ORISE--99-0164-Vol.2
CONF-960536-PROC.-Vol.2

SIXTH INTERNATIONAL RADIOPHARMACEUTICAL DOSIMETRY SYMPOSIUM

Proceedings of a Conference
Held in Gatlinburg, Tennessee

May 7-10, 1996

Edited by

Audrey T. S.-Stelson
Michael G. Stabin
Richard B. Sparks

Compilers
Fanny B. Smith
Audrey T. S.-Stelson

SPONSORS

Oak Ridge Associated Universities
U.S. Food and Drug Administration
U.S. Department of Energy

January 1999

This report was prepared under contract number DE-AC05-76OR00033 between the U.S. Department of Energy and Oak Ridge Asssociated Universities

DISCLAIMER

CONTENTS

VOLUME 1

QUANTITATIVE ANALYSIS AND TREATMENT PLANNING (CONTINUED)

Session Chairmen: A. Bertrand Brill and Terry Smith

CELLULAR AND SMALL-SCALE DOSIMETRY

Session Chairman: Claude Brihaye and James Stubbs

CELLULAR AND SMALL SCALE DOSIMETRY (CONTINUED)

Session Chairmen: Robert Atcher and Darrell Fisher

POSTERS

VOLUME 2

POSTERS (CONTINUED)

DOSIMETRIC MODELS

Session Chairmen: Peter Roberson and Michael Stabin

RADIOPHARMACEUTICAL KINETICS AND DOSIMETRY (CONTINUED)

Session Chairmen: Wesley Bolch and Richard Toohey

ANIMAL MODELS, EXTRAPOLATION, AND UNCERTAINTY

DOSIMETRY OF RADIUM-223 AND PROGENY

Fisher DR[1] and Sgouros G[2]
[1]Pacific Northwest National Laboratory
P.O. Box 999, Richland, WA 99352
[2]Memorial Sloan-Kettering Cancer Center
New York, NY 10021

ABSTRACT

Radium-223 is a short-lived (11.4 d) alpha emitter with potential applications in radioimmunotherapy of cancer. Radium-223 can be complexed and linked to protein delivery molecules for specific tumor-cell targeting. It decays through a cascade of short-lived alpha- and beta-emitting daughters with emission of about 28 MeV of energy through complete decay. The first three alpha particles are essentially instantaneous. Photons associated with Ra-223 and progeny provide the means for tumor and normal-organ imaging and dosimetry. Two beta particles provide additional therapeutic value. Radium-223 may be produced economically and in sufficient amounts for wide-scale application. Many aspects of the chemistry of carrier-free isotope preparation, complexation, and linkage to the antibody have been developed and are being tested. The radiation dosimetry of a Ra-223-labeled antibody shows favorable tumor to normal tissue dose ratios for therapy. The 11.4-d half-life of Ra-223 allows sufficient time for immunoconjugate preparation, administration, and tumor localization by carrier antibodies before significant radiological decay takes place. If 0.01 percent of a 37 MBq (1 mCi) injection deposits in a one gram tumor mass, and if the activity is retained with a typical effective half-time (75 h), the absorbed dose will be 163 mGy MBq^{-1} (600 rad mCi^{-1}) administered.

INTRODUCTION

Several characteristics of a radionuclide determine whether it has potential applications in medicine. The choice of suitable radionuclides is limited by practical considerations involving physical half-life, radiation emissions (energies and abundances), availability, cost and difficulty of production, decay products, and chemistry of complexation, linkage to monoclonal antibodies or other cell-directed delivery systems, and suitability to specific applications (1,2,3). Alpha-emitting radionuclides currently considered for systemic radiotherapy include astatine-211 (7.2 h) (4, 5), bismuth-212 (60 min) (6, 7, 8), bismuth-213 (46 min) (9, 10, 11), actinium-225 (10 d) (9, 10), terbium-149 (4.15 h) (12) and radium-223 (11.4 d) (13). It is well known that alpha particles provide a more effective radiation than beta particles for tumor cell-killing in radioimmunotherapy of cancer (14, 13). Alpha emitters such as Bi-213 and At-211 will soon be used in the U.S. and elsewhere for systemic therapy of cancer. Their potential applications are described in more complete detail in the report of a recent

Department of Energy Workshop on *Alpha-Emitters for Medical Therapy*, May 30-31, 1996, Denver, Colorado (1996, in press). The main *advantages* of alpha emitters over beta-emitters are

- limited availability
- high linear energy transfer (LET) and effective cell killing
- ideal path length for treating micrometastases and for sparing adjacent normal tissues
- effective under hypoxic conditions
- not subject to dose-rate limitations
- high specific activities are achievable.

The *disadvantages* of alpha emitters are

- high cost of production
- difficult chemistry of preparation and linkage to antibodies
- undesirable decay chains and progeny
- half-lives that may be too long or too short
- short alpha-particle ranges in tumor tissue (40 to 90 μm), which can be problematic if the antibody uptake in tumors is not uniform.

Given the experimental results of studies using alpha emitters in the treatment of implanted cancer cell lines in mice (15, 16, 17, 7, 8, 18), alpha emitters appear to have outstanding potential for therapy of cancer. The main challenge will be to overcome difficulties associated with (1) radionuclide production, and (2) chemistry of labeling the radionuclide to antibodies.

Radium-223 is an alpha-particle emitter with a physical half-life of 11.4 days. It decays through a chain of progeny, from which are emitted a four alpha and two beta particles before reaching stability as Pb-207. Gamma rays are also emitted by Ra-223 and some of its progeny.

Radium-223 can be produced relatively inexpensively (compared to other proposed alpha emitters) and in relatively large amounts by chemical extraction from a generator system containing Th-227 or Ac-227. These starting materials are obtained by neutron irradiation of common Ra-226. The main challenge in applying Ra-223 to therapy of cancer is the difficulty of complexing radium, which is highly electropositive and averse to forming complexes with most ligands.

The absorbed radiation dose to a patient receiving a Ra-223 radiopharmaceutical will depend on both physical and biological parameters. The biological parameters, which depend on the pharmacokinetics of the radiopharmaceutical, include the time-activity curves describing the uptake and retention of Ra-223 and its progeny in specific tissues of interest. In this work, the physical characteristics of Ra-223 are examined in terms of dosimetric and microdosimetric considerations. In addition, the potential concerns of use of this radionuclide in cancer therapy are addressed.

CHARACTERISTICS OF RADIUM-223 AND PROGENY

Radium-223 and its short-lived progeny emit four alpha particles through complete decay to stable Pb-207 (Figure 1). Following decay of Ra-223, three alpha particles with energies of 5 to 7 MeV are emitted within seconds. The fourth alpha particle is emitted by Bi-211 following decay of the beta emitter Pb-211, which has a half-life of 36 min. An additional beta particle and several gamma rays are also emitted by members of the Ra-223 decay chain (Table 1). The 11.4 d half-life of Ra-223 is sufficiently long to allow radionuclide production using a generator system (or process chemistry) and allow the isotope to be linked to the antibodies or other delivery system and be administered to a patient.

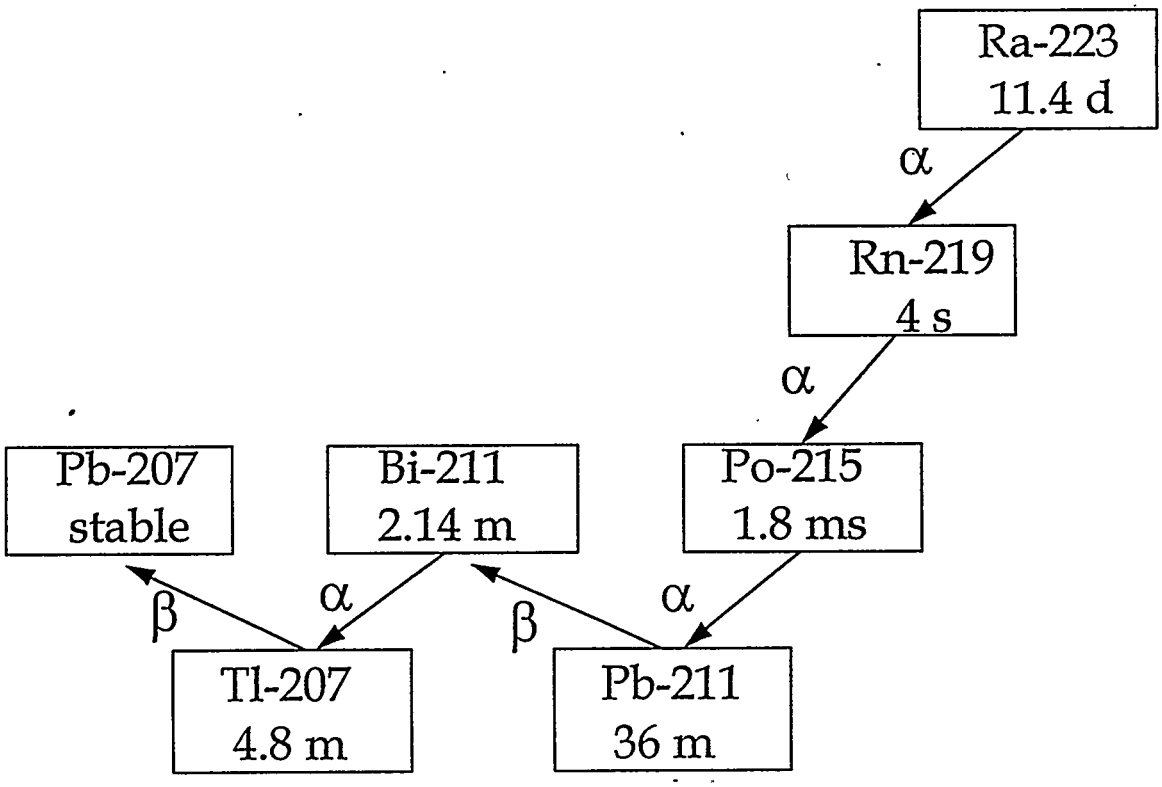

Figure 1. The Radium-223 decay chain. Shown are the Ra-223 progeny, physical half-lives of each, and mode of decay (alpha- or beta-particle emission).

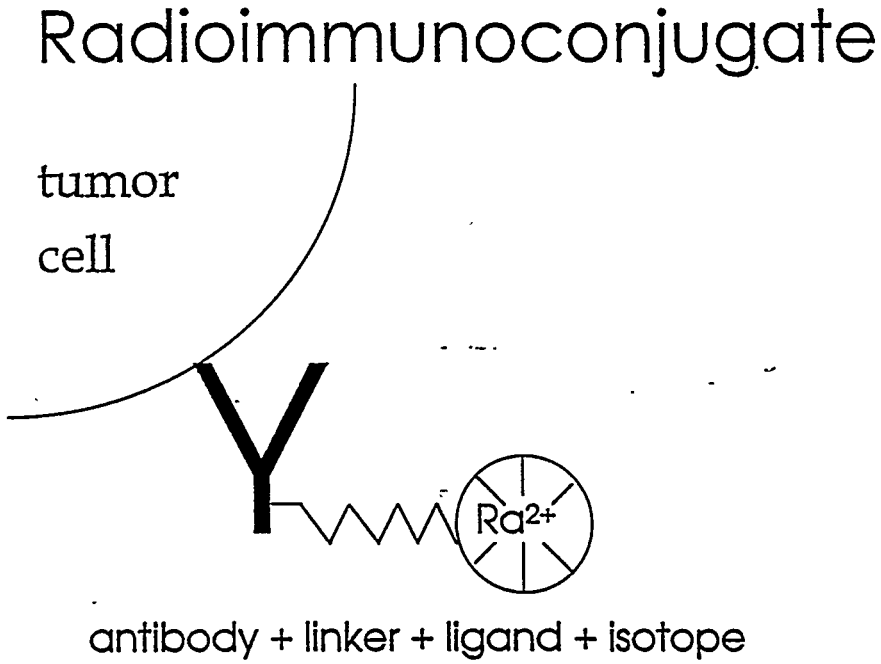

Figure 2. Schematic of a Radium-223 immunoconjugate. The immunoconjugate consists of an antibody recognizing a specific tumor-cell-surface antigen binding site. The antibody is linked to a macrocyclic ligand containing a positively charged Ra-223 atom.

Table 1
Principle Emissions of Radium-223 and Decay Progeny
Radon-219, Polonium-215, Lead-211, Bismuth-211, and Thallium-207
(Listed are relative emission yield, energy, and dose constant in traditional and S.I. units (19).)

Isotope	Emission	Yield $(Bq\ s)^{-1}$	Energy (MeV)	dose constant Δ (g rad $\mu Ci^{-1}\ h^{-1}$)	dose constant Δ (Gy kg $Bq^{-1}\ s^{-1}$)
Radium-223	alpha	0.52	5.72	6.33	4.76E-13
		0.24	5.61	2.87	2.16E-13
		0.094	5.75	1.15	8.66E-14
		0.091	5.54	1.07	8.07E-14
		0.02	5.43	0.231	1.74E-14
		0.01	5.50	0.117	8.81E-15
	X or gamma ray	0.15	0.081	0.0259	1.95E-15
		0.25	0.084	0.0447	3.36E-15
		0.086	0.094	0.0172	1.29E-15
		0.028	0.098	0.00584	4.39E-15
		0.097	0.117	0.0242	1.82E-15
		0.012	0.122	0.00312	2.34E-16
		0.10	0.142	0.0302	2.27E-15
		0.032	0.144	0.00982	7.38E-16
		0.056	0.154	0.0184	1.38E-15
		0.14	0.269	0.0802	6.03E-15
		0.039	0.324	0.0269	2.02E-15
		0.028	0.338	0.0202	1.52E-15
		0.013	0.445	0.0123	9.26E-16
Radon-219	alpha	0.074	6.42	1.01	7.61E-14
		0.12	6.55	1.67	1.23E-13
		0.80	6.82	11.6	8.74E-13
	X or gamma ray	0.01	0.111	0.00236	1.78E-16
		0.099	0.271	0.0571	4.30E-15
		0.066	0.402	0.0565	4.25E-15
Polonium-215	alpha	1.0	7.39	15.7	1.18E-12
Lead-211	beta	0.99	0.405	0.854	6.42E-14
	X or gamma ray	0.03	0.405	0.0259	1.78E-16
		0.014	0.427	0.0127	9.57E-16
		0.028	0.832	0.0496	3.73E-15
Bismuth-211	alpha	0.16	6.28	2.14	1.61E-13
		0.84	6.62	11.8	8.91E-13
	X or gamma ray	0.02	0.070 to 0.073	0.00305	2.29E-16
		0.127	0.351	0.0200	1.51E-15
Thallium-207	beta	1.0	0.494	1.05	7.91E-14

Potential Applications

For cancer therapy, Ra-223 will linked to a monoclonal antibody or other specific tumor-cell targeting agent (Figure 2). In other applications not requiring a specific delivery system, colloidal Ra-223 could be directly administered into a tumor or lymph node during a surgical procedure if precautions were taken to limit the biodistribution of Ra-223 and progeny in normal tissues and systemic circulation. Other potential applications of Ra-223 are palliation of bone pain and treatment of arthritis or other joint diseases. Additional research, animal biodistribution and toxicity studies, and experience in safe handling will be needed before Ra-223 products can be safely used in human patients.

Radium-223: Advantages and Disadvantages

As part of the general discussion in the published literature and at scientific symposia on the radiation dosimetry and microdosimetry of alpha emitters, there has been considerable discussion concerning the comparative advantages and disadvantages of different radionuclides for systemic radioimmunotherapy.

The principal advantages of Ra-223 over other candidate alpha emitters are: relative ease of production in amounts needed; relatively low cost of production; suitable half-life for many applications; potential for commercial distribution as a generator-supplied carrier-free radionuclide; photons for imaging and dosimetry; and high energy per decay for effective cell killing.

The principal disadvantages of Ra-223 are: the difficulty of complexation and linkage to protein delivery systems; long decay chain; and relatively long third daughter (Pb-211, half-life = 36 min.). The individual concerns sometimes associated with potential use of Ra-223 are examined in the following sections.

Concern No. 1: Radium Complexation. It is difficult to chelate and link the radium atom to a delivery protein (e.g., monoclonal antibody).

Studies have shown that radium can be complexed by certain ligands. These studies fall within three classes: (1) studies of Ra^{2+} solvent extraction from aqueous solutions using size-selective crown-ethers, (2) molecular dynamics simulations of Ra^{2+} in aqueous solutions, and (3) competing metal ion challenge experiments using plasma or serum to test Ra^{2+} complexation in competition with other metals in a physiological medium. Progress has been made at Pacific Northwest National Laboratory in each of these areas.

Initial investigations focused on ~~crown ethers, which~~ are a class of selective ligands that form stable complexes with metal ions based primarily on the ionic radius-cavity size compatibility concept. (20, 21, 22) reported the extraction of radium with dicyclohexano-21-crown-7 in the presence of organo-carboxylic acids as counteranions. The possibility of transporting radium through a liquid membrane with dicyclohexano-18-crown-6 was also described in a patent (23). Proton-ionizable crown ethers with attached carboxylate groups have been shown to effectively extract alkali metals (24, 25, 26, 27), alkaline earth metals (28, 29), and lanthanides (30). Ehrenfeld (31) proposed a diagnostic and therapeutic agent for treatment of cancer using the 3.66-day half-life alpha emitter Ra-224 complexed with a crypt and (Kryptofix 222 precursor, available from Merck, Darmstadt, Germany), a three-dimensional crown ether. However, the stability of the Ra^{2+} complex with the Kryptofix 222 precursor was not strong ($\log K = 6.64$), but did exceed that for other competing metal ions. Case and McDowell (32) showed the selectivity of ion-size-selective macrocyclic crown ether carboxylic acids for Ra^{2+} in toluene solutions containing also barium, strontium, calcium, magnesium, and other metal ions. The crown ether used was dicyclohexano-21-crown-7. The challenge of radium

complexation was further investigated by our collaborators in the Department of Chemistry of the University of Idaho. Beklemishev, Elshani, and Wai (33) recently demonstrated effective complexation of radium with crown ether carboxylic acids. Twin crown ethers were found to form a cage structure around the radium atom. Chemical side-arm "latches" were designed to give the cage structure additional stability.

Current studies at Pacific Northwest National Laboratory involve testing of a large variety of carboxylic acid macrocycle structures other than crown ethers. Favorable radium complexation has been obtained with three macrocyclic polyethers (to be described in a future publication), and other potentially favorable complexing agents are to be tested. Stability constants are being determined for radium complexation in aqueous solution and in the presence of competing metal ions typical of physiological media (calcium, potassium, manganese, zinc, etc.).

Concern No. 2: Biodistribution of Decay Products. Decay products of Ra-223 are not complexed and will freely migrate in extracellular fluids.

It is not necessary to complex the daughter products to achieve a favorable therapeutic dose ratio in tumors. The first decay product (Rn-219) has a 4-second half-life, and the second decay product (Po-215) has a 1.8-millisecond half-life. This means that the first three alpha emissions occur almost simultaneously before they have opportunity to migrate from the initial binding site.

Concern No. 3: Half-life of Lead-211. The third decay product, Pb-211, has a half-life of 36 minutes. Lead-211 could migrate away from the initial binding site and irradiate normal tissue.

One of two things could happen: The Pb-211 daughter will either remain in the tumor, or it will migrate away from the tumor before it decays to Bi-211. It is more likely that Pb-211 will bind to tissue or constituents of extracellular fluids in the tumor and contribute to tumor dose as it decays, rather than migrate some distance away and irradiate normal tissue. The absorbed dose delivered by Ra-223 decay prior to Pb-211 will be 3.4 Gy per Bq-sec (45 rad per microcurie-hour) in one gram of tumor tissue, and the additional dose from Pb-211 and progeny is 1.1 Gy per Bq-sec (15 rad per microcurie-hour). Assuming that one percent of the administered Ra-223 activity deposits in tumors and the remaining 99 percent circulates and clears from the body without depositing in tumor tissue, the effect of loosing Pb-211 and progeny from the tumor is to change this ratio to 0.75 percent in the tumor tissue and 99.25 percent in the remainder of the body. In other words, the increase in background absorbed dose to normal tissues from circulating activity will not significantly increase. Alternatively, if Pb-211 and progeny are lost from the tumor and localize in a particular normal tissue, then the absorbed dose to that tissue could exceed the background absorbed dose to the remainder of the whole body. Biodistribution experiments are needed to understand the fate of Pb-211 and its progeny to fully address this concern.

Concern No. 4: Radon Migration. The first decay product of Ra-223 is an isotope of radon, which is an inert noble gas that will not bind with anything in the extracellular environment. On formation, it will recoil away from initial binding site and diffuse away in extracellular fluids.

The maximum diffusion of the 4-second half-life Rn-219 in water, including recoil, was calculated from standard equations for radon diffusion in water. The maximum diffusion is 30 micrometers (about three cancer-cell diameters). Radon-219 in the tumor will contribute to the tumor dose. Microdosimetry calculations predict an enhanced radiobiological effect of the slight

redistribution of the Rn-219 daughter. This is because any slight diffusion or recoil increases the uniformity of distribution within a tumor and increases the probability of alpha-particle hits to cancer-cell nuclei.

Concern No. 5: Laboratory Safety. The first decay product (Rn-219) will make the handling of Ra-223 in the laboratory difficult and dangerous. It will increase alpha-particle creep and contamination. Radon may permeate gloves on a glove box, presenting contamination hazards to the user unless precautions are taken.

Experience with the preparation, extraction, and purification of Ra-223 at this Laboratory shows that Ra-223 can be safely prepared and handled. Collaborating scientists at other universities have successfully handled and used Ra-223 in their research. Precautions should be taken to contain the short-lived Rn-219 decay product; however, its short half-life precludes diffusion through rubber gloves used in glove boxes. Care should be taken to prevent release of Rn-219 into general room air, which could cause surface contamination. Our laboratory experience shows that radon characteristically remains fixed in liquids unless air is bubbled through the liquids. A radiochemistry hood with adequate ventilation is normally sufficient to carry the short-lived Rn-219 away from the work area, where it quickly decays before transport to the environment. Gamma exposures to chemistry and hospital personnel and beta radiation exposure to hands and fingers will be only a small fraction of what they currently are with present techniques for handling therapeutic amounts of I-131 and Y-90-labeled antibodies.

Concern No. 6: Radiotoxicity and Carcinogenicity of Radium-223. Radium is known to be a bone-seeker and a carcinogen.

It is desirable that a radionuclide for therapy of cancer be sufficiently toxic to destroy targeted tissue, and at the same time not present unwanted toxicity to normal organs and tissues. The key to achieving successful cancer therapy while minimizing normal tissue toxicity it to selectively deliver more radiation to tumors than to normal tissues. This is accomplished by putting the radionuclide in a chemical form that will minimize its uptake and retention in normal tissues (i.e., by putting it in a chelate or complexing agent), and by linking it to an effective delivery system (e.g., monoclonal antibodies). The behavior of a radionuclide immunoconjugate in the body will be much different than the behavior of a free (chloride or citrate) form of the radionuclide.

Few studies have been conducted on the biodistibution and toxicity of Ra-223 and progeny *in vivo*. These studies did not involve the complexed form of Ra-223 linked to a monoclonal antibody. Nonetheless, they do provide important information on the toxicity of the free forms of Ra-223 and progeny. Campbell et al. (34) studied the metabolism, retention, and toxicity of Ac-227, Th-227, and Ra-223 in rats. The Ac-227 in equilibrium with its decay products was administered in a soluble chloride form by intravenous injection, by oral feeding, and by direct contact with animal skin (broken and unbroken). They showed that Ac-227, Th-227, and Ra-223 were each metabolized differently in the body and that differences in radionuclide biodistribution greatly influenced their relative radiotoxicities. They found Ra-223 uptake in the skeleton, which resulted in localized irradiation of bone marrow.

Durbin et al. (35) also studied the biodistribution and toxicity of Ra-223 and progeny. They administered Ra-223 intramuscularly as $RaCl_2$ to young adult female Sprague-Dawley rats at levels ranging from 0.148 kBq to 3.7 kBq (0.004 to 0.1 μCi) per g body weight. Radium was absorbed from the injection site, assimilated into body fluids, and excreted in feces (about 67 percent of the

administered amount). The total excretion rate (percent per day) was described by the function

$$E_t = 13.5\ T^{(-0.95)}, \quad (1)$$

where T is the number of days after injection. In general, the excretion of Ra-223 was more rapid than other lighter alkaline earth elements. Radium-223 was unstable in crystal bone mineral and readily exchanged with systemic calcium. Its short half-life prevented long-term observation.

Durbin et al. (35) also showed that the major organs and tissues of early Ra-223 deposition were the skeleton (3.41 percent per g) and kidneys (0.25 percent per g). Other tissues, such as the liver, spleen, muscle, and gastrointestinal tract wall contained 0.04 percent per g, 0.08 percent per g, 0.02 percent per g and 0.17 percent per g, respectively. The skeletal content was 2.1 to 2.8 percent per gram at 16 days postinjection, whereas all other tissues contained less than 0.02 percent per gram. The midpoint for death at 30 days was found to be 1.85 kBq (0.05 μCi) per g body weight. Gross tissue effects of high-dose Ra-223 included reduced lymphopoietic activity, hemorrhagic infiltration of lymph nodes, decreased cellularity of bone marrow and complete absence of marrow cells, ulceration of mucosal surfaces of the stomach, and degeneration of liver and kidney tissues consistent with high dose irradiation. Lung pneumonitis was found in varying degrees, but was not well correlated with dose level or time after injection (35). Bone growth was impaired at high dose levels as both cell proliferation and bone resorption ceased.

Howell et al. (36) studied the relative biological effectiveness of uncomplexed Ra-223 citrate in equilibrium with its progeny in mouse testes with spermhead survival serving as an indicator of toxicity. Survival fraction was determined as a function of testicular absorbed dose. They obtained an RBE for Ra-223 and progeny of 5.6 relative to external 120 kVp X-rays.

The high toxicity of Ra-223 is necessary from the viewpoint of potential for cell-directed cancer therapy, where normal-tissue uptake and retention can be minimized. The animal toxicity studies of Durbin et al. (35) demonstrate that it will be important to tightly complex the Ra^{2+} ion within a stable configuration that will withstand exchange with and competition from other metallic cations in physiologic solution, to prevent uptake on bone surfaces, and to enhance excretion from soft tissues and blood. Studies have not yet been conducted to determine the decrease in toxicity to normal tissues when Ra-223 is complexed in a chemical form that causes it to be cleared rapidly from normal tissues. Applications in therapy of cancer will require (1) efficient targeting of tumor tissue, and (2) nonspecific uptake and rapid clearance from normal tissues to maximize the therapeutic ratio and limit undesirable side effects.

Method of Production

The parent (Ac-227) of Ra-223 can be produced efficiently in both thermal and fast reactors by neutron irradiation of a long-lived radioactive waste material, common Ra-226 (1600 y), which is used in well-logging sources, neutron starters, and radium needles. Disposal of old radium sources is a major problem for many institutions. The conversion of a waste material (that is very expensive to package and dispose of) to a medically useful radionuclide has inherently attractive features. The irradiation reaction and ingrowth of Ra-223 from parent material is given by

$$^{226}Ra(n,\gamma)^{227}Ra(T_{1/2} = 42\ m) \rightarrow \beta^- + {}^{227}Ac(T_{1/2} = 21.77\ y) \text{ and} \quad (2)$$

$$^{227}Ac \rightarrow \beta^- + {}^{227}Th(T_{1/2} = 18.7\ d) \rightarrow \alpha + {}^{223}Ra(T_{1/2} = 11.4\ d). \quad (3)$$

After irradiation, the Ac-227 can be chemically separated from the target irradiation product

mixture. Actinium-227 can then be purified to remove silica solids, any actinide contaminants (uranium or plutonium) that may be present, and elemental iron. The Ac-227 in equilibrium with decay products is then transferred to an anion exchange column and is eluted with 0.35 M nitric acid. The Th-227 remains alone on the column. Actinium-227 and Ra-223 are recycled back into the original container for later use. Ten days later, the anion exchange column is eluted again with 0.35 M nitric acid to obtain pure Ra-223. The resulting solution is boiled down with hydrochloric acid to form the final product Ra-223-chloride.

Principal Emissions

The principal alpha, beta, and gamma emissions, relative yield (>1 percent), and energy of decays from Ra-223 and progeny are shown in Table 1. Figure 3 shows the alpha spectrum obtained from a source of Ra-223 in equilibrium with its progeny, where the energies of the peaks corresponding to Ra-223, Bi-211, Rn-219, and Po-215 are given in MeV. Figure 4 shows the gamma spectrum obtained from the same source of Ra-223 in equilibrium with its progeny, where the principal gamma lines are highlighted for emissions at 154, 270, 351, and 405 keV. The high-energy peaks have low abundance and do not interfere with imaging.

Half-life

The radionuclide half-life is an important consideration for maximizing the tumor absorbed dose. The half-life of Ra-223 is long enough to allow the antibodies to circulate in blood, be taken up by tumor tissues or cleared from the body, and to irradiate tumor tissue over a period of time. Antibody uptake by some tumors is protracted over extended periods of time. Rao and Howell (37) showed that the optimum physical half-life of the radionuclide is one to three times the biological retention half-time of the radiolabeled antibody in the tumor. Typical tumor retention half-times are 48 to 96 hours (2 to 4 days), and therefore optimal physical half-lives are 2 to 12 days, with the longer half-lives preferred over shorter half-lives. Ideally, the half-life of the radionuclide should be about three times the biological retention half-time of the material in the tumor for maximum therapeutic effect. The 8-day half-life of iodine-131 has proven effective in the treatment of lymphoma (38) and acute and chronic leukemia (39, 40).

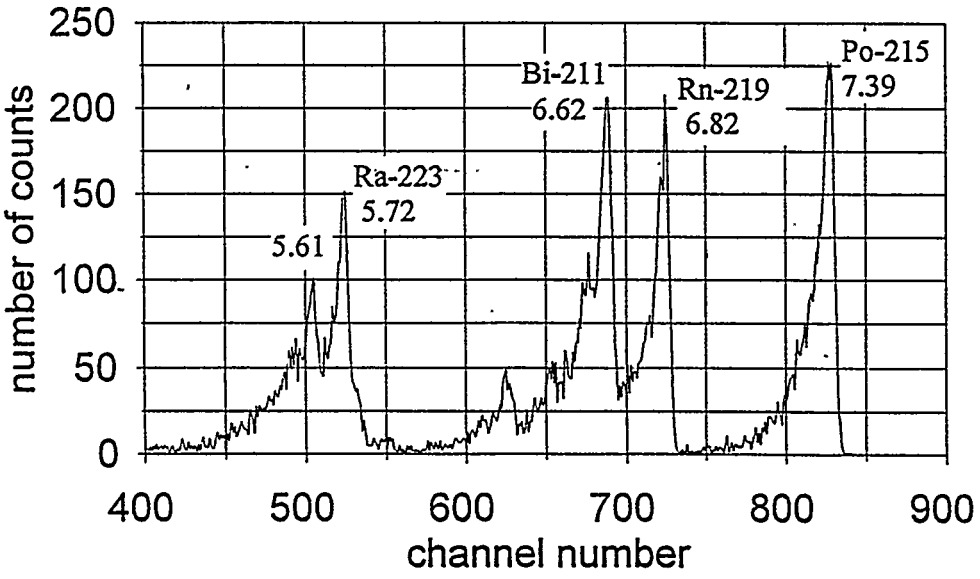

Figure 3. Alpha particle energy spectrum from radium-223 in equilibrium with its decay products. The principal alpha emissions are shown with alpha particle energies (MeV).

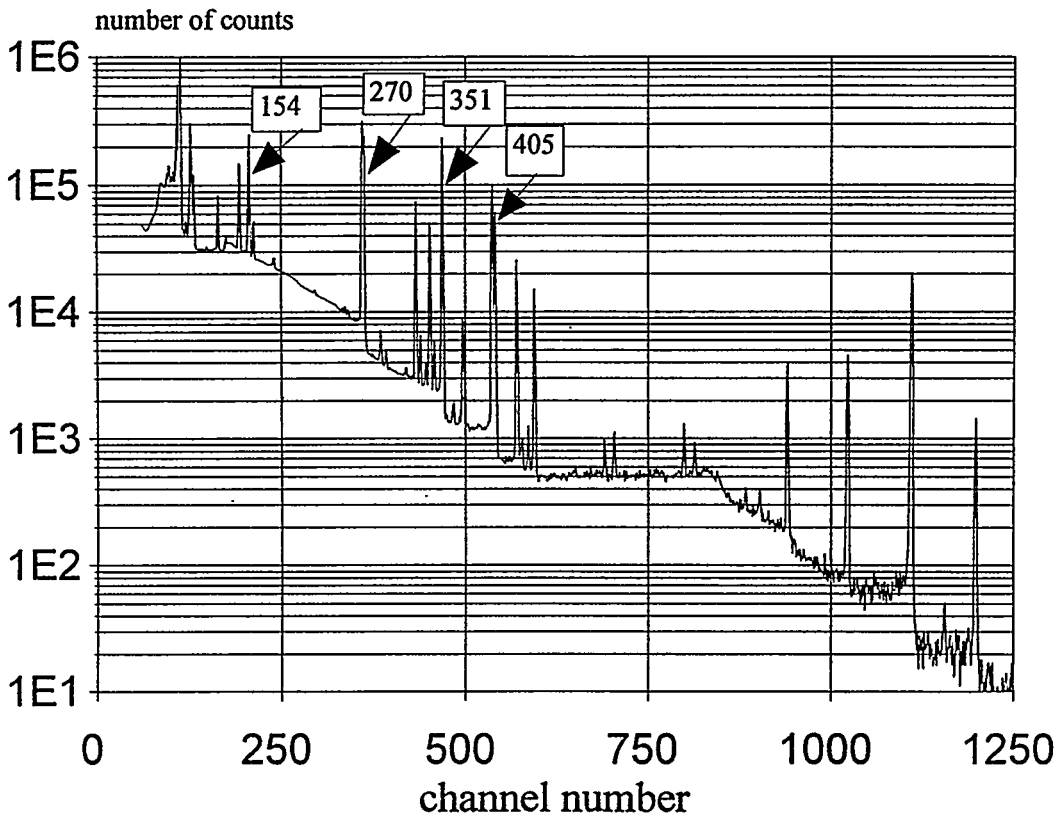

Figure 4. Gamma-ray energy spectrum from radium-223 in equilibrium with its decay products. Shown are the major peaks from Ra-223 at 154 keV and 269 keV (together with the 270 keV line from Rn-219), and the 351 keV line from Bi-211, and the 405 keV line from Pb-211.

IMAGING OF RADIUM-223 *IN VIVO*

One of the important features of a radionuclide proposed for cell-directed radiation therapy is the ability of nuclear medicine specialists to image its biodistribution in major organs and tumors as well as its clearance from the body with time. Imaging is essential for characterizing the uptake, biodistribution, and clearance of the radiolabeled antibody with time, for assessing internal dose, and for treatment planning.

Radium-223 emits several gamma rays in its decay to stable Pb-207. A plastic block containing Ra-223 in a unique shape, with hot spots and cold spots, was constructed to test whether Ra-223 and its decay products could be imaged inside the body. Initial results (Figure 5) show that Ra-223 can be imaged with a conventional nuclear a medicine gamma camera fitted with medium- or high-energy collimators. Photo-peaks at both 155 keV (FWHM = 15 percent) and 270 keV (FWHM = 10 percent) produced high-quality images of the test phantom at activity levels corresponding to therapeutic levels of administered Ra-223. These results provide another important indicator of the potential of Ra-223 as a therapeutic radionuclide against cancer.

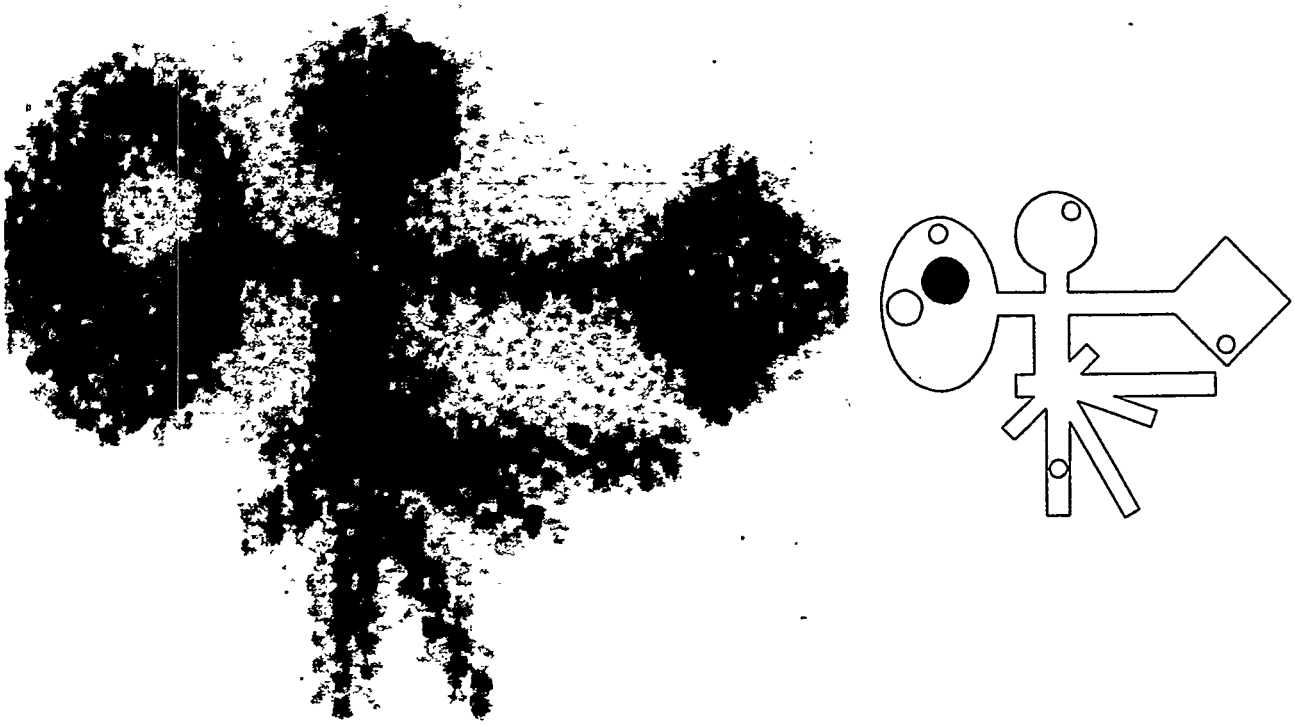

Figure 5. Gamma camera image of a Ra-223 test phantom at surface (at left). The energy window of the camera was set for dual-peak detection at 154 keV ± 17 percent and at 270 keV ±8 percent full-width at half-maximum (FWHM), using a high-energy collimator. The camera was a General Electric MaxiCamera. The test phantom contained 0.4 mCi Ra-223 embedded in epoxy distributed in a unique pattern (see schematic) cut into a 4-cm thick ABS plastic block, with hot (light) and cold (dark) regions.

ABSORBED DOSE CALCULATIONS

The basic quantity for energy imparted to matter by ionizing radiation is the absorbed dose, which is the ratio of the energy imparted by ionizing radiation and the mass of the tissue in which the energy is deposited. In the formalism developed by the Medical Internal Radiation Dose (MIRD) committee of the Society of Nuclear Medicine (41), the absorbed dose $\bar{D}$ (Gy) to a target region (r_k) from a source region (r_h) from an internally administered radionuclide is

$$\bar{D} = \tilde{A}\, S(r_k \leftarrow r_h), \tag{4}$$

where $\tilde{A}$ is the cumulated activity or total number of transformations (Bq s) that have taken place in the source tissue, and S (Gy Bq^{-1} s^{-1}) is the mean dose to a target tissue per unit cumulated activity in a source tissue.

The cumulated activity $\tilde{A}$ in a source region (r_h) is the total number of radioactive transformations over time *t*:

$$\tilde{A}_h = \int_0^\infty A_h(t)\, dt. \tag{5}$$

The S value is the product of the reciprocal mass m (kg) of the target organ or tissue containing the activity and the sum of the products of the dose constant or mean energy emitter per nuclear transition (Δ_i, in Gy kg Bq^{-1} s^{-1}) and the energy absorbed fraction of the *i*th emission (ϕ_i),

$$S(r_k \leftarrow r_h) = 1/m_k \sum_i \Delta_i \phi_i. \quad (6)$$

The absorbed fraction (ϕ_i) is the fraction of energy emitted by the *i*th emission from activity in the source region that is absorbed in the target region. Given the short range of alpha and beta particles, and where the source and target regions are the same, the energy absorbed fractions (ϕ_i) for alpha and beta particles are assumed to be 1.0, and $\phi_i = 0$ where the source and target regions are not the same.

The equilibrium dose constant Δ_i is the sum of the products of a unit conversion constant (*k*), the fractional abundance of each emission (n_i) and the energy of the *i*th emission (E_i),

$$\Delta_i = \sum_i k\, n_i\, E_i. \quad (7)$$

Values of Δ_i are given in Table 1 in both S.I. units and traditional units for the principal emissions from Ra-223 and progeny radionuclides. These values may be used with Equations 4 to 7 to estimate the dose to tissue from Ra-223 and progeny if the biological retention over time and the mass of the tissue are known. This information may be obtained, for example, from groups of serially sacrificed mice injected with Ra-223, where specific tissues are obtained and counted with a gamma spectrometer. Table 2 summarizes the effective energies and dose constant of each radionuclide in the Ra-223 decay chain. Values are presented for all emissions combined and for only the alpha particle emissions. Totals are also presented for Ra-223 in equilibrium with decay progeny. Table 2 shows that 28.2 MeV of energy is liberated by the decay of Ra-223 through complete decay, of which 93 percent is by alpha emission.

If 0.01 percent of a 37 MBq (1 mCi) injection of Ra-223 deposits in a 1-g tumor mass, and if the activity is retained with an effective retention half-time of 75 hours (which is typical of many radiolabeled antibodies), the absorbed dose will be 163 mGy MBq^{-1} (600 rad mCi^{-1}). Alpha recoil contributes less than 2 percent of the total absorbed dose (19). Photons contribute only a small fraction of the total absorbed dose.

MICRODOSIMETRY CALCULATIONS

Microdosimetry is a statistical analysis of the probability of small targets receiving any possible radiation dose. The concepts of specific energy and lineal energy form the foundation of stochastic microdosimetry. Microdosimetry involves the calculation or experimental determination of probability densities in specific energy for various types of radiation and various sizes of the target. These probability densities correspond to the distribution of doses received by cells or cell nuclei in a biological system, including the probability that such targets are not irradiated. The calculations are complex and must be performed using computer techniques. The concepts of microdosimetry in the radioimmunotherapy were reviewed recently by Humm et al. (42).

Table 2
Summary of Effective Energy and Dose Constants for Radium-223 and Progeny for All Emissions Combined.

Isotope	Effective energy (MeV disint.$^{-1}$)	dose constant Δ (g rad μCi^{-1} h^{-1})	dose constant Δ (Gy kg Bq^{-1} s^{-1})
Radium-223	5.96* 5.56**	12.7 11.8	9.54E-13 8.91E-13
Radon-219	6.94* 6.72**	14.8 14.3	1.11E-12 1.08E-12
Polonium-215	7.52* 7.39**	16.0 15.7	1.20E-12 1.18E-12
Lead-211	0.505*	1.08	8.09E-14
Bismuth-211	6.73* 6.57**	14.3 14.0	1.08E-12 1.05E-12
Thallium-207	0.495*	1.05	7.93E-14
TOTAL	28.2* 26.2**	60.0 55.9	4.51E-12 4.20E-12

*Includes alpha, beta, photon, X-ray, Auger electron, and conversion electron energies
**Includes only alpha particle energies

Microdosimetry is important for the study of interactions by alpha particle tracks with single cells. Since each target (cell nucleus) receives a unique dose depending on the exact chord length for each alpha particle "hit," the number of hits, and the total amount of energy deposited per hit, a probability histogram may be constructed indicating the relative frequency of any such dose. The exact amount of energy imparted to a microscopic target is the specific energy (z). It is defined as the quotient of e by m, where e is the energy imparted by ionizing radiation to a small target having mass m,

$$z = e/\mathrm{m}. \tag{8}$$

The specific energy may be due to one or more energy-deposition events. The possible values of the specific energy are described by a probability density, $f(z)$. The mean specific energy is the absorbed dose, D, which has the same units as the absorbed dose,

$$\bar{z} = \mathrm{D}. \tag{9}$$

The probability density also includes the probability that no energy is deposited in a site, or $z = 0$. This component, called the delta function (δ), is the fraction of unirradiated sites.

$$\delta = \exp(-\mathrm{M}), \text{ and} \tag{10}$$

$$\mathrm{M} = -\ln(\delta), \tag{11}$$

where M is the mean number of "hits" per target. The delta function can be a useful parameter for interpreting microdosimetry distributions for radiobiological experiments.

Calculation of Microdosimetric Parameters

Probability densities in specific energy may be calculated using the mathematical methods such as fast-Fourier analytical techniques (43, 44) or Monte Carlo methods (45, 46, 47, 48), where

$$z = (1/m) \int_{v1}^{v2} (dE/dx)\, dx, \tag{12}$$

where m is the target mass, dE/dx is the energy deposited per unit length of track in the target, and v1 and v2 are the entrance and exit coordinates of the alpha track through the target. Microdosimetric evaluations of the potential for alpha emitters in radioimmunotherapy have been performed for Bi-212 (49), and for astatine-211 (46, 47), among others.

SUMMARY AND CONCLUSIONS

Alpha emitters will play an important future role in cancer therapy. Radium-223 exhibits certain desirable features that are not shared by other alpha-particle-emitting radionuclides under consideration for cancer therapy. The favorable characteristics of Ra-223 include its longer half-life, greater availability, and potency. The 11.4-d physical half-life provides sufficient time for preparation, labeling, delivery, and administration of a labeled agent to patients. The supply of Ra-223 may be obtained from an Ac-227 or Th-227 generator system. The starting material Ac-227 may be obtained by neutron irradiation of common Ra-226, a long-lived radioactive waste material. Photons associated with Ra-223 and progeny provide means for tumor and normal-tissue imaging in patients at levels of administered activity corresponding to anticipated levels for therapeutic infusion.

The decay scheme of Ra-223 includes the emission of four alpha particles, three of which are immediate for effective irradiation of targeted cancer tissue. The short-range alpha particles are well matched for irradiation of small cancer metastases. The alpha emissions provide a potentially high absorbed dose to the target tissue, which can result in a highly favorable therapeutic ratio. Beta particles in the decay chain also contribute to tumor dose. Absorbed doses on the order of 160 mGy MBq^{-1} (600 rad mCi^{-1}) may be achieved.

These desirable features of Ra-223 are, however, accompanied by a number of concerns. Studies in animals, using non-protein-bound (free ion) Ra-223, have demonstrated high biological toxicity. This toxicity may be minimized by effective complexation of the Ra^{2+} ion, which is difficult. Linkage of the Ra-223 complex to effective delivery agents will improve the likelihood of successful tumor-cell targeting, a high therapeutic ratio, and sparing of normal tissues.

It is likely that some of the 36-minute half-life Pb-211 in the decay chain will diffuse away from the target site. Potentially high therapeutic ratios diminish the concern of Pb-211 diffusion away from the target tissue. Further study is needed to determine the fate of Pb-211 and progeny.

Safe handling is a necessary concern to prevent the spread of alpha contamination when Ra-223 and complexing agents are prepared. Recent experience by our laboratory and others shows that the material can be handled safely, and that in general, the use of alpha emitters in cancer treatment is not precluded.

ACKNOWLEDGMENTS

This work was conducted for the U.S. Department of Energy under contract No. DE-AC06-76-RLO 1830. The Hanford Isotopes Program is operated at Pacific Northwest National Laboratory in Richland, Washington for the Department's Isotope Production and Distribution Program. Richard Ratner of Pacific Northwest National Laboratory provided the alpha and gamma spectra for Ra-223. Lane Bray and Jackie Deschane provided Ra-223 for this study, and David Alexander helped cast the Ra-223 test phantom. Larry Durack at the University of Washington Medical Center provided the Ra-223 test phantom image shown in Figure 5. Other imaging studies were performed by Mark Vandermalle and Dr. Thomas Mahoney at the Kadlec Medical Center in Richland, Washington, and by Barbara Ratliff at the Virginia Mason Medical Center in Seattle.

REFERENCES

1. Schubiger PA, Alberto R and Smith A. Vehicles, chelators, and radionuclides: choosing the 'building blocks' of an effective therapeutic radioimmunoconjugate. Bioconjugate Chem 7:165-179, 1996.
2. Wessels BW and Rogus RD. Radionuclide selection and model absorbed dose calculations for radiolabeled tumor associated antibodies. Med Phys 11:638-645, 1984.
3. Adelstein SJ and Kassis AI. Radiobiologic implications of the microscopic distribution of energy from radionuclides. Nucl Med Biol. 14:165-169, 1987.
4. Brown I. Astatine radiopharmaceuticals. Astatine-211: its possible applications in cancer therapy. Appl Radiat Isot 37:789-798, 1986.
5. Richardson TC. Astatine-211 as a therapeutic radionuclide. The plasma: blood cell distribution in vitro. Nucl Med Biol 13:583-584, 1986.
6. Kozak RW, Atcher RW, Gansow OA, Friedman AM, Hines JJ and Waldmann TA. Bismuth-212-labeled anti-Tac monoclonal antibody: Alpha-particle-emitting radionuclides as modalities for radioimmunotherapy. Proc Natl Acad Sci USA 83:474-478, 1986.
7. Macklis RM, Kinsey BM, Kassis AI, Ferrara JL, Atcher RW, Hines JJ, Coleman CN, Adelstein SJ and Burakoff SJ. Radioimmunotherapy with alpha-particle-emitting immunoconjugates. Science 240:1024-1026, 1988.
8. Macklis RM, Kaplan WD, Ferrara JL, Atcher RW, Hines JJ, Burakoff SJ and Coleman CN. Resident's essay award: Alpha particle radioimmunotherapy: animal models and clinical prospects. Int J Radiat Oncol Biol Phys 16:1377-1387, 1989.
9. Geerlings MW. Radionuclides for radioimmunotherapy: criteria for selection. Int J Biol Markers 8:180-186, 1993.
10. Geerlings MW, Kaspersen FM, Apostolidis C and Van der Hout R. 1993. The feasibility of Ac-225 as a source of alpha particles in radioimmunotherapy. Nucl Med Commun 14:121-125, 1993.
11. Sgouros, G, Graham MC, Jureidini IM, Humm JL, Larson SM and Scheinberg DA. Pre-clinical dosimetry for alpha-emitter-labeled antibody therapy of hematologic disease. J Immunother 16:156, 1994 (abstract).
12. Allen BJ and Blagojevic N. Alpha- and beta-emitting radiolanthanides in targeted cancer therapy: the potential role of terbium-149. Nucl Med Comm 17:40-47, 1996.
13. Wilbur DS. Potential use of alpha emitting radionuclides in the treatment of cancer. Antibody Immunocon and Radiopharm 4:85-97, 1991.
14. Hall EJ. LET and RBE. Chapter 8 in *Radiobiology for the Radiologist*, 3rd ed, pp. 161-178. J. B. Lippincott Company, Philadelphia, 1988.

15. Harrison A and Royle L. Efficacy of astatine-211-labeled monoclonal antibody in treatment of murine T-cell lymphoma. *National Cancer Institute Monographs* 3:157-158, 1987.
16. Black CV, Atcher RW, Barbet J, Brechbiel MW, Holton OD, Hines JJ, Gansow OW and Weinstein JN. Selective ablation of B lymphocytes in vivo by an alpha emitter, bismuth-212, chelated to a monoclonal antibody. Antibody Immunocon and Radiopharm 1:43-53, 1988.
17. Kurtzman SH, Russo A, Mitchell JB, DeGraff W, Sindelar WF, Brechbiel MW, Gansow OA, Friedman AM, Hines JJ, Gamson J and Atcher RW. Bismuth-212 linked to an antipancreatic carcinoma antibody: Model for alpha-particle-emitter radioimmunotherapy. J Natl Cancer Inst 80:449-452, 1988.
18. Huneke, RB, Pippin CG, Squire RA, Brechbiel MW, Gansow OA and Strand M. Effective alpha-particle-mediated radioimmunotherapy of murine leukemia. Cancer Res 52:5818-5820, 1992.
19. International Commission on Radiological Protection (ICRP). *Radionuclide Transformations, Energy and Intensity of Emissions.* ICRP Publication 38. Oxford: Pergamon Press, 1983.
20. McDowell, WJ, Case GN and Aldrup DW. Separ Sci Technol 18:1483, 1983.
21. McDowell WJ. Crown ethers as solvent extraction reagents: where do we stand? Separ Sci Technol 23:1251-1268, 1988.
22. McDowell WJ, Arndston BA and Case GN. Solv Extr Ion Exch 7:1377, 1989.
23. Rollat A, Sabot JL, Burgard M and Delloye T. European patent application EP 188394 A1 860723; Chem Abstr 106:35491v, 1987.
24. Walkowiak W, Charewicz WA, Kang SI, Sang I, Yang I-W, Pugia MJ and Bartsch RA. Anal Chem 62:2018, 1990.
25. Walkowiak W, Kang SI, Sang I, Stewart LE, Ndip G and Bartsch RA. Anal Chem 62:2022, 1990.
26. Bartsch RA. Solv Extr Ion Exch 7:829, 1989.
27. Bartsch RA, Kim JS, Olsher U, Purkiss DW, Ranesh V, Dalley KN and Hayashita T. Pure Appl Chem 65:399, 1993.
28. Uhlemann E, Geyer H, Gloe K and Muhl P. Anal Chim Acta 185:279, 1986.
29. Uhlemann E, Bukowsky H, Dietrich F, Gloe K, Muhl P and Mosler H. Anal Chim Acta 224:47, 1989.
30. Wood DW, Elshani S, Du HS, Natale NR and Wai CM. Anal Chem 65:1350, 1993.
31. Ehrenfeld U. *Jomol derivatives as agents for use in malignant tumors and lowered immune defenses.* U.S. Patent No. 5,116,614, May 26, 1992.
32. Case GN and McDowell WJ. Separation of radium and its determination by photon/electron-rejecting alpha liquid scintillation spectrometry. Radioactivity and Radiochemistry 1:58-69, 1990.
33. Beklemishev MK, Elshani S and Wai CM. Solvent extraction of radium with crown ether carboxylic acids. Anal Chem 66:3521-3524, 1994.
34. Campbell JE, Robajdek ES and Anthony DS. The metabolism of Ac-227 and its daughters Th-227 and Ra-223 by rats. Radiat Res 4:294-302, 1956.
35. Durbin PW, Asling CW, Jeung N, Williams MH, Post J, Johnston ME and Hamilton JG. *The metabolism and toxicity of radium-223 in rats.* UCRL-8189. University of California Radiation Laboratory, Berkeley, California, 1958.
36. Howell RW, Goddu SM, Narra VR, Fisher DR, Schenter RE and Rao DV. Radiotoxicity of Gd-148 and Ra-223 in mouse testes: RBE of alpha particle emitters *in vivo*. Radiat Res (submitted for publication), 1996.
37. Rao DV and Howell RW. Time-dose fractionation in radioimmunotherapy: Implications to selection of radionuclides (abstract). J Nucl Med 34:1801-1810, 1993.

38. Press OW, Eary JF, Appelbaum, FR, Martin PJ, Nelp WB, Glenn S, Fisher DR, Porter B, Matthews DC, Gooley T and Bernstein ED. Phase II trial of I-131-B1 (anti-CD-20) antibody therapy with autologous stem cell transplantation for relapsed B cell lymphomas. Lancet 346:336-340, 1995.
39. Matthews DC, Appelbaum FR, Eary JF, Fisher DR, Durack LD, Bush SA, Hui TE, Martin PJ, Mitchell D, Press OW, Badger CC, Storb R, Nelp WB and Bernstein ID. Development of a marrow transplant regimen for acute leukemia using targeted hematopoietic irradiation delivered by I-131-labeled anti-CD45 antibody, combined with cyclophosphamide and total body irradiation. Blood 85:1122-1131, 1995.
40. Jurcic JG, Caron PC, and Scheinberg DA. Monoclonal antibody therapy of leukemia and lymphoma. Adv Pharmacol 33:287-314, 1995.
41. Loevinger R, Budinger TF and Watson EE. *MIRD Primer for Absorbed Dose Calculations*, revised ed. New York: The Society of Nuclear Medicine, 1991.
42. Humm JL, Roeske JG, Fisher DR and Chen GTY. Microdosimetric concepts in radioimmunotherapy. Med Phys 20:535-541, 1993.
43. Roesch WC. Microdosimetry of internal sources. Radiat Res 70:494-510, 1977.
44. Stinchcomb TG and Roeske JC. Analytic microdosimetry for radioimmunotherapeutic alpha emitters. Med Phys 19:1385-1393, 1992.
45. Wilson WE and Paretzke HG. Calculation of ionization frequency distributions in small sites. Radiat Res 81:326-335, 1980.
46. Humm JL. A microdosimetric model of astatine-211 labeled antibodies for radioimmunotherapy. Int J Radiat Onc Biol Phys 13:1767-1773, 1987.
47. Humm JL, Chin LM, Cobb LM and Begent R. Microdosimetry in radioimmunotherapy. Radiat Prot Dosim 31:433-436, 1990.
48. Charlton DE and Sephton R. A relationship between microdosimetric spectra and cell survival for high-LET irradiation. Int J Radiat Biol 59:447-457, 1991.
49. Fisher DR. The microdosimetry of monoclonal antibodies labeled with alpha emitters. In: Fourth International Radiopharmaceutical Dosimetry Symposium, Schlafke-Stelson AT and Watson EE, eds., pp. 26-36, CONF-851113. Oak Ridge Associated Universities, Oak Ridge, Tennessee, 1986.

TARGETED CANCER THERAPY: THE POTENTIAL ROLE OF TERBIUM-149

Allen BJ [1], Goozee G[1], Imam S[1], Sarkar S[2], Leigh J[3], Beyer GJ[4]
[1]St George Cancer Care Centre, Gray St, Kogarah, NSW 2217 Australia
[2]Faculty of Life Sciences, University of Sydney, NSW 2006 Australia
[3]Department of Nuclear Physics, Australian National University, Canberra, ACT, Australia
[4]Department of Nuclear Medicine, University Hospital Geneva, Switzerland

ABSTRACT

Cancer proceeds through a number of quite separate stages in the development of lethal disease. Early stages offer the potential for control if alpha-emitting radioimmunotherapy (RIT) is applied. Later stages may be more appropriate for both alpha and beta RIT. In this paper, the properties of various alpha- and beta-emitting radionuclides are examined. Prophylactic therapy requires the localization of dose to the cancer cell and rules out radioactive beta-emitting radionuclides. Alpha-emitting radionuclides, however, are much more appropriate toxins, as their efficacy depends on the energy and range of the alpha particles. After matching the cancer stage, radiolabel and carrier, we find that ^{149}Tb is the radionuclide of choice in all aspects except production. We report the production of ^{149}Tb in μCi quantities using the heavy-ion reaction at a tandem accelerator and in multi-mCi quantities using the spallation reaction in combination with on-line isotope separation technology.

INTRODUCTION

The efficacy of radionuclide therapy depends on the type and energy of radiation, the specificity of the carrier and the nature of the target cancer (1). Orthodox radionuclide therapy of cancer rests on a very limited quantitative basis. Traditionally ^{131}I labeled carriers are used, and more recently radiolanthanides are being applied for palliative treatment of bone cancer. With the exception of thyroid cancer, radionuclide therapy has been markedly unsuccessful in controlling cancer. The use of radiolabeled monoclonal antibodies was expected to improve the situation, but complete responses are rare and long term control is generally not achieved.

CANCER TARGETS

There are four stages of cancer which require quite different approaches to effect control. These are:

a) **Cells in transit** - Blood borne cancer cells from the primary tumor break away and travel through the lymphatic system or vasculature, lodging in the lymph nodes or on the walls of capillaries. These cells may be in a dormant state, i.e. the G_0 phase, and as such are not receptive to chemotherapy which relies on high mitotic rates for compounds to enter the cell

and cause damage to DNA. Thus to target these cells, a short range toxicity is required with a highly selective carrier.

b) **Preangiogenic lesions** - Small nests of cells develop in appropriate sites which might stimulate cell division. However, the numbers of cells is insufficient to secrete growth factors which would induce angiogenesis in nearby capillaries.

c) **Subclinical lesions** - Sufficient cells are present to stimulate capillary growth, which leads to rapid development of the tumor. However, lesions are still too small to be observable clinically, i.e. tumor diameter is less than 3 mm, and the patient is asymptomatic.

d) **Clinical lesions** - The tumor now manifests itself clinically with symptoms and can be readily observed by various diagnostic methods. For malignant cancers, metastatic disease is widespread, and treatment is mostly palliative in nature.

The current approach is to use beta-emitting radionuclides bound to monoclonal antibodies for the management of clinical cancer (2,3). We propose that different stages of cancer require different approaches.

RADIATION DOSES

The tumorcidal dose required to kill cancer cells in lesions depends on the number of viable or clonogenic cells present; nominally 60 Gy is required for 10^{12} cells, 40 Gy for 10^{8} cells, 20 Gy for 10^{4} cells and 10 Gy for 10^{2} cells. However, the tolerance dose for bone marrow is 1-5 Gy, for the GI tract is 1-5 Gy, for the vascular system is 10-20 Gy, and for the whole body is 2 Gy.

The lethal dose for a subclinical lesion of 10^{4} cells is 20 Gy. In order to limit the systemic dose to 2 Gy to the body, a 10:1 tumor:tissue dose is required. For 100 cancer cells in circulation, only 10 Gy and a 5:1 dose ratio is required. But for beta therapy, only 2.5% of the beta energy is deposited in a cancer cell with I-131, so only a 1:40 dose ratio is achievable. Thus, control of isolated cells is not possible because there is a 5x40=200 fold short fall in dose ratio, and beta-RIT cannot reasonably be expected to control cancer. For this reason alpha-RIT must be examined. Alpha particles have much higher linear energy transfer (LET) than betas, so fewer hits are required to kill a cell. The short range of alphas means much lower doses will be received by surrounding normal cells if a carrier with cancer cell-specific properties is used. However, cross-fire is not an important aspect of dose delivery as it is with betas. Microdosimetry calculations are required to determine median cell dose and cell survival probabilities. Monte Carlo methods have been applied for determining cell survival after boron neutron capture therapy (4,5); similar calculations would be required for alpha-RIT.

PROPERTIES OF ALPHA-EMITTING RADIONUCLIDES

The properties of some alpha-emitting radionuclides are shown in Table 1. The most efficacious of those listed is Boron-10, with a range less than a cell diameter. However, this activity must be initiated by neutron capture, and as such is most suitable for local therapy, as for glioblastoma multiforme. The next shortest range is that for Terbium-149. Radium-223, 224 and Actinium-225 have much higher alpha yields than Tb-149, and therefore require lower administered concentrations. The transuranium nuclides, however, require improved chelation chemistry. Astatine-211 is a halide with low in-vivo stability and the alpha particle range is more than twice that of Tb-149. Bismuth-212 has a very short half-life, but can be produced by a generator. However, the average energy and range of the alpha particles are more than twice that for Tb-149.

Table 1
Selected Alpha-Emitting Radionuclides with Therapeutic Potential
(Decay Data taken from NUCLEUS O.E.C.D./NEA Data Bank 1993)

Nuclide daughter	$T_{1/2}$	E_α [keV]	I_α(*) [%]	Range [μm]	dE/dx [keV/μm]	E_γ [keV]	I_γ(*) [%]	Production Route
10-B (n,α)	0	1470 1780	100	7.2 8.9	204 200	478	93	Thermal Neutron Source
149-Tb	4.1 h	3967	17	28	142	Eγ 165 352 652 817 853	>10 27 30 17 12 16	141-Pr (12-C;5n)149-Tb 142-Nd (12-C;4n)149-Dy HI accelerator (Tandem) Ta (p;spall)
211-At 211-Po	7.2 h 0.5 s	5867 7450	42 48	59	114	687 570 898	0.25 0.25 0.25	209-Bi (α,2n) 211-At Cyclotron
212-Bi 212-Po	60.6 m 0.3 ms	6051 6090 8785	25 10 65	74	106	727	6.75	228-Th--α-->224-Ra -α-α-α-> 212-Pb Generator
223-Ra 219-Rn 215-Po 211-Bi	11.4 d 4.0 s 1.8 ms 2.1 m	5434 5540 5607 5716 5747 weak 6425 6553 6819 7386 6279 6623	2 9 24 53 10 2 7.5 11.5 81 100 16.4 83.4	57	115	Eγ 154 269 351	>5 6 13.6 13	227-Ac--β-->227-Th --α--> 223-Ra Generator
224-Ra 220-Rn 216-Po 212-Pb 212-Bi 212-Po	3.7 d 55.6 s 0.15 s 10.6 h 60.6 m 0.3 ms	5449 5686 6288 6779 - 6051 6090 8785	5 95 99.9 100 - 25 10 65	58	114	240 239 300 727	4 43.4 3.2 6.75	228-Th--α--> 224-Ra Generator
225-Ac 221-Fr 217-At 213-Bi 213-Po	10.0 d 4.9 m 32 ms 45.6 m 4.2 μs	5637 5723 5731 5791 5793 5829 others 6127 6341 7067 5870 8376	4.5 2.9 10 8.6 18.1 50.7 5.2 15.1 83.4 100 2 98	60	113	 218 440	 11.6 26.1	 U, Th (p,spall) 229-Th--α--> 225-Ra --β-->225-Ac Generator
225-Fm	20.1 h	6963 7022	5 93.4	63	111			HFIR 255-Es--β--> 255-Fm Generator

*only strong relevant α and γ lines are presented

RADIOLANTHANIDES

The wide range of radiolanthanides available enables the efficacy of RIT to be optimized for each given stage of cancer. Lanthanides have almost identical biokinetic behavior in vivo, as long as they are bound via bifunctional linkers to biospecific molecules such as EDTMP, as shown by Beyer et al. (6). A great deal of chelation chemistry has already been developed for attaching lanthanides generally (7), as well as ^{153}Sm (8) and ^{166}Ho (9), to monoclonal antibodies (MoAbs). Chelators include DTPA, DOTA and TETA (10). Thus the relative efficacy of alpha- and beta-emitting radiolanthanides for killing cancer cells can be readily determined by chelation to the same MoAb.

The different decay properties of the radiolanthanides are given in Table 2. The volume factor is the cube of the range of the alpha particle, or of the average range of the beta particle, and represents the effective volume of interaction. Normalized to Tb-149, the volume factor varies by many orders of magnitude, even between ^{153}Sm and ^{166}Ho. Clearly, if a specific monoclonal antibody is used as a carrier which targets individual cancer cells, then the probability of cell killing relates to the fraction of energy deposited in the cell and the hits to kill a cell. These quantities therefore determine the required dose to be administered, which may exceed the critical normal tissue tolerance dose. The number of hits to kill a cell differs by two orders of magnitude between alphas and betas (1).

The half-life for Tb-149 is very much shorter than that of the beta emitters. As an iodine labeled MoAb may take as long as 24-48 h to reach peak uptake in solid tumors, such tumors are not the target for Tb-alpha-RIT. Uptake times required for cells in transit or preangogenic lesions are expected to be very short, and as such, the short half-life of Tb-149 may be of advantage (1).

PRODUCTION

We have used two modes of production to produce Tb-149. The first method uses a tandem accelerator to bombard a Pr or Nd target with C-12 ions. The saturated yield curve is shown in Figure 1 for both Pr and natural Nd targets. Two such measurements have been made with good agreement for Pr, but the first Nd measurement suffered from poor beam alignment.

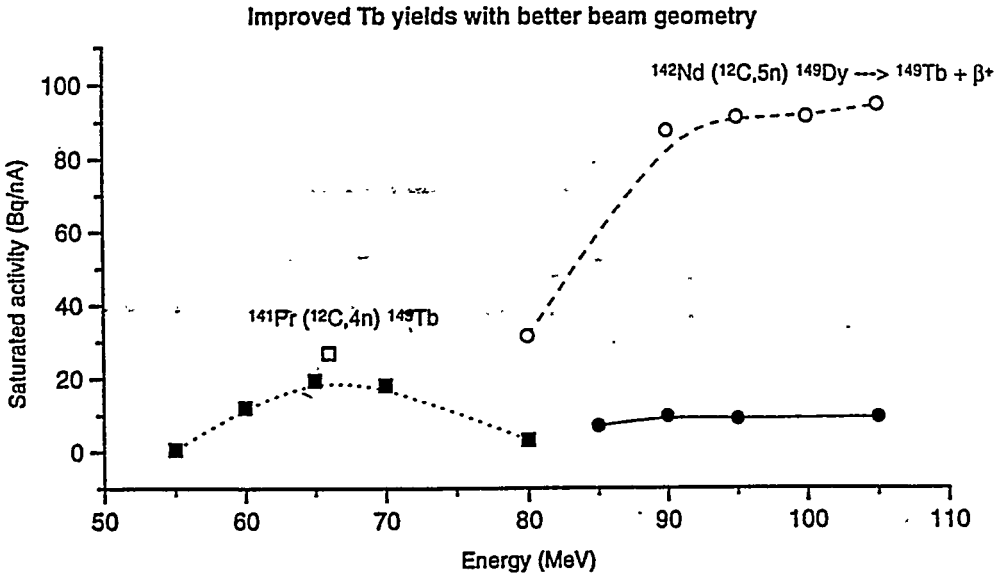

Figure 1. Saturated activities for the production of ^{149}Tb from ^{12}C bombardment of Pr (squares) and Nd (circles) at the ANU tandem accelerator. The open points represent a second measurement in each case.

Table 2
Selected Radionuclides of Rare Earth Elements with Therapeutic Potential
(Nuclear Data taken from NUCLEUS O.E.C.D./NEA Data Bank 1993)

NUCLIDE	$T_{1/2}$	Radiation	E(max) [MeV]	E(mean) [MeV]	Range [μm]	Volume Factor	Eγ [keV]	Iγ(*) [%]	Production Route
149-Tb	4.1 h	α	3.967	3.97	28	1	See Table 1		See Table 1
47-Sc	3.3 d	β, γ	0.6	0.161	300	1200	159	70	47--Ti(n,p) 47-Sc reactor
90-Y	64.1 h	β	2.3	0.934	4200	3400000	no		90-Sr--β ---> 90-Y generator
137m-Ce	34.4 h	e	0.2	0.203	500	5700	254	11	136-Ce (n,γ) 137m-Ce reactor
141Ce	32.5 d	β, γ	0.6	0.171	400	2900	145	48.4	235-U (n,f) fission product reactor
									141-Pr (p,n) 141-Ce cyclotron
142-Pr	19.1 h	β, γ	2.2	0.809	3500	2000000	1576	3.7	142-Pr (n,γ) 142-Pr reactor
143-Pr	13.6 d	β	0.9	0.315	900	33000	no		142-Ce(n,γ)143-Ce--β-->143-Pr reactor
147-Nd	11 d	β, γ	0.9	0.27	700	16000	91	28	235-U (n,f) fission product reactor
							531	13	146-Nd (n,γ) 147-Nd reactor
149-Pm	53.1 h	β	1.1	0.366	1100	61000	weak		148-Nd(n,γ)149-Nd--β-->149-Pm reactor
153-Sm	46.7 h	β, γ	0.8	0.269	600	121300	103	28.3	152-Sm (n,γ)153-Sm reactor
159-Gd	18.6 h	β, γ	1.0	0.312	800	23000	364	10.8	158-Gd(n,g) 159-Gd reactor
161-Tb	6.9 d	β, γ	0.6	0.195	450	4200	75	9.8	160-Gd(n,γ)161-Gd--β--> 161-Tb reactor
166-Ho	26.8 h	β, γ	1.9	0.694	2800	1000000	80.6	6.2	164-Dy(2n,γ)166-Dy--β-->166-Ho reactor
169-Er	9.4 d	β	0.3	0.103	200	360	no		168-Er (n,γ) 169-Er reactor
175-Yb	4.2 d	β, γ	0.5	0.13	250	700	396	6.5	174-Yb (n,γ) 175-Yb reactor
177-Lu	6.7 d	β, γ	0.5	0.147	300	1200	208	11	176-Yb(n,γ)177-Yb--β-->177-Lu reactor

(*) Only the strong gamma lines are summarized. For more data on ^{149}Tb see Table 1

Nd provides the higher yield, but may require an enriched target of ^{142}Nd in order to obtain high radionuclidic purity. The production and decay scheme of Tb-149 is shown in Figure 2. Most decays are by electron capture which generates Auger and Coster Kronig electrons. Such radiations are of little consequence as long as the Tb is not bound to DNA.

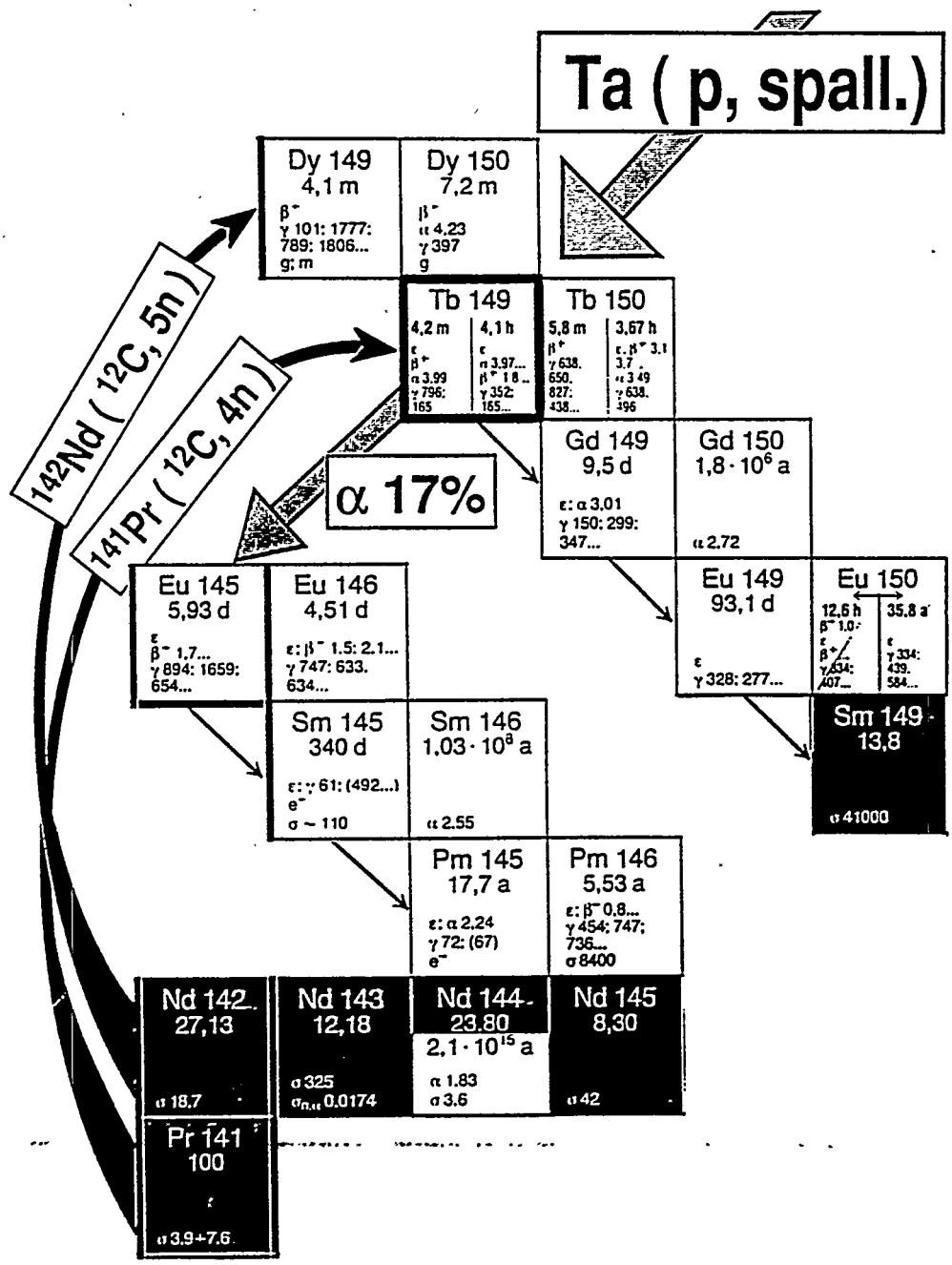

Figure 2. Production and decay scheme of Tb-149

Much higher yields, however, can be obtained via GeV energy proton spallation on Ta targets. Extremely high isotopic purity is obtained when the spallation production is followed by an on-line isotope separation process. We have produced multi-mCi quantities of ^{149}Tb at the CERN on-line isotope separation facility ISOLDE (6). The one GeV proton beam from the CERN booster hits a

120 g cm^{-2} Ta foil kept at a temperature of around 2400 ^{0}C. The radiolanthanides are preferentially produced in the spallation reaction and are released very quickly from the target and ionized in high yields by a surface ionization ion source. The ions are extracted from the target ion source unit and separated according to the mass:charge ratio electromagnetically. Theoretical production yields are 2 x 10^{10} atoms s^{-1} compared with the practical production rate of 20-30 mCi (about 1 Gbq) for a 4 h collection time. The collected samples contain isobaric impurities which are separated by using cation exchange chromatography (Aminex A5/ a-hydroxy-isobutyric acid). The alpha and gamma ray spectra obtained from such a carrier free isotopically clean ^{149}Tb preparation at the CERN ISOLDE facility is shown in Figure 3.

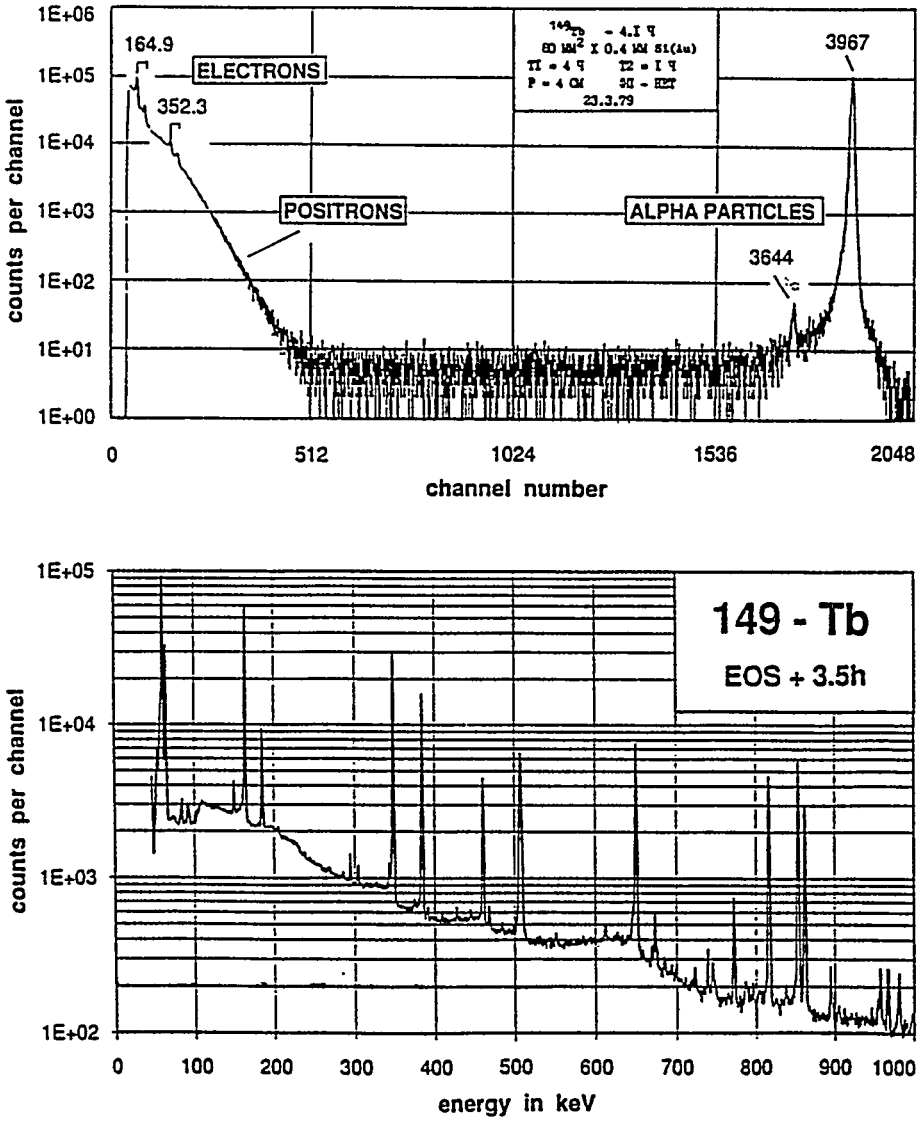

Figure 3. Spectra of particles (e^-, β^+ and α) (upper part) and gamma rays (lower part) emitted from mass-separated and chemically purified ^{149}Tb samples 4 and 3.5 h after end of separation. The spectra were recorded using a 80 mm^2 x 0.4mm Si(Au) surface barrier detector (upper part) and a 80 cm^3 HP-Ge-detector (lower part).

CONCLUSIONS

Tb-149 offers a better approach to the control of early stage cancer or leukemia. It possesses properties which are superior to other alpha emitters and offers efficacy very much greater than that for beta emitters. It can be produced in quantities adequate for in vitro studies at a high energy tandem accelerator. However, at present a spallation reaction combined with an on-line isotope separator facility allows production of quantities of this isotope required for patient therapy. The next step is the determination of efficacy in the control of cancer via *in vitro* and *in vivo* models.

REFERENCES

1. Allen BJ and Blagojevic N. Alpha and beta -emitting radiolanthanides in targeted cancer therapy: the potential role of terbium-149. Nucl Med Comm 17:40-47, 1996.
2. Scheinberg DA, Lovett D, Divigi CR et al. A phase 1 trial of monoclonal antibody M195 in acute myelogenous leukemia: specific bone marrow targeting and internalization of radionuclide. J Clin Oncol 9(3):478-490, 1991.
3. Papanastassiou P, Pizer BL, Chandler CL et al. Pharmacokinetics and dose estimates following intrathecal administration of 131I-monoclonal antibodies for the treatment of central nervous system malignancies. Int J Radiat Oncol Biol Phys 31(3):541-552, 1995.
4. Charlton DE and Allen BJ, Monte Carlo calculations of ion passages through brain endothelial nuclei during boron neutron capture therapy. Int J Radiat Biol 64(4):739-747, 1993.
5. Humm JL. A microdosimetric model of astatine-211 labelled antibodies for radioimmuotherapy. Int J Radiat Oncol Biol Phys 13:1767-1773, 1987.
6. Beyer GJ, Allen BJ, Morel Ch, Offord R, Aleksandrova Yu and Jahn S. The alpha and positron emitter Tb-149 - a suitable isotope for radionuclide therapy. Deutche Gesellschaft fur Nuklearmedizin, Munster, April 1996.
7. Beyer GJ, Offord RE, Kunzi G, Jones RML, Ravn U, Aleksandrova Yu, Werlen RC, Macke H, Lindroos M, Jahn S and Tengblad D. Biokinetics of monoclonal antibodies labelled with radio-lanathanides and Ac-225 in xenografted mice: preliminary results. J Labelled Compounds Radiopham. XXXVII:529-530, 1995.
8. Izard ME, Boniface GR, Hardiman KL et al. An improved method for labelling monoclonal antibodies with Samarium-153: use of the bifunctional chelate Mx-DTPA. Bioconjugate Chem 3(4):346-350, 1992.
9. Dadachova E, Smith SV, Di Bartolo et al. Labelling of proteins with ^{166}Ho. Proc 11th Int Symp on Radiopharmaceutical Chemistry, 13-17 August 1995, Vancouver, 526-528.
10. McMurry TJ, Brechbiel M, Kumar K and Gansow OA. Convenient synthesis of bifunctional tetraaza macrocycles. Bioconjugate Chem 3:108-117, 1992.

DOSIMETRY OF BNCT EPITHERMAL NEUTRON BEAMS USING MOSFET DOSIMETERS

Carolan MG[1,2], Rosenfeld AB[2], Allen BJ[2,3] and Kaplan GI[2]
[1]Illawarra Cancer Care Centre, Wollongong NSW 2500, Australia
[2]Department of Physics, University of Wollongong, NSW 2500, Australia
[3]St. George Cancer Care Centre, Kogarah, NSW 2217, Australia

ABSTRACT

Metal Oxide Field Effect Transistors (MOSFET) can be used as integrating dosimeters. Their small size (the actual device can be fabricated to be 0.1 x 0.1 x 0.01 mm^3 or smaller) suggests their application as internal in-vivo dosimeters. We have determined experimentally the photon energy response of MOSFETs when packaged in TO-18 transistor packages. We have also determined the neutron energy response of the MOSFETs in the same package and with a ^{6}LiF neutron attenuating shield by using Monte Carlo techniques. Measurements using LiF covered MOSFETs were performed in phantoms exposed in an epithermal neutron beam designed for Boron Neutron Capture Therapy (BNCT). These measurements are compared with Monte Carlo calculations of the gamma dose in the phantoms and show reasonable agreement. Further refinement of the device packaging is required to minimize the MOSFET neutron response. We have also experimented with MOSFETs as microdosimeters for determining pulse-height spectra in the source and drain p-n junctions. Using these junctions, the sizes of which are of the same order as biological cells, we have successfully discriminated between high- and low-LET radiations and acquired LET spectra.

INTRODUCTION

The very small size of the sensitive volume of MOSFET dosimeters suggests their application to internal dosimetry and the possibility of attaching them to a catheter in order to provide online and high spatial resolution in-vivo dosimetry.

We have investigated their application in photon and mixed gamma neutron fields such as those which occur in Boron Neutron Capture Therapy, (BNCT) (1,2,3). BNCT is currently undergoing Phase I clinical trials at Brookhaven National Laboratory and the MIT medical research reactor. BNCT is a binary therapy for cancer which depends upon delivery of ^{10}B to tumor cells by drugs which localize selectively in tumors. The tumor region is then irradiated with a neutron beam from either a filtered reactor beam or an accelerator neutron source. Any gamma component in the beam deposits a nonspecific dose.

Some gamma dose will be generated due to neutron interactions in the epithermal beam filters and structures. However in epithermal neutron beams designed for BNCT, by far the largest contribution to gamma dose comes from photons generated within the patient or phantom material, primarily from the H(n,γ) reaction. This dose can be of the order of several cGy per minute for a typical geometry and generally makes up 80 - 90 % of the total gamma dose. Though the dose can be

calculated to quite a good degree of accuracy using Monte Carlo radiation transport techniques, it is still necessary to be able to measure directly the gamma dose at points within phantoms to validate these calculations. We have investigated the use of metal oxide field effect transistors (MOSFETs) for gamma dosimetry in mixed gamma neutron fields, in particular those in phantoms exposed in BNCT beams.

In the case of BNCT, a large flux of epithermal or thermal neutrons are present and the neutron contribution to the MOSFET detector response must be taken into account. We have used Monte Carlo techniques to calculate the neutron energy response of MOSFETs and then used this response to correct MOSFET measurements in phantoms exposed to epithermal neutron beams.

For characterizing the biological effect of radiation in a mixed gamma-neutron radiation field, or in the case of short-range emitters such as immunotherapy with alpha-emitting isotopes or in BNCT, it is necessary to know more than just the average absorbed dose. The distribution of energies deposited on the micron scale (LET spectrum) in typical cell volumes is the most important additional characteristic of such radiation fields.

We investigated single dosimetric n-MOSFET devices with a 1 mm oxide thickness, measuring simultaneously charge collection from the reverse biased p-n drain and source junctions and also the threshold voltage shift. Such an approach can be applied for dosimetry in BNCT where mixed radiation gamma-neutron fields contain alpha particles and ^{7}Li ions with energies of 1.5 and 1.3 MeV respectively, resulting from neutron capture in ^{10}B.

MATERIALS AND METHODS

The operation of MOSFET dosimeters relies upon the buildup of trapped positive charges (holes), in the silicon oxide insulator under the gate electrode of the MOSFET. Any incident ionizing radiation will generate electron-hole pairs in this oxide layer. Some of these holes will be immobilized in traps throughout the oxide predominantly close to the substrate-oxide interface (Figure 1a). These trapped holes are quite stable. The accumulation of this positive charge in the oxide leads to a modification of the source-drain conduction characteristics. An n-type channel is induced in the p-type substrate of the MOSFETs used in this study. This effect is measured via observable changes in the threshold voltage, V_{TH}. The sensitivity of the MOSFET can be enhanced by applying a positive bias to the gate electrode during irradiation.

The MOSFETs used were obtained from Gammasonics Pty Ltd (Australia) and were fabricated on a p-type substrate with an oxide layer thickness of 1.0 μm. The MOSFET package was a standard kovar TO-18 encapsulation which must be taken into account when determining the neutron and gamma response of the dosimeters.

Photon Energy Response

The photon energy response of the MOSFET in free air geometry was determined using a number of sources including a Varian 2100C linear accelerator and a Pantak Therapax Orthovoltage x-ray source as well as some isotopic sources (2).

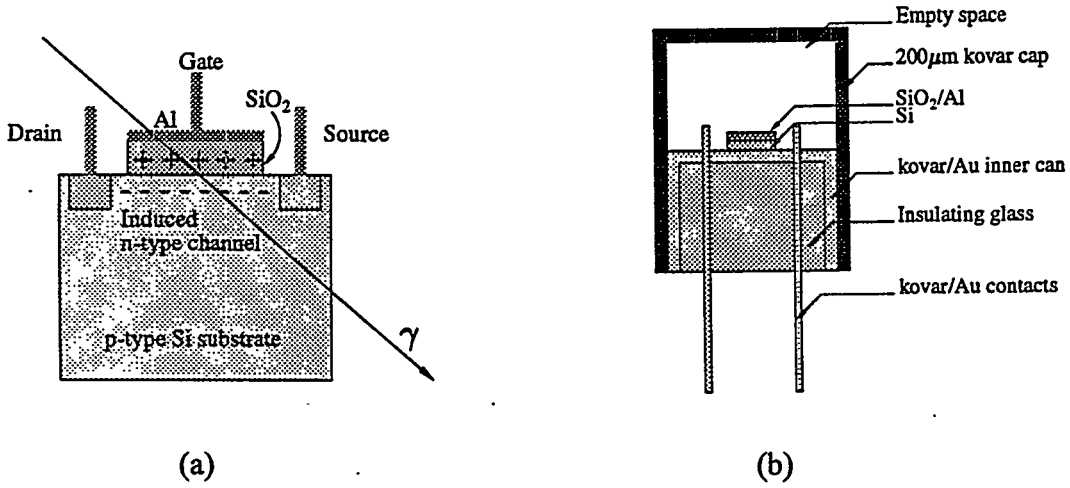

Figure 1.(a) MOSFET mechanism of operation. Ionizing radiation creates electron hole pairs in SiO_2 layer which leads to an induced n-type channel between the source and drain. (b) The geometry of the MCNP model used to calculate the neutron energy response of the MOSFET. The diagram is not to scale.

Neutron Energy Response

In order to determine the neutron energy response of the MOSFET as packaged in a TO-18 encapsulation, a Monte Carlo model of the device was developed using the Los Alamos Neutron Photon Monte Carlo transport code, MCNP4A (4). A detailed model was required to adequately represent the contribution due to secondary particles generated in the TO-18 package.

The geometry used in the model is shown in Figure 1b, which is not to scale. Some approximations were used in the model to improve the statistics of the photon flux at a position corresponding to the silicon oxide region. These included enlarging the silicon oxide tally region to a thickness of 450 μm rather than the actual thickness of 1 μm.

In order to minimize the neutron contribution to the MOSFET response, lithium fluoride neutron attenuating covers of wall thickness ~ 2 mm were fabricated. These were made by mixing polyester resin with enriched ^{6}LiF powder and molding the resultant mixture into rods which were then machined to allow the insertion of a MOSFET. To determine the energy response of the MOSFET in this configuration, it was modeled in an isotropic field of neutrons. For both the covered and the uncovered MOSFET, several MCNP4A runs were done each using source neutrons in groups covering the epithermal range of energies. The photon flux through the silicon oxide region of the model was tallied and convolved with the silicon photon KERMA. To a first approximation, we can assume that the tallied quantity is proportional to the response of the device to neutrons. These responses were normalized using MOSFETs exposed in a thermal neutron beam at the MOATA reactor at Ansto and also by exposing the MOSFETs in the free epithermal neutron beam at the JRC reactor in Petten, where the neutron spectrum and flux was assumed to be known.

MOSFET Gamma Dose Measurements in Phantoms

A number of phantoms were exposed in an epithermal neutron beam in a series of experiments performed on the HB11 epithermal neutron beam at Petten High Flux Reactor (HFR) in the Netherlands (1,5). In these experiments the MOSFETs were exposed in passive mode, that is with no bias applied to the gate during irradiation. The MOSFETs were covered with ^{6}LiF/polyester shields, and calibrated in a standard ^{60}Co photon field to determine individual photon sensitivity factors for

each device. These sensitivities were of the order of 1.8 mV cGy^{-1}.

MOSFET measurements were made in two different phantoms. One was a 15 cm perspex cube and the other was a cylindrical phantom 18 cm in diameter filled with an agar based tissue-equivalent gel. Measurements were performed with the phantoms placed at a distance of 20 cm from the 15 cm diameter beam exit aperture. Irradiations varied in duration from approximately 5 min to 15 min and yielded changes in threshold voltage of 20 - 100 mV.

Using MCNP, models of the cylinder phantom and the cube phantom were developed, and the neutron silicon and tissue doses, the gamma dose and MOSFET neutron responses were calculated along the axes where measurements were made. Resonance activation foil measurements were performed using bare and cadmium covered gold foils to validate these Monte Carlo models. MCNP was used to generate the expected activities of these foils at each location of interest in the phantoms.

Microdosimetry Using MOSFETs

For initial microdosimetry tests, we removed the covers from the MOSFETs and placed them in the vacuum chamber of an alpha spectrometer. Tests were performed using alpha spectra from ^{210}Po with the drain and source under reverse bias. A reverse bias of 18 volts was used and the pulse signals were amplified and stored using a standard alpha spectrometry amplifier and multichannel analyzer setup. A small ^{60}Co source and a ^{90}Sr source were also tested in this configuration to observe the MOSFET pulse mode response to low-LET radiations. The MOSFET threshold voltage shift was measured for the MOSFET exposed to alpha particles from the ^{210}Po source.

RESULTS

For photon energies greater than approximately 660 keV, the response of the MOSFET in free air is proportional to tissue response. Below this energy, an over response of up to ten times is observed, as a result of buildup in the kovar cap. When the MOSFET is embedded in a phantom or in any location where electronic equilibrium exists, this over response is not so accentuated. Dose-depth profiles in phantoms measured in x-ray photon beams show good agreement with ionization chamber measurements of the same. For MOSFET gamma measurements in epithermal neutron beams the MOSFET response has been assumed to be proportional to tissue dose. This is a reasonable assumption, since, as previously noted, one of the main sources of gamma dose is from the $H(n,\gamma)$ reaction which yields gamma photons of approximately 2.2 MeV.

The neutron energy response of the MOSFET when exposed to an isotropic neutron field without any LiF shield shows a strong neutron response at thermal energies which decreases with increasing energy until it is approximately three orders of magnitude lower at 10 keV. This thermal neutron response is attenuated by a factor of $\sim 10^2$ when exposed encapsulated in a ^6LiF/polyester shield. The attenuation is greatest at thermal energies and decreases as the neutron energy increases. The response of a LiF covered MOSFET, assuming a 100% Ni TO-18 package, has a peak response between 1 eV and 10 eV. This probably results from neutron resonance capture in gold at 4.9 eV. For the case of the kovar package, there is a peak response for the 100 - 500 eV neutron energy group, resulting from the added Co content. The use of a LiF shield attenuates the thermal neutron response of the MOSFET by a factor of ~ 100, but only by 2 - 3 times at energies of 1 eV. Since this is in the desirable epithermal region, the neutron fluxes will be significant and therefore the MOSFET will still have an observable response at this energy. A correction must be applied for this neutron contribution.

The gold activation foil experimental data were in good agreement with Monte Carlo generated foil activities. From this we can conclude that the neutron fluxes are accurately predicted by the

MCNP calculations (to better than 10% difference), and therefore we can have reasonable confidence in the MCNP-generated neutron responses of the shielded MOSFETs at each measurement point in the phantoms. Figure 2 shows the MOSFETs data with the Monte Carlo calculated neutron response subtracted from the experimental MOSFET measurements, which are then presented in terms of gamma dose per hour. Also shown are argon-filled magnesium ionization chamber measurements at the same locations. These ion chamber measurements were performed with a lithium carbonate/epoxy cover to further minimize neutron response. Good agreement is seen between these three sets of data when the uncertainty in the MOSFET readout is considered.

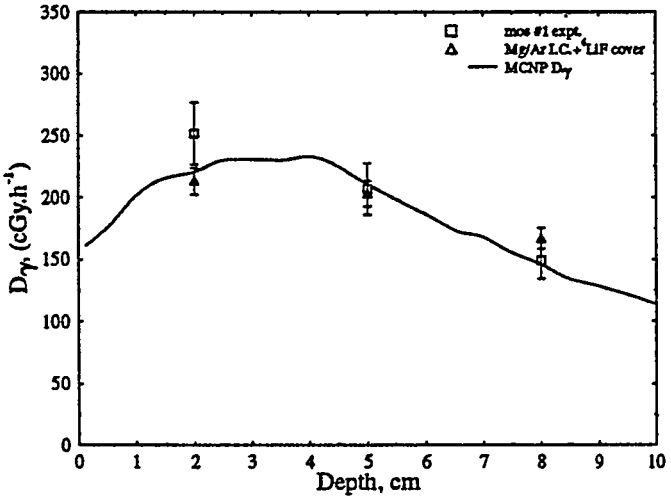

Figure 2. The MOSFET measured gamma dose with the MCNP-predicted neutron response subtracted from the experimental measured data. Ionization chamber measurements are shown for comparison.

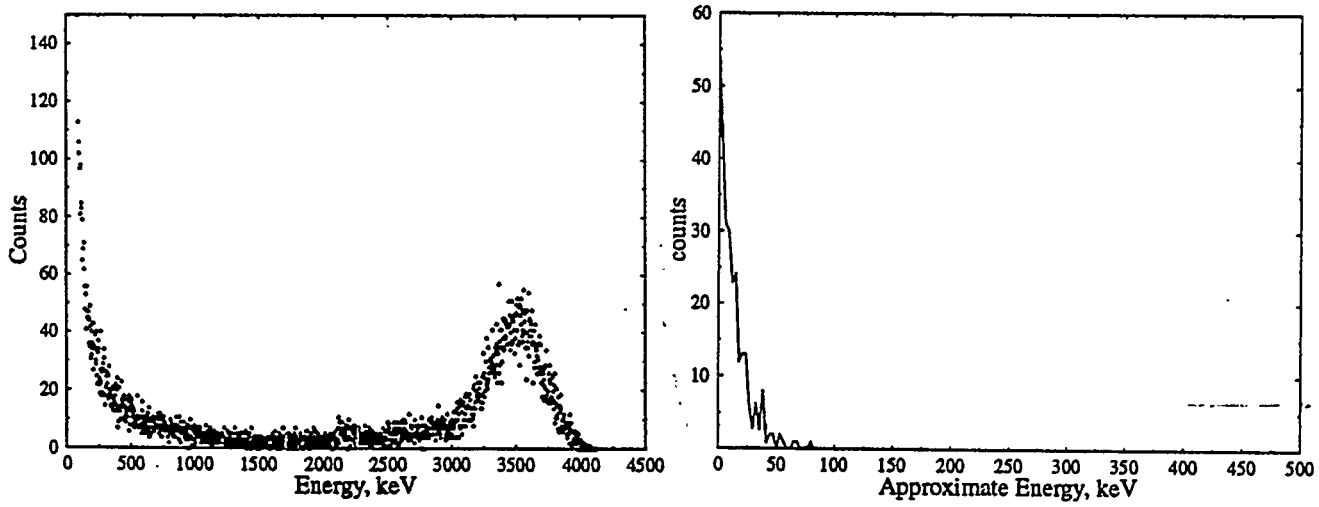

(a) (b)

Figure 3. (a) The pulse-height spectra obtained using a MOSFET drain p-n junction exposed to ^{210}Po alpha particles, and (b) the pulse-height spectrum obtained using the same MOSFET with ^{60}Co photons.

Figure 3 shows the pulse-height distribution for Po-210 alpha particles and gamma photons for the same bias condition. For the case of polonium, the main peak corresponds to a deposited energy of 3.8 MeV rather than 5.3 MeV, as a result of losses in the entrance window and recombination. The observed peak corresponds to charge collection due to drift in the depletion region of several microns (for 18V bias) and also due to diffusion because of the large time constant of the charge-sensitive preamplifier used.

These results clearly show the possibility of separately measuring the contributions of high-LET and low-LET particles. Variation of the bias on the drain p-n junction from 0-18V does not change the amplitude of the spectra, which confirms that most of the charge is collected by diffusion processes. Thus it should be possible to measure LET spectra using pulse-height spectra from MOSFET source and drain p-n junctions. This is important for short-range charged particles in BNCT, where the particle range is of the same order as a cell size and the effect of nonlinearity of LET is important. The cell size could be adjusted by bias on the drain p-n junction.

Despite the fact that photons and electrons do not contribute to the pulse-height spectra, they do make a strong contribution to the threshold shift because of ionization in the thick oxide layer. This contribution represents the average absorbed dose from low-LET particles. The threshold voltage shift due to the contribution of alpha particles has been studied using an ^{241}Am alpha source with a flux of alphas similar to that expected in BNCT treatment, i.e. $\sim 4 \times 10^3$ $s^{-1}cm^{-2}$. Figure 4 shows the linear dependence of the threshold voltage versus alpha particle fluence for a gate voltage of 18V applied during the irradiation.

The study of pulse-height distribution spectra from alpha particles incident on the MOSFET shows that the spectra obtained are independent of the charge build up in the silicon oxide, i.e. the average absorbed dose. This is important for the application of MOSFET dosimeters where they are to be used simultaneously in microdosimetry and macrodosimetry modes.

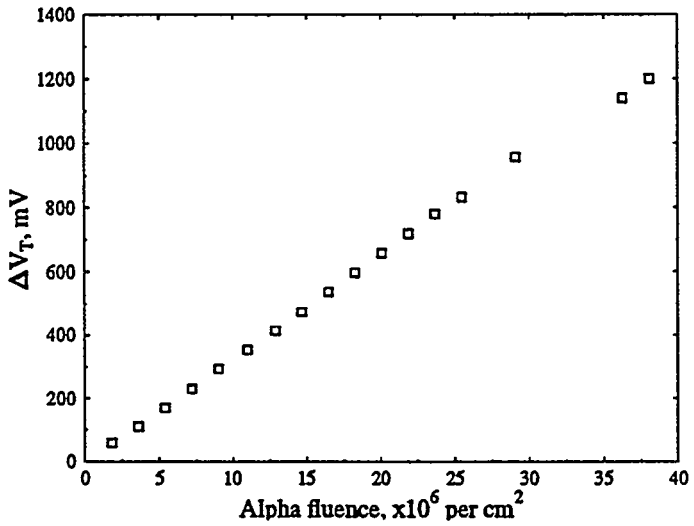

Figure 4. The change in V_{TH} when the MOSFET is exposed to a flux of alpha particles from a ^{241}Am source.

CONCLUSIONS

We have measured the photon-energy response function of the MOSFET in free air relative to the tissue-equivalent response. The effect of the kovar metal casing is significant and must be taken into account for photon energies below 660 keV. The dose enhancement effect can result in an over response relative to tissue of ~ 10 times. This is not critical in situations where electron equilibrium exists, if a calibration relative to tissue is done in a photon field of similar energy to the one in which the MOSFET is to be used for measurements. However, a plastic or near tissue-equivalent encapsulation material would minimize the over response and should be used in future measurements.

The relative neutron response function of the MOSFET as a function of energy has been calculated using Monte Carlo techniques. This has been normalized using measurements in known neutron fields. Though a LiF shield on the MOSFETs reduces the thermal neutron response by ~100 times the response to epithermal neutrons is not much reduced because of the lower absorption cross section of the ^6Li. The undesired neutron response of the MOSFET could be further minimized by elimination of the kovar and by having a device package consisting of low cross section materials, possibly plastic.

Currently it is necessary to calculate a neutron response correction factor using Monte Carlo or some other technique to adjust the MOSFET response for the neutron contribution. If this neutron response can be reduced adequately by alternate packaging this may not be necessary. Otherwise the MOSFET measurements in mixed neutron gamma fields still provide a useful check on Monte Carlo or other dose calculations. The rather large uncertainties in the MOSFET measured data can be minimized to 3 - 4% at most by the use of MOSFETs in active mode rather than in passive mode, because of the increased sensitivity and the consequent larger change in V_{TH}. Applying a temperature correction to each data point would also reduce uncertainties from temperature variation.

We have shown that it is possible to measure the gamma dose in a mixed gamma neutron field using MOSFET detectors. With some further packaging development and taking advantage of their very small size, it should be possible to use them for phantom dosimetry in BNCT beams or even for in-vivo dosimetry.

ACKNOWLEDGMENTS

The authors would like to acknowledge the assistance of Gammasonics Pty Ltd for providing some of the MOSFETs used in this study. The first author would also like to acknowledge the guidance and assistance of Dr. J.M. Mathur of the Department of Physics, at the University of Wollongong. Thanks also to the BNCT group at Petten HFR for their assistance with the measurements performed on their reactor.

REFERENCES

1. Carolan MG, Wallace SA, Allen BJ, et al. Validation of Monte Carlo dose planning by epithermal beam dose distribution measurements in phantoms. Proceedings of the 6th International Symposium on Neutron Capture Therapy, Kobe Japan 1994, edited by Y Mishima, Plenum Publishers, New York, in press.
2. Rosenfeld AB, Carolan MG, Kaplan GI, Allen BJ and Khivrich VI. MOSFET Dosimeters: The role of encapsulation on dosimetric characteristics in mixed gamma-neutron and megavoltage x-ray fields. IEEE Trans Nuc Sci, NS-42, N6, 1870-1877, 1995.
3. Butson MJ, Rosenfeld AB, Mathur JN, Carolan MG, Wong TPY and Metcalfe PE. A New Radiotherapy Surface Dose Detector: The MOSFET. Med Phys 23(5):655-658, 1996.
4. Briesmeister JE, Ed. MCNP - A General Monte Carlo N-Particle Transport Code, Version 4A, LA-12625, 1993.
5. Carolan MG, Rosenfeld AB, Wallace SA, Meriaty HA, Storr GJ, Khivrich VI, Moss R and Allen BJ. Silicon dosimetric diode for BNCT using epithermal neutron sources. Proceedings of the First International Workshop on Accelerator Based Neutron Sources for Boron Neutron Capture Therapy, CONF-940976, 299 -309, 1994.

MINI-TLD ABSORBED DOSE MEASUREMENTS FOR IN VIVO USE: PARAMETERS AFFECTING THE DOSIMETER SIGNAL

Strandh M[1], Strand S-E[1] and Spanne P[2]
[1]Jubileumsinstitutionen, Radiation Physics Department
Lund University Hospital
S-221 85 Lund, Sweden
[2]European Synchrotron Radiation Facility
Grenoble, France.

ABSTRACT

Mini-TLDs are small rods of Teflon with $CaSO_4$:Dy or LiF as dosimeter material. Their dimensions are 0.2x0.4x5mm, produced from ordinary TLD-discs. The mini-TLD method has been used for absorbed dose measurements in different tumor models and animal experiments, reported in the literature. However, no thorough examination of the different properties of these mini-TLDs has been performed. We investigated different parameters affecting the signal and thus the accuracy of the mini-TLDs, such as fading in daylight and darkness, signal loss in gel and muscle tissue, pH dependence and supralinearity.

For $CaSO_4$:Dy mini-TLDs, we found that fading in air in darkness is small. For LiF mini-TLDs, the signal increased up to at most 135%. The observed signal loss after implanting mini-TLDs in gel and muscle tissue is considerable. For $CaSO_4$:Dy mini-TLDs, the signal decreased to 32% of its original value after 9 days at room temperature. The corresponding value for LiF is 65%. The signal losses in gel and muscle tissue are the same at a single temperature, but increase with increasing temperature. Signal losses are still seen after pretreating mini-TLDs with liquid or gel, although to a lesser extent. The explanation may be that the luminescent crystals are dissolved in the material. This has been visualized by SEM-and micro-CT-imaging of treated dosimeters. The pH dependence of the Tl-signal is high. For external irradiation, supralinearity starts around 1 Gy for both kinds of dosimeter materials.

The use of mini-TLDs for in vivo measurements requires that the above corrections be considered or that the dosimeters are calibrated in a similar milieu.

INTRODUCTION

There is an increasing need for measurements of absorbed doses in radionuclide therapy. It is important to know both the absorbed dose to normal tissues and to the tumor. The use of small thermoluminescent dosimeters (TLDs) has been suggested to make direct measurements of absorbed dose in vivo. A good knowledge of absorbed dose in systemic radiation therapy (SRT) is a prerequisite for understanding the therapy effect (1, 2).

Since 1985, several groups have used these dosimeters (3-9, 13, 14). $CaSO_4$:Dy has been chosen as a dosimeter material because its sensitivity is 30 times greater than that of LiF. A disadvantage of $CaSO_4$:Dy is that it is not tissue equivalent (Zeff = 15.3), and has comparatively high sensitivity to low-energy photons. LiF, however, is almost tissue equivalent (Zeff-LiF = 8.2, Zeff-tissue = 7.4) and has low dependence on photon energy. Wessels et al. suggested the mini-TLD method, and have implanted $CaSO_4$:Dy dosimeters in animal organs (3, 4). The same group (5) has also constructed phantoms with artificial tumors contained in a tissue-equivalent medium. The mini-TLDs were used to characterize the absorbed dose distribution in a radial direction from the center of the cylindrical tumor volumes. Griffith et al. (6, 7) showed, using microtomed sections, that implanted mini-TLDs in conjunction with autoradiographic section profiles provide a correlation of absorbed dose to the heterogeneous radioactivity in the tumor.

After several in vivo studies, questions arose about the accuracy of the method. Demidecki et al. (8) reported signal loss with $CaSO_4$:Dy dosimeters. Heidorn et al (9) similarly suggested fading effects with these dosimeters. Fading in air has been investigated by McKinlay (10) for $CaSO_4$:Dy-Teflon-dosimeters at storage temperatures 25 degrees C and 100 degrees C. Recently our group, in collaboration with others, investigated the effect of signal loss in $CaSO_4$:Dy dosimeters (13). Strand et al. (14) examined prepared and unprepared mini-TLDs with electron microscopy and μ-CT. The above reports show that several factors affect mini-TLDs in vivo.

The aim of this work was to carefully examine the different properties of $CaSO_4$:Dy and LiF mini-TLDs in order to evaluate the accuracy of these dosimeters in determination of the absorbed dose in vivo in radionuclide therapy. In a recent study (15), we have mentioned that careful calibrations of $CaSO_4$:Dy mini-TLDs in similar milieus is necessary for measuring the absorbed dose with reasonable accuracy.

MATERIALS AND METHODS

Preparation of the Mini-TLDs

Mini-TLDs were prepared from TLD-discs with a thickness of 0.4 mm and a diameter of 13 mm, which were sectioned into 0.2 mm thin strips. The strips were then cut into rods with a length of 5 mm.

Irradiation of the Dosimeters

The calibrations were done by irradiating the mini-TLDs in a Teflon phantom with photons from a ^{60}Co-source. The phantom consisted of two plates of 7.5 mm thickness between which 20 rod-shaped mini-TLDs can be placed in cavities fitted to their shape. The absorbed dose in the calibrations was about 0.2 Gy for the $CaSO_4$:Dy dosimeters and about 0.6 Gy for the LiF dosimeters. For each investigation a group of 10 dosimeters was used.

Sensitivity of the Dosimeters to Daylight and Ambient Illumination

In a clinical situation, the mini-TLDs spend most of their time in the tissue or the tumor, thus in darkness. However, during shorter periods after irradiation, e.g. during washing and waiting for readout in the TLD-reader, they may be exposed to ambient light. In order to investigate the influence of exposure of the dosimeters to light, irradiated mini-TLDs were placed close to a window and were exposed to daylight and illumination with laboratory fluorescent tubes for between 2 hours and 2 days.

Signal Loss of the Dosimeters in Air, Gel, Muscle Tissue at Different Temperatures

Irradiated mini-TLDs were left in air and in darkness for between 2 hours and 10 days at the three different air temperatures; 4°C, 22°C (room temperature) and 37°C (body temperature). Another set of irradiated mini-TLDs was put into solid gelatine gel and into fresh piece of murine muscle tissue, and were left there in darkness from 1 to 9 days at 4°C and at room temperature. The temperature 37°C could not be used for gel, because it liquidizes, nor for muscle tissue, because at that temperature decomposition of the meat was a problem.

Dosimeter pH Sensitivity

Irradiated mini-TLDs were placed into liquids and gels with various pHs and were left there for 4 days in darkness. The pHs of the liquids and the gels were prepared by adding concentrated NaOH or HCl solutions to distilled water or the warm and fluid gel.

Supralinearity of the Dosimeters

The thermoluminescence response per unit absorbed dose in any material is an important characteristic of a thermoluminescent phosphor. At relatively low values of absorbed dose, the response is linear. Above a critical dose level, the response becomes supralinear, saturating at a high dose and then falling off rapidly. Supralinearity is due to multiplication of the traps in the thermoluminescent material. In order to investigate the supralinearity of the mini-TLDs, dosimeters were irradiated for absorbed doses up to 20 Gy.

RESULTS

Preparation of the Mini-TLDs

Despite careful cutting of the dosimeters, the mini-TLDs showed large individual variations in sensitivity after irradiation with equal absorbed doses. The maximum variation of sensitivity for new dosimeters was about 20%, and the mini-TLDs were therefore calibrated individually.

Sensitivity of the Dosimeters to Daylight and Ambient Illumination.

$CaSO_4$:Dy: A significant difference in signal between dosimeters exposed to light compared to dosimeters left in darkness was seen (Figure 1). Uncertainty for all data is reported as one standard deviation (σ).

From the extrapolated curve, it appears that the signal loss due to UV irradiation in the light is greatest during the first few hours. After about 40 hours of exposure, the rate of signal loss is the same for the dosimeter groups. Fading in air is small in darkness, being about 10% after 9 days. No large differences could be seen between the fading curves at the three different temperatures.

Signal Loss of the Dosimeters in Air, Gel and Muscle Tissue

$CaSO_4$:Dy: Signal loss in gel and muscle tissue is presented in Figure 2. The signal loss is more important in gel and muscle tissue than in air (Figure 1). There is an increase in signal loss between 4° C and 22° C.

LiF: In air, the signal first increases (Figure 3), reaching a maximum between 4 and 6 days, and then declines.

For incubation in gel, the signal loss is much smaller for LiF than for $CaSO_4$:Dy dosimeters. For example at 6 days, the corresponding signals are 35% and 65%, respectively.

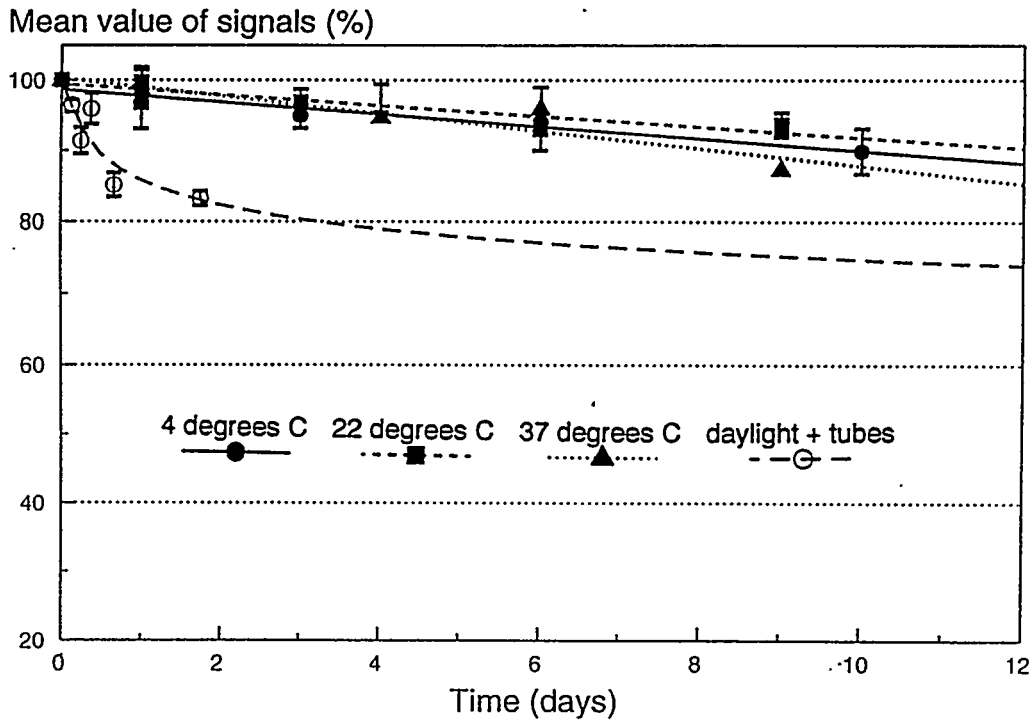

Figure 1. $CaSO_4$:Dy fading in air in darkness at different temperatures and fading in daylight and illumination with laboratory fluorescent tubes.

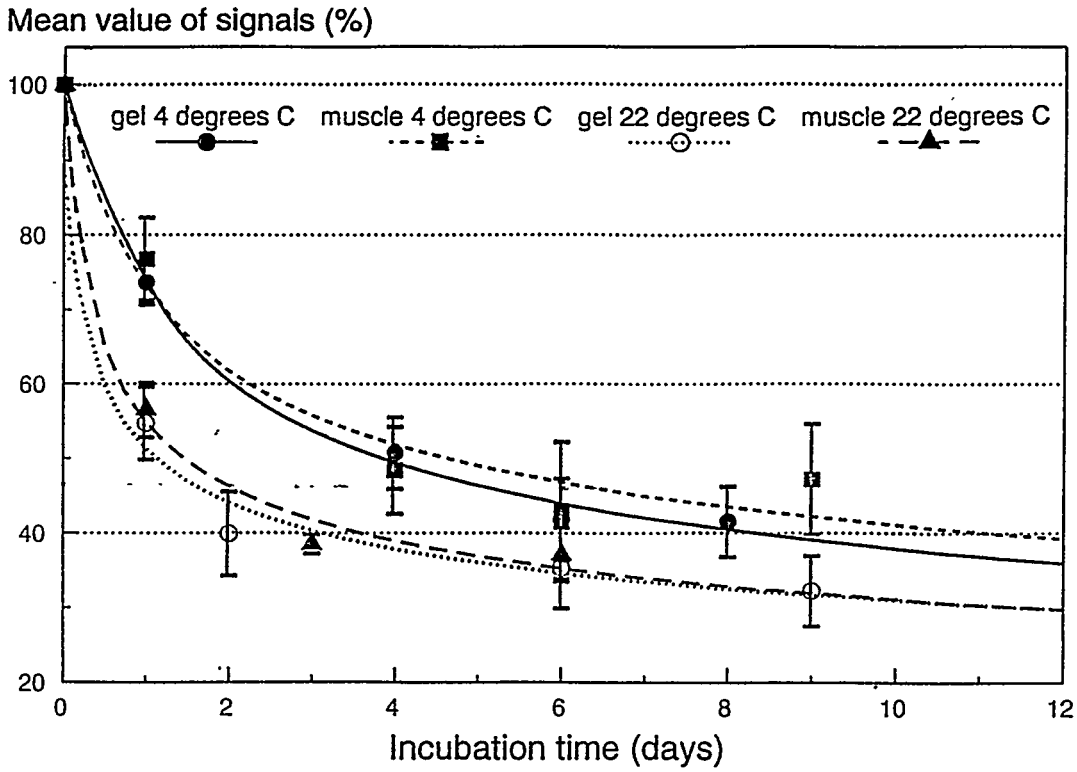

Figure 2. $CaSO_4$:Dy signal loss in gel and muscle tissue at two different temperatures, in darkness.

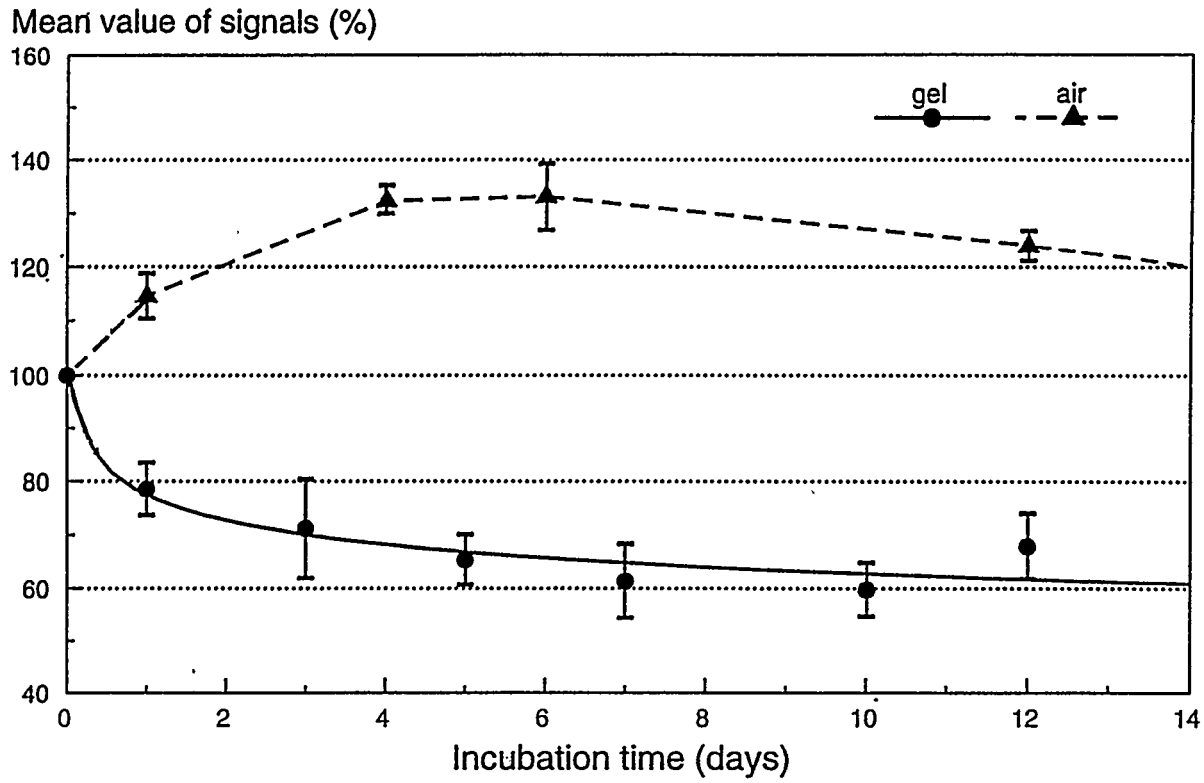

Figure 3. LiF fading in air and signal loss in gel, both at room temperature in darkness.

pH Sensitivity of the Dosimeters

$CaSO_4$:Dy: The relative signals at the different pHs are presented in Figure 4, normalized to the mean value of a group of mini-TLDs left in air for zero time.

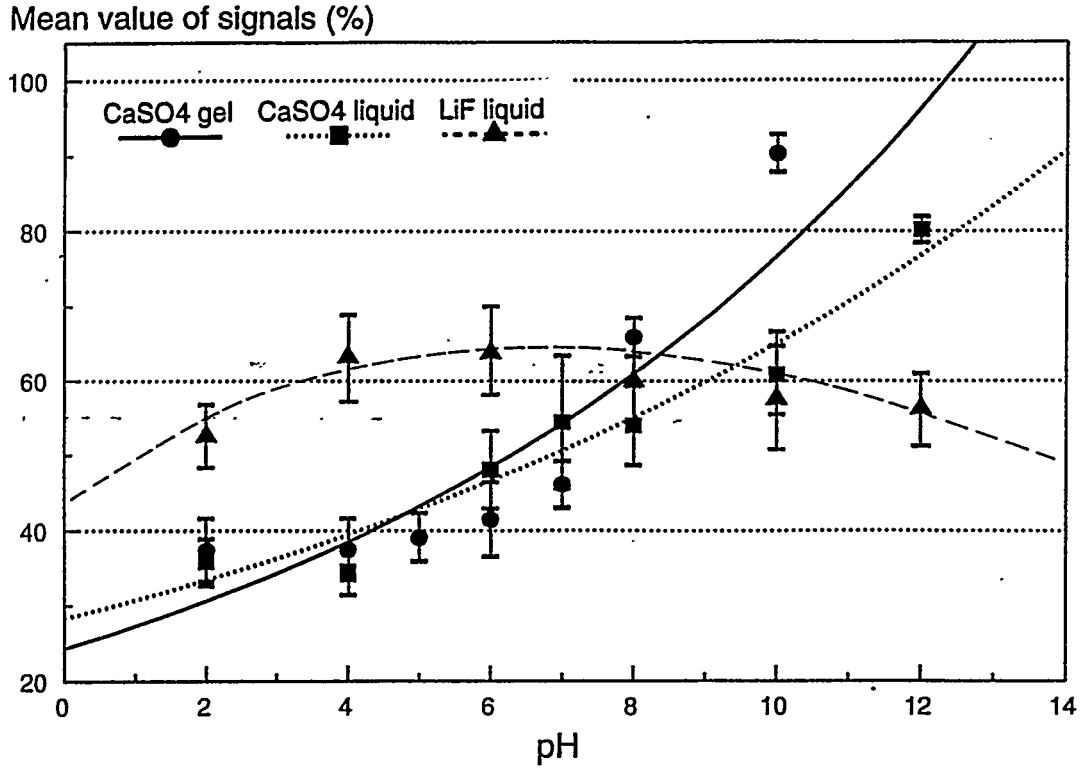

Figure 4. pH dependence of the dosimeters, in darkness

The dosimeters exhibit a strong dependence on the pH, being about the same in liquid as in gel. The loss of sensitivity is highest for pH below six, reaching a value of 35% of the original signal for a pH of two. For pH above six, the loss of sensitivity is smaller, around 10% loss of signal for a pH of 12 for gel.

LiF: The signal for LiF is dependent on the pH, however not as much as for $CaSO_4$:Dy. Figure 4 shows the loss of sensitivity is smallest for a neutral pH. For higher and lower pH the signal decreases.

Supralinearity of the Dosimeters

The relative sensitivity (R) is related to the sensitivity at 0.1 Gy, according to the expression

$$\mathbf{R = TL(D)/TL(0.1),}$$

where TL(D) is the TLD-signal at the dose D (Gy) and TL(0.1) the TLD-signal at 0.1 Gy. The onset of supralinearity can be seen between 0.5 and 1 Gy for both $CaSO_4$:Dy and LiF dosimeters (Figure 5). At absorbed doses above 1 Gy, the sensitivity enhancement increases rapidly.

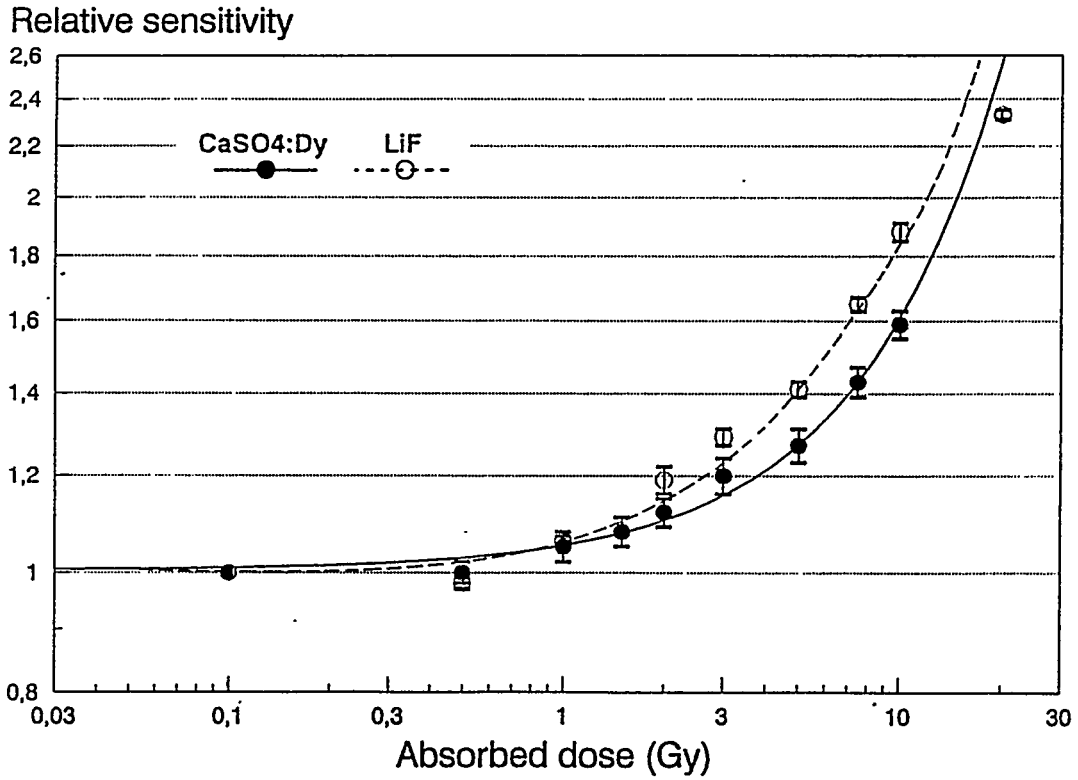

Figure 5. Supralinearity of the dosimeters.

DISCUSSION

In this investigation we have shown that several physical parameters affect the dosimeter signal when applying these mini-TLDs for in vivo dosimetry. Demidecki et al. (13) and Strand et al. (14) have made investigations showing signal effects for the mini-TLDs. The large sensitivity variation of the freshly prepared mini-TLDs (up to 20%) might be due to irregularity of crystal density in the original dosimeter discs, depending on the manufacturing method. However, a sensitivity variation of

20% is acceptable in clinical situations. Also, the cutting procedure might remove crystals close to the surface. This was clearly seen in earlier SEM- and μ-CT studies (13, 14). The dosimeters must be calibrated and handled individually, because it is practically impossible to find a sufficiently large group of dosimeters with the same sensitivity.

Fading in air has previously been studied by McKinlay (10) for $CaSO_4$:Dy discs at storage temperatures of 25°C and 100°C, respectively. Our results for mini-TLDs show a fading in air of 5-10% after 10 days of storage, which is similar to those reported by McKinlay.

The curve for storage of LiF mini-TLDs in darkness (Figure 3) differs significantly from that for $CaSO_4$:Dy mini-TLDs (Figure 1). The increase of the signal between 1 and 4 days (Figure 3) probably depends on migration and aggregation of traps in the thermoluminescent material (11, 12). Our results show that this effect is more pronounced during the first days of storage and removes any effect of fading. After 6 days, however, a decrease in the signal can be seen.

The curve for signal loss after incubation in gel for LiF mini-TLDs (Figure 4) is similar to the corresponding curve for $CaSO_4$:Dy mini-TLDs. The signal loss is, however, more pronounced for the $CaSO_4$ dosimeters. LiF dosimeters are slightly soluble in water (11). They appear to be less hygroscopic than $CaSO_4$ dosimeters.

Since measurements at body temperature (37°C), which is very important for in vivo measurements, could not be made for gel or muscle tissue introduces an error in the estimation of the signal loss for in vivo conditions. According to Figure 2, the signal loss with temperature changes is about 10% between 4°C and 22°C. Assuming linearity then between 22°C and 37°C, an additional 8 % signal loss may be anticipated.

The pH effect was shown to be significant. It is a well-known fact that $CaSO_4$ crystals are soluble in acids (12). According to a recent investigation by Demidecki et al. (13) and Strandh et al. (14), sour solutions make small "holes" on the surface of the dosimeter at the $CaSO_4$ sites on the crystals. This can be seen in the SEM and μ-CT pictures of treated dosimeters compared to pictures of untreated dosimeters (13, 14). However, LiF crystals appear to be soluble in both acids and bases. This is quite in accordance with what is known about LiF in inorganic chemistry.

The supralinearity is slightly more pronounced for LiF mini-TLDs. McKinlay has mentioned 30 Gy as the point for the onset of supralinearity for $CaSO_4$:Dy dosimeters. According to Figure 5, the start of supralinearity for those dosimeters is much earlier, between 0.5 and 1 Gy. Horowitz, however, has mentioned 1 Gy as the point for onset of supralinearity for LiF dosimeters. Supralinearity has effects in a clinical situation, because, depending on the type of therapy used, absorbed doses up to several tenths of Gy may be reached.

A large disadvantage of the LiF mini-TLDs is the toxicity of the material LiF for in vivo use (18, 19); 200 mg/kg by oral intake may kill a guinea pig. It is a well-known fact that LiF is very toxic, whereas $CaSO_4$ is not (19). The closely related material, $BaSO_4$, is a well-known contrast agent administered in diagnostic radiology. One way to overcome the problem with LiF toxicity, might be to encapsulate the mini-TLDs. Mini-TLDs encapsulated in plastic or placing the dosimeter in a catheter would take away any effect of signal loss or pH dependence.

CONCLUSIONS

We have found that the signal of the mini-TLDs varies with several factors. To be able to use mini-TLDs successfully in vivo, these parameters have to be taken into consideration before using the dosimeters. One of the most striking effects is the pH dependence. In tumor tissue, a pH of around 3 may be seen (compared to a pH of 5 in normal tissue), thus possibly causing a change in the TLD signal of up to 5%. Without corrections for supralinearity, an absorbed dose of 1 Gy gives an

excessive signal value a few percent. On the other hand, an absorbed dose of 10 Gy gives an increase in signal value of about 60%. Therefore, an estimate of the absorbed dose delivered to the tumor must be made, e.g. with a suitable dose planning system, before direct calculations of the absorbed dose are made with regard to the sensitivity enhancement. Thus we conclude that the mini-TLDs should be recalibrated after each measurement.

ACKNOWLEDGMENTS

We would like to thank professor Barry Wessels for initiating this work and M.Sc. Agneta Svedberg for help with the materials and giving good advice on the methods.

REFERENCES

1. Flower AF, Al-Saadi A, Harmer CL, McCready R and Ott RJ. Dose-response study on thyrotoxic patients undergoing positron emission tomography and radioiodine therapy. Eurp J Nucl Med 21:531-536, 1994.
2. Begent RHJ, Lane DM, Hope-Stone LD and Green AJ. Correlation of patient clinical response with dosimetry of 131-I labeled antibodies (Abstract). Anti Immunoconj and Radiopharm 7, No 1:73, 1994.
3. Wessels BW, Bach P and Quadri SM. Microdosimetric TLD measurements for tumor associated antibody therapy (Abstract). J Nucl Med 25:39, 1984.
4. Wessels BW, Vesella RL, Palme DF, Bercopec JM, Smith GK and Bradley EW. Radiobiological comparison of external beam irradiation and radioimmunotherapy in renal cell carcinoma xenografts. Int J Radiat Oncol Biol Phys 117:1257-1263, 1989.
5. Wessels BW and Griffith MH. Miniature thermoluminescent dosimeter absorbed dose measurements in phantom models. J Nucl Med 27:1308-1314, 1986.
6. Griffith MH, Wijewardene C and Wessels BW. Micro-TLD and autoradiographic measurements for radiolabelled antibody uptake in tumor bearing mice. Med Phys 12:672, 1985.
7. Griffith MH, Yorke ED and Wessels BW. Direct dose confirmation of quantitative autoradiography with micro-TLD measurements for radioimmunotherapy. J Nucl Med 29:1795-1809, 1988.
8. Demidecki AJ, Williams LE and Wong JYC. Calibration on thermoluminescent dosimeters (TLD's) for beta radiation. Anti Immunoconj and Radiopharm 4:52, 1991.
9. Heidorn DB, Ten Haken RK, Robertson PL and Buchsbaum DJ. A sensitivity study of micro-TLD for in vivo dosimetry of radioimmunotherapy. Med.Phys 18:1195-1199, 1991.
10. McKinlay AF. Thermoluminescent Dosimetry, pp 22-69, Medical Physics Handbook 5, Adam Hilger Ltd, England, 1981.
11. Robertson MEA. Identification and Reduction of Errors in Thermoluminescence Dosimetry Systems. DA Pitman Ltd, Weybridge, Surrey, England.
12. Horowitz YS. Thermoluminescence and Thermoluminescent Dosimeters, pp 89-172, CRC-Press, Vol. 1, 1984.
13. Demidecki AJ, Williams LE, Wong JYC, Yorke ED, Wessels BW, Strandh M and Strand S-E. Considerations on the calibration of small thermoluminescent dosimeters of beta particle absorbed dose in liquid environments. Med Phys 20(4):1079-1087, 1993.
14. Strand S-E, Strandh M and Spanne P. Electron microscopy and computed microtomography studies of in vivo implanted mini-TL dosimeters. Acta Oncologica 7/8:787-791, Vol. 32, 1993.
15. Strand S-E and Strandh M. Parameters to consider for measurements of absorbed doses in vivo

with mini-TLDs. CANCER No. 3:985-988, Vol. 73, February 1, 1994.
16. Piesch E. Application of TLD to Personnel Dosimetry in Applied Thermoluminescence Dosimetry edited by Oberhofer M and Scharmann A, pp 167-195, Adam Hilger Ltd, Bristol, England, 1981.
17. Hasman A and Groothedd RT. Comparison of some TLD dosimetry systems. British Journal of Radiology 16:637-640, 1973.
18. Oberhofer M and Scharmann A. Applied Thermoluminescence Dosimetry, pp 135-141, Adam Hilger Ltd, Bristol, England, 1981.
19. Sax NI. Dangerous Properties of Industrial Materials, 8th edition, van Nostrand Reinhold Cop, New York, 1992.

THE SIMDOS MONTE CARLO CODE FOR THE CONVERSION OF ACTIVITY DISTRIBUTIONS TO ABSORBED DOSE AND DOSE RATE DISTRIBUTIONS

Tagesson M, Ljungberg M and Strand S-E
Department of Radiation Physics
Lund University
S-221 85 Lund
SWEDEN

ABSTRACT

A generalized Monte Carlo code, SIMDOS, has been developed for the conversion of arbitrary activity distributions to absorbed dose and absorbed dose rate distributions. Geometries from cellular level to organs and total body can be simulated. The activity distribution can either be described analytically or be voxel-based. A density distribution, obtained either by CT or transmission SPECT, and matched with the activity distribution, is used in the Monte Carlo simulation. Photons and electrons are followed until they either escape the patient/phantom or drop below a predefined cutoff energy. To verify results from SIMDOS, absorbed fractions and S values have been compared with results from both the MIRD/ORNL phantom (incorporated in the code) and other published data. Absorbed fractions and S values for photons and electrons show good agreement with published data, typically within ±10-15%. On tissue and cellular levels (absorbed fractions and absorbed dose distributions), the results are within 10% of published data.

The SIMDOS code is generally applicable for internal dosimetry. It is possible to define arbitrary volumes mathematically and derive absorbed fractions and S values. An important application is the use in a treatment planning system for systemic radiation therapy. The code can also serve as a tool in converting activity distributions obtained from other imaging modalities, such as autoradiography and beta camera imaging, into absorbed dose distributions.

INTRODUCTION

In radionuclide therapy planning, an accurate knowledge of the absorbed dose to tumors and to other tissues is important, both for patient safety and treatment optimizing, but also when evaluating the radiobiological effect of the therapy. The absorbed dose to normal tissues may also set a limit to the maximum activity that may be administered. In radiotherapy, the dose planning should be within 5% of the actual absorbed dose delivered to the patient. In systemic radiation therapy (SRT), however, dose calculations to date have often been in terms of administered activity, "MBq/kg" or "MBq/m^2", instead of the absorbed dose, in Gy, to tumor and normal tissue.

We have previously suggested the use of quantitative SPECT for absorbed dose calculations (1, 2). Quantitative SPECT images reflect the activity distribution, within the limits of the spatial

resolution of the scintillation camera, and serve as a base for calculation of the absorbed dose distribution. By repetitive SPECT studies over several days, the biokinetics, the absorbed dose-rate and the cumulated absorbed dose can be obtained.

The MIRD formalism (3) is the most commonly used method for calculation of the mean absorbed dose to organs and other regions of the human body. Calculated absorbed fractions and S values (4, 5), as well as descriptions of computer codes with the possibility to include the biokinetics in the calculations (6-8) have been published since the late 1960s. The main limitation using the MIRD formalism is the assumption of a standardized geometry with no patient-specific activity distribution. This assumption is valid for radiation protection calculations in diagnostic imaging using radionuclides where the mean values of absorbed dose are sufficient for evaluating safety. In SRT, however, a more general method, that takes patient-specific parameters into account, is needed.

The definition of the S value is not restricted to standard geometries. Data published in MIRD Pamphlet no 11 (5) are, however, restricted to standardized masses, shapes and locations of the organs, obtained from the ICRP-23 publication "Reference Man" (9). The S values have also been calculated for a homogeneous activity distribution in the source organs. All electrons and β-particles are assumed to be locally absorbed.

The shape, location and mass of organs differ from human to human, and radiopharmaceuticals are rarely distributed uniformly in the organs. Also not routinely considered in traditional dose calculations are additional activity distributions, e.g. tumors. The use of the MIRD S values in SRT may therefore give significant discrepancies from real clinical situations. The absorbed dose calculation in radionuclide therapy therefore should be based on information regarding the individual patient organs, tumor localization and size.

METHODS FOR CONVERSION OF ACTIVITY TO ABSORBED DOSE

Several methods for conversion of activity distributions to absorbed dose distributions have been suggested in the literature. The use of analytical dose point kernels (10, 11) with a convolution procedure is straightforward, but generally has the disadvantage of not including inhomogeneities in the calculations. The kernel may, however, be rescaled to correct for the inhomogeneities if the convolution procedure is made in the spatial domain. Uncertainty in the absorbed dose still exists in the lung and bone regions due to differences in photon/electron cross sections and scattering properties for soft tissue, bone and lung.

The Monte Carlo technique (e.g. (12)) can be used to overcome these limitations. The method is numerical and solves stochastic problems by sampling from probability distributions. Applying the method to absorbed dose calculations allows accurate calculations of photon and electron transport over arbitrary boundaries and interfaces. The method also makes it possible to study nonmeasurable parameters, such as the energy distribution of photons and electrons at a certain points of interest, and the absorbed dose distribution in a specific volume.

PHANTOMS

Phantoms can be defined either mathematically or by digital images (obtained from specific computer codes or from imaging modalities, such as CT and MRI). For analytically described body phantoms, both body and organ surfaces must be defined. For a sphere or an ellipsoid, the outer boundary is defined analytically. A digital phantom consists of voxels of a certain size. The contents of the voxels can then reflect some parameter, such as the activity or the density.

Mathematical Phantoms

The program can read mathematical phantoms, such as the MIRD and Cristy-Eckerman pediatric phantoms (13) from ASCII-files. In addition to the standard organs, defined by MIRD and ORNL, extensions such as the separation of left and right organ, as for the lungs, kidneys, ovaries, testis and adrenals, have been implemented in the code. The skeleton has been separated into bone matrix and inactive and active bone marrow, where each skeletal part has its own fractional mass. The densities and atomic composition given for the MIRD and ORNL phantoms are used to make the comparison with published data. It is also possible to define new 'organs' with arbitrary positions, shapes and sizes.

Voxel-based phantoms

When calculating a 3-D absorbed dose distribution from SPECT, autoradiography, or beta camera images, the number of simulated decays are proportional to the count density in each of the voxels of the matrix. The density distribution in the volume is defined from a density map. In SPECT, this is obtained from X-ray Computed Tomography, Transmission SPECT, or from Compton scatter segmentation of the acquired SPECT data.

RADIATION TRANSPORT CODE

For a more detailed description of the sampling procedure and the photon simulation, see (14).

Scoring of Energy Depositions

For the calculation of absorbed fractions and S values from the mathematical phantoms, the absorbed energy in an organ/region is accumulated to an organ/region-specific vector, if the energy absorption point (x,y,z) is located within the mathematically described organ or region. For a voxel-based conversion, the absorbed energy matrix is recalculated if the energy deposition (x,y,z) occurred within the voxel. The program stores the absorbed energy distribution in a 3D absorbed energy matrix and writes data as an absorbed energy or absorbed dose distribution. An example with a density and activity map are shown in Figure 1. The radionuclide is ^{131}I.

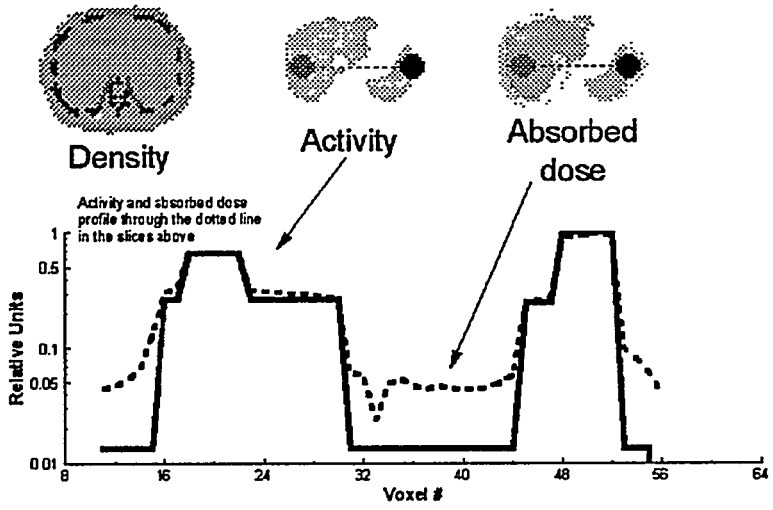

Figure 1. An example of an activity distribution (^{131}I) with two tumors, one in the liver and one in the spleen. From the upper left: density, activity and absorbed dose distribution. Both the activity and absorbed dose distribution are shown in the same diagram, despite the different units.

Photons

Figure 2 shows calculated S-value distributions inside the liver from three different activity distributions of ^{131}I in the MIRD phantom (left and right kidney and both kidneys). The arrows indicate the mean value of each distribution. The solid, middle arrow is close to the tabulated MIRD S(liver←kidneys) value of 3.1 x 10^{-6} Gy/MBq-h. The figure clearly shows that uniform distributions of activity result in a nonuniform distribution of absorbed dose, especially in large volumes close to the source activity. The figure therefore concludes that use of the mean S value may produce an inaccurate estimate of the absorbed dose in a particular volume.

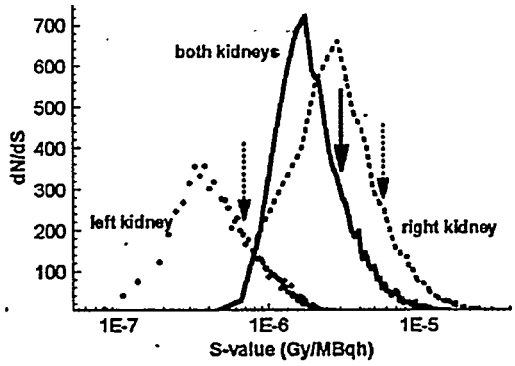

Figure 2. Distributions of S values to liver from uniform activity in the kidney(s) in the MIRD phantom. The arrows indicate the mean value of the three distributions.

Electrons

A model for simulation of electrons, based on fractional energy depositions, macroscopic steps, and the continuous slowing down approximation (CSDA) with small energy depositions along the electron track, has been implemented (15). The total mass stopping power is taken from ICRU-37 (16). Secondary δ-particles and bremsstrahlung photons are not sampled. An energy-dependent Gaussian function, based on mass scattering powers from ICRU-35 (17) is used to sample the angular distribution of the electron.

If the simulated geometry (mathematical phantom or voxel-based activity distribution) or the dimensions of organs/regions or voxels are smaller than or of the same order as the electron range, then explicit electron simulation needs to be performed.

Absorbed fractions as a function of sphere mass are shown in Figure 3 for monoenergetic electrons. The comparison with Siegel and Stabin (18) shows discrepancies typically less than 5%. In some points, however, the deviations are as much as 16%.

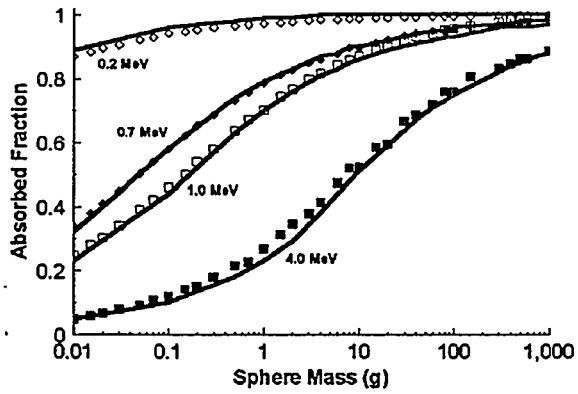

Figure 3. Absorbed fractions for monoenergetic electrons. Comparison with Siegel and Stabin (18) (solid lines).

Another simulation example is shown in Figure 4, in which a tumor (radius 0.66 cm) with a necrotic center (radius 0.22 cm) was simulated assuming a uniform distribution within the shell around the necrosis. Three beta emitting radionuclides, ^{90}Y, ^{32}P and ^{131}I, and three hypothetical radionuclides emitting monoenergetic photon with energies 15, 30 and 100 keV were simulated. For ^{131}I, the contribution from photons becomes significant at some distances (>0.8 cm) away from the center. The stochastic nature of the Monte Carlo simulation is seen, especially in the ^{131}I curve.

To further show the potential of the code, a simulation for spheres of cellular dimensions was made. In Figure 5 the calculated absorbed fraction in the cell nucleus from uniform activity in the cytoplasm is shown. Our results are within 30% of published data of Goddu et al (19).

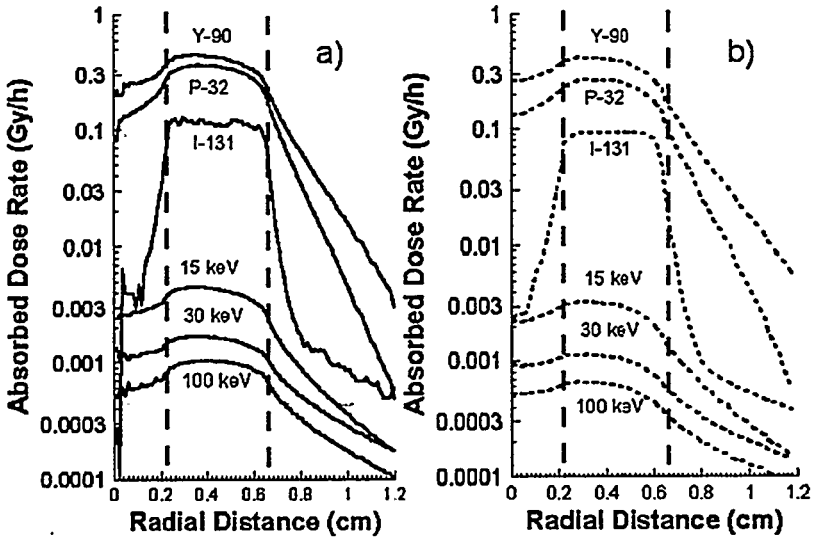

Figure 4. In a), radial absorbed dose rate profiles thru a tumor with a necrotic center are seen. The radius of the tumor is 6.6 mm and the necrotic center has a radius of 2.2 mm. Shown for three beta-emitters and three monoenenergetic photons. In b), data from Howell et al (20).

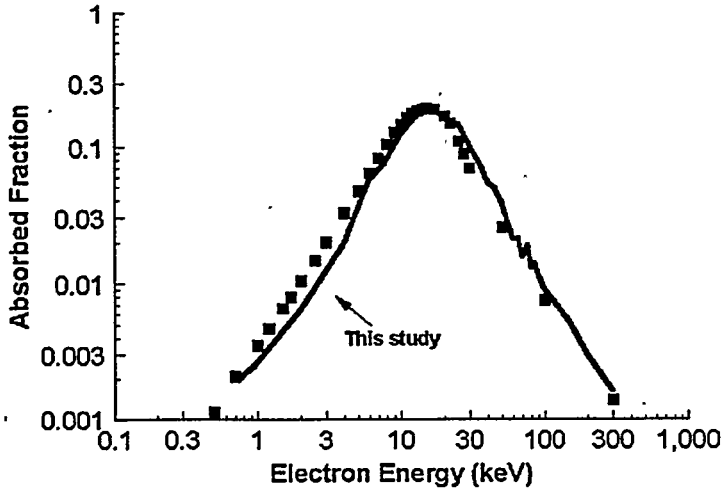

Figure 5. Absorbed fraction for monoenergetic electrons on the cellular level. A cell (radius 8 μm) and a cell nucleus is modeled (radius 6 μm). Comparison with Goddu et al (19).

PROGRAM FEATURES

Data necessary for a simulation include the decay scheme, the phantom definition and the interaction coefficients. For the MIRD or the ORNL phantoms, differential photon interaction coefficients and densities for the specific material composition are chosen. For a voxel-based activity distribution, the input files include the activity and density maps. Calculated results from any simulation include the absorbed fractions, S values, the number of photon and electron interactions in each organ. Additional calculations, such as 3D absorbed dose distributions, photon/electron energy spectra through chosen surfaces, and radial absorbed dose distributions, can also be included.

A specific simulation is divided into parts after which accumulated results are written to result files. Each of these subparts is divided into multiple batches for calculation of statistical errors, expressed as the standard deviation of the mean value. Below is a brief description of some program features.

1) Input files are available with single monoenergetic photons, electrons or a complete radionuclide decay scheme with a list of photon and electron energies and relative abundances. Decay schemes are at present taken from Snyder et al. and Weber et al. (21,22).

2) Bremsstrahlung emission is not included in the electron simulation. However, a complete bremsstrahlung spectrum (such as for ^{32}P and ^{90}Y (23)) can be simulated as a part of the particle emission from a decay. This omission may give inaccurate results at short distances (a few cm) from the decay.

3) Any elemental composition and density of the tissues/materials can be defined.

4) Calculation of photon and electron energy distributions may be made in various locations inside the phantom.

5) Absorbed fractions and S-values can be simulated in mathematical phantoms with the activity either as a point source or homogeneously or nonhomogeneously distributed within a sphere or an organ. Scoring of energy depositions in spherical shells and photon/electron energy spectra can be made to calculate dose point kernels, radial absorbed dose distributions, etc.

6) When simulating the MIRD or ORNL phantoms, lung and skeleton regions can be included, as well as soft tissue - an option useful when investigating scattering effects of lungs and skeleton in certain regions of the phantom.

7) A 3D distribution of the absorbed energy or absorbed dose can be calculated - which is optional when converting voxel-based phantoms, but available when converting analytically described phantoms. The 3D distribution could, for instance, be used for a dose-volume histogram calculation for the volume of interest.

Further work on the code includes:

1) Integrating the program in a radionuclide treatment planning system for systemic radiation therapy.

2) Increasing the accuracy in the calculation of the absorbed dose to the bone marrow. In the ORNL phantoms (13), the secondary electrons are simulated in a unique way, thus giving a better estimate of the absorbed dose to the active marrow. Similar type of simulation procedure will be implemented in this code.

3) More accurate sampling of the angular distribution for the secondary electrons emission in the photo absorption or pair production interaction. Presently, electrons are emitted in the same direction as the indicant photon direction prior to the interaction. Furthermore, bremsstrahlung photons should be emitted from the electron path and not as a part of the decay scheme.

Computional Conditions

The code is written in ANSI FORTRAN-77 using some of the VAX extensions included in most modern compilers. The program has been tested on a DEC AXP 3000/600 workstation with OSF/1 and on IBM compatible computers with Microsoft 32-bit Powerstation Compiler. Some benchmark examples: 1 million decays of ^{131}I in the MIRD liver without electron simulation takes approximately 2 hours on the workstation and 26 hours on a 486/33MHz PC. A point source with 200,000 emissions of 4 MeV monoenergetic electrons takes approximately 0.5 and 10 hours, respectively.

CONCLUSION

We have developed a very useful, generalized photon-electron Monte Carlo program for conversion of arbitrary activity distributions to absorbed dose and absorbed dose rate distributions. An activity map, obtained from, e.g. quantitative SPECT, autoradiography images, or a beta camera can be converted using a density map to give an absorbed dose rate map. Integration of these absorbed dose-rate maps over time gives the absorbed dose. The program plays an important role in our development of a treatment planning system for systemic radiation therapy.

ACKNOWLEDGMENTS

This work has been supported by grants from the Swedish Cancer Foundation, grant 2353-B94-08XAB, 3559-B95-02XBB, the Swedish Radiation Protection Institute #893.95, the Nilsson Foundation, the Medical Faculty of Lund University, the Royal Physiographic Society, the J&A Persson Foundation, the Kamprad Foundation and the Swedish Foundation for Medicine.

REFERENCES

1. Strand S-E, Jönsson B-A, Ljungberg M and Tennwall J. Radioimmunotherapy dosimetry - A review. Acta Oncol 33:807-817, 1993.
2. Strand S-E, Ljungberg M, Tennwall J, Norrgren K and Garkavij M. Radioimmunotherapy dosimetry with special emphasis on SPECT quantification and extracorporeal immunoadsorption. Med Biol Eng Comput 32:551-561, 1994.
3. Loevinger R and Berman M. A Revised Schema for Calculating the Absorbed Dose from Biologically Distributed Radionuclides: MIRD Pamphlet No. 1, Revised, The Society of Nuclear Medicine, New York, 1976.
4. Snyder WS, Ford MR and Warner GG. Estimates of Specific Absorbed Fractions for Photon Sources Uniformely Distributed in Various Organs of a Heterogeneous Phantom: MIRD Pamphlet No. 5, Revised, The Society of Nuclear Medicine, New York; 1978.

5. Snyder WS, Ford MR, Warner GG and Watson SB. "S," Absorbed Dose per Unit Cumulated Activity for Selected Radionuclides and Organs: MIRD Pamphlet No. 11, The Society of Nuclear Medicine, New York, 1975.
6. Watson EE, Stabin MG and Bolch WE. MIRDOSE Version 2, Oak Ridge Associated Universities, Oak Ridge,TN, USA, 1984.
7. Johnson TK. MABDOS: A generalized program for internal radionuclide dosimetry. Comput Programs Biomed 27:159-167, 1988.
8. Stabin M. MIRDOSE 3, Documentation Package, Radiation Internal Dose Information Center, Oak Ridge Institute for Science and Education, Oak Ridge, TN, 1994.
9. Report of the Task Group on Reference Man, ICRP Report 23, Snyder WS et al, 480 P, Pergamon Press, 1975.
10. Sgouros G, Barest G, Thekkumthala J, Chui C, Mohan R, Bigler RE and Zanzonico PB. Treatment planning for internal radionuclide therapy: Three-dimensional dosimetry for nonuniformly distributed radionuclides. J Nucl Med 31:1884-1891, 1990.
11. Giap HB. Development of a SPECT-based three-dimensional treatment planner for radionuclide therapy with iodine-131 (Thesis), The University of Texas, Houston, Texas, 1994.
12. Andreo P. Review: Monte Carlo techniques in medical radiation physics. Phys Med Biol 36:861-920, 1991.
13. Cristy M and Eckerman KF. Specific Absorbed Fractions of Energy at Various Ages from Internal Photon Sources I-VII, TM/8381/V1-V7, Oak Ridge National Laboratory, Oak Ridge, TN, USA, 1987.
14. Ljungberg M and Strand SE. A Monte Carlo program for the simulation of scintillation camera characteristics. Comput Programs Biomed 29:257-272, 1989.
15. Berger MJ. Monte Carlo Calculation of the Penetration and Diffusion of Fast Charged Particles, Methods in Computional Physics Vol. 1 Fernbach S, Rotenberg M pp 135-215, Academic, New York, 1963.
16. Stopping Powers for Electrons and Positrons, ICRU Report 37, 271 P, 1984.
17. Radiation Dosimetry: Electron Beams with Energies Between 1 and 50 MeV, ICRU Report 35, 157P, 1984.
18. Siegel JA and Stabin MG. Absorbed fractions for electrons and beta particles in spheres of various sizes. J Nucl Med 35:152-156, 1994.
19. Goddu SM, Rao DV and Howell RW. Multicellular dosimetry for micrometastases - Dependence of self-dose versus cross-dose to cell nuclei on type and energy of radiation and subcellular distribution of radionuclides. J Nucl Med 35:521-530, 1994.
20. Howell RW, Rao W, Sastry DV and Kandula SR. Macroscopic dosimetry for radioimmunotherapy: Nonuniform activity distributions in solid tumors. Med Phys 16:66-74, 1989.
21. Snyder WS, Fors MR, Bernard SR, Dillman LT, Eckerman KF, Poston JW and Watson SB. ICRP 38: Radionuclide Transformations, Energy and Intensity of Emissions, Pergamon Press, New York, 1983.
22. Weber DA, Eckerman KF, Dillman LT and Ryman JC. MIRD: Radionuclide Data and Decay Schemes, The Society of Nuclear Medicine, New York, 1989.
23. Simpkin DJ, Cullom SJ and Mackie TR. The spatial and energy dependence of bremsstrahlung production about beta point sources in H_2O. Med Phys 19:105-114, 1992.

MABDOSE: A COMPUTER PROGRAM FOR THE CALCULATION OF DOSE

Johnson TK, McClure DL, McCourt SL, Andl GJ, Berman BD, Koss J and Newman FD
University of Colorado Health Sciences
Denver, Colorado 80262

ABSTRACT

MABDOSE is a computer program that offers a unique computation tool for the calculation of internal radionuclide dose. The software integrates time-activity data modeling functions with the computation of 'S' values into a seamless environment. Additionally, it allows the interactive definition of arbitrary sources and targets of radioactivity (representative of solid tumors) within a selected lattice target geometry.

The software makes use of an intuitive graphical interface that runs under the Windows operating system. An operator initially selects from a collection of check boxes those source organs for inclusion in the current patient dosimetry estimate. Right-clicking on a "checked" source organ pops-up a spreadsheet containing the time-activity curve data associated with that source organ. Data may be entered and erased.

The operator selects a 3-D lattice target geometry, along with a nuclide. If a tumor has been designated a source organ, the operator locates the tumor within the selected target lattice using sequential coronal and transverse projections of the target.

The operator selects one of four techniques to compute cumulated activities for each checked source organ. A Monte Carlo simulation of radiation transport is then completed to obtain organ dose estimates. The program is currently being validated against the published MIRD 11 'S' tables. The system has the ability to provide greater precision of organ dose estimates, in addition to functioning as a general dosimetry tool. The computationally intensive simulation of radiation transport can be offloaded onto a parallel processor array, achieving a linear decrease in computation time.

RADIOIMMUNOTHERAPY - THE DOSIMETRY PROBLEM

The Medical Internal Radiation Dose (MIRD) methodology constitutes the traditional method for performing internal radionuclide dosimetry. This methodology has proved adequate for estimating doses to normal organs since its initial formulation by Snyder et al [1]. Until recently, the goal of Nuclear Medicine has been the imaging and treatment of regular human organs. Questions of internal dosimetry that inevitably arose as a result of this goal could be answered adequately using the practical implementation of the MIRD methodology found in MIRD pamphlet 11 [2].

In contrast, the goal of current radioimmunotherapy (RIT) trials is to deliver therapeutic amounts of radioactivity to a cancer. This cancer is, by definition, of arbitrary shape and location within the body. Although the MIRD methodology itself is completely general, its practical implementation (as embodied in MIRD Pamphlet 11) is deficient in that it does not account for arbitrary sources and

targets of radiation within the human body. Consequently, individuals providing dose estimates have been forced to use approximations of widely varying accuracy depending on patient specific circumstances.

The second problem with the traditional MIRD methodology is its predominant use in *diagnostic* Nuclear Medicine. By definition, the term diagnostic defines a range of activities that are not expected to have a therapeutic effect on the human body. The goals of RIT, however, are precisely to deliver a therapeutic effect. Because of imperfect specificity on the part of the antibody to localize at a cancer site, normal organs can be expected to receive possibly toxic amounts of radiation dose. The use of standard mathematical phantoms belie the fact that individuals differ from mathematical phantoms, sometimes substantially. These differences are uniformly treated as insignificant when diagnostic amounts of radioactivity are used. This assumption may not be warranted when using therapeutic amounts of radioactivity in RIT. It is readily seen that the current system, while not necessarily broken, is in need of some modifications to make it flexible enough to answer the dosimetry questions posed by modern day advances in molecular medicine.

One Solution: Recalculate Absorbed Fractions

One solution to the dosimetry problem is to allow for the introduction of arbitrary sources/targets of radioactivity, and recalculate the absorbed fractions by simulating radiation transport. The Monte Carlo method, whereby one simulates the physical decay of radioactivity and builds up a statistical answer with respect to dose distribution, is one alternative that can be adapted to estimate tumor dose. MABDOSE is a program that exploits this approach to providing dose estimates. It provides for the introduction of an arbitrary lattice serving as the target geometry. The program currently selects a subset of lattice voxels to serve as the radiation source from which Monte Carlo histories are started.

MABDOSE DESCRIPTION

A Brief History

The MABDOSE program [3-5] was originally created to allow the interactive definition of arbitrary sources and targets of radioactivity (representative of solid tumors) within the adult male Reference Man geometry. In contrast with other programs, MABDOSE integrated the calculation of cumulated activity into the dose computation environment. The program's user interface was written in Fortran and Intel assembler language for a Texas Instrument's Professional microcomputer, and was specific to that piece of hardware. Data was input during an interactive modeling session, and subsequently uploaded to a Cray Y-MP supercomputer for simulation of radiation transport. The transport code executing on the Cray was also written in Fortran. Simulation results were downloaded and combined with the input data to provide a standard dosimetry printout. The hardware dependence of MABDOSE meant that the program was not portable to other computer platforms. General distribution of the program, and acceptance by the dosimetry community, was viewed as being dependent on significant hardware advances in computer speed, memory, and storage capacity.

Because of its size, MABDOSE had become extremely difficult to maintain. Advances in computer language design, development tools and libraries, made it attractive to consider the possibility of rewriting the program in an object oriented language. At the same time, the user interface could be updated to comport with current expectations, making for an interface better suited to the data manipulation necessary for internal dosimetry. The task of rewriting MABDOSE was begun in 1990 and continues to this day. The current program has an executable size of approximately

3 Mbytes and consists of approximately 10,000 lines of C++ code using the Borland Object Windows Library application framework.

MABDOSE Data Structures

MABDOSE is composed of six principle objects that represent instances of a Patient class, a TargetGeometry class, an Isotope class, a Modeling class, a Simulation class, and a Dose class. All objects are created dynamically (i.e. at runtime rather than compile time) from within a MABDOSE dosimetry session. Each class is outlined below. Additionally, the TargetGeometry class contains a method for tumor location that warrants separate discussion.

Patient Class

The **Patient** class represents the fundamental data abstraction of a patient's time-activity data. It encapsulates fundamental identifiers that make the patient unique: name, number, sex, radiopharmaceutical, isotope infused, activity infused. This object can loosely be equated with the base worksheet displayed when the program opens.

Target Geometry Class

The **Target Geometry** class corresponds to a three-dimensional lattice that is created from user selections within a popup dialog window. The operator selects from among male and female versions of six Reference Man phantoms, creating a "virtual" phantom. Lattice resolution is determined by the user, and limited only by system RAM. The largest Reference Man phantom is the adult male, with dimensions of 170 cm x 40 cm x 20 cm. If one byte is devoted per voxel, 1 cm^3 voxel resolution requires 170 x 40 x 20, = 136,000 bytes of memory. In contrast, 1 mm^3 voxel resolution requires 1700 x 400 x 200, = 136 Mbytes of memory. These limits represent the two extremes between which dose resolution appears to be adequate.

The target lattice is traversed, with the coordinates of each voxel tested against a set of mathematical phantom definitions codified in Cristy et al [6]. When a voxel satisfies the equations defining a given organ system, the voxel is assigned an index representing that organ. Each voxel in the lattice therefore contains a single integer that identifies the organ system of which the voxel is a member, i.e. the target lattice is segmented. The target lattice is stored to disk, with the file name coded to represent the phantom type (newborn, 1 yr old, etc), phantom sex, and x/y/z resolution. In the event that an identical phantom is used for subsequent dosimetry sessions, recalling a stored target lattice reduces the time necessary to create the **Target Geometry** object. Specification of the **Target Geometry** class in terms of a lattice means that any other three-dimensional lattice, such as that from a series of CT or MRI scans, may be loaded into the dosimetry program.

Isotope Class

The **Isotope** class encapsulates the physical decay properties of an isotope. The dynamic allocation feature of C++ allows a variable list of penetrating radiations and nonpenetrating radiations to be composed at run-time. In fact, each **Isotope** object is composed of instances of two base class types called ***discrete_radiations*** and ***continuous_radiations***. The former are represented by alpha particles, electrons and photons; the latter by positrons and beta particles. ***Discrete_radiations*** have a *size* data member, and variable arrays *energy* and *abundance*. ***Continuous_radiations*** have *max_energy* and *mean_energy* arrays in place of the single *energy* array. All arrays are sized and filled at run time when a user selects a specific isotope.

Modeling Class

The **Modeling** class encapsulates the methods for assigning cumulated activities to each identified source organ. To date, four techniques are offered to accomplish this. The first three are simple curve fitting routines: Riemann integration, Trapezoidal integration, and monoexponential curvefitting. Selecting a method provides a cumulated activity for each identified source organ. The curve fitting method is subsequently stored along with the cumulated activity. In the case of monoexponential fitting, the slope (rate of activity decrease) is also stored with the individual source organ cumulated activities.

The fourth technique is mathematical modeling. The model is solved using eigenvector analysis. Solutions to a set of linear differential equations are obtained by sums of exponentials, the time-activity curve for each source organ is therefore represented by a sum of exponential terms. The eigenvalues that comprise the solution to the set of simultaneous differential equations represent the time dependent exponential coefficients; the eigenvectors coupled with initial boundary conditions give the exponential amplitudes. Each source organ function is integrated numerically using a Newton-Raphson integration. The model is stored for future recall.

Tumor Location Method

Tumor location is more properly a method of the **Target Geometry** class than an object unto itself. This method allows, in the event of a tumor declaration, to reassign the organ indices stored within the **Target Geometry** object. It can consequently be viewed as a graphical editor that allows the editing of the target geometry.

Simulation Class

The **Simulation** class has two principle data members, a dose lattice and an array of sources. The dose lattice has dimensions equal to that of the target geometry object selected. Each element of the dose lattice is a floating point counter. The counter holds and updates the accumulated energy deposited within that element's lattice location.

Each member of the source array corresponds to one of the selected source organs, and is itself a vector container. Each container is constructed of elements representative of voxels in the target lattice. Each container element consists of an ordered integer triplet corresponding to the x/y/z location of a voxel in the target lattice (Figure 1).

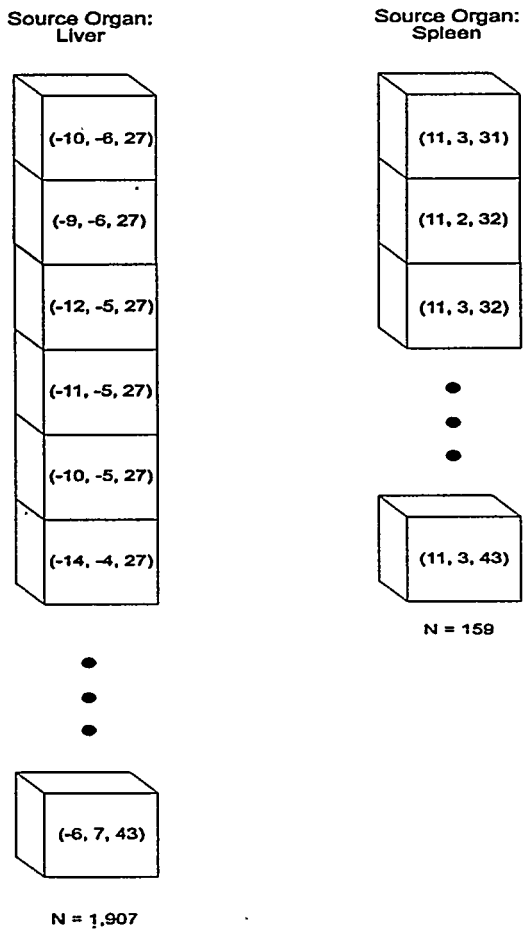

Figure 1. Schematic illustrating the construction of Source Organ vector containers for the Liver and Spleen.

The vector containers are composed dynamically at run time, immediately prior to the simulation of radiation transport. The target lattice is traversed for each declared source organ, searching for indices that match the source organ under construction. When a target voxel index matches, the x/y/z location of the voxel is added to the source organ vector container.

The principle method contained in the **Simulation** class is the radiation transport simulation itself. Currently, only penetrating radiations are simulated (photons with energy >= 10 keV), but electron simulation will be added in the future. This method selects a starting coordinate by: 1) counting the number of elements contained in the source organ column vector; 2) sequentially calling a pseudo-random number generator giving a distribution between 0 (inclusive) and 1 (exclusive); and 3) multiplying the number of elements by the returned random number to yield the container element whose ordered integer triplet will serve as the random starting coordinate. The **Simulation** object currently calls the random number generator three more times in order to select an arbitrary starting point from within the determined voxel. This additional overhead of three function calls is probably not warranted for the gain in statistical accuracy, and will be incorporated into a "simulation parameters" grouping of radiobuttons in the future (see below).

Other methods accomplish the typical features required to simulate radiation transport: 1) accessing a table of interaction coefficients appropriate for the photon's current energy [7]; 2) transporting the photon, subsequently sampling the probability distribution for a given interaction type; 3) depositing the energy at the current location if a photoelectric interaction occurs; sampling Klein-Nishina if a Compton interaction occurs (depositing scattered electron energy at interaction site, reducing the photons energy, selecting a new direction); simulating pair-production if appropriate (local deposition of electron energy; local deposition of positron energy - 1.02 MeV; tracking of two 511 keV photons in opposite directions).

Each energy in the selected isotope's spectrum undergoes the same number of histories, currently 50000. Upon completion of the histories, the lattice is multiplied by the energy's percent abundance. The results are then added into a second dose lattice that serves to accumulate the energy deposition pattern from each spectral emission.

Dose Class

An instance of the **Dose** class is constructed using the results of the **Simulation** object. The primary data member is a one dimensional array whose length equals the number of target organs. The dose accumulator lattice is subsequently traversed. Each voxel in the dose lattice is checked against the index stored in the **Target Geometry** lattice to determine which target organ the voxel belongs. The appropriate target organ element is updated by the amount stored in the dose lattice voxel. Upon completing the traversal of the dose lattice, the results are increased by the contributions from nonpenetrating radiations (electrons, alpha particles, beta particles, photons less than 10 keV). Organs selected as sources of radioactivity have corresponding contributions depending on one of three types: regular organs distribute the nonpenetrating component uniformly and homogeneously over the source organ; organs having a lumen whose contents are the pharmaceutical target divide the absorbed dose by 2; mass fraction composite organs (bone marrow) use a lookup table to determine the mass of source organ in a particular organ space, and ascribe the absorbed dose based on the ratio of (source organ mass)/(organ space). For example, the mass of active bone marrow in the clavicles of the adult male reference phantom is 10.3 g. The mass of the clavicle space itself is 76.5 g. The activity assigned to the marrow, and hence assigned as local deposition, is (Activity $_{Clavicle}$) * (Red Marrow mass $_{clavicle}$) / (Clavicle mass), = (Activity $_{Clavicle}$) * 0.135.

MABDOSE - Current Status

The rewrite of MABDOSE began in the winter of 1990-1991. The user interface was designed to run under the Windows operating system, and make use of an intuitive graphical interface that users have come to expect from modern software. In addition to the input of basic patient data, the user selects from a collection of check boxes those source organs for inclusion in the current patient dosimetry estimate. Right-clicking on a "checked" source organ pops-up a spreadsheet that contains the time-activity data for that source organ. In Figure 2, Tumor 1 has been selected as a source organ for patient "Tumor Test", presumably based on a knowledge of radioactivity distribution provided by Nuclear Medicine scintigrams or biopsy. Right-clicking the Tumor 1 source organ pops up the associated spreadsheet containing the tumor's time-activity data. Consistent with the functioning of all current spreadsheets, data may be entered and erased dynamically. The collected time-activity curve spreadsheets represent the main data set from which all subsequent dosimetry calculations proceed.

Selecting **Targ Geom** from the main menu selects the Reference Man phantom desired for dose estimates (Figure 3). Male and female versions of the 6 Reference Man phantoms are provided with resolution of 1 cm^3. The user is given the option of creating higher resolution data sets. Although only the Reference Man phantoms are currently selectable, efforts are currently underway to incorporate

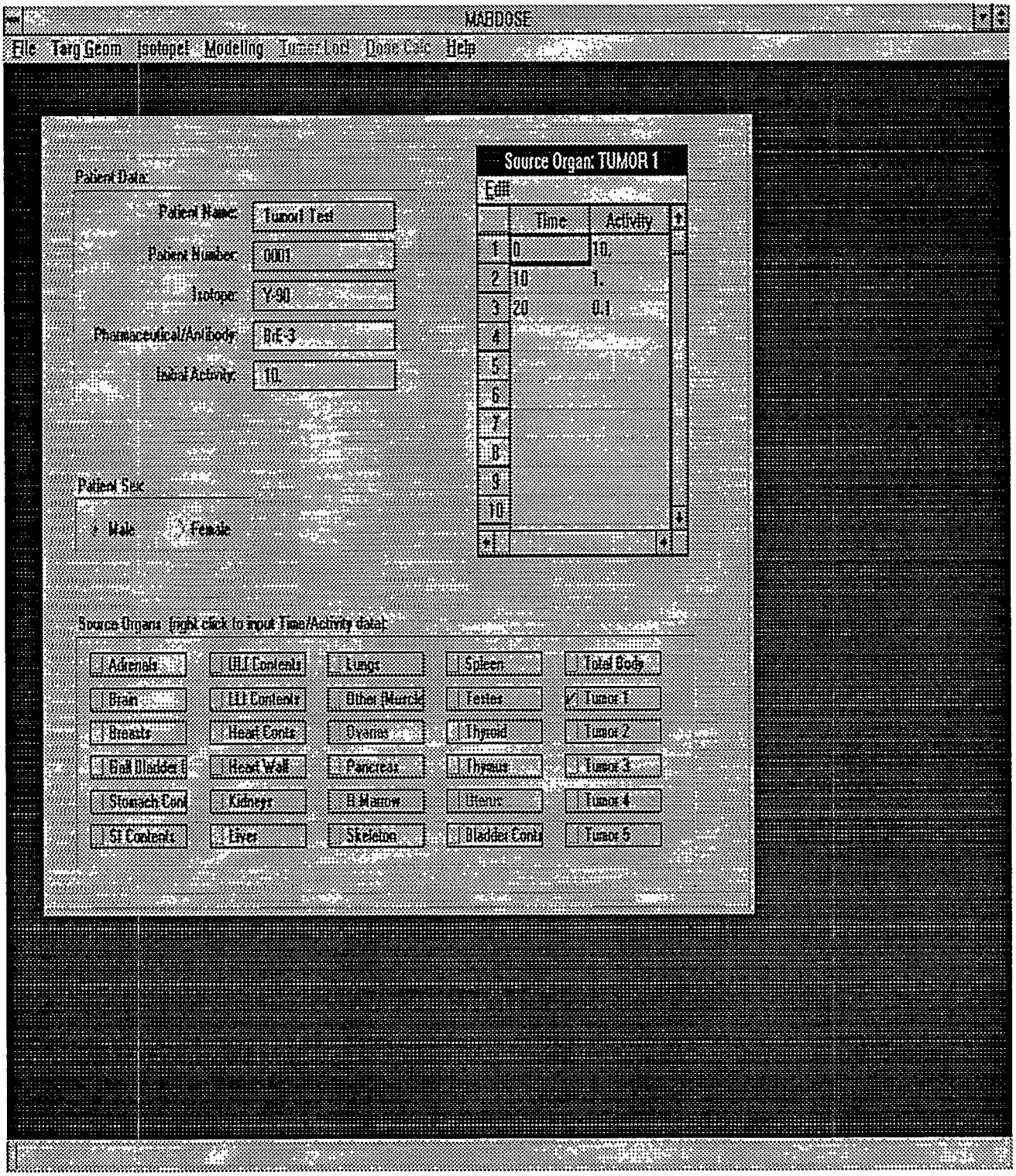

Figure 2. Screen capture of the base MABDOSE window. In addition to descriptive patient data, "Tumor 1" has been declared a source organ. Right-clicking on the "Tumor 1" check box pops-up a spreadsheet to contain the time-activity data associated with this source organ.

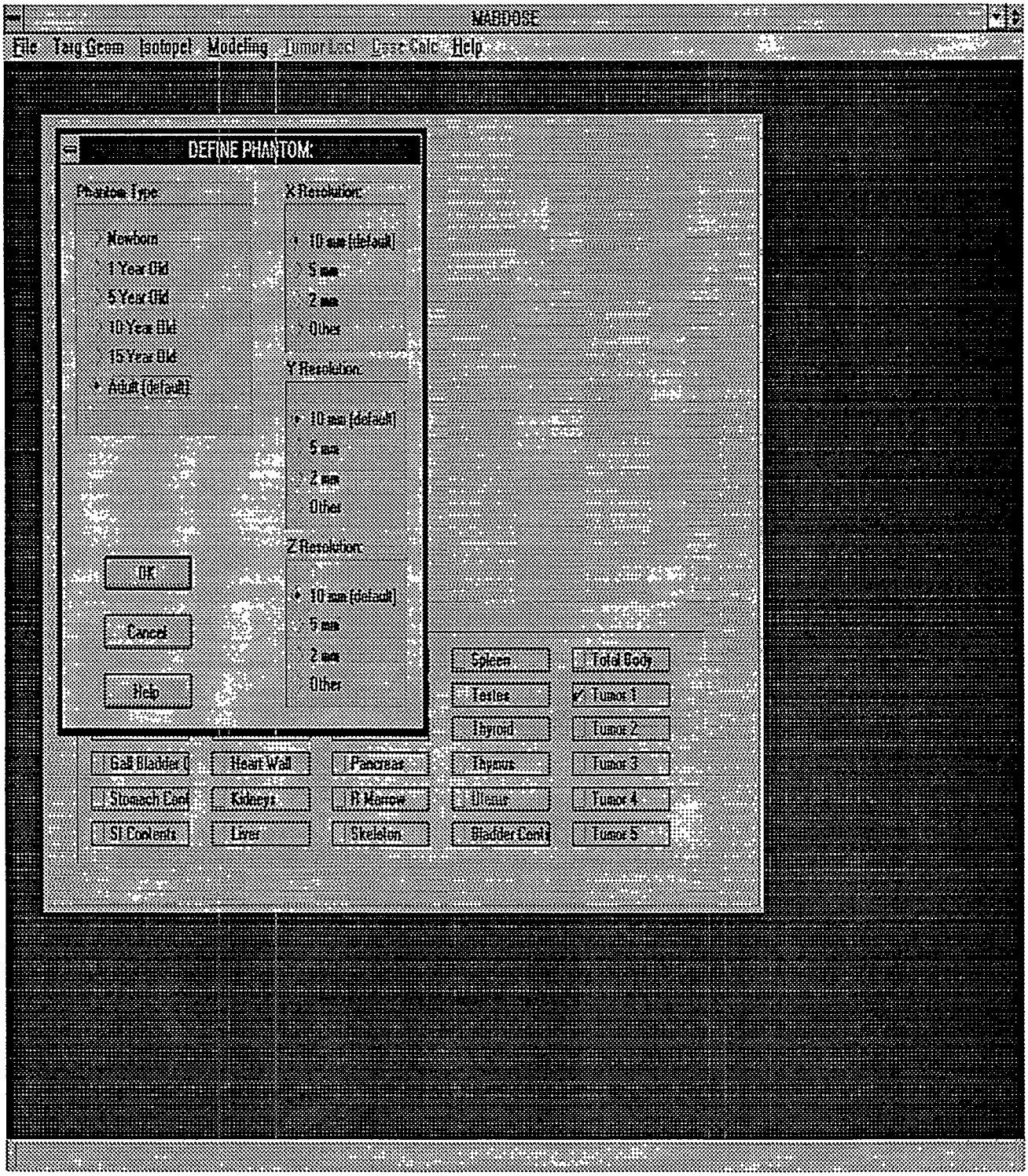

Figure 3. Screen capture displaying the Phantom Definition pop-up window. Male and female versions of six Reference Man phantoms can be selected. X, y, and z axis voxel resolutions are selected independently. Available resolutions are 10 mm, 5 mm, 2 mm, and user defined.

several digital human data sets.

Selecting **Isotope!** from the main menu pops up a window displaying a scrollable list of isotopes derived from the DLC-80 database of Kocher [8]. Selection of any one pops up that isotope's spectrum in an adjacent List Box (Figure 4). Clicking on the "Select" button uses that decay spectrum in the dosimetry estimate.

Selecting **Modeling** from the main menu offers the user one of four techniques to compute cumulated activities for each checked source organ: Riemann integration; trapezoidal integration; mono-exponential curve fitting; and mathematical modeling. The curve fitting routines are straightforward, displaying the raw data, fitted-points (where appropriate), and the cumulated activity using the public-domain "gnuplot" plotting program (Figure 5).

The mathematical modeling routine is similar to that demonstrated originally on the Texas Instruments Professional. Representations of the selected source organs are displayed as rounded rectangles, and the user positions them using a standard drag-and-drop interface. Models representative of the movement of radioactivity through the body are then created by double clicking within a box to establish the start of a kinetic pathway; double clicking within a second box terminates the pathway. An edit field is associated with each created pathway. The user is queried for initial estimates of organ rates, creating a series of simultaneous differential equations that denote the mathematical model. The set of differential equations defined are solved using an eigenvalue/least squares optimization routine. The equations are integrated and cumulated activities provided for each of the selected source organs. Database facilities allow the storage and recall of previously validated models.

Provided a tumor has been declared a source organ, the **Tumor Loc!** menu item becomes active. The operator must locate the tumor within the selected target geometry before proceeding to a calculation of dose. Initially, a coronal projection of the selected target geometry is displayed on the left side of the screen (Figure 6). The operator positions a mouse cursor at the height of the tumor. The transaxial slice associated with that height is composed on the right side of the screen. The operator is queried to locate the tumor's center with the mouse. A popup dialog box next queries the operator for the tumor's radius, assuming spherical geometry. Upon input, the program accesses the target lattice voxels enclosed by the tumor's boundary and changes the index to represent tumor.

Provided a target geometry and isotope have been selected, and provided that cumulated activities exist for all declared source organs, the **Dose Calc** menu item becomes active. MABDOSE currently performs a Monte Carlo simulation of photon transport for photon energy deposition, and assumes local energy deposition for all nonpenetrating radiation. Dose is calculated for a vector of approximately 70 target organs. The vector of dose values is displayed in a tabular array, with three columns (Figure 7). The columns correspond to the target organ system name, dose for the administered activity, and dose per unit administered activity. Two additional dose calculation options are planned. These are: 1) reading in the MIRD 11 S values from disk, obviating the need for performing a simulation at all; and 2) simulating both photon and electron transport.

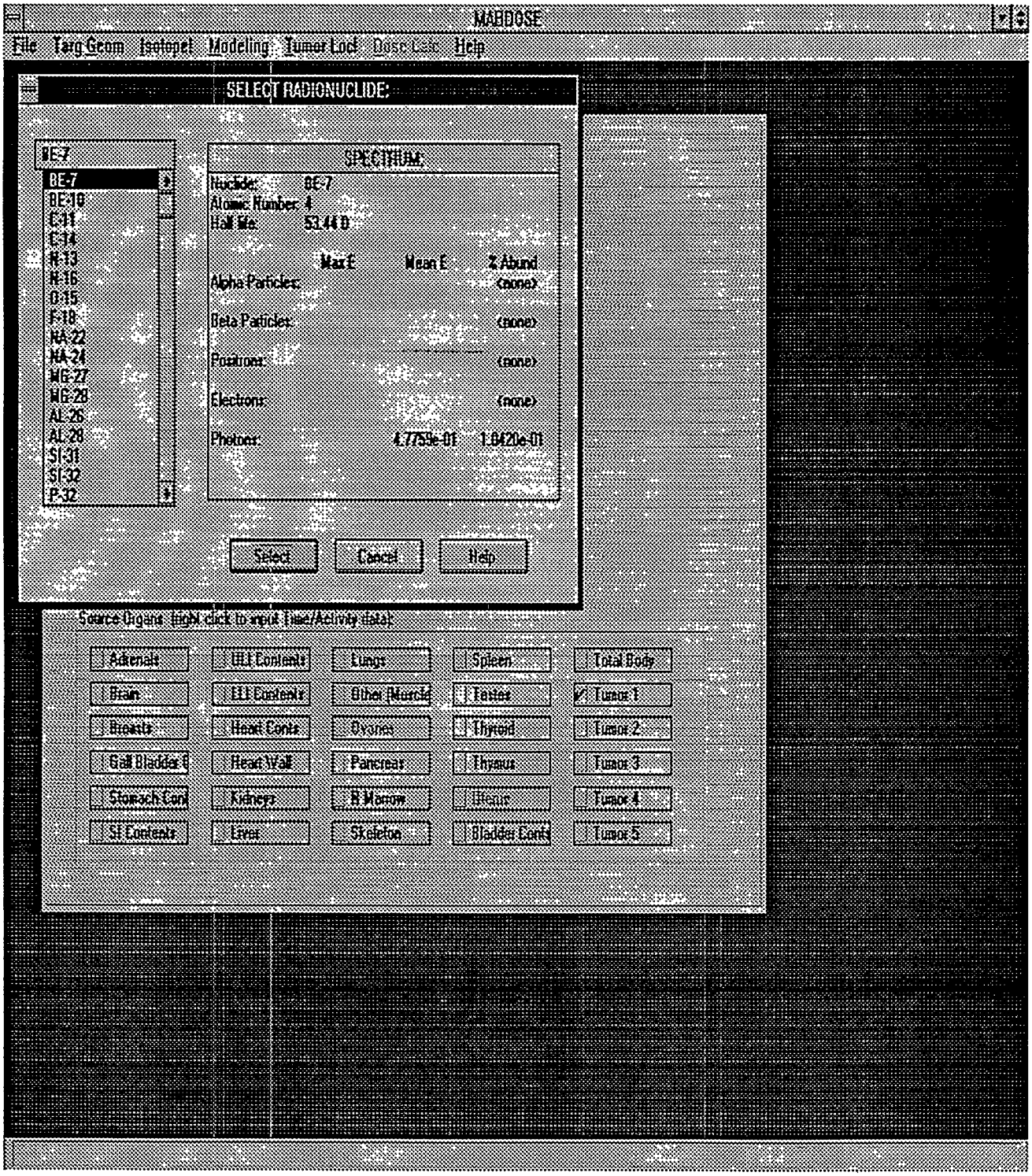

Figure 4. Screen capture displaying the Isotope Selection pop-up window. A scrollable list box of isotopes is presented on the left side of the window; the spectrum of a selected isotope is displayed on the right.

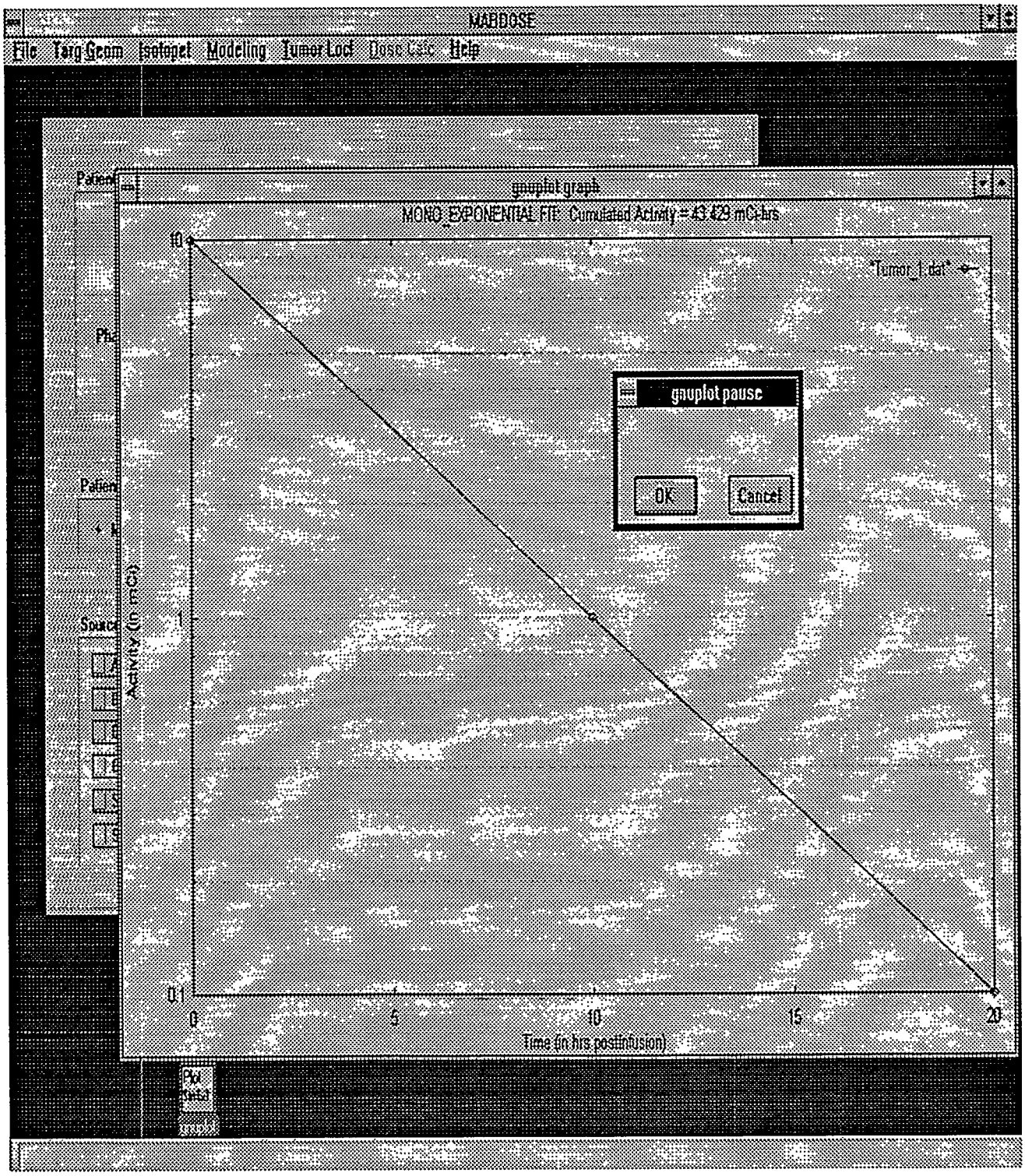

Figure 5. Screen capture displaying the calculation of cumulated activity for the "Tumor 1" source organ after fitting the time-activity data set with a mono-exponential function.

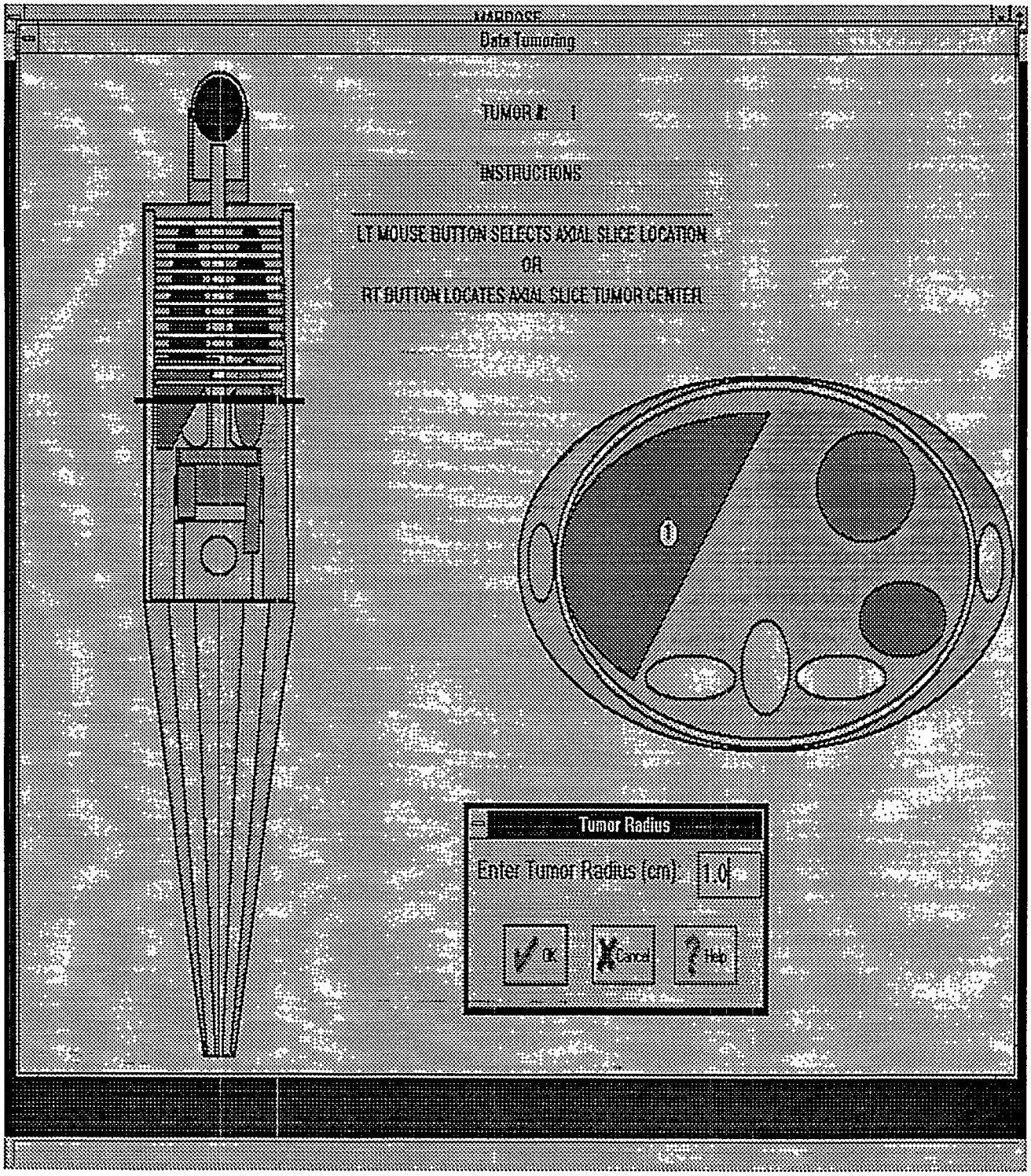

Figure 6. Screen capture displaying the interface for locating a tumor. The user locates a mouse cursor on the coronal projection of the Reference Man target geometry. The transverse slice correspondent with this height is composed adjacent. Locating the tumor on the transverse slice fixes the tumor with respect to the Reference Man geometry. Upon entering a tumor radius, MABDOSE redefines the target geometry voxels that compose this spherical space to be tumor.

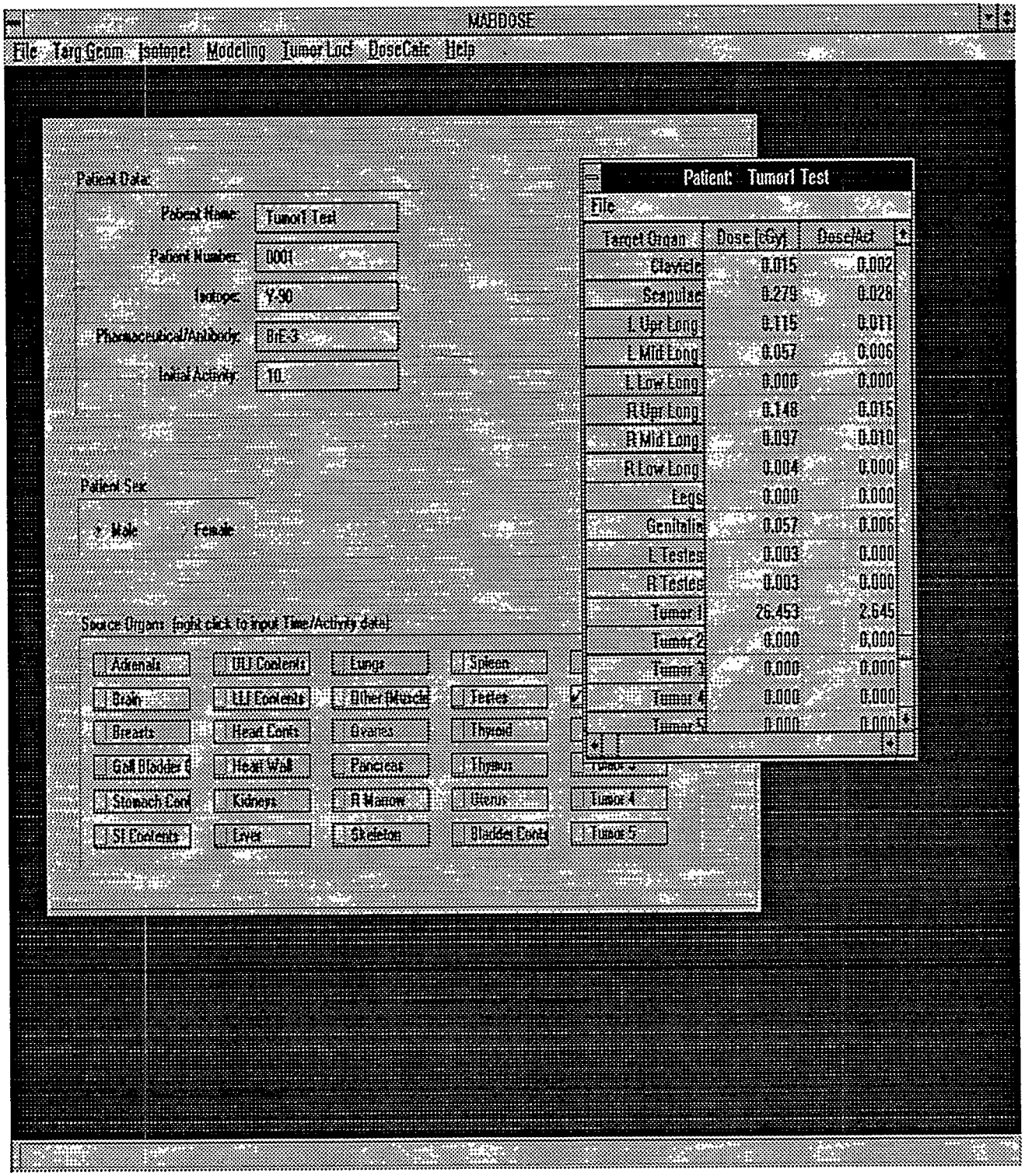

Figure 7. Screen capture showing target organ dose output. The previous user selection of the isotope Be-7 overrides the isotope Y-90 displayed in the "Isotope" edit field (seen on the underlying base MABDOSE window). This allows for "what-if" scenarios assuming antibody kinetics remain constant with different isotopic labels (e.g. a diagnostic tracer of In-111; a therapeutic agent of Y-90).

MABDOSE - Future Developments

Although the design of MABDOSE addresses the inclusion of tumors into the Reference Man phantoms, significant deviations from these geometries require the substitution of a patient's own anatomy. Substitution of a patient's own anatomy however, requires that surfaces corresponding to an individual patient's major organs be composed. This problem - commonly referred to as the image segmentation problem - is not an easy one to solve. A parallel research effort involving a neural network solution is currently under study at the University of Colorado Health Sciences. With respect to the major organs, the method appears extremely favorable [9]. The casting of the radiation transport problem into a three-dimensional matrix means that the result of a successful segmentation could be plugged into the current MABDOSE software: a different **Target Geometry** "object" would be substituted for the current lattice representations of the Reference Man series of mathematical phantoms.

The radiation transport code is being rewritten to take advantage of a collection of parallel microprocessors to decrease computation time. Monte Carlo solutions can be extremely time consuming - a factor which may prove prohibitive in radioimmunotherapy. Restrictions on calculation time are necessary because a human anti-mouse antibody response can develop within 7-14 days of an initial diagnostic infusion, effectively changing a patient's antibody kinetics and negating the utility of a diagnostic study for therapeutic planning. Parallel processors provide an inexpensive solution to achieving the computation power necessary to arrive at dosimetry estimates in an acceptable time interval. The computationally intensive simulation of radiation transport can be offloaded onto an array or network of microprocessors, achieving a linear decrease in computation time.

Various updates to the user interface are also planned. These include: (1)adding information boxes that the computer is performing an action during source organ creation and simulation. In place of an hourglass icon, a gadget object would communicate to the user the source organ currently being simulated, and the estimated time necessary to complete the simulation; (2)placing the values of the various objects into the status bar. Currently the user must remember the specific target geometry (i.e. reference phantom) selected, the isotope selected, whether time-activity data has been entered for each checked source organ, and whether cumulated activities have been generated. The status bar would display the current state of the MABDOSE session, so that a user working on multiple dosimetry estimates would not have to open up subsequent windows in order to determine the current values of these objects and (3)incorporating a Print menu item with the project. Initially this is planned for the **Dose** object only, for hard copy of dosimetry results. This would be extended in future to other objects, although the stored model and patient files can currently be read with any text editor and transferred to a printer.

SUMMARY

The MABDOSE program offers a unique computation tool for the calculation of internal radionuclide dosimetry. The goal of this application is to construct a definitive internal radionuclide dosimetry system that is capable of yielding dosimetry estimates appropriate for monoclonal antibodies currently undergoing clinical trials throughout the country. The software integrates the functions describing the time course of radioactivity in defined source organs, and incorporates the cumulated activity with S values into an integrated environment. The program is currently being validated against the published MIRD 11 S tables. The system will provide greater precision of tumor dose estimates, as well as functioning as a general dosimetry tool for use in radiation dosimetry.

ACKNOWLEDGMENTS

This work was supported in part by NIH Grant No R29CA59026-02.

REFERENCES

1. Snyder WS, Ford MR and Warner GG. Estimates of Specific Absorbed Fractions for Photon Sources Uniformly Distributed in Various Organs of a Heterogeneous Phantom, MIRD Pamphlet No. 5, Revised. New York: Society of Nuclear Medicine. 1975.
2. Snyder WS, Ford MR, Warner GG and Watson SB. "S": Absorbed Dose per Unit Cumulated Activity for Selected Radionuclides and Organs, MIRD Pamphlet No. 11. New York: Society of Nuclear Medicine. 1975.
3. Johnson TK. MABDOS: a generalized program for internal radionuclide dosimetry. Comput Methods Programs Biomed 27:159-167, 1988.
4. Johnson TK and Vessella RL. On the application of parallel processing to the computation of dose arising from the internal deposition of radionuclides. Comp Phys 3:69-72, 1989.
5. Johnson TK and Vessella RL. On the possibility of 'real-time' Monte Carlo calculations for the estimation of absorbed dose in radioimmunotherapy. Comput Methods Programs Biomed 0-31
6. Cristy M and Eckerman KF. Specific Absorbed Fractions of Energy at Various Ages from Internal Photon Sources. I. Methods. ORNL/TM-8381/V1. April, 1987.
7. Roussin RW, Knight JR, Hubbell JH and Howerton RJ. Description of the DLC-99/HUGO Package of Photon Interaction Data in ENDF/B-V format. Oak Ridge National Laboratory (ORNL/RSIC-46). December, 1983.
8. Kocher DC. DLC-80/DRALIST Data Package (RSIC Data Library DLC-80, Oak Ridge National Laboratory.
9. Koss JE, Newman FD, Johnson TK and Kirch DL: Abdominal organ segmentation using a hopfield neural network. Proceedings, Symposium on Computer Assisted Radiology, Denver, CO, June 6-9, 1996.

SOME ISSUES IN THE USE OF THE REMAINDER OF THE BODY S-VALUE CORRECTION

Stabin MG and Sparks RB
Oak Ridge Institute for Science and Education
Radiation Internal Dose Information Center
P.O. Box 117
Oak Ridge, TN 37831-0117

ABSTRACT

In 1973, Cloutier et al. developed a method for correcting absorbed dose equations to account for activity in the total body with residence times in the "remainder of the body" (total body minus a variable number of specified source organs). To provide accurate use of the equations, this correction should always be made when calculating internal dose estimates; the magnitude of the correction will vary depending on the problem. This correction method is based on the assumption that activity is uniformly distributed in the remainder of the body. In three situations, however, the use of the correction is not a straightforward application of the standard equations. For organs with separate walls and contents, complications arise in correcting the specific absorbed fraction for nonpenetrating emissions originating in the contents and striking the wall. Also, the activity uniformly distributed in the "remainder" probably should be apportioned to the wall and not the contents. For bone and marrow, adjustments are needed to the standard equations if activity is not assumed to be distributed throughout bone. For brain, the assumption that activity uniformly distributed throughout the body will also be uniform throughout brain tissue may not be justified, and a special correction for this case will be needed. The appropriate equations for correcting S values in these three situations will be described.

INTRODUCTION

In the standard MIRD schema, the absorbed dose (D) to a target region r_k from a source region r_h is designated as:

$$D(r_k \leftarrow r_h) = A_0 \sum_h \tau_h \, S(r_k \leftarrow r_h), \quad (1)$$

where A_0 is the administered activity, τ_h is the residence time in region h and $S(r_k \leftarrow r_h)$ is the so-called "S value", the absorbed dose in target region r_k per unit cumulated activity in source region r_h (1). S values have been routinely derived for many source and target regions within the heterogeneous phantom often used in internal dosimetry (2). Included in the definition of these regions is the "total body", that is the entire interior of the phantom. Biodistribution data used to estimate absorbed doses may include several identified source regions (where radioactivity tends to concentrate) and the "rest of the body" or the "remainder of the body." In 1973, Cloutier et al. (3) developed a method for correcting absorbed dose equations to account for the activity in the total body with residence times

in the "remainder of the body"(total body minus a variable number of specified source organs). To provide accurate use of the equations, this correction should always be made when calculating internal dose estimates; the magnitude of the correction will vary depending on the problem. Coffey and Watson (4) showed that the relationship between S values calculated for the total body (TB) and the remainder of the body (RB) is

$$S(r_k \leftarrow RB) = S(r_k \leftarrow TB)\frac{m_{TB}}{m_{RB}} - \sum_h S(r_k \leftarrow r_h)\frac{m_h}{m_{RB}}, \quad (2)$$

where m represents the mass of any particular region (source h, target k, TB or RB). This correction seeks to eliminate double counting of emissions occurring in a source region (which is, by definition, contained in TB) within the S value for TB.

Organs with Separate Wall and Contents Fractions

A small difficulty arises in the use of Equation 2 for organs with separate absorbed fractions for wall and contents (gallbladder, heart, stomach, small intestine, upper and lower large intestine and urinary bladder). The difficulty is that the apportioning of activity in the "remainder of the body" to organ contents does not make physiological sense. Such activity is more likely distributed throughout the bloodstream (thus including *heart* contents), intra- and extracellular fluids, etc., but not distributed in gallbladder, intestine or bladder contents. However, the S values for a hollow organ's contents irradiating its wall is contained in the second part of Equation 2, and many photon absorbed fractions estimated for "total body" have included photons originating in organ contents (e.g. 2, 5). Therefore, the straightforward relationship shown in Equation 2 does not hold.

Applying Equation 2 to a walled organ, we obtain

$$S(w \leftarrow RB) = S(w \leftarrow TB)\frac{m_{TB}}{m_{RB}} - \sum_h S(w \leftarrow r_h)\frac{m_h}{m_{RB}}, \quad (3)$$

where w indicates the wall of the hollow organ. The important correction occurs when r_h is the contents of the walled organ. In that case, the S values on the right side of Equation 3 are

$$S(w \leftarrow TB) = \frac{\sum_i \Delta_{np_i}\phi_{np}(w \leftarrow w)_i Q_{np_i}}{m_w}\frac{m_w}{m_{TB}} + \frac{\sum_i \Delta_{p_i}\phi_p(w \leftarrow TB)_i Q_{p_i}}{m_w} \quad (4)$$

$$S(w \leftarrow TB) = \frac{\sum_i \Delta_{np_i}\phi_{np}(w \leftarrow w)_i Q_{np_i}}{m_{TB}} + \frac{\sum_i \Delta_{p_i}\phi_p(w \leftarrow TB)_i Q_{p_i}}{m_w} \text{ and} \quad (5)$$

$$S(w \leftarrow c) = \frac{\sum_i \Delta_{np_i}\phi_{np}(c \leftarrow c)_i Q_{np_i}}{2m_c} + \frac{\sum_i \Delta_{p_i}\phi_p(w \leftarrow c)_i Q_{p_i}}{m_w}. \quad (6)$$

In these equations, w refers to wall and c refers to contents, Δ is the mean energy emitted for nuclear transition I (either nonpenetrating, np, or penetrating, p), ϕ is the fraction of energy absorbed in a

target region from transition I in a source region, Q is the quality factor (or radiation weighting factor) associated with transition I, and ν is a factor suggested by the ICRP (7), as being 1 for β particles, but only 0.01 for alpha particles. The factor $\phi_{np}(c \leftarrow c)$ is assumed to be 1.0. If we define $\phi_{np}(w \leftarrow c) = \phi_{np}(c \leftarrow c)\ \nu$, we could write

$$S(w \leftarrow c) = \frac{\sum_i \Delta_{np_i} \phi_{np}(w \leftarrow c)_i Q_{np_i}}{2m_c} + \frac{\sum_i \Delta_{p_i} \phi_p(w \leftarrow c)_i Q_{p_i}}{m_w}. \quad (7)$$

The factor Q also assumes that nonunity values for alpha emissions (6,7). The S values shown in these equations include a radiation weighting factor, although published definitions may not (e.g. (1)). An S value including a radiation weighting factor is similar to the Specific Effective Energy (SEE), as defined by the ICRP (7).

Now, if we assume that activity in the remainder of the body is *not* distributed throughout the contents of walled organs, the penetrating component of S(w←TB) contains contributions from these contents, and should be corrected. The nonpenetrating component, however, does not need to be corrected. Therefore, the total S value for the irradiation of a walled organ from the remainder of the body should be calculated as:

$$S(w \leftarrow RB) = \left[\frac{\sum_i \Delta_{np_i} \phi_{np}(w \leftarrow w)_i Q_{np_i}}{m_{TB}} + \frac{\sum_i \Delta_{p_i} \phi_p(w \leftarrow TB)_i Q_{p_i}}{m_w} \right] \frac{m_{TB}}{m_{RB}} - \frac{\sum_i \Delta_{p_i} \phi_p(w \leftarrow c)_i Q_{p_i}}{m_w} \frac{m_c}{m_{RB}}. \quad (8)$$

(This equation only accounts for the contributions to the wall from the hollow organ's contents and the remainder of the body. It will need to be extended in the general case involving other source organs, using the form of Equation 2.)

If the standard formulation in Equation 5 and 6 is followed, however, this quantity becomes

$$S(w \leftarrow RB) = \left[\frac{\sum_i \Delta_{np_i} \phi_{np}(w \leftarrow w)_i Q_{np_i}}{m_{TB}} + \frac{\sum_i \Delta_{p_i} \phi_p(w \leftarrow TB)_i Q_{p_i}}{m_w} \right] \frac{m_{TB}}{m_{RB}} - \left[\frac{\sum_i \Delta_{np_i} \phi_{np}(w \leftarrow c)_i Q_{np_i}}{2m_c} + \frac{\sum_i \Delta_{p_i} \phi_p(w \leftarrow c)_i Q_{p_i}}{m_w} \right] \frac{m_c}{m_{RB}}. \quad (9)$$

If $\phi_{np}(w \leftarrow w) = \phi_{np}(w \leftarrow c)$, as for electrons,

$$S(w \leftarrow RB) = \frac{\sum_i \Delta_{np_i} \phi_{np}(w \leftarrow w)_i Q_{np_i}}{2m_{RB}} + \frac{\sum_i \Delta_{p_i} \phi_p(w \leftarrow TB)_i Q_{p_i}}{m_w} \frac{m_{TB}}{m_{RB}} - \frac{\sum_i \Delta_{p_i} \phi_p(w \leftarrow c)_i Q_{p_i}}{m_w} \frac{m_c}{m_{RB}}. \quad (10)$$

Here, the nonpenetrating component has been artificially reduced by about half over that in Equation 8. If $\phi_{np}(w \leftarrow w) \neq \phi_{np}(w \leftarrow c)$, as for alpha particles, Equation 9 does not reduce to Equation 10, but the nonpenetrating component is still incorrectly reduced, due to the first term in the second half of Equation 9.

Not standard in most S-value tables is the use of the wall as a source region, except for the heart wall. There are situations in which it is more reasonable to assign activity in a walled organ to the wall itself, and not the contents (e.g. I-131 NaI in the stomach). In these cases, the S value for the wall irradiating the wall must be calculated, as for any other soft tissue organ, and the correction in Equation 3 may be applied normally. Photon SAFs for contents irradiating wall must generally be substituted for wall irradiating wall, as the latter values are not generally available. This substitution should introduce only negligible errors.

Bone and marrow

The skeleton is another site where cross irradiation among organs result in absorbed fractions that are not equal to zero. In reality, activity uniformly distributed throughout the body is not distributed throughout the volume of mineral bone; however, this assumption is usually applied in the absence of any quantitative information to the contrary. It is probably reasonable to assume that there is some level of activity in the marrow similar to that in other soft tissues, because of the vascularity of the marrow spaces.

If activity is uniformly distributed throughout all tissues of the body, these target tissues (T) should receive the same dose per disintegration from the nonpenetrating emissions, equal to

$$\frac{\sum_i \Delta_{np_i} \phi_{np_i} Q_{np_i}}{m_T} \frac{m_T}{m_{TB}} = \frac{\sum_i \Delta_{np_i} \phi_{np_i} Q_{np_i}}{m_{TB}}. \quad (11)$$

If, however, we assume that the activity is only distributed throughout the marrow cavities, the total energy deposited in bone surface cells will be considerably less than the quantity in Equation 11. Cristy and Eckerman (7) have assigned an absorbed fraction for red marrow irradiating bone surface cells of

$$f_{ET/RM} \frac{m_{ET}}{m_{RM}} \quad (12)$$

where $f_{ET/RM}$ is the fraction of endosteal tissue associated with red marrow, m_{ET} is the mass of endosteal tissue and m_{RM} is the mass of red marrow in a particular phantom. In addition, the absorbed fractions for marrow and bone surfaces as targets for alphas or betas/electrons originating within the marrow or bone are case and energy specific, even for marrow irradiating marrow (9). As long as these absorbed fractions and assumptions are properly incorporated into the S values for total body as

a source, the remainder of the body correction should work properly. But if the usual assumption is made that all body tissues that do not have assigned residence times contain a uniform distribution of the remaining activity, the dose to these tissues will be overestimated. In this situation, the mass assigned to "remainder of the body", must be adjusted, if one assumes that the entire mass of skeleton (~5 kg) contains no activity. This will increase concentrations in the other tissues.

Brain

Because of the function of the blood brain barrier (BBB), radionuclides uniformly distributed throughout the body may not be taken up in significant quantities in the brain. If a nuclide is thought to be uniformly distributed in all tissues except the brain, the brain should receive no dose from nonpenetrating emissions. The RB correction may be applied to the penetrating emissions. Some photons may originate within the blood vessels in the brain, even though the material does not cross the BBB. Therefore, an S value for RB irradiating brain could be developed as:

$$S(brain \leftarrow RB) = \frac{\sum_i \Delta_{p_i} \phi_p(brain \leftarrow TB)_i Q_{p_i}}{m_{brain}} \frac{m_{TB}}{m_{RB}} - \sum_h \frac{\sum_i \Delta_{p_i} \phi_p(brain \leftarrow r_h)_i Q_{p_i}}{m_{brain}} \frac{m_h}{m_{RB}}. \quad \textbf{(13)}$$

Normally, there will be no nonpenetrating component in the S value from a region r_h to the brain. Therefore, if Equation 2 is applied as usual, the effect will be to have an additional factor of

$$\frac{\sum_i \Delta_{np_i} \phi_{np}(brain \leftarrow brain)_i Q_{np_i}}{m_{RB}} \quad \textbf{(14)}$$

in S(brain←RB).

It may be argued that a small dose may result from nonpenetrating activity in the blood vessels in the brain irradiating the brain tissue. This component will be specific to the type and energies of the nonpenetrating emissions, and can be estimated in particular cases if desired.

REFERENCES

1. Loevinger R, Budinger T and Watson E: MIRD Primer for Absorbed Dose Calculations, Society of Nuclear Medicine, 1988.
2. Snyder W, Ford M and Warner G. Estimates of Specific Absorbed Fractions for Photon Sources Uniformly Distributed in Various Organs of a Heterogeneous Phantom. MIRD Pamphlet No. 5, Revised. Society of Nuclear Medicine, New York, 1978.
3. Cloutier R, Watson E, Rohrer R and Smith E. Calculating the radiation dose to an organ. J Nucl Med 14(1):53-55, 1973.
4. Cristy M and Eckerman K. Specific Absorbed Fractions of Energy at Various Ages from Internal Photon Sources. ORNL/TM-8381 V1-V7. Oak Ridge National Laboratory, Oak Ridge, TN, 1987.
5. International Commission on Radiological Protection. Limits for Intakes of Radionuclides by Workers. ICRP Publication 30, Pergamon Press, New York, 1979.
6. International Commission on Radiological Protection. 1990 Recommendations of the

International Commission on Radiological Protection. ICRP Publication 60, Pergamon Press, New York, 1991.
7. Cristy M and Eckerman K. SEECAL: Program to Calculate Age-Dependent Specific Effective Energies. ORNL/TM-12351, Oak Ridge National Laboratory, Oak Ridge, TN, 1993.
8. Stabin M and Eckerman K. Dose conversion factors for marrow and bone by skeletal region. J Nucl Med 35:112P, 1994. (Abstract)

THE EFFECT OF SCATTER SUBTRACTION ON SPECT QUANTITATION

Dunn WL and Wiseman GA
Mayo Clinic
200 First Street S.W.
Rochester, Minnesota 55905

ABSTRACT

Radiation scatter removal is important if SPECT imaging is to become quantitatively accurate because scatter adds to background and makes it difficult to perform accurate attenuation correction.

We have investigated the effect of an Elscint technique called Compton free imaging (CFI) on SPECT absolute activity quantitation. In this technique, the SPECT study is acquired with 32 discriminator windows set over the photon peak and Compton region. The spectrum is decomposed into photopeak and scatter photon portions based on probability of distribution of photon scatter at any energy in the spectrum of interest.

A circular Jaszczak phantom (22 cm long x 21 cm diameter) with fillable internal spheres was scanned in the CFI SPECT and standard SPECT modes on an Elscint Helix dual headed camera. The effect of scatter was evaluated for ^{123}I, ^{111}In, ^{67}Ga, and ^{131}I for both single- and dual-head 360° acquisitions - step and shoot - 30 sec. at 6° steps. Two separate Helix systems were used. Three 22 ml sources were taped to the outside of the phantom, and spherical sources (2.6 to 38.5 ml) were placed inside the Jaszczak. These sources ranged in specific activity from 12.6 to 200 kBq/ml. ROI's were drawn over all sources, and one of the sources outside the phantom was chosen as a standard. The average quantitation error was about 6% with CFI and approximately 31% in non-CFI SPECT acquisitions for ^{67}Ga and ^{123}I. In a ^{111}In Pentetreotide patient study, tumor counts were reduced by 36% using CFI.

We reached the conclusion that CFI for scatter reduction significantly improves SPECT absolute quantitation. This will enhance SPECT quantitation for dosimetry and uptake determinations.

INTRODUCTION

Accurate radioactivity quantitation in single-photon emission computed tomography (SPECT) is hindered by the presence of scattered radiation. This study investigates the effect on absolute activity quantitation of a technique for scatter removal called Compton free imaging (CFI). This technique is offered on the Elscint Helix scintillation camera system.

Radiation scatter removal is important since gamma photons emitted from one region in the patient scatter into other regions and, therefore, increase background causing error in quantitation. The predominate interaction between photons and body tissue and bone in the 50 to 500 keV energy range is Compton scattering. This range encompasses the energy emissions of most of the common

radionuclides used in nuclear medicine. Almost all photon scatter in this range is due to the Compton effect.

In Compton scattering, the energy of the scattered photon is given by the following:

$$E_{st} = \frac{E_i}{1 + \frac{E_i}{0.511} \cdot (1-\cos(\theta))},$$

where E_i = incident photon energy in MeV
E_{st} = scattered photon energy in MeV and
θ = scatter angle between incident and scattered photon.

A portion of the incident photon energy is transferred to a recoil electron leading to an energy distribution of scattered radiation below the photopeak energy.

There are a number of possible approaches to correcting for radiation scatter(1-4). One technique employs two adjacent or abutted energy discriminator windows placed over the photopeak. The ratio of counts in these windows is used to calculate the magnitude of the scatter present. Another method uses two energy discriminator windows, one placed over the photopeak and another in the Compton scatter region below the photopeak. A fraction of the scatter as determined by the low-energy window is subtracted from the photopeak window. A problem with this is that the scatter fraction is dependent on the geometry of the patient under study. Therefore, the value measured in phantom studies may not be the true scatter fraction value.

In the CFI technique, the data is acquired with up to 32 discriminator windows set over the photopeak and Compton region. The spectrum is decomposed into photopeak and scatter photon portions based on the probability of distribution of photon scatter as a function of energy in the spectrum. The Compton scatter probability distribution is calculated theoretically from the quantum electrodynamic differential cross section for photons that collide with an electron. The scatter-free image is created by subtracting the scatter portion from the photopeak portion.

MATERIALS AND METHODS

A circular Jaszczak phantom with dimensions of 22 cm long by 21 cm diameter was scanned on an Elscint Helix scintillation camera. Both the CFI SPECT and standard SPECT non-CFI modes were used. The phantom has fillable spheres that can be mounted inside its water filled interior. The effect of the CFI technique on determining activity in the spheres was evaluated for I-123, In-111 and Ga-67. CFI would not function for I-131.

Three 22 ml cylinders were filled with the isotope under evaluation and taped to the outside of the phantom. Spherical sources of 2.6 to 38.5 ml were mounted inside the phantom. The sources ranged in specific activity of 12.6 to 200 kBq/ml. In order to ensure the cylinders would be resolved in the SPECT reconstruction, they were spaced 5 cm apart, edge to edge around the phantom. This facilitated drawing regions of interest (ROIs) around each cylinder.

SPECT of the phantom was performed in 360° acquisitions in the step and shoot mode in which the camera heads arc through 6° steps, pause and acquire data for 30 sec. Following reconstruction of transaxial slices and attenuation correction with a Chang technique, ROIs were drawn over all sources. One of the sources outside the phantom was chosen as a standard.

A SPECT study was also performed on a patient injected with In-111 Pentetreotide to determine the effect of CFI on tumor counts.

RESULTS

Tables 1 and 2 list the results for I-123 absolute activity quantitation in the CFI and standard SPECT acquisition modes, respectively. Quantitation error, true vs. measured activity, in both cylinders and spheres, ranges from -37.5 to +30.7% in the standard acquisition mode. With CFI, error ranges from -1 to +10.5%. The average absolute error (AAE) is 25.8% without CFI and 4.1% with CFI.

Table 1
I-123 Compton Free Imaging

Source	Activity MBq	Measured Activity MBq	Error %
22 ml cylinder	1.931	1.913	1.0
22 ml cylinder	0.348	0.385	10.5
38.5 ml sphere	2.523	2.549	1.0
8.2 ml sphere	0.171	0.178	3.7

Table 2
I-123 Standard or Non-CFI Mode

Source	Activity MBq	Measured Activity MBq	Error %
22 ml cylinder	4.022	3.593	10.7
22 ml cylinder	0.348	0.455	30.7
38.5 ml sphere	2.523	1.576	37.5
8.2 ml sphere	0.171	0.130	24.4

The results for Ga-67 are shown in Tables 3 and 4. With CFI, quantitation error extended from -17.0 to +4.3%. The standard mode error ranges from -.95 to -34.6%. The AAE is 5.6% with CFI and 20.3% without CFI. Combining the results for I-123 and Ga-67, the AAE was 30.8% in the non-CFI mode and 5.7% using CFI for the spherical sources inside the Jaszczak phantom.

In-111 results are given in Tables 5 and 6. Utilizing CFI, the error ranges from -40.5 to +8.8% with an AAE of 23.1%. In the standard mode, error extends from -43.9 to +5.9% with an AAE of 21.2%. In a In-111 Pentetreotide patient study, tumor counts were reduced by 36 % using CFI.

Table 3
Ga-67 Compton Free Imaging Mode

Source	Activity MBq	Measured Activity MBq	Error %
22 ml cylinder	1.558	1.624	4.3
22 ml cylinder	4.044	4.048	0.09
2.6 ml sphere	0.210	0.218	3.9
38.5 ml sphere	0.696	0.714	2.7
15.6 ml sphere	1.003	0.833	17.0

Table 4
Ga-67 Standard or Non-CFI Mode

Source	Activity MBq	Measured Activity MBq	Error %
22 ml cylinder	1.558	1.543	0.95
22 ml cylinder	4.044	3.696	8.6
2.6 ml sphere	0.210	0.148	29.6
38.5 ml sphere	0.696	0.455	34.6
15.6 ml sphere	1.003	0.725	27.7

Table 5
In-111 Compton Free Imaging Mode

Source	Activity MBq	Measured Activity MBq	Error %
22 ml cylinder	1.935	2.105	8.8
22 ml cylinder	0.977	0.903	7.6
38.5 ml sphere	1.088	0.648	40.5
8.2 ml sphere	0.810	0.533	35.6

Table 6
In-111 Standard or Non-CFI Mode

Source	Activity MBq	Measured Activity MBq	Error %
22 ml cylinder	1.935	2.050	5.9
22 ml cylinder	0.977	0.918	6.1
38.5 ml sphere	1.088	0.611	43.9
8.2 ml sphere	0.810	0.577	28.8

CONCLUSIONS

CFI for scatter reduction significantly improves SPECT absolute quantitation with I-123 and Ga-67. This will enhance SPECT quantitation for dosimetry and uptake determinations. In-111 absolute quantitation does not improve using the CFI technique.

REFERENCES

1. Berlad G, Maor D, Natanzon A, et al. Compton free imaging (CFI): Validation of a new scatter correction method. J Nucl Med 35(5):143p (abst), 1994.
2. O'Connor MK, Caiati C, Christian TF, et al. Effects of scatter correction on the measurement of infarct size from SPECT cardiac phantom studies. J Nucl Med 36(11):2080-2086, 1995.
3. Tsui BMW, Zhao X, Frey EC, et al. Quantitative single-photon emission computed tomography: Basics and clinical considerations. Semin Nucl Med 24(1):38-65, 1994.
4. Haynor DR, Kaplan MS, Miyaoka RS, et al. Multiwindow scatter correction techniques in single-photon imaging. Med Phys 22(12):2015-2024, 1995.

THE WORK OF THE ICRP DOSE CALCULATIONAL TASK GROUP: ISSUES IN IMPLEMENTATION OF THE ICRP DOSIMETRIC METHODOLOGY

Keith F. Eckerman
Oak Ridge National Laboratory

ABSTRACT

Committee 2 of the International Commission on Radiological Protection (ICRP) has had underway efforts to provide the radiation protection community with age-dependent dose coefficients, i.e., the dose per unit intake. The Task Group on Dose Calculations, chaired by the author, is responsible for the computation of these coefficients. The Task Group, formed in 1974 to produce ICRP Publication 30, is now international in its membership and its work load has been distributed among the institutions represented on the task group. This paper discusses: 1) recent advances in biokinetic modeling; 2) the recent changes in the dosimetric methodology; 3) the novel computational problems with some of the ICRP quantities; and 4) quality assurance issues which the Task Group has encountered. Potential future developments of the dosimetric framework which might strengthen the relationships with our emerging understanding of radiation risk will also be discussed.

INTRODUCTION

The Task Group on Dose Calculations (DOCAL) of Committee 2 of the International Commission on Radiological Protection (ICRP) was formed in 1974 to calculate the radiation protection quantities for ICRP Publication 30 (1). The Task Group was centered at Oak Ridge National Laboratory (ORNL) and ORNL personnel and their consultant served on the task group. Following the completion of Publication 30 and upon issuance of its report on nuclear decay data (Publication 38 (2)), the task group expected to be disbanded. However, the Commission, sensing a need to maintain the computational expertise and reflecting concern in relying on a single institution for such a capabilities, decided to make DOCAL a standing task group with the stipulation that its membership become international. DOCAL's current membership (see Table 1) includes individuals from institutions within Brazil, Germany, Ukraine, United Kingdom, and the United States. The computational efforts in support of Committee 2 activities are now shared among the institutions represented on the task group.

ICRP DOSIMETRIC FORMULATION

ICRP's dosimetric formulation shares a common physical foundation with Medical Internal Radiation Dose (MIRD) Schema of the Society of Nuclear Medicine. The MIRD system (3) is based

Table 1

Members of ICRP Committee 2 DOCAL Task Group

K. F. Eckerman (Chairman)	Oak Ridge National Laboratory; Oak Ridge, TN, USA
V. Berkovski	All Union Scientific Center for Radiation Medicine; Kiev, Ukraine
L. Bertelli	Instituto de Radioprotecao e Dosimetria; Rio de Janeiro, Brazil
G. M. Kendall	National Radiation Protection Board, Didcot, UK
R. W. Leggett	Oak Ridge National Laboratory; Oak Ridge, TN, USA
I. A. Likhtarev	All Union Scientific Center for Radiation Medicine; Kiev, Ukraine
D. Noβke	Bundesamt fur Strahlenschutz; Munich, Germany
A. W. Phipps	National Radiation Protection Board; Didcot, UK

on physical quantities and is formulated for application to the short-lived radionuclides used in nuclear medicine procedures which emit only electrons and photons; i.e., radiations of low-linear energy transfer (low-LET). The ICRP dosimetry (1) system address all radionuclides, without regard to their physical half-life, and all emitted radiations; including high-LET radiations such as alpha and neutron particles. Some radionuclides of interest in radiation protection reside within the body for extended periods of time and hence their dose is protracted throughout the lifetime of the exposed individual. In addition, many radionuclides form radioactive decay products (decay chains) within the body and these daughter products may behave differently from the parent radionuclide. The primary dosimetric quantity in the ICRP system is equivalent dose while absorbed dose serves that role in the MIRD system. The relationship of the various quantities of the two dosimetric systems is given in Table 2.

Table 2

Dosimetric Quantities[1] of the ICRP and MIRD Systems

Quantity	**ICRP**	**MIRD**
Activity[2]	A	A
Cumulated activity	U_τ, τ is the time period	$\tilde{A}$
Absorbed Dose[3]	D	D
Equivalent Dose[4]	H	-
Mean absorbed dose per cumulated activity	-	S
Specific equivalent energy per unit cumulated activity	SEE	-
Particles per transition	Y	n
Energy per particle	E	E
Absorbed fraction	AF	ϕ
Specific absorbed fraction	SAF	Φ

[1] Both system employ SI units.
[2] The special name of the SI unit of activity is the becquerel (Bq).
[3] The special name of the SI unit of absorbed dose is the gray (Gy).
[4] The special name of the SI unit of equivalent dose is the sievert (Sv).

Following the Chernobyl accident in 1986, the ICRP began a series of publications (4-7) tabulating age-dependent dose coefficients for ingestion and inhalation intakes of radionuclides. This effort required extending the ICRP dosimetric formulations to reflect changes in the behavior of the radionuclide in the body with respect to age and changes in the absorption of ionizing energy with body growth. The equivalent dose rate $\dot{H}_T(t)$ in tissue T at time t following an acute intake of one unit of activity of a radionuclide by an individual of age t_0 at the time of intake can be expressed as

$$\dot{H}_T(t) = \sum_S A_S(t)\ SEE(T\leftarrow S; t_0+t)\ , \tag{1}$$

where $A_S(t)$ is the activity of radionuclide residing in source region S at time t, $SEE(T\leftarrow S; t_0+t)$ is the equivalent dose rate in target tissue T per unit activity of the radionuclide in source region S in an individual of age t_0+t, and the summation extends over all source regions within which the radionuclide may reside. The set of *SEE* values at any age are obtained by interpolation of the *SEEs* at the six standard ages (newborn, 1-, 5-, 10-, 15-, and 20-year old) using the inverse of total-body mass as the interpolation variable (4). Figure 1 illustrates the *SEE* for ^{131}I self-irradiation of the thyroid gland as a function of age computed in this manner. The equivalent dose in tissue T, $H_{T,\tau}$, delivered during the time period τ following the intake is given by the integral of the equivalent dose rate,

$$H_{T,\tau} = \int_0^\tau \sum_S A_S(t)\, SEE(T\leftarrow S; t_0+t)\, dt\ . \tag{2}$$

If the *SEEs* are independent of age (as during adulthood) or if body growth is negligible during the period over which nuclear decays accumulated (short-lived radionuclides), then the above equation reduces to

$$H_{T,\tau} = \sum_S U_{S,\tau}\, SEE(T\leftarrow S; t_0)\ , \tag{3}$$

where $U_{S,\tau}$ is the number of nuclear decays occurring in source region S during the time period τ per unit intake and is given by

$$U_{S,\tau} = \int_0^\tau A_S(t)\ dt\ . \tag{4}$$

ICRP refers to the period τ as the commitment period and denotes the committed equivalent dose per unit intake at age t_0 as the dose coefficient $h_{T,\tau}(t_0)$.

The *SEEs* for the radionuclides are computed as

$$SEE(T\leftarrow S; t_0) = \sum_R Y_R\, w_R\, E_R\, SAF(T\leftarrow S; E_R, t_0)_R\ , \tag{5}$$

where Y_R is the yield of radiation R of unique or average energy E_R per nuclear transformation of the radionuclide, w_R is the radiation weighting factor for radiation R (see Table 3), and $SAF(T\leftarrow S; E_R, t_0)_R$ is the specific absorbed fraction for radiation R of unique or average energy E_R for an individual of age t_0. The radiation weighting factor is a radiation protection quantity which puts the various radiations on a common scale with regard to their biological effectiveness (8).

Table 3

Radiation weighting factors of ICRP Publication 60 (8)

Radiation type and energy[1]	Weighting factor, w_R
Photons, all energies	1
Electrons, all energies[2]	1
Neutrons, fission	10
Alpha particles, fission fragment, heavy nuclei	20

[1] All values related to the radiation emitted from an internal source.
[2] Excluding Auger electrons emitted by nuclei bound to DNA.

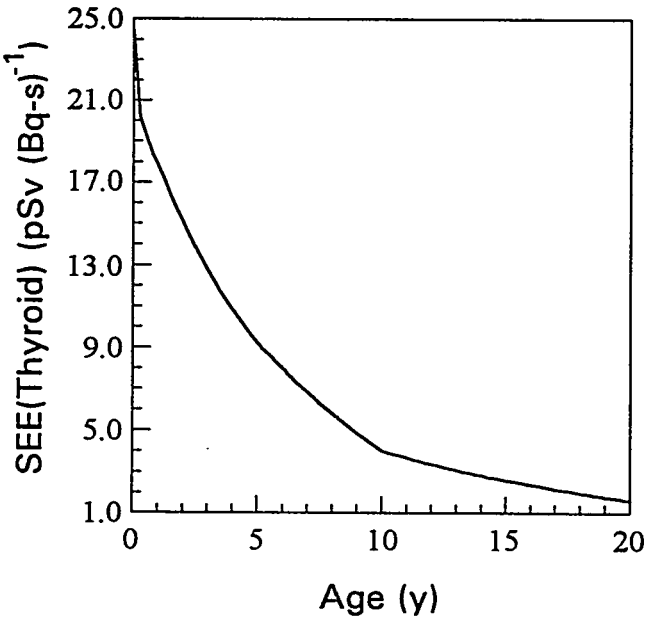

Figure 1. SEE for self-irradiation of the thyroid by ^{131}I as a continuous function of age based on interpolation of the values at the six ages in the inverse of the total body mass.

The ICRP dosimetric system is based on health risk considerations (8). Radiation health effects can be categorized as deterministic effects, where severity of the effect increases with dose above a threshold and stochastic effects, where the probability of the effect occurring increases with dose without threshold. Work practices are planned to avoid deterministic effects and to limit the frequency that stochastic effects occur within the worker population. The stochastic effects of concern are genetic effects and cancer. The organs and tissues of the body exhibit a range of sensitivity with regard to stochastic effects. The ICRP introduced the effective dose quantity to reflect the contribution of the irradiated tissues to the health risk. The effective dose coefficient is defined as (8):

$$E = \sum_T w_T H_T + w_{rem} H_{rem} , \qquad (6)$$

where w_T is the tissue weighting factor for tissue T (see Table 4) , H_T is the equivalent dose in tissue T, and the subscript *rem* denotes the remainder group of tissues (see Table 4). The remainder group represents those tissues of the body for which it has not been possible to assign specific w_T values, but there is no reason to rule out the occurrence of stochastic effects in these tissues. As noted in the footnote to Table 4, the equivalent dose to the remainder tissue group is computed as the mass average of the equivalent dose to each tissue within the remainder. However, if a tissue of the remainder is the most highly irradiated tissue in the body, then the weighting factor for the remainder, w_R, is split and one-half is applied to the equivalent dose for the highly irradiated tissue and the other half is applied to the equivalent dose for the remainder, excluding the highly irradiated tissue.

Table 4

Tissue Weighting Factors of ICRP Publication 60 (8)

Tissue or organ	Weighting factor, w_T
Gonads	0.20
Red Marrow	0.12
Colon	0.12
Lung	0.12
Stomach	0.12
Bladder	0.05
Breast	0.05
Liver	0.05
Esophagus	0.05
Thyroid	0.05
Skin	0.01
Bone Surface	0.01
Remainder[1,2]	0.05

[1] The remainder is composed of the following tissues: adrenals, brain, extrathoracic airways, upper large intestine, small intestine, kidney, muscle, pancreas, spleen, thymus, and uterus.
[2] If a remainder tissue receives the highest equivalent dose then a weighting factor of 0.025 should be applied to that tissue and a weighting factor of 0.025 to the average equivalent dose in the rest of the remainder.

BIOKINETIC MODELS

In the ICRP computations, information on the behavior of radionuclides in the body is condensed into three main types of biokinetic models: a respiratory tract model, a gastrointestinal tract model, and an element-specific systemic model (see Figure 2). Inhalation and ingestion are the routes of intake of the radionuclide into the body.

The ICRP recently introduced a new respiratory tract model (9) that involves considerably greater detail and physiological realism than the previous model (1). The model structure is shown in Figure 3. The model divides the respiratory tract into extrathoracic (ET) and thoracic regions. The airways of the ET region are further divided into two categories: the anterior nasal passages (ET_1), in which deposits are removed by extrinsic means such as nose blowing, and the posterior nasal passages including the nasopharynx, oropharynx, and the larynx (ET_2), from which deposits are swallowed. The airways of the thorax include the bronchi (compartment labeled BB_i), bronchioles (compartments labeled bb_i), and alveolar region(compartments labeled AI_i). Material deposited in the thoracic airways may be cleared into blood by absorption to the GI tract by mechanical processes (that is, transported upward and swallowed), and to the regional lymph nodes via lymphatic channels. Unlike the mechanical clearance, the absorption to blood depends on the chemical and physical form of the inhaled material. Although the model permits consideration of compound-specific absorption rates, three default absorption types are defined; Type F (fast rate of absorption to blood), Type M (an intermediate rate of absorption), and Type S (slow rate of absorption). With the exception of compartment ET_1, absorption to blood occurs from all other compartments. Equivalent doses are calculated for specific cells within the respiratory tract considered to be at risk. The dose to the lung is computed as the weighted equivalent dose to the cells at risk in the BB, bb, AI, and LN_{TH} compartments; weighting factors of 0.333, 0.333, 0.333, and 0.001, respectively, are applied. The dose to the extrathoracic airways is computed as the weighted equivalent dose to the cells at risk in the ET_1, ET_2, and LN_{ET} compartments; weighting factors of 0.001, 0.998, and 0.001, respectively are applied. The extrathoracic airways are considered to be part of the remainder tissue group when computing the effective dose.

The model of the gastrointestinal tract in current use is that which has been used by the ICRP for many years (1). The model, shown in Figure 2, divides the GI tract into four segments or compartments and depicts the transfer of material from one segment to the next by first-order kinetics. Absorption to blood is generally assumed to occur only in the small intestine. Absorption is

described by the fraction f_1 which denotes, in the absence of radioactive decay, the fraction of ingested material that is absorbed.

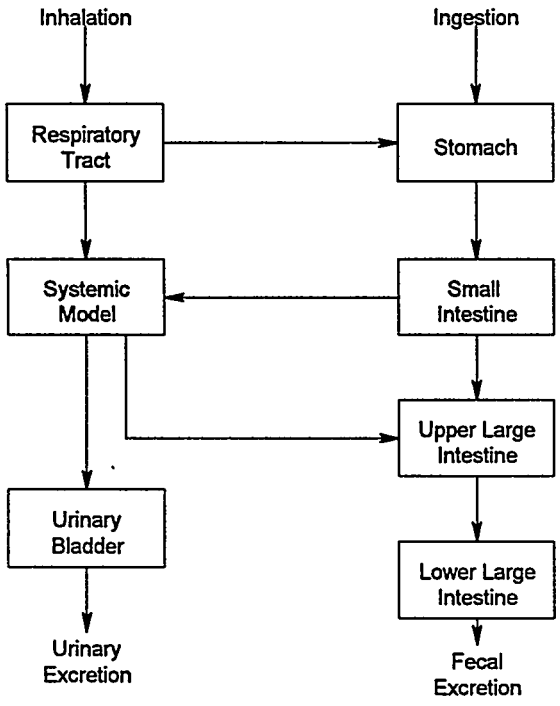

Figure 2. Structure of the ICRP models for computation of dose following ingestion and inhalation intakes of radionuclides.

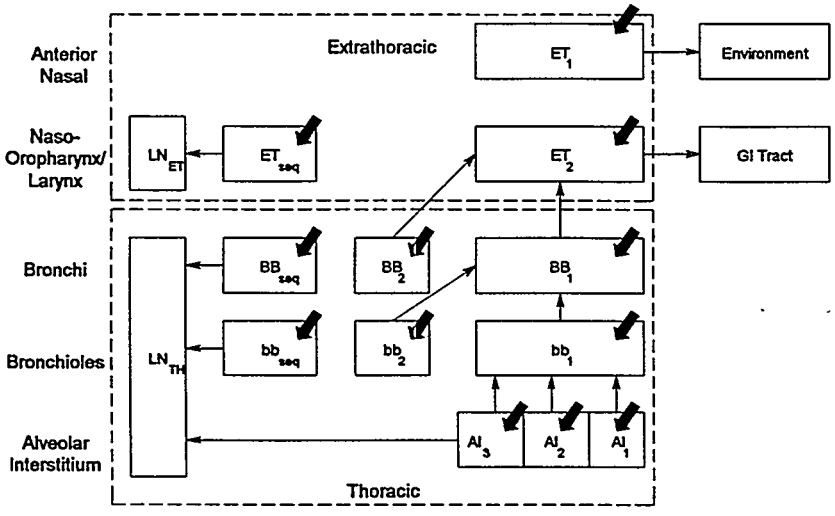

Figure 3. Structure of the ICRP's respiratory tract model (9). The broad arrows denote deposition of the inhaled particulate matter and the thin arrows the routes of mechanical clearance of the deposited material.

The systemic biokinetic models used in ICRP's recent series of publications (5-8) on age-dependent dose coefficients may be divided into two main classes, referred to here as "retention models" and "physiologically based models." A retention model is not intended as a biologically realistic depiction of actual paths of movement of a radionuclide in the body; rather, it is a mathematically convenient representation of the inventories of the radionuclide in its major repositories at times following its initial entry into blood. The initial distribution of activity leaving blood is represented by compartment-specific deposition fractions, and subsequent inventories in the compartments are described in terms of compartment-specific biological removal half-times.

Material leaving a compartment is assumed either to move directly to excretion or to enter an excretion pathway such as the contents of the urinary bladder or the gastrointestinal tract (see Figure 1).

In the ICRP publications on age -dependence (5-7), physiologically based models have been developed for a number of elements. This modeling framework depicts loss of material by specific excretion pathways, feedback of material from organ to blood plasma, and certain physiological processes that are known to influence the distribution and movement of the element within the body. Clearly, the degree of biological realism incorporated into each of the models is limited by practical considerations regarding the amount and quality of information available to determine actual paths of movement and the

values of the model parameters. Figure 4 shows the ICRP physiologically based model for "calcium-like" or bone volume-seeking radionuclides (5). A similar model has also been formulated for "plutonium-like" or bone surface-seeking elements (5).

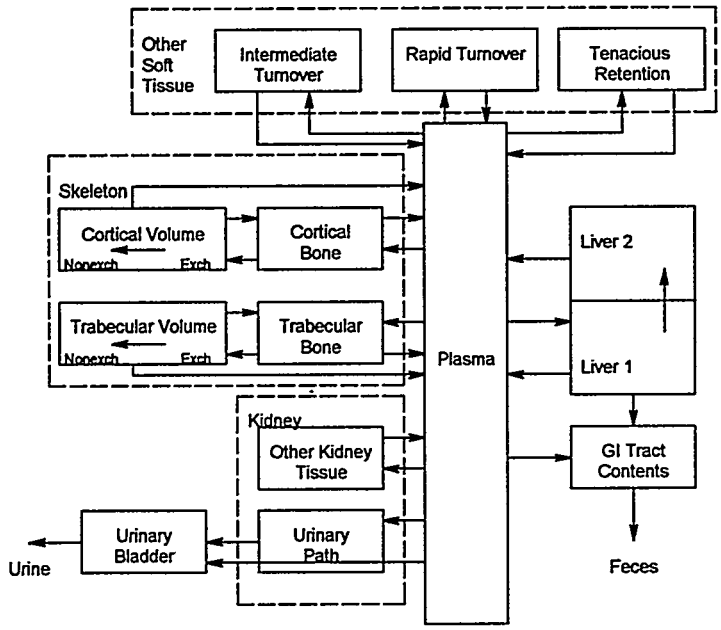

Figure 4. Structure of the ICRP's generic model for calcium-like elements (5). EXCH = exchangeable bone volume, NONEXCH = nonexchangeable bone volume.

TASK GROUP OPERATIONS

ICRP Committee 2 considered it desirable that DOCAL carry out its computations using the software that existed within the institutions represented on the task group rather than develop a standard "ICRP code." However, the software of some institutions was not capable of age-specific calculations and members had to substantially revise their software. This effort was facilitated by agreeing in advance on the specific formulations, data sources, and procedures. The selection of specific numerical methods was left to the individual members who, of course, adopted the method already implemented in their software. Thus, for example, a variety of numerical methods are used to solve the system of differential equations describing the behavior of radionuclides in the body. Table 5 lists some of the decisions adopted by DOCAL with regard to data sources and procedures.

The most computational intense aspect of the calculations is solving the system of differential equations governing the behavior of the radionuclides in the body. The system of equations is said to be "stiff" in that they involve transfer coefficients which vary over orders of magnitude (e.g., removal of activity from the volume of mineral bone may be many orders of magnitude slower than its removal from the circulating blood). In addition, the equations involve time-dependent (or age-dependent) transfer coefficients governing the movement of material from one compartment to another. Furthermore, the number of equations involved can be quite large; for example, inhalation intakes of ^{232}Th, Type S, requires solving a system of 605 simultaneous differential equations. The numerical solvers used by DOCAL members were able to cope with such system of equations. However, the solvers varied considerably in their computational times and, some solvers, required that extreme care be taken to ensure the validity of the solution.

Table 5

Example of DOCAL Standard Data Source and Procedures

- ICRP 38 nuclear decay data; electronic decay data files of Eckerman *et al* (10).
- Photon specific absorbed fractions of Cristy and Eckerman (11).
- Source and target regions masses as in Cristy and Eckerman (11).
- Bone dosimetry of ICRP Publication 30 (1).
- Respiratory tract model and absorbed fractions of ICRP Publication 66 (9).
- Linear interpolation of specific absorbed fractions and biokinetic rate constants.
- Interpolation of *SEE*s in the inverse total body mass.
- Thymus dose used as surrogate for esophagus.
- Colon dose computed as mass average of dose to upper and lower large intestine.

QUALITY ASSURANCE AND CONTROL

Considerable quality assurance and quality control (QA/QC) efforts have been undertaken by DOCAL to ensure the validity of the published dose coefficients. These efforts were greatly aided by agreement on the data sources and procedures outlined in Table 5. Prior to publication all coefficients were calculated by a least two different institutions and their values were compared at a meeting of the task group. Often the comparisons were limited to the effective dose coefficient when it was the only coefficient to appear in the publication. Because of the robust nature of this quantity, agreement in its value did not ensure that the computations were error free. If a discrepancy in the effective dose was noted, then it was necessary to examine the equivalent dose for the various organs and tissues. It became apparent that differences in equivalent dose for the remainder tissue group was frequently the source of the discrepancy in the effective dose values. For inhalation intakes of short-lived radionuclides, the dose to the extrathoracic airways, a member of the remainder, often is the most highly irradiated tissue of the body. As noted above, if an organ of the remainder is the most highly irradiated tissue of the body, then the tissue weighting factor for the remainder is "split" and half is applied to the equivalent dose from the organ and the other half is applied to the average dose to the remainder (exclusive of the organ). Computationally, this is an unstable procedure since two different software packages can produce numerical values that are in agreement yet the representation of these numbers within the machine results in different decisions regarding splitting and hence different values for the effective dose. For example, consider a hypothetical irradiation in which only bone surface (w_T of 0.01) and the extrathoracic airways (mass 15 g) of the remainder (mass 30 kg, w_T of 0.05) each received an equivalent dose H. If the latter were computed to be $H + \epsilon$ (where ϵ is a small positive number), then the remainder is split and the effective dose is $0.01\ H + 0.025\ (H + \epsilon)$ or 0.035 H. However, if ϵ is 0, the remainder is not split (dose is mass averaged) and effective dose is $0.01\ H + 0.05 * 15\ H / 30000$ or 0.01 H. The two values for the effective dose differ by a factor of 3.5.

It was possible to reduce the frequency at which the software packages made different decisions by rounding the values to two significant figures prior to the decision regarding splitting. While this

procedure reduces the frequency it, of course, did not eliminate the problem. Among the DOCAL members, discrepancies in the values of equivalent doses to specific tissues generally were found to be associated with differences in the interpretation of the biokinetic model and are best confirmed by comparing the calculated number of nuclear transformation for the source regions.

Although no attempt was made to standardize the input streams of the various software packages, sufficient interchange took place among the members enabling some members to read the input stream of the other software packages. Similarly, as the work proceeded a number of utility routines were developed to read the output files produced by the different software packages and automate the numerical comparisons. Further automation of the comparisons might well have been undertaken.

CONCLUSIONS

The need for more realistic and physiologically meaningful models in radiation protection is generally well recognized. Such models, by their nature will be more complex and demanding with regard to computational procedures. DOCAL has demonstrated that with today's computing hardware, and with appropriate software, one can deal with these models even in a production mode. DOCAL has successfully established computational support for the activities of ICRP Committee 2 at a number institutions world wide. This has accomplished while issuing a number of publications which were subjected to appropriate QA/QC procedures. The difficulties encountered with respect to the definition of the effective dose suggests that greater attention needs to be given to the computational considerations when defining quantities within the dosimetric systems.

REFERENCES

1. International Commission on Radiological Protection. Limits for Intakes by Workers, ICRP Publication 30, Part 1, Pergamon Press, Oxford, 1979.
2. International Commission on Radiological Protection. Radionuclide Transformations Energy and Intensity of Emissions, ICRP Publication 38. Pergamon Press, Oxford, 1983.
3. Loevinger R. Berman M. A Revised Schema for Calculating the Absorbed Dose from Biologically Distributed Radionuclides. MIRD Pamphlet No. 1, Revised, The Society of Nuclear Medicine, New York, 1976.
4. International Commission on Radiological Protection. Age-Dependent Doses to Members of the Public from Intake of Radionuclides, Part 1, ICRP Publication 56, Pergamon Press, Oxford, 1989.
5. International Commission on Radiological Protection. Age-Dependent Doses to Members of the Public from Intake of Radionuclides, Part 2, ICRP Publication 67, Pergamon Press, Oxford, 1993.
6. International Commission on Radiological Protection. Age-Dependent Doses to Members of the Public from Intake of Radionuclides, Part 3, ICRP Publication 69, Pergamon Press, Oxford, 1995.
7. International Commission on Radiological Protection. Age-Dependent Doses to Members of the Public from Intake of Radionuclides, Part 4, ICRP Publication 71, Pergamon Press, Oxford, 1995.
8. International Commission on Radiological Protection. 1990 Recommendations of the International Commission on Radiological Protection, ICRP Publication 60, Pergamon Press, Oxford, 1991.

9. International Commission on Radiological Protection. Human Respiratory Tract Model for Radiological Protection, ICRP Publication 66, Pergamon Press, Oxford, 1994.
10. K. F. Eckerman, R. J. Westfall, J. C. Ryman, and M. Cristy. "Availability of nuclear decay data in electronic form, including beta spectra not previously published, Health Phys 67:338-345, 1994.
11. M. Cristy and K. F. Eckerman. Specific absorbed fractions of energy at various ages from internal photon sources, ORNL/TM-8381/V1-7 (Oak Ridge National Laboratory, Oak Ridge, TN), 1987.

QUESTIONS

Bolch: In the calculation of effective dose under the ICRP dosimetry system, how is the gonadal dose assigned considering the Cristy and Eckerman phantoms contain both ovaries and testes and the resulting doses are not broken down by sex?

Eckerman: In ICRP Publication 30, the gonadal dose was assigned the higher of the value for testes and ovaries. For internal emitters this is typically the ovaries. In ICRP Publication 51 on external dosimetry, the gonadal dose was considered as the average of the ovaries and testes or calculated in gender-specific phantoms.

Stelson: Keith, this is not directed to you but to the powers that be in the ICRP. I mention this because there are several ICRP committee members in this audience and I hope that you will all pass this on to the publication committee. The numbering system for the ICRP is a librarian's nightmare! It is difficult to catalog issues that are not sequential in year and date and one report doesn't even have a number. Also, I'd like to suggest that updates to previous publications be printed in pamphlet from so that they can be placed into the original publication. It is difficult to remember that it has been updated and where the update is located.

Lathrop: I want to endorse everything Audrey just said. Dr. Eckerman, in addition to the excretory pathways you have indicated, i.e., the urinary bladder and intestine, and the lungs, have you given any consideration to losses from skin, hair and perspiration?

Eckerman: Loses from the body from these removal pathways are generally considered in the biokinetics, e.g. the lead biokinetic model. However, no dosimetric considerations are given to those routes of excretion.

MODEL DEVELOPMENTS AND REVISED DOSES IN MACRODOSIMETRY

Phipps AW, Fell TP and Silk TJ
National Radiological Protection Board,
Chilton, Didcot, Oxon OX11 0RQ, UK

ABSTRACT

Since the issue of ICRP Publications 52 and 53 in 1987, the field of internal dosimetry has seen many improvements in both modeling and computational capabilities. Driven principally by a need to provide more realistic estimates of organ or tissue doses to members of the public (including children) the ICRP has recommended new models for the respiratory tract and for the systemic behavior of many of the more important elements. Also, a general calculation method has been developed for age-dependent dosimetry which involves an effectively continuous variation of both biokinetic parameters and dosimetric quantities (S values).

This paper presents a review of recent developments in the computation of internal doses at the organ and suborgan (macrodosimetric) level with reference to a few important radiopharmaceuticals. Revised dose coefficients (dose per unit intake values) are presented and discussed for Tc and In aerosols to illustrate the effect of the new lung model, and for Ca, Sr and Ba to illustrate the effect of the new (age-dependent) biokinetic models. The results given here differ significantly from those of ICRP Publication 53 in some cases and can be seen as an indicator of what may be in store in future dose compendia.

INTRODUCTION

Since the issue of ICRP Publications 52 (1) and 53 (2) in 1987, the ICRP has recommended new models for the respiratory tract and for the systemic behavior of many of the more important elements. These developments have been driven principally by a need to provide more realistic estimates of organ or tissue doses to members of the public (including children), particularly following the Chernobyl accident. A detailed review of the evolution and development of the new ICRP models, which also discusses their advantages and limitations, has been published by Leggett and Eckerman (3).

Where relevant, for example for alkaline earth elements, models include a detailed recycling model for bone which allows for bone remodeling and burial of activity. As well as the new biokinetic models, a general calculation method has been developed for age-dependent dosimetry which involves an effectively continuous variation of both biokinetic parameters and dosimetric quantities (S values).

Although developed mainly for assessing doses to the public from general exposures, these new models should find application in the field of nuclear medicine. ICRP Publication 53 states that

'complicated multicompartment models' were intentionally avoided, nevertheless, it is interesting to explore the implications that these new ICRP models may have in the field of radiopharmaceutical dosimetry.

THE ICRP MODEL FOR THE RESPIRATORY TRACT

Overview

In 1994 the ICRP recommended a new model of the respiratory tract in ICRP Publication 66 (4). This model replaces the previous model given in ICRP Publication 30 (5), which was the current model during the preparation of ICRP Publication 53. The new model was used in recent ICRP Publications of dose coefficients (doses per unit intake) for workers (6) and members of the public (7) and is employed in the calculations described here. The new model divides the respiratory tract into extrathoracic and thoracic regions (Figure 1). The former subdivides into ET_1 (anterior nasal passage) and ET_2 (posterior nasal passage, pharynx and larynx). The thoracic region is subdivided into BB (bronchial: airway generations 1-8), bb (bronchiolar: generations 9-15) and AI (alveolar-interstitial: the region where gases exchange). In addition, lymphatic tissue is associated with both extrathoracic and thoracic regions LN_{ET} and LN_{TH}, respectively.

The model includes a submodel for the deposition of material of different characteristics in the various parts of the lung. Following deposition, there is competition between mechanical clearance and absorption to blood. The former is taken to be independent of the material while the latter depends on its solubility.

It is recognized, of course, that inhalation is not normally an important intake path for radiopharmaceuticals, except for lung ventilation studies. However, recent work (8) has shown that the uniquely permeable nature of the lung epithelium to macromolecules may lead to the pulmonary delivery route for pharmaceuticals finding wider application.

Deposition of Inhaled Aerosols

The total deposition in the new model for 1 μm AMAD aerosols is lower than in the ICRP Publication 30 model by about 25% (Table 1). Moreover, a large part of this total is in the nasal region, where material is mostly removed by extrinsic processes or by mucociliary action and thus does not usually contribute significantly to lung dose or to doses to systemic tissues. Deposition in the deep lung is approximately half that predicted by the old model, and lung doses can be correspondingly lower.

Clearance from the Respiratory Tract

Previously, in the ICRP Publication 30 model, individual chemical compounds of radionuclides were assigned to one of three default inhalation Classes (D, W and Y), and rates of overall clearance were given for each compartment for each Class. Of course, these defaults may not have been relevant for calculations involving radiopharmaceuticals. In the new model, removal from compartments is taken to be a competition between absorption to blood and mechanical clearance within the lung (and to the GI tract). Absorption rates are then given for three default solubility Types (F, M and S; for fast, moderate and slow), and mechanical clearance is taken to be the same for all particles, irrespective of solubility. The processes of mechanical clearance and absorption to blood are thus treated separately. This means that the new model is more adaptable for specific materials; data on absorption for a particular pharmaceutical can be easily built into the model. This, in turn, should mean that the new model will find greater application to radiopharmaceutical dosimetry.

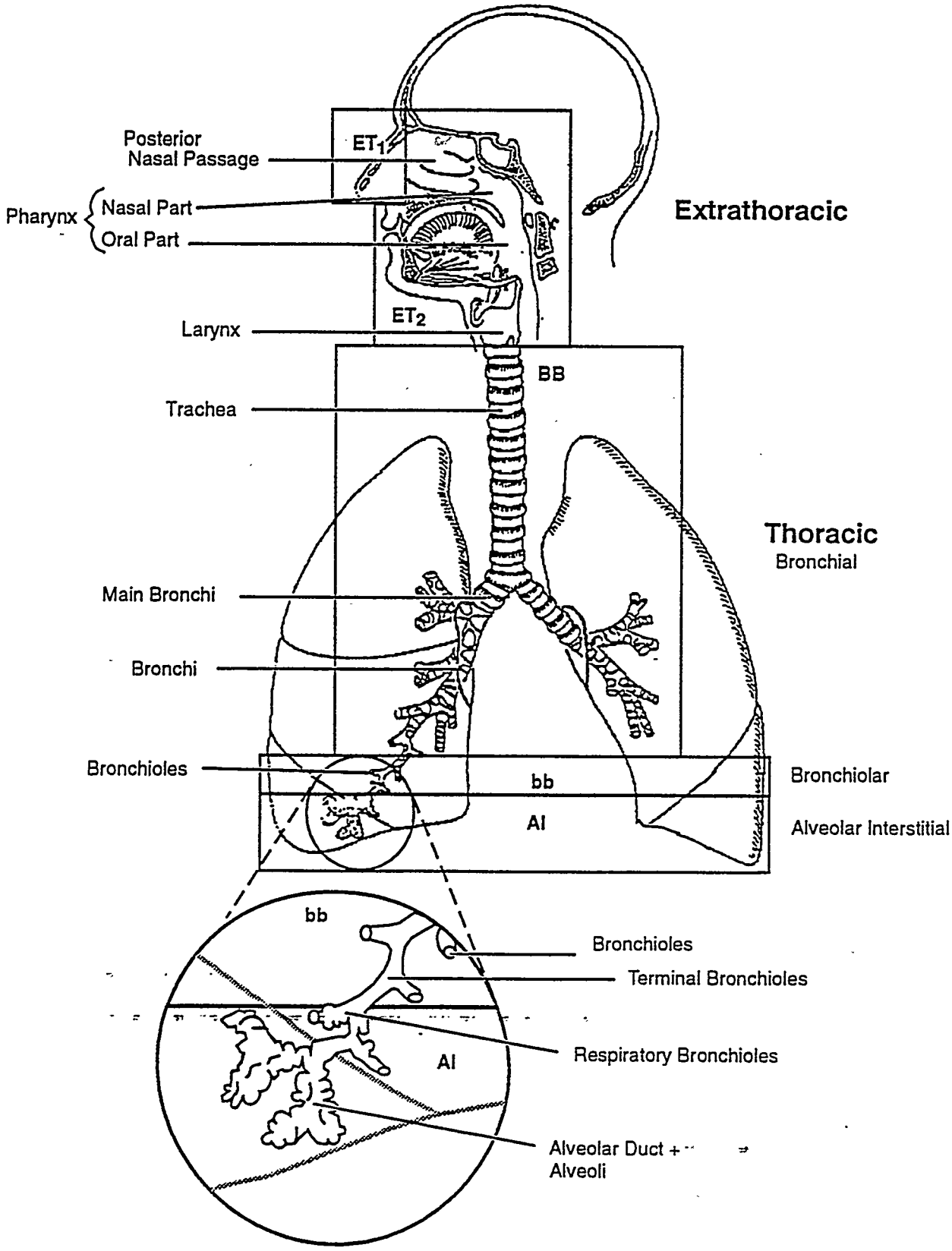

Figure 1. Anatomical regions of respiratory tract.

Table 1
Regional Depositions for 1 μm AMAD Aerosols[a]

Publication 30 model		Publication 66 model	
Region	**(%)**	**Region**	**(%)**
Nasal passage (N-P)	30	Extrathoracic (ET_1)	15
		Extrathoracic (ET_2)	19
		(Total)	(34)
Trachea and bronchial tree (T-B)	8	Bronchial (BB)	1.3
		Bronchiolar (bb)	2.0
		(Total)	(3.3)
Pulmonary parenchyma (P)	25	Alveolar-interstitial (AI)	11
Total	63		48

a) Calculated for a combination of activity levels suitable for an average member of the public. Different deposition fractions may be appropriate for radiopharmaceuticals administered in controlled circumstances.

It is interesting to consider the fraction of deposited activity which reaches systemic circulation based on total deposition patterns and subsequent removal to blood. This can give an indication of the effects on systemic tissue doses of the new model. Although this is only valid for materials whose physical half-life is long compared with the residence times in the lung, it does provide a useful insight. Simple calculations show that for soluble compounds one might expect about 75% of the previous values, and for insoluble compounds about one tenth (9).

Lung Dosimetry

A major difference in the new lung model is that whereas the ICRP Publication 30 model gave the average dose to lung tissue, the new model allows for the calculation of doses to specific groups of cells that are considered to be at risk; it can thus take into account differing radiosensitivity within the lung. Absorbed fractions (the fraction of energy emitted in a source region which is absorbed in a target region) are given in ICRP Publication 66 as functions of energy for each source and target pair and for each radiation type. These functions allow beta dosimetry in the lung to be based on beta spectra rather than mean beta energies and this approach has been adopted in recent ICRP Publications on dose coefficients (6,7).

The new absorbed fractions vary widely over the range of energies and particle types and are often substantially less than one. However, the masses of the target regions are much lower than the 1000g of the lung in the ICRP Publication 30 model. These changes act in opposition, and generalizations regarding the effect on lung doses and effective doses are not possible.

The target cells identified are: basal cells of the epithelium in both extrathoracic regions; basal and secretory cells in the bronchial epithelium; Clara cells (a type of secretory cell) in the bronchiolar epithelium; and endothelial cells, such as those of capillary walls and type II epithelial cells, in the alveolar-interstitial (AI) region.

In each respiratory tract region, there are also several possible source regions (Figure 2). In the bronchiolar (bb) region, for example, activity in the fast phase of clearance (bb_1) is taken to be in the mucous layer above the cilia, activity in the slow phase of clearance (bb_2) is in the mucus between the cilia and particles sequestered in the airway wall (bb_{seq}) are in a macrophage layer at a depth of 20-25 μm (i.e., below the target cells). The same naming system for source regions is used in the Bronchial

(BB) region. Account is also taken of irradiation of all regions from activity present in the AI region (AI_1, AI_2 and AI_3).

The overall dose to the lung is then taken to be a weighted sum of the doses to the three different regions: bronchial, bronchiolar and alveolar-interstitial. These weights, known as regional apportionment factors, are not to be confused with the tissue weighting factors used in the calculation of effective dose. They represent the contribution from each region towards the total detriment associated with lung and are given in Table 2.

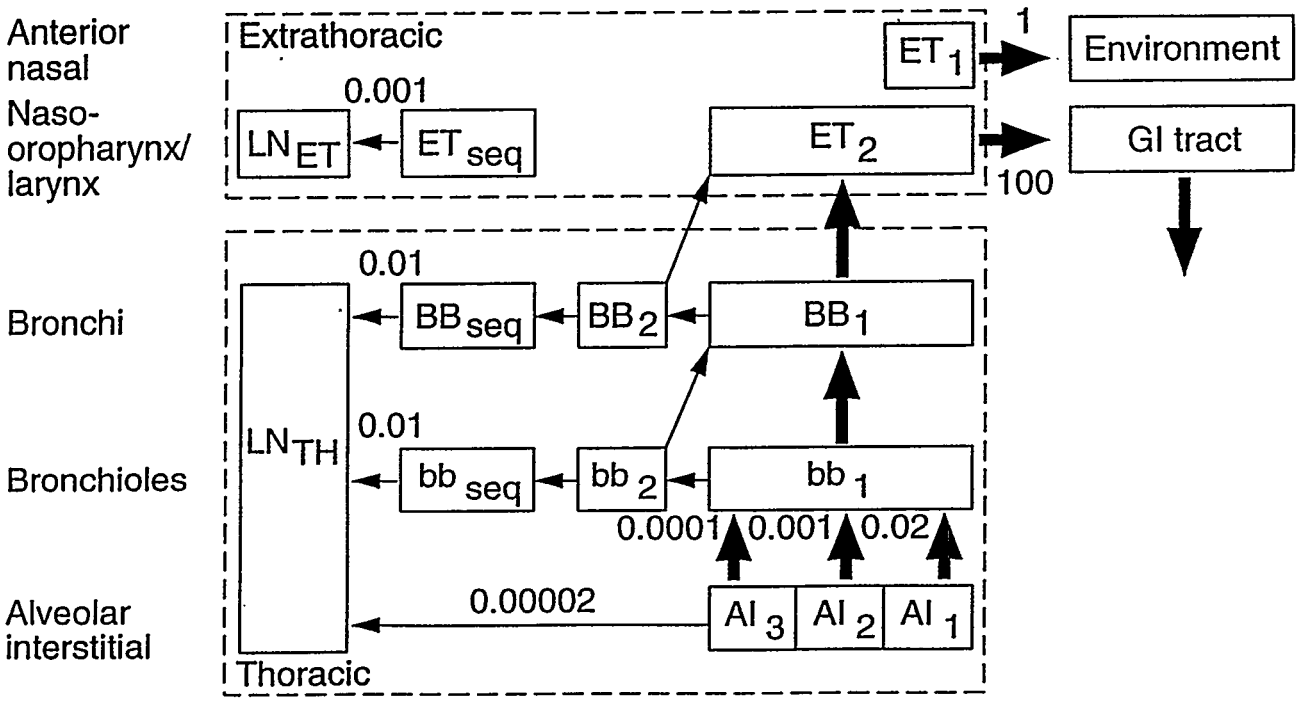

Figure 2. Compartment model representing particle transport in the respiratory tract model.

Example: In-113m

Table 2 compares doses to regions of the lung, based on the new model, for an insoluble 1μm AMAD aerosol labelled with In-113m to the corresponding lung dose taken from ICRP Publication 53. A biological half-time for absorption to blood of 24 hours is used in order to maintain consistency with Publication 53. Lung doses under the new model are less than half those of ICRP Publication 53, reflecting the lower deposition in the deep lung.

Doses to certain groups of target cells, are, however, substantially higher than the overall lung dose. For example, doses are higher by a factor of about two for the cells of the bronchial region. It is interesting to note that the dose to the ET_1 (anterior nasal) region is much larger than the dose to the lung, by between two and three orders of magnitude (this is a common feature of doses for short-lived nuclides under the new model). The detriment associated with the ET_1 region is low, this is reflected by the low regional apportionment factor for ET_1 and the assignment of ET region as a whole to the remainder tissues, thus the contribution of this high tissue dose to effective dose is small. If decisions regarding administered quantities are based on consideration of stochastic effects, then high ET_1 doses are not likely to be of importance. However, consideration of possible deterministic effects in this region should be borne in mind. Doses to the nasal passage region were not considered in the ICRP Publication 30 lung model.

Table 2
Absorbed Doses (μGy/MBq) to the Respiratory Tract from In-113m (insoluble, e.g. albumin)

	Dose	RAF[a]	Weighted dose
ET_1	$2.9\ 10^4$	0.001	29
ET_2	230	0.998	230
ET lymph nodes	110	0.001	0
ET region			**259**
Bronchial (secretory)	160	0.167	27
Bronchial (basal)	140	0.167	23
Bronchiolar	46	0.333	15
Alveolar-interstitial	21	0.333	7
Thoracic lymph nodes	3	0.001	0
Lung			**72**
ICRP 53 lung dose			**190**

a) Regional Apportionment Factor

NEW MODELS FOR ALKALINE EARTH ELEMENTS

In ICRP Publication 53 biokinetic models for simple chemical forms of radionuclides were often taken from ICRP Publication 30. These models were, broadly speaking, empirical in nature setting out to represent the gross retention of the radionuclide in important organs with sufficient precision for purposes of dosimetry. The models for the alkaline earth elements treated radionuclides as either 'bone surface seekers' or 'bone volume seekers'. Initial deposition was taken to occur either on bone surface or volume, from where activity was removed according to recommended retention parameters. No account was taken of transfer of activity between surface and volume.

Recently however, the ICRP has recommended models (10) which include underlying physiological processes. These models are much more complicated and involve recycling of activity (Figure 3). In particular, the simple ICRP Publication 30 classification of isotopes as either surface or volume seekers is replaced by a dynamic model for the bone which involves continual bone burial, remodeling and resorption. Nuclides which previously were simply taken to reside on bone surfaces (e.g. Ca-47, see below) now deposit on bone surfaces, and are then gradually buried in bone volume, where less irradiation of bone target tissues occurs. Bone doses can therefore be lower (although this effect is small for short-lived nuclides). On the other hand, nuclides which were simple bone volume seekers (e.g. Sr-85, see below) are now initially deposited on bone surfaces (where they reside for a short period before being buried in bone volume), leading to higher irradiation of bone target tissues. In contrast to surface seekers, the effect here is most marked for short-lived nuclides.

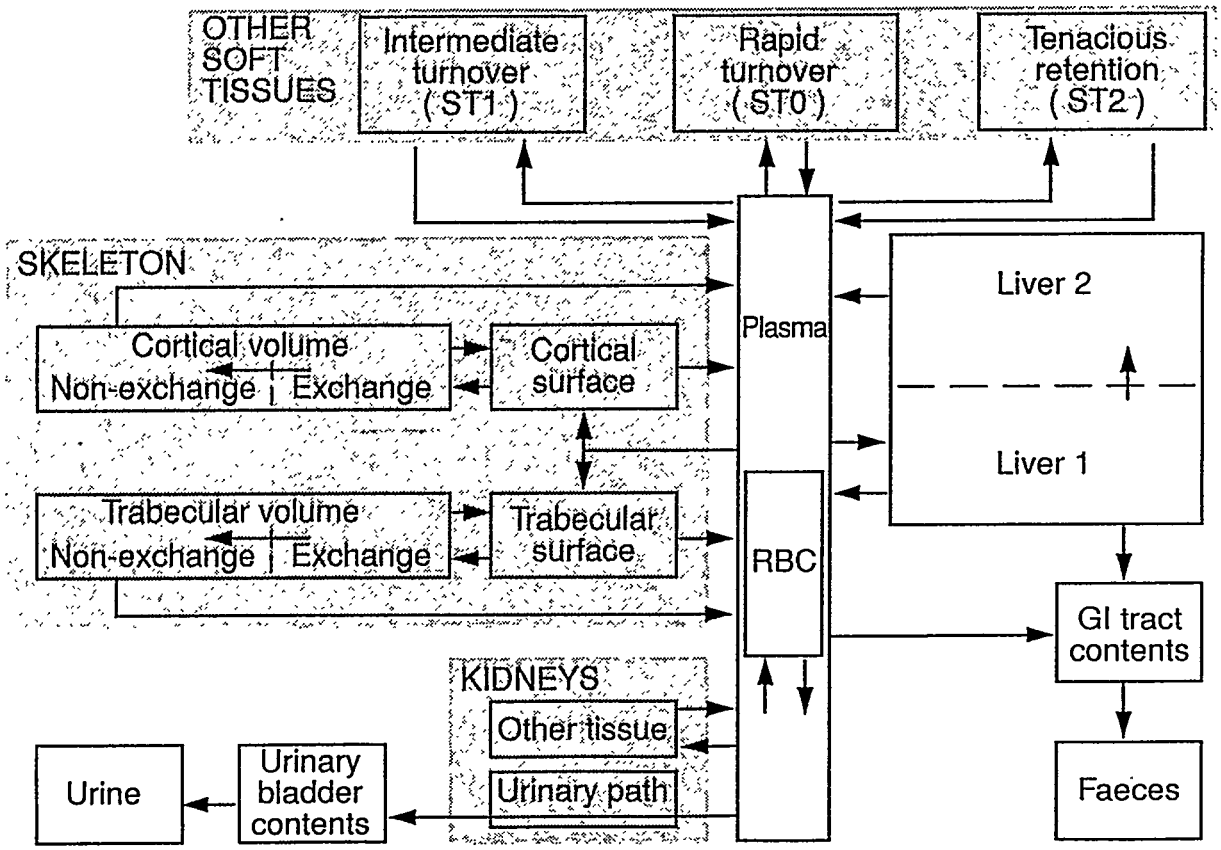

Figure 3. Generic biokinetic model for alkaline earth elements.

Example: Ca-47 and Sr-85

Table 3 compares adult dose coefficients (doses per unit intake) for a few tissues based on the new models to those taken from ICRP Publication 53 for intravenous administration of Ca-47 and Sr-85 in ionic form (fuller tables are given in the Appendix). Bone doses for Ca-47 under the new models are lower by a factor of over two, while for Sr-85 the new doses are higher by about 50%, which is in line with the effects noted above. The large difference in colon doses for Ca-47 results from the explicit consideration of excretion pathways (Figure 3).

Table 3
Comparison of Tissue Doses (mGy/MBq) for I.V. Administration of Ca-47 and Sr-85 in the Adult

	Ca-47 ($T_{1/2}$ = 4.5 d) (ICRP 30 - surface)		Sr-85 ($T_{1/2}$ = 65 d) (ICRP 30 - volume)	
Tissue	ICRP 53	New model	ICRP 53	New model
Bone surface	13	5.6	2.0	2.7
Red marrow	5	3.4	1.8	2.7
Colon	0.5	2.4	0.7	0.7
Others	0.5	0.6	1.0	1.2
Effective	1.4	1.2	0.9	1.1

AGE-DEPENDENT DOSIMETRY

The results given in ICRP Publication 53 were usually based on calculations where the adult biokinetic model was applied to all age groups (a notable exception was for iodide). It was acknowledged that this could lead to overestimates of the doses to children, since turnover of material in children is usually more rapid. It should be noted that this effect is often small for the radionuclides commonly used in nuclear medicine since many are of short physical half-life. Age-specific S values, taking into account the lower tissue masses and different anatomical shape of children were, however, used in ICRP Publication 53.

Recently the ICRP has published age-specific dose coefficients based on an implementation of age-dependent dosimetry developed by the ICRP Task Group on Dose Calculations (10). A brief outline of this method, as it is implemented in the NRPB computer code PLEIADES, is given below. Different implementations are used at other laboratories (11). As part of the ICRP's commitment to quality assurance, results from these different computer codes have been compared and discrepancies resolved.

Biokinetics

In Publication 67 (10) the ICRP has recommended age-specific biokinetic models for alkaline earth elements at six standard ages (3 months, 1, 5, 10, 15 years, and adult) for 31 elements judged to be of most importance in assessing environmental doses. These models are given in terms of rate constants which specify the rate at which material is transferred between the different parts of the body. Rate constants at intermediate ages are derived using linear interpolation. In the calculations presented here, the continuous variation of transfer rates is modeled discretely using a time-stepping method. Starting at the age of intake the calculation is advanced by a time-step small enough for the interpolated rates to be considered constant.

The computed activities at the end of the preceding time-step are then used as the initial conditions for the next step. In this way the number of nuclear decays in each step or interval can be computed. The size of the time-steps used by PLEIADES is of the order of tens of days; it is not governed by the concerns of a numerical method, but in order to model a smooth change of parameters.

S values

Absorbed fraction data for photons and charged particles are available at six standard ages (newborn, 1, 5, 10, 15 years and the adult) from the MIRD phantoms (12, 13). Thus, full sets of S values can be generated at these six ages. At intermediate ages, S values are derived using a suitable interpolation scheme (in the calculations given here a method based on inverse total body mass is used). As described above, calculations proceed by breaking down the time period into a series of steps or intervals. S values calculated at the beginning of a step are assumed to be constant within the interval.

Example: Ca-47 and Sr-85

Table 4 compares dose coefficients based on the new models to those taken from ICRP Publication 53 for intravenous administration of Ca-47 and Sr-85 for 15-year old children. As noted above, Publication 53 did employ age-dependent S values, thus the major development reported here is the application of the new age-dependent biokinetic models. The discussion given above for adults regarding increased doses for ICRP 30 'volume seekers' also applies here, thus we would expect higher bone doses for Sr-85. However, the new model also allows for much higher skeletal uptakes

of alkaline earth elements in the 15-year old to account for the phase of rapid skeletal growth at that age. Figure 4 shows that initial skeletal uptake is about three times higher than in the adult. These two factors act in synergy, the result being that bone doses for Sr-85 in the 15-year old are about a factor of four higher than the previous values (compared to the increase in adult bone doses of only 50%).

Table 4
Comparison of Tissue Doses (mGy/MBq) for Intravenous Administration of Ca-47 ($T_{½}$ = 4.5 days)and Sr-85 ($T_{½}$ = 65 days) in the 15-year Old

Tissue	Ca-47 (ICRP 30 - surface)		Sr-85 (ICRP 30 - volume)	
	ICRP 53	New model	ICRP 53	New model
Bone surface	17	12	2.4	9.5
Red marrow	6.4	5.3	2.2	7.4
Others	0.6	0.6	0.8	2.1
Colon	0.6	1.2	1.1	2.4
Effective	1.8	1.3	1.0	2.7

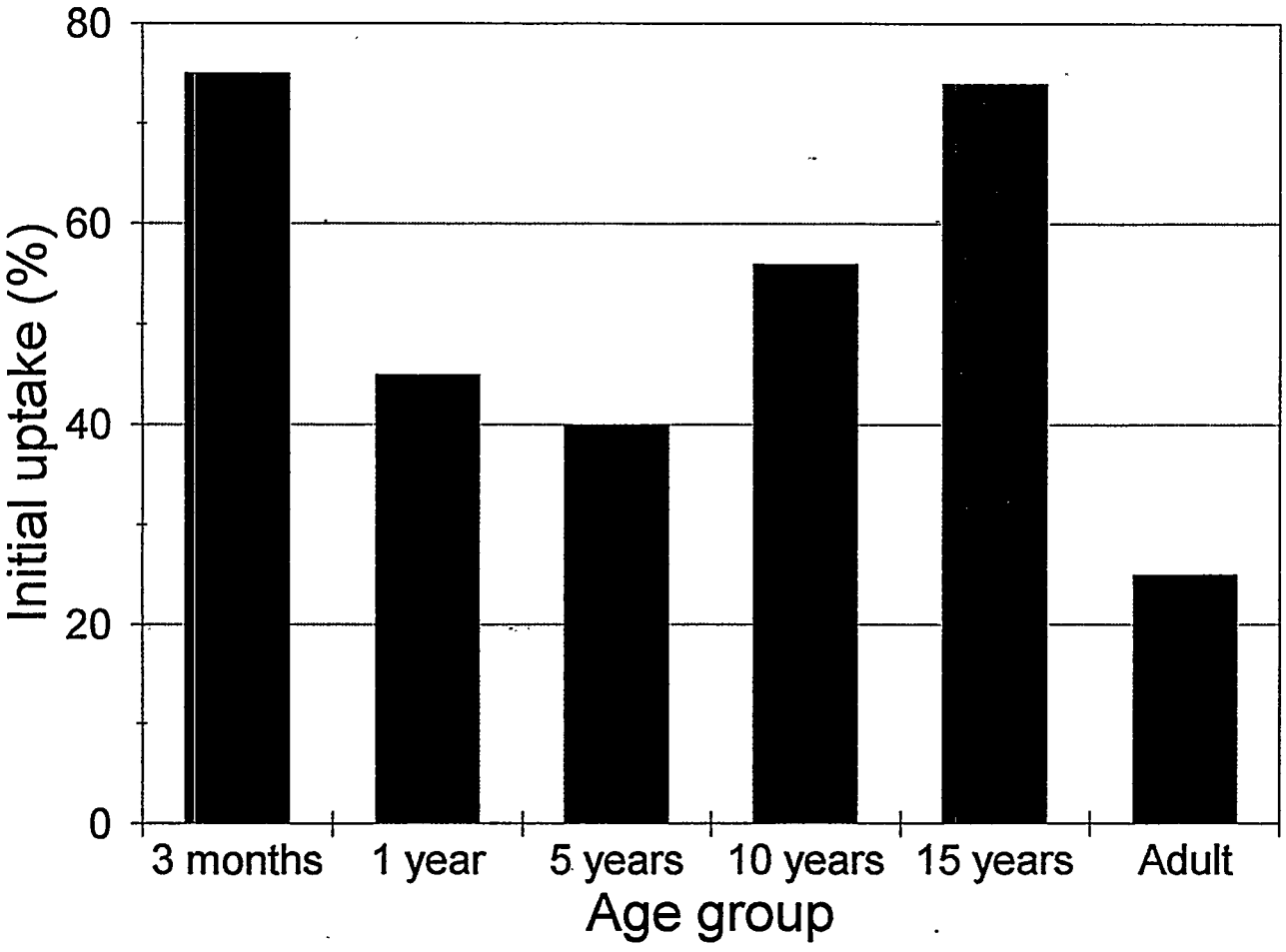

Figure 4. Age-dependent initial skeletal uptakes of strontium.

In the case of Ca-47, the higher skeletal uptake acts in opposition to the lowering effects of the new model for 'ICRP 30 surface seekers'; doses are slightly lower. Figure 4 illustrates that the effect of high skeletal uptake in the 3-month old could also lead to doses that are higher than would otherwise be expected.

RESULTS

Tables 5 to 18 present results for intravenous administration of isotopes of Ca, Sr (note, the values for Sr-89 may be of interest for administrations of 'Metastron') and Ba; and for inhalation of 1μm AMAD aerosols labeled with Tc-99m, In-111 and In-113m. Calculations were performed using the NRPB code PLEIADES and are based on the latest ICRP models described above. PLEIADES is one of the codes used by the ICRP Task Group on Dose Calculations in recent calculations for ICRP Publications (6,7); results are thus consistent in approach with recent ICRP dose coefficients. It should be noted that this approach includes modeling of loss of activity from the gut and from the gallbladder and urinary bladder as a continuous process.

The six age groups given here include the infant (3 month), which was not considered in Publication 53, presumably since radiopharmaceuticals are rarely administered to infants. Nevertheless, results for the infant are given for consistency with recent ICRP Publications.

Table 5
Injection Doses: Committed Equivalent and Effective Doses (mGy/MBq) for Ca-45

Age at intake f1	3 Months 0.6	1 Year 0.4	5 Years 0.4	10 Years 0.4	15 Years 0.4	Adults 0.3
Adrenals	7.9E-01	7.5E-01	3.9E-01	1.8E-01	7.9E-02	1.3E-01
Bladder wall	9.1E-01	9.3E-01	5.9E-01	3.0E-01	1.4E-01	2.7E-01
Bone surfaces	2.4E+02	1.4E+02	8.8E+01	6.5E+01	4.8E+01	2.1E+01
Brain	7.9E-01	7.5E-01	3.9E-01	1.8E-01	7.9E-02	1.3E-01
Breast	7.9E-01	7.5E-01	3.9E-01	1.8E-01	7.9E-02	1.3E-01
GI tract						
St wall	7.9E-01	7.5E-01	3.9E-01	1.8E-01	7.9E-02	1.3E-01
SI wall	7.9E-01	7.5E-01	3.9E-01	1.8E-01	7.9E-02	1.3E-01
ULI wall	2.5E+00	2.9E+00	1.5E+00	6.5E-0	2.2E-01	5.1E-01
LLI wall	5.5E+00	6.7E+00	3.6E+00	1.5E+00	5.0E-01	1.2E+00
Colon	3.8E+00	4.5E+00	2.4E+00	1.0E+00	3.4E-01	8.2E-01
Kidneys	7.9E-01	7.5E-01	3.9E-01	1.8E-01	7.9E-02	1.3E-01
Liver	7.9E-01	7.5E-01	3.9E-01	1.8E-01	7.9E-02	1.3E-01
Muscle	7.9E-01	7.5E-01	3.9E-01	1.8E-01	7.9E-02	1.3E-01
Ovaries	7.9E-01	7.5E-01	3.9E-01	1.8E-01	7.9E-02	1.3E-01
Pancreas	7.9E-01	7.5E-01	3.9E-01	1.8E-01	7.9E-02	1.3E-01
Red marrow	1.1E+02	5.3E+01	2.7E+01	2.2E+01	1.8E+01	1.0E+01
Respiratory tract						
ET airways	7.9E-01	7.5E-01	3.9E-01	1.8E-01	7.9E-02	1.3E-01
Lungs	8.0E-01	7.5E-01	3.9E-01	1.8E-01	7.9E-02	1.3E-01
Skin	7.9E-01	7.5E-01	3.9E-01	1.8E-01	7.9E-02	1.3E-01
Spleen	7.9E-01	7.5E-01	3.9E-01	1.8E-01	7.9E-02	1.3E-01
Testes	7.9E-01	7.5E-01	3.9E-01	1.8E-01	7.9E-02	1.3E-01
Thymus	7.9E-01	7.5E-01	3.9E-01	1.8E-01	7.9E-02	1.3E-01
Thyroid	7.9E-01	7.5E-01	3.9E-01	1.8E-01	7.9E-02	1.3E-01
Uterus	7.9E-01	7.5E-01	3.9E-01	1.8E-01	7.9E-02	1.3E-01
Remainder	7.9E-01	7.5E-01	3.9E-01	1.8E-01	7.9E-02	1.3E-01
Effective dose	1.6E+01	8.8E+00	4.7E+00	3.5E+00	2.7E+00	1.6E+00

GI tract Gastrointestinal tract
St Stomach
SI Small intestine
ULI Upper large intestine
LLI Lower large intestine
ET Extrathoracic

Table 6

Injection Doses: Committed Equivalent and Effective Doses (mGy/MBq) for Ca-47

Age at intake	3 Months	1 Year	5 Years	10 Years	15 Years	Adults
f1	0.6	0.4	0.4	0.4	0.4	0.3
Adrenals	4.8E+00	3.6E+00	1.9E+00	1.3E+00	8.9E-01	7.6E-01
Bladder wall	3.1E+00	3.0E+00	2.0E+00	1.1E+00	5.9E-01	9.9E-01
Bone surfaces	6.5E+01	3.7E+01	2.3E+01	1.7E+01	1.2E+01	5.6E+00
Brain	3.6E+00	2.9E+00	1.7E+00	1.0E+00	6.9E-01	5.6E-01
Breast	2.8E+00	2.3E+00	1.3E+00	7.2E-01	4.0E-01	4.7E-01
GI tract						
St wall	3.0E+0	2.5E+00	1.5E+00	8.1E-01	4.8E-01	5.6E-01
SI wall	3.5E+00	3.1E+00	1.8E+00	1.1E+00	6.7E-01	7.5E-01
ULI wall	6.1E+00	7.5E+00	4.3E+00	2.0E+00	9.1E-01	1.7E+00
LLI wall	1.1E+01	1.5E+01	8.6E+00	3.8E+00	1.6E+00	3.3E+00
Colon	8.2E+00	1.1E+01	6.1E+00	2.8E+00	1.2E+00	2.4E+00
Kidneys	4.0E+00	3.1E+00	1.7E+00	1.0E+00	6.8E-01	6.6E-01
Liver	3.3E+00	2.7E+00	1.5E+00	8.7E-01	5.2E-01	5.8E-01
Muscle	3.6E+00	2.9E+00	1.6E+00	9.5E-01	6.0E-01	5.7E-01
Ovaries	3.7E+00	3.3E+00	1.9E+00	1.1E+00	7.4E-01	8.0E-01
Pancreas	3.6E+00	2.9E+00	1.6E+00	9.7E-01	6.1E-01	6.6E-01
Red marrow	4.1E+01	1.8E+01	8.9E+00	6.8E+00	5.3E+00	3.4E+00
Respiratory tract						
ET airways	3.0E+00	2.6E+00	1.5E+00	8.8E-01	5.6E-01	5.6E-01
Lungs	3.6E+00	2.9E+00	1.5E+00	9.2E-01	5.8E-01	5.7E-01
Skin	3.1E+00	2.5E+00	1.3E+00	7.8E-01	4.6E-01	4.6E-01
Spleen	3.5E+00	2.8E+00	1.5E+00	9.0E-01	5.3E-01	5.8E-01
Testes	2.8E+00	2.4E+00	1.4E+00	7.5E-01	4.4E-01	5.0E-01
Thymus	3.0E+00	2.6E+00	1.4E+00	8.2E-01	5.0E-01	5.5E-01
Thyroid	3.0E+00	2.6E+00	1.5E+00	8.8E-01	5.6E-01	5.6E-01
Uterus	3.2E+00	2.9E+00	1.6E+00	9.6E-01	5.9E-01	6.8E-01
Remainder	3.6E+00	2.9E+00	1.6E+00	9.6E-01	6.1E-01	5.8E-01
Effective dose	9.0E+00	6.0E+00	3.2E+00	2.0E+00	1.3E+00	1.2E+00

Table 7

Injection Doses: Committed Equivalent and Effective Doses (mGy/MBq) for Sr-85

Age at intake	3 Months	1 Year	5 Years	10 Years	15 Years	Adults
f1	0.6	0.4	0.4	0.4	0.4	0.3
Adrenals	1.6E+01	7.4E+00	3.7E+00	3.6E+00	3.8E+00	1.4E+00
Bladder wall	6.4E+00	3.4E+00	2.1E+00	1.8E+00	1.4E+00	8.0E-01
Bone surfaces	4.7E+01	1.9E+01	1.0E+01	9.8E+00	9.5E+00	2.7E+00
Brain	1.0E+01	4.8E+00	2.8E+00	2.7E+00	2.7E+00	8.2E-01
Breast	6.4E+00	3.0E+00	1.5E+00	1.4E+00	1.2E+00	4.7E-01
GI tract						
St wall	6.3E+00	3.0E+00	1.7E+00	1.6E+00	1.4E+00	6.2E-01
SI wall	8.9E+00	4.5E+00	2.5E+00	2.4E+00	2.3E+00	1.0E+00
ULI wall	8.3E+00	4.4E+00	2.5E+00	2.2E+00	1.9E+00	1.0E+00
LLI wall	1.1E+01	6.2E+00	3.6E+00	3.3E+00	3.0E+00	1.4E+00
Colon	9.7E+00	5.2E+00	3.0E+00	2.7E+00	2.4E+00	1.2E+00
Kidneys	1.1E+01	5.3E+00	2.7E+00	2.6E+00	2.5E+00	1.0E+00
Liver	7.8E+00	3.8E+00	1.9E+00	1.7E+00	1.7E+00	6.9E-01
Muscle	9.8E+00	4.5E+00	2.4E+00	2.2E+00	2.1E+00	7.3E-01
Ovaries	9.7E+00	5.0E+00	2.7E+00	2.6E+00	2.7E+00	1.2E+00
Pancreas	9.3E+00	4.5E+00	2.3E+00	2.2E+00	2.2E+00	9.5E-01
Red marrow	2.8E+01	1.2E+01	6.2E+00	6.7E+00	7.4E+00	2.7E+00
Respiratory tract						
ET airways	6.7E+00	3.5E+00	2.1E+00	1.9E+00	1.9E+00	7.1E-01
Lungs	1.0E+01	4.7E+00	2.3E+00	2.1E+00	2.1E+00	7.8E-01
Skin	8.0E+00	3.6E+00	1.8E+00	1.6E+00	1.4E+00	4.8E-01
Spleen	9.1E+00	4.3E+00	2.1E+00	1.9E+00	1.8E+00	7.0E-01
Testes	6.0E+00	3.0E+00	1.6E+00	1.3E+00	1.2E+00	4.7E-01
Thymus	7.3E+00	3.6E+00	1.8E+00	1.7E+00	1.6E+00	6.4E-01
Thyroid	6.7E+00	3.5E+00	2.1E+00	1.9E+00	1.9E+00	7.1E-01
Uterus	7.6E+00	3.9E+00	2.2E+00	2.0E+00	2.0E+00	9.1E-01
Remainder	9.9E+00	4.6E+00	2.4E+00	2.3E+00	2.2E+00	7.5E-01
Effective dose	1.1E+01	5.3E+00	2.8E+00	2.7E+00	2.7E+00	1.1E+00

GI tract Gastrointestinal tract
St Stomach
SI Small intestine
ULI Upper large intestine
LLI Lower large intestine
ET Extrathoracic

Table 8
Injection Doses: Committed Equivalent and Effective Doses (mGy/MBq) for Sr-87m

Age at intake	3 Months	1 Year	5 Years	10 Years	15 Years	Adults
f1	0.6	0.4	0.4	0.4	0.4	0.3
Adrenals	4.0E-02	3.1E-02	1.7E-02	1.1E-02	7.3E-03	6.4E-03
Bladder wall	4.9E-02	6.2E-02	5.2E-02	3.2E-02	1.7E-02	3.4E-02
Bone surfaces	1.4E-01	7.6E-02	4.5E-02	3.3E-02	2.4E-02	1.3E-02
Brain	3.2E-02	2.5E-02	1.4E-02	8.6E-03	5.5E-03	4.6E-03
Breast	2.5E-02	2.0E-02	1.1E-02	6.3E-03	3.8E-03	4.0E-03
GI tract						
St wall	2.9E-02	2.3E-02	1.3E-02	7.9E-03	4.7E-03	5.3E-03
SI wall	3.5E-02	3.0E-02	1.8E-02	1.1E-02	6.4E-03	7.1E-03
ULI wall	6.4E-02	7.5E-02	4.3E-02	2.1E-02	9.4E-03	1.6E-02
LLI wall	4.8E-02	4.7E-02	2.7E-02	1.5E-02	7.9E-03	1.1E-02
Colon	5.7E-02	6.2E-02	3.6E-02	1.8E-02	8.7E-03	1.4E-02
Kidneys	3.6E-02	2.7E-02	1.5E-02	9.5E-03	6.0E-03	5.8E-03
Liver	3.2E-02	2.6E-02	1.4E-02	8.6E-03	5.2E-03	5.5E-03
Muscle	3.2E-02	2.5E-02	1.4E-02	8.4E-03	5.2E-03	5.1E-03
Ovaries	3.6E-02	3.0E-02	1.8E-02	1.1E-02	6.8E-03	7.4E-03
Pancreas	3.5E-02	2.8E-02	1.6E-02	9.6E-03	6.0E-03	6.2E-03
Red marrow	1.4E-01	6.4E-02	3.3E-02	2.5E-02	2.0E-02	1.2E-02
Respiratory tract						
ET airways	3.1E-02	2.6E-02	1.5E-02	8.6E-03	5.2E-03	5.1E-03
Lungs	3.3E-02	2.5E-02	1.4E-02	8.3E-03	5.3E-03	5.0E-03
Skin	2.7E-02	2.0E-02	1.1E-02	6.4E-03	3.8E-03	3.8E-03
Spleen	3.3E-02	2.6E-02	1.4E-02	8.7E-03	5.2E-03	5.4E-03
Testes	2.8E-02	2.3E-02	1.4E-02	7.8E-03	4.4E-03	5.0E-03
Thymus	3.0E-02	2.4E-02	1.3E-02	8.0E-03	4.9E-03	5.0E-03
Thyroid	3.1E-02	2.6E-02	1.5E-02	8.6E-03	5.2E-03	5.1E-03
Uterus	3.4E-02	3.0E-02	1.9E-02	1.1E-02	6.3E-03	7.5E-03
Remainder	3.2E-02	2.5E-02	1.4E-02	8.5E-03	5.3E-03	5.1E-03
Effective dose	5.0E-02	3.7E-02	2.2E-02	1.3E-02	8.4E-03	8.9E-03

Table 9
Injection Doses: Committed Equivalent and Effective Doses (mGy/MBq) for Sr-89

Age at intake	3 Months	1 Year	5 Years	10 Years	15 Years	Adults
f1	0.6	0.4	0.4	0.4	0.4	0.3
Adrenals	4.9E+00	4.2E+00	2.1E+00	1.1E+00	5.4E-01	6.5E-01
Bladder wall	6.5E+00	6.5E+00	4.7E+00	2.9E+00	1.5E+00	2.2E+00
Bone surfaces	2.7E+02	1.2E+02	7.7E+01	6.4E+01	5.4E+01	2.0E+01
Brain	4.9E+00	4.2E+00	2.1E+00	1.1E+00	5.4E-01	6.5E-01
Breast	4.9E+00	4.2E+00	2.1E+00	1.1E+00	5.4E-01	6.5E-01
GI tract						
St wall	4.9E+00	4.2E+00	2.1E+00	1.1E+00	5.4E-01	6.5E-01
SI wall	4.9E+00	4.2E+00	2.1E+00	1.1E+00	5.4E-01	6.5E-01
ULI wall	1.4E+01	1.5E+01	8.0E+00	3.9E+00	1.5E+00	2.4E+00
LLI wall	3.2E+01	3.5E+01	1.9E+01	8.9E+00	3.4E+00	5.7E+00
Colon	2.2E+01	2.4E+01	1.3E+01	6.0E+00	2.3E+00	3.8E+00
Kidneys	4.9E+00	4.2E+00	2.1E+00	1.1E+00	5.4E-01	6.5E-01
Liver	4.9E+00	4.2E+00	2.1E+00	1.1E+00	5.4E-01	6.5E-01
Muscle	4.9E+00	4.2E+00	2.1E+00	1.1E+00	5.4E-01	6.5E-01
Ovaries	4.9E+00	4.2E+00	2.1E+00	1.1E+00	5.4E-01	6.5E-01
Pancreas	4.9E+00	4.2E+00	2.1E+00	1.1E+00	5.4E-01	6.5E-01
Red marrow	2.7E+02	9.4E+01	4.3E+01	3.9E+01	3.6E+01	1.6E+01
Respiratory tract						
ET airways	4.9E+00	4.2E+00	2.1E+00	1.1E+00	5.4E-01	6.5E-01
Lungs	4.9E+00	4.2E+00	2.2E+00	1.1E+00	5.4E-01	6.5E-01
Skin	4.9E+00	4.2E+00	2.1E+00	1.1E+00	5.4E-01	6.5E-01
Spleen	4.9E+00	4.2E+00	2.1E+00	1.1E+00	5.4E-01	6.5E-01
Testes	4.9E+00	4.2E+00	2.1E+00	1.1E+00	5.4E-01	6.5E-01
Thymus	4.9E+00	4.2E+00	2.1E+00	1.1E+00	5.4E-01	6.5E-01
Thyroid	4.9E+00	4.2E+00	2.1E+00	1.1E+00	5.4E-01	6.5E-01
Uterus	4.9E+00	4.2E+00	2.1E+00	1.1E+00	5.4E-01	6.5E-01
Remainder	4.9E+00	4.2E+00	2.1E+00	1.1E+00	5.4E-01	6.5E-01
Effective dose	4.2E+01	1.9E+01	9.2E+00	6.9E+00	5.6E+00	3.1E+00

GI tract Gastrointestinal tract
St Stomach
SI Small intestine
ULI Upper large intestine
LLI Lower large intestine
ET Extrathoracic

Table 10
Injection Doses: Committed Equivalent and Effective Doses (mGy/MBq) for Ba-131

Age at intake	3 Months	1 Year	5 Years	10 Years	15 Years	Adults
f1	0.6	0.3	0.3	0.3	0.3	0.2
Adrenals	3.1E+00	1.3E+00	6.2E-01	5.9E-01	6.1E-01	1.9E-01
Bladder wall	1.6E+00	1.0E+00	6.2E-01	4.7E-01	2.9E-01	2.2E-01
Bone surfaces	4.2E+01	1.6E+01	8.9E+00	7.9E+00	7.1E+00	1.7E+00
Brain	2.1E+00	8.1E-01	4.5E-01	4.4E-01	4.7E-01	1.1E-01
Breast	1.2E+00	5.0E-01	2.4E-01	2.2E-01	1.8E-01	6.2E-02
GI tract						
St wall	1.5E+00	7.8E-01	4.2E-01	3.2E-01	2.4E-01	1.3E-01
SI wall	2.6E+00	1.9E+00	1.1E+00	7.7E-01	5.5E-01	4.3E-01
ULI wall	6.3E+00	6.3E+00	3.5E+00	2.0E+00	9.7E-01	1.2E+00
LLI wall	1.4E+01	1.4E+01	8.0E+00	4.3E+00	2.0E+00	2.7E+00
Colon	9.6E+00	9.8E+00	5.5E+00	3.0E+00	1.4E+00	1.9E+00
Kidneys	2.3E+00	1.0E+00	5.0E-01	4.5E-01	4.2E-01	1.6E-01
Liver	1.6E+00	7.7E-01	3.8E-01	3.1E-01	2.7E-01	1.1E-01
Muscle	2.1E+00	9.0E-01	4.6E-01	4.0E-01	3.6E-01	1.3E-01
Ovaries	3.1E+00	2.4E+00	1.4E+00	9.5E-01	6.8E-01	5.2E-01
Pancreas	1.9E+00	8.7E-01	4.3E-01	3.7E-01	3.5E-01	1.4E-01
Red marrow	1.1E+01	3.7E+00	1.8E+00	1.8E+00	1.9E+00	6.2E-01
Respiratory tract						
ET airways	1.2E+00	5.3E-01	3.0E-01	2.8E-01	2.9E-01	8.7E-02
Lungs	2.1E+00	8.3E-01	3.8E-01	3.5E-01	3.4E-01	1.0E-01
Skin	1.6E+00	6.4E-01	3.0E-01	2.6E-01	2.3E-01	7.1E-02
Spleen	1.9E+00	8.1E-01	3.9E-01	3.2E-01	2.8E-01	1.1E-01
Testes	1.3E+00	6.7E-01	3.3E-01	2.5E-01	2.0E-01	8.8E-02
Thymus	1.4E+00	5.7E-01	2.8E-01	2.5E-01	2.5E-01	8.3E-02
Thyroid	1.2E+00	5.3E-01	3.0E-01	2.8E-01	2.9E-01	8.7E-02
Uterus	2.0E+00	1.3E+00	7.3E-01	5.0E-01	3.9E-01	2.5E-01
Remainder	2.1E+00	9.1E-01	4.7E-01	4.1E-01	3.7E-01	1.4E-01
Effective dose	4.4E+00	2.7E+00	1.5E+00	1.0E+00	7.6E-01	4.8E-01

Table 11
Injection Doses: Committed Equivalent and Effective Doses (mGy/MBq) for Ba-133m

Age at intake	3 Months	1 Year	5 Years	10 Years	15 Years	Adults
f1	0.6	0.3	0.3	0.3	0.3	0.2
Adrenals	1.9E-01	1.4E-01	7.0E-02	4.5E-02	3.6E-02	2.4E-02
Bladder wall	2.0E-01	2.3E-01	1.7E-01	1.0E-01	5.4E-02	9.5E-02
Bone surfaces	8.5E+00	4.1E+00	2.5E+00	1.9E+00	1.5E+00	5.5E-01
Brain	1.6E-01	1.2E-01	6.2E-02	4.0E-02	3.2E-02	2.0E-02
Breast	1.3E-01	1.0E-01	5.3E-02	3.0E-02	1.7E-02	1.8E-02
GI tract						
St wall	1.4E-01	1.3E-01	6.9E-02	3.7E-02	2.1E-02	2.3E-02
SI wall	2.1E-01	2.2E-01	1.3E-01	7.1E-02	3.8E-02	5.1E-02
ULI wall	7.3E+00	1.0E+01	5.6E+00	2.5E+00	8.2E-01	1.9E+00
LLI wall	1.4E+01	2.0E+01	1.1E+01	4.8E+00	1.6E+00	3.8E+00
Colon	1.0E+01	1.5E+01	8.0E+00	3.5E+00	1.2E+00	2.7E+00
Kidneys	1.7E-01	1.3E-01	6.7E-02	4.0E-02	2.7E-02	2.4E-02
Liver	1.5E-01	1.2E-01	6.5E-02	3.6E-02	2.2E-02	2.1E-02
Muscle	1.6E-01	1.2E-01	6.6E-02	3.9E-02	2.6E-02	2.2E-02
Ovaries	2.4E-01	2.5E-01	1.5E-01	8.1E-02	4.4E-02	5.7E-02
Pancreas	1.5E-01	1.2E-01	6.5E-02	3.8E-02	2.5E-02	2.2E-02
Red marrow	5.9E+00	2.1E+00	9.8E-01	8.2E-01	7.0E-01	3.4E-01
Respiratory tract						
ET airways	1.3E-01	1.0E-01	5.6E-02	3.3E-02	2.3E-02	1.9E-02
Lungs	1.6E-01	1.2E-01	6.0E-02	3.6E-02	2.5E-02	2.0E-02
Skin	1.4E-01	1.1E-01	5.6E-02	3.2E-02	2.0E-02	1.8E-02
Spleen	1.5E-01	1.2E-01	6.2E-02	3.5E-02	2.2E-02	2.1E-02
Testes	1.3E-01	1.1E-01	6.0E-02	3.2E-02	1.8E-02	2.0E-02
Thymus	1.3E-01	1.1E-01	5.5E-02	3.2E-02	2.1E-02	1.9E-02
Thyroid	1.3E-01	1.0E-01	5.6E-02	3.3E-02	2.3E-02	1.9E-02
Uterus	1.7E-01	1.7E-01	9.2E-02	4.9E-02	2.8E-02	3.1E-02
Remainder	1.6E-01	1.2E-01	6.7E-02	4.0E-02	2.7E-02	2.3E-02
Effective dose	2.2E+00	2.2E+00	1.2E+00	5.8E-01	2.6E-01	4.0E-01

GI tract Gastrointestinal tract
St Stomach
SI Small intestine
ULI Upper large intestine
LLI Lower large intestine
ET Extrathoracic

Table 12
Injection Doses: Committed Equivalent and Effective Doses (mGy/MBq) for Ba-135m

Age at intake	3 Months	1 Year	5 Years	10 Years	15 Years	Adults
f1	0.6	0.3	0.3	0.3	0.3	0.2
Adrenals	1.3E-01	1.0E-01	5.2E-02	3.0E-02	1.8E-02	1.7E-02
Bladder wall	1.5E-01	1.8E-01	1.4E-01	8.3E-02	4.0E-02	8.0E-02
Bone surfaces	4.3E+00	2.1E+00	1.3E+00	1.0E+00	7.4E-01	3.0E-01
Brain	1.1E-01	8.8E-02	4.7E-02	2.7E-02	1.6E-02	1.5E-02
Breast	9.2E-02	7.8E-02	4.1E-02	2.2E-02	1.1E-02	1.3E-02
GI tract						
St wall	1.1E-01	1.0E-01	5.3E-02	2.7E-02	1.3E-02	1.8E-02
SI wall	1.6E-01	1.7E-01	1.0E-01	5.2E-02	2.4E-02	3.9E-02
ULI wall	5.8E+00	8.4E+00	4.6E+00	2.0E+00	6.5E-01	1.5E+00
LLI wall	1.0E+01	1.5E+01	8.2E+00	3.5E+00	1.2E+00	2.8E+00
Colon	7.7E+00	1.1E+01	6.2E+00	2.6E+00	8.7E-01	2.1E+00
Kidneys	1.2E-01	9.6E-02	5.1E-02	2.8E-02	1.5E-02	1.7E-02
Liver	1.1E-01	9.5E-02	5.0E-02	2.6E-02	1.3E-02	1.6E-02
Muscle	1.1E-01	9.5E-02	5.0E-02	2.7E-02	1.4E-02	1.7E-02
Ovaries	1.7E-01	1.9E-01	1.1E-01	5.8E-02	2.7E-02	4.3E-02
Pancreas	1.1E-01	9.5E-02	4.9E-02	2.6E-02	1.4E-02	1.7E-02
Red marrow	4.2E+00	1.5E+00	7.2E-01	5.8E-01	4.8E-01	2.5E-01
Respiratory tract						
ET airways	9.3E-02	8.1E-02	4.3E-02	2.3E-02	1.3E-02	1.4E-02
Lungs	1.1E-01	8.9E-02	4.5E-02	2.5E-02	1.4E-02	1.5E-02
Skin	9.9E-02	8.2E-02	4.3E-02	2.3E-02	1.2E-02	1.4E-02
Spleen	1.1E-01	9.1E-02	4.7E-02	2.5E-02	1.3E-02	1.6E-02
Testes	9.7E-02	8.8E-02	4.6E-02	2.4E-02	1.1E-02	1.5E-02
Thymus	9.6E-02	8.2E-02	4.2E-02	2.3E-02	1.2E-02	1.4E-02
Thyroid	9.3E-02	8.1E-02	4.3E-02	2.3E-02	1.3E-02	1.4E-02
Uterus	1.3E-01	1.3E-01	7.0E-02	3.5E-02	1.7E-02	2.3E-02
Remainder	1.1E-01	9.5E-02	5.0E-02	2.8E-02	1.5E-02	1.7E-02
Effective dose	1.6E+00	1.6E+00	8.9E-01	4.3E-01	1.8E-01	3.0E-01

Table 13
Injection Doses: Committed Equivalent and Eff. Doses (mGy/MBq) for Tc-99m (Soluble) AMAD 1.0μm

Age at intake	3 Months	1 Year	5 Years	10 Years	15 Years	Adults
f1	1.0	0.8	0.8	0.8	0.8	0.8
Adrenals	1.6E-02	1.1E-02	5.3E-03	3.5E-03	2.1E-03	1.8E-03
Bladder wall	1.2E-02	9.6E-03	4.7E-03	3.2E-03	2.0E-03	1.6E-03
Bone surfaces	2.1E-02	1.5E-02	7.5E-03	5.1E-03	3.2E-03	2.9E-03
Brain	1.3E-02	8.0E-03	4.2E-03	2.8E-03	1.7E-03	1.5E-03
Breast	1.2E-02	7.9E-03	3.9E-03	2.4E-03	1.4E-03	1.2E-03
GI tract						
St wall	7.7E-02	4.7E-02	2.1E-02	1.3E-02	7.6E-03	6.3E-03
SI wall	1.6E-02	3.0E-02	1.4E-02	9.1E-03	4.7E-03	4.1E-03
ULI wall	1.8E-02	5.4E-02	2.4E-02	1.5E-02	7.9E-03	6.6E-03
LLI wall	1.6E-02	4.1E-02	1.8E-02	1.2E-02	5.9E-03	5.0E-03
Colon	1.7E-02	4.8E-02	2.1E-02	1.4E-02	7.0E-03	5.9E-03
Kidneys	1.4E-02	9.8E-03	5.0E-03	3.3E-03	2.0E-03	1.7E-03
Liver	1.5E-02	1.1E-02	5.3E-03	3.4E-03	2.0E-03	1.7E-03
Muscle	1.7E-02	1.2E-02	5.5E-03	3.5E-03	2.1E-03	1.8E-03
Ovaries	1.4E-02	1.5E-02	7.5E-03	5.1E-03	2.9E-03	2.5E-03
Pancreas	1.9E-02	1.4E-02	6.9E-03	4.7E-03	2.8E-03	2.4E-03
Red marrow	1.3E-02	8.7E-03	4.5E-03	3.2E-03	2.0E-03	1.8E-03
Respiratory tract						
ET airways	1.7E+00	1.4E+00	6.9E-01	4.1E-01	2.4E-01	2.0E-01
Lungs	6.6E-02	4.9E-02	3.0E-02	2.3E-02	2.2E-02	1.7E-02
Skin	1.0E-02	6.5E-03	3.1E-03	2.0E-03	1.2E-03	1.0E-03
Spleen	1.6E-02	1.1E-02	5.5E-03	3.7E-03	2.2E-03	1.9E-03
Testes	1.1E-02	7.1E-03	3.4E-03	2.2E-03	1.3E-03	1.2E-03
Thymus	3.0E-02	2.1E-02	8.4E-03	4.9E-03	2.6E-03	2.0E-03
Thyroid	1.5E-02	9.6E-03	5.0E-03	3.3E-03	2.0E-03	1.8E-03
Uterus	1.4E-02	1.3E-02	6.5E-03	4.3E-03	2.5E-03	2.1E-03
Remainder	8.6E-01	7.0E-01	3.5E-01	2.1E-01	1.2E-01	1.0E-01
Effective dose	7.1E-02	6.0E-02	2.9E-02	1.9E-02	1.2E-02	9.7E-03

GI tract Gastrointestinal tract
St Stomach
SI Small intestine
ULI Upper large intestine
LLI Lower large intestine
ET Extrathoracic

Table 14

Injection Doses: Committed Equivalent and Eff. Doses (mGy/MBq) for Tc-99m (Insoluble) AMAD 1.0μm

Age at intake	3 Months	1 Year	5 Years	10 Years	15 Years	Adults
f1	0.02	0.01	0.01	0.01	0.01	0.01
Adrenals	1.2E-02	9.1E-03	4.8E-03	3.0E-03	1.9E-03	1.5E-03
Bladder wall	1.3E-02	9.8E-03	5.0E-03	3.3E-03	1.7E-03	1.4E-03
Bone surfaces	1.4E-02	1.1E-02	5.5E-03	3.8E-03	2.4E-03	2.1E-03
Brain	2.9E-03	2.0E-03	1.3E-03	9.6E-04	6.5E-04	6.4E-04
Breast	8.0E-03	6.1E-03	3.6E-03	2.2E-03	1.2E-03	1.1E-03
GI tract						
St wall	9.0E-02	5.5E-02	2.4E-02	1.5E-02	9.0E-03	7.3E-03
SI wall	1.4E-01	9.3E-02	4.2E-02	2.8E-02	1.4E-02	1.1E-02
ULI wall	2.9E-01	2.0E-01	8.7E-02	5.6E-02	2.8E-02	2.3E-02
LLI wall	2.1E-01	1.4E-01	6.1E-02	3.9E-02	1.9E-02	1.6E-02
Colon	2.6E-01	1.7E-01	7.6E-02	4.9E-02	2.4E-02	2.0E-02
Kidneys	1.1E-02	8.4E-03	4.5E-03	3.0E-03	1.8E-03	1.5E-03
Liver	1.5E-02	1.1E-02	5.6E-03	3.5E-03	2.0E-03	1.6E-03
Muscle	1.3E-02	9.5E-03	4.7E-03	3.0E-03	1.8E-03	1.5E-03
Ovaries	3.9E-02	3.0E-02	1.5E-02	1.0E-02	5.8E-03	4.7E-03
Pancreas	1.8E-02	1.4E-02	6.8E-03	4.6E-03	2.7E-03	2.2E-03
Red marrow	7.3E-03	5.8E-03	3.6E-03	2.8E-03	1.9E-03	1.7E-03
Respiratory tract						
ET airways	1.8E+00	1.5E+00	7.1E-01	4.3E-01	2.5E-01	2.1E-01
Lungs	2.4E-01	1.9E-01	1.2E-01	9.2E-02	9.0E-02	7.0E-02
Skin	4.9E-03	3.5E-03	1.7E-03	1.1E-03	6.5E-04	5.7E-04
Spleen	1.3E-02	9.6E-03	5.0E-03	3.3E-03	2.0E-03	1.7E-03
Testes	5.5E-03	3.9E-03	1.7E-03	1.0E-03	4.9E-04	3.7E-04
Thymus	2.3E-02	1.7E-02	7.1E-03	4.1E-03	2.3E-03	1.8E-03
Thyroid	5.3E-03	4.0E-03	2.3E-03	1.6E-03	1.0E-03	9.4E-04
Uterus	2.7E-02	2.1E-02	1.0E-02	7.0E-03	3.7E-03	3.0E-03
Remainder	9.0E-01	7.3E-01	3.6E-01	2.2E-01	1.3E-01	1.0E-01
Effective dose	1.3E-01	9.5E-02	4.9E-02	3.3E-02	2.3E-02	1.8E-02

Table 15

Injection Doses: Committed Equivalent and Eff. Doses (mGy/MBq)for In-111 (Soluble) AMAD 1.0μm

Age at intake	3 Months	1 Year	5 Years	10 Years	15 Years	Adults
f1	0.04	0.02	0.02	0.02	0.02	0.02
Adrenals	3.2E-01	2.4E-01	1.3E-01	9.2E-02	6.5E-02	5.6E-02
Bladder wall	2.9E-01	2.2E-01	1.1E-01	7.6E-02	4.4E-02	3.8E-02
Bone surfaces	1.3E+00	7.7E-01	3.1E-01	1.8E-01	1.2E-01	8.6E-02
Brain	1.4E-01	9.8E-02	5.1E-02	3.3E-02	2.3E-02	2.1E-02
Breast	1.4E-01	9.8E-02	5.0E-02	3.2E-02	2.0E-02	1.7E-02
GI tract						
St wall	4.8E-01	3.3E-01	1.6E-01	1.0E-01	6.2E-02	5.2E-02
SI wall	9.2E-01	6.7E-01	3.3E-01	2.2E-01	1.2E-01	1.0E-01
ULI wall	2.3E+00	1.6E+00	7.4E-01	4.8E-01	2.4E-01	2.0E-01
LLI wall	4.4E+00	3.0E+00	1.3E+00	8.5E-01	4.2E-01	3.6E-01
Colon	3.2E+00	2.2E+00	1.0E+00	6.4E-01	3.2E-01	2.7E-01
Kidneys	1.0E+00	7.2E-01	4.1E-01	2.8E-01	2.1E-01	1.8E-01
Liver	8.0E-01	5.9E-01	3.2E-01	2.2E-01	1.6E-01	1.3E-01
Muscle	2.5E-01	1.8E-01	9.2E-02	5.9E-02	3.8E-02	3.2E-02
Ovaries	7.3E-01	5.5E-01	2.8E-01	1.9E-01	1.1E-01	8.8E-02
Pancreas	3.4E-01	2.5E-01	1.4E-01	9.1E-02	6.0E-02	5.2E-02
Red marrow	1.2E+00	7.4E-01	3.7E-01	2.1E-01	1.4E-01	1.2E-01
Respiratory tract						
ET airways	1.4E+01	1.2E+01	6.3E+00	3.7E+00	2.1E+00	1.7E+00
Lungs	3.0E-01	2.2E-01	1.2E-01	8.7E-02	7.0E-02	5.6E-02
Skin	1.3E-01	9.3E-02	4.6E-02	2.9E-02	1.9E-02	1.7E-02
Spleen	5.0E-01	3.5E-01	1.9E-01	1.3E-01	8.7E-02	6.8E-02
Testes	1.7E-01	1.2E-01	5.9E-02	3.8E-02	2.3E-02	1.9E-02
Thymus	3.1E-01	2.2E-01	9.3E-02	5.3E-02	3.2E-02	2.6E-02
Thyroid	1.5E-01	1.0E-01	5.7E-02	3.7E-02	2.6E-02	2.3E-02
Uterus	4.3E-01	3.2E-01	1.6E-01	1.1E-01	6.4E-02	5.3E-02
Remainder	7.0E+00	6.2E+00	3.2E+00	1.9E+00	1.1E+00	8.6E-01
Effective dose	1.2E+00	9.1E-01	4.5E-01	2.8E-01	1.6E-01	1.3E-01

GI tract Gastrointestinal tract
St Stomach
SI Small intestine
ULI Upper large intestine
LLI Lower large intestine
ET Extrathoracic

Table 16

Injection Doses: Committed Equivalent and Eff. Doses (mGy/MBq) for In-111 (Insoluble) AMAD 1.0μm

Age at intake	3 Months	1 Year	5 Years	10 Years	15 Years	Adults
f1	0.04	0.02	0.02	0.02	0.02	0.02
Adrenals	2.6E-01	2.0E-01	1.1E-01	7.3E-02	5.2E-02	4.4E-02
Bladder wall	2.8E-01	2.1E-01	1.0E-01	7.1E-02	3.9E-02	3.4E-02
Bone surfaces	8.4E-01	4.9E-01	2.1E-01	1.2E-01	8.4E-02	6.3E-02
Brain	8.7E-02	6.1E-02	3.4E-02	2.2E-02	1.6E-02	1.5E-02
Breast	1.3E-01	1.0E-01	5.7E-02	3.7E-02	2.2E-02	2.0E-02
GI tract						
St wall	4.9E-01	3.3E-01	1.6E-01	1.0E-01	6.3E-02	5.1E-02
SI wall	1.0E+00	7.2E-01	3.5E-01	2.4E-01	1.3E-01	1.1E-01
ULI wall	2.7E+00	1.9E+00	8.4E-01	5.5E-01	2.8E-01	2.3E-01
LLI wall	5.2E+00	3.5E+00	1.6E+00	1.0E+00	5.0E-01	4.2E-01
Colon	3.7E+00	2.6E+00	1.2E+00	7.4E-01	3.7E-01	3.1E-01
Kidneys	6.4E-01	4.5E-01	2.6E-01	1.8E-01	1.4E-01	1.2E-01
Liver	5.4E-01	4.0E-01	2.2E-01	1.5E-01	1.1E-01	9.1E-02
Muscle	2.2E-01	1.6E-01	8.2E-02	5.3E-02	3.4E-02	2.8E-02
Ovaries	7.8E-01	5.9E-01	2.9E-01	2.0E-01	1.2E-01	9.0E-02
Pancreas	2.9E-01	2.2E-01	1.2E-01	7.5E-02	5.0E-02	4.2E-02
Red marrow	7.3E-01	4.5E-01	2.4E-01	1.4E-01	1.0E-01	8.2E-02
Respiratory tract						
ET airways	1.4E+01	1.2E+01	6.4E+00	3.7E+00	2.2E+00	1.7E+00
Lungs	1.3E+00	1.0E+00	6.4E-01	4.8E-01	4.5E-01	3.5E-01
Skin	1.1E-01	7.3E-02	3.7E-02	2.3E-02	1.5E-02	1.3E-02
Spleen	3.6E-01	2.6E-01	1.4E-01	9.2E-02	6.4E-02	5.1E-02
Testes	1.5E-01	1.0E-01	4.8E-02	3.1E-02	1.8E-02	1.5E-02
Thymus	2.9E-01	2.1E-01	9.5E-02	5.5E-02	3.4E-02	2.8E-02
Thyroid	1.1E-01	8.3E-02	4.7E-02	3.0E-02	2.1E-02	1.9E-02
Uterus	4.2E-01	3.1E-01	1.6E-01	1.1E-01	6.0E-02	4.9E-02
Remainder	7.0E+00	6.2E+00	3.2E+00	1.9E+00	1.1E+00	8.6E-01
Effective dose	1.3E+00	1.0E+00	5.1E-01	3.3E-01	2.1E-01	1.7E-01

Table 17

Injection Doses: Committed Equivalent and Eff. Doses (mGy/MBq) for In-113m (Soluble) AMAD 1.0μm

Age at intake	3 Months	1 Year	5 Years	10 Years	15 Years	Adults
f1	0.04	0.02	0.02	0.02	0.02	0.02
Adrenals	9.8E-03	7.1E-03	3.6E-03	2.3E-03	1.4E-03	1.2E-03
Bladder wall	8.7E-03	6.0E-03	2.9E-03	1.8E-03	1.0E-03	8.7E-04
Bone surfaces	2.4E-02	1.4E-02	5.8E-03	3.4E-03	2.1E-03	1.6E-03
Brain	5.6E-03	3.9E-03	2.0E-03	1.4E-03	9.0E-04	8.3E-04
Breast	7.7E-03	5.5E-03	2.7E-03	1.7E-03	9.4E-04	8.0E-04
GI tract						
St wall	3.3E-01	1.9E-01	7.6E-02	4.5E-02	2.5E-02	2.1E-02
SI wall	2.8E-01	1.8E-01	7.7E-02	4.7E-02	2.2E-02	1.8E-02
ULI wall	2.7E-01	1.8E-01	7.6E-02	4.7E-02	2.2E-02	1.8E-02
LLI wall	7.7E-02	5.1E-02	2.2E-02	1.4E-02	6.5E-03	5.5E-03
Colon	1.9E-01	1.3E-01	5.3E-02	3.3E-02	1.5E-02	1.3E-02
Kidneys	1.8E-02	1.2E-02	6.3E-03	4.2E-03	2.8E-03	2.3E-03
Liver	1.6E-02	1.1E-02	5.4E-03	3.4E-03	2.1E-03	1.7E-03
Muscle	1.1E-02	7.9E-03	3.7E-03	2.3E-03	1.4E-03	1.1E-03
Ovaries	1.9E-02	1.4E-02	6.9E-03	4.5E-03	2.5E-03	2.1E-03
Pancreas	1.5E-02	1.1E-02	5.7E-03	3.8E-03	2.2E-03	1.9E-03
Red marrow	2.2E-02	1.4E-02	6.9E-03	4.1E-03	2.6E-03	2.1E-03
Respiratory tract						
ET airways	2.2E+00	1.7E+00	7.8E-01	4.8E-01	2.7E-01	2.4E-01
Lungs	1.2E-01	9.1E-02	5.7E-02	4.3E-02	4.2E-02	3.3E-02
Skin	6.2E-03	4.3E-03	2.0E-03	1.3E-03	7.8E-04	6.7E-04
Spleen	1.4E-02	9.7E-03	4.9E-03	3.3E-03	2.0E-03	1.7E-03
Testes	5.6E-03	3.9E-03	1.8E-03	1.1E-03	6.4E-04	5.4E-04
Thymus	2.0E-02	1.4E-02	5.6E-03	3.0E-03	1.5E-03	1.2E-03
Thyroid	6.6E-03	4.6E-03	2.4E-03	1.6E-03	1.0E-03	9.5E-04
Uterus	1.6E-02	1.2E-02	5.8E-03	3.8E-03	2.0E-03	1.7E-03
Remainder	1.1E+00	8.4E-01	3.9E-01	2.4E-01	1.4E-01	1.2E-01
Effective dose	1.4E-01	9.7E-02	4.5E-02	2.9E-02	1.8E-02	1.5E-02

GI tract Gastrointestinal tract
St Stomach
SI Small intestine
ULI Upper large intestine
LLI Lower large intestine
ET Extrathoracic

Table 18

Injection Doses: Committed Equivalent and Eff. Doses (mGy/MBq) for In-113m (Insoluble) AMAD 1.0μm

Age at intake	3 Months	1 Year	5 Years	10 Years	15 Years	Adults
f1	0.04	0.02	0.02	0.02	0.02	0.02
Adrenals	7.8E-03	5.9E-03	3.0E-03	1.9E-03	1.2E-03	9.9E-04
Bladder wall	5.7E-03	4.1E-03	1.9E-03	1.2E-03	5.9E-04	4.8E-04
Bone surfaces	7.7E-03	5.1E-03	2.4E-03	1.5E-03	9.5E-04	8.1E-04
Brain	2.0E-03	1.4E-03	8.4E-04	6.6E-04	4.5E-04	4.4E-04
Breast	5.9E-03	4.4E-03	2.5E-03	1.6E-03	8.3E-04	7.4E-04
GI tract						
St wall	3.8E-01	2.1E-01	8.6E-02	5.1E-02	2.9E-02	2.3E-02
SI wall	3.2E-01	2.1E-01	8.7E-02	5.4E-02	2.4E-02	2.0E-02
ULI wall	3.1E-01	2.1E-01	8.6E-02	5.4E-02	2.5E-02	2.1E-02
LLI wall	8.4E-02	5.6E-02	2.4E-02	1.5E-02	7.0E-03	5.8E-03
Colon	2.1E-01	1.4E-01	5.9E-02	3.7E-02	1.7E-02	1.4E-02
Kidneys	7.6E-03	5.4E-03	2.9E-03	1.9E-03	1.1E-03	9.4E-04
Liver	9.5E-03	7.0E-03	3.4E-03	2.1E-03	1.2E-03	9.5E-04
Muscle	8.4E-03	6.2E-03	2.9E-03	1.9E-03	1.1E-03	8.7E-04
Ovaries	1.8E-02	1.3E-02	6.4E-03	4.2E-03	2.2E-03	1.8E-03
Pancreas	1.4E-02	1.0E-02	5.3E-03	3.6E-03	2.1E-03	1.7E-03
Red marrow	6.0E-03	4.2E-03	2.4E-03	1.7E-03	1.2E-03	1.0E-03
Respiratory tract						
ET airways	2.3E+00	1.8E+00	8.3E-01	5.2E-01	2.9E-01	2.5E-01
Lungs	2.6E-01	2.0E-01	1.3E-01	9.7E-02	9.4E-02	7.3E-02
Skin	3.4E-03	2.4E-03	1.1E-03	7.3E-04	4.5E-04	3.8E-04
Spleen	9.5E-03	7.0E-03	3.6E-03	2.5E-03	1.5E-03	1.3E-03
Testes	2.3E-03	1.6E-03	6.3E-04	3.9E-04	1.7E-04	1.3E-04
Thymus	1.7E-02	1.2E-02	5.1E-03	2.8E-03	1.4E-03	1.1E-03
Thyroid	3.4E-03	2.5E-03	1.5E-03	1.0E-03	6.7E-04	6.2E-04
Uterus	1.4E-02	1.1E-02	5.1E-03	3.4E-03	1.7E-03	1.3E-03
Remainder	1.2E+00	9.0E-01	4.2E-01	2.6E-01	1.5E-01	1.3E-01
Effective dose	1.7E-01	1.2E-01	5.6E-02	3.7E-02	2.5E-02	2.0E-02

GI tract Gastrointestinal tract
St Stomach
SI Small intestine
ULI Upper large intestine
LLI Lower large intestine
ET Extrathoracic

ACKNOWLEDGMENT

This work was partially supported by the European Commission under contract number FI4P CT95 0011.

REFERENCES

1. Protection of the Patient in Nuclear Medicine. ICRP Publication 52. Ann ICRP 17(4), 1987.
2. Radiation Dose to Patients from Radiopharmaceuticals. ICRP Publication 53. Ann ICRP 18(1-4), 1987.
3. Leggett RW and Eckerman KF. Evolution of the ICRP's biokinetic models. In: Intakes of Radionuclides: Detection, Assessment and Limitation of Occupational Exposure. Bath, England. Editors, J W Stather and A Karaoglou. pp 147-155. Radiat Prot Dosim 53(1-4), 1994.
4. Human Respiratory Tract Model for Radiological Protection. ICRP Publication 66. Ann ICRP 24(1-3), 1994.
5. Limits for Intakes of Radionuclides by Workers. ICRP Publication 30 Part 1. Ann ICRP 2(3/4), 1979.
6. Dose Coefficients for Intakes of Radionuclides by Workers. Replacement of ICRP Publication 61. ICRP Publication 68. Ann ICRP 24(4), 1994.
7. Age-dependent Doses to Members of the Public from Intake of Radionuclides: Part 4 Inhalation

Dose Coefficients. ICRP Publication 71. Ann ICRP 25(3/4), 1995.
8. Guy RH, Kalia YN, Lim CS, Nonato LB and Turner NG. Drug smuggling - creative ways to cross biological barriers. Chemistry in Britain 32 (7), The Royal Society of Chemistry, London, 1996.
9. Silk TJ, Phipps AW and Bailey MR. New inhalation dose coefficients for workers. Radiol Prot Bull 172, 1995.
10. Age-dependent Doses to Members of the Public from Intake of Radionuclides: Part 2 Ingestion Dose Coefficients. ICRP Publication 67. Ann ICRP 23(3/4), 1993.
11. Eckerman KF, Leggett RW and Williams LR. An elementary method for solving compartmental models with time-dependent coefficients. In: Radiation Protection Dosimetry, Age-dependent Factors in the Biokinetics and Dosimetry of Radionuclides. Schloss Elmau, Germany. Editors DM Taylor, GB Gerber, JW Stather. Radiat Prot Dosim 41(2-4), 1992.
12. Cristy M and Eckerman KF. Specific Absorbed Fractions of Energy at Various Ages from Internal Photon Sources. Oak Ridge, Tennessee. ORNL/TM-8381/v1-7, 1987.
13. Cristy M and Eckerman K F. SEECAL: Program to Calculate Age-dependent Specific Effective Energies. Oak Ridge, Tennessee. ORNL/TM-12351, 1993.

QUESTIONS

Bolch: In the general systemic circulation model you showed, activity is partitioned in a variable fashion over time between surface deposition and bone volume incorporation. In the new ICRP model, do you explicitly consider burial in bone as a function of depth from bone surface and do you have electron absorbed fractions as a function of depth in bone?

Phipps: The burial of activity from bone surface to volume is modeled as a continuous process governed by first-order kinetics. However, since we are using a compartmental model, activity is either in the 'surface box' as in the 'volume box'; an activity-depth profile is not available from this kind of model. Different absorbed fractions (AF) are applied to activity in the surface and volume boxes; thus, activity passing from surface to volume undergoes a discontinuous change in the AF associated with it.

Kennel: What sort of considerations went into the determination of the RAF value in the lung model?

Phipps: The regional apportionment factors (RAF) represent the fraction of the total lung detriment that is associated with each region. They are based on observed rates of tumor incidence in the various regions of the lung; this is mainly available from the group of occupationally exposed uranium miners. In fact, the final recommended values for RAFs are substantially rounded (to 0.333 for each of the 3 lung regions) to reflect the uncertainties in the epidemiological data.

PROPRIETY OF THE ICRP MODEL FOR ESTIMATION OF RADIATION DOSE TO THE GASTROINTESTINAL TRACT FROM INTRAVENOUSLY ADMINISTERED ^{201}TlCl

Lathrop KA[1],Lathrop DA[2],and Harper PV[1]
[1]University of Chicago Hospitals
Department of Radiology, MC 2026
5841 Maryland Ave., Chicago IL 60637
[2]Department of Medical Physiology
University of Tromsø
N-9037 Tromsø, Norway

ABSTRACT

A detailed biodistribution study of intravenously administered ^{201}TlCl in mice indicated a very substantial intestinal localization, especially in the small intestine wall. This is of interest because all the current published radiation absorbed dose estimates make use of the ICRP 30 distribution model which assumes that all the activity associated with the intestine is in the lumen. The human studies by Krahwinkel et al. provide data on intestinal localization of ^{201}Tl for comparison with the mouse data. The residence times in the gut in both mouse and human studies were nearly the same, and on this basis revised radiation absorbed dose estimates in human subjects were made, suggesting that especially the small intestine was receiving substantial exposure from routine ^{201}Tl imaging studies.

INTRODUCTION

Some time ago we undertook to carry out a detailed biodistribution study of ^{201}TlCl administered intravenously to mice (1,2,3) with particular attention to the gastrointestinal tract (4,5). Animals were sacrificed at intervals of a few minutes during the early period of rapid equilibration. Beginning at one day, sacrifices were made daily through seven days. The principal organs and tissues, twenty-seven samples in all, were assayed for ^{201}Tl. The wall and contents of the sections of the intestinal tract were analyzed separately.

RESULTS AND DISCUSSION

With the mouse data base obtained as described above, the SAAM program (6) was used to produce a compartmental model (Figure 1). This disclosed that the injected ^{201}Tl rapidly entered into a complex equilibrium. Note that the rate constant for small intestine content and small intestine wall is remarkably higher than any other observed.

Figure 2 shows a semilog plot of the activity contained in the various intestinal components over time, corrected for physical decay. The effect of the high rate constant mentioned above can be seen since the small intestine wall contains five times more activity than the content. The rate constants in general were quite high, so that equilibrium was reached rapidly and was maintained for the seven day observation period. The biologic disappearance of ^{201}Tl for all the intestinal components was the same; the ratios of activity in the various segments remained constant with a disappearance half-time of 62.5 hours, corresponding to a rate constant of 0.016 h^{-1}.

A portion of this equilibrium is demonstrated in Table 1, in which $^{201}TlCl$ was injected into an isolated segment of the upper small intestine. A ligature was placed at each end of this section to prevent direct passage of the activity to other parts of the lumen. As shown, the activity rapidly entered the wall of the tied segment and from there

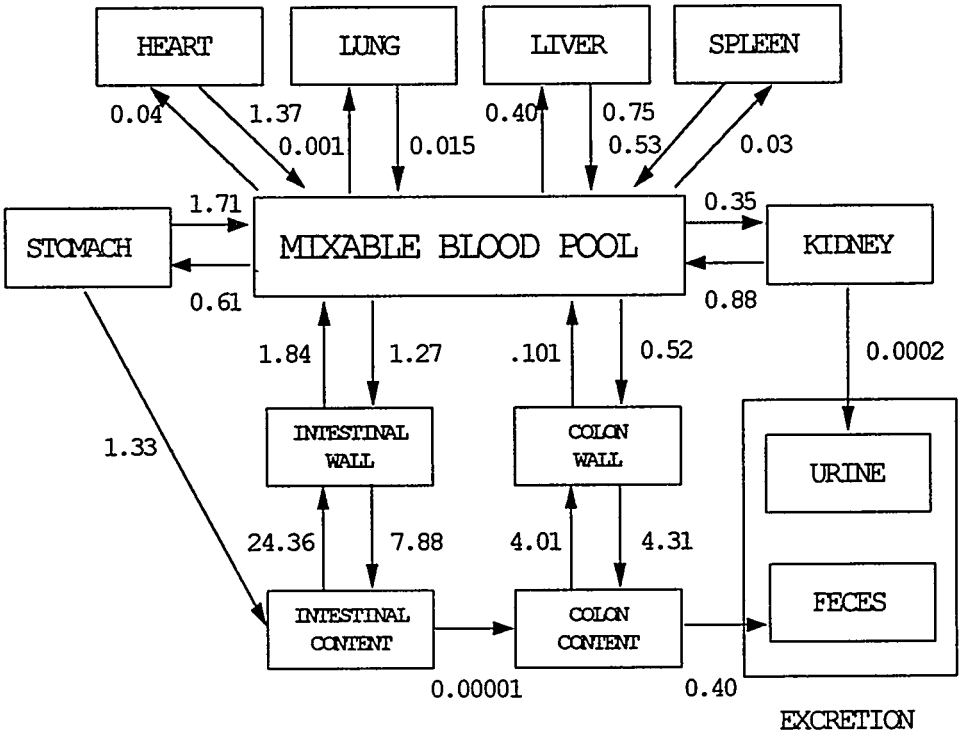

Figure 1. Rate constants expressed as fraction of ^{201}Tl per hour.

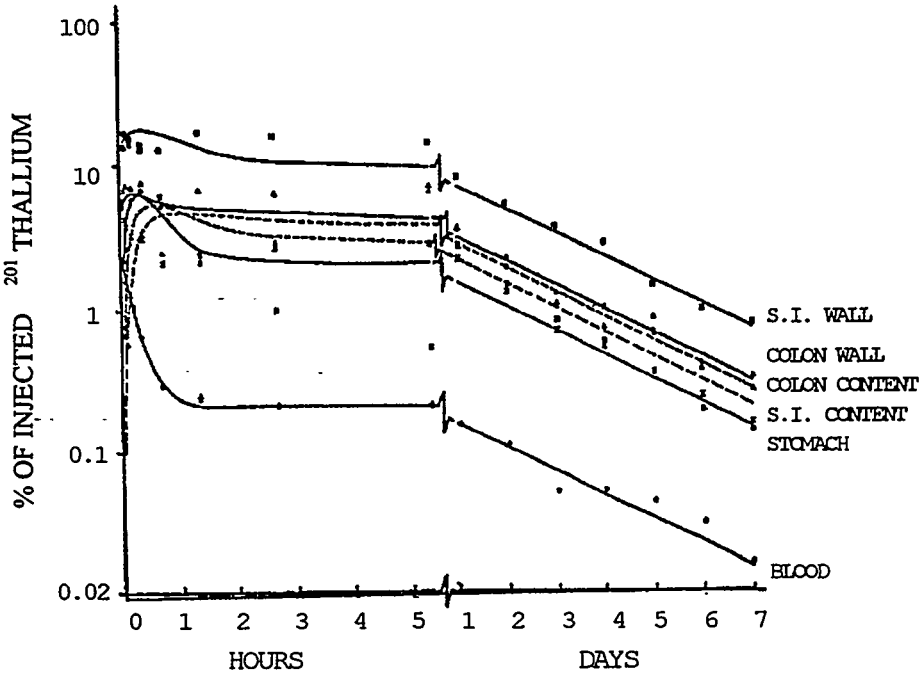

Figure 2. Gastrointestinal tract biokinetics for ^{201}Tl in mice following intravenous administration.

was transported via the circulation throughout the body and returned to lower portions of the small intestine and its contents. The initial disappearance rate of activity from the lumen of the isolated segment shown in Table 1 of 87.5% in five minutes (rate constant of 24.9 h^{-1}) agrees well with that shown in Figure 1.

Table 1
Absorption of ^{201}Tl from Isolated Upper Small Intestinal Segment

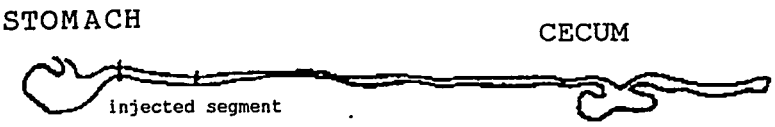

% OF INJECTED ^{201}THALLIUM

MINUTES AFTER	ISOLATED SEGMENT		REMAINDER OF SMALL INTESTINE	
INJECTION	WALL	CONTENTS	WALL	CONTENTS
0	0.	100.	0.	0.
5	69.2	12.5	0.	0.07
10	60.6	18.1	1.09	0.05
60	22.9	5.83	17.35	0.48

The publication by Krahwinkel et al. (7) of their studies in humans of ^{201}Tl localization after I.V. injection as TlCl afforded human data to compare with the mouse data. These data were obtained by conjugate imaging and were reported as small and large intestines combined together with their contents. Measurements were made at 2 h, 24 h, 48 h, 120 h, and 168 h. The data for these time intervals, together with the mouse data for the same time points, are shown in Table 2. A time-activity curve for the mouse intestinal data, comparable to the Krahwinkel data was generated by summing the data for the small intestine and large intestine with their contents and combining the biologic disappearance constant of 0.016 h^{-1} with the physical decay constant for ^{201}Tl ($T_{½}$ = 73 h or 0.00949 h^{-1}) to give 0.0255 h^{-1}. The corresponding value for the human data, which lumped together the whole gut and contents (determined in a similar way from Krahwinkle's data) was 0.0131 h^{-1} (Figure 3). The time-activity curves determined in this way differed little from the least squares exponential fit of the actual data points. The areas under the curves agreed within 10% - 15%. The residence times for human and summed mouse data, determined by dividing the estimated initial activity by the rate constant, were 11.7 h and 15.3 h for the mouse and human. This close agreement was remarkable in view of the ratio of body masses of ~3000:1. This is due to the fact that thallous ion has been shown to be a good potassium analogue (8), and as such is strongly retained in the body in the intracellular space, and is excreted very slowly so that the physical decay of the thallium is strongly reflected in the retention curves.

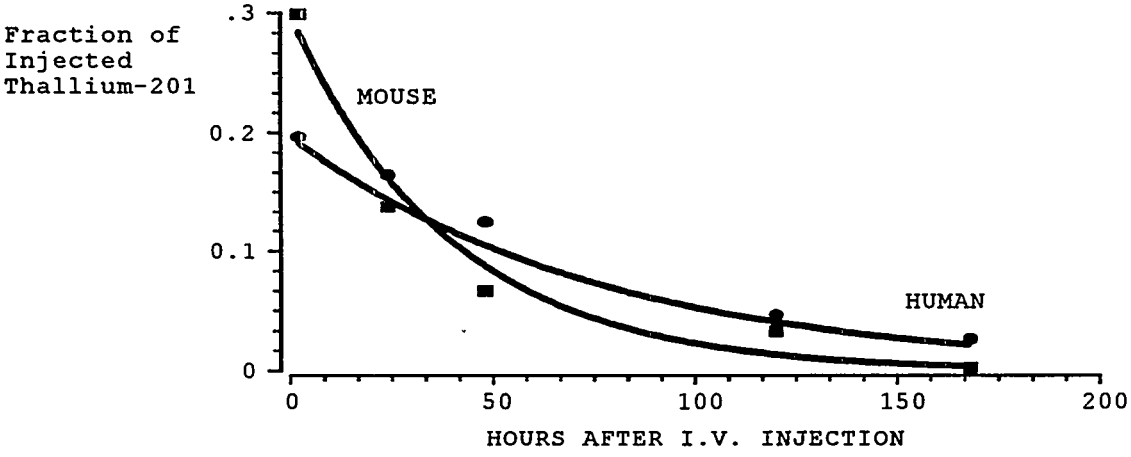

Figure 3. ^{201}Tl retention in whole gut and in mouse and human. Points from Table 2. Curves: $\lambda_{eff} = \lambda_{biol}$ (Figure 2) + λ_{phys}. Area under curves (i.e. residence time): τ = initial value / λ_{eff}.

Table 2

Time:Activity Data for ^{201}Tl in Mouse and Human

ORGAN	SAMPLE	2 H	24 H	48 H	120 H	168 H
SMALL INTESTINE	Wall	*19.2	6.51	3.24	1.37	0.16
	Content	1.43	2.32	0.89	0.2	0.02
UPPER LARGE INTESTINE	Wall	4.12	1.58	0.75	0.12	0.03
	Content	1.52	1.03	0.56	1.36	0.31
LOWER LARGE INTESTINE	Wall	2.14	1.15	0.61	0.07	0.02
	Content	1.04	1.33	0.61	0.13	0.03
SUMMED MOUSE DATA	Wall + Content	29.9	13.8	6.66	3.34	0.3
HUMAN DATA (5)	Wall + Content	19.7	16.5	12.5	4.7	2.7

*Values not corrected for physical decay.

Since the various portions of the mouse intestines and contents appear to be in constant ratio with each other (Figure 2), it seems reasonable to assume that the human residence times could be approximated from corresponding portions of the mouse gut and contents by assuming that the ratios of their residence times are the same as the total gut ratio, i.e. 1.31. The residence times calculated in this way are shown in Table 3.

The ICRP 30 model (Figure 4) (9) for activity in the intestinal tract assumes that all activity associated with the intestinal tract is in the lumen of the bowel and moves along at various rates. Furthermore, this assumption is usually made in the calculation of S values (10). Because most of the thallium is in the wall, not in the contents, the ICRP model will not adequately model the behavior of thallous ion in the intestine. Published S values as well must be modified to account for the appropriate patterns of energy absorption.

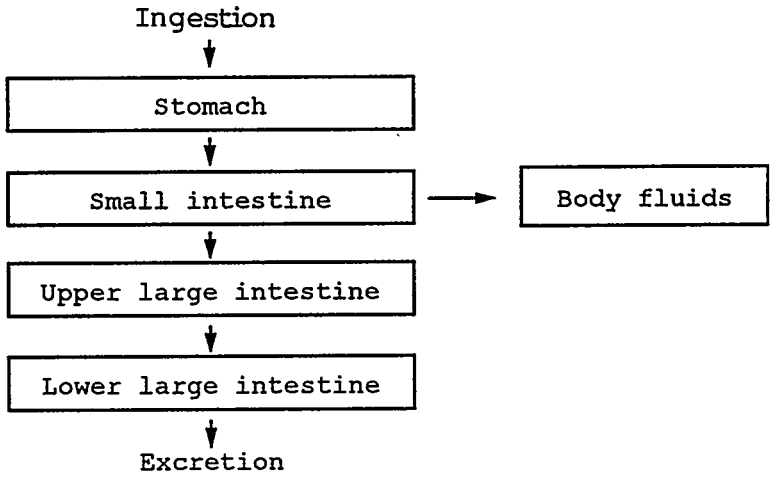

Figure 4. ICRP gastrointestinal tract model.

For comparison with published dose estimates (7,11,12), partial (i.e. self-dose) estimates of the human radiation absorbed dose to the intestinal walls were carried out (Table 3). The particle self-dose presented no problems since it does not depend on organ position and the absorbed fractions are assumed to be one. Residence times are taken from this study, target masses from MIRD 5, Revised, (13) and delta values were calculated using MIRD decay data (14). The effective target mass was assumed to be limited to the highly metabolic, highly cellular mucosa. This was estimated from animal data (15) as 60% of small bowel mass, and 20% of colon wall mass (due to absence of villi). Note that although the colon activity was less than the small bowel activity, the target mass was much lower, so that the radiation absorbed dose is about the same. One-half of the electron dose to the contents is assumed to be absorbed in the wall.

The photon dose to the small intestine wall was calculated using a model suggested in ORNL/TM-12907 (16). The activity in entire wall and content was assumed to be distributed evenly in the total mass of 1040 g. The small intestine as described in MIRD 5 (Revised) is assumed to be contained in a cylindrical volume; absorbed fractions for the Brownell thick ellipsoid were used (17). The values from the present study, although they represent only partial doses, in general exceed the published values

These findings raise some interesting questions and possibilities. Consider the small intestine; the average particle self-dose is 26.6 mGy/37 MBq. For a routine imaging study, 259 MBq gives a dose of 186 mGy to the bowel wall. Assuming that the thallium localization is largely in the mucosa the estimated dose will be substantially increased. Since an RBE as high as 5 has been reported for ^{201}Tl (18) relative to beta emitting ^{204}Tl (Figure 5), this suggests that the intestinal mucosa might be receiving a dose on the order of 2 Sv during an imaging procedure with 259 MBq. These speculations need to be examined carefully as they probably represent a worst case. The MIRD decay scheme tabulation for ^{201}Tl lists thirty-eight transitions giving rise to low-energy electrons. Summing the probabilities for these transitions gives an average of about five electrons per disintegration. It has been suggested by Dr. Feinendegen (personal communication) that low-energy electrons originating within the cytoplasm, unlike the effect of Auger disintegration processes in atoms

Table 3
Estimated Self Dose to Human Intestine from 37 MBq (1 mCi) of Intravenous ^{201}TlCl.

Organ	Effective Mass (kg)*	Residence Time (hr)**	Absorbed Dose (mGy)			
			Electrons	Photons	Total	Published Value
SI Wall	0.39	10.1	23.4	3.6	26.6	0.61 (6)
						4.64 (10)
SI Contents	0.4	2.8	6.4	3.6		3.9 (11)
ULI Wall	0.23	2.2	8.5		12.4	0.28 (6)
						15.7 (10)
ULI Contents	0.09	0.77	7.9			3.0 (11)
LLI Wall	0.1	1.22	11.1		15.7	5.39 (6)
						44.0 (10)
LLI Contents	0.12	1.25	9.2			2.2 (11)

* Effective mass assumed to be limited to mucosa (13,15)

** human (assumed) = $\tau_{mouse} \times \frac{\tau_{human}\ (Krahwinkel)}{\tau_{mouse}(summed\ data)}$

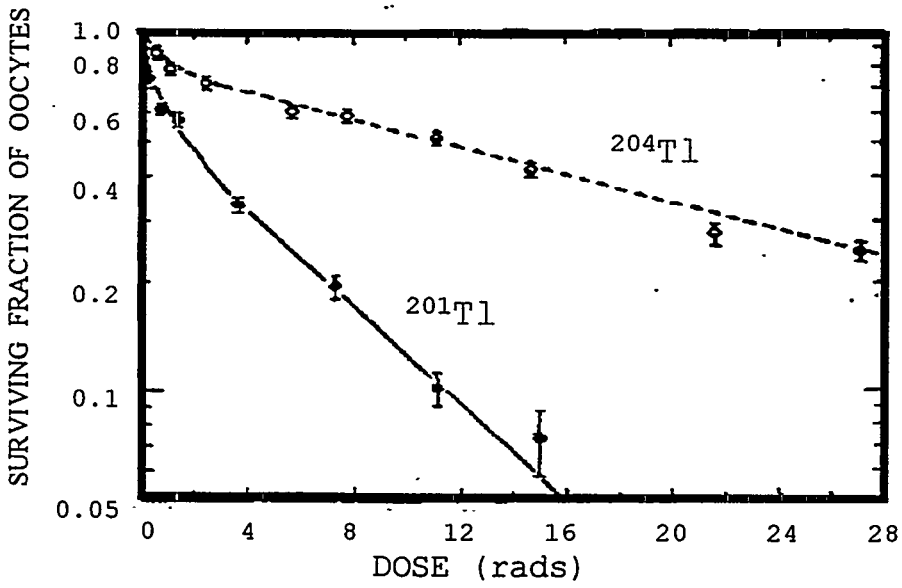

Figure 5. Contrasting effect of β (^{204}Tl) and Auger plus conversion electrons (^{201}Tl) in cell suspensions (17).

chemically bound to the DNA, behave very much like beta rays terminating their paths within the cell. Furthermore, such low-energy electrons have a specific ionization several times higher than that of the initial track of the ^{204}Tl beta originating in a cell. This could increase the difference between the ^{201}Tl and ^{204}Tl survival curves. On the other hand, the total energy of the ^{204}Tl beta is several times higher than the total of the low energy electrons of ^{201}Tl and their range is a number of cell diameters. In closely packed cells in a tissue, ^{204}Tl cross fire would result in a reduction of the difference between the survival curves. An intermediate situation would occur with cells in a single layer of epithelium. The effect of such geometrical considerations is eliminated in the experiment shown in Figure 5, since

the probability of the ^{204}Tl beta encountering more than one cell would be negligible in a cell suspension. The dominant factor in this situation is probably the target geometry. A realistic compromise might be the use of an RBE of 2.5, so that the estimated exposure would be equivalent to about 1 Sv to the small bowel mucosa. These findings suggest that it would be wise to reduce the routine clinical dosage of ^{201}Tl as much as feasible.

Similar studies are in progress using a larger species, i.e. 5 kg rabbits whose body mass exceeds that of the mouse by a factor of about 200. Data will be generated at the same time points and in the same intestinal segments as in the mouse experiments. Localization data in the intestinal mucosa will be collected using the methods in reference 15. Thallium localization, as well as tissue mass will be examined. Using the mouse data, prediction of the residence times will be carried out in the rabbit, with one difference that direct measurements of the rabbit intestinal localization will be available for comparison. In addition human residence times will be generated using rabbit data in the same way the mouse data was used. Comparison of these different analyses may furnish an objective evaluation of assumptions in the present studies.

REFERENCES

1. BMW Tsui, KA Lathrop, PV Harper. Extrapolation from animals to human for the retention of radiothallium in the blood. Third International Radiopharmaceutical Dosimetry Symposium. pp. 283-291. HHS Publication FDA 81-8166. June 1981.
2. BMW Tsui, KA Lathrop, KR Fultz, PV Harper. Prediction of time-concentration curves in the human from animal data. J Nucl Med 23(5):P103, 1982.
3. C-T Chen, KA Lathrop, PV Harper, RD Bartlett, VJ Stark, KR Fultz, PF Faulhaber. Quantitative measurement of long-term in vivo thallium distribution in the human. J Nucl Med 24(5):P50, 1983.
4. KA Lathrop, PV Harper, IV Gloria, M Rich. Intestinal localization of ^{201}thallium. J Nucl Med 16(5):P545, 1975.
5. BMW Tsui, IV Gloria, KA Lathrop. Biokenetics of Tl-201 in mice after intravenous and oral administration of TlCl J Nucl Med 18(6):633, 1977.
6. SAAM II User Guide. SAAM Institute, University of Washington, 1994.
7. W Krahwinkel, H Herzog, IE Feinendegen. Pharmacokinetics of thallium-201 in normal individuals after routine myocardial scintigraphy. J Nucl Med 29(9):1582-1586, 1988.
8. PJ Gehring and PB Hammond. The Interrelationship between thallium and potassium in animals. J Pharmacol Exp Ther 155(1):187-201, 1967.
9. ICRP Publication 30. Report of committee 2 of the International Commission on Radiological Protection. Limits for Intake of Radionuclides by Workers. Dosimetric Model for the Gastrointestinal Tract. p 33, 1978.
10. WS Snyder, MR Ford, GG Warner, SB Watson. "S", Absorbed Dose per Unit Cumulated Activity for Selected Radionuclides and Organs. MIRD Pamphlet No. 11, Society of Nuclear Medicine. 1975.
11. FP Castronovo. ^{201}Tl-labelled TlCl dosimetry revisited. Nucl Med Comm 14:104-107, 1993.
12. M. Stabin. Radiation dose estimates for thallium-201 chloride. ORAU: Radiopharmaceutical Internal Dose Information Center. 1988.
13. WS Snyder, MR Ford, GG Warner. Estimates of Specific Absorbed Fractions for Photon Sources Uniformly Distributed in Various Organs of a Heterogeneous Phantom. MIRD Pamphlet No. 5, Revised. Society of Nuclear Medicine, 1978.

14. DA Weber, KF Eckerman, LT Dillman, JC Ryman. MIRD radionuclide data and decay schemes. p.370. The Society of Nuclear Medicine, 1989.
15. MK Younoszai and JC Ranshaw. Quantitation of intestinal-tissue layers from their histology. Am J Dig Dis 20(8):764-769. 1975.
16. MG Stabin, EE Watson, M Cristy, JC Ryman, KF Eckerman, JL Davis, D Marshall, MK Gehlen. Mathmatical models and specific absorbed fractions of photon energy in the non-pregnant adult female and at the end of each trimester of pregnancy. ORNL/TM-12907 p. 28. National Technical Information U.S. Department of Commerce, 5285 Port Royal Rd., Springfield, VA 22161.
17. GL Brownell, WH Ellett, AR Reddy. Absorbed fractions for photon dosimetry. J Nucl Med Suppl 1:28-39, 1968.
18. DV Rao, VB Mylavarapu, GF Govelitz, VK Lanka, KSR Sastry, RW Howell. Biological and biophysical dosimetry of Auger-emitters in vivo: A review. in Selected Topics in Physics of Radiotherapy and Imaging: (U. Madhvanath, KS Parthasarathy, and TV Venkateswaran, Eds.) pp. 232-258. Tata McGraw-Hill, New Delhi, 1988.

A BLOOD CIRCULATION MODEL FOR REFERENCE MAN

Leggett RW[1], Williams LR[2] and Eckerman KF[1]
[1]Dosimetry Research Group, Health Sciences Research Division,
Oak Ridge National Laboratory, Oak Ridge, Tennessee 37831-6480
and [2]Division of Liberal Arts and Sciences,
Indiana University South Bend, South Bend, IN 46634

ABSTRACT

This paper describes a dynamic blood circulation model that predicts the movement and gradual dispersal of a bolus of material in the circulation after its intravascular injection into an adult human. The main purpose of the model is to improve the dosimetry of internally deposited radionuclides that decay in the circulation to a significant extent. The total blood volume is partitioned into the blood contents of 24 separate organs or tissues, right heart chambers, left heart chambers, pulmonary circulation, arterial outflow to the systemic tissues (aorta and large arteries), and venous return from the systemic tissues (large veins). As a compromise between physical reality and computational simplicity, the circulation of blood is viewed as a system of first-order transfers between blood pools, but outflow from any given pool is delayed during the first pass of material through the circulation with the delay time depending on the mean transit time across the pool. The model allows consideration of incomplete, tissue-dependent extraction of material during passage through the circulation and return of material from tissues to plasma.

INTRODUCTION

The International Commission on Radiological Protection (ICRP) currently is revising its document on Reference Man (1). As part of this revision, we have reviewed information on the human circulation and in previous papers and reports (2-4) have proposed reference values for total and regional blood volumes, cardiac output, and regional blood perfusion rates. In this paper we summarize the main features of a dynamic blood flow model that unifies the information described in the previous papers, and we illustrate how the model can be used to predict the distribution of decays of short-lived radionuclides after intravenous injection into an adult human. Details concerning model parameters and solution of the model have been published elsewhere (5).

The model is a compromise between physical reality and computational simplicity. The circulation of blood is viewed as a system of first-order transfers among 29 blood pools, together with a set of delays in transfer of material from one pool to the next. The delays are used only during the first pass after injection of material into blood, because use of subsequent delays would complicate the implementation of the model while making little difference in dosimetric estimates. For purposes

of radiation dosimetry, the first-pass delays may be ignored for radionuclides with half-lives longer than about three minutes.

Transfer rates between compartments are derived from input values for total blood volume, total cardiac output, the fraction of the total blood volume contained in each compartment, and the fraction of cardiac output received by each compartment. A full set of input values has been derived only for the baseline case of a 35-year old, resting adult male. In subsequent work we will extend input values to females and children and use the model to address the age- and gender-specific dosimetry of some medically important radionuclides.

MODEL STRUCTURE

A schematic diagram of the model is shown in Figure 1. The total blood volume is partitioned into 29 compartments, including 24 compartments representing the nutrient blood supplies of organs or tissues and five compartments corresponding to venous return from the systemic tissues (large veins in Figure 1), contents of right and left heart chambers, contents of the pulmonary circulation, and arterial outflow to the systemic tissues (aorta and large arteries in Figure 1, sometimes referred to as the "large artery pool"). The 24 nutrient compartments include a pool called "all other" that represents the collective nutrient blood supply of organs and tissues not explicitly identified in Figure 1, such as the eyes, pituitary gland, and salivary glands. As described later, an additional compartment called "injection vein" is used to address the delayed entry of intravenously injected material into the right heart.

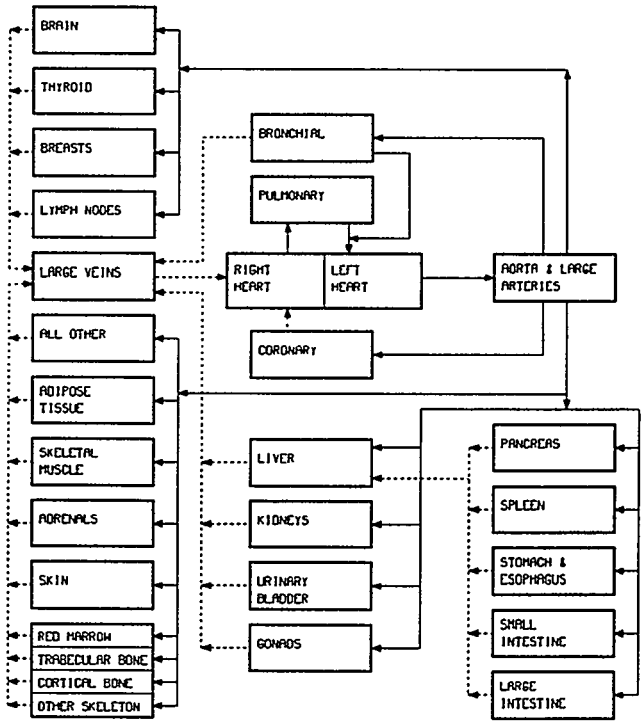

Figure 1. Diagram of the blood flow model.

The blood content of the heart is partitioned into right heart (right atrium plus right ventricle), left heart (left atrium plus left ventricle), and the coronary pool that supplies nutrients to the heart. Venous return from the systemic circulation flows into the right heart, is pumped via the pulmonary circulation through the lungs, enters the left heart, and then is pumped into the aorta. The coronary circulation is fed by the aorta. In reality, blood leaves the coronary circulation through a complicated system of vascular connections with the various cardiac chambers (6), but in this model the simplifying assumption is made that venous outflow from the coronary pool is received by the right heart.

The blood in the lungs is partitioned into a pulmonary pool that receives oxygen from the lungs and a bronchial pool that supplies nutrients to the lungs. The bronchial circulation is assumed to be

fed by the aorta and to return blood to the systemic venous system (one-third of venous outflow) and the left heart (two-thirds of venous outflow). The model does not include some generally less important aspects of the bronchial circulation, such as shunting of bronchial arterial flow to the systemic circulation or various connections between the bronchial and the pulmonary circulations (6,7-10).

The portion of the cardiac output known as the portal circulation flows through capillary beds of the spleen, pancreas, stomach, intestines, and part of the esophagus, merges in the portal vein, and is then circulated through the liver. The stomach and esophagus are lumped because of their close relation in the body and because the limited amount of data on the esophagus suggest a blood perfusion rate similar to that of the stomach (11). Although venous outflow from much of the esophagus and from the anal canal do not pass through the liver, this "nonportal" flow typically represents a small portion of the total venous outflow from the alimentary tract and is not depicted in this model. The model also does not depict collateral circulation from the liver to the lungs, which may become important in some diseases (2).

The kidneys, urinary bladder, gonads, brain, thyroid, breasts, lymph nodes, adipose tissue, skeletal muscle, adrenals, skin, skeletal compartments, and all other (all remaining tissues combined into a single compartment) are assumed to be fed only by the large arteries, and venous outflow is assumed to be only to the large veins. The breasts are included as a separate compartment for application of the model to mature or adolescent females. The complex blood supply of the skeleton (12) is simplified considerably by viewing the four skeletal compartments as parallel blood pools (Figure 1).

The model may be thought of as describing the flow of blood or some component of blood such as blood plasma or red blood cells, or the movement of an internally deposited substance as it is carried in blood. The simplifying assumption is made that all components of blood have the same kinetics. This assumption is not strictly true. For example, it is known that red blood cells and plasma have different rates of transfer through some vascular beds (13,14). However, there is insufficient information to model the differential kinetics of different blood components with much confidence.

For the case of intravenous injection of a substance, the injected material is depicted as passing in series through the injection vein, the right heart chambers, the pulmonary pool, the left heart chambers, and the aorta and large arteries, with brief delays in each pool before outflow to the next pool begins. Outflow from the large artery pool is assumed to be distributed among the vascular beds of the different tissue compartments according to the distribution of cardiac output. After compartment-specific delays in the blood and tissue pools of each of the tissue compartments, material begins to flow out of the different compartments into the large veins. After a brief delay, material in the large veins reaches the right heart and begins a new cycle through the circulation. As described below, no further delays are imposed after the first pass through the circulation.

DERIVATION OF TRANSFER RATES AND DELAYS FOR THE REFERENCE ADULT MALE

Baseline Parameter Values

The kinetics of blood circulation is complex but for most practical purposes can be viewed as a system of first-order transfers among the different blood pools, together with a set of delays, or minimal transit times, in transfer of material from one pool to the next. These delays are used only during the first pass after injection of material into blood, because depiction of subsequent delays would complicate the implementation of the model and would make little difference in predictions of the distribution of the material.

The first-order transfer rates between compartments and the delays imposed during the first pass are all secondary values that are derived from the following input parameters: the total blood volume (ml); the cardiac output (ml d^{-1}); 29 regional blood volumes (i.e., the fraction of the total blood volume contained in each of the 29 compartments shown in Figure 1); 24 fractional blood flows to compartments fed by aorta and large arteries; and, for the case of intravenous injection of material, a delay period in the injection vein representing the time between the start of injection and the beginning of inflow into the right heart, and a transfer rate from the injection vein into the right heart.

Baseline values for total blood volume and cardiac output in a healthy, reclining, 35-y-old male are 5300 ml and 6500 ml min^{-1}, respectively (4). Baseline values for regional blood volumes and the distribution of cardiac output in a healthy, reclining, 35-y-old male are given in Table 1. These reference values are based on the authors' review and reanalysis of data from about 500 studies of blood flow and blood volume in human subjects and laboratory animals. Data reduction and selection of reference values, as well as the potential variability of blood volume and flow with such factors as sex, age, and level of activity, are described elsewhere (2-4). Additional information on the division of skeletal blood flow among red marrow, trabecular bone, cortical bone, and other skeletal tissues was found in the literature (12, 15-19). Reference values for blood volume and blood flow of the four skeletal compartments are more reflective of the relative sizes of nutrient blood supplies of these compartments than of their total internal vasculature; this approach was judged to be appropriate for purposes of radiation dosimetry.

Delays in Transfer Between Blood Pools During the First Pass

If a radioactive tracer is injected into an arm vein of an adult male at time 0, activity could reach the pulmonary circulation in as little as 5-6 s, some systemic tissues in 11-12 s, and venous outflow from some tissues in 15 s (Table 2). The initial appearance time (AT) of the tracer in the right heart, lung, or large arteries is noticeably smaller than the mean transit time (MTT) of the tracer to these points. Even smaller ratios of AT:MTT have been determined for transit across the nutrient beds of organs and tissues. Reported measurements of AT and MTT for various injection and measurement sites in the circulation indicate a ratio AT:MTT in the range 0.6-0.85 for flow through portions of the central circulation and a median ratio near 0.5 for flow across a nutritive vascular bed (5).

To model the delay between injection of material into blood and the initial appearance of material at different points in the circulation, we assign to each blood pool a delay between the appearance time of material in the pool and the time material begins to flow out of the pool. The delay times for the different blood pools are related to the mean transit times across the pools. For right heart, left heart, pulmonary blood, aorta and large arteries, and large veins, the delay is assumed to be 0.7 times the mean transit time across the pool. For each nutrient blood pool, the delay is assumed to be 0.5 times the mean transit time across the organ. For a given pool, the delay period begins when material first reaches the pool and applies only to the first pass of material through the pool; after the end of the delay period, outflow from the pool is assumed to follow first-order kinetics. The simple first-pass delay scheme used in this model is likely to overestimate the actual transit times of small portions of material through short circuits of some organs and tissues, but such overestimates will be of little practical consequence with regard to radiation dosimetry.

The mean transit time for a given pool is calculated as the volume of blood in the pool divided by the rate of flow of blood into the pool. For example, the brain is assumed to contain 1.2% of the total blood and to receive 12% of the cardiac outflow (Table 1). Based on a total-body blood volume of 5300 ml and cardiac output of 6500 ml min^{-1}, the mean transit time across the brain (i.e., from arterial inflow to venous outflow) is calculated as $(0.012 \times 5300 \text{ ml})/(0.12 \times 6500 \text{ ml min}^{-1}) = 4.89$ s. For a material injected into blood, the delay between the first appearance in the brain circulation and the

first appearance in venous outflow is assumed to be 0.5 × 4.89 s = 2.45 s. As a second example, the aorta and large arteries receive virtually 100% of the cardiac output and are assumed to contain 6% of the total blood (Table 1). Therefore, the mean transit time between entry of material into the aorta and exit into the systemic tissues is calculated as (0.06 × 5300 ml)/(1.0 × 6500 ml min^{-1}) = 2.94 s. After injection of a substance into blood, the delay between the first appearance in the aorta and large arteries and the beginning of exit from this pool (i.e., the first appearance in systemic organs) is assumed to be 0.7 × 2.94 s = 2.05 s.

The default value for the delay time in the injection vein (i.e., appearance time in the right heart) for the reference adult male is 4 s. This value is based on observations of Kuikka and coworkers (20-21) for material injected into the antecubital (midarm) vein of resting subjects. When cardiac output is elevated above the resting level, a shorter delay time may be appropriate. The default delay for intra-arterial injection is 2 s, which is about the same as the delay for aorta and large arteries.

Table 1
Reference Regional Blood Volumes and Flow Rates for Organs of a Recumbent Adult Male

Organ or tissue	% of total blood volume	% cardiac output received
adipose tissue	5.0 (4-8)	5.0 (3.5-9)
brain	1.2 (0.8-1.4)	12.0 (10-15)
stomach and esophagus	1.0 (0.2-1.3)	1.0 (0.5-2)
small intestine	3.8 (0.9-4.4)	10.0 (7-13)
large intestine	2.2 (0.5-2.5)	4.0 (2.8-6)
heart		
chambers	9.0 (6-12)	
coronary tissue	1.0 (0.5-1.5)	4.0 (3-6)
kidneys	2.0 (1.3-2.9)	19.0 (16-21)
liver	10.0 (4-12)	6.5 (5.5-8.5) arterial
pulmonary	10.5 (8-13)	25.5 (17-30) total
bronchial tissue	2.0 (1.8-2.5)	2.5 (1-5.5)
skeletal muscle	14.0 (8-21)	17.0 (10-21)
pancreas	0.6 (0.1-0.7)	1.0 (0.6-1.9)
skeleton	7.0 (4-8) total	5.0 (2.5-10) total
red marrow	4.0	3.0
trabecular bone	1.2	0.9
cortical bone	0.8	0.6
other skeleton	1.0	0.5
skin	3.0 (1-6)	5.0 (3.3-7)
spleen	1.4 (1.2-1.9)	3.0 (2.5-5)
thyroid	0.06 (0.02-0.1)	1.5 (0.7-2.2)
lymph nodes	0.2 (0.05-0.4)	1.7 (0.5-3.5)
testes	0.04 (0.01-0.1)	0.05 (0.01-0.1)
adrenals	0.06 (0.01-0.1)	0.3 (0.1-1)
urinary bladder	0.02 (0.01-0.05)	0.06 (0.01-0.2)
all other tissues	1.92 (1-4)	1.39 (0.5-3.5)
aorta and large arteries	6.0 (3-9)	
large veins	18.0 (11-25)	

Table 2
Comparison of Experimentally Determined Circulation Times with Model Predictions
(Based on Table 2 of Reference 5, where Original Studies are Cited)

Path	Appearance time (s)		Mean transit time (s)	
	Observed	Model	Observed	Model
Right heart to left heart	5	5.2	6.5	7.5
Right heart to aorta			8	9.7
Right heart to radial artery	9.5	8.4	6.5	7.9
Arm vein to pulmonary artery				
Pulmonary artery to radial artery	9	6.8	12	9.6
Pulmonary artery to tongue	7	7.3		
Arm vein to femoral artery	12	12	18	18
Basilic vein to brachial artery			19	17
Brachial vein to brachial artery	5	8.8	14	12
Arm vein to brain	12	13	18	18
Brachial vein to jugular vein	9	13	17	19
Antecubital vein to hepatic vein	27	22		
Liver to hepatic vein	10	9.7		
Superior mesenteric artery to spleen	4	11	19	23
Sup. mesenteric artery to portal vein	8.5	9.3		
Sup. mesenteric vein to sup. mes. artery	19	18		
Jugular vein to jugular artery			22	17
Carotid artery to jugular vein	3	3.5	7	6.3

The model may be applied to a continuous infusion as well as to acute injection of material into blood. The first-pass delays of continuously infused material can be accounted for by first generating a time-dependent activity curve for each compartment based on acute injection into the appropriate blood compartment and then convoluting the organ activity curves against the continuous infusion rate.

First-order Transfer Rates between Blood Pools

After the delay time is exceeded during the first pass of material through a given pool, outflow from the pool is assumed to follow first-order kinetics. The total transfer rate from a given pool to the receiving compartment(s) is calculated as the number of total blood volumes flowing into the pool per day, divided by the fraction of the total blood volume contained in the pool.

For example, the large veins are assumed to collect all of the venous outflow and hence all of the cardiac output, except that the coronary outflow is assigned to the right heart and two-thirds of the bronchial outflow is assigned to the left heart. Since the coronary pool receives 4% and the bronchial pool 2.5% of cardiac output, the large veins receive 100% - 4% - (2/3 × 2.5%) = 94.333% of cardiac output. The cardiac output is 1440 min d^{-1} × 6500 ml min^{-1} / 5300 ml = 1766 d^{-1}. Since the large veins are assumed to contain 18% of the total blood volume, the transfer rate from large veins to the right heart is calculated as 0.94333 × 1766 / 0.18 = 9255 d^{-1}.

The transfer rate (volumes d^{-1}) from the large artery pool into the blood pool of a systemic organ is calculated as $F_O \times CO / F_A$, where F_O = the fraction of cardiac output received by the organ, CO is the cardiac output (d^{-1}), and F_A is the fraction of the blood volume of the large artery pool. For

example, the transfer rate from aorta and large arteries to coronary circulation is $0.04 \times 1766\ d^{-1} / 0.06 = 1177\ d^{-1}$.

The transfer rate from the blood pool of a systemic organ into the compartment designated as large veins (or into the liver via the portal vein) is calculated as the daily inflow into the pool, divided by the amount of blood in the pool. For example, the transfer rate from the kidney blood pool to large veins is calculated as $0.19 \times 1766\ d^{-1} / 0.02 = 16{,}777\ d^{-1}$.

Venous outflow from the spleen, pancreas, and alimentary tract is assumed to flow into the portal vein, which feeds the liver. The portal vein is not depicted explicitly in this model; rather, outflow from the pancreas, spleen, and alimentary tract is assigned directly to the liver blood pool. Outflow from the liver blood pool is assigned to the large veins.

The default transfer rate from injection vein to right heart in the reference resting adult male is 1/D, where D is the duration of injection. A transfer rate greater than (1/D) may be appropriate when cardiac output is elevated above the resting level.

Application of Model to Substances that Transfer between Blood and Tissues

As will be illustrated later, the blood flow model may be used as a framework for modeling the kinetics of a substance that transfers between blood and extravascular pools. This requires the addition of extravascular compartments and derivation of substance-specific transfer rates between the blood compartments and extravascular compartments. Essentially, each of the organs fed by the large arteries (Figure 1) is viewed as consisting of a blood compartment and one or more tissue compartments. In general, each tissue compartment may be treated as a peripheral compartment that exchanges material only with the blood compartment of the same organ. Transfer rates from one blood compartment to another are the same as described above for the blood flow model, and transfer rates between tissue compartments and blood are substance-specific.

The number of tissue compartments assigned to an organ will vary with the substance and/or the available biokinetic information. For short-lived radionuclides, it will often suffice to treat each organ as a single, well-mixed pool, because only short-term transfer from tissue to blood is of interest.

Depending on the type of biokinetic data available for a given substance, it may be possible to simplify the derivation of transfer rates to tissue compartments by treating the tissue and blood compartments of an organ as parallel rather than serial compartments. That is, one may assume that the tissue and blood compartments of an organ are both fed directly by the large artery pool (and portal vein, in the case of the liver) and that both lose material directly to the large vein pool. Such a scheme is physically incorrect but does not introduce significant temporal errors and has the advantage of allowing direct application of reported "extraction fractions" for substances. An extraction fraction for a given organ and a given substance in plasma (and for a given physiological condition) is the fraction of material removed by the organ during a single pass from arterial to venous plasma.

If the extraction fraction for a given substance and organ is known, then the transfer rates from the large artery pool to the organ blood pool and the organ tissue pool can be determined from that extraction fraction and the transfer rates of the basic blood flow model. For example, the extraction fraction for Rb by brain appears to be on the order of 0.01. Since the brain is assumed to receive 12% of cardiac output, the transfer rate of blood from the large artery pool to the brain blood pool is $0.12 \times 1766\ d^{-1} / 0.06 = 3532\ d^{-1}$. With the parallel-compartment configuration, the transfer rate of Rb from the large artery pool to the brain blood pool would be $0.99 \times 3532\ d^{-1} = 3497\ d^{-1}$ and from the large artery pool to brain tissue would be $0.01 \times 3532\ d^{-1} = 35.32\ d^{-1}$.

COMPARISON OF MODEL PREDICTIONS WITH OBSERVATIONS OF THE EARLY KINETICS OF RADIOTRACERS

Model predictions of transit times between different points in the circulation of a reference adult male are compared in Table 2 with observed values, i.e., central reported values for reasonably healthy adult humans, mainly males less than 50 years old. A model prediction for a given path, "Pool A to Pool B", refers to a travel time between the point of entry into Pool A and the point of entry into Pool B. To account for travel time between injection or sampling points and the receiving or feeding organs, the following appearance times are assumed: antecubital vein or median basilic vein to right heart, 4 s; brachial vein or jugular vein to right heart, 2 s; left heart to brachial artery or superior mesenteric artery, 1 s; left heart (exit) to radial or femoral artery, 2 s; brain (exit) to jugular vein, 0.5 s; carotid artery to brain, 0.5 s. For each of these portions of the "large veins" or "aorta and large artery" pools, the mean transit time is assumed to be 1.4 times the appearance time. For purposes of this exercise, "aorta" is interpreted as the point of entry into the "aorta and large artery" pool.

In Figure 2, model predictions are compared with observations (22) of the concentration of ^{131}I in arterial and venous blood as a function of time after intravenous injection of ^{131}I-labeled human serum albumin into a resting adult human subject. The age, gender, or other characteristics of the subject were not reported. The observations in Figure 2 represent radioactivity in blood samples collected over 15- or 30-s intervals from the brachial artery and hepatic vein. For purposes of this exercise the aorta and large artery pool of the model was used as a surrogate for brachial artery blood. A hepatic vein pool was created by separating venous outflow from the liver from all other flow into the large vein pool. The model curves in Figure 2 are moving averages of predicted ^{131}I concentrations in these arterial and hepatic vein pools over 15-s intervals. All observations and model predictions were normalized to an arbitrary number (0.5) representing the concentration of ^{131}I in blood after a uniform distribution is attained. The model predictions were based on parameter values for the reference resting adult male. The default value of 4 s was used as the delay period in the injection vein, and the transfer rate from injection vein into right heart after the delay was assumed to be 0.5 s^{-1} (rapid injection).

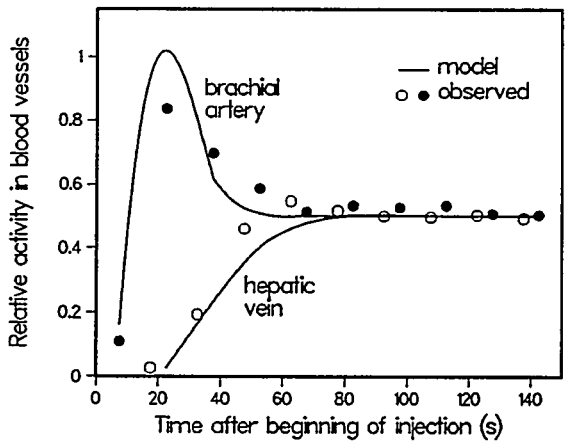

Figure 2. Observations and model predictions of radioactivity in arterial and venous blood of a subject after intravenous injection of ^{131}I-labeled human serum albumin.

APPLICATIONS AND DISCUSSION

Application to a Radiotracer that Remains in Blood

We consider the distribution of systemic decays of ^{11}C after inhalation of the tracer ^{11}C-labeled carbon monoxide (CO), which is rapidly absorbed to blood. Because absorbed CO is virtually completely bound to hemoglobin, it is reasonable to assume that all systemic decays of ^{11}C ($T_{1/2}$ = 20.4 min) occur in blood (23). In ICRP Publication 53 (23), this tracer is assumed to be distributed among tissues according to their blood contents at all times after absorption from the lungs to blood. With the present model, activity entering blood in the pulmonary compartment is viewed as passing in

series through the pulmonary compartment, the left heart chambers, and the aorta and large arteries, and then distributing among the vascular beds of the different tissue compartments according to the distribution of cardiac output, which differs considerably from the distribution of blood volume.

To simplify comparison of predictions of the present blood flow model with those of the blood model of ICRP Publication 53, attention is confined to the integrated activity in the various blood pools, and the assumption is made that inhaled activity is instantaneously absorbed to blood. Predictions of the blood volume model of ICRP Publication 53 (23) were derived from fractional blood volumes given in Table A.2, p. 16, of that document.

Since ^{11}C has a relatively long half-life compared with the time required for activity in blood to become reasonably uniformly distributed (< 2 min), differences between predictions of the present model and that of ICRP Publication 53 (Table 3) arise mainly from differences in assumptions concerning regional blood volumes. The present model generates a considerably more detailed distribution of activity than does the model of ICRP Publication 53, which addresses only a small number of blood pools.

The model predictions for ^{11}C given in Table 3 are based on the baseline parameter values described earlier and hence do not consider differences between the distributions of red blood cells and plasma in the circulation. Such differences are conceivably important for ^{11}CO because of its rapid and nearly complete binding to red blood cells but were not addressed here due to a paucity of information for most of the compartments in this model.

Table 3
Comparisons of Predicted Cumulative Activities in Selected Organs, Based on the Present Blood Flow Model and the Blood Model of ICRP Publication 53 (23) for Two Cases: Inhalation of ^{11}C-labeled Carbon Monoxide and Intravenous Injection of ^{82}Rb

Organ or tissue	Ratio, ICRP Pub. 53 to this model	
	^{11}CO	^{82}Rb
adrenals	1.0	6.2
bone, cortical	2.7	7.8
bone, trabecular	0.4	1.3
red marrow	0.9	2.0
heart wall	1.3	1.6
kidneys	0.7	2.0
liver	0.5	0.9
lungs, pulmonary	0.8[a]	1.3
lungs, bronchial	--	0.2
pancreas	b	1.6
skeletal muscle	b	1.0
spleen	1.2	1.1
stomach and esophagus	b	2.1
small intestine	b	1.0
large intestine	b	1.4
thyroid	1.1	3.8

[a]Total lungs (pulmonary plus bronchial blood).
[b]Not included in blood volume model of ICRP Publication 53.

Application to an Ultrashort-lived Radionuclide that Transfers to Extravascular Spaces

The blood flow model is next used to predict the distribution of decays of intravenously injected ^{82}Rb, an ultrashort-lived radionuclide ($T_{1/2}$ = 75 s) used clinically in imaging of the myocardium, brain, and kidneys. Because Rb transfers rapidly from blood plasma to extravascular spaces, it is necessary to append extravascular compartments to the blood flow model and derive rates of transfer of Rb into these compartments. For each of the blood compartments fed by the large artery compartment, a corresponding tissue compartment is added to the model. We use the "parallel compartment" approach described in an earlier section and define transfer rates to these compartments in terms of Rb extraction fractions. Because of the short half-life of ^{82}Rb, we may assume that there is no transfer from tissues back to blood provided the applied extraction fractions are effective values over a few minutes rather than "first-pass" values. First-pass values sometimes overstate effective or steady-state extraction due to a brief delay in the onset of back diffusion of material from extravascular spaces to plasma.

In an earlier paper (24), biokinetic data on Rb were reviewed and a detailed biokinetic model for Rb was developed. That model included most of the tissue compartments indicated in Figure 1 and made use of Rb extraction fractions but depicted plasma as a static, uniformly mixed pool that exchanged Rb with peripheral organs. The Rb extraction fractions derived in that paper are applied here to ^{82}Rb, except that extraction fractions for skeletal muscle and kidneys have been modified to accommodate differences in model structure and, in the case of kidneys, to reflect newer experimental data (25). The following extraction fractions are applied here: gastrointestinal tract compartments, lung, spleen, pancreas and skin = 0.80; skeletal muscle = 0.6; heart = 0.45; liver and skeleton = 0.4; brain = 0.01; and all other organs = 0.5.

These extraction fractions may be used, together with the transfer rates between blood pools described earlier, to derive transfer rates for this extension of the blood flow model to Rb. That is, each organ fed by aorta and large arteries is partitioned into a blood pool and a tissue pool. As illustrated in an earlier section, the transfer rate from aorta and large arteries to the tissue pool of a given organ is set at E × T and from aorta and large arteries to the blood pool of that organ is (1 - E) × T, where E is the extraction fraction for the organ and T is the transfer rate from the aorta and large artery compartment to the organ. For each tissue pool, the transfer rate to the large veins (or liver) is set at zero; i.e., there is assumed to be no loss of ^{82}Rb from tissues. Transfers to or from heart chambers remain unchanged. Movement of ^{82}Rb along excretion pathways and uptake by red blood cells do not significantly influence the systemic distribution of decays of this ultrashort-lived radionuclide (24) and are not considered in the present calculations.

Table 3 compares integrated activity in the various organs as predicted by this extended blood flow model with estimates from ICRP Publication 53 (23, p. 161). The assumed delay in the injection vein was 4 s. The transfer rate from injection vein to right heart was set at 0.2 s^{-1} for comparison of model predictions with ^{82}Rb-injection data of Ryan and coworkers (26), whose injection and subsequent saline flush were completed in 5-6 s. The estimate of the present model for an organ is the sum of activities in the blood pool and tissue pool of that organ. In ICRP Publication 53, the distribution of decays of ^{82}Rb is based on a model of the distribution of cardiac output. For example, 23% of the systemic decays were assigned to kidneys based on the assumption that the kidneys receive 23% of cardiac output. The delay time in the injection vein and the transfer rate to right heart assumed above do not apply to the model of ICRP Publication 53, because the residence time or location of activity in blood is not considered in that model. As indicated in Table 3, the method of ICRP Publication 53 yields higher estimates of integrated activity in most organs than does the present method. The differences in estimates result from two factors: 1) the present method considers decays of ^{82}Rb that occur in blood pools outside the indicated organs; and 2) the two different blood

flow models underlying the two approaches depict considerably different blood flow rates to some pools (e.g., bronchial tissue and adrenals). For some of the listed organs, estimates of integrated activity cannot be derived from the blood flow model of ICRP Publication 53 (e.g., testes, urinary bladder).

Ryan and coworkers (26) used external measurements to estimate the integrated activity of intravenously injected ^{82}Rb in organs of two healthy men, ages 23 and 27 years. For organs that could be reasonably well isolated by the external counting technique (liver, kidneys, and testes), model predictions were within 2-33% of experimentally determined values.

In Table 4 we compare estimates of absorbed dose, from intravenously injected ^{82}Rb based on the present model as applied here to Rb (Method A), with absorbed dose estimates derived from four other models or methods for describing cumulative activities of ^{82}Rb (Methods B-E). Method B is the blood volume model of ICRP Publication 53 (23) as applied in that document to ^{82}Rb. Method C is based on the experimentally determined values of Ryan and coworkers (26) described above, using the average of cumulative activities for two subjects and assuming uniform distribution of activity in tissues not measured by Ryan and coworkers. Method D is based on cumulated activities of ^{86}Rb in rats at 1-180 min after injection and the assumption that individual organ concentrations per initial mean whole-body concentration are the same for humans and rats (27). As with Method C, activity not accounted for by measured pools was assumed to be uniformly distributed in the remainder of the body. Method E is the assumption of uniform distribution of activity in the body at all times after injection, which is equivalent to applying the Rb kinetic model of ICRP Publication 30 (28).

Table 4

Comparison of Absorbed Dose Estimates for Intravenously Injected ^{82}Rb in the Adult Male Based on Different Models or Methods

Organ or tissue	This model (Gy Bq^{-1} x 10^{12})	ICRP Pub. 53 (23) / This model	Ryan et al. (26)/ This model	Kearfott (27)/ This model	Uniform distribution/ This model
adrenals	3.6	5.9	0.1	0.2	0.1
red marrow	0.6	1.7	0.7	0.8	0.8
kidneys	9.2	2.0	1.0	0.6	0.05
liver	1.0	1.0	1.0	0.7	0.5
lungs	2.5	1.0	0.7	0.8	0.2
testes	0.3	0.4	0.8	0.4	1.3
thyroid	10	3.8	0.05	0.05	0.05

All absorbed dose estimates in Table 4 were based on specific effective energies and dosimetric methods described in a recent document by Cristy and Eckerman (29). Absorbed dose estimates based on Methods B, C and D were generally close but not identical to estimates given in the original documents describing those methods (respectively, Refs. 23, 26, 27). Discrepancies appear to be due mainly to differences in the specific effective energies applied to total-body activity not contained in separately identified source organs, that is, activity in "other" or "remainder".

ACKNOWLEDGMENT

The work described in this paper was sponsored by the Office of Health and Environmental Research, U. S. Department of Energy, under contract DE-AC05-84OR21400 with Martin Marietta Energy Systems, Inc.

REFERENCES

1. International Commission on Radiological Protection (ICRP). Report of the Task Group on Reference Man. ICRP Publication 23. Pergamon Press, Oxford, 1975.
2. Williams LR and Leggett RW. Reference values for resting blood flow to organs of man. Clin Phys Physiol Meas 10:187-217, 1989.
3. Leggett RW and Williams LR. Suggested reference values for regional blood volumes in humans. Health Phys 60:139-154, 1991.
4. Williams LR. Reference Values for Total Blood Volume and Cardiac Output in Humans. ORNL/TM-12814, Oak Ridge National Laboratory, Oak Ridge, TN, 1994.
5. Leggett RW and Williams LR. A proposed blood circulation model for Reference Man. Health Phys 69:187-201, 1995.
6. Brobeck JR. Best and Taylor's physiological basis of medical practice. Tenth edition. Williams and Wilkins, Baltimore, 1979.
7. Aramendia P, Martinez de Letona J and Aviado DM. Responses of the bronchial veins in a heart-lung bronchial preparation. Circ Res 10:3-10, 1962.
8. Aramendia P, Martinez de Letona J and Aviado DM. Exchange of blood between pulmonary and systemic circulations via bronchopulmonary anastomoses. Circ Res 11:870-879, 1962.
9. Aviado DM. The Lung Circulation. Vol. I, Physiology and Pharmacology. Pergamon Press, New York, 1965.
10. Cudkowicz L. The Human Bronchial Circulation in Health and Disease. Williams and Wilkins, Baltimore, 1968.
11. Pennanen MF, Bass BL, Dziki AJ and Harmon JW. Adenosine: differential effect on blood flow to subregions of the upper gastrointestinal tract. J Surg Res 56:461-465, 1994.
12. Kelly PJ. Pathways of transport in bone. In: Handbook of Physiology, Section 2: The Cardiovascular System, Vol. III, Peripheral Circulation and Organ Blood Flow. Shepherd JT, Abboud FM, eds. pp. 371-396, American Physiological Society, Bethesda, MD, 1983.
13. Larsen OA, Tygstrup N and Winkler K. The splanchnic hematocrit in man. Acta Physiol Scand 57:397-406, 1963.
14. Ladefoged J and Pedersen F. Renal blood flow, circulation times and vascular volume in normal man measured by the intra-arterial injection -- external counting technique. Acta Physiol Scand 69:220-229, 1967.
15. Whiteside LA, Simmons DJ and Lesker PA. Comparison of regional bone blood flow in areas with differing osteoblastic activity in the rabbit tibia. Clin Orthop Rel Res 124:267-270, 1977.
16. Morris MA and Kelly PJ. Use of tracer microspheres to measure bone blood flow in conscious dogs. Calcif Tissue Int 32:69-76, 1980.
17. Gross PM, Marcus ML and Heistad DD. Current concepts review: Measurement of blood flow to bone and marrow in experimental animals by means of microsphere technique. J Bone Jt Surg 63-A:1028-1031, 1981.
18. Light TR, McKinstry MP, Schnitzer J and Ogden JA. Bone Blood Flow: Regional Variation with Skeletal Maturation. In: Bone Circulation, Arlet J, Ficat RP, Hungerford DS (eds.), pp. 178-185,

Williams and Wilkins, Baltimore, 1984.
19. Tøndevold E and Bülow J. Microsphere Determined Regional Bone Blood Flow in Conscious Dogs at Rest and Long Time Muscular Exercise. In: Bone Circulation, Arlet J, Ficat RP, Hungerford DS (eds), pp. 175-177, Williams and Wilkins, Baltimore, 1984.
20. Kuikka JT, Pyorala T, Lehtovirta P and Rekonen A. Cardiopulmonary blood volumes at rest and during muscular exercise measured by ^{113m}In radiocardiography. Acta Physiol Scand 95:145-152, 1975.
21. Kuikka J and Ahonen A. A simple and rapid non-invasive radioisotope method to determine ventricular ejection fractions and cardiopulmonary transit times. Nucl-Med Band XVI/Heft 2:57-62, 1977.
22. Bradley SE, Marks PA, Reynell PC and Meltzer J. The circulating splanchnic blood volume in dog and man. Transactions of the Association of American Physicians 66:294-302, 1953.
23. International Commission on Radiological Protection (ICRP). Radiation Dose to Patients from Radiopharmaceuticals. ICRP Publication 53. Pergamon Press, Oxford, 1987.
24. Leggett RW and Williams LR. A biokinetic model for Rb in humans. Health Phys 55:685-702, 1988.
25. Mullani NA, Ekas RD, Marani S, Kim EE and Gould RL. Feasibility of measuring first pass extraction and flow with rubidium-82 in the kidneys. Amer J Physiologic Imaging 5:133-140, 1990.
26. Ryan JW, Harper PV, Stark VS, Peterson EL and Lathrop KA. Radiation absorbed dose estimate for rubidium-82 determined from in vivo measurements in human subjects. In: 4th Int. Radiopharmaceutical Dosimetry Symposium, Schlafke-Stelson AT, Watson EE (eds), pp. 346-358, Springfield, VA., NTIS, CONF-85113, 1985.
27. Kearfott KJ. Radiation absorbed dose estimates for positron emission tomography (PET): K-38, Rb-81, Rb-82, and Cs-130. J Nucl Med 23:1128-1132, 1982.
28. International Commission on Radiological Protection. Limits for Intakes by Workers. ICRP Publication 30, Part 2. Pergamon Press, Oxford, 1980.
29. Cristy M and Eckerman KF. SEECAL: Program to Calculate Age-dependent Specific Effective Energies. ORNL/TM-12351, Oak Ridge National Laboratory, Oak Ridge, TN, 1993.

THE RADIATION DOSIMETRY OF INTRATHECALLY ADMINISTERED RADIONUCLIDES

Stabin MG[1] and Evans JF[2]
[1]Oak Ridge Institute for Science and Education
P.O. Box 117
Oak Ridge, TN 37831-0117
[2]Ohio State University
Columbus, OH

ABSTRACT

The radiation dose to the spine, spinal cord, marrow, and other organs of the body from intrathecal administration of several radiopharmaceuticals was studied. Anatomic models were developed for the spine, spinal cerebrospinal fluid (CSF), spinal cord, spinal skeleton, cranial skeleton, and cranial CSF. A kinetic model for the transport of CSF was used to determine residence times in the CSF; material leaving the CSF was thereafter assumed to enter the bloodstream and follow the kinetics of the radiopharmaceutical as if intravenously administered. The radiation transport codes MCNP and ALGAMP were used to model the electron and photon transport and energy deposition. The dosimetry of Tc-99m DTPA and HSA, In-111 DTPA, I-131 HSA, and Yb-169 DTPA was studied. Radiation dose profiles for the spinal cord and marrow in the spine were developed and average doses to all other organs were estimated, including dose distributions within the bone and marrow.

INTRODUCTION

Several radiopharmaceuticals have been administered intrathecally for cisternography. A paper at this meeting in 1991 (1) gave some details about the model in ICRP Publication 53 (2) describing the kinetics of activity introduced into the cerebrospinal fluid (CSF), and also gave values of photon-specific effective energy (SEE) (3) to various organs of the body from activity in the spinal and cranial CSF, as well as mean doses to the spinal cord from electrons. In this study, we extend these results to give dose estimates to major organs of the body from intrathecal administrations of five radiopharmaceuticals (Tc-99m DTPA and HSA, In-111 DTPA, I-131 HSA, and Yb-169 DTPA). In addition, dose distributions within the spinal cord are given, based on radiation transport calculations for electrons from these nuclides. Radiation dose distributions to the marrow and bone surfaces are also given for these five radiopharmaceuticals, using the bone and marrow model of Eckerman (4).

METHODS

The kinetic model from ICRP 53 (2), as given by Johansson and Nosslin (1), was adopted. This model is shown in Figure 1, which was taken directly from Johansson and Nosslin (1). In this model, material administered into the CSF is assumed to move through the CSF space in the spinal column and into the CSF in the brain, with removal of activity into the bloodstream from each region. Radionuclides introduced into the CSF space were assumed to remain in the spinal or cranial CSF according to the ICRP model, and then pass into the bloodstream. At that point, they were treated with standard biokinetic models, as if they were due to an intravenous injection. The residence times for the intravenously administered radiopharmaceuticals are shown in Table 1.

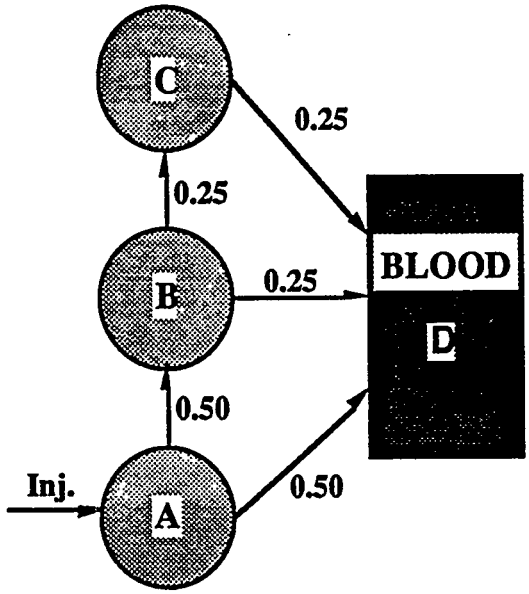

Flow	Fraction of dose	T	a
A → B	0.5	20 min 8 h	0.25 0.75
A → D	0.5	8 h 30 d	0.97 0.03
B → C	0.25	18 h	1.0
B → D	0.25	18 h 30 d	0.97 0.03
C → D	0.25	18 h 30 d	0.97 0.03

Figure 1. ICRP 53 biokinetic model for the CSF (taken from Johansson and Nosslin (1)).

Table 1
Residence Times (hr) for Intravenously Administered Radiopharmaceuticals Considered in this Study

Organ	Tc-99m DTPA	Tc-99m HSA	In-111 DTPA	I-131 HSA	Yb-169 DTPA
Brain	---	0.424	---	9.45	---
Small	---	---	0.0288	---	---
Intestine	---	---	0.0225	---	---
Stomach	---	0.813	---	18.1	---
Heart	0.092	0.11	0.0748	2.46	0.103
Contents	---	0.457	0.0622	10.2	---
Kidneys	---	0.847	---	18.9	---
Liver	---	---	0.223	---	---
Lungs	---	0.144	0.0045	3.22	---
Muscle	1.84	0.0553	3.6	0.78	2.15
Spleen	2.84	5.67	2.23	127	4.3
Urinary Bladder					
Remainder					

We also adopted, with slight modification, the ICRP geometric model of the spinal CSF and spinal cord. In our model, the spinal cord was modeled as a circular cylinder of radius 0.45 cm. The spinal CSF region was modeled as a circular cylinder of radius 0.8 cm. The spinal cord and CSF region were surrounded by a cylindrical region representing the spine; the radii of this region in the x and y directions (using the x, y, z axes as described in the Cristy-Eckerman phantom series (5)) were 2.0 and 2.5 cm. The cranium was modeled after the skull in the Cristy and Eckerman phantom for the reference adult; the cranial CSF was modeled as a cylindrical shell of thickness 0.09 cm. There were three materials used in the model: soft tissue, bone, and a special material used to represent the tissue in the spinal cord. These materials had densities of 1.04, 1.4, and 1.04 g cm^{-3}; their elemental compositions are shown in Table 2.

Table 2
Elemental Compositions of the Three Materials Used in this Model

Element	f-soft	f-bone	f-spinal cord
H	0.104	0.0734	0.107
C	0.227	0.255	0.145
N	0.0249	0.0306	0.022
O	0.635	0.479	0.712
F	----	0.00025	----
Na	0.00112	0.00326	0.002
Mg	0.00013	0.00112	----
Si	0.0003	0.00002	----
P	0.00134	0.0509	0.004
S	0.00204	0.00173	0.002
Cl	0.00133	0.00143	0.003
K	0.00208	0.00153	0.003
Ca	0.00024	0.102	----
Fe	0.00005	0.00008	----
Zn	0.00003	0.00005	----
Rb	0.00001	0.00002	----
Sr	----	0.00003	----
Zr	0.00001	----	----
Pb	----	0.00001	----

The entire spine and cranial region was enclosed in the trunk and head regions of the Cristy and Eckerman model for the reference adult (no attempt was made to model the lung or other bone spaces within the trunk; all material inside of the trunk and head other than specified above were assumed to be soft tissue, as in the first column of Table 2). Within the spinal cord, 10 concentric shells of 0.045 cm radius each were defined for scoring the energy deposition of electrons originating in the spinal CSF.

The computer code MCNP (version 4A) was used to model the transport of electrons and photons originating within the spinal CSF. Electron and photon emissions from the various radionuclides were encoded, and calculations were carried out for times sufficient to obtain acceptable uncertainties in the reported results. In general, about 300,000 to 800,000 photons were created and 7 to 14 million electrons were created. This resulted in uncertainties in the reported

values of the order of 1-5% for most photon doses reported and 1-15% for the electron doses reported (the electron doses due to bremsstrahlung generally had higher uncertainties, ranging up to 30%, but were not very significant to the total dose for any region). Photon doses to other organs were estimated using the results of Evans et al. (6). They gave photon-specific absorbed fractions (SAFs) for sources in the spinal and cranial CSF to major organs of the body in the Cristy-Eckerman reference adult for a broad spectrum of photon energies; values for energies corresponding to those emitted by the radionuclides considered in this study were obtained by interpolation. They also gave photon SAFs for each of the different regions of the regional bone and marrow dosimetry model of Eckerman (5); these results were also used to obtain estimates of the dose distributions within the skeleton from the intrathecal administration of these radionuclides. For the material reaching the bloodstream, the standard dosimetry for the various organs was estimated using the MIRDOSE (version 3.1) software (7). Finally, contributions from all sources were added and total doses per unit activity administered were calculated.

RESULTS

The radionuclide residence times in the CSF and the fractions of each radionuclide reaching the blood are shown in Table 3. Absorbed doses to several major organs within the body and the effective dose equivalent (3) are given in Table 4. These results contain contributions from emissions occurring within the CSF as well as from activity which reached the bloodstream. Dose distributions within the active marrow and to the endosteal cells on the surfaces of growing bone are given in Tables 5 and 6 and plotted in Figures 2 and 3. Electron, photon, and total doses to the different segments of the spinal cord are given in Tables 7 and 8. In Table 7, the results are given per disintegration for the four radionuclides; in Table 8, they are given per unit administered activity for the five radiopharmaceuticals studied. The absorbed doses to the spinal cord, in absorbed dose per disintegration, are given for each radionuclide in Figures 4-7 (showing the electron and photon contributions and the totals) and for all four radionuclides (only the total dose) in Figure 8.

Table 3
Residence Times in Different Segments of the CSF and Fractions Reaching the Blood, for the Radiopharmaceuticals Considered in this Study

	Residence time (hr)			
Radionuclide	**Spinal CSF - A**	**Spinal CSF - B**	**Cranial CSF - C**	**Fraction to Blood**
Tc-99m	4.45 hr	1.83 hr	0.23 hr	0.251
In-111	10.3 hr	9.92 hr	4.11 hr	0.752
I-131	12.9 hr	12.9 hr	6.57 hr	0.884
Yb-169	17.9 hr	16.4 hr	9.87 hr	0.96

Table 4
Absorbed Doses (mGy/MBq) to Major Organs from Intrathecal Administration of the Radiopharmaceuticals Considered in this Study

	Tc-99m DTPA	**Tc-99m HSA**	**In-111 DTPA**	**I-131 HSA**	**Yb-169 DTPA**
Brain	0.00262	0.0042	0.0935	1.03	0.17
Heart Wall	0.00416	0.00896	0.0399	2.67	0.0551
Kidneys	0.00957	0.0103	0.0928	1.2	0.141
Liver	0.00316	0.00475	0.0296	0.893	0.0412
Lungs	0.00394	0.00737	0.0377	2.27	0.0549
Ovaries	0.00254	0.00227	0.0306	0.373	0.034
Red Marrow	0.0137	0.0143	0.154	0.613	0.205
Bone Surfaces	0.0116	0.0125	0.121	0.488	0.284
Spleen	0.00335	0.00675	0.0316	2.19	0.0452
Testes	0.000989	0.000785	0.0145	0.312	0.0152
Urinary Bladder Wall	0.0193	0.0017	0.329	0.459	0.419
Uterus	0.00366	0.00224	0.0521	0.397	0.05
Effective Dose Equivalent	0.00703	0.00696	0.0864	1.03	0.121

Table 5
Radiation Dose Distributions (mGy/MBq) within the Active Marrow for Intrathecal Administration of the Radiopharmaceuticals Considered in this Study

	Tc-99m DTPA	Tc-99m HSA	In-111 DTPA	Yb-169 DTPA	I-131 HSA
Upper Arm Bones	1.18E-03	1.72E-03	1.39E-02	4.41E-01	1.69E-02
Clavicles	1.56E-03	2.10E-03	1.84E-02	4.47E-01	2.29E-02
Upper Leg Bones	5.68E-04	1.11E-03	6.45E-03	4.31E-01	9.17E-03
Pelvis	1.90E-03	2.44E-03	2.03E-02	4.48E-01	2.56E-02
Ribs	2.92E-03	3.47E-03	3.05E-02	4.62E-01	3.90E-02
Scapulae	1.81E-03	2.35E-03	1.97E-02	4.49E-01	2.44E-02
Skull - Cranium	3.17E-03	3.71E-03	9.75E-02	5.63E-01	1.90E-01
Skull - Facial Skeleton	2.11E-03	2.66E-03	3.59E-02	4.75E-01	5.48E-02
Lower Spine	9.22E-02	9.27E-02	1.04E+00	1.82E+00	1.31E+00
Middle Spine	7.18E-02	7.24E-02	8.26E-01	1.55E+00	1.03E+00
Upper Spine	6.35E-02	6.41E-02	7.28E-01	1.43E+00	9.28E-01
Average	1.37E-02	1.43E-02	1.54E-01	6.13E-01	2.05E-01

Table 6
Radiation Dose Distributions (mGy/MBq) within the Endosteal Cells on the Surfaces on Growing Bone for Intrathecal Administration of the Radiopharmaceuticals Considered in this Study

	Tc-99m DTPA	Tc-99m HSA	In-111 DTPA	Yb-169 DTPA	I-131 HSA
Lower Arm Bones	1.61E-03	2.56E-03	1.43E-02	3.90E-01	2.52E-02
Middle Arm Bones	2.68E-03	3.63E-03	2.26E-02	3.99E-01	3.80E-02
Upper Arm Bones	2.54E-03	3.49E-03	2.32E-02	3.99E-01	3.95E-02
Clavicles	3.78E-03	4.73E-03	3.37E-02	4.10E-01	6.10E-02
Lower Leg Bones	8.14E-04	1.76E-03	7.73E-03	3.82E-01	1.65E-02
Middle Leg Bones	8.21E-04	1.77E-03	7.82E-03	3.82E-01	1.66E-02
Upper Leg Bones	8.97E-04	1.85E-03	8.60E-03	3.83E-01	1.73E-02
Pelvis	4.55E-03	5.50E-03	3.56E-02	4.10E-01	6.94E-02
Ribs	6.94E-03	7.89E-03	5.43E-02	4.31E-01	1.10E-01
Scapulae	4.23E-03	5.18E-03	3.49E-02	4.12E-01	6.29E-02
Skull - Cranium	6.03E-03	6.98E-03	1.73E-01	5.49E-01	5.13E-01
Skull - Facial Skeleton	4.39E-03	5.34E-03	5.79E-02	4.43E-01	1.43E-01
Lower Spine	1.88E-01	1.88E-01	1.81E+00	2.20E+00	3.91E+00
Middle Spine	1.45E-01	1.46E-01	1.37E+00	1.85E+00	2.98E+00
Upper Spine	1.25E-01	1.26E-01	1.29E+00	1.66E+00	2.76E+00
Average	1.16E-02	1.25E-02	1.21E-01	4.88E-01	2.84E-01

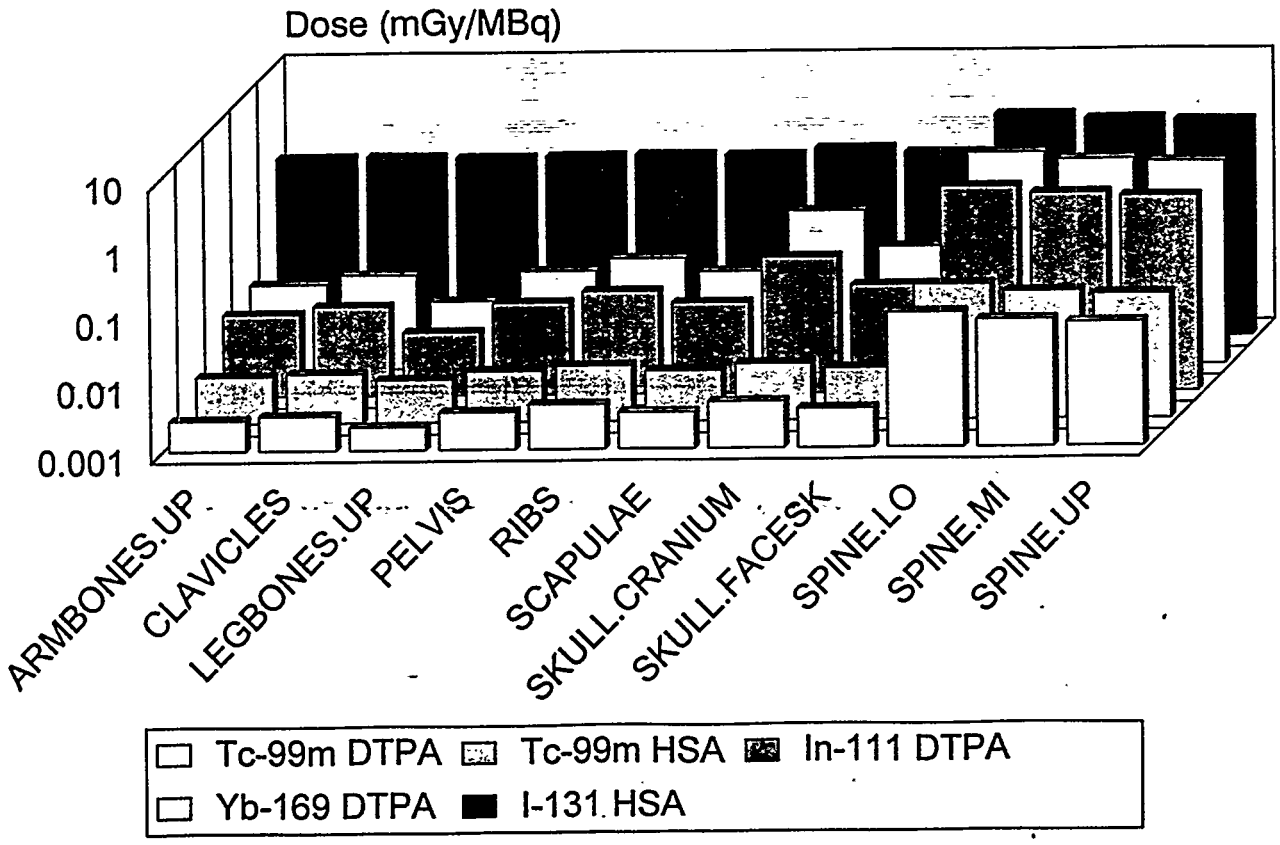

Figure 2. Dose distributions within the active marrow.

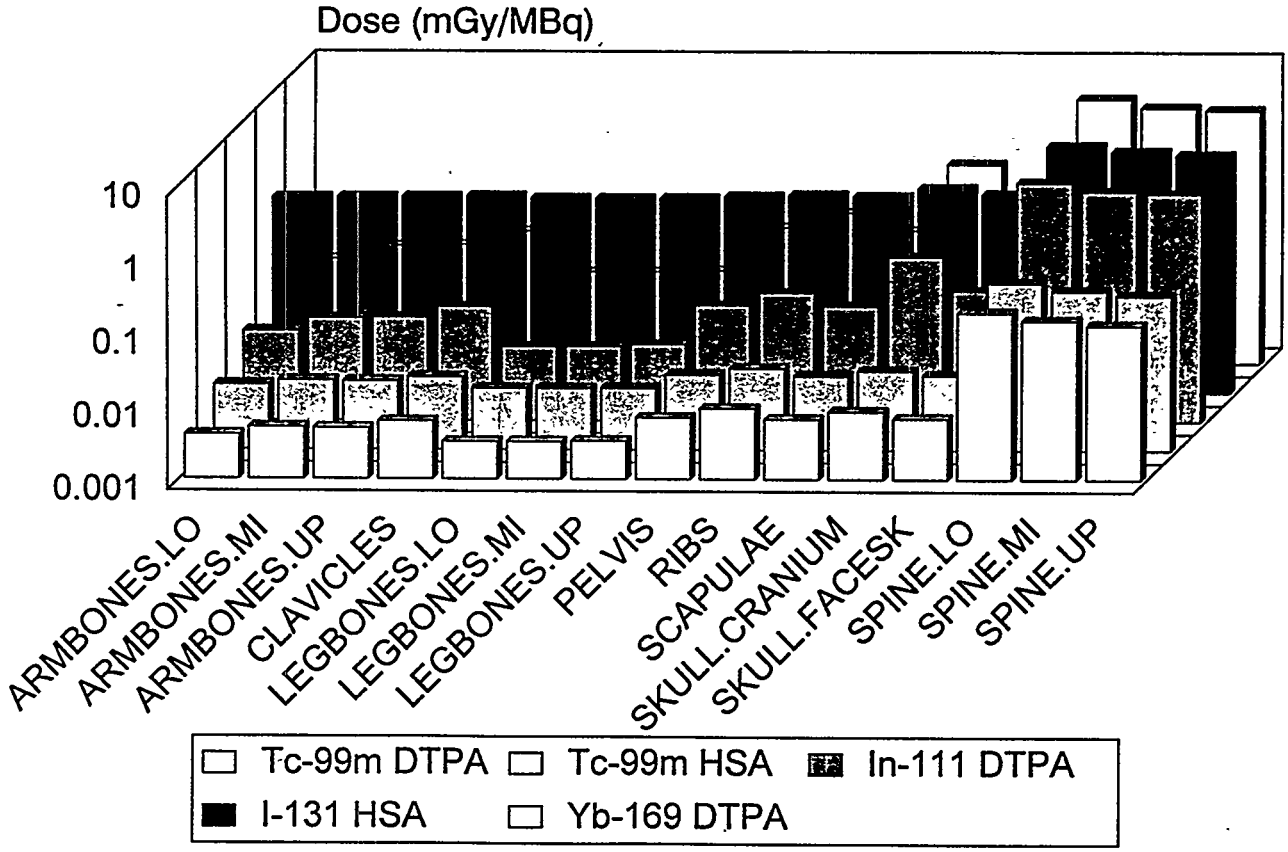

Figure 3. Dose distributions for endosteal cells on the surfaces of growing bone.

Table 7

Electron, Photon, and Total Doses (Gy dis^{-1}) to the Different Segments of the Spinal Cord for the Radionuclides Considered in this Study (uncertainties are shown as one standard deviation errors)

	Tc-99m					
Distance (cm)*	Electron Dose	1 s.d.	Photon Dose	1 s.d.	Total Dose	1 s.d.
0.43	1.97E-15	2.14E-17	7.37E-15	1.18E-16	9.34E-15	1.20E-16
0.38	3.07E-18	4.04E-19	6.76E-15	1.15E-16	6.77E-15	1.15E-16
0.34	2.23E-18	3.70E-19	6.91E-15	1.24E-16	6.91E-15	1.24E-16
0.29	2.07E-18	3.44E-19	6.39E-15	1.28E-16	6.40E-15	1.28E-16
0.25	2.15E-18	4.15E-19	6.21E-15	1.37E-16	6.21E-15	1.37E-16
0.20	1.50E-18	3.67E-19	6.04E-15	1.49E-16	6.04E-15	1.49E-16
0.16	1.92E-18	4.91E-19	6.21E-15	1.74E-16	6.21E-15	1.74E-16
0.11	2.14E-18	6.18E-19	6.01E-15	1.98E-16	6.02E-15	1.98E-16
0.07	1.76E-18	6.87E-19	5.88E-15	2.59E-16	5.88E-15	2.59E-16
0.02	----	----	6.06E-15	4.36E-16	6.06E-15	4.36E-16

Table 7 (continued)

	In-111					
Distance (cm)*	Electron Dose	1 s.d.	Photon Dose	1 s.d.	Total Dose	1 s.d.
0.43	8.37E-15	7.86E-17	3.00E-14	4.53E-16	3.84E-14	4.60E-16
0.38	9.40E-18	1.23E-18	2.75E-14	4.56E-16	2.75E-14	4.56E-16
0.34	5.94E-18	7.87E-19	2.70E-14	4.84E-16	2.70E-14	4.84E-16
0.29	7.06E-18	1.06E-18	2.57E-14	5.06E-16	2.57E-14	5.06E-16
0.25	6.16E-18	9.60E-19	2.44E-14	5.30E-16	2.44E-14	5.30E-16
0.20	6.68E-18	1.17E-18	2.40E-14	5.81E-16	2.40E-14	5.81E-16
0.16	3.90E-18	9.31E-19	2.48E-14	6.78E-16	2.48E-14	6.78E-16
0.11	5.08E-18	1.33E-18	2.31E-14	7.68E-16	2.31E-14	7.68E-16
0.07	----	----	2.36E-14	9.97E-16	2.36E-14	9.97E-16
0.02	----	----	2.40E-14	1.75E-15	2.40E-14	1.75E-15
	I-131					
Distance (cm)*	Electron Dose	1 s.d.	Photon Dose	1 s.d.	Total Dose	1 s.d.
0.43	1.10E-13	7.27E-16	2.22E-14	5.55E-16	1.32E-13	1.32E-13
0.38	1.91E-14	3.13E-16	2.10E-14	5.68E-16	4.02E-14	6.49E-16
0.34	2.86E-15	1.24E-16	1.95E-14	1.95E-14	2.24E-14	5.99E-16
0.29	3.13E-16	3.76E-17	1.92E-14	6.15E-16	1.95E-14	6.16E-16
0.25	5.13E-17	9.26E-18	1.90E-14	6.67E-16	1.91E-14	6.67E-16
0.20	4.51E-17	7.31E-18	1.75E-14	7.17E-16	1.75E-14	7.17E-16
0.16	4.44E-17	7.74E-18	1.95E-14	8.58E-16	1.95E-14	8.58E-16
0.11	4.30E-17	8.17E-18	1.74E-14	9.38E-16	1.74E-14	9.38E-16
0.07	4.25E-17	1.19E-17	1.69E-14	1.18E-15	1.69E-14	1.18E-15
0.02	----	----	1.54E-14	1.98E-15	1.54E-14	1.98E-15
	Yb-169					
Distance (cm)*	Electron Dose	1 s.d.	Photon Dose	1 s.d.	Total Dose	1 s.d.
0.43	1.07E-14	1.53E-16	1.91E-14	3.14E-16	2.97E-14	3.50E-16
0.38	1.62E-17	2.88E-18	1.84E-14	3.25E-16	1.84E-14	3.25E-16
0.34	1.52E-17	2.72E-18	1.82E-14	3.49E-16	1.82E-14	3.49E-16
0.29	1.54E-17	2.83E-18	1.70E-14	3.61E-16	1.70E-14	3.61E-16
0.25	1.37E-17	3.20E-18	1.64E-14	3.80E-16	1.64E-14	3.80E-16
0.20	1.12E-17	2.99E-18	1.60E-14	4.13E-16	1.60E-14	4.13E-16
0.16	1.24E-17	3.94E-18	1.66E-14	4.87E-16	1.66E-14	4.87E-16
0.11	1.47E-17	4.39E-18	1.62E-14	5.48E-16	1.62E-14	5.48E-16
0.07	----	----	1.66E-14	7.42E-16	1.66E-14	7.42E-16
0.02	----	----	1.53E-14	1.16E-15	1.53E-14	1.16E-15

* Distance = 0 represents the center of the spinal cord.

Table 8
Total Doses (mGy/MBq) to Different Segments of the Spinal Cord for all Radionuclides Considered in this Study

	Tc-99m		In-111		I-131		Yb-169	
Distance(cm)*	Total Dose	1 s.d.	Total Dose	1 s.d.	Total Dose	1 s.d.	Total Dose	1 s.d.
0.43	0.061	7.9E-4	1.37	0.016	6.13	0.042	1.75	0.021
0.38	0.044	7.5E-4	0.98	0.016	1.86	0.030	1.08	0.019
0.34	0.045	8.2E-4	0.96	0.017	1.04	0.028	1.07	0.021
0.29	0.042	8.4E-4	0.91	0.018	0.91	0.029	1.00	0.021
0.25	0.041	9.0E-4	0.87	0.019	0.88	0.031	0.96	0.022
0.20	0.040	9.8E-4	0.86	0.021	0.81	0.033	0.94	0.024
0.16	0.041	1.1E-3	0.88	0.024	0.91	0.040	0.98	0.029
0.11	0.040	1.3E-3	0.82	0.027	0.81	0.043	0.95	0.032
0.07	0.038	1.7E-3	0.84	0.036	0.78	0.055	0.98	0.044
0.02	0.040	2.9E-3	0.86	0.062	0.72	0.092	0.90	0.068

* Distance = 0 represents the center of the spinal cord.

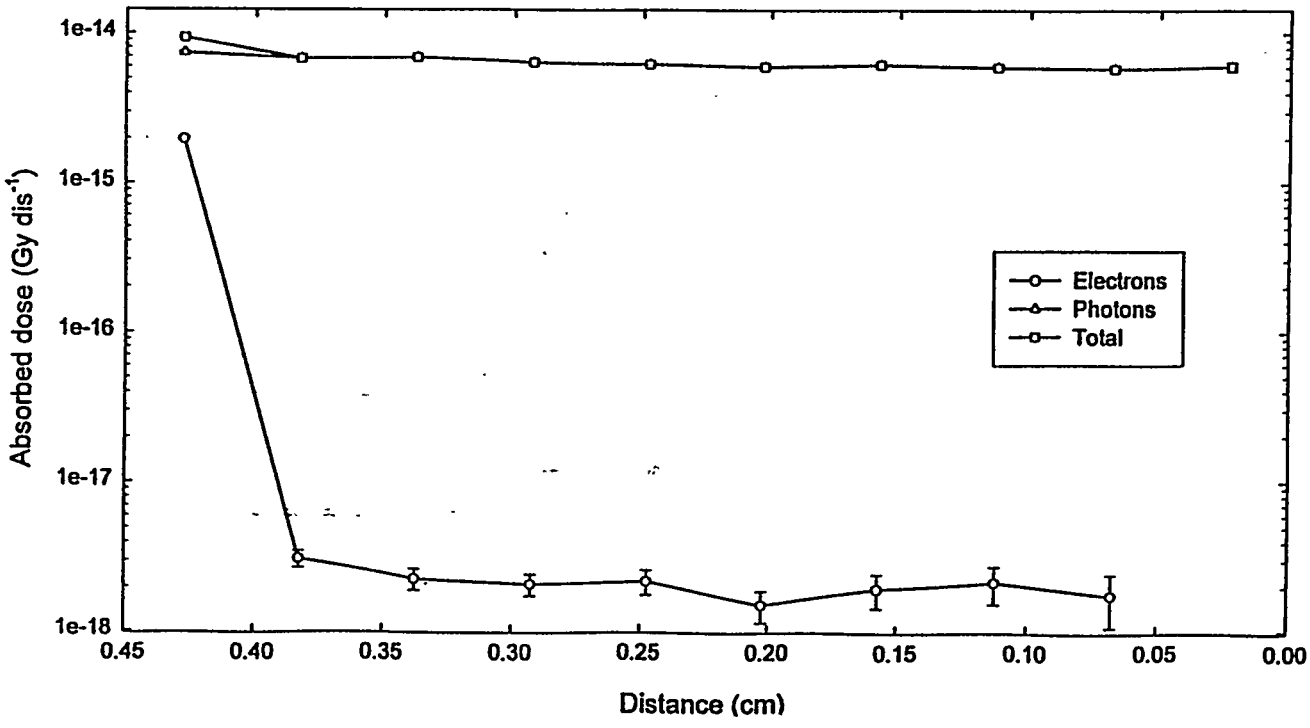

Figure 4. Dose per disintegration within the spinal cord - Tc-99m.
(Distance = 0 represents the center of the cord)

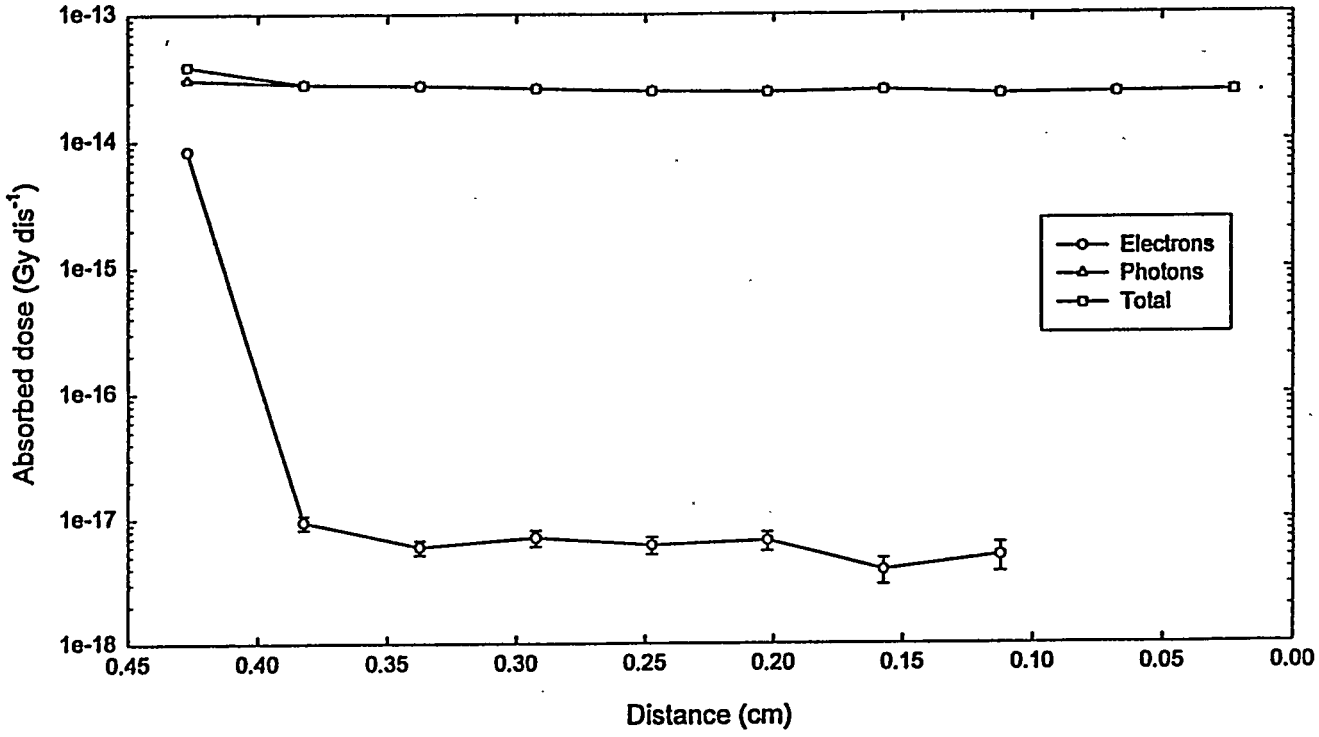

Figure 5. Dose per disintegration within the spinal cord - In-111.
(Distance = 0 represents the center of the cord)

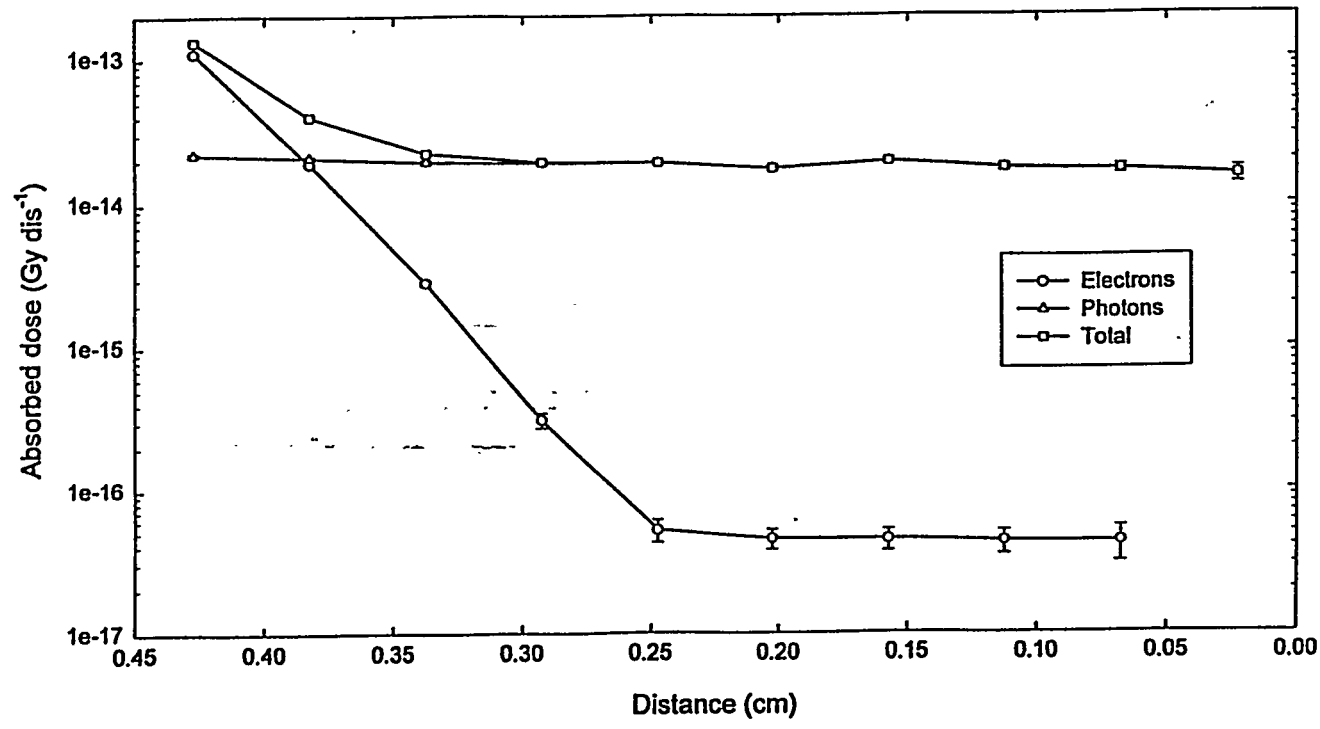

Figure 6. Dose per disintegration within the spinal cord - I-131.
(Distance = 0 represents the center of the cord)

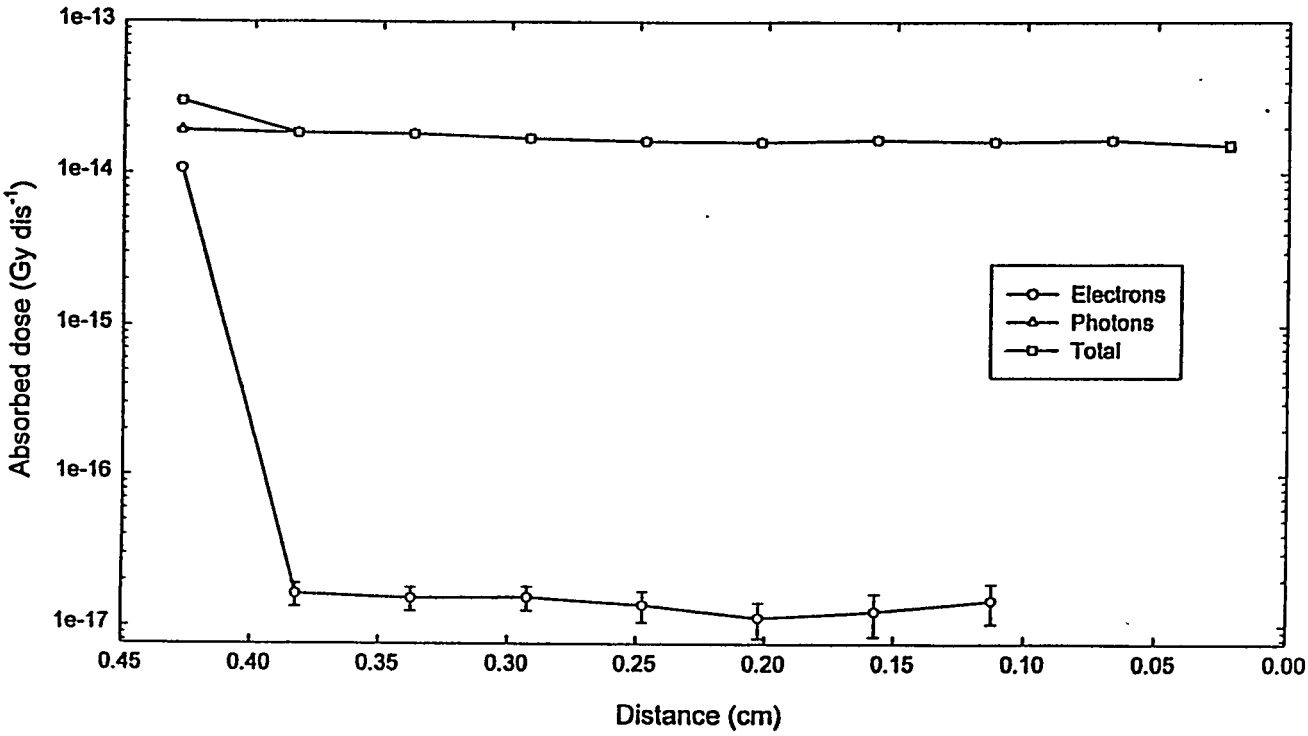

Figure 7. Dose per disintegration within the spinal cord - Yb-169.
(Distance = 0 represents the center of the cord)

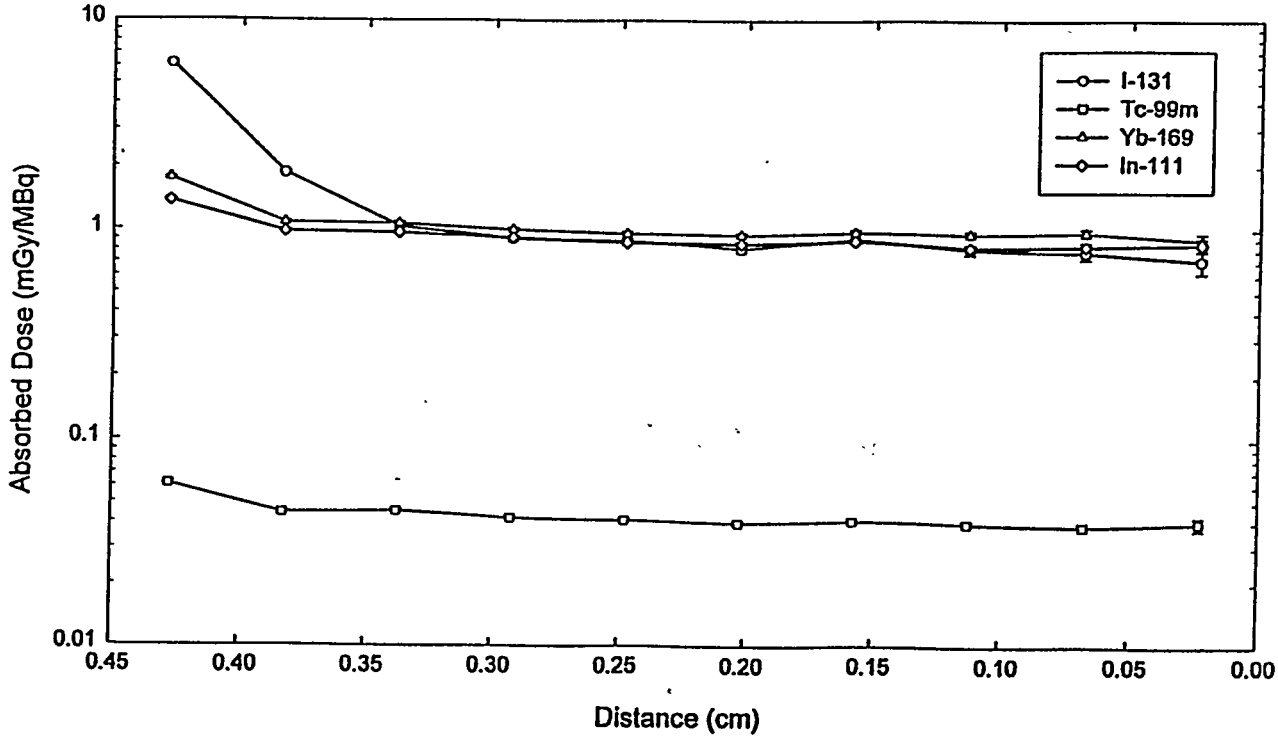

Figure 8. Dose per unit administered activity within the spinal cord - all nuclides.
(Distance = 0 represents the center of the cord)

DISCUSSION

The dose to the spinal cord is often of central concern in studies involving the intrathecal administration of radionuclides. In this study, the use of a coupled electron-photon transport code provided very good detail about the dose to this region. Figures 4-7 show the contribution to the total spinal cord dose from the photon and electron components of each radionuclide's decay scheme. In all of the cases except for I-131, a small initial electron dose component is quickly reduced to a very low and relatively constant level due to bremsstrahlung radiation. Thereafter, the photon contribution, which is relatively uniform across the cord, dominates. In the case of I-131, due to the higher energy beta rays, the beta dose is attenuated over the first 0.15-0.20 cm, and then the total dose is determined solely by the photon contributions. The data in Tables 7 and 8 and in Figures 4-8 show in detail the dose distributions (and associated uncertainties) within the spinal cord for the four radionuclides employed. Figure 8 shows that Tc-99m delivers a much lower total dose than any of the other radionuclides, per unit administered activity.

This study also reports absorbed doses to many organs of the body, as well as detailed dose distributions within the bone and marrow, for these studies. The organ doses from I-131 HSA are the highest, as would be expected from the decay characteristics and radionuclide half-time. Those for In-111 and Yb-169 DTPA are about an order of magnitude lower (per unit activity administered), and those of Tc-99m DTPA and HSA are about another order of magnitude lower. The specific organs which receive the highest dose are determined by the characteristics of the radiopharmaceutical biokinetics, to a large degree, although in the case of Tc-99m, and to a lesser degree of In-111 and Yb-169, the influence of the CSF activity in enhancing the bone and marrow dose are evident. In the marrow and endosteal cell dose distributions, the high contributions to the spine are obvious (Figures 2 and 3). It is interesting, however, that Yb-169 delivers the highest doses to the endosteal cells, while I-131 delivers the highest dose to marrow in the spine. No modeling was done to look at the electron dose to the bone or marrow of the spine. Although a "vertebrae" model was defined, it was in a very simple geometry, and the complex geometry of the vertebrae, bone surfaces, and marrow were not modeled. Therefore, these doses reflect only the photon dose to these regions. Yb-169 has a generally lower energy photon spectrum than I-131, including a large x-ray component (8). Examination of the specific absorbed fractions of Evans et al. (6) reveals that photon absorption in the bone surface cells for a source in the spinal CSF is much higher for the low-to-moderate energy photons of Yb-169 than of the higher energy I-131 photons. For the marrow, the specific absorbed fractions in this region do not vary as strongly with energy, and the higher abundance of the I-131 photons are more important to determining the dose (although Yb-169 has some high abundance x-rays, these have significantly smaller SAFs in the marrow than photons of higher energy).

CONCLUSION

A model of the spine and CSF was developed, and radiation dose distributions within the spinal cord, major organs of the body, and the bone and marrow were developed for intrathecal administrations of Tc-99m DTPA and HSA, In-111 and Yb-169 DTPA, and I-131 HSA. The data should be useful in answering radiation safety concerns involving the intrathecal administration of the five radiopharmaceuticals studied. The model can easily be extended to include other radionuclides and pharmaceuticals as needed.

ACKNOWLEDGMENTS

This work was performed for the U.S. DOE under contract DE-AC05-76OR00033 and for the U.S. FDA under Interagency Agreement No. FDA 224-75-3016, DOE 40-286-71.

The submitted manuscript has been authored by a contractor of the U.S. Government under contract DE-AC05-76OR00033. Accordingly, the U.S. Government retains a nonexclusive, royalty-free license to publish or reproduce the published form of the contribution, or allow others to do so, for U.S. Government purposes.

REFERENCES

1. Johansson L and Nosslin B. Dosimetry of intrathecally administered radiopharmaceuticals, in Fifth International Radiopharmaceutical Dosimetry Symposium, edited by EE Watson and AT Schlafke-Stelson, pp 188-201, Oak Ridge Associated Universities, 1992.
2. International Commission on Radiological Protection. Radiation Dose to Patients from Radiopharmaceuticals. ICRP Publication 53, Pergamon Press, New York, 1988.
3. International Commission on Radiological Protection. Limits for Intakes of Radionuclides by Workers. ICRP Publication 30, Pergamon Press, New York, 1979.
4. Eckerman K. Aspects of dosimetry of radionuclides within the skeleton with particular emphasis on the active marrow In Fourth International Radiopharmaceutical Dosimetry Symposium; edited by A.T. Schlafke-Stelson and E. E. Watson. CONF-851113, pp 514-534, Oak Ridge Associated Universities, Oak Ridge, TN 37831, 1986.
5. Cristy M and Eckerman K. Specific Absorbed Fractions of Energy at Various Ages from Internal Photon Sources. ORNL/TM-8381 V1-V7. Oak Ridge National Laboratory, Oak Ridge, TN, 1987.
6. Evans JF, Stabin MG and Stubbs JB. Specific absorbed fractions of energy from internal photon sources in brain tumor and cerebrospinal fluid. Med Phys 22(3):331-340, 1994.
7. Stabin M. MIRDOSE - the personal computer software for use in internal dose assessment in nuclear medicine. J Nucl Med 37:538-546, 1996.
8. Weber D, Eckerman K, Dillman LT and Ryman J. (1989): MIRD: Radionuclide Data and Decay Schemes. Society of Nuclear Medicine, New York.

ABSORBED DOSE IN THE SALIVARY GLANDS FROM TECHNETIUM-99m LABELED RADIOPHARMACEUTICALS

Lennart Johansson
Radiation Physics Department, Umeå University Hospital
S-901 85 Umeå, Sweden

ABSTRACT

A number of technetium-99m labeled radiopharmaceuticals have been found to concentrate in the salivary glands. At present no readily available S values or absorbed fractions to be used for calculation of the absorbed dose in this organ are found in the literature. For the calculation of absorbed dose a simple mathematical model for the salivary glands can be used. This was done for the calculations performed in ICRP 53. In this model, the salivary glands are represented by three pairs of small spheres, with masses of 5, 12.5 and 25 g, for each of the respective glands. With the approximation that all nonpenetrating radiation is absorbed in the glands, and that the amount of energy transported from one gland to another is negligible, S factors for Tc-99m have been estimated. The validity of these approximations, as well as S factors for other ages, is discussed and presented.

INTRODUCTION

In nuclear medicine investigations significant activity concentration is sometimes observed in the salivary glands. For two of the substances found in ICRP Publication 53, (1) and in the addendum in ICRP Publication 62 (2), ^{99m}Tc-pertechnetate and ^{99m}Tc- MIBI, the salivary glands are included as source organ for the dose calculations, with uptakes of 3 and 1.5 % respectively. At the time of the preparation of these ICRP-reports and at present no general model for the calculation of absorbed dose in salivary glands has been published.

For the preparation of the ICRP Publication 53 (1) it was necessary to make a simple model in order to estimate the absorbed dose. The aim with this work is to present and evaluate this model, which earlier has not been published.

ANATOMIC MODEL

Man has three pairs of salivary glands, the parotid, submaxillary and sublingual glands. Their locations in the head are illustrated in Figure 1. For adult males, the "Reference Man" report ICRP 23 (3) gives their masses to be 25, 12.5 and 5 g, respectively, for a single gland. This adds up to a total mass of 85 g. For children of different ages, the assumed masses are presented in Table 1. The total

mass for each age was obtained from ICRP 23, and the proportion of the mass for the single glands was assumed be independent of age.

For the purpose of dosimetry the glands were assumed to be spherically shaped. Assuming unit density, the radii of these spheres in adults are 18.1, 14.4 and 10.6 mm, respectively. The positions of the glands were irrelevant since it was assumed that "cross-fire" of penetrating radiation from one gland to another, only contributed insignificantly to the absorbed dose, and was thus omitted form the calculation.

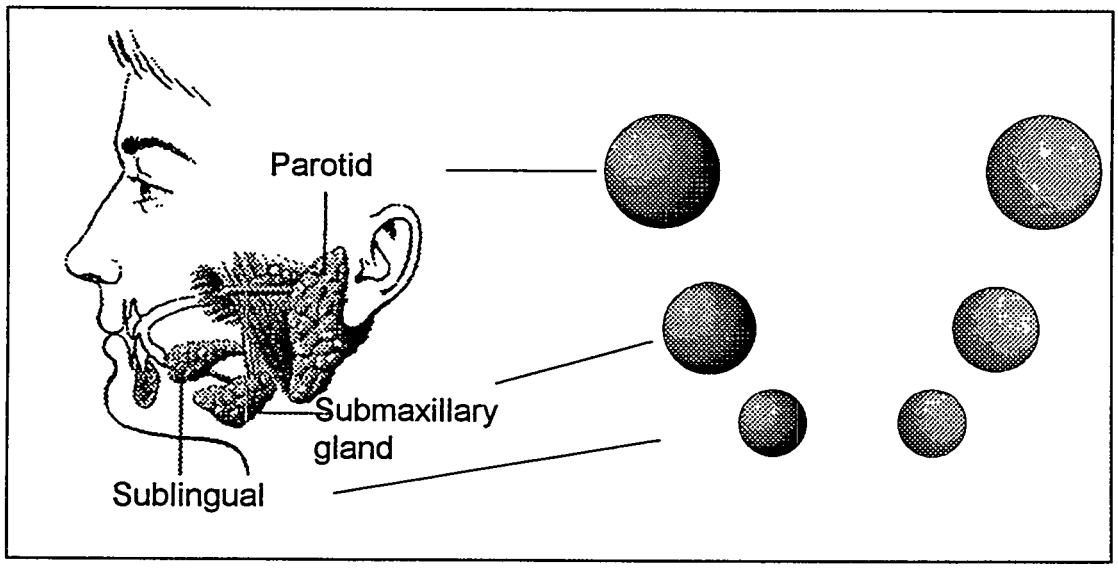

Figure. 1. Illustration of the anatomy and the location of the salivary glands, together with their schematic representation.

Table 1

Mass of the Salivary Glands, in Grams, for Different Ages (3)

Age	Total mass	Parotid	Submaxillary	Sublingual
Adults	85	25	12.5	5
15 years	68	20	10	4
10 years	51	15	7.5	3
5 years	37.5	11	5.5	2.25
1 years	25.2	7.4	3.7	1.5

CALCULATION METHODS

To obtain the absorbed fraction of energy in a single gland for 140 keV photons, data found in MIRD Pamphlet No. 8 (4) were used. The energy emitted as nonpenetrating radiation was assumed to be completely absorbed within the gland. The S factor for a single gland of mass m_n, with the source in the same gland, $S_{n \leftarrow n}$, is given by the expression

$$S_{n\leftarrow n} = \frac{k}{m_n}\sum_i Y_i\, E_i\, \phi_i \qquad [1]$$

Y_i is the yield of radiation type i, E_i the energy of the photon or electron, and ϕ_i is the absorbed fraction of energy for radiation type i. For nonpenetrating radiation $\phi = 1$. k is a dimension constant. For the dose calculations in ICRP 53 it was assumed that the contribution of "cross-fire" is insignificant.

The cumulated activity in gland n is given by

$$\tilde{A}_n = \left(\frac{m_n}{m_{tot}}\right)\tilde{A}_{tot} \qquad [2]$$

As the mean dose in all glands D_{tot} may be written

$$D_{tot} = S_{tot}\tilde{A}_{tot} \qquad [3]$$

or

$$D_{tot} = \sum_n \left(\frac{m_n}{m_{tot}}\right) D_n \qquad [4]$$

$$D_{tot} = \sum_n \left(\frac{m_n}{m_{tot}}\right) S_n\tilde{A}_n, \qquad [5]$$

the total S factor for salivary glands as both target and source then becomes

$$S_{tot} = \sum_{n=1}^{6}\left(\frac{m_n}{m_{tot}}\right)^2 S_{n\leftarrow n} \qquad [6]$$

m_{tot} is the total mass of all salivary glands together. $S_{n\leftarrow n}$ is obtained from Equation 1.

For calculation of the absorbed dose in other organs due to radiation emitted in the salivary glands S factors calculated using the thyroid as a source organ. Based on absorbed fractions published by Cristy and Eckerman (5) together with nuclear decay data, such S factors may derived for different ages. For adults similar values are also found in MIRD Pamphlet No. 11 (6).

In a similar way the absorbed dose to the salivary glands due to irradiation from other source organs, can be assumed to be equal to that of the thyroid. Similar methods are in common use when calculating the dose in other organs for which no S factors are found, e.g. the esophagus.

In cases in which the thyroid is either a target or source, and the salivary glands are the corresponding organ, the method described above will not work. In such cases the absorbed dose may be taken as the average of the dose to the brain and thymus.

EVALUATION OF THE VALIDITY OT THE ICRP MODEL

To sum up, the following approximations and assumptions have been made for the dose calculation:

i. no "cross fire"
ii: all nonpenetrating radiation is absorbed in the gland in which it is emitted.
iii: the spherical shape in place of a more anatomical realistic geometry.
iv: calculation of dose in other organs with the source in salivary glands replaced by the thyroid.
v: calculation of the dose contribution from other organs to the salivary glands in a similar way.

No "Cross Fire"

For the evaluation of the significance of the first assumption, the absorbed dose was calculated in five of the glands when the source was located in the remaining sixth gland. For this reason distances between the glands had to be established. For simplicity, and for the purpose of evaluating the model, it is assumed that the center of all the glands is found in the same plane in space. Two dimensional coordinates for these centers are assigned, and those are presented in Table 2, together with the radius of the spheres.

Table 2

Assumed Coordinates (mm) for the Salivary Glands in Adults, Used for the Evaluation of the Influence of "Cross-fire"

	x	y	radius
Parotid gland, left	50	60	18.1
right	50	-60	
Submaxillary gland, left	0	45	14.4
right	0	-45	
Sublingual gland, left	-30	25	10.6
right	-30	-25	

Consider a small tissue element of a gland, located at the distance d from a point source. The absorbed dose in this element per photon of energy E_g, emitted from the point source is given by

$$D_{E_\gamma} = k\, Y_i\, E_\gamma \left[\frac{\mu_{en}(E_\gamma)}{\rho} \frac{1}{4\pi d^2} e^{-\mu d} \right] B_{en}(\mu d); \qquad [7]$$

k, Y_i and E_g have been defined earlier, μ_{en} is the linear energy attenuation coefficient and ρ is the density of the gland, which approximately equals 1.0 g cm^{-3} . The energy build-up factor, B_{en} is taken from MIRD Pamphlet No. 2 (7). By integrating this equation (point-kernel) over the source and target volume, the absorbed fraction of energy in a gland with a source in another gland may be estimated. The technique has been described by Loevinger and Berman (8) and by Berger (1968). By calculating the absorbed dose at different points in the "target" gland for a large number of point-pairs (~10000), chosen at random, the contribution of the absorbed dose in the "target" gland from the "source" glands is estimated. This was then repeated for all combinations of glands (utilizing

symmetry), whereupon the average absorbed dose in all the glands was calculated using Equation 2. The result of these calculations shows that the increase absorbed energy from 140 keV photons due to "cross fire" within the gland packet is approximately 8 %. This means that the total S factor is underestimated by about 2 % if cross-fire is not considered (Figure 2).

Completely Absorbed Nonpenetrating Radiation

The range of the Auger and conversion electrons from ^{99m}Tc is very short. To evaluate the assumption that these electrons is completely absorbed in the "source gland" the most extreme case is considered, i.e. using the smallest single gland, which is the sublingual gland in a newborn child, which has a mass of 1.5 g. Siegel and Stabin (9) have estimated absorbed fractions for spheres of different sizes. Utilizing their data, the absorbed fraction of energy for monoenergetic electrons of 140 keV is found to be 0.98 with a uniformly distributed source in a sphere with a mass of 1.5 g.

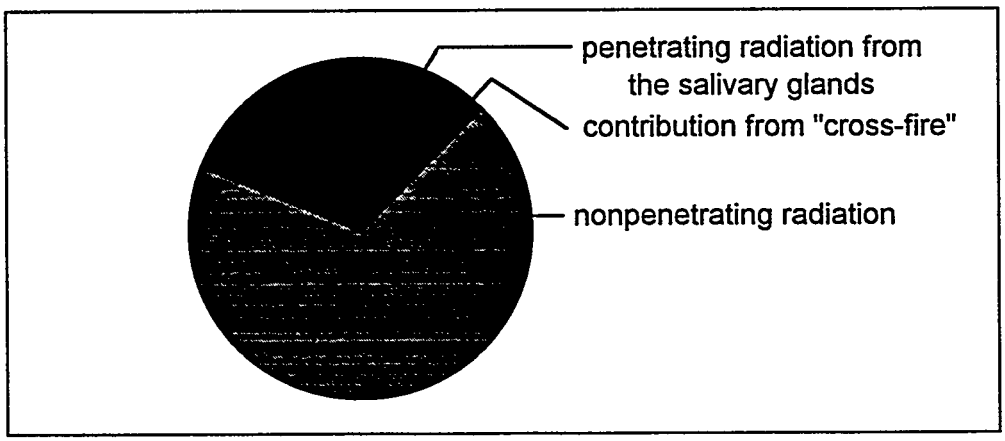

Figure 2. The relative contribution from different components to the absorbed dose in the salivary glands from Tc-99m located in the same organ.

Thus, even the smallest gland is large enough to absorb almost 100 % of the nonpenetrating radiation at the highest electron energy. Setting the absorbed fraction to 1.00 in this case is thus a very good approximation. It may be pointed out that even if other radionuclides may emit non-penetrating radiation with higher energies, assuming complete absorption is usually still a good approximation. For example for I-131, 95 % of the energy of the beta particles is absorbed in the smallest gland (9).

Spherical Shape of the Glands

The spherical shape is the most efficient one for absorbing radiation. In reality, the salivary glands are more irregular (Figure 1), and an ellipsoidal shape would perhaps fit better. The influence of the absorbed fraction of energy as a function of the mass for different shapes is shown in Figure 3. From this graph, it is seen that the absorbed fraction for penetrating radiation may be overestimated by about 20 %. This will, however, influence the final S factor to a smaller degree, since the energy absorbed from nonpenetrating radiation is about a factor of two higher (Figure 2). The overestimation in absorbed dose due to this assumption is thus only about 5 - 10 %, depending on mass and actual shape of the gland.

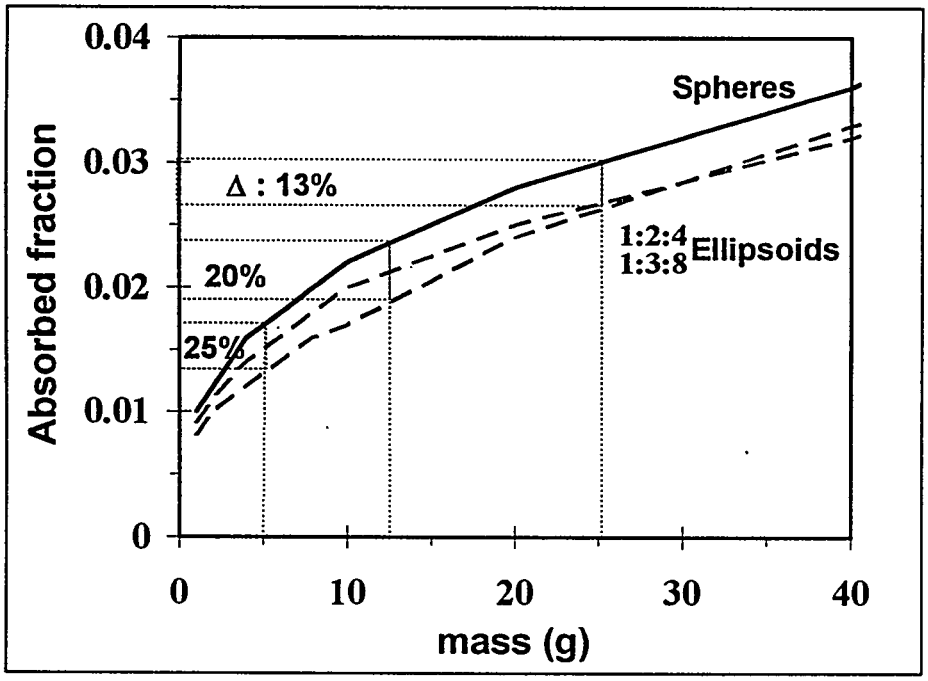

Figure 3. Absorbed fraction of energy for small volumes of different shapes as a function of mass (4). The photon energy is 140 keV, and the source is uniformly distributed in the volumes which are surrounded by a scattering medium.

Table 3A

S Factors (mGy/MBq-h) for Thyroid and Thymus as Target with Different Source Organs Located in the Upper Part of the Body (10)

Target	Brain	Breast	Lungs	Stomach cont.	Bone
Thyroid	4.9E-04	1.1E-04	3.2E-04	9.4E-06	2.8E-4
Thymus	2.5E-05	8.2E-04	1.0E-03	1.3E-04	1.7E-4
ratio	20	1 / 7.6	1 / 3.2	1 / 14	1.6

Table 3B

S Factors (mGy/MBq) for Different Target Organs with Thyroid and Thymus as Source (10)

Source	Brain	Breasts	Lungs	Red marrow	Ovaries
Thyroid	4.9E-04	1.1E-04	3.2E-04	2.9E-04	8.2E-07
Thymus	2.5E-05	8.2E-04	9.7E-04	3.0E-04	6.9E-06
ratio	20	1 / 7.5	1 / 3.0	1.0	1 / 8.4

Substituting the Salivary Glands with another Organ.

To get an idea of the uncertainty in the method used for estimating the absorbed dose to other organs, the dose in two slightly separated target organs may be compared for a number of source organs. This is shown in Table 3, where the thymus and the thyroid are compared. From the data in this table, the error introduced by replacing the thymus with the thyroid can be estimated. Assuming that the error introduced by replacing the salivary glands with the thyroid is similar, typically the error is about a factor of five. Except for the brain, the dislocation of the activity in the salivary glands to the thyroid tends to overestimate the absorbed dose in the other organs. For the brain however, the underestimation of the absorbed dose is considerable. The significance of this error in the total S value is strongly dependent on the distribution of the cumulated activity in the different organs.

In the opposite direction, the significance of the error which is introduced by replacing the salivary glands with another target organ is similar (Table 3B). In reality, however, this error is smaller as the contribution from other organs to the total absorbed dose in the salivary glands is small. For Tc-99m pertechnetate, this contribution is 18 % (Figure 4), when the thyroid dose is substituted for the dose to salivary glands. An indication of the degree of overestimation introduced by using the thyroid dose as a substitute may be obtained by considering the absorbed dose in the brain from other tissues. It is reasonable to assume that this dose is smaller than the corresponding dose in the salivary glands, due to the larger distance from the source. Thus, the absorbed dose to the salivary glands would be a factor of two smaller than that in the thyroid from other tissues. This would result in an overestimation of the total dose of about 10 %.

CALCULATION OF THE EFFECTIVE DOSE

For the calculation of the effective dose, the ICRP has in Publication 60 (11) identified a number of radiosensitive organs, to which are assigned specific weighting factors. Besides these organs, a number of other organs to be included in the "remainder" is listed. The salivary glands can not be found in any of these groups of organs. However, the ICRP also says that the latter group may also include other tissues or organs selectively irradiated; therefore, the salivary glands may be included.

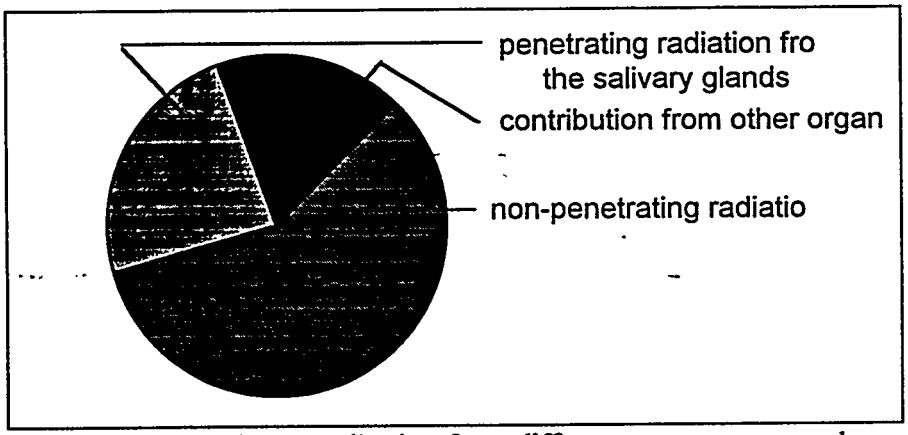

Figure 4. The relative contribution from different components to the absorbed dose in the salivary glands from Tc-99m pertechnetate. The activity is distributed according to ICRP 53 (1), and the thyroid is substituted for the salivary glands.

ICRP 60 also says that in those exceptional cases in which any of the organs in the "remainder" receives the highest absorbed dose of all organs and tissues, half of the weighting factor for the remainder should be applied to that tissue. This exception may also be applicable if the salivary glands receive the highest absorbed dose. In the two cases considered here, Tc-99m pertechnetate and MIBI, this has not been the case.

RESULTS AND DISCUSSION

Table 4 shows the S factors for Tc-99m in salivary glands. The first column presents those that were used in ICRP 53, and the second column shows recalculated data using the MIRDOSE 3 program (10) that calculates S factors in small spheres. The same approximations have been made in both cases.

Table 4

Tc-99m S Factors (Salivary Glands ← Salivary Glands)
(mGy MBq^{-1} h^{-1})

Age	ICRP 53	*MIRDOSE 3*
Adults	0.13	*0.15*
15 year	0.16	*0.19*
10 year	0.21	*0.24*
5 year	0.29	*0.32*
1 year	0.42	*0.46*

The method presented for estimating the absorbed dose the salivary is comparatively simple and fast. It may be applied also to other radionuclides. For Tc-99m, the greatest uncertainties are introduced when the contribution from activity in other organs is estimated. An overestimation of 10 - 15 % in the total S value is estimated, of which the majority is due to activity in other organs. In the two cases in ICRP 53 and 62 (1,2), in which the method has been used, the accuracy of the estimated absorbed dose, both in salivary glands and other organs, as well as the effective dose is within acceptable limits.

REFERENCES

1. International Commission of Radiological Protection. Radiation Dose to Patients from Radiopharmaceuticals. ICRP Publication 53, Pergamon Press, Oxford, 1987.
2. International Commission of Radiological Protection. Addendum to Publications 53. ICRP Publication 62. Radiological Protection in Biomedical Research. Pergamon Press, Oxford, 1993.
3. International Commission of Radiological Protection. Report of the Task Group on Reference Man. ICRP Publication 23. Pergamon Press, Oxford, 1975.
4. Ellet WH and Humes RM. Absorbed Fractions for Small Volumes Containing Photon-emitting Radioactivity. MIRD Pamphlet No. 8. J Nucl Med 12 (Suppl no. 5): 25- 32, 1971.
5. Cristy M and Eckerman KF. Specific Absorbed Fractions of Energy at Various Ages from Internal Photon Sources. Report ORNL/TM-8381/V1 - V7, 1987.

6. Snyder WS, Ford MR, Warner GG and Watson SB. "S" Absorbed Dose per Unit Cumulated Activity for Selected Radionuclides and Organs. MIRD Pamphlet No 11, Society of Nuclear Medicine, New York, 1975.
7. Berger MJ. Energy deposition in water by photons from biologically-distributed radionuclides. MIRD Pamphlet No. 2. J Nucl Med 9 (Suppl No. 1): 15-26, 1968.
8. Loevinger R and Berman M. A schema for absorbed-dose calculations for biologically-distributed radionuclides. MIRD Pamphlet No. 1. J Nucl Med 9 (Suppl. No. 1): 7-14, 1968
9. Siegel JA and Stabin MG. Absorbed fractions of electrons and beta particles in spheres of various sizes. J Nucl Med 35 (1): 152-156, 1994.
10. Stabin M, 1996 MIRDOSE: Personal computer software for internal dose assessment in nuclear medicine. J Nucl Med 37: 538-546, 1996.
11. International Commission of Radiological Protection. 1990 Recommendations of the International Commission on Radiological Protection. ICRP Publication 60, Pergamon Press, Oxford 1991.

QUESTIONS

Gardin: Have you used your model with HMPAO-Tc-99m in the case of brain SPECT Images? When the quality of the HMPAO is not perfect, the Tc-99m concentration is very high in salivary glands.

Johansson: No, I have only used the model for calculation in those cases where the salivary glands were identified as a source organ by the ICRP 53. This is not the case for ^{99m}Tc HMPAO.

Stabin: You said that using the thyroid as a surrogate for salivary glands to calculate the dose to other organs might overestimate the dose by a factor of five. How did you arrive at this number?

Johansson: This factor is dependent on where your source is located. The figure you mention represents a worst case, and has been obtained as a rough estimate by comparing absorbed doses to different organs in some cases.

EXTRAVASATION OF RADIOPHARMACEUTICALS A STUDY OF ITS FREQUENCY AND ESTIMATION OF ABSORBED DOSES IN DIAGNOSIS AND THERAPY

Grafström G, Strand S-E, Kontestabile E, Almén A, Bergqvist L, Larsson I[1]
Radiation Physics Department, Lund University, 221 85 Lund, Sweden
[1]Clinical Physiology Department, Helsingborg Hospital, 251 87 Helsingborg, Sweden

ABSTRACT

With all injection procedures there is a risk for extravasation. When injecting a radiopharmaceutical the absorbed dose at the injection site may be increased due to high activity concentration and/or charged particle emission. This may cause deterministic effects such as tissue necrosis, especially in radionuclide therapy (RNT), and also with some radionuclides used for diagnostic studies. To estimate the risk for extravasation, we studied various injection techniques at two nuclear medicine clinics. We looked at the frequency and magnitude of extravasations in randomly selected patients.

Clinic A used peripheral venous catheters (PVC), and clinic B used direct injections with injection needles (IN). At clinic A and clinic B, 192 patients and 90 patients were investigated, respectively. All of these patients were injected with either Tc-99m-DTPA, Tc-99m-MAA, Tc-99m-MDP, Tc-99m-pertechnetate or Tl-201-chloride. Both arms were imaged with a scintillation camera as soon as possible after the injection. In the case of an extravasation, a volume estimate and the retention time at the injection site was determined with multiple imaging.

The results for PVC injected patients showed one complete extravasation. In 8% of the patients, a detectable activity at the injection site, up to 2% of injected activity, was found. None of the IN injected patients had complete extravasation. However, in 33% of these patients a remaining activity of up to 18%, was detected.

The mean absorbed doses at the injection site, estimated using the MIRD formalism, were up to 0.1 Sv. Projecting the results to RNT, absorbed doses could be a thousand times higher. In addition to the calculated absorbed doses, radionuclides localizing in or close to the cell nucleus might further enhance the deterministic effects.

INTRODUCTION

All injections are associated with a risk for extravasation. Special attention should be given to this possibility when injecting a radiopharmaceutical. Long retention time at the site of the extravasation of the radiopharmaceutical, and high emission of charged particles may cause a high local absorbed dose. More than one hundred thousand radiopharmaceutical injections are performed each year in Sweden (population of 8.9 million). Of these injections, the majority is administered for

diagnostic purposes, and less than one percent of the injections are for radionuclide therapies. Most of the radionuclides used for diagnostic studies decay with emission of low-energy electrons such as beta, conversion or Auger electrons. For radiotherapy, the desire is to have as much particle emission as possible. For this reason, alpha-emitting radionuclides have been suggested (1,2).

To determine the magnitude of locally absorbed doses and to estimate the possible biological consequences it is of interest to study extravasation frequencies for different injection techniques and for various radiopharmaceuticals.

Extravasations of radiopharmaceuticals have been reported in only a few articles. Driedger and Breen (3) described a case where the extravasated substance was lipid-soluble I-131-iodocholesterol. The slow clearance lead to a very large local absorbed dose and radiation injury at the injection site (erythema, pruritus and tenderness). The absorbed dose was estimated to be in the range of 245-490 Gy. Minsky et al. (4) reported an extravasation of aqueous P-32, where the estimated maximal absorbed dose was 5 Gy. Pier and Beekhuis (5) described a case where a chronic ulcerous lesion was diagnosed as radiation induced three years after an administration of Tl-201. The absorbed dose was calculated to be 33-250 Gy. They also found that in nine other patients, a small part of the injected Tl-201 was extravenously located. The absorbed dose in the patients was estimated to be 80-190 mGy/MBq, in a tissue mass of one g.

Very little data have been published concerning retention times for different radiopharmaceuticals after extravasation. In two papers, Castronovo et al. (6,7) give retention data for subcutaneously injected rats. Pedersen et al. (8) give retention for intracutaneously injected patients. Sarby et al. (9) have published data from eight patients injected extravasally or interstitially with one of the following radiopharmaceuticals: Tc-99m-HDP, Tc-99m-colloid, Tc-99m-DPD, Tc-99m-MAA, Tl-201-chloride and Xe-131 in saline. Retention times have earlier been studied for several radiopharmaceuticals in our group have previously been investigated (10,11,12,13).

To estimate the risk for extravasation, we have studied various injection techniques with special attention given to the frequency and magnitude of extravasations in randomly selected patients.

MATERIALS AND METHODS

The study was performed at two nuclear medicine departments at two hospitals (A and B) in southern Sweden. Department A uses peripheral venous Teflon catheters (PVC), and department B uses syringes with an injection needle for i.v. injection of the radiopharmaceuticals.

The Teflon Catheter Technique

The radiopharmaceutical was injected through a Teflon catheter (Venflon, Spectramed-Viggo, diameter 0.8 (1.0) mm, length 25 (32) mm). After the injection, the catheter was flushed with 5 ml saline solution. After the injection and before the scintillation camera measurement, the injection site was wiped with a cotton swab moistened with alcohol. Measurements were performed with a scintillation camera (Toshiba GCA-901A) on randomly selected patients as soon as possible after the injection, usually 10-20 min. A radioactive marker was placed close to the injection site. Data were collected for two minutes, and the images were stored in a 256x256-matrix. For the evaluation the image, processing software provided with the medical image processor (Toshiba GMS-550U) was used. Regions of interest were selected by drawing contours around the area of elevated count rates and the extravased activity ($A_{measured}$) was calculated. In these calculations, background was subtracted by using a nearby area of approximately the same thickness without an elevated count rate. When correction for attenuation was performed, all activity was assumed to be at a depth of 0.5 cm. A linear attenuation coefficient (μ) of 0.1522 cm^{-1} was used for the 140 keV photons. Correction for

decay in the time interval between the injection and the measurement (t) was also done, with a physical decay constant (λ) equal to 0.1149 h^{-1} for Tc-99m, using the formula

$$A = A_{measured} \cdot e^{\mu \cdot depth} \cdot e^{\lambda \cdot t}.$$

The volume was considered a rotational ellipsoid with the same length and width as the image area with elevated activity.

$$V_{ellipsoid} = \frac{4\pi}{3} \cdot \frac{length}{2} \cdot \left(\frac{width}{2}\right)^2, \text{ where the length} > \text{width}$$

The density of tissue (ρ) is assumed to be 1 g/cm^3. With nuclide data from ICRP 38 (14) and absorbed fractions from MIRD Pamphlet 7-8 (15), the mean absorbed dose in the injection site ($\overline{D}(v)$) can be calculated (12) by the formula

$$\bar{D}(v) = \int_0^\infty \dot{D}v(t)dt = \int_0^\infty \frac{A(t) \cdot \sum_i \Delta_i \cdot \phi_i(v(t))}{\rho \cdot v(t)} dt.$$

In this study, extravasations increased to their final volume within 1 minute, and so the volume was not assumed to change with time. However, in general, the reader should be aware that the extravasation volume may vary with time. Also, in this study, all electron absorbed fractions were assumed to be 1.0; for smaller volumes and/or higher energy electrons, the application of different absorbed fractions may be appropriate.

The total number of patients examined at clinic A was 192. The patients were randomly selected from all patients examined at the clinic. Table 1 gives a summary of the study. Of the patients, 128 were injected with Tc-99m-MDP in a volume of about 1 ml and an activity of ~ 400 MBq for the purpose of bone scanning, 14 were injected with ~ 35-80 MBq Tc-99m-MAA in volumes of 0.3-0.8 ml for lung perfusion studies, 15 were injected with ~ 100 MBq Tc-99m-O_4^- in a volume of ~ 0.3 ml for thyroid studies, 9 were injected with Tc-99m-O_4^- and stannous ions (RNAK) for blood flow measurements, 15 were injected with ~ 75-85 MBq Tc-99m-DTPA for renographies, and 11 were injected with ~ 75 MBq Tl-201- chloride for brain scanning.

Table 1
Number of Patients and Radiopharmaceuticals Investigated for Extravasation Frequencies

Investigation	Clinic A	Clinic B	Total
Tc-99m-MDP	128	90	**218**
Tc-99m-MAA	14		**14**
Tc-99m-O_4^-	15		**15**
Tc-99m-O_4^- + Sn^{2+}	9		**9**
Tc-99m-DTPA	15		**15**
Tl-201-Cl	11		**11**
Total	**192**	**90**	**282**

The Syringe Technique

Data collection and image analysis were performed in the same way at clinic B as described above. The radiopharmaceutical was injected directly into the vein after checking the position of the needle by drawing some blood into the hub of the syringe. The cannulas had a diameter of 0.6 mm and a length of 25 mm. Ninety patients were injected with ~ 500 - 600 MBq Tc-99m-MDP in volumes of 0.4 - 1.2 ml.

RESULTS

Results of extravasation frequencies of the two injection techniques are given in Table 2.

Table 2
Extravasation Frequencies
for the Two Injection Techniques

	Catheter	Syringe	Total
Patients	192	90	**282**
Complete extravasation	1 (0.5%)		**1 (0.4%)**
Small extravasation	15 (8%)	30 (33%)	**45 (16%)**
External uptake in vessels	4 (2%)		**4 (1.4%)**
Total	**20 (10%)**	**30 (33%)**	**53 (19%)**

The Teflon Catheter Technique

Of the 192 randomly selected patients, a complete extravasation (100%) was found in one case (0.5%) injected with Tc-99m-MDP. A retention study was performed, and in Figure 1 the activity at the extravasation site is compared with a retention study by Castronovo (6) with Tc-99m-MDP in rats. The local mean absorbed dose was calculated to be 0.22 Gy. An increased level of radioactivity was detected at the injection site in 15 cases (8%), where up to 2% of the injected activity was extravasated. The results for these cases are shown in Figure 2. The local absorbed doses were calculated to be in the range of 0.3 to 51 mGy.

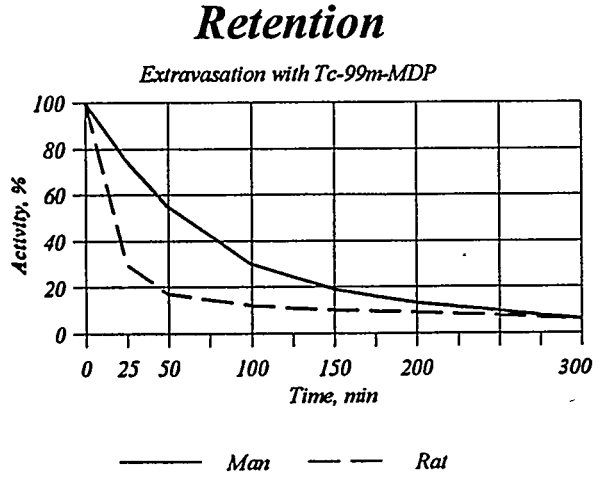

Figure 1. Retention of extravasated Tc-99m-MDP in one of the patients with complete extravasation, compared to rats (7).

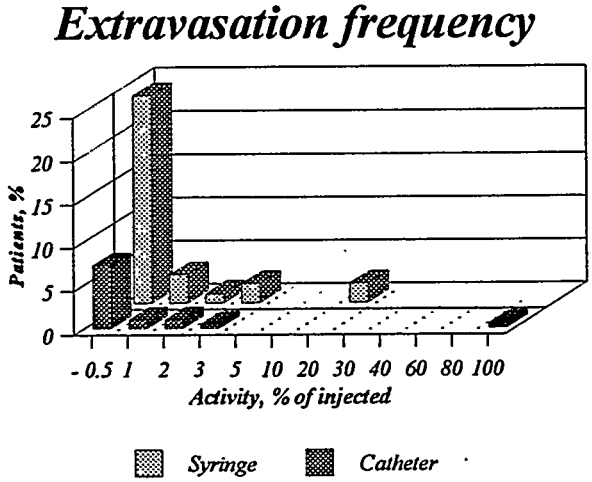

Figure 2. Extravasation frequency and measured activity at injection site for the two different injection techniques examined. Note the complete extravasation for the catheter technique and the high frequency of low activities for the syringe technique.

The Syringe Technique

When the 90 randomly selected examinations were analyzed, an increased level of radioactivity was detected at the injection site in 30 cases (33%) where up to 18% of the injected activity was extravasated. (Two cases with 18% and two cases with an extravased fraction of about 3%.) The estimated absorbed dose did in not exceed 130 mGy in any case.

To be able to compare the two injection techniques, extravasation frequencies for the patients injected with Tc-99m-MDP are compared. For catheter, 6 cases (5%) were detected. (Three cases with 0.1%, two cases with 1.5% and one case with 100% of the injected activity extravasated.) The results are shown in Table 2. As shown, the syringe technique had most cases of extravasation. The overall extravasation frequency for the 282 patients was 19%.

DISCUSSION

To make a comparison for some of the different radionuclides used in diagnosis and therapy, a dose calculation was performed assuming the extravasation activity in a volume of 10 ml and no activity outflow. The results from this "worst case" (no biologic clearance) scenario is shown in Table 3. These data indicate that even a small fraction of the injected activity of some radionuclides, if extravasated, may result in very high local tissue doses and possibly tissue damage. After extravasation, however, in most cases there is an outflow of activity from the injection site, as exemplified in Figure 1. The influence of retention on the absorbed dose is illustrated in Figures 3 and 4. Recalculations with an assumption of an effective half-time of 5 h results in much lower absorbed doses (37, 243 and 18 times for I-131, Sr-89 and Re-186, respectively). These results show how very important it is to measure the actual retention parameters for a specific radiopharmaceutical in a specific patient in order to correctly estimate the absorbed dose.

Table 3
Absorbed Dose (Gy/100MBq) for Some Commonly Used Isotopes in Diagnosis and Therapy in a 10 ml Volume at the Injection Site, i.e. "Worst-Case" Scenario.

^{18}F	3.9	^{90}Y	495	^{186}Re	261
^{32}P	1980	^{99m}Tc	0.22	^{188}Re	120
^{67}Cu	81.4	^{114m}In	9076	^{198}Au	211
^{67}Ga	26.5	^{125}I	321	^{211}At	419
^{89}Sr	5882	^{131}I	322	^{212}Bi	4500

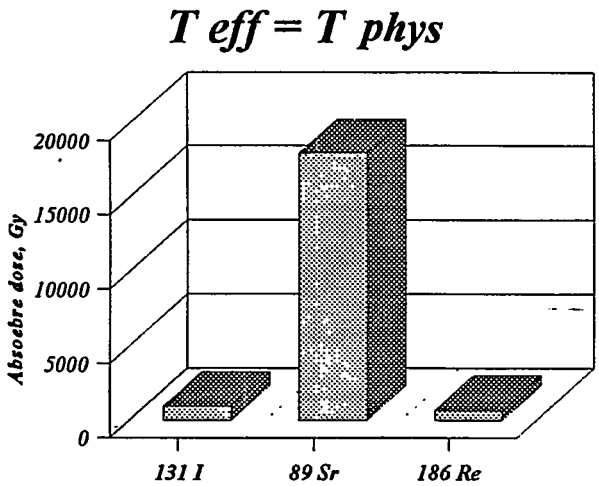

Figure 3. Absorbed doses for I-131, Sr-89 and Re-186 in "worst case" i.e. no retention from the injection site.

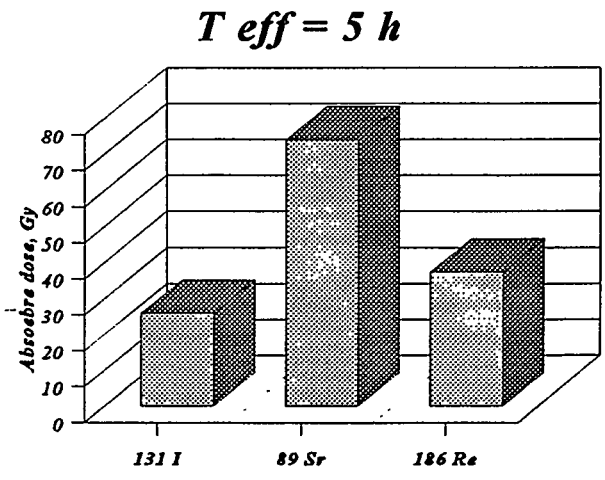

Figure 4. Absorbed doses for I-131, Sr-89 and Re-186 in a more realistic case with an effective retention half-time of 5 hours.

Figure 5 is an example of Tc-99m-MDP extravasation with images saved at different times after the injection. Figure 6 shows an RNAK related phenomenon with activity in the vessels, which can

not be attributed to extravasation. The proximal blood vessels are easily distinguishable. Due to the very high concentration of Sn^{2+} and Tc-99m-O_4^- in the boluses just after injection, it might be that the endothelial cells in the blood vessels are labeled by diffusion.

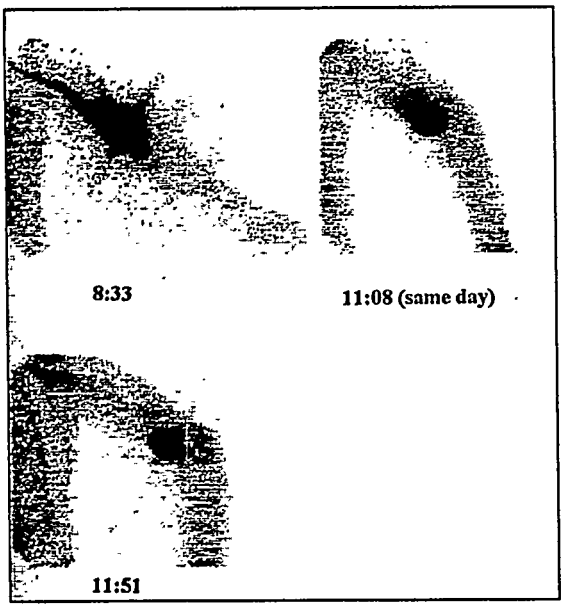

Figure 5. Example of a Tc-99m-MDP extravasation with images saved at three different times after the injection. In the image one can see a large area of elevated activity (18% of the activity was extravasated). An average absorbed dose of 130 mGy was calculated.

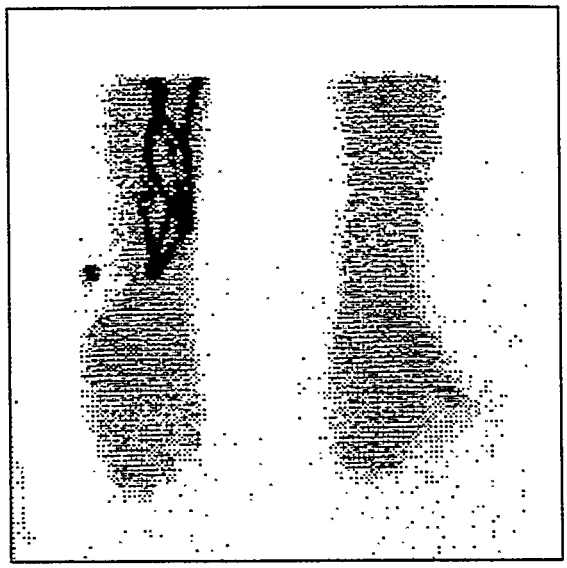

Figure 6. Example of RNAK related phenomenon which is not an extravasation. The blood vessels are easily distinguised.

The results show that extravasations do occur even when using safe techniques such as catheters. When injecting a radiopharmaceutical with a catheter, extravasation (or an area with increased activity) occurs in 8% of the patients. For smaller extravasations, the estimated average absorbed dose in the "worst case" did not exceed 50 mGy for Tc-99m radiopharmaceuticals. When injecting a radiopharmaceutical with a syringe, an extravasation or an area with increased activity occurs in about 33% of the cases. The estimated average absorbed doses in this study were in the range of 10-130 mGy for Tc-99m. This means that the biologic effect caused by the Tc-99m-radiopharmaceuticals used in the study must be considered small (the largest permissible absorbed dose to any part of the body for a single occupational exposure is 500 mGy). The extravasation frequency after injection of Tc-99m-MDP was 16%. In bone scans performed with Tc-99m-MDP, Ongseng et al (16) have reported that an axillary uptake was found ipsilateral to the injection site in 2% of the injections, and in each of these cases activity was found near the injection site. Because their criteria was decreased image quality, it is plausible that in the patients a higher total extravasation frequency was apparent.

Larger or total extravasations are too few in our study for firm conclusions. It is not possible to say with certainty that the risk of a major extravasation is larger with a syringe than with a catheter injection technique. However, extravasations occur, also total, and can not be neglected. During our study one nonrandomized patient had a large extravasation of Tc-99m-MAA. The distribution of the activity within the ROI was studied. The radioactivity was four times higher in the center than the

activity in the area close to the edge of the extravasated volume. From images at different times after the extravasation, it was observed that the activity stayed within the volume ("worst case"). Even though this measurement was made in only one patient, a likely assumption is that the maximum absorbed dose in the center exceeds the average absorbed dose and may reach the order of Gys instead of mGys, depending on the radionuclide. No general strategy to minimize the effects of an extravasation has been recommended.

The problem of extravasation is not only related to radiopharmaceuticals. Whenever drugs are injected intravenously, one can not automatically assume that the injection is successful. This is a serious problem, for instance when administering chemotherapy agents because of their high cytotoxicity.

When administering chemotherapy agents that are vesicant (for instance doxorubicin) the effects of an extravasal injection may be more apparent in comparison to a failed radiopharmaceutical injection, since an ulcer may appear at the injection site. References (17,18,19,20,21,22,23,24,25,26, 27,28,29,30) are all case reports of extravasal injections of chemotherapy agents often causing tissue damage. There are also reports of problems with catheters for long-term access (22) and an extravasation incidence of 1.1% (31). There is a call for procedures in chemotherapy concerning extravasation (32,33), and a follow-up suggestion is also presented (34).

As far as chemotherapy agents are concerned, there are different suggestions about the appropriate actions to take in case of an extravasation. The most common way of reducing the injury is by cooling or by heating (to increase the blood circulation and thereby the clearance of the vesicant substance). Surgery may also apply, but only after necrosis has developed. For chemotherapeutic agents it is difficult to locate and quantify any extravasation with precision.

The suggestions about what to do when an extravasal injection of a radiopharmaceutical injection has occurred, should in principle correspond to those mentioned above. Injection of saline solution would be a possible way to increase the volume and consequently diminish the mean absorbed dose. Injection of hyaluronidase has also been suggested to stimulate the spread into the neighboring tissue and thereby increasing the volume (9). Another way of possibly increasing the blood flow in the area might be to move the arm repeatedly so that the muscular activity increases blood flow and clearance by the lymphatic system.

There is very little information in the literature about at what level of absorbed doses one may expect biological effects. A lower "limit" of 20 Gy has been proposed for radionuclides by Shapiro (35). Threshold for moist desquamation in skin is 20 Gy, and cell death in epidermal and dermal layers resulting in necrosis is about 50 Gy, according to ICRP 60 (36). As shown in Table 3, even a very small extravasation of some radiopharmaceuticals may result in doses far in excess of these limits. In ICRP 59 (37) it is stated that as the stochastic risk of skin cancer mortality is low (2×10^{-4}/Sv); the deterministic effect is the limiting endpoint for chronic exposures, with a threshold of 20 Gy for large areas. For smaller areas (< 25mm diameter) and lower energies of beta radiation, the threshold is higher.

One practical realization resulting from this study was the necessity of educating nuclear medicine personnel about the possibility of extravasation. It would be appropriate to check after an administration of a radiotoxic nuclide to be sure that the injection was successful. This is important because extravasation may not have been noticed, and enough radioactivity may have reached other parts of the body when imaging. Hoop (38) stresses that "unexpected costs associated with ignorance of risk, are generally greater than anticipated costs associated with rational understanding".

To gain full cooperation of the staff it might also be valuable to emphasize the fact that extravasations may occur even if great care is taken. In other words, an extravasation should not be regarded either as embarrassing or as just as a minor incident that could be ignored.

CONCLUSION

Our study shows that extravasations do occur when injecting radiopharmaceuticals at nuclear medicine departments. Depending on the radiopharmaceutical used, the absorbed dose may be significant. Different techniques give different risks of extravasation. In our study we have shown an overall extravasation rate of 8% for the Teflon catheter technique, whereas for the syringe technique extravasation occurs in as much as 33% of the cases. Our observations show the importance of checking for possible extravasations when administering radiopharmaceuticals with potential high absorbed doses e.g., radiotherapeutic agents.

ACKNOWLEDGMENTS

The project was financially supported by the Swedish Radiation Protection Institute (Project number: P563.90).

REFERENCES

1. Wilder GB, DeNardo GL and DeNardo SJ. Radioimmunotherapy: Recent results and future directions. J Clin Onc 14(4):1383-1400, 1996.
2. Srivastava SC. Criteria for the selection of radionuclides for targeting nuclear antigens for cancer radioimmunotherapy. Canc Bioth Radiopharm 11(1):43-45, 1996.
3. Driedger AA and Breen SL. Radiation injury from interstitial injection of I-131- idocholesterol. J Nucl Med 32:892, 1991.
4. Minsky BD, Siddon RL, Recht A and Nagel JS. Dosimetry of aqueous P-32 after soft-tissue infiltration following attempted intravenous administration. Health Phys 52:87-89, 1987.
5. Pier DA and Beekhuis H. Local radiation dose from extravasal Tl-201. J Nucl Med 28:684, 1987.
6. Castronovo FP, McKusick KA and Strauss HW. Dosimetric implications of the infiltrated injection. J Nucl Med 25:40, 1984.
7. Castronovo FP, Jr, McKusick KA and Strauss HW. The infiltrated radiopharmaceutical injection: Dosimetric considerations. Eur J Nucl Med 14:93-97, 1988.
8. Pedersen BN, Bertilsson G, Fregert S, Lidén K and Rorsman H. Disappearance of chromium injected intracutaneously. Int Arch Allegry 36:82-88, 1969.
9. Sarby B, Cederlund T and Svensson L. Dosimetry, radiation protection and possible biologic effects of radionuclides administered in small volumes of tissue. Proceedings from the 18th International Symposium on Radioactive Isotopes in Clinical Medicine and Research, Badgastein, Austria, 11-14 Jan, 1988.
10. Bergqvist L, Strand S-E and Persson BRR. Particle sizing and biokinetics of interstitial lymphoscintigraphic agents. Sem Nucl Med 13:9-19, 1983.
11. Bergqvist L, Strand S-E, Hafström L and Jönsson P-E. Lymphoscintigraphy in patients with malignant melanoma: Quantitative and qualitative evaluation of its usefulness. Eur J Nucl Med 9:129-135, 1984.
12. Bergqvist L, Strand S-E, Persson B, Hafström L and Jönsson P-E. Dosimetry in lymphoscintigraphy of Tc-99m antimony sulfide colloid. J Nucl Med 23:698-705, 1982.
13. Rydén S, Bergqvist L, Hafström L and Strand S-E. Reticuloendothelial function in normal and tumor-bearing rats. Measurements with a scintillation camera technique. Eur J Ca Clin Oncol 19:965-970, 1983.

14. ICRP Publication 38. Radionuclide Transformations, Energy and Intensity of Emissions, Pergamon Press, Oxford, 1983.
15. MIRD Pamphlet 7-8. J Nucl Med 5:Supplement, 1971.
16. Ongseng F, Goldfarb CR and Finestone H. Axillary lymph node uptake of technetium-99m-MDP. J Nucl Med 36(10):1797-1799, 1995.
17. Gahankari D, Rana RE and Tambwekar SR. An unusual complication following intralesional triamcinolone injections. Plast Reconstr Surg 97(5):1076, 1996.
18. Lauvin R, Miglianico L and Hellegouarc'h R. Skin cancer occurring 10 years after the extravasation of doxorubicin. N Engl J Med 332(11):754, 1995.
19. Shapiro J and Richardson GE. Paclitaxel-induced "recall" soft tissue injury occurring at the site of previous extravasation with subsequent intravenous treatment in a different limb. J Clin Oncol 12(10):2237-2238, 1994.
20. Raymond E, Cartier S, Canuel C, Louvet C, Demuynck B, Debray M, Varette C, Baux S, Mimoun M, de Gramont A et al. Extravasation of paclitaxel. Rev Med Interne 16(2):141-142, 1995.
21. Bharani A, Chattopadhyay BP, Dani P and Bhargava KD. Metronidazole extravasation causing digital gangrene. Indian J Physiol Pharmacol 39(3):307-308, 1995.
22. Williams JH, Hunter JE, Kanto WP Jr, Bhatia J. Hemidiaphragmatic paralysis as a complication of central venous catheterization in a neonate. J Perinatol 15(5):386-388, 1995.
23. du Bois A, Kommoss FG, Pfisterer J, Lück HJ, Meerpohl HG. Paclitaxel-induced "recall" soft tissue ulcerations occurring at the site of previous subcutaneous administration of paclitaxel in low doses. Gynecol Oncol 60(1):94-96, 1996.
24. Silverman HI. More skin cancer after the extravasation of doxorubicin. N Engl J Med 333(4):257, 1995.
25. Dini D, Forno G, Gozza A, Silvestro S, Bertelli G, Toma S, Filippi F and Passarelli B. Combined management in the treatment of epidoxorubicin extravasation. A case report. Support Care Cancer 3(2):150-152, 1995.
26. Banerjee A, Brotherston T M, Lamberty B G, Campbell R C. Cancer chemotherapy agent-induced perivenous extravasation injuries. Postgrad Med J 63:5-9, 1987.
27. Bhawan J, Petry J, Rybak M E. Histologic changes induced in skin by extravasation of doxorubicin (adriamycin). J Cutan Pathol 16:158-163, 1989.
28. Dorr RT, Dordal MS, Coinage LM, Taylor CW and McCloskey TM. High levels of doxorubicin in the tissues of a patient experiencing extravasation during a 4-day infusion. Cancer 64:2462-2464, 1989.
29. Dreizen S, McCredie KB, Bodey GP and Keating MJ. Necrotizing dermatitis in patients receiving cancer chemotherapy. Postgrad Med 81:263-271, 1987.
30. Kerr IG, DeAngelis C, Assad DM and Hanna SS. Drug extravasation along the route of a peritoneal catheter during intraperitoneal chemotherapy. Cancer 60:1731-1733, 1987.
31. Keeney SE and Richardson CJ. Extravascular extravasation of fluid as a complication of central venous lines in the neonate. J Perinatol 15(4):284-288, 1995.
32. Woodman C, Nicolson M, Hare L, So J, Hey R, McIllmurray M and Crowter D. Towards quality control in cancer chemotherapy. Br J Cancer 73(1):117-118, 1996.
33. Mayo DJ and Pearson DC. Chemotherapy extravasation: A consequence of fibrin sheath formation around venous access devises. Oncol Nurs Forum 22(4):675-680, 1995.
34. Davis ME, DeSantis D and Klemm K. A flow sheet for follow up after chemotherapy extravasation. Oncol Nurs Forum 22(6):979-983, 1995.
35. Shapiro B, Pillay M and Cox P H. Dosimetric consequences of interstitial extravasation

following i.v. administration of a radiopharmaceutical. Eur J Nucl Med 12:522-523, 1987.
36. ICRP Publication 60. Recommendations of the International Commission on Radiological Protection, Pergamon Press, Oxford, 1990.
37. ICRP Publication 59. The Biological Basis for Dose Limitation in the Skin, Pergamon Press, Oxford, 1991.
38. Hoop B. The infiltrated radiopharmaceutical injection: Risk considerations. J Nucl Med 32:890-891, 1991.

QUESTIONS

Wright: Have you any evidence of draining of activity via the lymph?

Grafstrom: You would expect it, but we have not seen any evidence for it.

Kopp: You showed some dose limits. Can you comment on from where they were derived? Do they hold true for that type of radiation?

Grafstrom: The dose limits used are from ICRP 60 (1990). For more details ICRP 60 refers to ICRP 59 (1991).

COMPARATIVE ANALYSIS OF DOSIMETRY PARAMETERS FOR NUCLEAR MEDICINE

R. E. Toohey and M. G. Stabin
Oak Ridge Institute for Science and Education, P.O. Box 117, Oak Ridge, TN 37831

ABSTRACT

For years many have employed the concept of "total-body dose" or "whole-body dose," i.e., the total energy deposited in the body divided by the mass of the body, when evaluating the risks of different nuclear medicine procedures. The effective dose equivalent (H_E), first described in ICRP Publication 26, has been accepted by some as a better quantity to use in evaluating the total risk of a procedure, but its use has been criticized by others primarily because the tissue weighting factors were intended for use in the radiation worker, rather than the nuclear medicine patient population. Nevertheless, in ICRP Publication 52, the ICRP has suggested that the H_E may be used in nuclear medicine. The ICRP also has published a compendium of dose estimates, including H_E values, for various nuclear medicine procedures at various ages in ICRP Publication 53. The effective dose (E) of ICRP Publication 60 is perhaps more suitable for use in nuclear medicine, with tissue weighting factors based on the entire population. Other comparisons of H_E and E have been published. We have used the program MIRDOSE 3.1 to compute total-body dose, H_E, and E for 62 radiopharmaceutical procedures, based on the best current biokinetic data available. As found by other investigators, the average ratio of E to H_E is about 0.9, with a relatively narrow range from 0.48 to 1.77. The ratio of E to total-body dose, however, ranges from 1.1 to almost 100. In children, the ratio of E to H_E was 0.92, with a standard deviation of 0.32. The ratio of E to total-body dose varied from 1.0 to 166. All ratios greater than 10 occur for the iodines; the values for most Tc-99m agents are greater than 2.0. In view of the nonuniform distributions of most radiopharmaceuticals, we believe the total-body dose is not a useful concept, and should be replaced by the effective dose. In those countries that have not as yet adopted the ICRP 60 methodology, the effective dose equivalent should be used in the interim.

INTRODUCTION

For years many physicians and physicists have employed the concept of "total-body dose" or "whole-body dose," i.e., the total energy deposited in the body divided by the total mass of the body, in evaluating the risks of different nuclear medicine procedures. Although this concept has been considered useful for comparing doses received from different procedures, it does not take into account the typical nonuniformity in dose distribution among the several body organs. The effective dose equivalent (H_E), first described in ICRP Publication 26 (1), has been accepted by some as a better quantity to use in evaluating the total risk of a procedure, but its use has been criticized by

others primarily because the tissue weighting factors were intended for use with the population of radiation workers, rather than of nuclear medicine patients (2). Nevertheless, the ICRP has suggested in Publication 52 (3) that the H_E may be used in nuclear medicine, and provided in Publication 53 (4) a compendium of dose estimates, including H_E values, for various nuclear medicine procedures undergone at various ages. The effective dose (E) of ICRP Publication 60 (5) is perhaps more suitable for use in nuclear medicine, with tissue weighting factors based on the entire population.

Comparisons of H_E and E for adults have previously been published (6). The pediatric phantom series of Cristy and Eckerman (7) and the adult female phantom, published in conjunction with the pregnant woman phantom series (8), permits extension of this previous study to other populations. In this work, we will compare total-body dose to both H_E and E for adults (men and women) and children of various ages, using available biokinetic models for a large number of radiopharmaceutical procedures.

METHODS

We have used the program MIRDOSE 3.1 (9) to compute total-body dose, H_E and E for 62 radiopharmaceutical procedures, involving 19 different radionuclides, based on the best current biokinetic data available. The MIRDOSE software permits the use of organ residence times (10) with phantoms representing the adult male, adult female, and children of various ages, from newborn through 15-year-old. The biokinetic models have been taken from a number of different sources. Many are described in a recent compendium of internal dose estimates for radiopharmaceuticals (11), however, many others are based on internal data at the Radiation Internal Dose Information Center (RIDIC) in Oak Ridge. A full description of the assumptions in these models is outside of the scope of this article. None of the biokinetic models are specific to a particular gender or age group, as no such data, in complete form, are currently available. The best biokinetic model for an agent was used to obtain residence times that were applied to all of the phantoms. After calculation of the total-body dose, H_E and E, ratios of these quantities were also calculated.

RESULTS

The computed values of total-body dose, H_E and E are listed in Table 1, for both the adult female and adult male phantoms. Ratios of total-body dose to H_E and E are shown in Table 2. Total-body dose, H_E and E and ratios of these quantities for children are listed in Table 3. Some of the ratios given in tables 2 and 3 are plotted in Figures 1-9. In addition, a comparison of many of the values of H_E calculated by MIRDOSE were compared to the same values reported in ICRP 53, for the different pediatric age groups and the adult male; this comparison is summarized in Table 4.

Abbreviations used in Tables 1-3:

Alb Mcrsph - albumin microspheres
Bladder Inf - infusion into urinary bladder
Brthld - breathhold
Dis - Diseased subjects
DISIDA - disofenin (iminodiacetic acid derivative)
DMSA - dimercaptosuccinic acid
DTPA - diethylentriaminpentaacetic acid
ECD - ethylene cystate dimer
FDG - fluorodeoxyglucose
Flsh - flushing dose administered
HDP - hydroxymethylene diphosphonate
Heat - heat treated
HEDP - hydroxyethylidene diphosphonate
HMPAO - hexamethylpropyleneamineoxine
HSA - human serum albumin
Hippuran - iodohippurate sodium
i.v. - intravenous
IMP - iodoamphetamine
MAA - macroaggregated albumin
MAG3 - mercaptoacetylglycylglycylglycine
MDP - methylene diphosphonate
mIBG - metaiodobenzylguanidine
MIBI - methoxyisobutyl isonitrile
Na2PO4 - sodium phosphate
NaF - sodium fluoride
NaI - sodium iodide
NH3 - ammonia
Nor - normal subjects
Nrml - Normal subjects
PA - percutaneous anemia subjects
PYP - pyrophosphate
RBC - red blood cells
Rebreath - rebreathing
Rt Hrt - right heart study
Slfr Cld - sulfur colloid
WBC- white blood cells

Table 1
Computed Values of Total-body Dose, H_E and E for Adult Females and Males
(Total-body Doses are given as mGy/MBq, H_E and E are mSv/MBq)

	FEMALES			MALES		
Pharmaceutical	Total-Body	H_E	E	Total-Body	H_E	E
Au-198 colloid	4.58E-01	1.72E+00	1.16E+00	3.59E-01	1.38E+00	9.14E-01
C-11 Tryptophane	3.60E-04	5.92E-04	5.03E-04	2.87E-03	5.16E-03	4.32E-03
C-11 Iomazenil	2.79E-03	1.54E-02	1.39E-02	2.20E-03	1.19E-02	1.06E-02
Co-57 B-12, Nor/flsh	1.91E+00	3.73E+00	2.90E+00	1.53E+00	2.94E+00	2.25E+00
Co-57 B-12, PA/flsh	2.68E-01	6.18E-01	5.99E-01	2.15E-01	5.00E-01	4.90E-01
Co-58 B-12, Nor/flsh	3.66E+00	7.08E+00	5.45E+00	2.96E+00	5.70E+00	4.35E+00
Co-58 B-12, PA/flsh	6.08E-01	1.61E+00	1.59E+00	4.93E-01	1.30E+00	1.30E+00
Co-60 B-12, Nor/flsh	5.61E+01	1.08E+02	8.01E+01	4.56E+01	8.67E+01	6.39E+01
Co-60 B-12, PA/flsh	7.49E+00	1.48E+01	1.24E+01	6.08E+00	1.19E+01	1.00E+01
F-18 FDG	1.51E-02	3.81E-02	3.10E-02	1.20E-02	2.98E-02	2.41E-02
F-18 NaF	1.10E-02	3.56E-02	3.10E-02	8.75E-03	2.70E-02	2.31E-02
Ga-67 Citrate	8.23E-02	1.23E-01	1.20E-01	6.62E-02	1.03E-01	1.00E-01
Hg-197 Chlormerodrin	3.84E-02	2.05E-01	1.13E-01	3.00E-02	1.81E-01	9.66E-02
I-123 Hippuran	3.52E-03	3.39E-02	2.90E-02	2.70E-03	2.38E-02	2.01E-02
I-123 IMP	1.43E-02	2.44E-02	2.34E-02	1.15E-02	1.91E-02	1.82E-02
I-123 mIBG	1.14E-02	2.56E-02	2.21E-02	9.12E-03	1.93E-02	1.66E-02
I-123 NaI	9.72E-03	1.47E-01	2.43E-01	8.03E-03	1.20E-01	2.00E-01
I-125 HSA	2.61E-01	3.89E-01	2.91E-01	2.07E-01	3.07E-01	2.29E-01
I-125 mIBG	2.93E-02	6.71E-02	4.86E-02	2.28E-02	5.08E-02	3.63E-02
I-125 NaI	1.61E-01	7.62E+00	1.35E+01	1.32E-01	6.37E+00	1.13E+01
I-131 Hippuran	9.71E-03	1.35E-01	1.17E-01	7.27E-03	1.00E-01	8.58E-02

Table 1 (continued)
Computed Values of Total-body Dose, H_E and E for Adult Females and Males
(Total-body doses are given as mGy/MBq, H_E and E are mSv/MBq)

	FEMALES			MALES		
Pharmaceutical	Total-Body	H_E	E	Total-Body	H_E	E
I-131 HSA	5.89E-01	1.30E+00	9.35E-01	4.68E-01	1.07E+00	7.43E-01
I-131 MAA	1.80E-01	6.35E-01	6.06E-01	1.41E-01	4.96E-01	4.72E-01
I-131 mIBG	1.03E-01	2.51E-01	1.95E-01	8.12E-02	1.95E-01	1.49E-01
I-131 NaI	2.32E-01	1.27E+01	2.24E+01	1.92E-01	1.04E+01	1.84E+01
I-131 Rose Bengal	1.02E-01	1.02E+00	1.33E+00	8.13E-02	9.02E-01	1.21E+00
In-111 DTPA	1.11E-02	5.75E-02	5.02E-02	8.75E-03	4.10E-02	3.56E-02
In-111 Platelets	1.92E-01	6.18E-01	3.95E-01	1.55E-01	5.13E-01	3.26E-01
In-111 RBC	1.80E-01	2.47E-01	2.24E-01	1.48E-01	2.04E-01	1.85E-01
In-111 WBC	2.04E-01	7.62E-01	4.88E-01	1.63E-01	6.38E-01	4.09E-01
In-111 Pentetreotide	3.77E-02	1.46E-01	1.03E-01	3.02E-02	1.18E-01	8.14E-02
Kr-81m	5.72E-06	3.35E-05	3.39E-05	4.42E-06	2.65E-05	2.65E-05
N-13 NH_3	1.99E-03	2.81E-03	2.56E-03	1.58E-03	2.22E-03	2.01E-03
P-32 Na_2PO_4	1.96E+00	2.40E+00	2.29E+00	1.51E+00	1.93E+00	1.80E+00
Tc-99m Alb Mcrsph	5.43E-03	1.78E-02	1.77E-02	4.30E-03	1.45E-02	1.45E-02
Tc-99m DISIDA	4.93E-03	3.00E-02	2.15E-02	3.99E-03	2.51E-02	1.78E-02
Tc-99m DMSA	4.76E-03	1.85E-02	1.07E-02	3.81E-03	1.62E-02	9.12E-03
Tc-99m DTPA - iv	2.85E-03	1.11E-02	9.66E-03	2.29E-03	8.19E-03	7.09E-03
Tc-99m DTPA Aerosol	2.20E-03	7.90E-03	7.50E-03	1.75E-03	6.06E-03	5.76E-03
Tc-99m glucoheptonate	3.36E-03	1.35E-02	1.00E-02	2.69E-03	1.04E-02	7.42E-03
Tc-99m HDP	4.20E-03	7.45E-03	6.07E-03	3.40E-03	6.12E-03	4.80E-03
Tc-99m HEDP	2.95E-03	7.86E-03	6.55E-03	2.37E-03	6.10E-03	4.96E-03
Tc-99m HMPAO	4.69E-03	1.68E-02	1.29E-02	3.78E-03	1.38E-02	1.09E-02
Tc-99m HSA	5.30E-03	9.59E-03	7.54E-03	4.28E-03	7.85E-03	6.21E-03
Tc-99m MAA	5.22E-03	1.62E-02	1.54E-02	4.12E-03	1.27E-02	1.20E-02
Tc-99m MAG3	2.04E-03	1.64E-02	1.40E-02	1.60E-03	1.18E-02	9.99E-03
Tc-99m MDP	3.27E-03	7.64E-03	6.19E-03	2.64E-03	6.08E-03	4.75E-03
Tc-99m MIBI/stress	4.65E-03	1.55E-02	1.31E-02	3.77E-03	1.27E-02	1.07E-02
Tc-99m MIBI/rest	5.26E-03	1.83E-02	1.63E-02	4.26E-03	1.49E-02	1.33E-02
Tc-99m Pertechnetate	3.94E-03	1.32E-02	1.40E-02	3.18E-03	1.06E-02	1.14E-02
Tc-99m PYP	4.12E-03	7.46E-03	6.31E-03	3.34E-03	6.03E-03	4.95E-03
Tc-99m RBC/in vitro	4.65E-03	9.19E-03	7.83E-03	3.75E-03	7.28E-03	6.11E-03
Tc-99m RBC/in vivo	4.95E-03	8.95E-03	7.59E-03	3.99E-03	7.17E-03	5.99E-03
Tc-99m RBC/heat	6.25E-03	5.55E-02	2.66E-02	4.94E-03	4.64E-02	2.24E-02
Tc-99m Slfr Cld/Nrml	6.24E-03	1.69E-02	1.03E-02	4.99E-03	1.36E-02	8.04E-03
Tc-99m Slfr Cld/Dis	6.11E-03	2.60E-02	1.59E-02	4.88E-03	2.16E-02	1.32E-02
Tc-99m Slfr Cld/Oral	5.28E-03	3.00E-02	2.88E-02	4.72E-03	2.77E-02	2.68E-02
Tc-99m Teboroxime	4.75E-03	1.49E-02	1.23E-02	3.86E-03	1.24E-02	1.00E-02
Tc-99m WBC	6.08E-03	2.39E-02	1.54E-02	4.87E-03	2.00E-02	1.29E-02
Tl-201 Chloride	6.79E-02	1.87E-01	1.65E-01	5.46E-02	3.16E-01	2.74E-01
Xe-127, 10 min brthld	2.22E-04	2.92E-04	2.92E-04	1.80E-04	2.36E-04	2.36E-04
Xe-133, 10 min brthld	2.59E-04	3.79E-04	3.86E-04	2.02E-04	2.98E-04	3.04E-04

Table 2
Ratios of H_E and E to Total-body Dose for Adult Females and Males

	FEMALES			MALES		
Pharmaceutical	H_E/TB	E/TB	E/H_E	H_E/TB	E/TB	E/H_E
Au-198 colloid	3.76	2.53	0.67	3.84	2.55	0.66
C-11 Tryptophane	1.6	1.40	0.85	1.80	1.51	0.84
C-11 Iomazenil	5.52	4.98	0.90	5.41	4.82	0.89
Co-57 B-12, Nor/flsh	1.95	1.52	0.78	1.92	1.47	0.77
Co-57 B-12, PA/flsh	2.31	2.24	0.97	2.33	2.28	0.98
Co-58 B-12, Nor/flsh	1.93	1.49	0.77	1.93	1.47	0.76
Co-58 B-12, PA/flsh	2.65	2.62	0.99	2.64	2.64	1.00
Co-60 B-12, Nor/flsh	1.93	1.43	0.74	1.90	1.40	0.74
Co-60 B-12, PA/flsh	1.98	1.66	0.84	1.96	1.64	0.84
F-18 FDG	2.52	2.05	0.81	2.48	2.01	0.81
F-18 NaF	3.24	2.82	0.87	3.09	2.64	0.86
Ga-67 Citrate	1.49	1.46	0.98	1.56	1.51	0.97
Hg-197 Chlormerodrin	5.34	2.94	0.55	6.03	3.22	0.53
I-123 Hippuran	9.63	8.24	0.86	8.81	7.44	0.84
I-123 IMP	1.71	1.64	0.96	1.66	1.58	0.95
I-123 mIBG	2.25	1.94	0.86	2.12	1.82	0.86
I-123 NaI	15.12	25.00	1.65	14.94	24.91	1.67
I-125 HSA	1.49	1.11	0.75	1.48	1.11	0.75
I-125 mIBG	2.29	1.66	0.72	2.23	1.59	0.71
I-125 NaI	47.33	83.85	1.77	48.26	85.61	1.77
I-131 Hippuran	13.90	12.05	0.87	13.76	11.80	0.86
I-131 HSA	2.21	1.59	0.72	2.29	1.59	0.69
I-131 MAA	3.53	3.37	0.95	3.52	3.35	0.95
I-131 mIBG	2.44	1.89	0.78	2.40	1.83	0.76
I-131 NaI	54.74	96.55	1.76	54.17	95.83	1.77
I-131 Rose Bengal	10.00	13.04	1.30	11.09	14.88	1.34
In-111 DTPA	5.18	4.52	0.87	4.69	4.07	0.87
In-111 Platelets	3.22	2.06	0.64	3.31	2.10	0.64
In-111 RBC	1.37	1.24	0.91	1.38	1.25	0.91
In-111 WBC	3.74	2.39	0.64	3.91	2.51	0.64
In-111 Pentetreotide	3.87	2.73	0.71	3.91	2.70	0.69
Kr-81m	5.86	5.93	1.01	6.00	6.00	1.00
N-13 NH_3	1.41	1.29	0.91	1.41	1.27	0.91
P-32 Na_2PO_4	1.22	1.17	0.95	1.28	1.19	0.93
Tc-99m Alb Mcrsphr	3.28	3.26	0.99	3.37	3.37	1.00
Tc-99m DISIDA	6.09	4.36	0.72	6.29	4.46	0.71
Tc-99m DMSA	3.89	2.25	0.58	4.25	2.39	0.56
Tc-99m DTPA - iv	3.89	3.39	0.87	3.58	3.10	0.87
Tc-99m DTPA Aerosol	3.59	3.41	0.95	3.46	3.29	0.95
Tc-99m glucoheptonate	4.02	2.98	0.74	3.87	2.76	0.71
Tc-99m HDP	1.77	1.45	0.81	1.80	1.41	0.78
Tc-99m HEDP	2.66	2.22	0.83	2.57	2.09	0.81
Tc-99m HMPAO	3.58	2.75	0.77	3.65	2.88	0.79
Tc-99m HSA	1.81	1.42	0.79	1.83	1.45	0.79
Tc-99m MAA	3.10	2.95	0.95	3.08	2.91	0.94

Table 2 (continued)
Ratios of H_E and E to Total-body Dose for Adult Females and Males

	FEMALES			MALES		
Pharmaceutical	H_E/TB	E/TB	E/H_E	H_E/TB	E/TB	E/H_E
Tc-99m MAG3	8.04	6.86	0.85	7.38	6.24	0.85
Tc-99m MDP	2.34	1.89	0.81	2.30	1.80	0.78
Tc-99m MIBI/stress	3.33	2.82	0.85	3.37	2.84	0.84
Tc-99m MIBI/rest	3.48	3.10	0.89	3.50	3.12	0.89
Tc-99m Pertechnetate	3.35	3.55	1.06	3.33	3.58	1.08
Tc-99m PYP	1.81	1.53	0.85	1.81	1.48	0.82
Tc-99m RBC/in vitro	1.98	1.68	0.85	1.94	1.63	0.84
Tc-99m RBC/in vivo	1.81	1.53	0.85	1.80	1.50	0.84
Tc-99m RBC/heat	8.88	4.26	0.48	9.39	4.53	0.48
Tc-99m Slfr Cld/Nrml	2.71	1.65	0.61	2.73	1.61	0.59
Tc-99m Slfr Cld/Dis	4.26	2.60	0.61	4.43	2.70	0.61
Tc-99m Slfr Cld/Oral	5.68	5.45	0.96	5.87	5.68	0.97
Tc-99m Teboroxime	3.14	2.59	0.83	3.21	2.59	0.81
Tc-99m WBC	3.93	2.53	0.64	4.11	2.65	0.65
Tl-201 Chloride	2.75	2.43	0.88	5.79	5.02	0.87
Xe-127, 10 min brthld	1.32	1.32	1.00	1.31	1.31	1.00
Xe-133, 10 min brthld	1.46	1.49	1.02	1.48	1.50	1.02
AVERAGE:	5.27	6.13	0.88	5.34	6.19	0.87

Table 3
Computed Values of Total-body Dose, H_E and E, and Ratios for Children
(Total-body doses are given as mGy/MBq, H_E and E are mSv/MBq)

Age (y)	TB	H_E	E	H_E/TB	E/TB	E/H_E
Ga-67 citrate						
0	0.885	1.28	1.16	1.446	1.311	0.906
1	0.372	0.538	0.487	1.446	1.309	0.905
5	0.203	0.32	0.304	1.576	1.498	0.950
10	0.129	0.205	0.197	1.589	1.527	0.961
15	0.0822	0.13	0.124	1.582	1.509	0.954
Kr-81m gas						
0	6.84E-05	4.64E-04	4.83E-04	6.784	7.061	1.041
1	2.77E-05	1.70E-04	1.76E-04	6.137	6.354	1.035
5	1.43E-05	8.71E-05	8.90E-05	6.091	6.224	1.022
10	8.99E-06	5.66E-05	5.75E-05	6.296	6.396	1.016
15	5.74E-06	3.96E-05	4.04E-05	6.899	7.038	1.020
I-123 mIBG						
0	0.114	0.173	0.147	1.518	1.289	0.850
1	0.0485	0.0771	0.0654	1.590	1.348	0.848
5	0.0266	0.0456	0.039	1.714	1.466	0.855
10	0.0171	0.0302	0.0257	1.766	1.503	0.851
15	0.0114	0.0248	0.0213	2.175	1.868	0.859

Table 3 (continued)
Computed Values of Total-body Dose, H_E and E, and Ratios for Children
(Total-body doses are given as mGy/MBq, H_E and E are mSv/MBq)

Age (y)	TB	H_E	E	H_E/TB	E/TB	E/H_E
I-125 mIBG						
0	0.396	0.679	0.492	1.715	1.242	0.725
1	0.156	0.286	0.209	1.833	1.340	0.731
5	0.0787	0.153	0.112	1.944	1.423	0.732
10	0.0485	0.0971	0.0679	2.002	1.400	0.699
15	0.0295	0.0684	0.0485	2.319	1.644	0.709
I-131 mIBG						
0	1.27	2.44	1.84	1.921	1.449	0.754
1	0.51	1.04	0.707	2.039	1.386	0.680
5	0.266	0.588	0.399	2.211	1.500	0.679
10	0.166	0.379	0.254	2.283	1.530	0.670
15	0.106	0.282	0.197	2.660	1.858	0.699
I-123 NaI						
0	0.101	1.59	2.71	15.743	26.832	1.704
1	0.0433	1.11	1.91	25.635	44.111	1.721
5	0.0239	0.593	1.02	24.812	42.678	1.720
10	0.0149	0.278	0.473	18.658	31.745	1.701
15	0.0101	0.188	0.317	18.614	31.386	1.686
I-125 NaI						
0	2.44	86.7	153	35.533	62.705	1.765
1	0.953	63.1	111	66.212	116.474	1.759
5	0.488	33.7	59.6	69.057	122.131	1.769
10	0.291	15.5	27.3	53.265	93.814	1.761
15	0.174	10.2	18	58.621	103.448	1.765
I-131 NaI						
0	3.05	161	283	52.787	92.787	1.758
1	1.24	116	206	93.548	166.129	1.776
5	0.646	60.5	107	93.653	165.635	1.769
10	0.394	26.7	47.1	67.766	119.543	1.764
15	0.245	17.2	30.4	70.204	124.082	1.767
I-123 Hippuran						
0	0.00894	0.064	0.0513	7.159	5.738	0.802
1	0.00381	0.0274	0.0219	7.192	5.748	0.799
5	0.00355	0.0296	0.0245	8.338	6.901	0.828
10	0.00228	0.0195	0.0163	8.553	7.149	0.836
15	0.00343	0.0302	0.0256	8.805	7.464	0.848
I-131 Hippuran						
0	0.0259	0.295	0.236	11.390	9.112	0.800
1	0.00983	0.116	0.0934	11.801	9.502	0.805
5	0.00849	0.124	0.104	14.605	12.250	0.839
10	0.00548	0.0801	0.0669	14.617	12.208	0.835
15	0.00952	0.129	0.111	13.550	11.660	0.860

Table 3 (continued)
Computed Values of Total-body Dose, H_E and E, and Ratios for Children
(Total-body doses are given as mGy/MBq, H_E and E are mSv/MBq)

Age (y)	TB	H_E	E	H_E/TB	E/TB	E/H_E
In-111 Platelets						
0	1.82	6.47	3.96	3.555	2.176	0.612
1	0.808	2.71	1.68	3.354	2.079	0.620
5	0.448	1.56	0.962	3.482	2.147	0.617
10	0.293	1.02	0.637	3.481	2.174	0.625
15	0.19	0.687	0.426	3.616	2.242	0.620
In-111 RBC						
0	1.76	2.39	2.11	1.358	1.199	0.883
1	0.776	1.05	0.938	1.353	1.209	0.893
5	0.431	0.591	0.527	1.371	1.223	0.892
10	0.275	0.388	0.349	1.411	1.269	0.899
15	0.18	0.26	0.232	1.444	1.289	0.892
In-111 WBC						
0	1.82	8.52	5.57	4.681	3.060	0.654
1	0.819	3.38	2.17	4.127	2.650	0.642
5	0.459	1.91	1.19	4.161	2.593	0.623
10	0.308	1.24	0.773	4.026	2.510	0.623
15	0.202	0.836	0.522	4.139	2.584	0.624
Kr-81m iv						
0	3.33E-05	5.73E-04	1.16E-03	17.207	34.835	2.024
1	1.44E-05	1.79E-04	3.55E-04	12.431	24.653	1.983
5	7.98E-06	9.04E-05	1.76E-04	11.328	22.055	1.947
10	5.17E-06	5.36E-05	1.02E-04	10.368	19.729	1.903
15	3.32E-06	3.70E-05	7.09E-05	11.145	21.355	1.916
Kr-81m Rt Hrt						
0	4.14E-05	2.51E-04	1.24E-04	6.063	2.995	0.494
1	1.74E-05	1.14E-04	4.80E-05	6.552	2.759	0.421
5	9.19E-06	6.27E-05	2.51E-05	6.823	2.731	0.400
10	5.97E-06	4.04E-05	1.63E-05	6.767	2.730	0.403
15	3.92E-06	2.74E-05	1.17E-05	6.990	2.985	0.427
Tc-99m Alb-Mcrsph.						
0	0.0495	0.198	0.205	4.000	4.141	1.035
1	0.0223	0.0799	0.083	3.583	3.722	1.039
5	0.0124	0.0433	0.0445	3.492	3.589	1.028
10	0.00805	0.0282	0.0284	3.503	3.528	1.007
15	0.00543	0.0197	0.0198	3.628	3.646	1.005

Table 3 (continued)
Computed Values of Total-body Dose, H_E and E, and Ratios for Children
(Total-body doses are given as mGy/MBq, H_E and E are mSv/MBq)

Tc-99m Bladder Inf						
0	9.56E-04	9.51E-03	8.18E-03	9.948	8.556	0.860
1	4.48E-04	4.22E-03	3.59E-03	9.420	8.013	0.851
5	2.68E-04	2.36E-03	2.00E-03	8.806	7.463	0.847
10	1.79E-04	1.60E-03	1.36E-03	8.939	7.598	0.850
15	1.35E-04	1.09E-03	9.27E-04	8.074	6.867	0.850
Age (y)	TB	H_E	E	H_E/TB	E/TB	E/H_E
Tc-99m DISIDA						
0	0.0398	0.347	0.217	8.719	5.452	0.625
1	0.0188	0.157	0.0953	8.351	5.069	0.607
5	0.011	0.072	0.0537	6.545	4.882	0.746
10	0.00723	0.0453	0.0346	6.266	4.786	0.764
15	0.00497	0.031	0.0228	6.237	4.588	0.735
Tc-99m DMSA						
0	0.043	0.159	0.0861	3.698	2.002	0.542
1	0.0193	0.0671	0.037	3.477	1.917	0.551
5	0.0109	0.039	0.0221	3.578	2.028	0.567
10	0.00692	0.0269	0.0151	3.887	2.182	0.561
15	0.00472	0.0197	0.0112	4.174	2.373	0.569
Tc-99m DTPA						
0	0.019	0.0335	0.03	1.763	1.579	0.896
1	0.00843	0.015	0.0136	1.779	1.613	0.907
5	0.00515	0.012	0.0107	2.330	2.078	0.892
10	0.00331	0.0081	0.00723	2.447	2.184	0.893
15	0.00282	0.0103	0.00895	3.652	3.174	0.869
Tc-99m DTPA Aerosol						
0	0.0164	0.0492	0.0521	3.000	3.177	1.059
1	0.00741	0.0207	0.0217	2.794	2.928	1.048
5	0.00446	0.0133	0.0133	2.982	2.982	1.000
10	0.0029	0.00884	0.00873	3.048	3.010	0.988
15	0.00219	0.00797	0.00766	3.639	3.498	0.961
Tc-99m ECD						
0	0.0214	0.0799	0.056	3.734	2.617	0.701
1	0.00988	0.0371	0.026	3.755	2.632	0.701
5	0.00651	0.0228	0.0181	3.502	2.780	0.794
10	0.00425	0.0146	0.0117	3.435	2.753	0.801
15	0.0034	0.0141	0.0115	4.147	3.382	0.816

Table 3 (continued)
Computed Values of Total-body Dose, H_E and E, and Ratios for Children
(Total-body doses are given as mGy/MBq, H_E and E are mSv/MBq)

Age (y)	TB	H_E	E	H_E/TB	E/TB	E/H_E
Tc-99m HDP						
0	0.0388	0.0797	0.0693	2.054	1.786	0.870
1	0.0174	0.0338	0.0283	1.943	1.626	0.837
5	0.00971	0.0187	0.015	1.926	1.545	0.802
10	0.00628	0.0114	0.00924	1.815	1.471	0.811
15	0.00417	0.00728	0.00591	1.746	1.417	0.812
Tc-99m HEDP						
0	0.0265	0.0703	0.0596	2.653	2.249	0.848
1	0.0119	0.0307	0.0258	2.580	2.168	0.840
5	0.00671	0.0172	0.0142	2.563	2.116	0.826
10	0.00434	0.0112	0.00934	2.581	2.152	0.834
15	0.00292	0.0075	0.0062	2.568	2.123	0.827
Tc-99m HMPAO						
0	0.0372	0.16	0.108	4.301	2.903	0.675
1	0.0171	0.0755	0.0544	4.415	3.181	0.721
5	0.0104	0.0379	0.0318	3.644	3.058	0.839
10	0.00681	0.0234	0.019	3.436	2.790	0.812
15	0.00469	0.0175	0.0138	3.731	2.942	0.789
Tc-99m MAA						
0	0.0478	0.172	0.171	3.598	3.577	0.994
1	0.0215	0.0695	0.0681	3.233	3.167	0.980
5	0.0119	0.0378	0.0365	3.176	3.067	0.966
10	0.00778	0.0252	0.0242	3.239	3.111	0.960
15	0.00523	0.0177	0.017	3.384	3.250	0.960
Tc-99m MAG3						
0	0.00476	0.0323	0.0265	6.786	5.567	0.820
1	0.00219	0.0142	0.0117	6.484	5.342	0.824
5	0.0021	0.0151	0.0126	7.190	6.000	0.834
10	0.00138	0.0103	0.0086	7.464	6.232	0.835
15	0.002	0.0148	0.0126	7.400	6.300	0.851
Tc-99m MDP						
0	0.0296	0.0747	0.0631	2.524	2.132	0.845
1	0.0133	0.032	0.0263	2.406	1.977	0.822
5	0.00747	0.0178	0.0142	2.383	1.901	0.798
10	0.00484	0.0113	0.00904	2.335	1.868	0.800
15	0.00324	0.00735	0.0059	2.269	1.821	0.803
Tc-99m MIBI						
0	0.0382	0.138	0.139	3.613	3.639	1.007
1	0.018	0.0653	0.0654	3.628	3.633	1.002
5	0.012	0.0443	0.0418	3.692	3.483	0.944
10	0.00791	0.0291	0.0264	3.679	3.338	0.907
15	0.00527	0.0189	0.0169	3.586	3.207	0.894

Table 3 (continued)
Computed Values of Total-body Dose, H_E and E, and Ratios for Children
(Total-body doses are given as mGy/MBq, H_E and E are mSv/MBq)

Age (y)	TB	H_E	E	H_E/TB	E/TB	E/H_E
Tc-99m Pertechnetate						
0	0.0392	0.117	0.144	2.985	3.673	1.231
1	0.0176	0.0533	0.0619	3.028	3.517	1.161
5	0.0101	0.0307	0.0349	3.040	3.455	1.137
10	0.00654	0.0192	0.0224	2.936	3.425	1.167
15	0.00456	0.0144	0.0156	3.158	3.421	1.083
Tc-99m PYP						
0	0.0382	0.0749	0.066	1.961	1.728	0.881
1	0.0171	0.0324	0.0278	1.895	1.626	0.858
5	0.00955	0.0179	0.015	1.874	1.571	0.838
10	0.00616	0.0112	0.00948	1.818	1.539	0.846
15	0.00409	0.00728	0.00614	1.780	1.501	0.843
Tc-99m RBC Heat						
0	0.0567	0.653	0.304	11.517	5.362	0.466
1	0.0255	0.259	0.122	10.157	4.784	0.471
5	0.0143	0.147	0.0697	10.280	4.874	0.474
10	0.00932	0.0967	0.0459	10.376	4.925	0.475
15	0.00617	0.0643	0.0305	10.421	4.943	0.474
Tc-99m RBC in vitro						
0	0.0433	0.0833	0.0709	1.924	1.637	0.851
1	0.0193	0.0369	0.0314	1.912	1.627	0.851
5	0.0108	0.0206	0.0174	1.907	1.611	0.845
10	0.00697	0.0138	0.0118	1.980	1.693	0.855
15	0.00462	0.00949	0.008	2.054	1.732	0.843
Tc-99m RBC in vivo						
0	0.0464	0.0821	0.0698	1.769	1.504	0.850
1	0.0207	0.0364	0.031	1.758	1.498	0.852
5	0.0116	0.0204	0.0172	1.759	1.483	0.843
10	0.00745	0.0136	0.0116	1.826	1.557	0.853
15	0.00493	0.00936	0.00786	1.899	1.594	0.840
Tc-99m Slfr Cld normal						
0	0.0568	0.152	0.0925	2.676	1.629	0.609
1	0.0256	0.0683	0.0421	2.668	1.645	0.616
5	0.0143	0.0385	0.0233	2.692	1.629	0.605
10	0.00971	0.026	0.0157	2.678	1.617	0.604
15	0.00623	0.0175	0.0103	2.809	1.653	0.589
Tc-99m Slfr Cld Dis						
0	0.0547	0.308	0.189	5.631	3.455	0.614
1	0.0246	0.121	0.0738	4.919	3.000	0.610
5	0.0139	0.0671	0.04	4.827	2.878	0.596
10	0.00922	0.0435	0.0259	4.718	2.809	0.595
15	0.00607	0.029	0.0172	4.778	2.834	0.593

Table 3 (continued)
Computed Values of Total-body Dose, H_E and E, and Ratios for Children
(Total-body doses are given as mGy/MBq, H_E and E are mSv/MBq)

Age (y)	TB	H_E	E	H_E/TB	E/TB	E/H_E
Tc-99m Slfr Cld oral						
0	0.0223	0.197	0.225	8.834	10.090	1.142
1	0.0125	0.0981	0.118	7.848	9.440	1.203
5	0.0115	0.0773	0.0804	6.722	6.991	1.040
10	0.00802	0.0504	0.049	6.284	6.110	0.972
15	0.00533	0.0319	0.0313	5.985	5.872	0.981
Tc-99m WBC						
0	0.0536	0.296	0.198	5.522	3.694	0.669
1	0.0242	0.113	0.0741	4.669	3.062	0.656
5	0.0137	0.0616	0.0391	4.496	2.854	0.635
10	0.0091	0.0396	0.0248	4.352	2.725	0.626
15	0.00604	0.0263	0.0165	4.354	2.732	0.627
Tl-201 Chloride						
0	0.795	4.03	3.65	5.069	4.591	0.906
1	0.33	2.28	2.08	6.909	6.303	0.912
5	0.175	1.5	1.34	8.571	7.657	0.893
10	0.11	1.16	1.01	10.545	9.182	0.871
15	0.0684	0.293	0.264	4.284	3.860	0.901
Xe-133 Rt Hrt						
0	0.00236	0.0179	0.0177	7.585	7.500	0.989
1	8.98E-04	0.00661	0.00631	7.361	7.027	0.955
5	4.48E-04	3.32E-03	3.13E-03	7.411	6.987	0.943
10	2.71E-04	2.13E-03	2.01E-03	7.860	7.417	0.944
15	1.62E-04	1.46E-03	1.40E-03	9.012	8.642	0.959
Xe-133 brthld						
0	2.09E-03	3.57E-03	3.66E-03	1.708	1.751	1.025
1	7.90E-04	1.32E-03	1.35E-03	1.671	1.709	1.023
5	3.94E-04	6.55E-04	6.71E-04	1.662	1.703	1.024
10	2.38E-04	4.09E-04	4.19E-04	1.718	1.761	1.024
15	1.41E-04	2.65E-04	2.73E-04	1.879	1.936	1.030
Xe-133 5 min rebreathing						
0	1.31E-02	1.41E-02	1.41E-02	1.076	1.076	1.000
1	4.97E-03	5.31E-03	5.33E-03	1.068	1.072	1.004
5	2.48E-03	2.65E-03	2.65E-03	1.069	1.069	1.000
10	1.49E-03	1.61E-03	1.62E-03	1.081	1.087	1.006
15	8.86E-04	9.88E-04	8.86E-04	1.115	1.000	0.897
Xe-133 10 min rebreathing						
0	0.0215	0.0217	0.0217	1.009	1.009	1.000
1	0.00816	0.00823	0.00822	1.009	1.007	0.999
5	0.00407	0.0041	0.00409	1.007	1.005	0.998
10	0.00245	0.00249	0.00249	1.016	1.016	1.000
15	0.00145	0.00151	0.00151	1.041	1.041	1.000

Table 3 (continued)
Computed Values of Total-body Dose, H_E and E, and Ratios for Children
(Total-body doses are given as mGy/MBq, H_E and E are mSv/MBq)

Age (y)	TB	H_E	E	H_ETB	E/TB	E/H_E
Xe-127 brthld						
0	1.28E-03	1.76E-03	1.77E-03	1.375	1.383	1.006
1	5.55E-04	7.58E-04	7.54E-04	1.366	1.359	0.995
5	3.02E-04	4.13E-04	4.12E-04	1.368	1.364	0.998
10	1.93E-04	2.71E-04	2.70E-04	1.404	1.399	0.996
15	1.25E-04	1.84E-04	1.83E-04	1.472	1.464	0.995
Xe-127 5 min rebreathing						
0	8.22E-03	8.99E-03	8.98E-03	1.094	1.092	0.999
1	3.56E-03	3.97E-03	3.95E-03	1.115	1.110	0.995
5	1.94E-03	2.18E-03	2.18E-03	1.124	1.124	1.000
10	1.24E-03	1.42E-03	1.42E-03	1.145	1.145	1.000
15	7.99E-04	9.47E-04	9.45E-04	1.185	1.183	0.998
Xe-127 10 min rebreathing						
0	0.0132	0.0141	0.014	1.068	1.061	0.993
1	5.71E-03	6.23E-03	6.20E-03	1.091	1.086	0.995
5	3.12E-03	3.43E-03	3.42E-03	1.099	1.096	0.997
10	1.99E-03	2.23E-03	2.23E-03	1.121	1.121	1.000
15	1.28E-03	1.49E-03	1.48E-03	1.164	1.156	0.993

Table 4
Ratios of MIRDOSE 3.1 to ICRP 53 Values of H_E

Phantom	MIRDOSE/ICRP
1-year-old	0.89 +/- 0.27
5-year-old	0.92 +/- 0.18
10-year-old	0.92 +/- 0.16
15-year-old	1.01 +/- 0.20
Adult	1.00 +/- 0.20
Mean	0.95 +/- 0.05

DISCUSSION

As reported by Johansson et al. (6), the average ratio of E to H_E for adults is about 0.8, with a relatively narrow spread from 0.48 to 1.77. The ratio of E to total-body dose in adults, however, ranges from 1.1 to almost 100. All ratios greater than 10 occur for the iodines; the values for Tc-99m agents fall between 1.4 and 6.9; it is of interest to note that Tc-99m and the iodines are the most widely used radiopharmaceuticals. In children, the ratio of E to H_E was 0.92, with a standard deviation of 0.32. The ratio of E to total-body dose varied from 1.0 to 166. Again, the largest ratios were observed in the iodine-labeled compounds.

Thus, a very different view of risk will be obtained by using the total-body dose versus either the value of E or H_E for a procedure. In view of the nonuniform distributions of most

radiopharmaceuticals, we believe the total-body dose is not a useful concept, and should be replaced by the effective dose. In those countries that have not as yet adopted the ICRP 60 (5) methodology, the effective dose equivalent should be used in the interim.

It is essential, however, to recognize the limitations on the use of these quantities. First, it is important to always study the actual organ doses. The calculation of E and H_E, involving multiplying individual organ doses by risk weighting factors and adding up individual contributions into a single value, necessarily causes a loss of information about the doses to different organs. It is important to remember also that the E and H_E are theoretical quantities; no organ or system, including the total body, actually received the value calculated. A second limitation on the use of the E or H_E is that it must never be used in situations involving radiation therapy. The risk weighting factors relate only to the induction of cancer or hereditary disease, and do not give any information about organ radiosensitivity to deterministic effects. Thirdly, it should be remembered that the E and H_E should always be applied to *populations*, never individuals. They have some usefulness in studying differences between procedures when used in large populations, or in estimating risks, but should not be used to calculate risks to individuals from specific procedures.

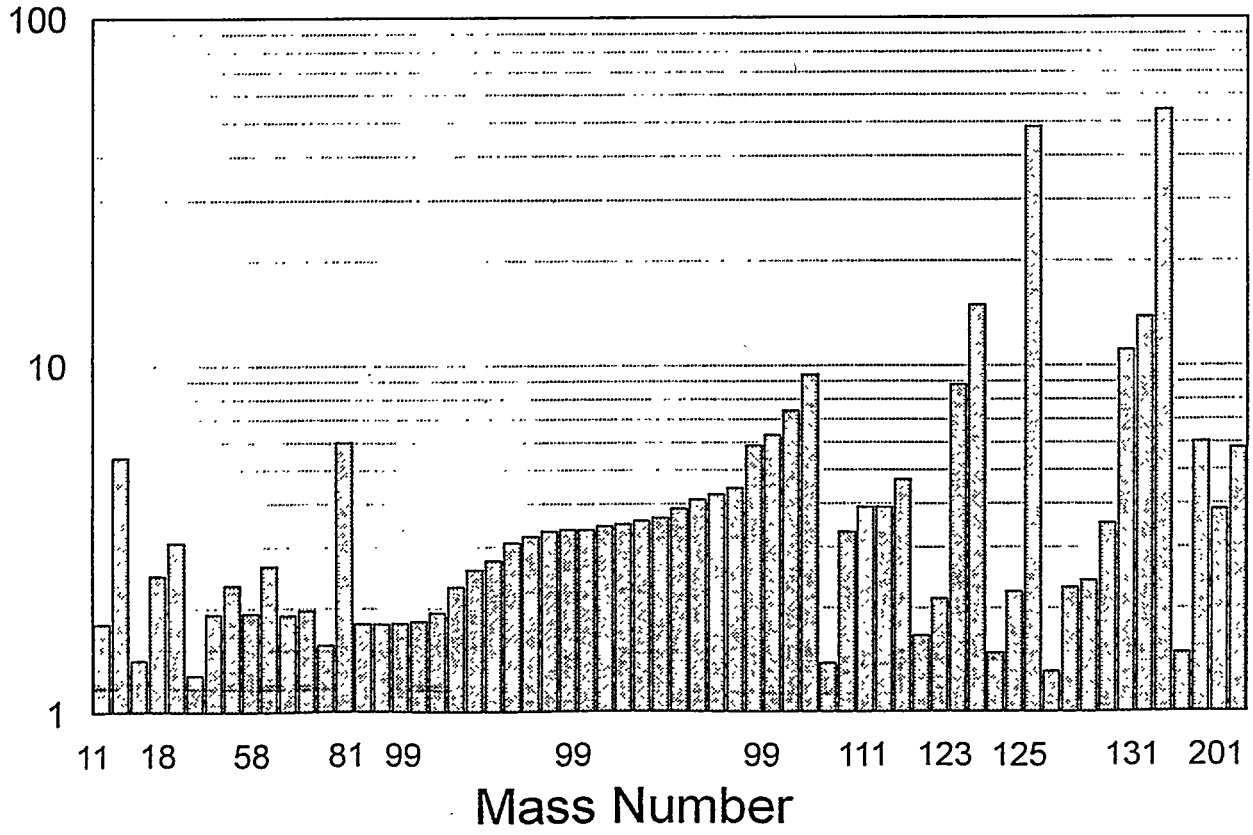

Figure 1. Ratio of H_E to total-body dose for the adult male.

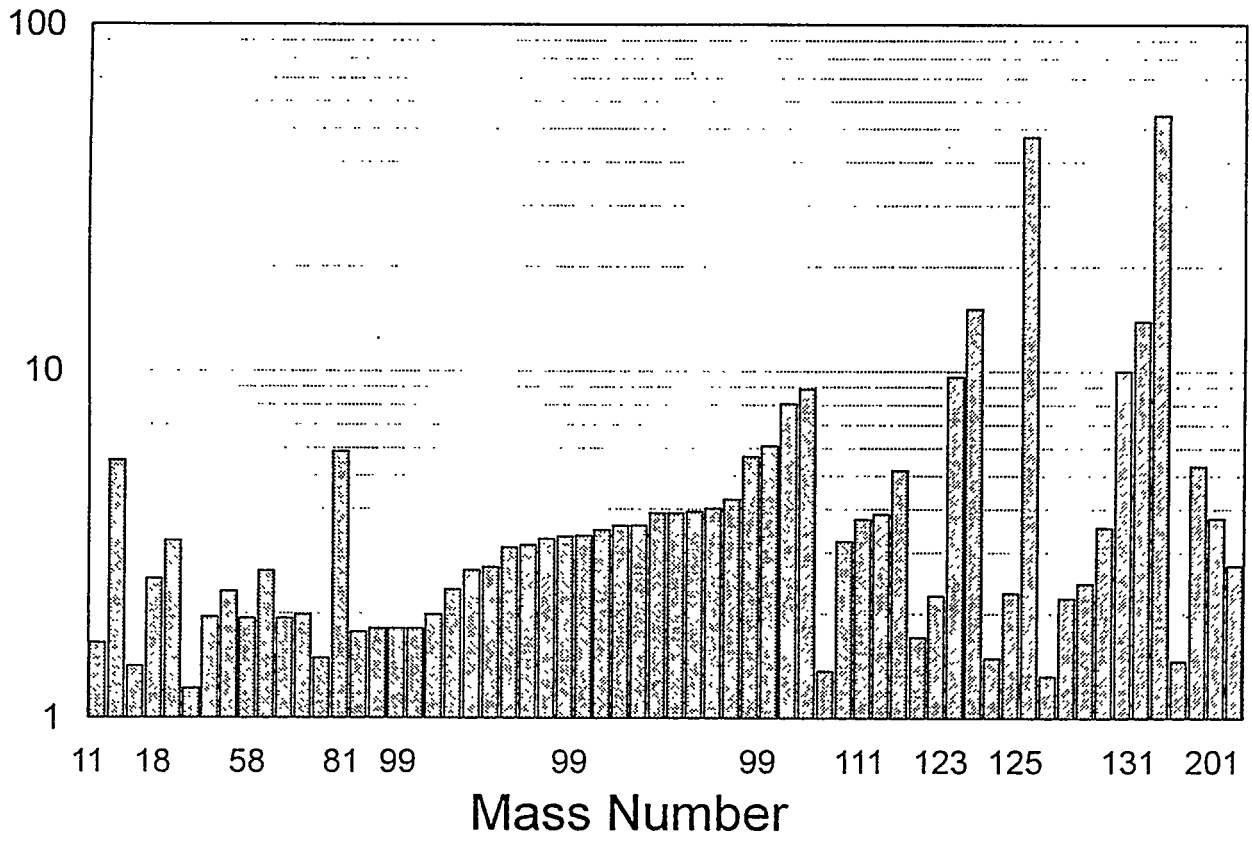

Figure 2. Ratio of H_E to total-body dose for the adult female.

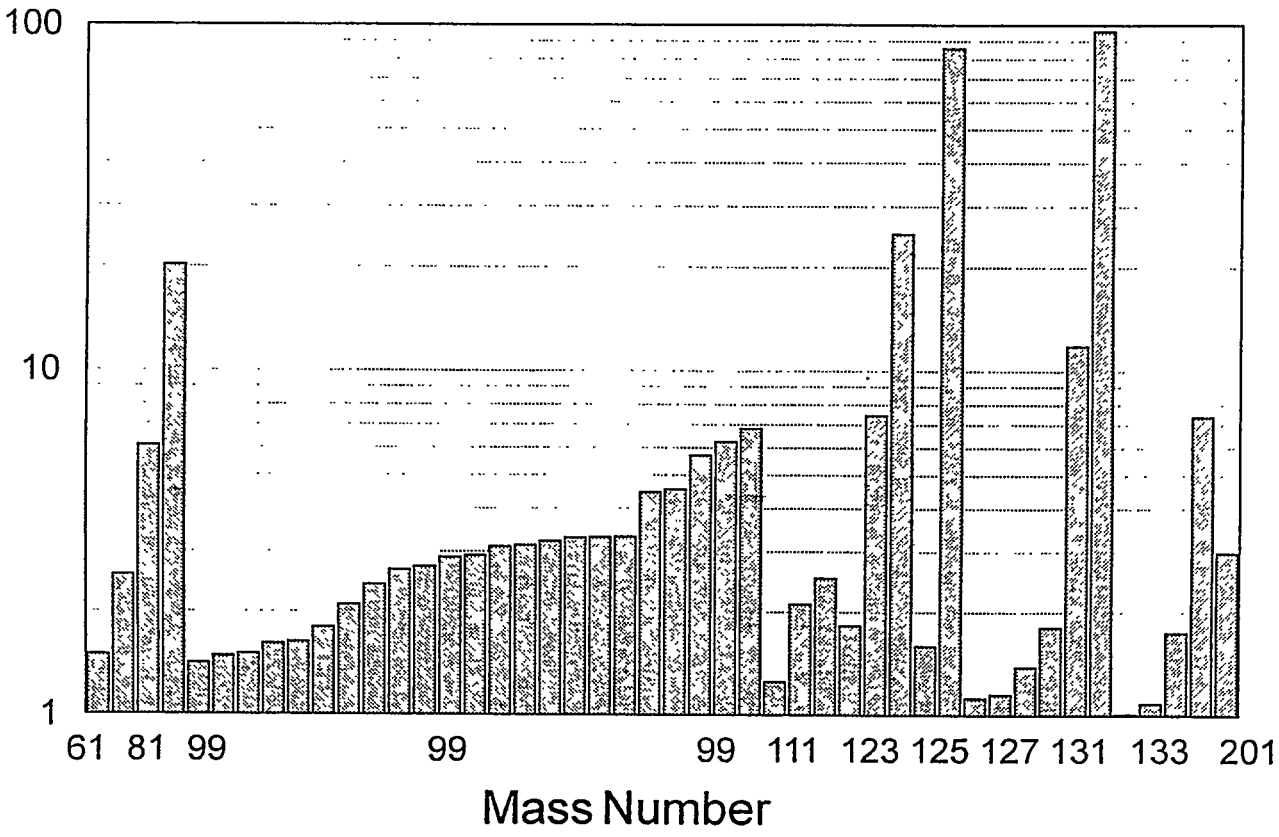

Figure 3. Ratio of E to total-body dose for the adult male.

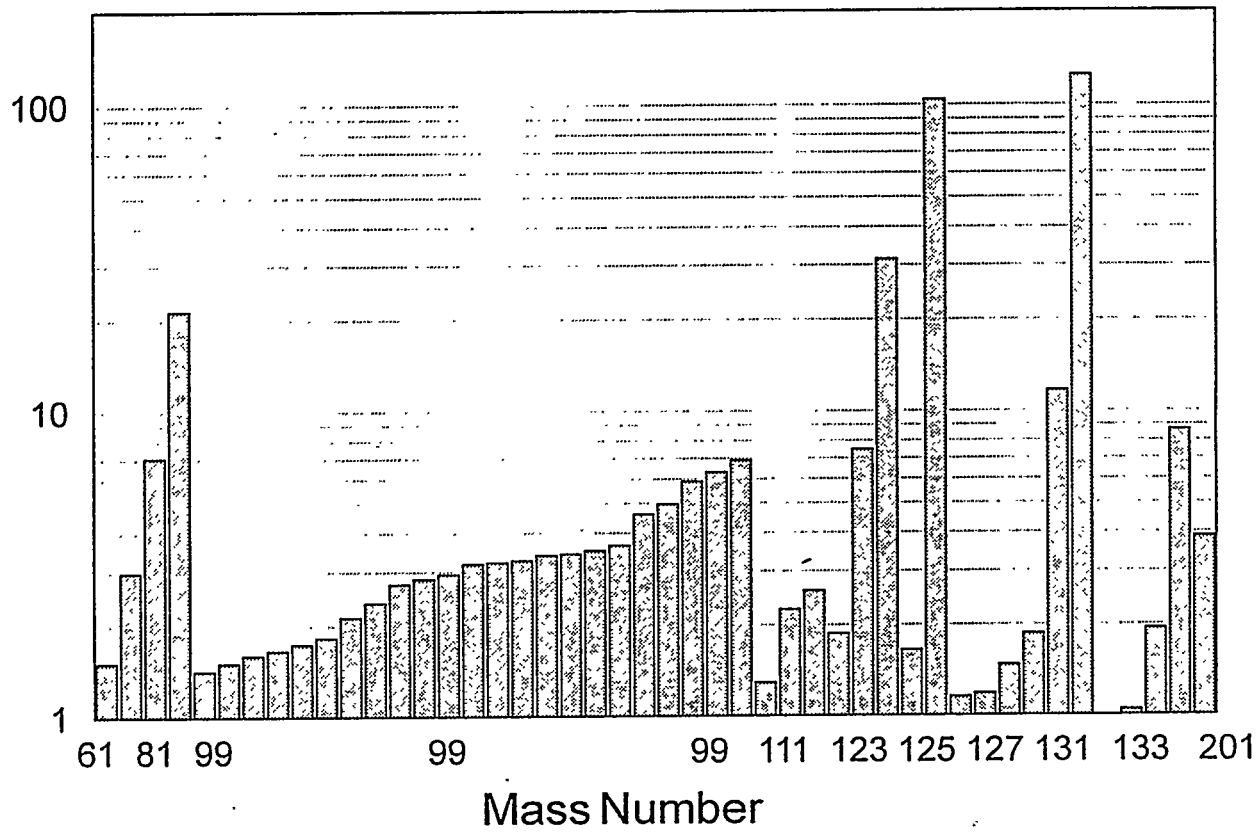

Figure 4. Ratio of E to total-body dose for the 15-year-old.

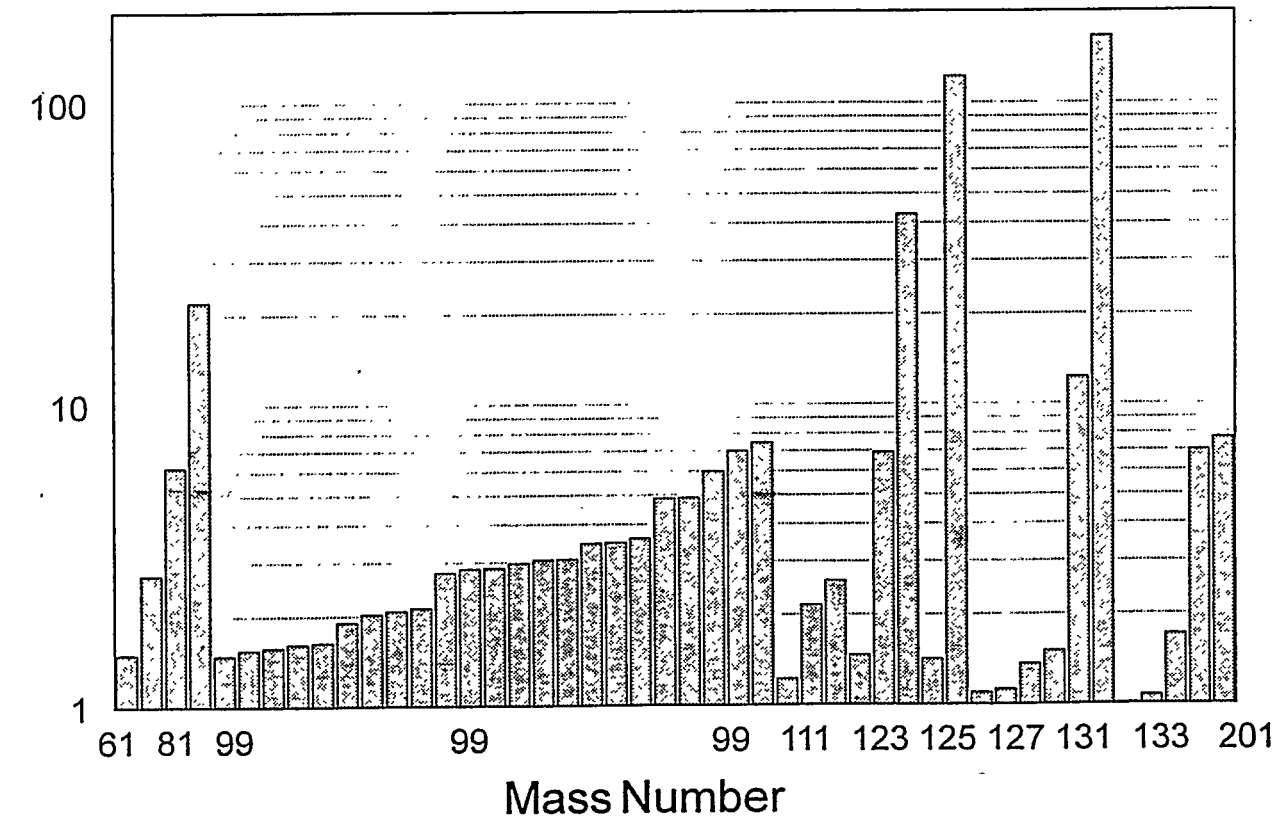

Figure 5. Ratio of E to total-body dose for the 5-year-old.

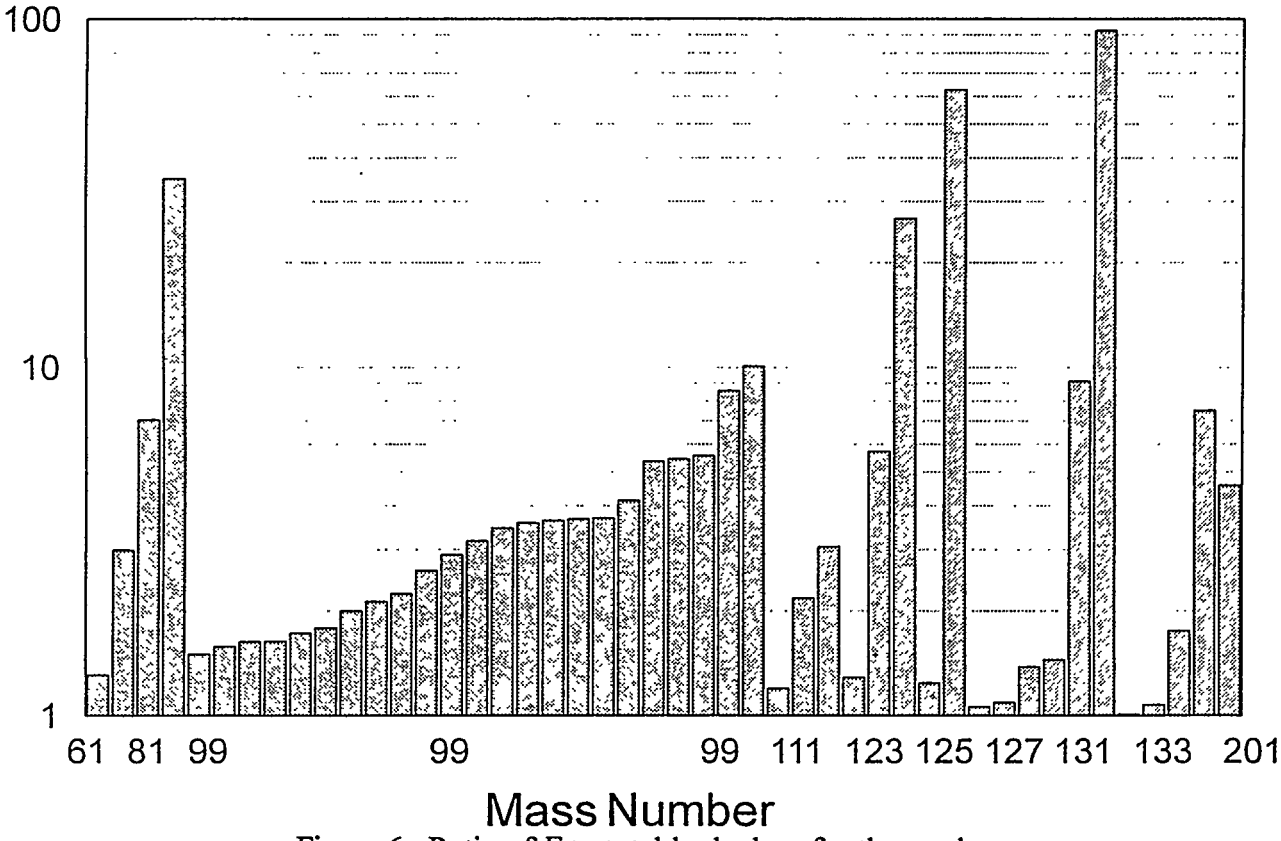

Figure 6. Ratio of E to total-body dose for the newborn.

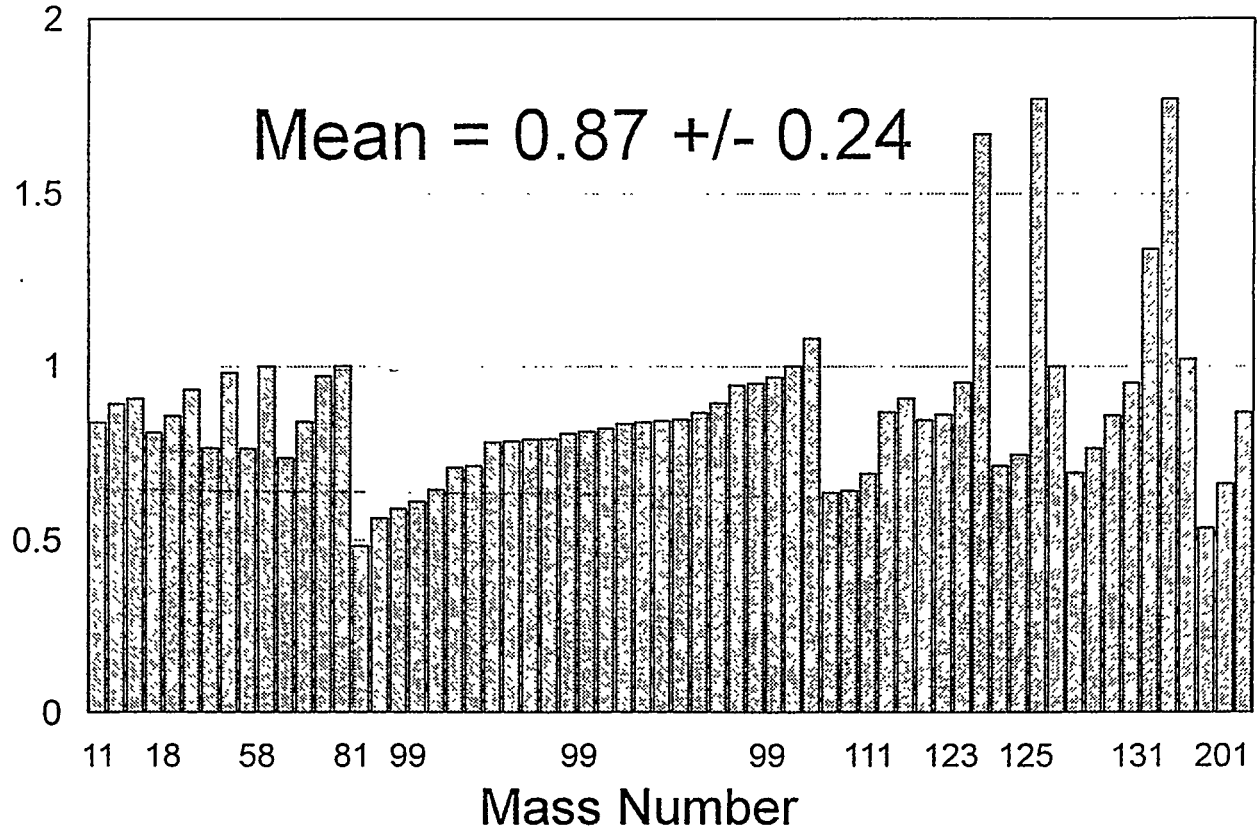

Figure 7. Ratio of E to H_E for the adult male.

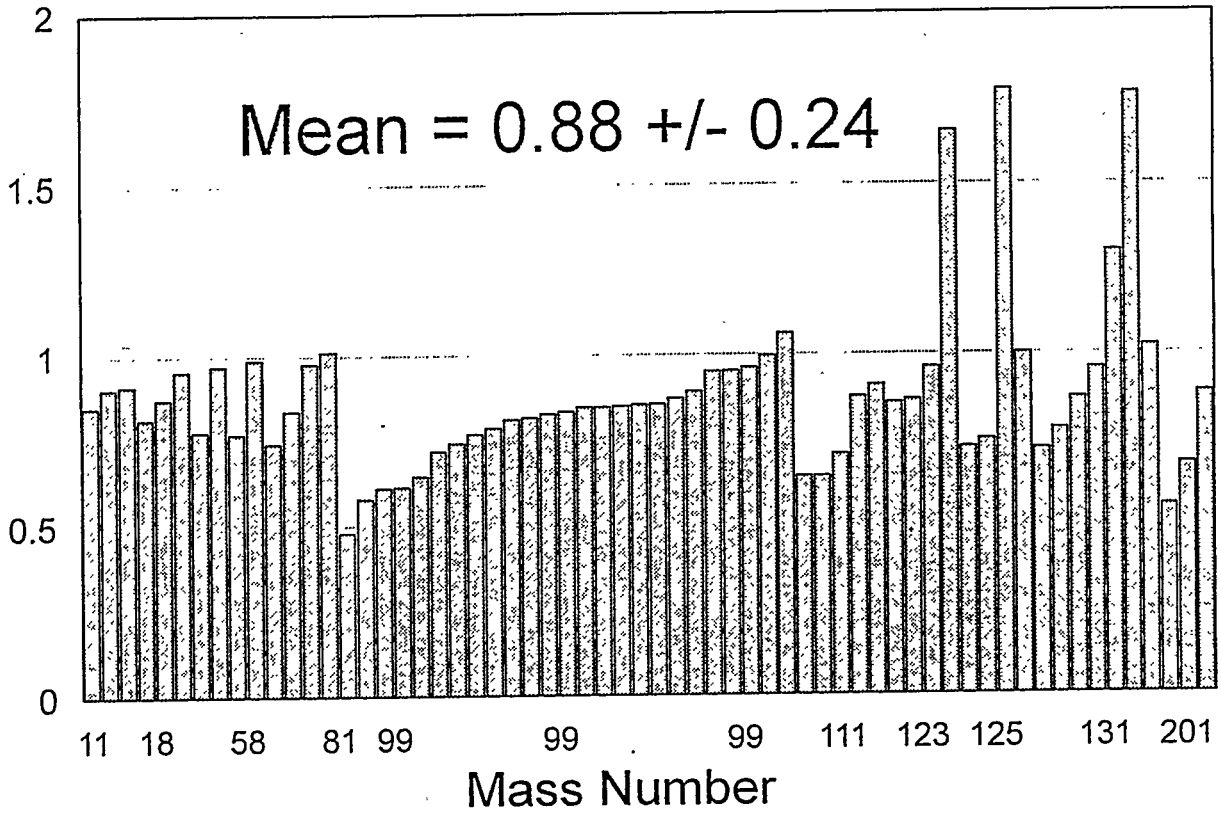

Figure 8. Ratio of E to H_E for the adult female.

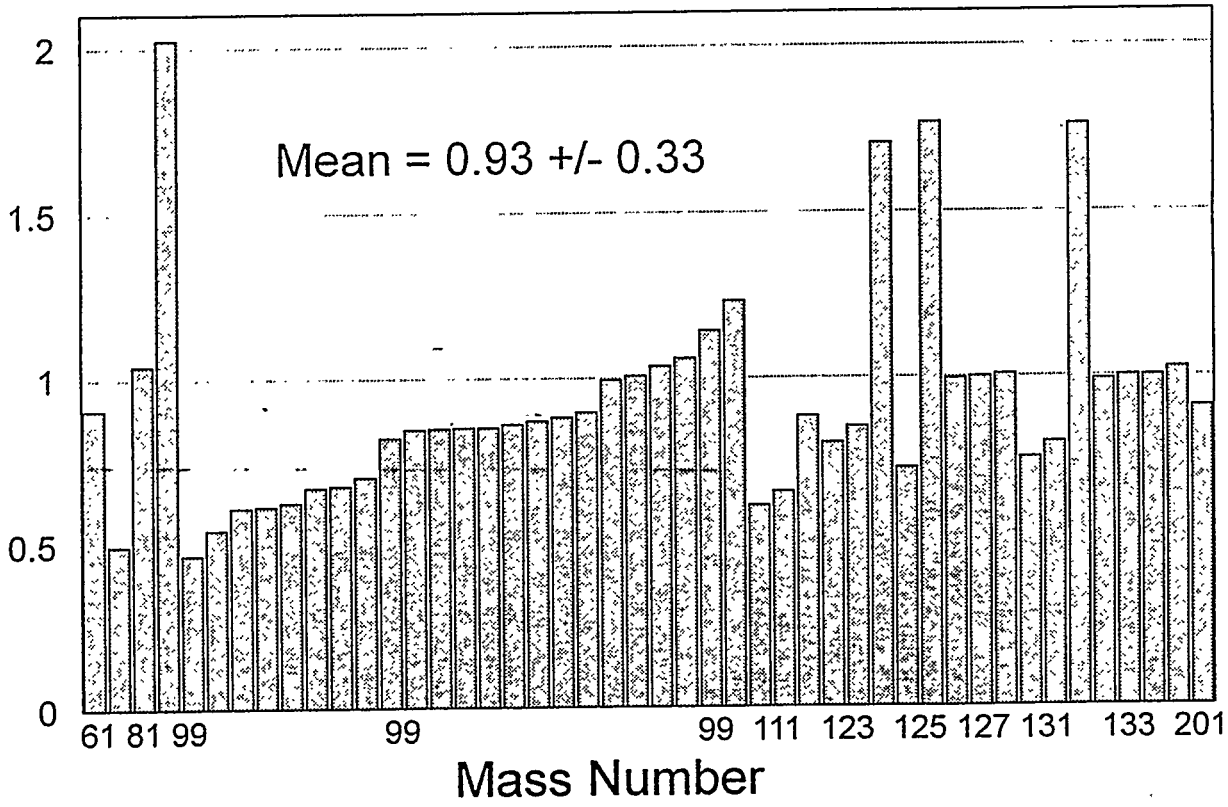

Figure 9. Ratio of E to H_E for the newborn.

REFERENCES

1. ICRP Publication 26, Recommendations of the International Commission on Radiological Protection Annals ICRP 1(3):1-53, 1977.
2. Poston JW. Application of the effective dose equivalent to nuclear medicine patients. J Nucl Med 34(4):714 1993.
3. ICRP Publication 52, Protection of the Patient in Nuclear Medicine, Annals ICRP 17 (4):1-37 1987.
4. ICRP Publication 53, Radiation Dose to Patients from Radiopharmaceuticals, Annals ICRP 18(1-4):1-377, 1987.
5. ICRP Publication 60, 1990 Recommendations of the International Commission on Radiological Protection, Annals ICRP 21 (1-3):1-201, 1991.
6. Johansson L, Mattsson S, Nosslin B and Leide S. Effective dose to the patient from radiopharmaceuticals calculated with the new ICRP tissue weighting factors. Proc. 5th Internat. Radiopharm. Dosimetry Symp., Oak Ridge, TN 1992.
7. Cristy M and Eckerman K. Specific Absorbed Fractions of Energy at Various Ages from Internal Photons Sources. ORNL/TM-8381 V1-V7. Oak Ridge National Laboratory, Oak Ridge, TN. 1987.
8. Stabin M, Watson E, Cristy M, Ryman J, Eckerman K, Davis J, Marshall D and Gehlen K. Mathematical Models and Specific Absorbed Fractions of Photon Energy in the Nonpregnant Adult Female and at the End of each Trimester of Pregnancy. ORNL Report ORNL/TM-12907, 1995.
9. Stabin M. MIRDOSE - the personal computer software for use in internal dose assessment in nuclear medicine. J Nucl Med, 37:538-546, 1996.
10. Loevinger R, Budinger T and Watson E. MIRD Primer for Absorbed Dose Calculations, Society of Nuclear Medicine, 1988.
11. Stabin M, Stubbs J and Toohey R. Radiation Dose Estimates for Radiopharmaceuticals. NUREG/CR-6345, U.S. Nuclear Regulatory Commission, Washington, D.C. 1996.

QUESTIONS

Rao: What is effective dose? It sounds as if it gives the effect, while it does not. Another point to be made is that when a somewhat higher dose is delivered to an organ with a radionuclide whose effective half-life is long compared to a short-lived radionuclide, it does not necessarily follow that the damage from the radionuclide with a long effective half-life is greater than that from the one with a short effective half-life, because of dose-rate effects.

Toohey: Effective dose is a construct developed by the ICRP to relate the risk of stochastic effects from highly nonuniform internal dose to those observed from more uniform, external whole-body radiation dose. The tissue weighting factors give the relative sensitivity of each organ or tissue to stochastic effects. Our position is that because the concept of effective dose takes into account the nonuniform irradiation of internal organs from any given radiopharmaceutical, as well as the sensitivity of each organ to stochastic effects, it is a more useful concept than "whole-body dose," which completely neglects the distribution of dose within the body. The ICRP does not take dose-rate effects into account in the definition of effective dose, so your point is well taken. However, because most radionuclides used in nuclear medicine have rather short physical half-lives, the issue of dose-rate effects may be less important in nuclear medicine than it is in occupational radiation.

Mattsson: When describing radiation risks to patients, I think we need modifying factors to the effective dose values, which perhaps are 2-3 for a group of pediatric patients and say 0.2 for a group of patients over 70 years. Would you like to comment on that?

Toohey: I agree with you completely. Because the effective dose concept was developed for occupational radiation protection, the tissue weighting factors do not include age-dependent factors. Unfortunately, no set of age-related correction factors to risk estimation has yet been developed and agreed upon by the radiation protection community.

Fisher: When using the effective dose equivalent or effective dose, we must keep in mind that the ICRP developed these concepts for application in occupational radiation protection, such as derivation of secondary limits. The radiation-weighting factors are conservatively chosen upper values, not necessarily actual values of relative biological effectiveness for specific endpoints. This system provides a construct of long-term detriment for population groups; it should not be applied to estimate short-term biological effects in individuals, such as patients treated for cancer with high-dose radiopharmaceuticals.

Toohey: Of course; in addition to the radiation weighting factors, the tissue weighting factors also are only for stochastic effects, not deterministic.

Rao: A comment to Dr. Fisher: the α-particle RBE values of 3-5 that you quoted are for deterministic effects, ie.g., cell killing. When you consider stochastic effects (e.g., chromosome aberrations), the RBE values reported for α-particles are as high as 80. Therefore using a radiation weighting factor of 20 for α-particles is not unreasonable when our interest is risk assessment.

Akabani: We have opened a Pandora's box. It is clear that the risk associated with a nuclear medicine procedure requires taking into consideration dose rate, age, and organ biokinetics, and must be based on radiation weighting factors for the specific-age population. The risk estimate must also consider the latency period for a specific illness to occur in a specific-age population.

Eckerman: Regarding age-dependent weighting factors, it appears that it would be much better to go directly from dose to risk in an age-dependent manner rather than attempt to construct and implement such considerations in the age-dependent scheme.

Toohey: All the comments are quite correct; effective dose does not meet all of our needs for a single parameter with which to perform risk-benefit evaluations in nuclear medicine; however, we still feel it is a much better parameter to use for this purpose than is whole-body dose, which we feel is essentially meaningless for any radiopharmaceutical that is not uniformly distributed in the body.

THE EFFECT OF $W_{R,AUGER}>1$ FOR RADIOPHARMACEUTICALS ON EQUIVALENT DOSE AND OTHER RELATED QUANTITIES

Wright A
Amersham International plc, UK
White Lion Road, Little Chalfont
Buckinghamshire, England HP7 9LL

ABSTRACT

Auger-electron emitters incorporated in DNA material have been shown to be extremely radiotoxic, with RBE values as high as 80 being reported. As a result, the American Association of Physicists in Medicine (AAPM) has recommended values of w_R=20 and 10 for stochastic and deterministic effects, respectively for Auger-electron emitters incorporated within DNA material. Assuming the ICRP tissue weighting factors, this report studies the relationship between effective dose and fraction incorporated in DNA (f_{DNA}). This relationship may be nonlinear, or even discontinuous. The ratio of highest organ dose to effective dose may be an important consideration for some therapeutic radiopharmaceuticals. The relationship between this ratio and f_{DNA} is shown to be complex and not easily predictable. These and other effects, including dependance on age, are discussed for a wide range of radiopharmaceuticals for both homogeneous and inhomogeneous distributions of f_{DNA}.

INTRODUCTION

A large number of radiopharmaceuticals use nuclides that emit Auger electrons. A fraction of these Auger-emitting nuclides may become bound to DNA, either by design or as a byproduct of the biochemistry of the product. Since the radiotoxicity of Auger electrons bound to DNA is significant (1,2), there is a greater likelihood of carcinogenesis than is currently estimated using standard calculations of equivalent dose and other similar quantities. This report studies one approach to the problem, which brings together the latest recommendations of the ICRP and those of the American Association of Physicists in Medicine (AAPM), estimates the effects of Auger electrons bound to DNA and considers whether there are artifacts of the models that, when combined, result in effects that may have no physical basis.

EQUIVALENT DOSE

The equivalent dose to an organ or tissue T is defined in ICRP 60(3) as follows:

$$H_T = w_R \cdot D_{T,R} , \qquad (1)$$

where w_R is the radiation weighting factor and $D_{T,R}$ is the absorbed dose to tissue T from radiation R. For a mixed radiation field, such as those generated by many radionuclides including Auger emitters,

$$H_T = \sum_R w_R \cdot D_{T,R} \cdot \quad (2)$$

w_R is 1 for all photons and electrons other than Auger electrons bound to DNA. However, Auger electrons that are bound to DNA are known to have a much greater radiotoxic effect for both stochastic and nonstochastic effects(1, 2). Thus, it has been proposed that for such emissions, a value of w_R=20 be assumed for all stochastic dose calculations and w_R=10 for all nonstochastic or deterministic dose calculations.

Humm et al. (3) propose that the equivalent dose specifically for Auger electrons may be expressed as:

$$H_{T,R(Auger)} = (1 + f_{DNA}(w_{Auger}-1)) \sum_{R(Auger)} D_{T,R(Auger)}, \quad (3)$$

where f_{DNA} is the fraction of the radioactivity in the organ bound to DNA. Since this fraction may vary from organ to organ, the value of f_{DNA} in organ T is denoted in this report $f_{DNA,T}$. Rearranging the above formulae and expanding the expression for D gives the following expression for equivalent dose to an organ considering DNA-bound Auger emitters (H_T^D) in terms of the ICRP definition of equivalent dose(H_T).

$$H_T^D = H_T + 9 f_{DNA,T} \frac{A_T \Delta^A}{m_T} \ (deterministic\ dose) \quad (4)$$

and

$$H_T^D = H_T + 19 f_{DNA,T} \frac{A_T \Delta^A}{m_T} \ (stochastic\ dose), \quad (5)$$

where A_T is the number of disintegrations within the target organ T, Δ^A is the mean energy per disintegration of Auger emissions, and m_T is the mass of the target organ T.

EFFECTIVE DOSE

Similarly, the expression for effective dose (ED) may be rearranged from

$$ED = \sum_T \sum_R w_T \cdot w_R \cdot D_{T,R} \quad (6)$$

to

$$ED^D = ED + 19 \sum_T \frac{f_{DNA,T}\, w_T\, A_T\, \Delta^A}{m_T}, \quad (7)$$

where w_T is the tissue weighting factor.

Variation of the Equivalent Dose and Effective Dose with $f_{DNA,T}$.

It may be seen that the values for both equivalent dose and the contribution to effective dose of organ T tend to increase linearly with $f_{DNA,T}$, the rate of increase being a function of the number of disintegrations in each organ, the mean energy of each disintegration, and the mass of the organ.

Values of w_T may vary to a limited extent. The sum of the tissue weighting factor for the remainder organs (adrenals, brain, small intestine, kidney, muscle, pancreas, spleen, thymus and uterus) remains fixed at 0.05, but the tissue factor for each of the organs within the remainder may change as described in Equation 8.

$$w_T = \frac{0.05\ m_T}{\sum_{T=1}^{T=9} m_T} \qquad if\ H_{T'} \le H_{max}$$

$$\left.\begin{aligned} w_{T'} &= 0.025 \\ w_T &= \frac{0.025\ m_T}{\sum_{\substack{T=1 \\ T \neq T'}}^{T=9} m_T} \quad \forall T \neq T' \end{aligned}\right\} \quad if\ H_{T'} > H_{max} \qquad (8)$$

In this equation, H_{max} denotes the maximum equivalent dose among all organs with explicit weighting factors, H_T, the equivalent dose to remainder organ T and $H_{T'}$, the maximum equivalent dose among organs of the remainder. Thus, if a remainder organ is the most exposed organ of the whole body, i.e. that for which the stochastic value of H_T^D is greatest, then the value of w_T for that organ will alter from $(0.05m_T/\sum_{rem}m_T)$ to 0.025. Values of w_T for other remainder organs will approximately halve, but since they have lower equivalent doses, the net effect will be an increase in ED^D. Since this increase in tissue weighting factor occurs over the whole of the organ dose, the increase in ED^D will be discontinuous with an attendant increase in slope.

Another effect occurs when the most exposed of the sex organs (ovaries and testes) changes. Since the tissue weighting factor of 0.2 for the gonads is attributed to the maximum of these two organs, if the dose to one becomes greater than the dose to the other, then there will be a change in slope of ED^D with $f_{DNA,gonads}$ but with no attendant discontinuity.

The ratio of highest organ dose to the effective dose is a consideration for some therapeutic radionuclides. Maximizing the dose to the cancerous tissue while not over-exposing normal tissue is one of the aims of cancer therapy. Borrowing an expression from external beam therapy, I have denoted the ratio of the maximum deterministic organ dose to the effective dose to the whole body as the "therapeutic ratio".

CALCULATIONS

In order to calculate the values of highest organ dose (HOD), effective dose (ED) and therapeutic ratio (TR) with respect to $f_{DNA,T}$, the following information is required:

A_T - the number of disintegrations occurring in organ T per Bq administered (this depends on the organ of interest, the nuclide and the chemical form of the radiopharmaceutical as well as its mode of administration (6)).

Δ^A- the mean energy emission of Auger electrons per disintegration (this will depend solely on the nuclide (7)).

m_T - the mass of organ T (6)

H_T - the equivalent dose to organ T with $f_{DNA,T}=0$ (or $w_{R,Auger}=1$) (this depends on the organ of interest, the nuclide and the chemical form of the radiopharmaceutical as well as its mode of administration (6)).

RESULTS

Organ doses increase linearly with $f_{DNA,T}$. This is because the expressions for ED in Equations 4 and 5 are of the form y=mx+c where $c=H_T$ and $m=(w_R-1)A_T\Delta^A/m_T$. Since w_R and Δ^A are not dependent on the organ, the factor that determines the slope for each organ with respect to $f_{DNA,T}$ is A_T/m_T. If this is high, then the effect of DNA-bound Auger electrons is greater than if it is low. It is by this means that the most exposed organ may change.

Homogeneous Distribution of f_{DNA}

The instance in which the fraction of Auger emitting nuclides that becomes bound to DNA material is independent of organ or tissue is referred to in this paper as homogeneous distribution of f_{DNA}. In this case the amount of Auger-emitting material bound to DNA is proportional to the time integral of concentration of activity in each organ or tissue (A_T). The only products for which there is no change in either ED or HOD are those orally administered and for which there is no gut uptake. These products do not become incorporated in any body tissue, and therefore the Auger component does not contribute to any dose.

Of those that remain, the majority of radiopharmaceuticals show a linear relationship between ED and f_{DNA} and between HOD and f_{DNA} with no discontinuities. Some of these products, like ^{67}Ga-citrate (Figure 1), exhibit a steadily rising therapeutic ratio, whereas others such as ^{51}Cr-chloride (iii) (Figure 2) exhibit a steadily falling therapeutic ratio. In other instances, the HOD changes slope with no discontinuity in ED, whereas in yet others, e.g. in ^{201}Tl, (Figure 3) there is both an increase in the slope of the highest organ dose v f_{DNA} and a discontinuity in the values of ED v f_{DNA}, leading to a complex relationship between therapeutic ratio (TR) and f_{DNA}. Unless there is such a discontinuity in the effective dose, it can be shown that the value of TR steadily increases with f_{DNA} if the following inequality is obeyed:

$$\frac{A_{T'}}{m_{T'}} < \frac{19}{9}\,\frac{HOD(0)}{ED(0)}\sum_T \frac{w_T A_T}{m_T}, \qquad (9)$$

where T' refers to the most exposed organ.

By using the above expression, one may identify those therapeutic radiopharmaceuticals whose properties may be perceived to be enhanced by a nonzero value of f_{DNA} (assuming the homogenous condition). This expression does not include a reference to the strength of Auger emissions and is solely dependent on distribution of activity throughout the body. It is important to note that the TR, i.e. the ratio between the ED and the HOD, is not simply dependent on w_T for those instances where the main contribution to ED is from one organ. In the case of I-125 iodide (Figures 4, 5 and 6), except where the thyroid is fully blocked (uptake in thyroid = 0%), the TR when $f_{DNA}=0$ is approximately 20, as would be expected with a value of w_T to the thyroid of 0.05. However, as f_{DNA}

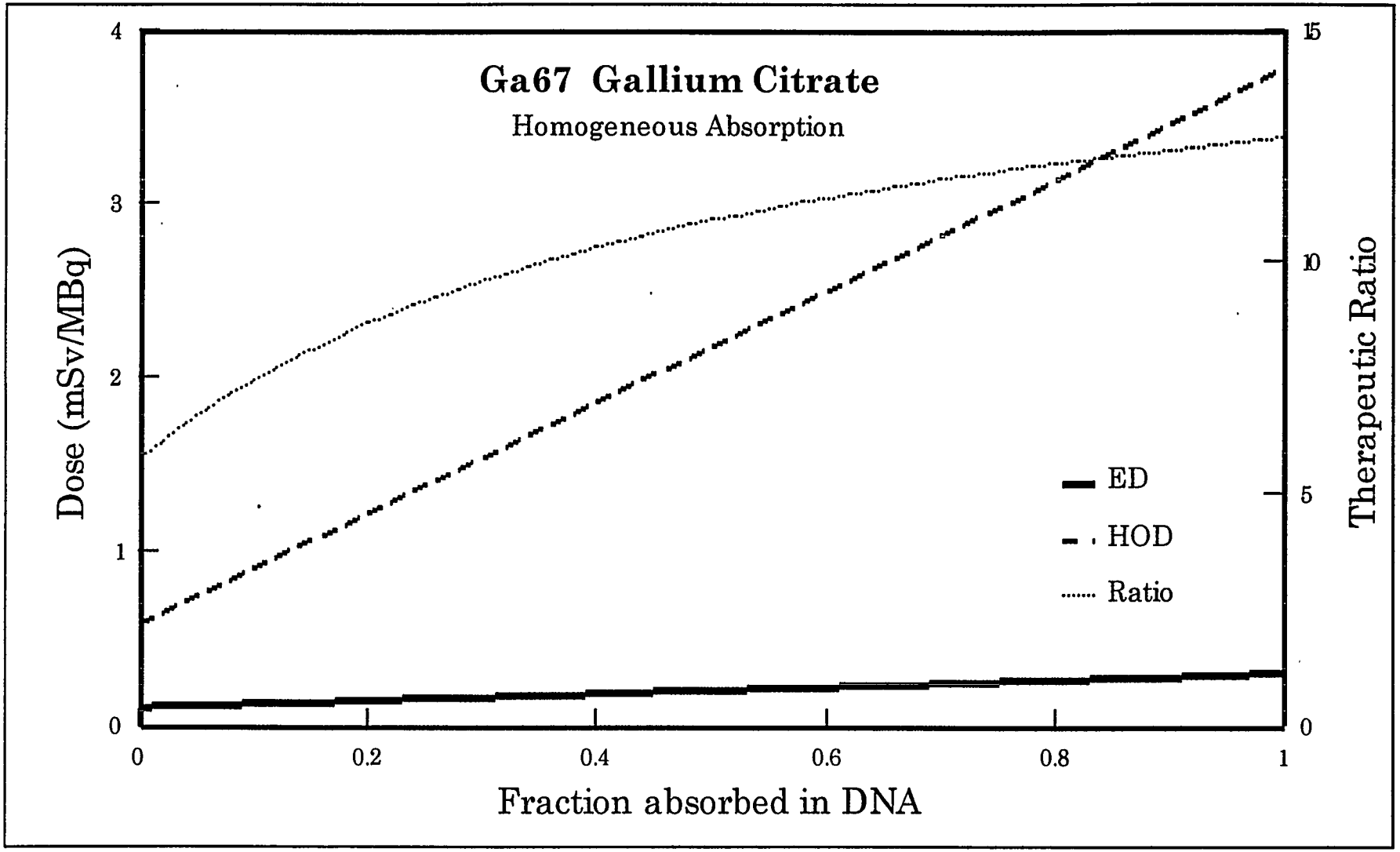
Ga67 Gallium Citrate
Homogeneous Absorption
Dose (mSv/MBq)
Therapeutic Ratio
Fraction absorbed in DNA
ED
HOD
Ratio
0
1
2
3
4
5
10
15
0
0.2
0.4
0.6
0.8
1

Figure 1.

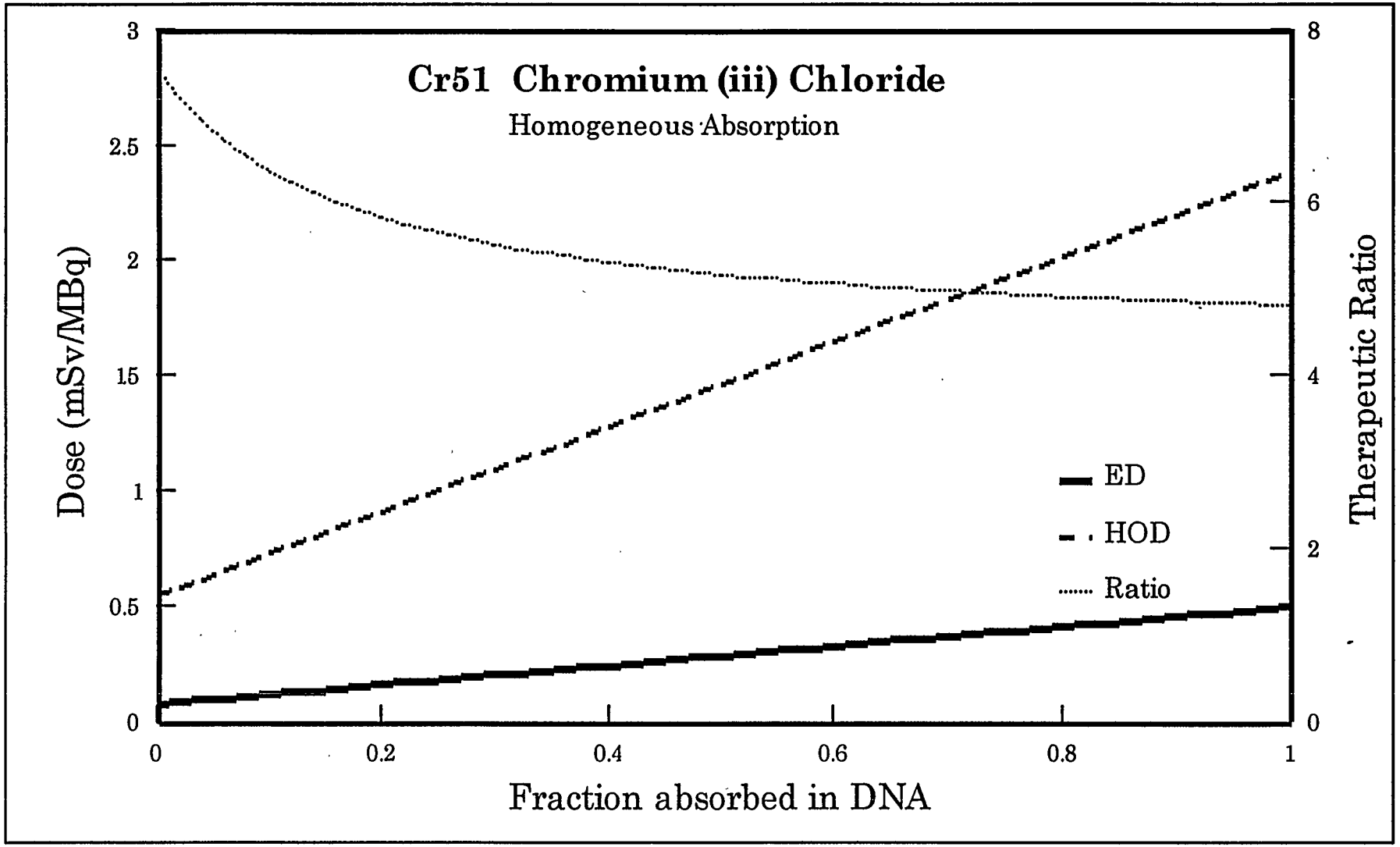
Cr51 Chromium (iii) Chloride
Homogeneous Absorption
Dose (mSv/MBq)
Therapeutic Ratio
Fraction absorbed in DNA
ED
HOD
Ratio
0
0.5
1
1.5
2
2.5
3
0
2
4
6
8
0
0.2
0.4
0.6
0.8
1

Figure 2.

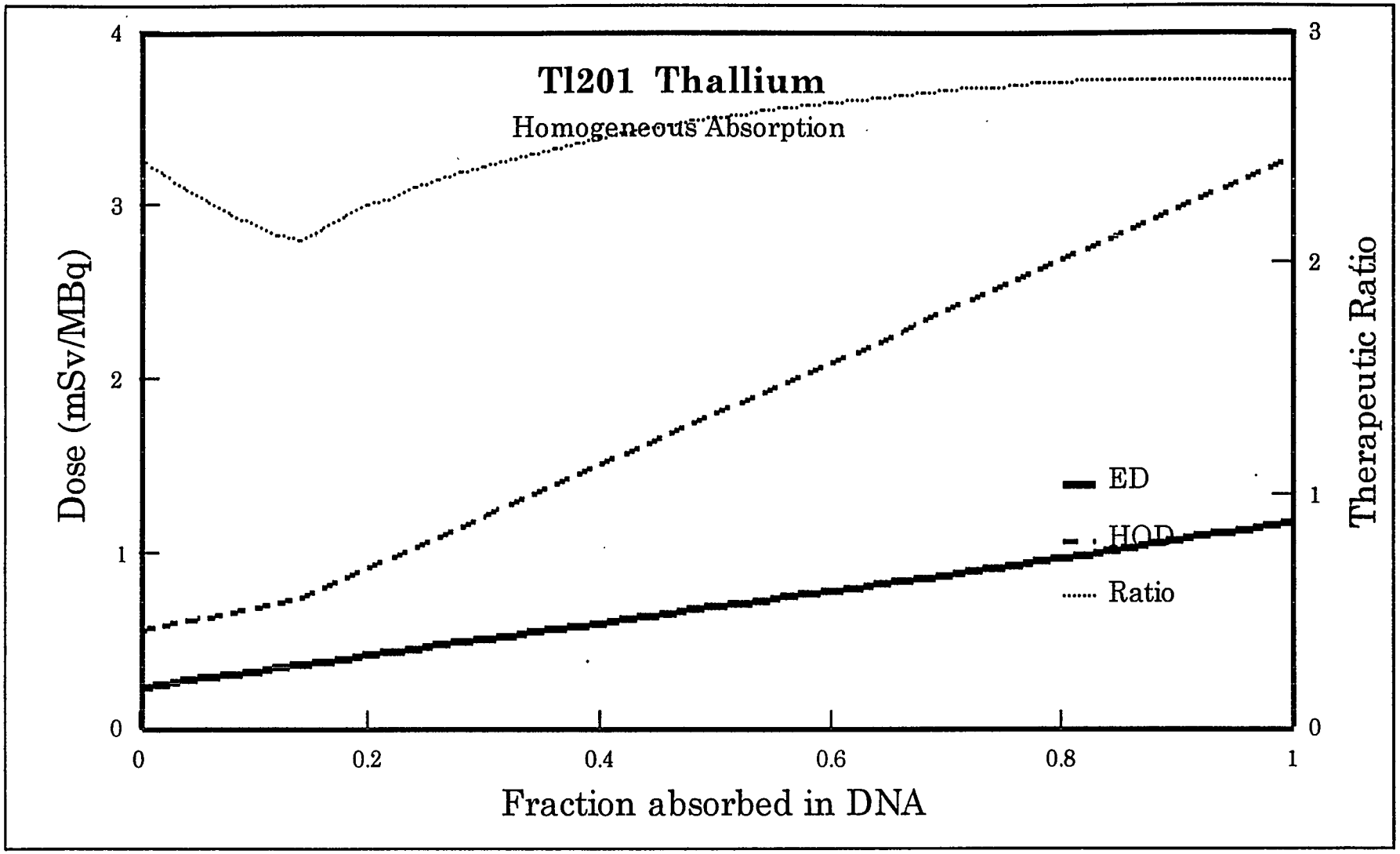
Tl201 Thallium
Homogeneous Absorption
Dose (mSv/MBq)
Therapeutic Ratio
Fraction absorbed in DNA
ED
HOD
Ratio
0
1
2
3
4
0
0.2
0.4
0.6
0.8
1

Figure 3.

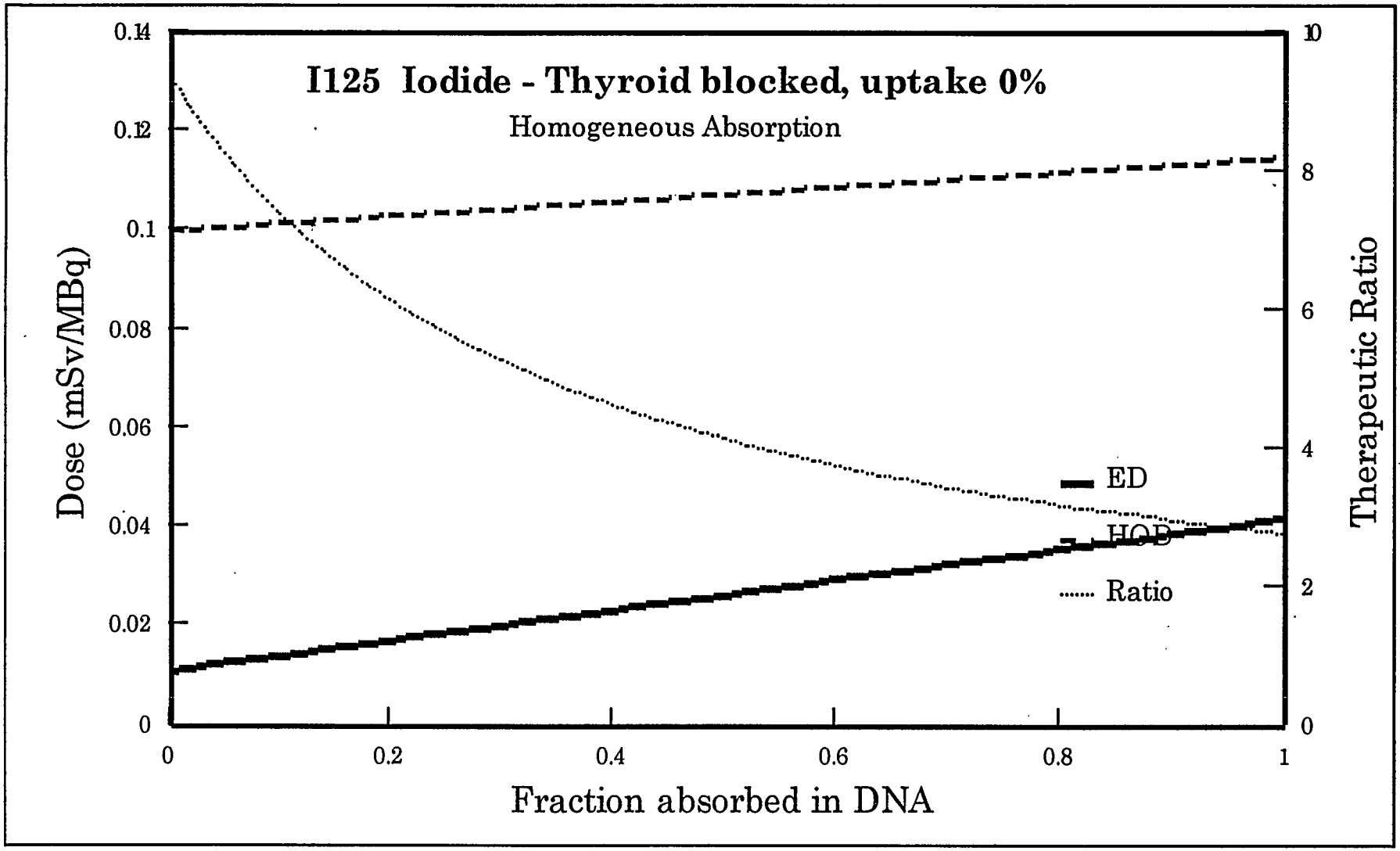
I125 Iodide - Thyroid blocked, uptake 0%
Homogeneous Absorption
Dose (mSv/MBq)
Therapeutic Ratio
Fraction absorbed in DNA
ED
HOD
Ratio
0.14
0.12
0.1
0.08
0.06
0.04
0.02
0
10
8
6
4
2
0
0
0.2
0.4
0.6
0.8
1

Figure 4.

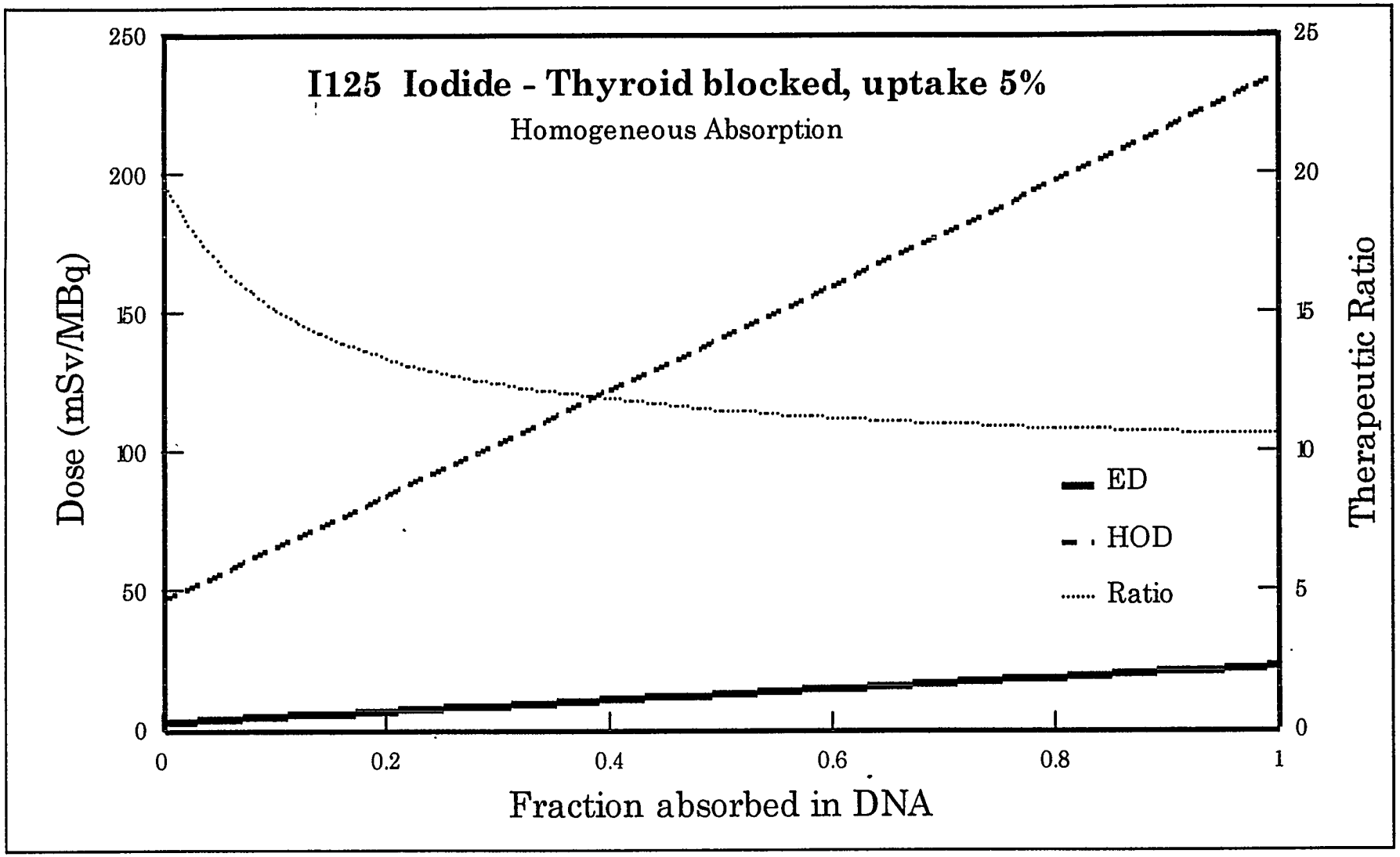
I125 Iodide - Thyroid blocked, uptake 5%
Homogeneous Absorption
Dose (mSv/MBq)
Therapeutic Ratio
Fraction absorbed in DNA
ED
HOD
Ratio
250
200
150
100
50
0
25
20
15
10
5
0
0
0.2
0.4
0.6
0.8
1

Figure 5.

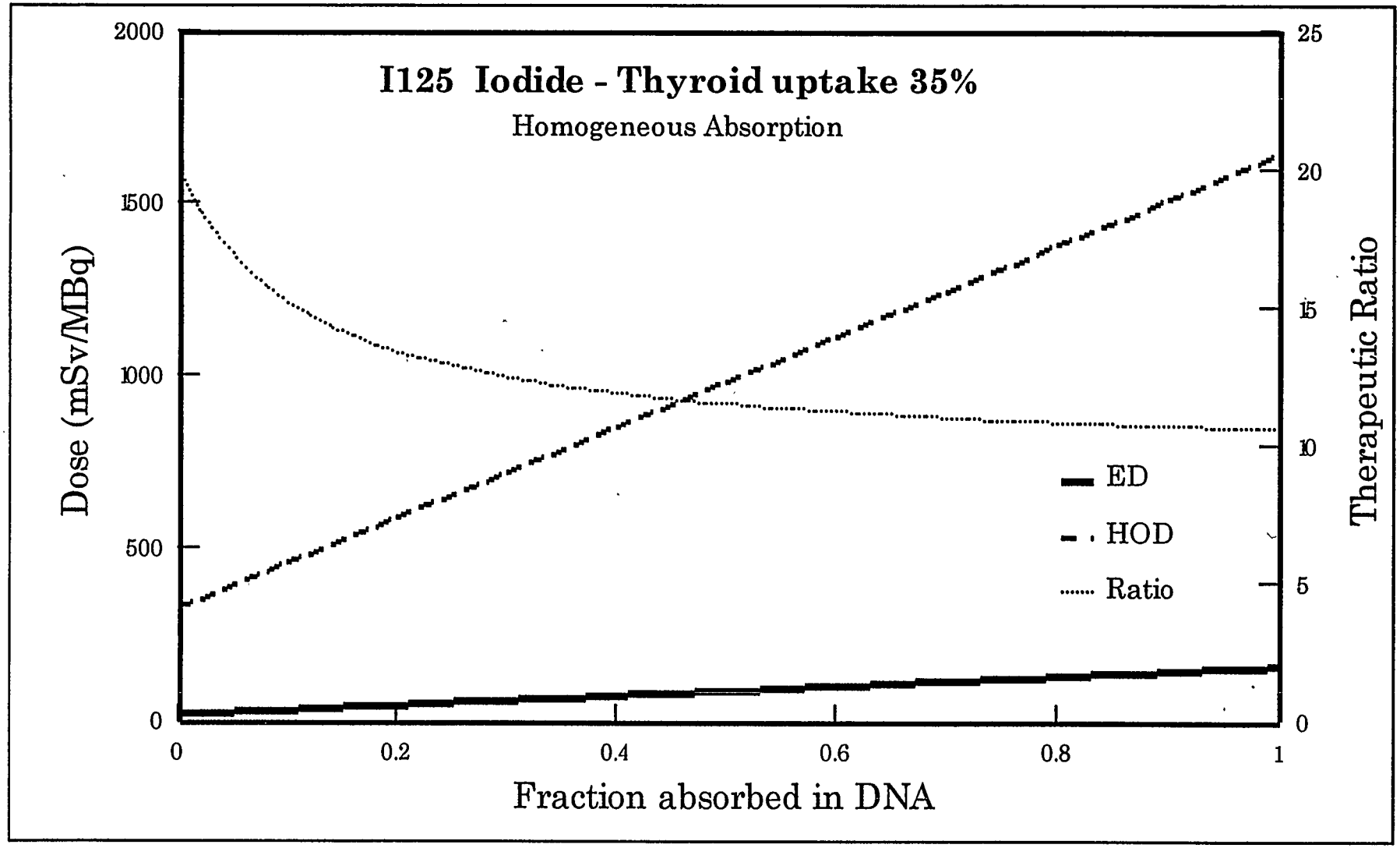
I125 Iodide - Thyroid uptake 35%
Homogeneous Absorption
Dose (mSv/MBq)
Therapeutic Ratio
Fraction absorbed in DNA
ED
HOD
Ratio
2000
1500
1000
500
0
25
20
15
10
5
0
0
0.2
0.4
0.6
0.8
1

Figure 6.

increases, so does the contribution to dose from Auger electrons, which have two values of w_R, one (20) for stochastic doses, the other (10) for deterministic dose. Thus, as the value of f_{DNA} increases, the TR being a ratio of deterministic and stochastic dose quantities asymptotically decreases to the value of 10.

Heterogeneous Absorption

In this report, a heterogeneous distribution of f_{DNA} assumes the limiting case where there is no binding of Auger emitting nuclides to DNA material, except for one particular organ or tissue, for which the fraction is f_{DNA}. If it is assumed that Auger emitters are absorbed within the DNA of one organ only, then differences from the homogeneous case arise. Two cases are considered, absorption only in the kidneys and only in the testes. The kidneys are organs normally considered among the remainder organs, and as such, may form discontinuities in ED when becoming the most exposed organ, e.g. ^{125}I iodinated polyvinylpyrrolidone (Figure 7) and ^{57}Co labeled Bleomycin (Figure 8).

The testes are organs with explicit tissue weighting factors, but which are only considered if exposed to a greater dose than the ovaries. Therefore, since there is no change of w_T from the gonads, there is no attendant discontinuity in ED when the testes become more exposed than the ovaries, e.g. ^{57}Co labeled bleomycin (Figure 9). In the case of ^{77}Br-bromide, however, some interesting effects occur with increasing f_{DNA}. (Figure 10) With f_{DNA}=0, the adrenals (a remainder organ) is the most exposed organ, and the dose to the ovaries is greater than that to the testes. When f_{DNA} reaches about 0.05 however, the dose to the testes exceeds that to the ovaries, with a linear change in ED and TR. When f_{DNA} reaches about 0.4, the dose to the testes (for the purposes of calculating stochastic dose) exceeds that to the adrenals, so there is a discontinuity in ED and TR, and when f_{DNA} exceeds about 0.7, then the testes becomes the most exposed organ (for the purposes of calculating deterministic doses), and so there is a continuous change in slope in HOD and TR vs. f_{DNA}.

Dependence on Age

It is not generally possible to study the dependence on age, since biokinetic models are often not available that adequately describe how the metabolism of normal individuals varies with age. However, in the case of iodide, it was decided that since, when the thyroid is not blocked such a large proportion of the dose is to the thyroid, and since the ICRP have published parameters for that gland for each of five ages, that it would be a valid subject of study. As may be expected, the dose to the thyroid and the EDE is greatest for the one year old, both the whole body and the thyroid being much less massive than when older. This is partially offset by the reduced residence time in the thyroid (30-day biological half-time for a 1-year old, cf. 80 days for an adult). What is interesting however, is therapeutic ratio is not age-dependant to any significant degree. For ^{125}I (Figure 6), the value of TR reduces from a value of approximately 20, falling with f_{DNA} asymptotically to 10.

DISCUSSION

It is accepted that a large number of the effects noted in this report are artifacts of the equations used to estimate effective dose and related quantities. Notably, the discontinuities that arise in ED when a remainder organ becomes the most exposed organ, and the distinction between organ dose for contributions to stochastic and nonstochastic organ doses from Auger emitters bound to DNA. It is not anticipated that the effects are real. However, it is important to understand the logical implications of current theories of the effects of Auger electrons when applied to radiopharmaceutical dosimetry as in particular the calculation of effective dose.

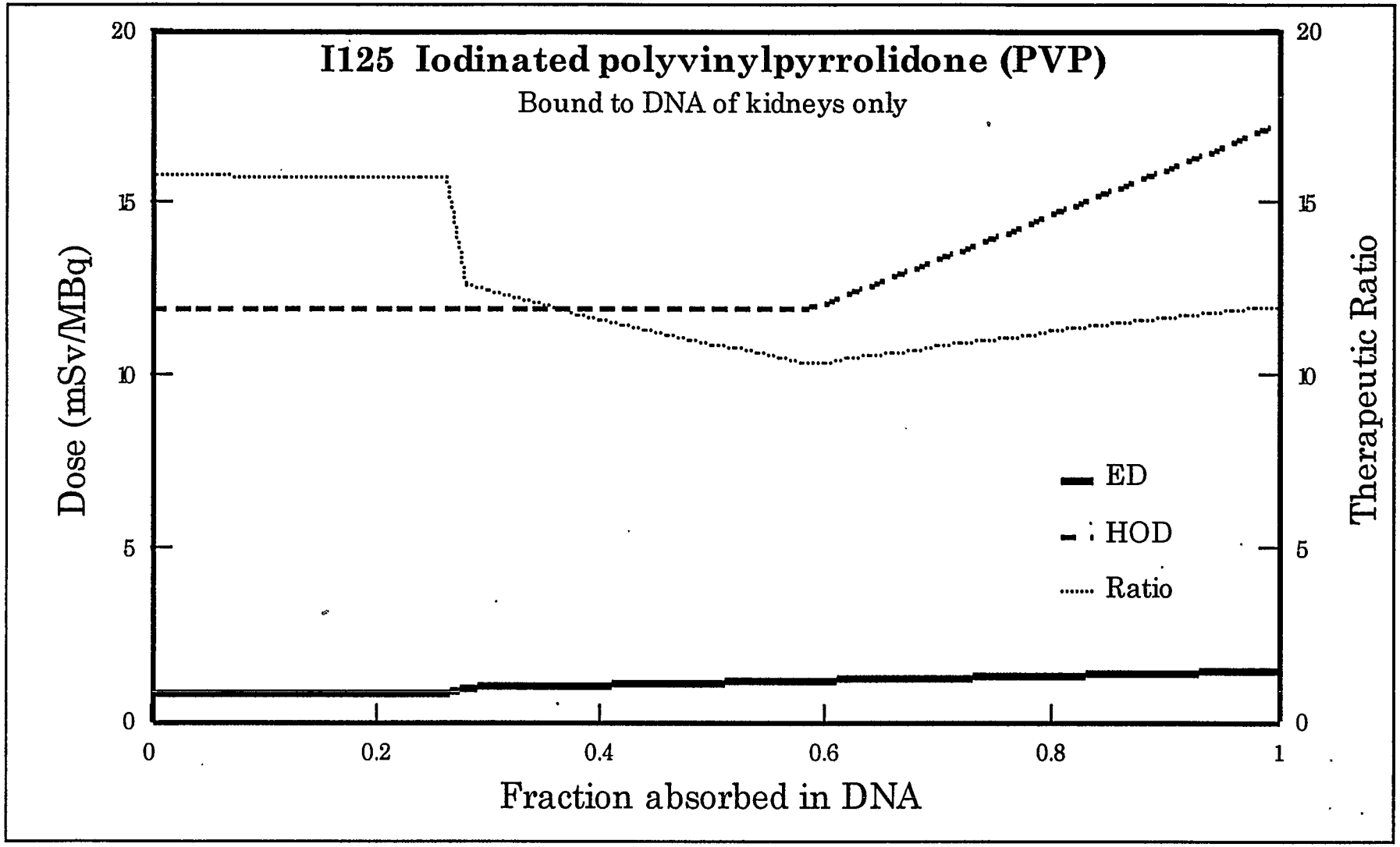
I125 Iodinated polyvinylpyrrolidone (PVP)
Bound to DNA of kidneys only
Dose (mSv/MBq)
Therapeutic Ratio
Fraction absorbed in DNA
ED
HOD
Ratio
0
5
10
15
20
0
0.2
0.4
0.6
0.8
1

Figure 7.

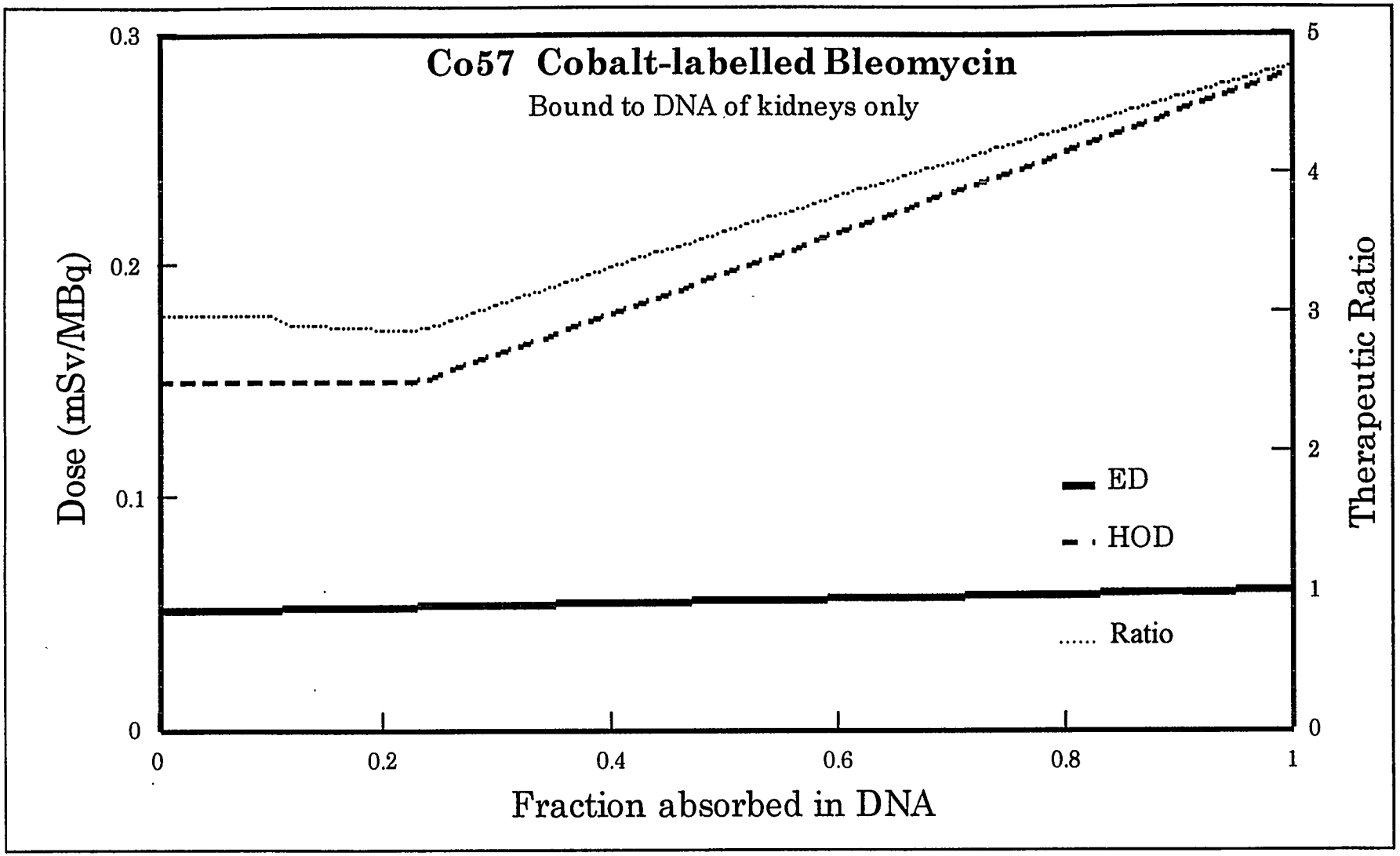
Co57 Cobalt-labelled Bleomycin
Bound to DNA of kidneys only
Dose (mSv/MBq)
Therapeutic Ratio
Fraction absorbed in DNA
ED
HOD
..... Ratio
0.3
0.2
0.1
0
5
4
3
2
1
0
0
0.2
0.4
0.6
0.8
1

Figure 8.

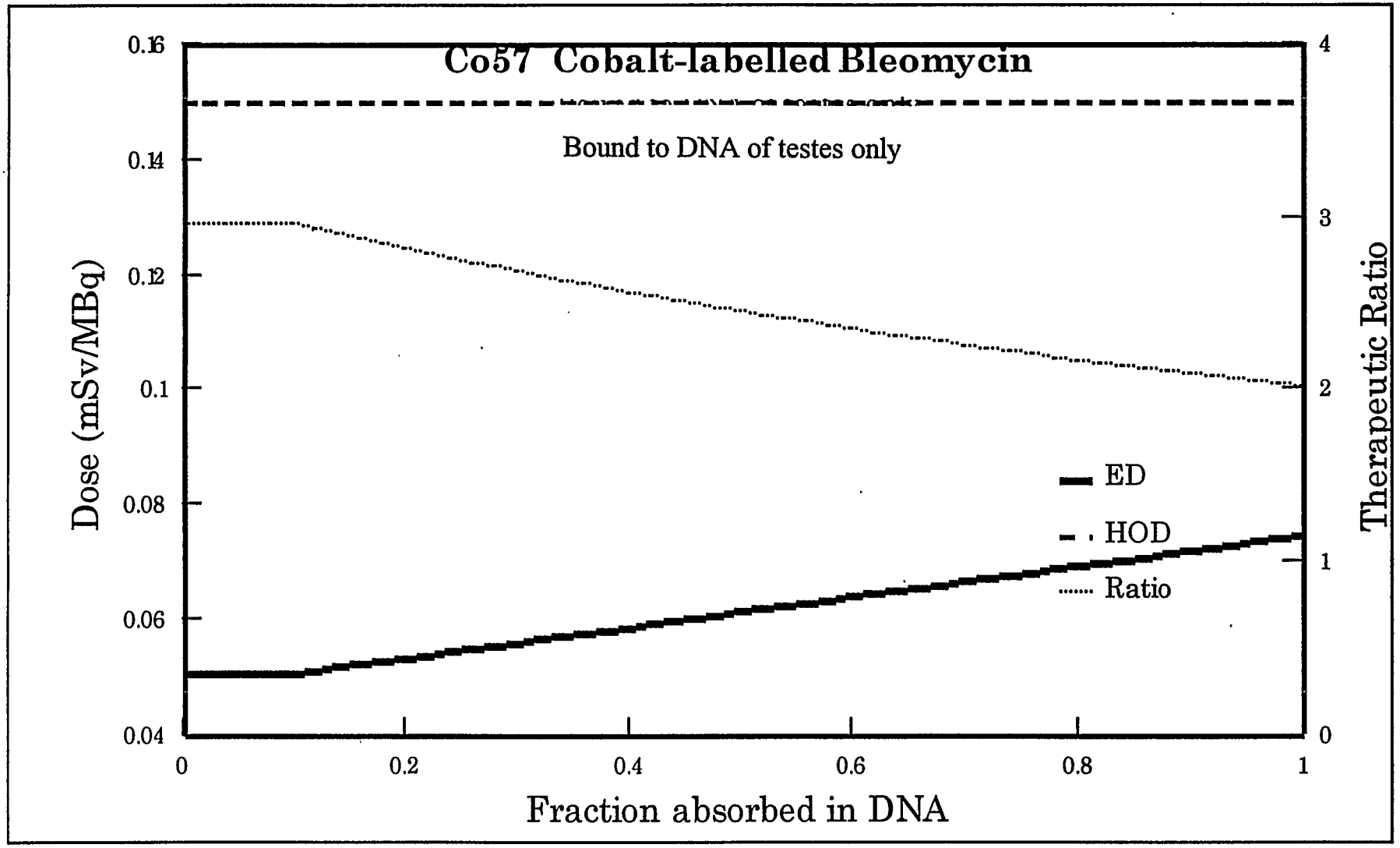
Co57 Cobalt-labelled Bleomycin
Bound to DNA of testes only
Dose (mSv/MBq)
Therapeutic Ratio
ED
HOD
Ratio
0.16
0.14
0.12
0.1
0.08
0.06
0.04
4
3
2
1
0
0
0.2
0.4
0.6
0.8
1
Fraction absorbed in DNA

Figure 9.

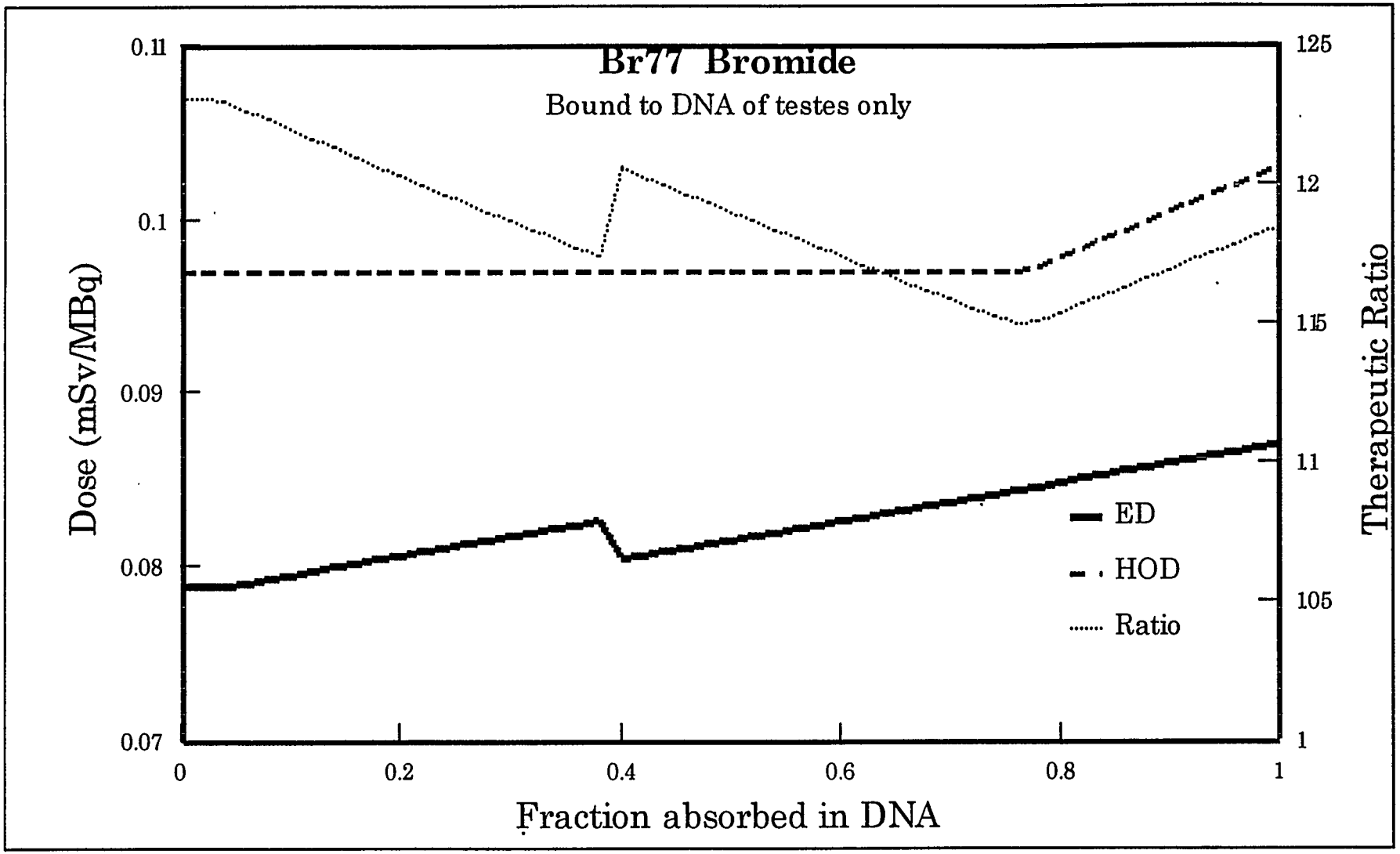
Br77 Bromide
Bound to DNA of testes only
Dose (mSv/MBq)
Therapeutic Ratio
Fraction absorbed in DNA
ED
HOD
Ratio
0.11
0.1
0.09
0.08
0.07
125
12
115
11
105
1
0
0.2
0.4
0.6
0.8
1

Figure 10.

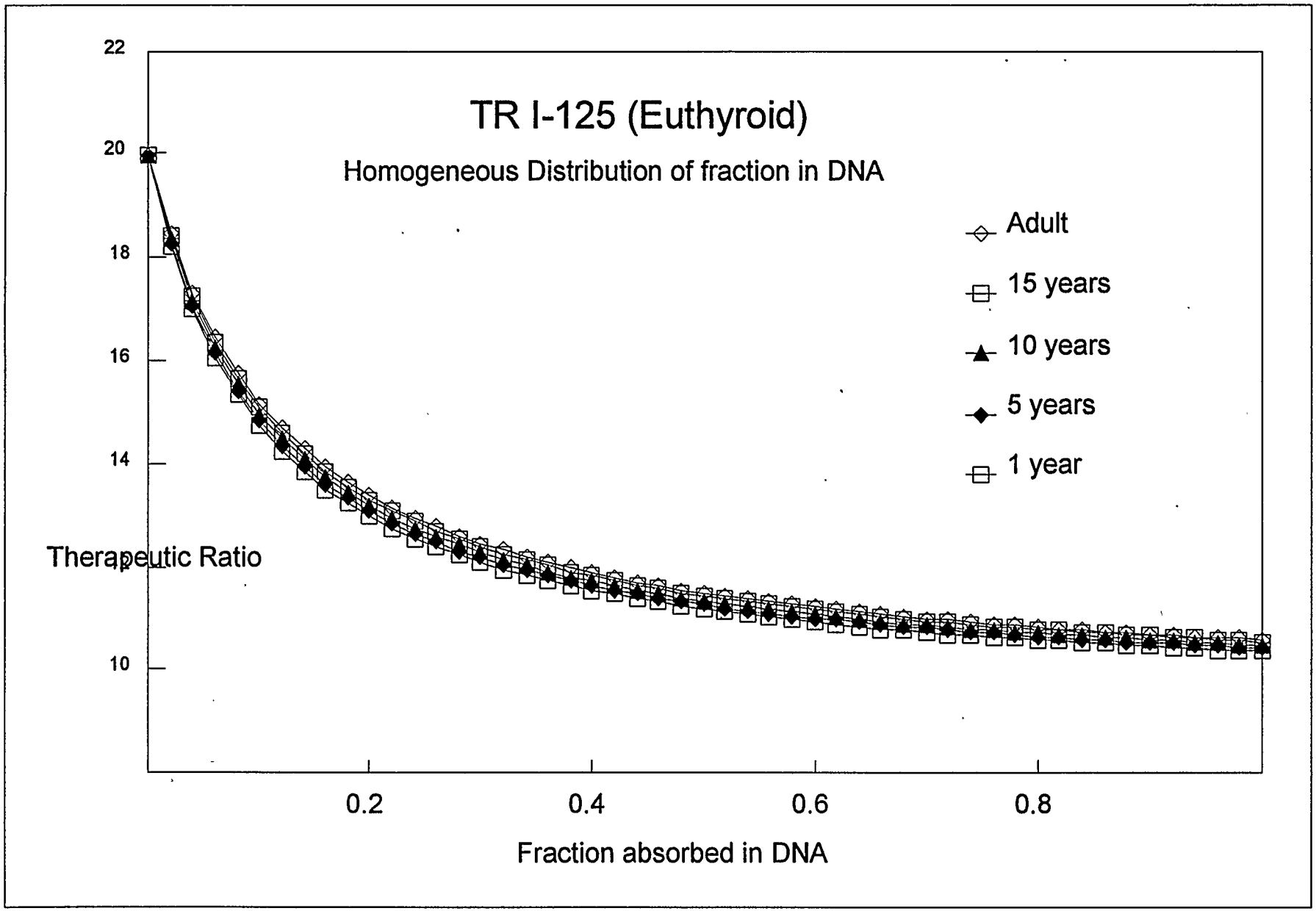
TR I-125 (Euthyroid)
Homogeneous Distribution of fraction in DNA
Adult
15 years
10 years
5 years
1 year
Therapeutic Ratio
22
20
18
16
14
12
10
0.2
0.4
0.6
0.8
Fraction absorbed in DNA

Figure 11.

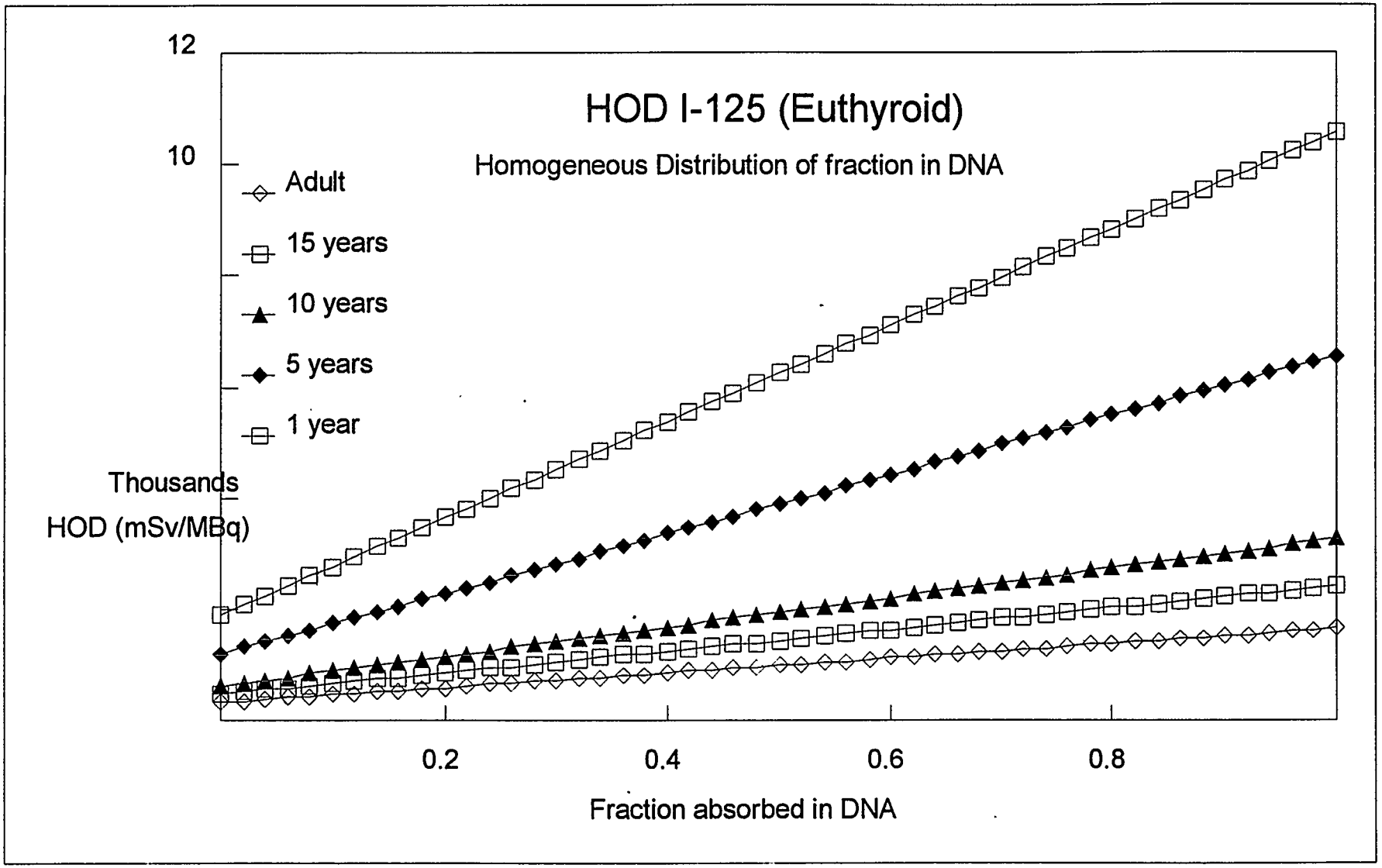
HOD I-125 (Euthyroid)
Homogeneous Distribution of fraction in DNA
Adult
15 years
10 years
5 years
1 year
12
10
Thousands
HOD (mSv/MBq)
0.2
0.4
0.6
0.8
Fraction absorbed in DNA

Figure 12.

The preliminary formalism and radiation weighting factors for equivalent dose calculations for Auger emitters should be updated as our understanding of the radiobiological effects of these radionuclides improves through experimental investigations. In this report values of f_{DNA} are assumed to be uniform within an organ or tissue, and further work is required to assess the impact of less uniform distributions.

REFERENCES

1. Persson L. The Auger electron effect in radiation dosimetry, Health Phys 67(5), 1994.
2. Dosimetry of Auger-Electron Emitting Radionuclides: Report No 3 of AAPM Nuclear MedicineTask Group No 6.
3. 1990 ICRP Recommendations of the International Commission on Radiological Protection, ICRP Publication 60, Permagon Press, 1991.
4. 1977 ICRP Recommendations of the International Commission on Radiological Protection, ICRP Publication 26, Permagon Press, 1977.
5. Age-dependant Doses to Members of the Public from Intake of Radionuclides: Part 2 Ingestion Dose Coefficients, ICRP Publication 67, Pergamon Press, 1993.
6. Radiation Dose to Patients from Radiopharmaceuticals, ICRP Publication 53, Pergamon Press, 1987.
7. Goddu MS et al, Multicellular dosimetry for micrometastases: Dependance of self-dose versus cross-cell dose to cell nucli on the type and energy of radiation and subcellular distribution of radionuclides, J. Nuc Med 35:521-530, 1994.

QUESTIONS

Mattsson: Could you comment on the possibilities of experimentally determining the f_{DNA}-values for various radiopharmaceuticals and organs in the future.

Wright: As you are well aware, there are enormous difficulties in establishing values of f_{DNA}. I only know of one study in which Zn-65 was found to be bound to the DNA of testes to a significant extent, I think between 0.3 to 0.5, I'm not sure. One way could be to perform estimates of the RBE using in-vitro studies and then work backwards to determine f_{DNA}.

Rao: I'd like to make comment on the slide you showed for I-125 in the thyroid which shows when ^{125}I is bound to the DNA in thyroid, the doses are very high. I don't want the audience to go home with a wrong impression that ^{125}I may be better than ^{131}I for thyroid therapy. The fact is that iodine does not bind to DNA in thyroid cells; it remains in thyroid follicles. The Auger electrons cannot effectively reach the cell nuclei. In fact, thyroid treatments with ^{131}I and ^{125}I showed that the Auger emitter ^{125}I is not more effective than ^{131}I. This has to be clearly understood.

Wright: As I said earlier, the radiopharmaceuticals I chose for my presentation were selected in order to emphasize the theoretical possibilities that exist. It was not my intention to suggest that large fractions of ^{125}I are bound to thyroidal DNA.

Humm: I think that it is probably naive to believe that there will be a single value of f_{DNA} for a given radiopharmaceutical in a given organ. Rather, it is more likely that a certain fraction of the cells have an f_{DNA} of say 0.0, a second fraction say 0.2, a third fraction perhaps 0.5 and so on.

Wright: I agree, but the number of possible permutations are infinite. Until such time as the values of f_{DNA} are available on an organ by organ basis, I would suggest that both the totally homogeneous and totally heterogeneous distributions of f_{DNA} are assumed. Then, the 'true' answer will be somewhere between.

BAYESIAN PARAMETER ESTIMATION FOR BIOKINETIC MODELS

Groer PG
Department of Nuclear Engineering
University of Tennessee
Knoxville, TN 37996-2300

ABSTRACT

In this paper we describe some aspects of the application of Bayesian methods to the estimation of parameters for biokinetic models and to the extrapolation of compartmental activities. These methods have several advantages of traditional methods. For example, the remaining uncertainty about the parameters is characterized by so called posterior probability densities after all available information has been used in the analysis. These densities can be graphed for a pictorial description of the uncertainty. The linkage among different compartments, expressed mathematically through coupled differential equations, is advantageous for parameter estimation in situations where activities in compartments are impossible to observe. The posterior densities can be used as prior densities should new data become available or they can serve as the starting point for patient-specific dosimetry. We use biokinetic data for ^{45}Ca to demonstrate these techniques. The methods described are, of course, general and can be applied to biokinetic data for any radiopharmaceutical.

INTRODUCTION

Estimation of parameters in compartmental models is a common problem in different scientific disciplines. We will focus here on Bayesian estimation techniques for parameters in biokinetic models.

The cornerstone of Bayesian inference is Bayes' theorem [1] as follows:

$$p(\theta|D) = p(D|\theta)p(\theta) / p(D) \qquad (1)$$

The left hand side of Equation 1, $p(\theta|D)$, is the so called posterior density of the parameter θ. It is equal to the Likelihood, $p(D|\theta)$, times the prior density $p(\theta)$. Parameter estimation using Equation 1 has some advantages over other methods.

1.. Prior information about parameters can be used by incorporating it into $p(\theta)$.

2. The estimation procedure is sequential. The posterior density can become the next prior, should new data become available.

3. Prediction of future outcomes is done with consideration of the existing parameter uncertainty.

4. Prior and posterior densities and probability based confidence intervals have natural interpretations. For instance, a 90% confidence interval [.5, 1.2] for the parameter θ simply means that the true value lies in this interval with probability 0.9. This interpretation is not valid for the classical confidence interval which needs a hypothetical repetition of identical experiments for its interpretation.

Complicated compartmental models have many parameters and it becomes computationally very challenging to calculate the marginal posterior distribution for each parameter. Here we will only consider estimation of biokinetic parameters for a two compartment model with excretion from one of the compartments. This model has three different parameters whose marginal distributions have to be determined by numerical integration. The detailed model, the observed data, the particulars of the estimation procedure and the resulting estimates are described in subsequent sections.

MODEL DESCRIPTION

The model used here links a bone surface compartment in dogs with an extracellular fluid compartment whose activity is assumed to be in equilibrium with a blood plasma compartment [2]. The differential equations describing the exchange of activity in the two compartments are

$$f_1' = -\rho f_1 + \sigma f_2 \qquad f_2' = \rho f_1 - (\sigma + \tau) f_2 \tag{2}$$

In Equations 2, f_1 is the specific activity in the bone surface compartment (μCi/mgCa) and f_2 is the plasma specific activity in the same units. There is leakage from the extracellular fluid compartment governed by the parameter τ. The solution of these differential equations is

$$\begin{aligned} f_1(t) &= C_1\left[e^{-\lambda_1 t} - e^{-\lambda_2 t}\right] \\ f_2(t) &= (C_1/\sigma)\left[(\rho - \lambda_1)e^{-\lambda_1 t} - (\rho - \lambda_2)e^{-\lambda_2 t}\right] \end{aligned} \tag{3}$$

where $C_1 = -27.1\sigma / \left[(\rho + \sigma + \tau)^2 - 4\rho\tau\right]^{1/2}$ and λ_1 and λ_2 are the eigenvalues of the system matrix for Equations 2

$$\begin{pmatrix} -\rho - \lambda, \sigma \\ \rho, -\sigma - \tau - \lambda \end{pmatrix}.$$

In terms of the parameters the two eigenvalues are given by

$$\lambda_1 = \left[\rho+\sigma+\tau+\sqrt{(\rho+\sigma+\tau)^2-4\rho\tau}\right]/2$$

$$\lambda_2 = \left[\rho+\sigma+\tau-\sqrt{(\rho+\sigma+\tau)^2-4\rho\tau}\right]/2$$

C_1 follows from the initial vector $\begin{Bmatrix}0.0\\27.1\end{Bmatrix}$. The unknown model parameters ρ,σ and τ are estimated using the available data on the compartmental activities with Equation 1 as described in the next section.

PARAMETER ESTIMATION

The parameter estimates are obtained by specializing a more general procedure developed by Box et al. [3]. The observed activities in the two compartments are represented by the two vectors

$$y_{1u} = \{y_{11}, y_{12}\cdots y_{1n}\}, y_{2u} = \{y_{21}, y_{22}\cdots y_{2n}\}, u = (1,2,3\ldots n).$$

The n observations for each compartment were selected to be at the same times x_u. Some of the observations for the two compartments [4] were not taken at the same times. These observations were left out since parameter estimation becomes more difficult computationally when missing observations are involved [5].

The observations are assumed to have normally distributed errors and are linked with the model through the following equations:

$$y_{1u} = f_1(x_u,\theta)+\varepsilon_{1u}, y_{2u} = f_2(x_u,\theta)+\varepsilon_{2u} \tag{4}$$

where u=1,2,...n and x_u is the same for each pair of observations y_{1u} and y_{2u}. The random errors ε_{iu} (i=1,2, u=1,2,...n) in Equation 4 are assumed to follow a multivariate normal distribution [3]. Under this assumption it is straightforward to construct the likelihood.

$$p(\vec{y}|\rho,\sigma,\tau,\Sigma) = (2\pi)^{-n}|A|^{n/2}e^{-1/2\sum_{i=1}^{2}\sum_{k=1}^{2}\Sigma_{ik}v_{ik}} \tag{5}$$

The symbol $\vec{y}$ in Equation 5 denotes the set of all observations y_{iu} and Σ or, in element notation, Σ_{ik} stands for the variance-covariance matrix [3]. The v_{ik} are defined as follows:

$$v_{ik} = \sum_{u=1}^{n}\left(y_{iu}-f_{iu}(x_u,\rho,\sigma,\tau)\right)\left(y_{ku}-f_{iu}(x_u,\rho,\sigma,\tau)\right). \tag{6}$$

|A| in Equation 5 is the determinant of the inverse of Σ. Using the following priors:

$p(\rho,\sigma,\tau) = $ const. and $p(\Sigma_{ij}) = |A|^{-3/2}$, the posterior density for the model parameters ρ,σ and τ is after integration over the Σ_{ij}'s is

$$p(\rho,\sigma,\tau|\vec{y}) \propto |v_{ij}|^{-n/2}. \tag{7}$$

To obtain the marginal posterior densities for individual parameters one has to integrate numerically over the other parameters. Graphs showing the posterior densities for ρ,σ and τ, respectively, are shown below.

By integrating over σ and τ one obtains the marginal posterior density for ρ (Figure 1). Similarly, we obtained the marginal density of σ by numerically integrating over the parameters ρ and τ (Figure 2).

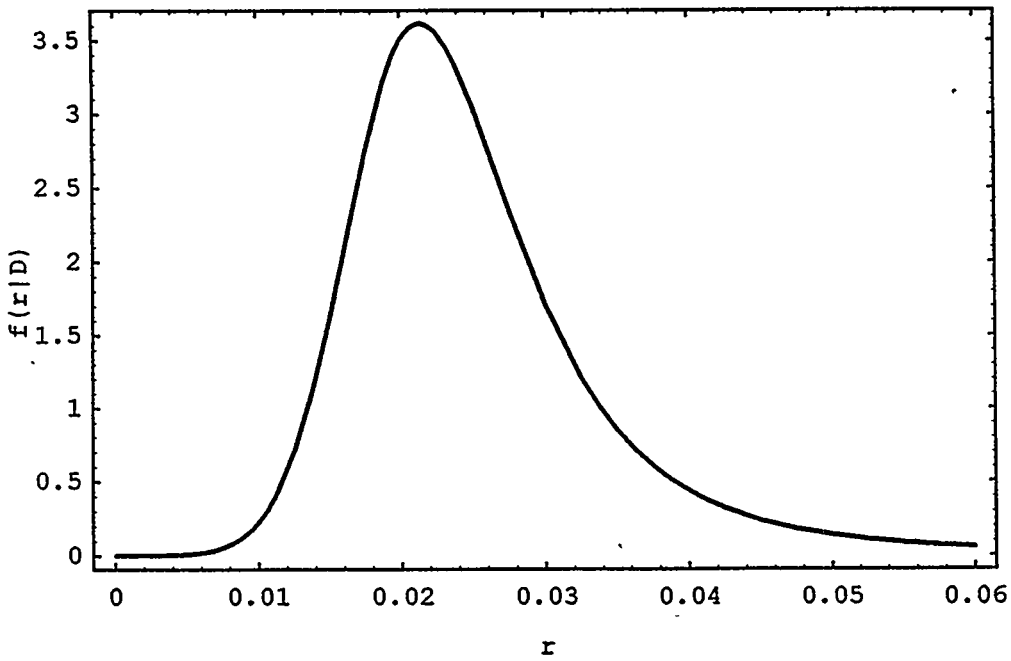

Figure 1. Marginal posterior density of ρ (r represents ρ).

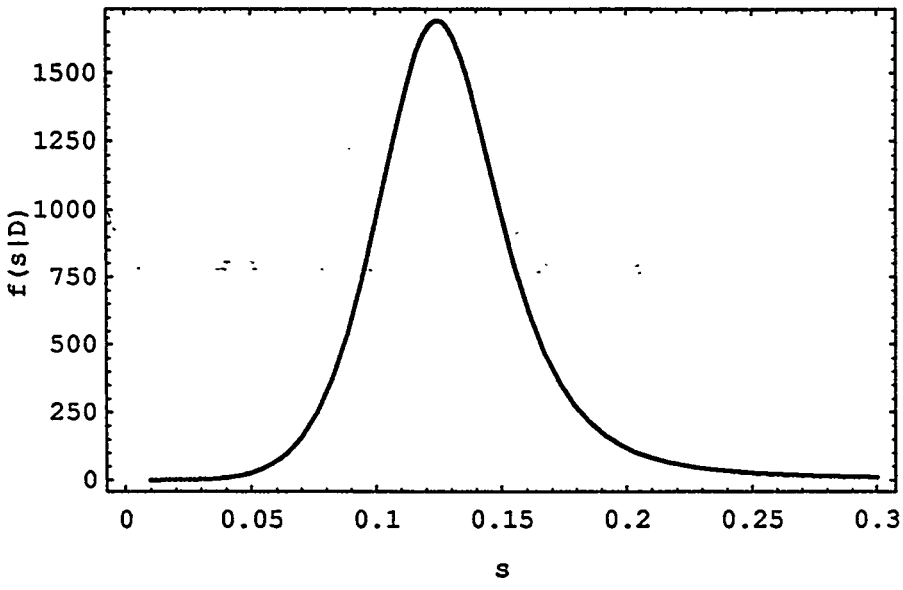

Figure 2. Marginal posterior density of σ (s represents σ).

Finally we determined the posterior density of τ by integrating over ρ and σ (Figure 3).

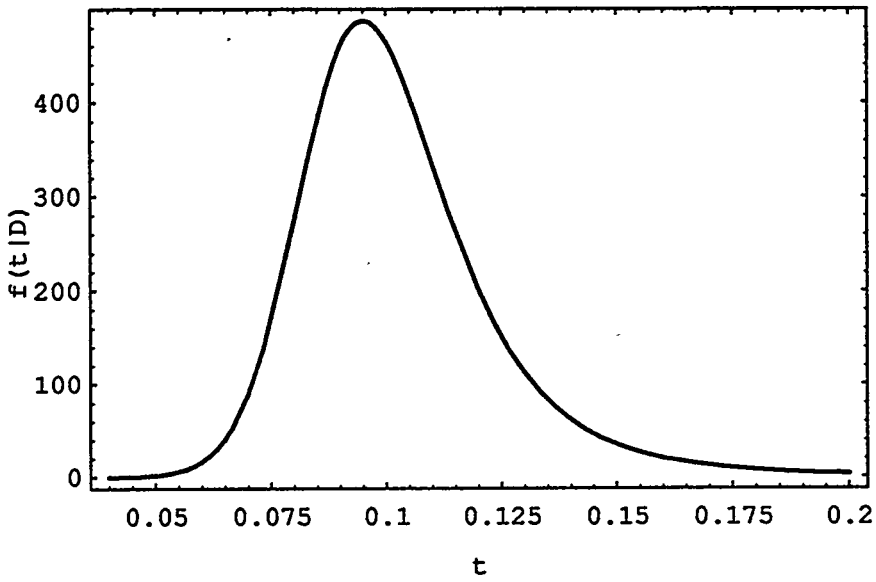

Figure 3. Marginal posterior density of τ (t represents τ).

The three figures show the remaining uncertainty about the model parameters in graphical form.

CONCLUSIONS

We demonstrated with a small data set describing the transfer of ^{45}Ca from plasma to bone surfaces how biokinetic parameters can be estimated using Bayesian methods. These methods yield as the final result posterior probability densities for the model parameters. These densities describe the remaining uncertainty about the parameters given the available information. Reduction of this uncertainty can be achieved if new information becomes available. The posterior densities become the new priors and are up-dated with the help of Bayes' theorem described by Equation 1. The sequential nature of Bayesian estimation is convenient since insufficient precision is displayed to the scientist and can be changed through further experimentation until precision satisfactory to the investigator has been reached. Point estimates for the parameters, like the posterior expectation or the mode of the posterior distribution, can easily be obtained. Such estimates do not provide any information about the uncertainty of the estimates and should not be used to predict future observations since prediction is influenced by parameter uncertainty. Instead prediction should be done with predictive densities [1] which incorporate uncertainty about parameters in the prediction process.

Another aspect of Bayesian analysis, not described here, is model comparison, which can be accomplished with the so called Bayes' factor [1]. This factor weighs the probability of the same data set under two different model assumptions. The "better" model assigns the higher probability to the given data.

Lastly, we want to point out that the uncertainty description offered by posterior densities as shown in Figures 1-3 is not based on hypothetical repetitions of experiments and, therefore, hypothetical data that have not been observed. This is the case for confidence intervals [6], which reflect the variation of estimates as unobserved data change.

REFERENCES

1. O'Hagan A. Kendall's Advanced Theory of Statistics, Vol.2b, pp 1-62, John Wiley & Sons, New York, 1994.
2. Groer PG and Marshall JH. Mechanism of calcium exchange on bone surfaces. Calc Tiss Res 12:175-192, 1973.
3. Box GEP and Draper NR, The Bayesian estimation of common parameters from several responses. Biometrika, 52:355-365, 1965.
4. Rowland RE. Exchangeable bone calcium. Clin Orthopaedics 49:233-248, 1966.
5. Stewart WE and Sorenson JP. Bayesian estimation of common parameters from multiresponse data with missing observations. Technometrics 23:131-141, 1981.
6. Neyman J. Frquentist probability and frequentist statistics. Synthese 36:97-115, 1977.

QUESTIONS

Sparks: Has there been significant progress lately in applying the Bayesian method to more complex compartmental models?

Groer: Yes, we have made some progress. One of my students is working on a three-compartment catenary model and he has also created probability contour plots for two parameters.

Sgouros: How does the probability distribution relate to parameter uniqueness?

Groer: The posterior probability density or distribution characterizes the remaining uncertainty about the parameter. Point estimates with standard deviations can be easily obtained from the posterior densities using standard formulas for mean and variance.

C. Johnson: Does the Bayesian mathematical technique used here differ from 'fuzzy' mathematics?

Groer: Yes, the Bayesian approach uses probability and its laws to measure uncertainty and calculate with uncertain quantities. This is not the case for fuzzy methods.

DEVELOPING AND TESTING INTEGRATED MULTICOMPARTMENT MODELS TO DESCRIBE A SINGLE-INPUT MULTIPLE-OUTPUT STUDY USING THE SAAM II SOFTWARE SYSTEM

Foster DM and Barrett PHR
Center for Bioengineering 352255
University of Washington
Seattle, WA 98195-2255

ABSTRACT

The fundamental problem in internal dosimetry is determining the radiation absorbed dose from an administered amount of a radiolabeled substance. As measurement devices become more sophisticated, it is possible to design more complex input-output studies. To interpret the resulting data requires models which can integrate known information about the system under study while simultaneously describing the data. In this paper, we will illustrate how to develop and test a model structure for a single-input multiple-output study using the SAAM II software system. This system has been designed to make the use of sound modeling principles easy. It will be assumed that a known amount of a radiolabeled substance was injected as a bolus into plasma, that this substance can bind to and be taken up by red cells, that its only route of elimination is through the urine, and that external measurements are possible over a target organ. The steps in developing a model structure will make use of SAAM II's forcing function capability to show how the system can be decoupled; this will permit us to postulate model structures for the various subsystem accessible to measurement. We will then show how to use this information to postulate a system model, and how to test the system model structure. This will permit us to comment on those parts of the system not accessible for experimental measurement. We will then show how to estimate the areas under the curves for the different components of the system and conclude with a general discussion of how to test for goodness-of-fit and model order.

INTRODUCTION

To determine the radiation absorbed from a given administered amount of a radiolabeled substance, i.e. a radiopharmaceutical (herein abbreviated RP), requires a sophisticated experimental design in which the material of interest is injected into plasma, and sequential plasma samples are taken together with data from target tissues of interest. In designing such experiments, one must be aware, to the best of one's ability, with which tissues the RP interacts. In the example discussed here, it is assumed that the RP can be taken up by red blood cells, and that its only loss from the body is via urinary excretion. Thus in designing the experiment, both plasma and red cells were isolated for quantitation of radioactivity, and 24-hour urine samples were taken in order to characterize

elimination of the RP. Finally, it is assumed that the RP can be quantitated via external counting over an organ.

Clearly the ideas presented herein can be modified to deal with more or less complicated situations. The main idea, however, as discussed in the next section, is that plasma can act as a forcing function to drive the rest of the system. That is, the RP is carried only in plasma, meaning that the only way the RP can move from one part of the body to another is through the plasma. This means that there can be no direct pathway between, for example, two organs.

The data to be used are given in Figures 1-4. It is assumed that a known amount of a RP was given as a bolus into plasma. By dividing all samples by this amount, the data have been converted either to fraction of amount injected per ml or fraction of amount injected.

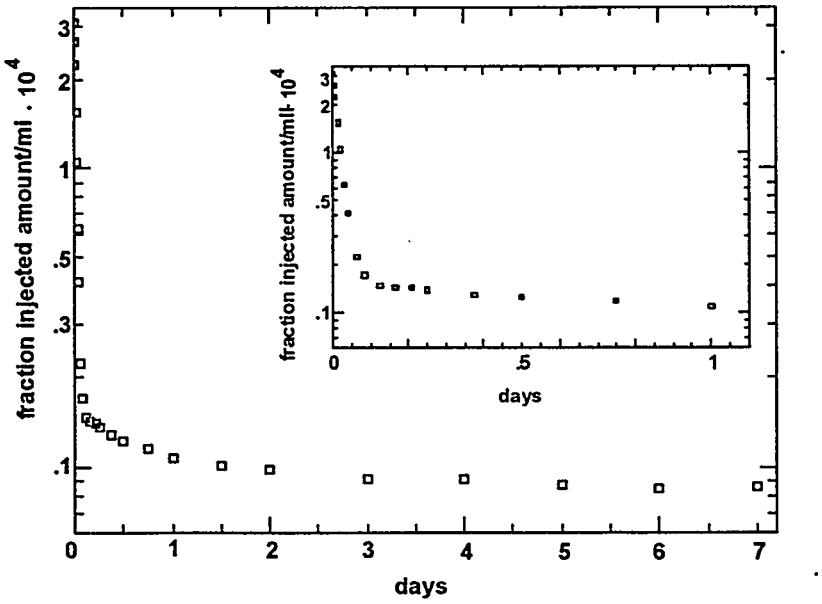

Figure 1. Plasma data collected following a bolus injection of labeled material into plasma. Data were collected at 2, 5, 10, 20, 30, 40 and 45 minutes, 1, 1.5, 2, 3, 4, 5, 6, 9, 12 and 18 hours, and 1, 2, 3, 4, 5, 6 and 7 days. Data are expressed in terms of fraction of amount injected amount per ml of plasma. The decay in plasma during the first day is shown in the inset.

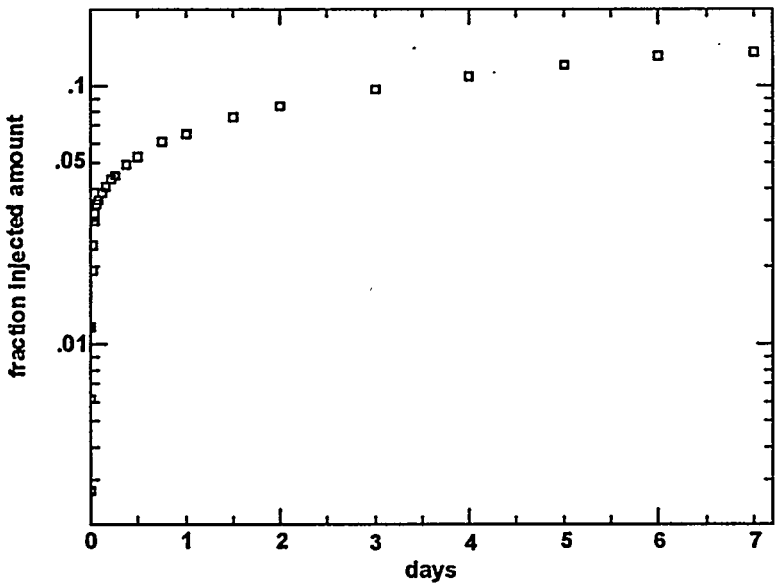

Figure 2. Red cell data collected following a bolus injection of labeled material into plasma. Data were collected at the same time plasma data were collected. Data are expressed as a fraction of the total amount injected.

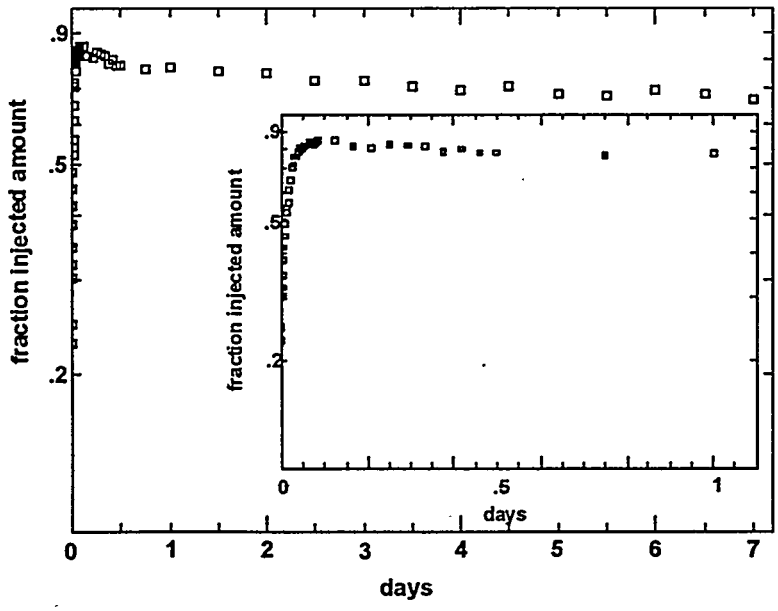

Figure 3. Data obtained from an external counter placed over a target organ. Data were collected at 1, 2, 4, 5, 8, 10, 12, 14, 16, 18, 20, 25, 30, 35, 40, 45, 50, 55, 60, 65, 70, 75, 80, 85, 90, 95, 100, 105, 110, 115 and 120 minutes, 3, 4, 5, 6, 7, 8, 9, 11, 12 and 18 hours, and 1, 1.5, 2, 2.5, 3, 3.5, 4, 4.5, 5, 5.5, 6, 6.5 and 7 days. Data are expressed in terms of fraction of amount injected. The appearance of radioactivity during the first day is shown in the inset.

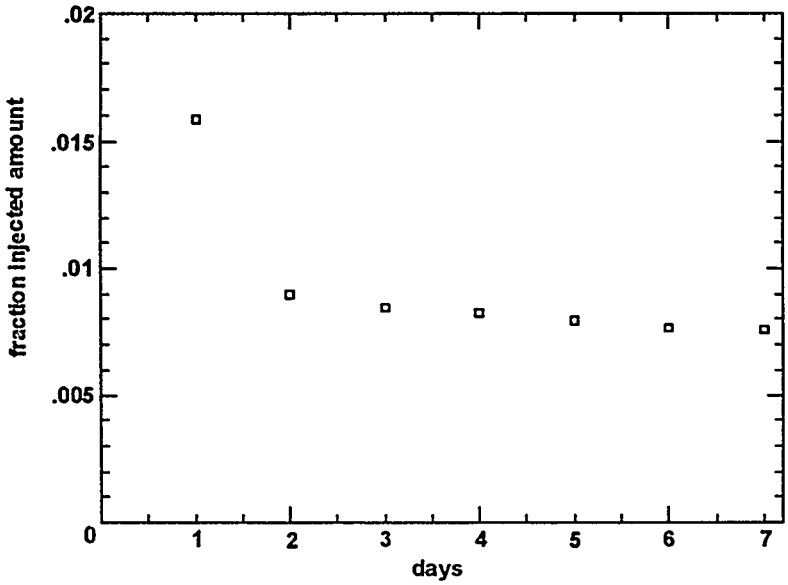

Figure 4. Twenty-four hr urine collections of RP. Data are expressed in terms of fraction of amount injected.

The problems discussed in the next sections relate to postulating a multicompartmental model structure which is compatible with these data, and using this model to estimate areas under various curves of interest. This will illustrate how to use many of the modeling tools incorporated in the SAAM II software system (1).

USING FORCING FUNCTIONS TO DECOUPLE THE SYSTEM

What is a forcing function, and what does it mean to decouple the system (2,3)? For the data given above, suppose we want to postulate a model structure for the red cell system, and describe elimination of the radiopharmaceutical through the urine. Since the only way the RP can interact with the red cells is via the plasma, and the only way it can leave the body is via the plasma through the urine, we can sketch the following relationships among plasma, red cells and urine (Figure 5). This figure indicates that the RP can exchange with plasma, and that there is a unidirectional loss from plasma into the urine.

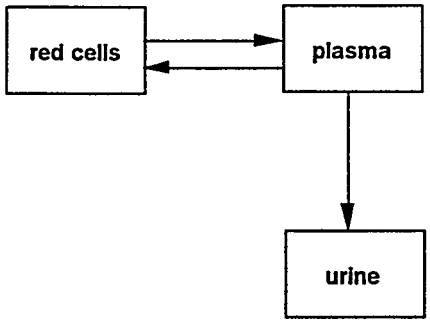

Figure 5. The metabolic relationships of the RP of interest among plasma, red cells and urinary excretion.

Assume that the RP in plasma is kinetically homogeneous. This means that the RP exists free in the plasma and does not bind in any significant way to any of the plasma proteins (or if it does, the binding equilibrium is too fast to be "seen" in these data). This assumption indicates that the plasma pool can be described by a single compartment in a multicompartmental model.

Without any a priori knowledge of the system, we do not know what kind of a multicompartmental structure will be required to describe red cells or urinary excretion. As a first attempt, we might want to try the following model (Figure 6).

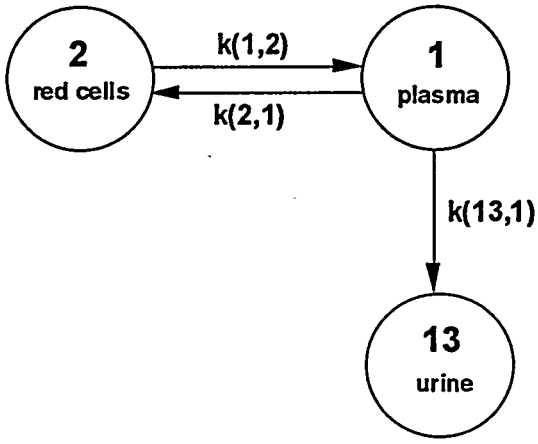

Figure 6. A potential model structure describing the interrelationships among plasma, red cells and urinary excretion.

The differential equations describing this model are

$$\frac{dq_1}{dt} = -(k(2,1)+k(13,1))q_1(t)+k(1,2)q_2(t) \quad q_1(0)=1, \qquad [1]$$

$$\frac{dq_2}{dt} = k(2,1)q_1(t)-k(1,2)q_2(t) \text{ and} \qquad [2]$$

$$\frac{dq_{13}}{dt} = k(13,1)q_1(t). \qquad [3]$$

Obviously this model will not completely describe the system, as the organ data are not represented. In particular, $q_1(t)$ will not describe the plasma data. However, if the plasma data were known, then the rate constants $k(2,1)$, $k(1,2)$ and $k(13,1)$ could be determined. That is, what is necessary for these rate constants to be determined, and to determine if compartments 2 and 3 can describe red cell and urine data respectively, is that these systems "see" what is actually in plasma.

To do this, we use the forcing function machinery in SAAM II to substitute for $q_1(t)$ in Equations 2 and 3, a function which has the characteristics of the plasma decay shown in Figure 1. In SAAM II, such a forcing function is denoted as $q_1.FF$. With the forcing function, Equations 1 - 3 become

$$\frac{dq_1}{dt} = -(k(2,1)+k(13,1))q_1(t)+k(1,2)q_2(t) \quad q_1(0)=1, \qquad [4]$$

$$\frac{dq_2}{dt} = k(2,1)q_1.FF(t)-k(1,2)q_2(t) \text{ and} \qquad [5]$$

$$\frac{dq_{13}}{dt} = k(13,1)q_1.FF(t). \qquad [6]$$

Notice Equations 1 and 4 are the same; the forcing function has no effect on $\frac{dq_1}{dt}$. However, in Equations 5 and 6 $q_1(t)$ is replaced with $q_1.FF(t)$. The system has been decoupled in the sense that we can now deal independently with the red cell and urinary subsystems.

Once we have a proposed model structure for these two subsystems, we will deal with the organ subsystem. At this point, we will have known model structures for the three subsystem models, and once we can reconstruct the plasma curve, we know these structures will be valid.

First we must postulate a functional description for $q_1.FF(t)$ and then develop and test model structures for the red cell and urinary subsystems. With the red cell model, we can postulate a structure for the organ subsystem estimating at the same time the blood volume of the organ.

The Forcing Function

To create the forcing function $q_1.FF(t)$, we must create a functional description of the data shown in Figure 1. There are two ways this can be done in SAAM II; both are invoked by opening the attribute box associated with compartment 1 shown in Figure 6. The first option to create $q_1.FF(t)$ is internally by letting SAAM II perform a linear interpolation between sequential pairs of data. Clearly this will recreate the shape of the input curve, but if the data are noisy, there can be problems.

Alternatively, we can write an expression directly for $q_1.FF(t)$; this normally will smooth the noise in the data. For the example here, we will describe the data shown in Figure 1 by a sum of four exponentials

$$plasma = \frac{1}{V}(A_1e^{-a_1t}+A_2e^{-a_2t}+A_3e^{-a_3t}+A_4e^{-a_4t}) \qquad [7]$$
$$A_1+A_2+A_3+A_4=1.$$

We need to make some observations about Equation 7 First, since the units of the plasma data are fraction of amount injected per ml, the units of Equation 7 are in these terms. However, the units of the forcing function must be in terms of fraction of amount injected. The constraint that the sum of the coefficients A_1, A_2, A_3 and A_4 equals 1 is equivalent to the bolus injection of 1 into the system. Dividing the sum by the unknown parameter V will permit making an estimate of the plasma volume and thus assure that the units of Equation 7 are fraction of amount injected per ml. When a fit has been obtained, the forcing function $q_1.FF(t)$ can be written

$$q_1.FF(t) = A_1e^{-a_1t}+A_2e^{-a_2t}+A_3e^{-a_3t}+A_4e^{-a_4t}. \qquad [8]$$

A fit of Equation 7 to the data given in Figure 1 is shown in Figure 7.

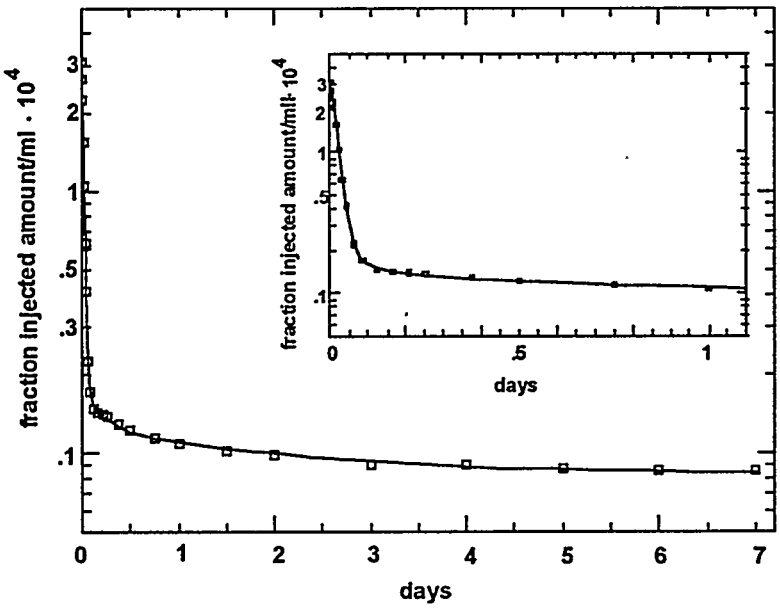

Figure 7. A fit of the plasma data given in Figure 1 to the sum of exponentials given by Equation 7. See text for additional explanation.

It is important to emphasize that Equation 7 is used to provide a functional description of the data given in Figure 1. It is not important to know the statistics of the fit; all that we are interested in is an accurate description of the shape of the plasma curve! In fact, if we tried to fit Equation 7 to these data using SAAM II, we will obtain a best fit, but learn the model is underdefined.

For this system, an estimate for the volume V is 2975 ml, and Equation 8 can be written for this example as follows:

$$q_1.FF(t) = 0.95e^{-62t} + 0.013e^{-5t} + 0.013e^{-0.5t} + 0.0247e^{-.0001t}. \qquad [9]$$

Equation 9 will be entered as the forcing function, and the individual subsystem models will be determined as described below.

The Red Cell System

To determine the red cell system model, we will first try the single compartment model suggested by Figure 6. An example of the model constructed in SAAM II is shown in Figure 8.

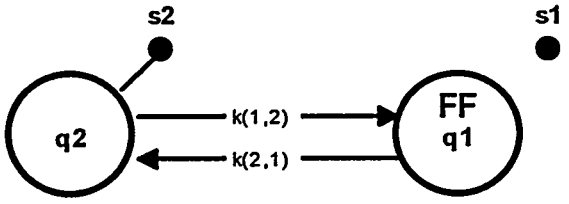

Figure 8. A model to determine the structure of the red blood cell system.

Compartment 1 is a forcing function with the equation given by Equation 9. Compartment 2 represents the red blood cell system. The bullets labeled "s1" and "s2" are samples. Sample "s2" is associated with the red blood cell data. Sample "s1" associated the forcing function with the plasma data, and is used to be sure the forcing function has been correctly specified; "s1" is not connected to compartment 1 because the sample equation is written in terms of $q_1.FF(t)$ and not $q_1(t)$ (1).

The differential equation for the red blood cell system represented by this model is

$$\frac{dq_2}{dt} = k(2,1)q_1.FF(t) - k(1,2)q_2(t) = \\ k(2,1)*(0.95e^{-62t} + 0.013e^{-5t} + 0.013e^{-0.5t} + 0.0247e^{-.0001t}) - k(1,2)q_2(t). \quad [10]$$

If this model is fitted to the red blood cell data, we will see the single compartment system for the red blood cells is not sufficient, and that a second compartment must be added. At this point, however, we have a choice of model structures, and to select the most appropriate, we must rely on what is known about the RP and its interaction with red blood cells. The two different model structures are shown in Figure 9.

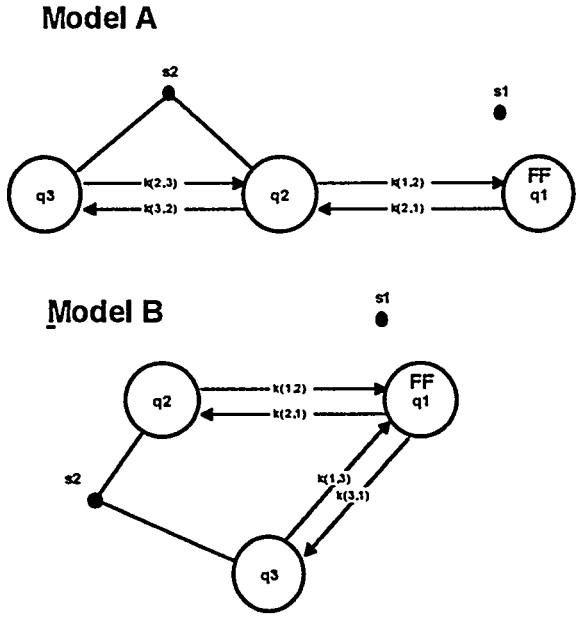

Figure 9. Two different models incorporating a second compartment into the red blood cell system. The red cell system is represented by compartments 2 and 3, and the red cell sample "s2" is the sum of the material in the compartments, $s2 = q2 + q3$; s1 was described in Figure 8.

The two models shown in Figure 9 have different physiological interpretations. It is essential to realize that both will produce the same fit to the data. Model A is consistent with the RP interacting with the red blood cell membrane, k(2,1). The RP can then be internalized, k(3,2), or return to plasma, k(1,2). The RP internalized can also bind to the interior of the membrane, k(2,3). Model B is consistent with there being two different classes of red blood cells, and that the RP has different

kinetic interactions with both classes. In general it is difficult to support this hypothesis, and so we will choose Model A.

It is of interest to note that derived parameters of interest can also be estimated from the primary parameters, the k(i,j). For example, if we wanted to know the fraction of RP bound to the red blood cell membrane that was internalized, we could write

$$frac\_in = \frac{k(3,2)}{k(3,2)+k(1,2)}. \qquad [11]$$

In this expression, the denominator $k(3,2)+k(1,2)$ is the total transfer from compartment 2, so *frac_in* is the fraction contributed by $k(3,2)$.

Thus if we assume that the RP of interest can bind to the red cell membrane and be internalized, then Model A is the model of choice. Figure 10 shows the best fit of this model to the red blood cell data, as it is the shape of the plasma curve as represented by the forcing function that is driving the system.

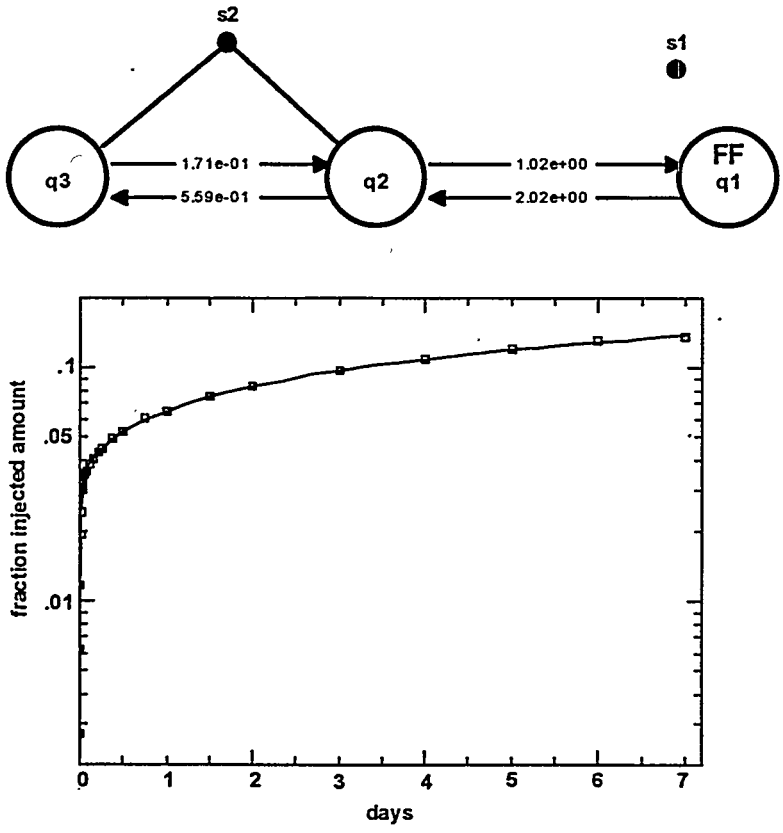

Figure 10. The best fit of Model A shown in Figure 9 to the red blood cell data. The model is shown at the top with the rate constants producing the best fit. The data (squares) and model prediction (continuous line) are shown in the bottom panel. Samples *s*1 and *s*2 are described in Figure 9.

It appears that the two-compartment system represented by compartments 2 and 3 will produce a good description of the red blood cell system. Technically, we should try a third compartment, say

compartment 4 exchanging with compartment 3, to determine if yet another component is required. In this situation, such a compartment is not justified; this can be tested using the tests for goodness-of-fit and model order discussed in a later section.

The Urinary Excretion System

As noted in Figure 4, the urine data represent 24-hour urine collections, and the data are expressed in terms of fraction of injected amount excreted during a 24-hour period. To simulate such an experimental protocol in SAAM II, we take advantage of the change condition capability. Basically, this permits us to reset the value for the urine compartment equal to zero at 24-hour intervals. The single-compartment urine system described in Figure 6 can be implemented in SAAM II as indicated by Figure 11.

It is important to note that this model is consistent with some urinary excretion happening immediately. If this were not the case, then an intermediary compartment could be placed between the forcing function and compartment 13, or if needed, the delay element in SAAM II could be used. The best fit of the model shown in Figure 11 to the urinary excretion data shown in Figure 4 is shown in Figure 12.

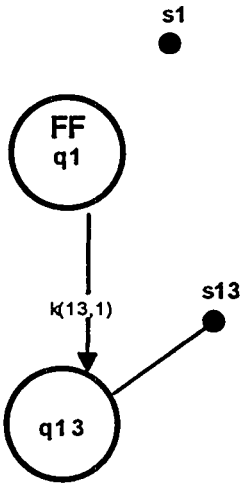

Figure 11. A single-compartment urinary excretion system being driven by the plasma forcing function. The model indicates there is no delay in appearance is RP in the urine. The sample *s*1 has been described previously; the sample *s*13 is the 24-hour excretion of RP.

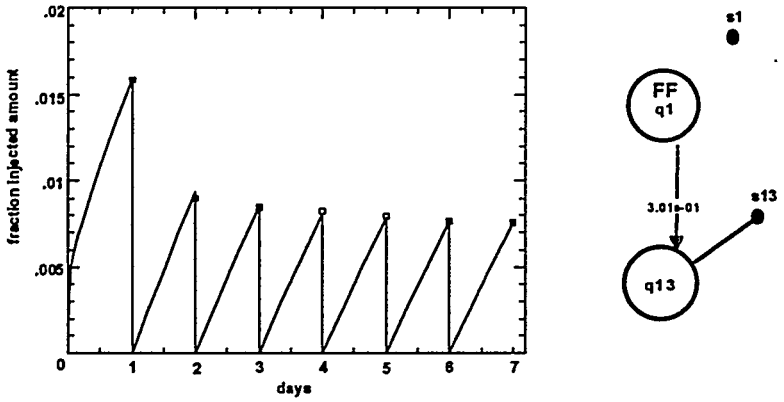

Figure 12. The best fit of the model shown in Figure 11 to the urinary excretion data. The model is shown to the right hand side of the fit, and indicates k(13,1)= 0.301/day. Notice the saw-tooth nature of the model predicted values; this reflects the fact that the data are 24-hour collections, hence the contents of compartment 13 are set equal to zero daily after the last collection. The samples $s1$ are $s13$ are described in Figure 11.

The Organ System

We are now in a position to postulate a model structure to describe the organ data. Remember that the organ data were collected using an external counter, and that this counter will quantitate material both in the organ cells and in the blood. That is, a fraction of the material "seen" by the counter will be due to the RP in blood and the rest presumably due to the RP in the organ's cells.

Suppose a two-compartment system is required to account for the radioactivity seen by the external counter. Then we are in a situation similar to that described above for the red blood cells. Specifically, there can be one compartment which exchanges with plasma and a second exchanging with this compartment; as before, this model would be consistent with the RP interacting with the organ cell's membrane with the possibility for uptake intracellularly. The second possibility would be two compartments exchanging with plasma. This would be consistent with the organ containing two different cell types with the RP having different kinetics with each type. In organ systems such as the liver this is not an unreasonable situation, and care should be taken in deciding which structure to use.

These two situations are illustrated in models A and B in Figure 13. Notice that the red blood cell subsystem is included; this is because it is assumed that plasma, represented by the forcing function $q_1.FF(t)$, and the red cells, represented by the sample $s2 = q2 + q3$, can account for the RP in the blood. The urinary subsystem is not included since it plays no part in quantitating the RP in the organ. For both model A and B shown in Figure 13, the measurement equation for the RP as seen by the external counter in the organ is

$$s3 = fraction * (q_1.FF(t) + s2) + q4 + q5. \qquad [12]$$

The parameter *fraction* can be estimated from the data as the fraction of blood in the organ. This is important information, as the blood volume of many organs is known; the estimate of the parameter *fraction* can be checked against the known blood volume as a step in validating the model structure.

The best fit of Model A to the organ data shown in Figure 3 is given in Figure 14. This indicates that a two-compartment subsystem is sufficient to describe the organ data. As with the red

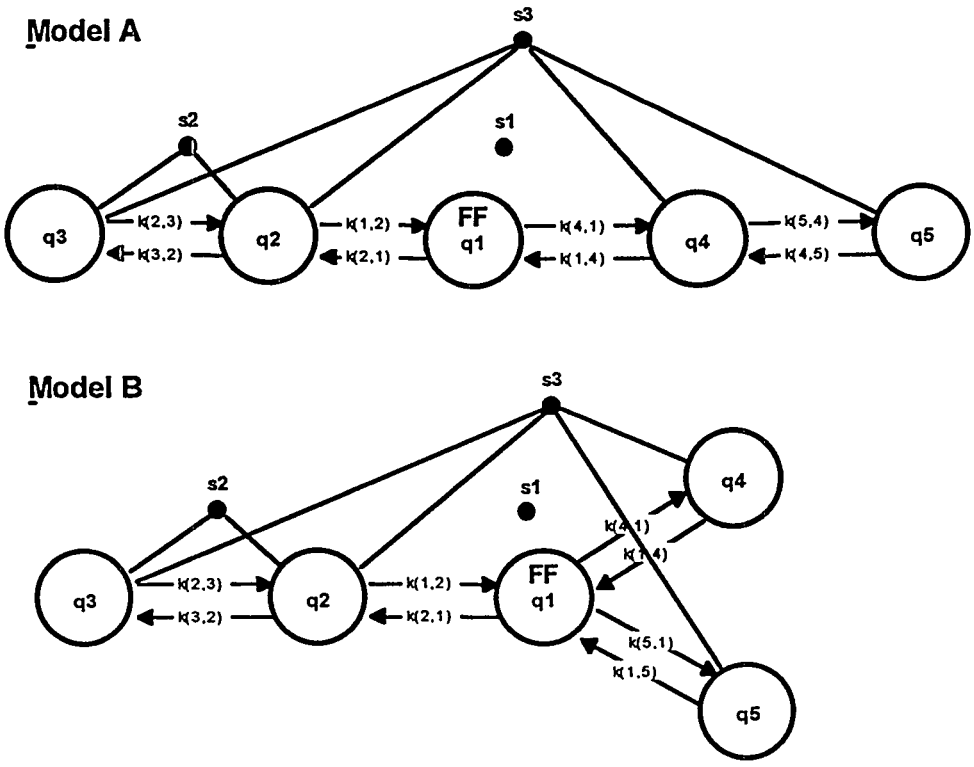

Figure 13. Two different multicompartmental models which can describe the organ kinetics of the RP being studied. See text for additional explanation. Samples *s*1 and *s*2 have been described previously; sample *s*3 accounts for the RP data seen by the external counter over the organ.

blood cell subsystem, we can add a third compartment to see if it improves the fit, and use the tests for goodness-of-fit and model order discussed below to determine the best model. However, as noted, we cannot distinguish with these data the difference between Models A and B. To do this would require additional experiments.

POSTULATING THE SYSTEM MODEL STRUCTURE

What is known at this stage of the model development process is that given the correct shape of the plasma input function, we have subsystem models which can describe the data. The system has thus been truly decoupled in that we have examined the subsystems first; we must now build the additional structure to account for the totality of the data. This is a two-step process. In the first step, we postulate the plasma model given the known structure and parameter values for the individual subsystems. In the second step, all parameters are permitted to be adjustable so that we can generate the best estimates for the system model parameters and their uncertainties. This is the first step towards evaluating the model; the last steps, which are discussed below, deal with tests for goodness-of-fit and model order.

The Plasma Model

In determining the plasma model, we first create a model in which all subsystems are incorporated with their rate constants fixed, remove the forcing function on plasma, and ask whether or not the plasma data can be fitted. Figure 15 describes this situation.

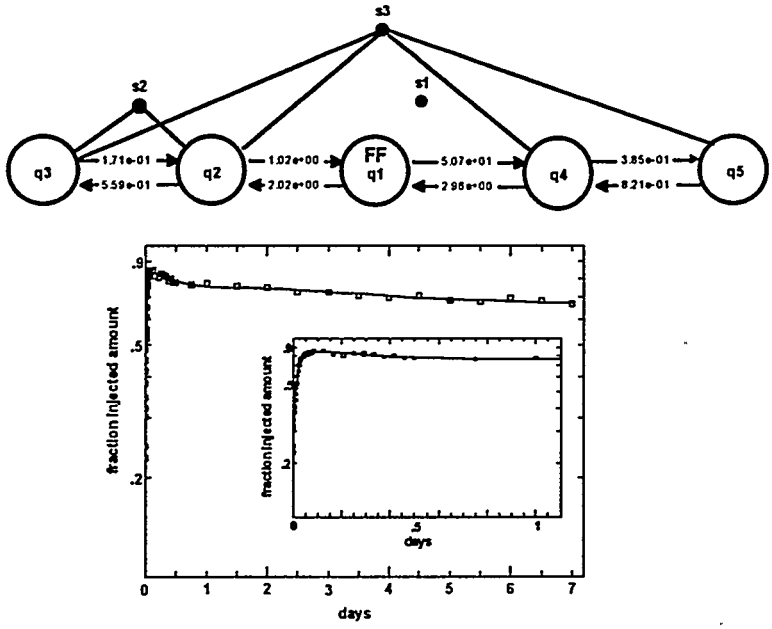

Figure 14. The best fit of Model A in Figure 13 to the organ data shown in Figure 3. The top figure shows the model and the parameter values for the exchange rate constants. The lower shows the fit with the inset giving the details for the first day. Samples $s1$ and $s2$ have been described previously; sample $s3$ accounts for the RP data seen by the external counter over the organ.

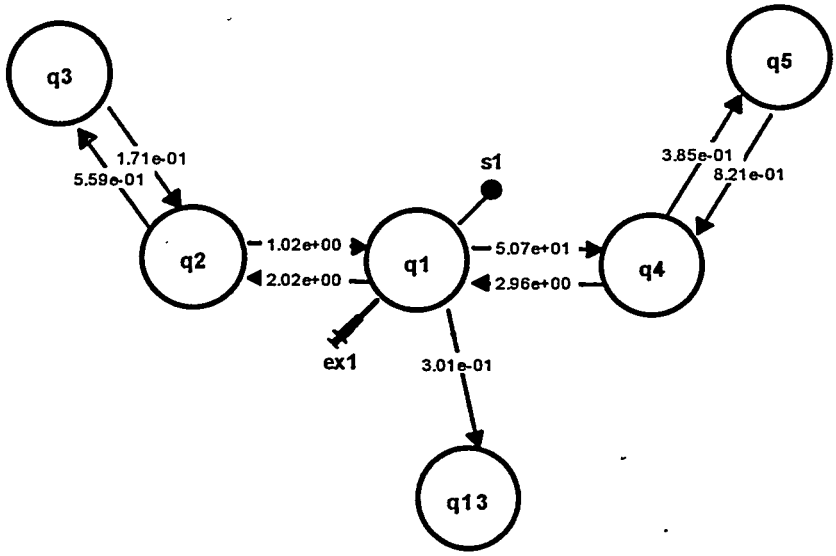

Figure 15. A model incorporating all known subsystems with rate constants fixed. Notice $s1$ is now attached to compartment 1; this is because the measurement equation is now given by Equation 12. The input $ex1$ represents the bolus input into Compartment 1. See text for additional explanation.

In removing the plasma forcing function, the differential equation for the compartments other than compartment 1 change from the form given in Equations 5 and 6 back to the form given by Equations 2 and 3. Now, however, since there is no function driving the system, we must specify $q_1(0)$ of Equation 1. In Figure 15, this is represented by "ex1", and is a bolus equal to 1. Since the units of the plasma data are fraction of injected amount per ml, the measurement equation $s1$ becomes

$$s1 = q1 / vol. \qquad [13]$$

The parameter *vol* provides an estimate for the plasma volume. With all the rate constants in the model shown in Figure 15 fixed, this is the only adjustable parameter. This model will either fit the plasma data or it will not. If it does, then the subsystems for which data are available completely specify the total system, and the structure given in Figure 15 would be the proposed system model structure.

If, on the other hand, this model does not fit the plasma data, then additional structure must be proposed. Such a situation is illustrated in the model shown in Figure 16. In this model, an additional compartment that exchanges with plasma, compartment 7, has been added. In this case, besides *vol* being an adjustable parameter, there are two adjustable rate constants, $k(7,1)$ and $k(1,7)$. It is important to realize that the rate constants characterizing the subsystems remain fixed. This is because we are trying to build a structure necessary to describe the plasma data, and if the subsystem rate constants were allowed to adjust, we would loose the subsystem fits. This is an important point behind the decoupling process, and the process of reconstructing the input function plasma.

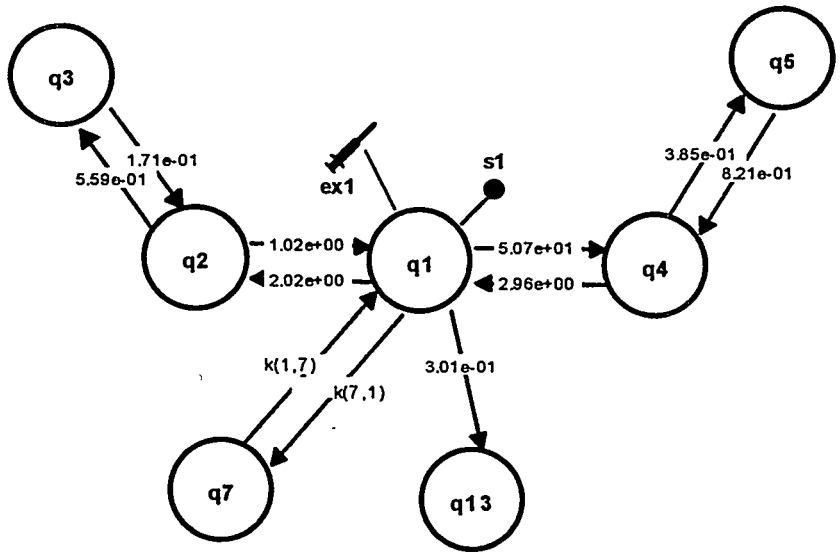

Figure 16. An expanded model to describe the plasma data. See text for additional explanation.

In the example we are discussing here, the model shown in Figure 16 can describe the plasma data, and hence it is proposed as the system model structure.

The System Model

With the system model structure proposed, it remains only to let all parameters of this system model adjust to fit the data. In the previous step, the subsystem parameters were fixed because we wanted to know the structure needed to recreate the plasma curve. Figure 17 shows the system

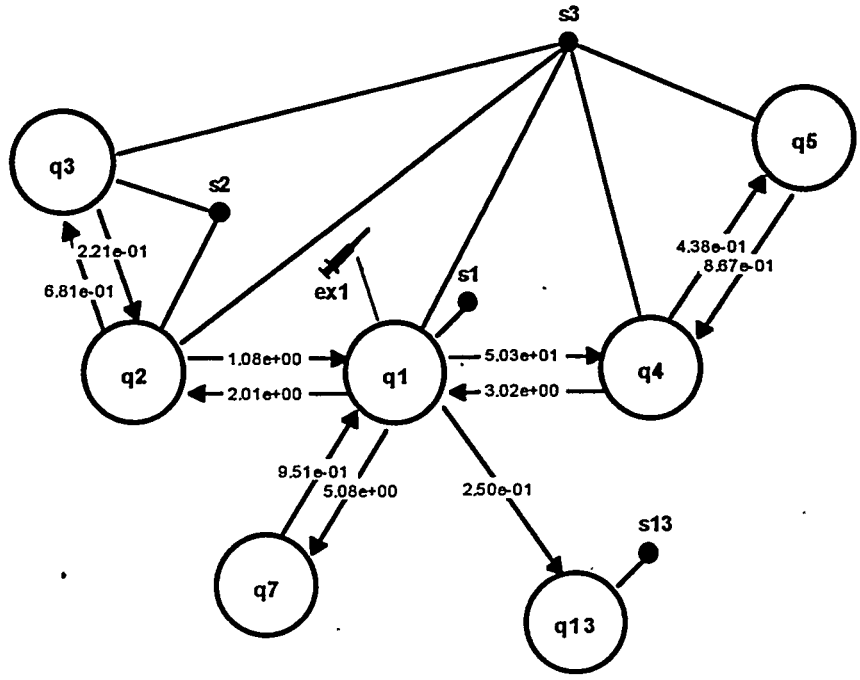

Figure 17. The system model with the best parameter estimates.
See text for additional explanation.

model indicating that all parameters are adjustable. We do not show any of the fits because they are essentially identical to those shown for the individual subsystem fits, and for the plasma forcing function.

The following tables, taken from SAAM II, provide statistical information about the fit. Table 1 lists the individual parameters, their values, the standard deviations and fractional standard deviations of the parameter estimates. Table 2 is the correlation matrix. The optimization routine used in SAAM II is as described by Bell et al. (4). More information on the theory and interpretation can be found in standard texts (5,6). We will summarize briefly how this information can be used.

Table 1
Parameter Estimates and Errors for System Model

Parameter	Value	Std.Dev.	Frac.Std.Dev.
k(13,1)	0.25004	4.32778e-02	1.73086e-01
frac	0.19913	1.70774e-03	8.57597e-03
vol	2993.90823	1.60974e+01	5.37670e-03
k(7,1)	5.08337	1.19459e-01	2.35000e-02
k(5,4)	0.43768	2.89504e-02	6.61450e-02
k(4,5)	0.86694	5.16487e-02	5.95756e-02
k(4,1)	50.28344	2.36637e-01	4.70607e-03
k(3,2)	0.68115	5.87808e-02	8.62963e-02
k(2,3)	0.22112	2.53242e-02	1.14525e-01
k(2,1)	2.01321	8.19272e-03	4.06947e-03
k(1,7)	0.95121	5.05240e-02	5.31155e-02
k(1,4)	3.02047	2.68551e-02	8.89102e-03
k(1,2)	1.08025	3.65733e-02	3.38564e-02

Table 2. Correlation Matrix for System Model

	k(1,2)	k(1,4)	k(1,7)	k(2,1)	k(2,3)	k(3,2)	k(4,1)	k(4,5)	k(5,4)	k(7,1)	vol	frac	k(13,1)
k(1,2)	1.00000	0.12028	-0.06614	0.39442	0.61115	0.87459	-0.21625	-0.07234	-0.04689	-0.14235	0.36797	0.06801	-0.06020
k(1,4)	0.12028	1.00000	0.15585	0.14228	0.08461	0.09491	0.37877	0.48268	0.67805	0.13256	0.11575	-0.10568	0.10222
k(1,7)	-0.06614	0.15585	1.00000	0.08685	0.00314	-0.05154	-0.08230	0.46549	0.49985	0.36909	-0.10877	0.11417	0.83590
k(2,1)	0.39442	0.14228	0.08685	1.00000	0.17458	0.28452	0.41962	0.05342	0.09995	0.18602	-0.34238	-0.13530	0.05485
k(2,3)	0.61115	0.08461	0.00314	0.17458	1.00000	0.89161	-0:06310	0.13454	0.14014	-0.04203	0.07030	0.02203	0.01963
k(3,2)	0.87459	0.09491	-0.05154	0.28452	0.89161	1.00000	-0.13016	0.02586	0.06096	-0.08100	0.16764	0.04145	-0.03928
k(4,1)	-0.21625	0.37877	-0.08230	0.41962	-0.06310	-0.13016	1.00000	0.17251	0.22466	-0.03099	-0.58264	-0.40956	0.01535
k(4,5)	-0.07234	0.48268	0.46549	0.05342	0.13454	0.02586	0.17251	1.00000	0.92158	-0.05015	-0.09685	-0.03706	0.56443
k(5,4)	-0.04689	0.67805	0.49985	0.09995	0.14014	0.06096	0.22466	0.92158	1.00000	0.12077	-0.15251	-0.04406	0.48634
k(7,1)	-0.14235	0.13256	0.36909	0.18602	-0.04203	-0.08100	-0.03099	-0.05015	0.12077	1.00000	-0.34425	0.16641	-0.05824
vol	0.36797	0.11575	-0.10877	-0.34238	0.07030	0.16764	-0.58264	-0.09685	-0.15251	-0.34425	1.00000	0.18409	-0.10479
frac	0.06801	-0.10568	0.11417	-0.13530	0.02203	0.04145	-0.40956	-0.03706	-0.04406	0.16641	0.18409	1.00000	0.04247
k(13,1)	-0.06020	0.10222	0.83590	0.05485	0.01963	-0.03928	0.01535	0.56443	0.48634	-0.05824	-0.10479	0.04247	1.0000

The fractional standard deviation (FSD) is the quotient of a parameter's estimated standard deviation and the parameter value. When multiplied by 100, it is the percent fractional deviation or coefficient of variation. The smaller the value, i.e. the closer it is to zero, is the better the estimate of the parameter. Thus parameters such as $k(4,1)$, with a FSD of 0.0047 or coefficient of variation 0.47%, are very well defined.

In this particular example, the highest coefficient of variation is less than 20%, so we can feel confident that the parameters have been estimated with very good precision. In general, depending upon the situation, mainly noise in the data, obtaining coefficients of variations for all parameters less than 50% is a reasonable goal. If we observe values in the range between 50% and 90%, we should be concerned, and above 90% we can probably conclude that the model contains more adjustable parameters than are supported by the data. Those parameters with high coefficients of variation need to be fixed at some reasonable value, or a constraint such as a functional relationship among parameters needs to be introduced in order to reduce the number of adjustable parameters.

The correlation matrix provides information on the relationship among the parameters in the model. It is especially useful when we are having difficulty optimizing the model to the data because some parameters have high coefficients of variation. This usually indicates a high correlation among some parameters in the model. Two parameters that are highly correlated, for example when the correlation coefficient is between 0.9 and 1, or between -1 and -0.9, means that one parameter can change and the other will change in such a way that the fit of the data doesn't change significantly. This will indicate which parameters are causing problems in the fitting process.

What we want is for the correlation coefficients to be close to zero. In our experience in biomedical research, this rarely happens, and often we are forced to live with correlation coefficients that are near 1 or -1. Because of the nature of the optimization problem, however, this situation can occur while the coefficients of variations for the parameters are acceptable.

Summary

The development and testing of an integrated model for a single input-multiple output experiment requires a number of steps. This example illustrates how to use the forcing function machinery to postulate a system model structure for such an experiment. In summary, the steps are:

- provide a functional description of the input function as a forcing function
- use the forcing function to develop and test model structures for the subsystems
- fix these subsystem structures and postulate a most for the input function
- optimize on all model parameters to obtain best estimates of the parameters and their uncertainties.

Estimating Areas Under the Curves

To estimate certain parameters, once a system model has been developed and tested, it is necessary to estimate the "areas under the curves" for the subsystems. In this section, we will illustrate how to do this using SAAM II and the model shown in Figure 18.

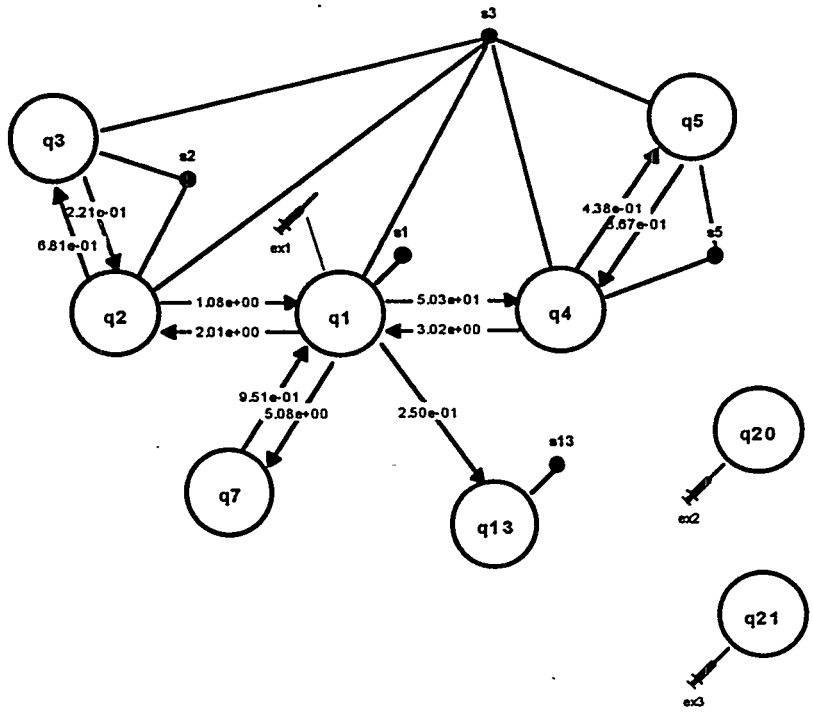

Figure 18. The system model shown in Figure 17. Compartments 20 and 21 have been added to estimate the area under the curve for the two liver compartments, compartments 4 and 5, and liver plus whole blood. See text for additional explanation.

Suppose we want to know the area under the organ curve cells and the organ curve with plasma. This can be accomplished as follows. First we create two compartments; in Figure 18, these are compartments 20 and 21. We then make the input into compartments 20 and 21 equation entries.

$$ex2 = q_5(t) + q_6(t) \qquad [14]$$

$$ex3 = fraction^{*}(q_1(t) + q_2(t) + q_3(t)) + q_5(t) + q_6(t) \qquad [15]$$

This will in essence create the following integrals

$$\int_0^{10000}(q_5(t) + q_6(t))dt = 100.20 \quad \text{and} \qquad [16]$$

$$\int_0^{10000}(fraction^{*}(q_1(t) + q_2(t) + q_3(t)) + q_5(t) + q_6(t))dt = 107.05. \qquad [17]$$

Two comments need to be made on this strategy. The first is a SAAM II requirement. As part of the inputs $ex2$ and $ex3$, we must put in a bolus of a small amount of material such as 0.001. The reason is that SAAM II's integrator requires some mass in the system prior to solving. The second deals with how long to integrate in order to obtain an accurate estimate for the area under the curve. As a rule of thumb, we can integrate to a number equal to the reciprocal of the smallest exponential

(eigenvalue) of the system. While SAAM II does not return these exponentials, we know from Equation 9 that the smallest exponential is 0.0001. Thus the integrals in Equations 15 and 16 go from 0 to 10,000.

A final comment on the areas under the curve is that the model will permit us to estimate areas under the curve for those parts of the system postulated as part of the model structure but not available for test measurement. In the example here, this would be the area under compartment 7. If we were to add another compartment to estimate this area, we would obtain

$$\int_0^{10000} q_7(t)\,dt = 2137. \qquad [18]$$

MODEL IDENTIFIABILITY AND GOODNESS-OF-FIT

In the above, we have concentrated on the steps needed to develop a model structure which is consistent with the experimental data. We assume in this discussion that the reader is aware of the principles of designing sound kinetic experiments, and is aware of tools, for example, to help in determining optimal sample selection time (for example, see Carson et al. (7))

When we have postulated a model structure which is consistent with the data, a number of questions arise:

- Given an ideal set of data and the correct model of the system, can I estimate uniquely the parameters of the model?
- Given the model of the system, can I estimate the parameters of the model with some statistical precision?
- How do the know the model "fits" the data?
- How do I know if I need more compartments in the model?

The first question is known as the a priori identifiability question (7). It is set in the context of knowing the correct model structure and noise-free, continuous time measurements (ideal data). The problem is that some model structures can have a finite number of solutions which will produce a best fit of the data, and others will have an infinite number of solutions. What is desired is a situation where there is a unique global minimum, i.e. a unique set of parameter values which will produce a best fit of the data. This question is very important, as physiological conclusions are drawn from the model, and with different sets of parameter values, these conclusions will be different. A general solution to the problem is difficult, but a software package, GLOBI (8) has recently been developed for linear compartmental models.

The second question relates to the a posteriori identifiability problem. Given a model structure and an initial set of parameter estimates, can a best fit be obtained where the error estimates of the parameters are acceptable?

To obtain statistical information about a model's fit to a set of data such as that presented above, the system model requires the assignment of weights to the data. Suppose $y(\vec{p},t)$ is the model being tested. Here t is the independent variable time, and $\vec{p} = (p_1,\cdots,p_n)$ are the parameters characterizing the model. For a linear compartmental model, these would be the rate constants k(i,j) and, for example, a volume term. Then for each time t_i for which there is a datum $y_{obs}(t_i)$, there is a model predicted value $y(\vec{p},t_i)$. There are two common, flexible error models that are used to calculate weights associated with data:

$$w_i = \frac{1}{A + B \cdot y_{obs}(t_i)^C} \qquad [19]$$

and

$$w_i = \frac{1}{A + B \cdot y(\bar{p}, t_i)^C}. \qquad [20]$$

In these equations, A, B and C are parameters that can be estimated from the data. SAAM II currently supports Equation 19 but in subsequent version will support both schemes.

There is a relationship between the weights assigned to a datum and the variance of the datum. In one case, known as absolute weights, the relationship is given by

$$\mathrm{var}(y_{obs}(t_i)) = \frac{1}{w_i}. \qquad [21]$$

This assumes that the weights are known. An alternate case, the case which is the default in SAAM II, is relative weights. This assumes that the error structure in the data are known up to a proportionality constant; this constant is estimated by the software. The advantage of this scheme is that SAAM II can deal with data sets that differ over several orders of magnitude. In the example we have just discussed, there would be separate estimates of this proportionality constant, the variance of the data set, for the plasma, red blood cell, urine and organ data. In this case, the relationship between the variance and weight is given by

$$\mathrm{var}(y_{obs}(t_i)) = \frac{v_j}{w_i}, \qquad [22]$$

where v_j is the variance of the j^{th} data set.

When the weights have been assigned to the data and when a best fit has been achieved, we can then investigate the statistical output. An example is given in Tables 1 and 2. As noted above, we should be sure that the estimated fractional standard or coefficients of variation are "reasonable"; we provided guidelines for this previously. Finally, the correlation coefficients should be checked.

When we have obtained a best fit and are satisfied with the statistical estimates, and have addressed the question of a priori identifiability, then it is possible to test for goodness-of-fit and model order. A common test for goodness-of-fit is the runs test. The runs test is based upon the residual or weighted residual where, if $\hat{p}$ is the parameter vector producing the best fit to the data, then the i^{th} residual or weighted residual is given respectively by

$$res(t_i) = y(\hat{p}, t_i) - y_{obs}(t_i) \qquad [23]$$

or

$$wres(t_i) = w_i(y(\hat{p}, t_i) - y_{obs}(t_i)). \qquad [24]$$

A run is a subset of sequential residuals having the same sign, plus or minus. The run test is described in standard statistical text books (e.g. (9) or (7)).

A final question deals with the number of compartments which are required to fit the data. Normally we can determine the number by examining the statistics of a fit and performing a runs test. Sometimes, however, different model structures will give similar fits. The question is whether or not there is a test to determine if there is a "best" structure.

Tests exist that are based on the principal of parsimony (7). These are the Akaike information criterion (AIC) and the Schwarz criterion (SC). Suppose WRSS is the value for the weighted residual sum of squares following a model fit to a set of data. For the absolute weight case, the AIC and SC are respectively

$$AIC = WRSS + 2P$$

and

$$SC = WRSS + P \cdot \ln(N), \qquad [25]$$

where P is the number of adjustable parameters and N is the number of data. For the relative weight case, these equations change to

$$\mathrm{AIC} = \mathrm{N} \cdot \ln(\mathrm{WRSS}) + 2\mathrm{P}$$

and

$$SC = N \cdot \ln(WRSS) + P \cdot \ln(N). \qquad [26]$$

The AIC and SC can be calculated for any number of model structures, and that model with the lowest criterion is said to be the best.

For the example given here, the total number of adjustable parameters is 13, the number of data points is 111 (plasma - 24, rbc - 24, urine - 7, organ - 56), and WRSS is 602. As relative weighting has been used, Equation 26 gives the proper formulas to calculate AIC and SC. We can calculate AIC = 736 and SC = 781. If a second model structure were proposed that had a different number of parameters, and if that model also gave a reasonable fit with reasonable statistical information on the parameters, one would calculate the AIC and SC for that model, and choose as the best model the one with the lower criterion. This is explained in more detail in Carson et al.(7).

The combination of tests for goodness-of-fit and model order can provide us with confidence that the model selected is the most appropriate for the specific set of experimental data.

CONCLUSION

The purpose of this paper has been to discuss the development and testing of integrated multicompartmental models to describe a single input-multiple output experiment, and to illustrate the application of modeling strategies using the SAAM II software system (1). A fundamental point is that through this process, one will actually learn the information content in the data set being analyzed, and thus extract the maximum amount of information and at the same time have confidence in the model that is developed. Very often, we will design an experiment and then try to apply an existing model to analyze the data. This can be a dangerous approach, as often the prior model may not fit the data for a variety of reasons due largely to differences in the experimental design. While the original model can be taken as a starting point, it should be subject to the same scrutiny we have described here.

In the first part of this text, we went through the steps to postulate a model which is compatible with a set of data, and summarized the main steps. We then showed how one can use the model to estimate areas under the curves of the various compartments in the model.

The second part of the text dealt with issues related to model identifiability and assessing the goodness-of-fit. These steps give us confidence in the validity of the model and its application.

We saw that the identifiability issue has two parts. A priori identifiability addresses the equation as to whether the models parameters can be estimated from the proposed experimental data. If the answer is no, then the experimental design must be changed. The other part is a posteriori identifiability. This relates to assessing the statistical information that is returned following optimization. If there are problems in the optimization process, i.e. some parameters are not well determined, there is information in the statistics that can help resolve which parameters are causing problems in optimization.

Finally, we discussed standard tests for goodness-of-fit and model order. These tests give us confidence in the model and its order, i.e. the number of compartments and interconnections that is required.

The SAAM II software system has been designed and is constantly being upgraded to make all of these processes easier so that the software can be a useful research tool as well as a tool for data analysis. We have described how the existing tools can help make the modeling process easier. New tools are being designed to help in the model development and testing process.

ACKNOWLEDGMENT

This work was supported by a grant from NIH/NCRR RR-02176.

REFERENCES

1. SAAM II User Guide. SAAM Institute. Seattle, WA, 1994.
2. Foster, DM and Boston RC. The use of computers in compartmental analysis: The SAAM and CONSAM programs. Compartmental Distribution of Radiotracers. JS Robertson, ed. CRC Press. Boca Raton, FL.1983.
3. Foster, DM, Aamodt RL, Henkin RI and Berman M. Zinc metabolism in humans: A kinetic model. Am J Physiol 237:R340-R349, 1979.
4. Bell, BM, Burke JV and Schumitzky A. A relative weighting method for estimating parameters and variances in multiple data sets. Computational Statistics and Data Analysis 22:119-135, 1996.
5. Neter, J and Wasserman W. Applied Linear Statistical Models. R. D. Irwin, Inc. Homewood, IL, 1974.
6. Bates, DM and Watts DG. Nonlinear Regression and its Application. John Wiley and Sons. New York. 1988
7. Carson, ER, Cobelli C and Finkelstein L. The Mathematic Modeling of Metabolic and Endocrine Systems. John Wiley and Sons. New York, 1983.
8. Audoly S, D'Angio' L, Saccomani MP and Cobelli C. Global identifiability of linear compartmental models--a computer algebra algorithm. IEEE Trans Biomed Eng 45(1):36-47, 1998. PMID: 9444838;UI: 98107291.
9. Dixon WJ and Massey FJ, Jr. Introduction to Statistical Analysis. McGraw-Hill, New York. 1969.

QUESTIONS

Aydrogan: Although the fit is good, you might have very large uncertainties associated with parameter estimates which propagate through residence time estimates. How do you relate such situations with the validity of acceptability of fit?

Foster: It is a complex question depending upon the model, the error in the data, and how you assign weights.

Muller: In the design of the user interface of SAAM II you use the word experiment. This word should be reserved for real experiments in the real world. A numerical experiment on a model is called a simulation. Because modelers, in time, tend to forget the real word, the word simulation should be used in the user interface.

Foster: An experiment on a model is a simulation. The model specifies the system of ODE while the experiment specifies the input output. There will be numerical values for parameters, you can solve (simulate). Simulation is sometimes awkward for experimentalists.

RADIATION DOSE ESTIMATES FOR RADIOLABELED ANTIBODIES AND FRAGMENTS

AJ Green, CJ Johnson, RHJ Begent and MJ Napier
CRC Labs, Royal Free Hospital School of Medicine
LONDON, UK

ABSTRACT

Antibodies and their fragments directed against tumor products can be used for a variety of diagnostic and therapeutic procedures. Radiation dose to normal tissues is one of the factors which determines the acceptability of these procedures, it is, thus, necessary to assess the dose delivered to nontumor (normal) tissues.

In a number of studies patients have been given whole antibody (150kD), $F(ab')_2$ (100kD), two linked F(ab) fragments (100kD) and a single chain variable region (SFv) (27kD) labeled with radioiodine (^{131}I or ^{123}I). Serial blood samples were taken and serial thorax and abdomen tomographic gamma camera imaging was performed to assess the distribution of radionuclide. Images were reconstructed with correction for scatter and attenuation, regions were chosen to represent the tissues of interest and percent injected dose per gram of tissue was calculated with correction for the different radionuclides used for measurement. It was assumed all the activity distributed homogeneously in the blood within a negligible time and the organ activity at time t=0 was taken to be proportional to the volume of blood in the organ. Simple (trapezoidal) integration was used to calculate the area under the time-activity curve, the "worst case" assumption (that only radioactive decay occurs after the final measurement point) was used to calculate the area under the tail of the curve. These areas were used to calculate the MIRD "residence times" for the significant organs.

The variation in size and location of tumor deposits meant that no account of dose to normal tissue from activity in the tumor could be made. MIRD doses and equivalent dose estimations, for the standard man and standard woman models, were calculated for the different size antibody fragments for therapeutic (^{131}I) and diagnostic (^{123}I) uses.

This work is supported by the Cancer Research Campaign.

COMPARISON OF CLINICAL DATA WITH A MATHEMATICAL MODEL OF ANTIBODY BIODISTRIBUTION, WITH RESCALING FOR DIFFERENT ANTIBODY FRAGMENTS

CJ Johnson, AJ Green, RHJ Begent, RB Pedley and JL Casey
CRC Labs Royal Free Hospital School of Medicine, LONDON, UK

ABSTRACT

Radioimmunotherapy uses antibodies against tumor expressed antigens to target radionuclides to tumors. Many factors influence the success of antibody targeting regimes. To investigate the relative importance of each factor, it is necessary to quantify its contribution. Expressing the whole system in a mathematical model gives a structure in which to study individual aspects, which should lead to strategies for improved targeting. Comparison of model predictions with clinical data determines the usefulness of the model.

We have given whole antibody (150kD), fragments with molecular weights 150kD and 100kD, and single chain Fv antibody fragments (27kD) to patients with colorectal cancer and measured the blood clearance and liver and tumor uptake. These results have been compared with a mathematical model that is driven by a time-dependent function describing the clinically observed concentration of antibody in the blood. Extravasation is modeled by the two-pore theory; process of antibody permeating into tissue, draining into lymph, binding to antigen in the tumor, are mathematically expressed. A minimal number of variable parameters, relating to the transcapillary convection and diffusion of antibody, are determined for the whole antibody by fitting the model to the clinical data. The same parameters are then rescaled for the other fragments. Rescaling considers not only molecular weight, but also the capillary pore size, which is consistent with the predictions of the two-pore theory. The resulting equations are solved to predict antibody levels in the tumor and in liver as functions of time.

Good agreement between the model and clinical data is seen for the whole antibody, and for the 150kD and 100kD antibody fragments. The model gave a poorer fit for the single chain Fv fragment. This model shows promise for evaluating the importance of factors influencing antibody targeting. This is demonstrated by calculating the effect of changing the affinity of the antibody-antigen interaction.

This work is supported by the Cancer Research Campaign.

QUESTIONS

Roesch: The database of your model consists of a correlation of type time versus activity. Did you analyze the chemical stability of the iodinated antibodies and fragments to make sure that the activity is really represented by the intact labels? Otherwise you would deal with combined processes of tracer uptake mechanism and deiodination kinetics of the labeled antibodies and fragments.

Johnson: The model contains no representation of deiodination, making the assumption that radiolabel remains bound to the protein.

Shen: The two parameters you identified to be sensitive in your kinetic modeling should be very useful information for developing new types of antibodies or fragments. Can you make some comments?

Johnson: The physiological interpretation of KE is unclear, and not readily identifiable with any specific characteristics of antibodies/antibody fragments. There is an explicit relationship between Jiso and antibody size, so the effect of changing antibody size can be investigated in the current model. However, there are other important considerations such as antibody shape, antibody charge distribution and diffusion of antibody within the interstitium which are not yet modeled but are considerations in the development of antibodies.

Kwok: How did you separate the amount of antibody in the blood compartment of an organ or tumor from that in the tissue in extravasation modeling?

Johnson: The amount of antibody in the vascular compartment is bound from the known blood function and the rates of plasma flow into and out of the organ and the rate of extravasation. Likewise the concentration in the interstitium is solved from the differential equations representing the system.

Foster: Comment. In your model, it is possible to account for blood volume depending upon your data.

PHARMACOKINETIC AND DOSIMETRY COMPARISON OF TWO HUMAN ANTIBODY CLONES (^{99M}Tc-88BV59)

Mardirossian[1], Baker SP[1], Foster D[3],
Wynant GE[2], Hanna MG[2] and Brill AB[1]
[1]University of Massachusetts Medical Center, Worcester MA 01655
[2]PerImmune Inc. Rockville, MD.20850
[3]University of Washington, MC

ABSTRACT

Two groups of colon cancer patients received a ^{99m}Tc-labeled human IgG monoclonal antibody, ^{99m}Tc-88BV59 (OncoSPECT), in a pharmacokinetic study. Forty-three of the patients received IV doses ranging from 0.5 to 1.4 GBq (14 to 37 mCi) (5.9 to 11.5 mg) of an antibody designated 88BV59H21-2 in a Phase IIA study. An additional 25 patients received a subclone of the antibody designated 88BVH21-2V67-66 in a Phase IIB study. This report analyzes the pharmacokinetic data observed in the two groups of patients which were infused with these agents to compare their pharmacokinetic behavior.

Pharmacokinetic (PK) analyses were performed at the University of Massachusetts Medical School using SAAM II. A two-compartment model was fit to the data using the actual length of the infusion each patient received. From this, plasma PK parameters including transition rates, AUC, FCR and MRT were deduced. Statistical analysis, using the multivariate analysis of variance (MANOVA), revealed no significant difference between the two tracers in PK behavior.

Absorbed dose estimates were calculated for the Phase II study following the administration of two OncoSPECT doses, separated by approximately one month, to colorectal cancer patients. Calculations were carried out using series of whole-body planar images and collecting blood and urine samples for up to 72 h postinfusion.

INTRODUCTION

Human monoclonal antibodies hold promise to improve radioimmunodetection by eliminating the immunogenicity problem encountered with nonhuman antibodies. OncoSPECT is an intact IgG human monoclonal produced by cells derived from cultured lymphocytes and has been tested in Phase I trials. The antibody is reactive with 74% of colon carcinomas, 83% of breast carcinomas, and 80% of ovarian carcinomas, as tested by immunohistochemistry. Normal tissue reactivity is confined to limited areas of glandular and ductal epithelium and certain neurological tissues. The antibody recognizes an antigen that is confined to the cytoplasm, not expressed on the cell surface and not released by the cell. The 88BV59

antibody retains its immunoreactivity following direct labeling with ^{99m}Tc with specific activity yields of 110-148 MBq/mg.

Two groups of patients received ^{99m}Tc-labeled OncoSPECT in a pharmacokinetic study at the State University of New York, at Buffalo. The studies included male and female patients with a high index of suspicion for, or known diagnosis of, metastatic colorectal carcinoma. Forty-three of the patients received an IV infusion with doses ranging from 518 to 1369 MBq (5.9 to 11.5 mg) of the antibody designated 88BV59H21-2 in a Phase IIA study (MAB-SUNY-9112-0), sponsored by PerImmune, Inc. An additional 25 patients received a subclone of the antibody designated 88BVH21-2V67-66 in a Phase IIB study (MAB SUNY 9112-1). The antibody was infused intravenously into patients over 10 to 45 minutes. Following the end of infusion, blood samples were obtained at 0, 15, 30, 60 min., 2, 4 and 24 hours. Typical infusion volumes were in the range of 60 ml, with final antibody concentrations in the range of 150 mg/ml. Data received by the sponsor (PerImmune) were entered into an Oracle data base, and the percent of the injected dose per ml at each sampling time was calculated.

PK analysis using the standard two-exponential fit to the data was not used because the material was administered over a variable period of time (not as a bolus). Instead, PK parameters were obtained using a two-compartment model with the actual time of the slow infusion, using the SAAM II computer software (1). The program, which provides a least-square best fit solution, enabled estimation of the tracer kinetic parameters of the system for each patient in the two study phases. We used the SPSS statistical software tool with multivariate analysis of variance (MANOVA) methods to determine whether the two injectates had similar or different pharmacokinetic characteristics in terms of their kinetic parameters.

In separate dosimetry protocols conducted at three sites (SUNY Buffalo, NY; Morgan Cancer Center Lehigh Valley, PA; and Centre Rene Huguenin St Cloud, FR), patients received the first dose of ^{99m}Tc-OncoSPECT followed approximately one month later by a second dose. Whole-body, planar images were collected immediately following infusion, and at 4-6, 14-20, and 24-30 hours. Blood samples were obtained at preinfusion, 5, 10, 15, 60, 120 minutes, 4, 24 and 48 hours. Urine samples were also collected in the following time intervals: 0-2, 2-4, 4-12, 12-24, 48-72 and 72-96 hours, whenever possible.

PHARMACOKINETIC STUDY

Patient Data

Patient selection criteria for the two study groups were identical. Eligibility criteria included patients above 18 years of age who were histologically diagnosed with colon cancer with diagnosed or suspected metastatic tumor involvement, based on biopsies or clinical and laboratory evidences including elevated CEA. All patients had Karnofsky test scores equal to or greater than 70, with adequate renal and hepatic function.

Following direct labeling of the antibody with ^{99m}Tc, the preparation was diluted in a saline (Abbott) human serum albumin (Cutter) solution and infused IV into patients over 15 to 45 minutes. Typical infusion volumes were in the range of 60 ml, with final antibody concentrations in the range of 150 µg/ml. The amount of antibody administered IV to patients in the two groups varied from 6 to 12 mg/patient and the administered activity ranged from 518 to 1369 MBq.

Starting at the end of infusion, blood samples were obtained at 0, 15, 30, 60 min, 2, 4, and 24 hours. Syringes were counted before and after injection to determine net infused activity. Samples were counted along with standards at the end of the collection period. Data received by the sponsor (PerImmune) from SUNY (Buffalo) were entered into an Oracle data base, and the percent of the injected dose at each sampling time was calculated. The injected activity, time intervals and assay data

were recorded and entered into spread sheets. Data on each patient, and the pereent of injected activity (%IA) as a function of time were transmitted by PerImmune to the University of Massachusetts Medical Center (UMMC), where the spread sheet computational method was verified and the %IA data entered into a PC computer for subsequent analyses.

Some patients from Phase IIA and Phase IIB (14 and 5 respectively) were excluded from the present analysis because too few blood samples were collected to permit fitting of the data to the model. Other patients which were imaged without collection of blood samples were also not included.

METHODS

Pharmacokinetic (PK) analyses were performed using the SAAM II software system (1) (a simulation analysis and modeling tool) based on Berman's SAAM (2). We used the PC version of SAAM II on a Gateway 486 DX2 66MHz computer.

A two-compartment model, as illustrated in Figure 1, was used to fit each individual patient's data using the actual time duration of the infusion for each patient. Data in terms of percent of injected activity (%IA) were entered into the SAAM II modeling program, which provides the computing machinery needed to converge on least squares best fit solutions for each of the model parameters for individual patients along with estimates of their uncertainties.

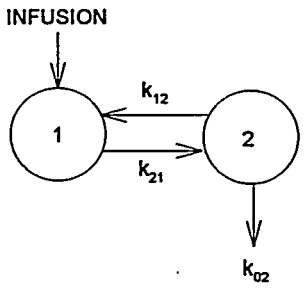

Figure 1. Two-compartment model

In Figure 1, compartment 1 is the plasma into which the material is continuously infused, and from which it exchanges with the extravascular space and remainder of the body (compartment 2). Compartment 2 also has an irreversible loss term. The SAAM II program provides estimates of the $k_{i,j}$ transition rates and the mean residence time matrix of the system. From the elements of this matrix, parameters (including the fractional clearance rates of the accessible pool and the total residence time in the system) can be expressed, as noted below.

The mean residence time in the accessible pool is the average time a single particle spends in that pool during all passages through it before irreversibly leaving the system. Covell et al. (3) have shown that the definition can be extended to any compartment in an n-compartment system. Since the time that a single particle spends in a specific compartment depends upon which compartment the particle enters the system, an n x n matrix, $\Theta = -K^{-1}$ of the mean residence times can be defined where the generic element $\theta_{i,j} = {}_{1,\ldots n}$ represents the average time a particle entering the system in compartment j spends in compartment i before irreversibly leaving the system. The compartmental matrix K is written

$$K = \begin{pmatrix} -k_{21} & k_{12} \\ k_{21} & -(k_{02} + k_{12}) \end{pmatrix}$$

and thus,

$$\Theta = \begin{pmatrix} \theta_{11} & \theta_{12} \\ \theta_{21} & \theta_{22} \end{pmatrix} = -K^{-1} =$$

$$\begin{pmatrix} \frac{k_{02} + k_{12}}{k_{21} k_{02}} & \frac{k_{12}}{k_{21} k_{02}} \\ \frac{k_{21}}{k_{21} k_{02}} & \frac{k_{21}}{k_{21} k_{02}} \end{pmatrix}$$

The following kinetic parameters have been defined based on the mean residence time matrix θ. The fractional clearance rate

$$FCR = \frac{1}{\theta_{ii}}$$

and mean total residence time (MRT) in the system

$$MRT_j = \sum_{i=1}^{n} \theta_{ij} .$$

The area under the curve (AUC) was estimated from the integration of activity in compartment 1.

Statistical Methods for Compartmental Analysis

Statistical tests of differences between the injected materials' kinetic parameters k_{02}, k_{21}, k_{12}, including AUC, MRT and FCR, were evaluated using a multivariate analysis of covariance (MANOVA) and the Hotellings T^2 test (4). A significant effect was defined as an effect having a probability less than 0.05. Analyses were carried out using univariate analysis of covariance (ANCOVA). The covariates controlled for included age, sex and CEA. The distributional assumption of normality was assessed graphically by inspection of histograms, then confirmed using the Kolmogorov-Smirnov one sample test for normality. All analysis were performed using the SPSS Statistical Software Package for Windows (Release 6) on a Dell Pentium PC.

DOSIMETRY STUDY

Patient Data

Patients (M/F with age range 65-83y) with histologic diagnosis of colorectal cancer who had at least one documented site of recurrent or metastatic tumor were studied. Each patient received two infusions (8-10 mg, 1147-1332 MBq) of the radiolabeled antibody separated by about one month.

Following each antibody infusion, whole-body and thoracic, abdominal and pelvic planar scans were performed immediately postinfusion and, 4-6, 14-20 and 24-30 hours later. Serial blood samples were collected preinfusion and at 5, 10, 15, 60, 120 minutes, 4, 24 and 48 hours later. Urine samples were also collected at intervals of 0-2, 2-4, 4-12, 12-24, 48-72 and 72-96 hours, whenever possible.

Methods

The fraction of the injected activity (FIA) in different source organs was determined by drawing regions of interest (ROIs) about the specified source organs. ROIs identified at early imaging sessions were linked to each other and moved as a group so that interorgan spatial relations were maintained and used at later times when not all organs were clearly visualized. The activity in each source organ ROI was calculated after background subtraction at each measurement time (counts per pixel in a background ROI, selected in the lower abdomen, were subtracted from each pixel in the source organ ROI). Serum clearance and urine excretion data were established by serum, urine and standards counting at the end of the sample collection period. Organ data were quantitated after correction for physical decay.

Regions of interest used in the study included the liver, spleen and kidneys. The remainder of the body activity at each sampling period was considered to be 100% of the injected activity minus the sum of all activities otherwise accounted for in the measured source organs and activity lost in urine. The partition of plasma activity included an assignment of 10% of the plasma pool to the heart and lungs, respectively (5). The bone marrow dose was calculated based on plasma activity as described by Sgouros (6) using each patient's hematocrit, as measured at time of infusion, and blood volume based on reference man data (adjusted for sex, height and weight).

The fraction of injected activity (FIA) in each source organ was calculated for each ROI and measurement time for each of the patients. Best fit parameters for a three-component exponential function were obtained for each patient using the CONSAM program (model type 2) (7,8). In this model, the values of the exponentials for the different measurements for each patient are the same for all organs, i.e. only the coefficients of the three terms varied. The strongest determinants of the values of the exponentials were the blood and whole-body activity measurements.

The absorbed radiation doses were calculated using the computer program MIRDOSE 3 developed by Stabin at Oak Ridge Institute for Science and Education (ORISE), based on the MIRD formalism (9).

RESULTS

Compartmental Analysis

Data expressed as fraction of injected activity (FIA) were entered into the model given in Figure 1 weighted by the reciprocal of the variance (10). Best-fit estimates of parameters were obtained based on the least squares criterion . The two-compartment model described in Figure 1 with continuous infusion input produced good fits to the data for all patients assuming only three adjustable parameters, the k_{ji}. The six parameters which adequately represent the plasma kinetic properties are the three transition rates (k_{02}, k_{21} and k_{12}), AUC, MRT and FCR. They are presented in Table 1 as obtained for each of the 29 patients who received Phase IIA and for the 20 patients who received the Phase IIB material.

Table 1
Mean and SD of Parameters Deduced from the Compartmental Analysis

	PHASE IIA	PHASE IIB
Number of Subjects	29	20
k_{02} (hr^{-1})	0.11 (0.03)	0.16 (0.10)
k_{21} (hr^{-1})	2.04 (1.84)	2.65 (3.33)
k_{12} (hr^{-1})	1.93 (1.81)	4.47 (6.26)
AUC (hr)	11.37 (3.22)	11.24 (2.82)
FCR (hr^{-1})	0.09 (0.02)	0.11 (0.08)
MRT (hr)	21.34 (2.91)	19.53 (4.16)

All but one kinetic parameter (AUC) required logarithmic transformation to achieve sufficient conformity to the normal distribution to satisfy the normality assumption of ANOVA. Despite some variations observed in the pharmacokinetic parameters in the two patient groups, the multivariate tests (Hotellings, Pillais and Wilks) of the pharmacokinetic parameters failed to show statistically significant differences in the two groups. The univariate results are presented in Table 2.

Table 2
The Group Effect on the Univariate F-test for all Parameters

Variable	Significance of F
AUC	0.756
FCR	0.411
MRT	0.076
k_{02}	0.042
k_{12}	0.317
k_{21}	0.706

Only k_{02} appeared to have marginal statistical significance (p=0.042), though this result is unadjusted for the number of parameters evaluated and the result is not supported by multivariate analysis, which was far from significant (p=0.25). Other variables such as age, sex and CEA levels (at time of administration), included as covariates in this analysis, expressed no significant association with any of the variates.

Ten patients who received Phase IIA material expressed positive HAMA values, which resulted from prior studies with nonhuman antibodies. The remaining patients from Phase IIA, as well as from Phase IIB, had negative HAMA. Having established no differences between the two clones of antibody, patients from both phases were selected and analyzed with respect to HAMA levels. Statistical analysis using SPSS software (MANOVA) revealed no statistically significant differences between the two groups of HAMA positive and negative (from both Phase IIA and B) patients (p=0.189). Covariates such as CEA, age and sex also appeared to have no significant association to the two groups. Patients did not develop HAHA during these studies.

Three other patients received two infusions and were included and analyzed in Phase IIA and B. Though HAMA values were reported negative for these patients, no linear correlation between CEA and any of the six parameters were observed despite the marginal increase in the CEA levels between the first and the second infusion.

PK Comparison

The biexponential function produced equally good fits to the plasma data, as obtained with the compartmental model. In order to compare results from the compartmental model and that of the bolus infusion model, we analyzed data from three patients who received two infusions, one month apart. Table 3 presents the deduced parameters for comparison for a representative patient with infusion duration of 29 and 20 min, respectively.

Table 3
Parameters Obtained with A) Two-Exponential Function and B) Compartmental Model

(A)

	A_1*	A_2*	$T_{\frac{1}{2}-1/2}$	$T_{\frac{2}{2}-1/2}$	AUC	FCR	MRT
			hr	hr	hr		hr
Phase IIA	0.45	0.36	12.34	0.34	0.101	0.1	17.43
Phase IIB	0.25	0.44	55.57	2.33	0.16	0.03	74.87

*FIA

(B)

	k_{02}	k_{21}	k_{12}	AUC	FCR	MRT
	hr^{-1}	hr^{-1}	hr^{-1}	hr		hr
Phase IIA	0.109	1.6	3.77	7.76	0.13	16.96
Phase IIB	0.116	2.97	3.29	9.93	0.1	18.62

Table 3A shows widely varying parameters while the parameters in Table 3B were much more consistent and reproducible.

Dosimetry

Absorbed dose estimates reported here are the results for three patients, each of whom received two infusions (study still underway). The residence times for all source organs are listed in Table 4 for each of the infusions.

Table 4
Mean Residence Times (hrs) and s.d. of Source Organs for Infusion 1 and 2

Source organs	Infusion 1	Infusion 2
Liver	0.96 (0.19)	0.98 (0.23)
Spleen	0.21 (0.02)	0.21 (0.03)
Kidneys	0.52 (0.07)	0.55 (0.12)
Red Marrow	0.78 (0.03)	0.77 (0.02)
Remainder	3.92 (0.23)	3.64 (0.06)
Heart Content	0.65 (0.08)	0.65 (0.05)
Lungs	0.65 (0.08)	0.65 (0.05)
Bladder Content *	0.28 (0.03)	0.27 (0.01)

* assuming 5 voids/day

The absorbed dose estimates as listed in Table 5 show no differences between the effective dose for both infusions (9 x10^{-3} mSv/MBq). Kidneys received the highest dose followed by the spleen, heart wall, urinary bladder and liver.

Table 5
Absorbed dose estimate (mGy/MBq x 1000)

Organ	Infusion 1	Infusion 2
Adrenals	9	9
Brain	3	3
Breasts	4	4
Gall Bladder Wall	8	8
LLI Wall	5	5
Small Intestine	5	5
Stomach	6	6
ULI Wall	5	5
Heart Wall	21	20
Kidneys	32	34
Liver	18	18
Lungs	16	16
Muscle	4	4
Ovaries	5	5
Pancreas	9	9
Red Marrow	9	9
Bone Surfaces	9	9
Skin	2	2
Spleen	26	26
Thymus	6	6
Thyroid	3	3
Urinary Bladder Wall	20	19
Uterus	6	5
Total Body	5	5
EFF Dose *	9	9

* mSv/MBq

DISCUSSION

Noncompartmental pharmacokinetic analysis assumes bolus input and is widely used to fit and describe plasma kinetic data. From the best fit parameters (multiexponential functions), one derives steady state physiological parameters which provide useful information about the system under study. Infusion of antibodies, especially those of murine origin, usually take place over several minutes to minimize the chance of adverse reactions to foreign protein. In the present studies, there was considerable variation between individual patients in duration of infusion (10-45 min.), despite the fact that the antibody was of human origin. This procedure introduced a bias, from the kinetic aspect, as a different fraction of the injected dose remained in the circulation at the end of infusion, depending on

the length of the infusion. Thus, the apparent slopes and intercepts varied widely in patients, even within the same group, depending on the duration of infusion. This is especially critical when the antibody is directly labeled with ^{99m}Tc, as fast clearance from the system is well documented (11). It seems clear that the continuous infusion model is preferable for use in analysis of antibody infusion data, especially when the infusion extends beyond 5 to 10 minutes. Statistical analysis of the pharmacokinetic behavior of Phase IIA and Phase IIB material is indistinguishable based on the more reliable parameters obtained from the compartmental analysis results presented.

With directly labeled antibodies, labeled catabolites clear rapidly from the system and the clearing organ pathways receive the highest dose. With ^{99m}Tc-OncoSPECT, the kidney dose is the highest (0.034 mGy/MBq), followed by the spleen, urinary bladder and liver. Primary doses delivered to the heart, lungs and bone marrow come from blood content contained in these tissues, the amounts of which were based on published values (5,6). No significant difference in absorbed dose was found in patients receiving two infusions approximately one month apart.

CONCLUSION

No significant difference in the pharmacokinetic behavior of the two subclones of antibodies designated 88BV59H21-2, vs 88BVH21-2V67-66 labeled with ^{99m}Tc was observed using compartmental analysis methods following IV injection in colorectal cancer patients. No significant correlation between patient age, sex, HAMA and CEA level was observed with any of the pharmacokinetic parameters. Kidneys received the highest dose (0.034 mGy/MBq), and basically there wasn't any difference in the organ doses in patients who received two consecutive doses one month apart. The effective dose was 0.009 mSv/MBq. This study was sponsored by PerImmune, Inc.

REFERENCES

1. "SAAM II User Guide" SAAM Institute, University of Washington, 1994.
2. Berman M and Weiss MF. SAAM Manual, U.S. Department of Health, Education, and Welfare. Publication No. (NIH) 78-180, 1978. Washington DC.
3. Covell DG, Berman M and Delisi C. Mean residence time, theoretical development, experimental determination and practical use in tracer analysis. Math Biosci 72:213-244, 1984.
4. Morrison DF. Multivariate statistical methods. McGraw-Hill Book Company, 1976.
5. Poston JW, Aissi A, Hui TY and Jimba BM. A preliminary model of the circulating blood for use in radiation dose calculations. In: Fourth International Radiopharmaceutical Dosimetry Symposium. CONF-851113 (DE86010102) p:574-586. Nov. 5-8, 1985, Oak Ridge, TN, 1986.
6. Sgouros G. Bone marrow dosimetry for radioimmunotherapy: Theoretical considerations. J Nucl Med 34:689-694, 1993.
7. Foster D, Boston R, Jacquez J and Zech L, The SAAM tutorials: An introduction to using conversational SAAM (CONSAM) Version 30. Seattle: Resource Facility for Kinetic Analysis, 1989.
8. Berman M, Belx WF, Greif PC, Chabay R and Boston RC. CONSAM User's Guide. U.S. Department of Health, Education and Welfare, Public Health Service. Manual version, July, 1983.
9. Stabin MG. MIRDOSE, Personal computer software for internal dose assessment in nuclear medicine. J Nucl Med 37:538-546, 1996.
10. Bell BM, Burke JV and Schumintzky A. A relative weighitng method for estimating parameters and variances in multiple data sets. Computational Statistics and Data Analysis 22:119-135, 1996.

11. Hnatowich DJ, Mardirossian G, Rusckowski M, Fogarasi M, Virzi F and Winnard P Jr. Directly and indirectly ^{99m}Tc-labeled antibodies: A comparison of in vitro and animal in vivo properties. J Nucl Med 34:109-119, 1993.

QUESTIONS

Breitz: How can the liver dose and the bone marrow doses be the same?

Mardirossian: The red marrow residence time was recorded off one decimal point resulting in high dose. This will be corrected in the submitted manuscript.

R Dunn: What were the associated tumor targeting parameters, e.g. dosimetry and pharmacokinetics? Also, were patients followed up for HAHA (human anti-human-antibody) postinjection, and if so, what were the results of the assay and any resultant effects on pharmacokinetics and dosimetry?

Mardirossian: Tumor dose was not obtainable from the first three patients studied to date. HAHA was observed in few patients included in the PK study. Several patients who had HAMA levels prior to injection of the OncoSpect antibody did not influence PK parameters for the humanized Ab.

Behr: What is the rationale for the high protein dose (10-12 mg) used for diagnostic purposes? Don't you think this high fraction amount may evoke "HAHA" formulism?

Maridrossian: High antibody dose was intended for further enhancing tumor and metastasis detection. To date, few patients have developed HAHA.

Fisher: I would like to follow up on the previous question by Dr. Hazel Breitz. Could you explain how you calculated the residence time for the marrow? Your values seem to be extraordinarily high.

Mardirossian: True. The red marrow residence time was recorded wrong by one decimal point (~ fraction of 10 higher) resulting in high dose.

A METHOD TO IMPROVE ABSORBED DOSE ESTIMATES FOR ^{14}C-LABELED PHARMACEUTICALS

Mattsson S[1], Leide-Svegborn S[1], Nilsson L-E[2], Nosslin B[1],
Stenström K[3], Erlandsson B[3], Hellborg R[3] and Skog G[4]
[1]Departments of Radiation Physics and [2]Clinical Physiology
Malmö University Hospital/Lund University, S-205 02 Malmö
[3]Department of Nuclear Physics
Lund University, Sölvegatan 14, S-223 62 Lund
[4]Department of Quaternary Geology
Lund University, Tornavägen 13, S-223 63 Lund, Sweden

ABSTRACT

This paper describes the use of accelerator mass spectrometry (AMS) for measurements of excreted ^{14}C activity after diagnostic investigations using ^{14}C-labeled triolein and urea, respectively. With the AMS technique it is possible to measure less than 100 times lower specific activities of ^{14}C (Bq/g of carbon) than with the standard liquid-scintillation technique.

After an intake of ^{14}C-triolein, about 30% of the ^{14}C activity is exhaled during the first 24 hours and another 7% during the following 8 days. The rest is assumed to be retained in body fat. Using AMS in conjunction with the patient fasting, excess ^{14}C can be measured in exhaled air years after a single administration of ^{14}C-triolein, indicating a half-time of about 300 days for ^{14}C retained in body fat. The results indicate that the long-term retention in adults is of the same magnitude as has been assumed earlier and that an investigation using 40-120 kBq gives a low effective dose (0.1-0.2 mSv) compared to other radiopharmaceuticals.

For ^{14}C-urea, similar studies are underway. For patients with *Helicobacter pylori* infection in the stomach, the expiration is more rapid. For three children studied, the $^{14}CO_2$ exhalation pattern was similar to that of the normal adult, indicating no considerable long-term retention. For ^{14}C-urea, bone biopsies should, if possible, be taken to estimate the fraction stored as carbonate in the skeleton. Even with very pessimistic assumptions concerning skeletal uptake, the absorbed doses to various organs and the effective doses from investigations with ^{14}C-urea will be low compared with other radiopharmaceuticals and comparable to that of the contribution from ^{14}C already present in our environment due to natural production and the testing of nuclear weapons in the atmosphere.

Accelerator mass spectrometry is a method for making extremely sensitive ^{14}C measurements. It can be used to improve dosimetry and makes it possible to use less than 1% of the activity needed for liquid-scintillation counting, without compromising the accuracy of the results. This may be of interest for very special investigations, e.g. in children and pregnant or breast-feeding women.

INTRODUCTION

Carbon-14 labeled organic substances are frequently used in biomedical research and when testing new pharmaceuticals. They are also used in clinical medicine. As the physical half-life is long (5,730 years) dose estimates need reliable long-term biokinetic information. Such data are difficult to obtain, as measurements of a pure β-emitter must be made for excreta and expired air or biopsy samples. Ethics committees, as well as government authorities and individual research groups, often request biokinetic and dosimetric information concerning ^{14}C-labeled pharmaceuticals. The aim of this investigation was two-fold: A) to use accelerator mass spectrometry (AMS) (1), which is a more sensitive technique than the currently used liquid scintillation counting, in order to improve biokinetic information and thus dose estimations; and B) to investigate how much less activity could be administered in an investigation if AMS was used for the analysis instead of liquid-scintillation counting.

EXAMPLES OF ^{14}C-LABELED SUBSTANCES IN CLINICAL USE

Today there is a renewed interest in using organic compounds labeled with ^{14}C to detect abnormalities in metabolism and organ function as well as the presence of an abnormal bacterial flora in the gastrointestinal tract. Some of the most frequently used ^{14}C-labeled substances and their clinical usefulness are shown in Table 1.

Table 1
^{14}C-labeled Radiopharmaceuticals in Current Clinical Use. Normally the Administered Activity is between 40 and 200 kBq per Investigation

^{14}C-labeled Substance	Investigation
Triolein	Fat malabsorption
Urea	*Helicobacter pylori* infection in upper GI-tract; associated with gastritis, ulcers and stomach cancer
Dimethylaminoantipyrine (DMA)	Liver function
Glycocholic acid	Ileum malfunction or abnormal bacterial flora in small intestine
Xylose	Abnormal intestinal bacterial flora
Lactose	Lactase deficiency (lactose intolerance)

All these substances are used in so called "breath tests". The ^{14}C-labeled compound is ingested and metabolized. The catabolic end-product carbon dioxide ($^{14}CO_2$) is exhaled and can be collected for measurements. The decay of the radionuclide is usually measured by liquid-scintillation counters or gas-flow counters. Clinically useful information is obtained from samples taken just a few hours after the administration of the test compound. However, a complete biokinetic study needed for calculation of the absorbed dose requires sampling for a much longer time, up to months or even years.

Of the substances mentioned, ^{14}C-urea is today among the most frequently used and is expected to become even more popular in the future, since it can be employed in a simple and reliable test for

the presence of *Helicobacter pylori* (HP) in the upper GI tract. More and more hospitals want to use it for screening investigations, also involving children.

MATERIALS AND METHODS

^{14}C-Triolein Test

After an overnight fast, three male volunteers were given 74 kBq ^{14}C-triolein according to the same routines as were used for patients (2). A fourth male volunteer was given 50 times less activity, 1.48 kBq. This later test was repeated 8 months later. The volunteers breathed through a plastic tube and a chamber filled with a drying agent into a glass vial containing NaOH on a solid support, Ascarite ® (Thomas Scientific, Swedesboro, NJ, USA), to trap the carbon dioxide. The volunteers made five expirations through the system for each sample. To establish the normal ^{14}C content in the expired air, samples were also taken before the intake of ^{14}C-labeled fat. New samples were then taken at 2, 4, 5 and 6 hours after the ingestion and then at longer intervals as indicated in Figure 1.

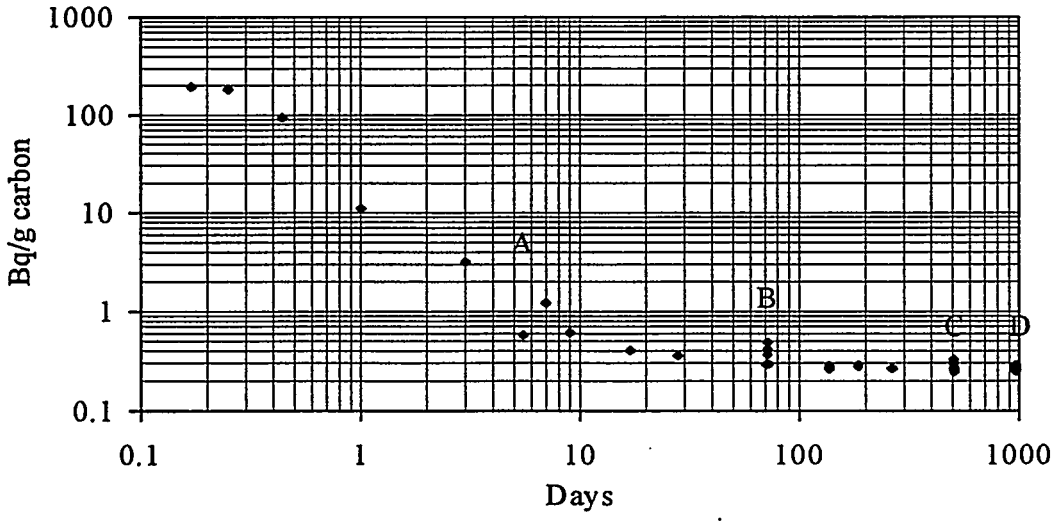

Figure 1. ^{14}C specific activity in expired air at various times after administration of 74 kBq^{14}C-triolein to a 94 kg male. The background, which was 0.258 Bq/g carbon, as determined from 8 samples taken before the ^{14}C-triolein administration, has not been subtracted. A-D are described in the text.

^{14}C-Urea Test

Two adult female volunteers were each given 1.1 kBq ^{14}C-urea. After 7 days, one of them was also given another 110 kBq. Three children (2 girls, aged 10 and 14 years, and one boy, 14 years) were each given 55 kBq ^{14}C-urea. Samples of expired carbon dioxide were taken before the administration and at 5, 10, 15 and 20 minutes after and then at various intervals up to 100 days after the administration. The carbon dioxide samples were converted to graphite through a catalytic reduction (2). The graphite samples were then analyzed using the AMS system at the Lund Pelletron tandem accelerator (3).

The studies were approved by the Ethics Committee of Lund University and performed after informed consent had been obtained.

RESULTS AND DISCUSSION

^{14}C-Triolein Test

Figure 1 shows the ^{14}C specific activity (Bq/g of carbon) in expired air from one of the volunteers at various times after the administration of 74 kBq ^{14}C-triolein. After 3 days, the detection limit for ordinary liquid-scintillation counting (around 3 Bq/g carbon) is passed. With AMS it is possible to follow the excess of ^{14}C in exhaled air over some years. The total expired activity has been calculated assuming a carbon dioxide expiration of 9 mmol per kg body weight per hour (4). The result shows that 30% left the body in 24 hours and another 7% during the following 8 days.

From the dosimetric point of view, it is of interest to know where the rest of the ^{14}C is to be found. The irregularities, which are seen in the curve (A-D) are interesting and can help to explain the kinetics. The dip in the curve after 5 days (A) came after the volunteer had had three full meals in a short time; this result gave rise to some controlled fasting periods (32 hours long) when the volunteer was allowed only to drink water. Such fasting periods started on days 72 (B), 500 (C) and 952 (D) after the administration of ^{14}C-triolein.

When the fast began, the exhalation of $^{14}CO_2$ increased, and then decreased to its starting value when the person began to eat again. For a reference person not given ^{14}C-triolein, no increase in ^{14}C specific activity was found during a 32-hour fast. Detailed curves from the three fasting sessions for the person who received ^{14}C-triolein are given in Figure 2. When the areas under the curves are calculated, the effect of the fasting can be expressed in terms of extra expired ^{14}C; the values are 3,400, 1,200 and 500 Bq-hr/g, respectively. This means that the effective half-time for the ^{14}C

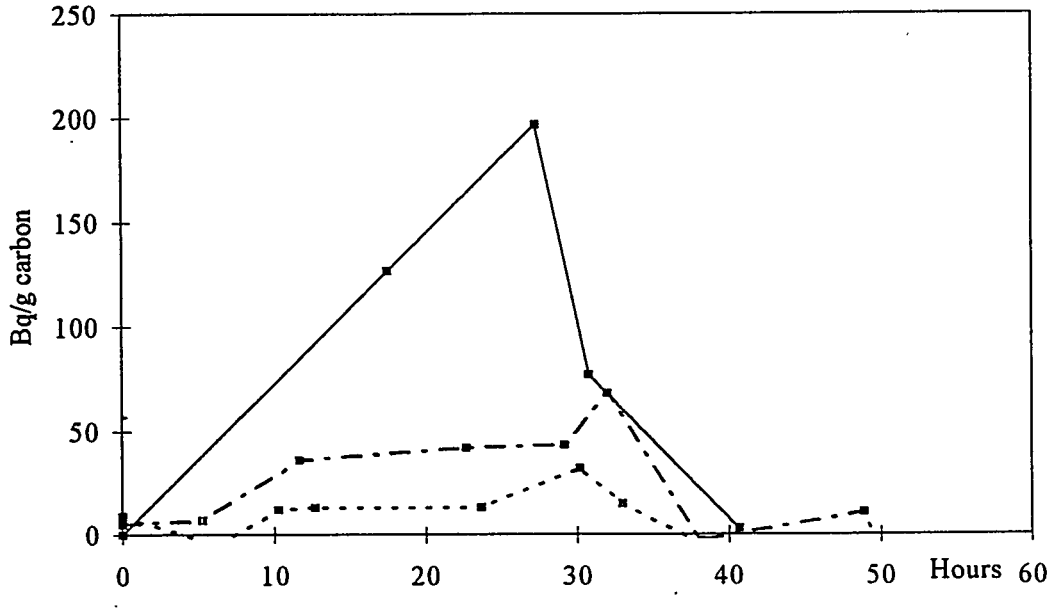

Figure 2. Increase in ^{14}C specific activity as a result of a controlled 32 hour fast (starting at time 0 and ending at 32 hours) at B: 72 (——), C: 500 (- — - —) and D: 952 (- - - -) days after administration of ^{14}C-triolein as in Figure 1.

remaining in the body (presumably in fat) is around 300 (260-340) days. The figure is at least valid for the fraction which is bound in such a way that it is available for use during a 32-h fasting period. The estimated half-time is considerably longer than 40 days, which is assumed for total body carbon in ICRP Reports 30 (5) and 56 (6). It is however in fairly good agreement with the ICRP Report 62 (7), which assumes that 30% of the ^{14}C-labeled fat is metabolized rapidly, with a half-time of 2 days, and that 70% is retained for a longer time (T = 400 days). We intend to follow 10 people in subsequent studies, including children. It will also be interesting to confirm the estimates above through analysis of a limited number of fat biopsies.

^{14}C-Urea Test

The results for the two adults are given in Figure 3. One was first given 1.1 kBq and 7 days later 110 kBq. The second volunteer received 1.1 kBq. The results for the three children, who were each given 55 kBq, (Figure 4), may indicate a similar or somewhat shorter half-time than for the normal adult. The excretion of ^{14}C via expired air during the first hour has been estimated for the adults as well as for the children and is given in Table 2. An exhalation of 0.1-0.5% during the first hour is considered normal. This means that one of the women is clearly HP-positive and one of the girls is a borderline case.

The urine samples have not yet been analyzed. In the future, it will be of interest to include analysis of bone biopsies to estimate the fraction of ^{14}C stored as carbonate in the skeleton. However, even if as much as 15% of the activity given were retained in the skeleton for the rest of the patient's life, it would result in dose rates which are comparable to those from ^{14}C already present in man and the environment mainly due to atmospheric nuclear weapons tests and natural production. Thus, there

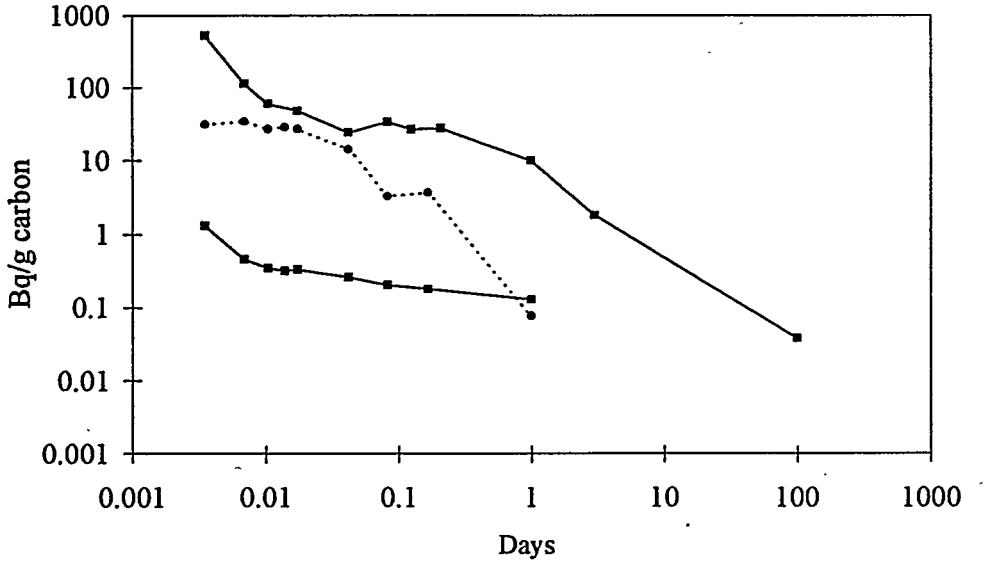

Figure 3. Excess $^{14}CO_2$ in expired air at various times after an intake of ^{14}C-urea in two adult female volunteers. Person A (■) was studied twice, first using 1.1 kBq ^{14}C-urea (lower curve) and 7 days later using 110 kBq (3 μCi)(upper curve). She was *Helicobacter pylori* negative. Person B (•) received 1.1 kBq ^{14}C-urea and was found to be HP positive.

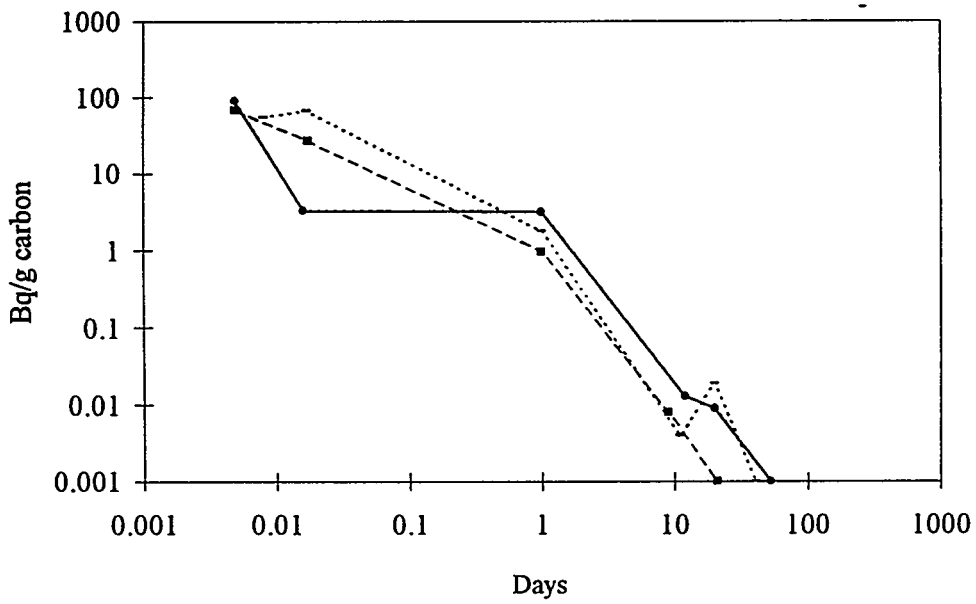

Figure 4. Excess $^{14}CO_2$ in expired air at various times after an intake of 55 kBq ^{14}C-urea in three children; (■ — — — = Person C), (– - - - - = Person D) and (● ——— = Person E).

Table 2
Estimated Fractional ^{14}C Exhalation during 0-60 Minutes after ^{14}C-urea Administration

Person	Sex, age and weight	Activity given, kBq	Fraction exhaled during the first 60 minutes, % of given ^{14}C-activity
A	F, 54 years, 55 kg	1.10	0.21
		110	0.46
B	F, 60 years, 70 kg	1.10	15.6
C	F, 10 years, 20 kg	55	0.10
D	F, 14 years, 70 kg	55	0.6-0.8
E	M, 14 years, 40 kg	55	0.15

is no reason to prevent the use of ^{14}C-labeled urea from a radiation protection point of view, either in adults or in children.

A detailed biokinetic and dosimetric model is under development to provide the nuclear medicine community with a rough estimate of the patient absorbed dose. These studies complement present estimates based on measurements using liquid-scintillation counters (8, 9).

In summary, we have a method available for extremely sensitive ^{14}C measurements. It can be used to improve our dosimetry and makes it possible to use less than 1% of the activity normally used today.

ACKNOWLEDGMENTS

This project was supported by the Swedish Medical Research Council (B95-39X-11272-01A), the Swedish Radiation Protection Institute and Malmö University Hospital. Johan Areberg M.Sc. assisted with the preparation of samples for AMS.

REFERENCES

1. Kutschera W. Accelerator mass spectrometry: Counting atoms rather than decays. Nucl Phys News 3(1):15-21, 1993.
2. Stenström K, Leide-Svegborn S, Erlandsson B, Hellborg R, Mattsson S, Nilsson L-E, Nosslin B, Skog G and Wiebert A. Application of accelerator mass spectrometry (AMS) for high-sensitivity measurements of $^{14}CO_2$ in long-term studies of fat metabolism. Appl Radiat Isot 47(4):417-422, 1996.
3. Stenström K, Leide-Svegborn S, Erlandsson B, Hellborg R, Skog G, Mattsson S, Nilsson L-E and Nosslin B. A program for long-term retention studies of ^{14}C-labeled compounds in man using the Lund AMS facility. Accepted for publication in Nucl Instr and Meth B.
4. Winchell HS., Stahelin H, Kusubov N, Slanger B, Fish M, Pollycove M and Lawrence JH . Kinetics of CO_2-HCO_3^- in normal adult males. J Nucl Med 11(12):711-715, 1970.
5. International Commission of Radiological Protection. Limits for Intakes of Radionuclides by Workers. ICRP Publication 30 Part 1. Pergamon Press, Oxford, 1979.
6. International Commission of Radiological Protection. Age-Dependent Doses to Members of the Public from Intake of Radionuclides: Part 1. Ingestion dose coefficients. ICRP Publication 56, Annals of the ICRP 20 (2) Pergamon Press, Oxford, 1989.
7. International Commission of Radiological Protection (1993). Addendum to Publication 53. ICRP Publication 62. Radiological Protection in Biomedical Research. Annals of the ICRP 22(3), Pergamon Press, Oxford.
8. Stubbs JB and Marshall BJ. Radiation dose estimates for the carbon-14-labeled urea breath test. J Nucl Med 34(5):821-825, 1993.
9. Combs MJ, Stubbs JB, Agarwal AK, Hoffman SR, Feng T, Teates CD and Marshall BJ. Dose estimates for a capsule-based ^{14}C-urea breath test. This publication, pp 620-630, 1999.

QUESTIONS

Muller: Why do you not use ^{13}C in the volunteer studies? Using a mass spectrometer it can also be distinguished from ^{12}C, and it could be used in a much higher amount than ^{12}C.

Mattsson: The aim is to study the kinetics and dosimetry of ^{14}C-labeled compounds which are used clinically. Labeling efficiency and stability might vary between ^{14}C and ^{13}C-labeled products, so therefore we have to use ^{14}C-substances. Another reason is that the background of ^{14}C is lower than that of ^{13}C. Therefore the detection limits with AMS will be lower when using ^{14}C-labeled compounds.

DOSE ESTIMATES FOR A CAPSULE-BASED ^{14}C UREA BREATH TEST FOR DETECTION OF *H.pylori*

Combs MJ[1], Stubbs JB[2], Sparks R[3], Teates CD[4],
Feng T[1], Hoffman SR[1], Agarwal AK[1,5] and Marshall BJ[1,4],

[1]Tri-Med Specialties, Charlottesville, VA
[2]Radiation Dosimetry Systems of Oak Ridge, Knoxville, TN.
[3]Radiation Internal Dose Information Center, Oak Ridge, TN
[4]University of Virginia Health Sciences Center, Charlottesville, VA
[5]Georgetown University Hospital, Washington, DC.

ABSTRACT

A 37 kBq (1μCi) ^{14}C urea breath test for the detection of *H. Pylori* has been developed (PYtest®) and is currently under clinical investigation. The purpose of this study was to examine the excretion and radiation doses estimated for the PYtest. A 37 kBq PYtest capsule was orally administered to 20 consenting human volunteers (5M, 15F, aged 19-60 years) along with 20 ml of water. Breath samples were collected frequently over the first hour and at 2, 3, 4, 5, 6, 12, 24, 36, 48, 60, and 72 hours postingestion. A five-day complete urine collection was also obtained for each subject in 12-hour increments. The ^{14}C concentration in the breath and urine samples was measured by liquid scintillation counting. The breath results were modeled using a modification of a published method to give percentage of the ^{14}C excreted as CO_2. The urinary excretion was measured directly since all urine was collected over 120 hours. Breath test results gave 9 *H. Pylori*-positive (HP+) and 11 *H. Pylori*-negative (HP-). The average 10-minute HP- breath activity was 7 disintegrations/minute (DPM) [range 0-41 DPM] and HP+ breath sample activity was 1536 DPM [range 217-2612 DPM]. Average total (120-hour) excretion of ^{14}C was measured to be 87% and 94% for HP- and HP+ subjects, respectively.

Residence times were obtained by averaging the individual pulmonary and urinary excretion data of the HP- and HP+ groups and applying a slightly modified version of the Stubbs and Marshall model(7). Radiation dose estimates were calculated using MIRDOSE3.1. Absorbed doses for the HP- and HP+ groups, respectively, were: stomach (0.38 and 0.22 mGy/kBq); lung (0.081 and 0.038 mGy/kBq); bladder wall (0.19 and 0.086 mGy/kBq). The EDEs were 0.10 and 0.049 mSv/kBq.

These results indicate that the long-term ^{14}C retention and radiation absorbed doses from the PYtest are very low. These data also reinforce previous excretion studies and dose estimates.

INTRODUCTION

The excretion of ^{14}C following administration of the PYtest® capsule which contains 37 kBq (1

μCi) ^{14}C urea has been studied previously (1). That study revealed an average excretion of 74% in HP-negative volunteers and 75% in HP-positive volunteers over the first 24 hr following administration of the test capsule. Munster (2) studied the excretion of orally administered liquid-form ^{14}C urea and found that 81% was recovered from HP-negatives and 79% recovered from HP-positives in the first 24 hr, which is in agreement with our results. Munster's study also looked at long-term retention of ^{14}C from a ^{14}C urea breath test, recovering an average of 97% from HP-negatives and 85% from HP-positives over a period of 3 days.

AIM OF STUDY

To determine the excretion of ^{14}C following ingestion of the PYtest capsule and using that information, calculate radiation dose estimates.

MATERIALS AND METHODS

Experimental Protocol and Data Collection

A total of 20 volunteers (5 Male, 15 Female, average age 41 yr, range 19-60) were enrolled in the protocol which was approved by the University of Virginia Human Investigation Committee and the Medical Isotopes Subcommittee of the Radiation Safety Committee. All volunteers participating in the study gave informed consent.

A blood test (Flexsure, SmithKline Diagnostics) for *H. pylori* antibodies was performed on each volunteer. Pregnancy tests were performed on women of childbearing potential since pregnancy was one of the exclusion criteria. Baseline breath samples were obtained from each volunteer and baseline urine samples were obtained in all but one volunteer who could not produce a sample. Standard procedures for administering the PYtest were employed by having each volunteer ingest a capsule containing 37.7 kBq (1.02 μCi) ^{14}C urea along with 20 ml water. Three minutes later, each volunteer was given an additional 20 ml water.

Following capsule administration, breath samples were collected using the normal PYtest breath collection procedure. The procedure is to trap 1 mMol CO_2 in PYtest breath collection fluid (1 ml 1 M benzethonium hydroxide, 1.5 ml methanol). Ten milliliters of liquid scintillation fluid (EconoSafe, Research Products International, Mt. Prospect IL) were added to each breath sample. The samples were counted in a liquid scintillation counter (Beckman, Fullerton CA) for 5 minutes and results expressed as DPM per millimole of CO_2 collected (DPM/mMol). Breath samples were collected at 0, 5,1 0, 15, 20, 25, 30, 40, 50, and 60 minutes after capsule administration, and at 2, 3, 4, 5, 6, 12, 24, 36, 48, 60, and 72 hr after capsule administration.

All urine was collected in 12-hour increments for a total of 5 days following capsule administration. The volume of each 12-hour collection was measured, and 1 ml of each container was placed in a liquid scintillation vial along with 10 ml of liquid scintillation fluid (EconoSafe, RPI, Mount Prospect, IL). Samples were counted in a liquid scintillation counter (Beckman, Fullerton, CA) for 5 minutes and the number of DPM/ml was obtained for each sample.

^{14}C Excretion Calculations

Cumulative urinary excretion results were obtained by direct multiplication of urine concentrations and urine volumes obtained throughout the collection period. Since not all breath could be collected, a model was used to describe pulmonary excretion. The method described by Munster (2) was used to model pulmonary $^{14}CO_2$. This model uses the trapezoid rule for integration of breath radioactivity excretion and multiplies that by a constant factor for amount of CO_2 excreted

per unit time. The only deviation from Munster's model was that, in this study, individual basal metabolic rate (BMR) values were calculated based on the volunteer's sex, height and weight using standard data tables (3) rather than the average value used by Munster. The population in the Munster study was almost entirely male so an average male BMR was justified. The individual values calculated in this study provide a more realistic model. All results were expressed as a percentage of administered activity.

Radiation Dose Estimation

The radiation dosimetry model previously developed by Stubbs and Marshall(4) utilized measured urinary excretion in HP- and HP+ subjects. In that report, the cumulative excretion of ^{14}C urea in the urine of humans receiving oral doses of ^{14}C urea was 70% and 40% in HP- and HP+ subjects, respectively. The cumulative excretion of ^{14}C labeled CO_3^{-2}-CO_2 in the breath was 30% and 60% in HP- and HP+ subjects, respectively. A more recent dose estimate for this compound was provided by the Radiation Internal Dose Information Center (RIDIC) at the Oak Ridge Institute for Science and Education (5). That estimate used a slightly modified version of the Stubbs and Marshall dosimetry model, applied to the mean cumulative urinary excretion values for each group of volunteers. These two earlier dose estimates for ^{14}C urea breath tests assumed that activity excreted in the breath accounted for all activity not excreted in the urine. Long-term assessment of breath excretion had not been performed prior to this study, thus actual breath excretion data were not available to validate the use of the biokinetic model of ^{14}C carbon dioxide. For this report's radiation absorbed dose estimate, the modified model of Stubbs and Marshall(4) was applied to the average urinary and pulmonary excretion and an additional compartment was utilized to more accurately account for activity not immediately excreted. Figure 1 shows the diagram of the biokinetic model used in this report.

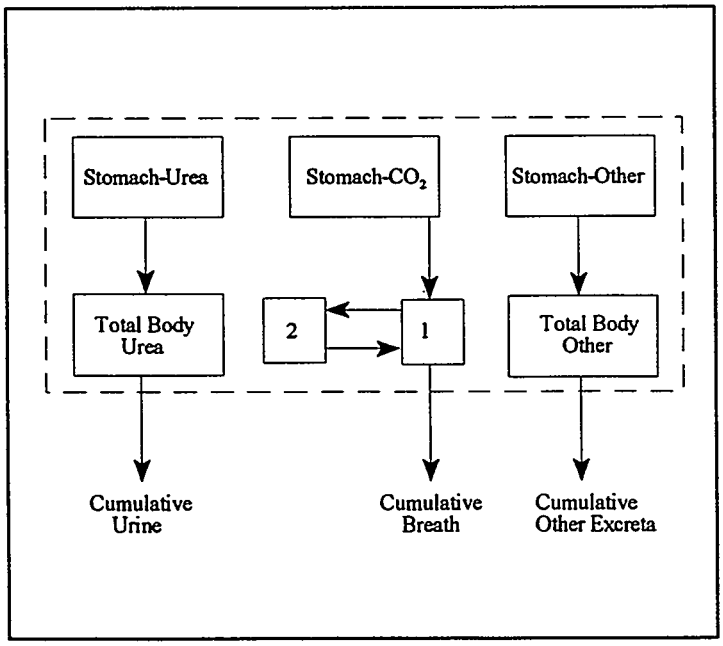

Figure 1. Biokinetic model for the 37-kBq (1-μCi) ^{14}C Urea Breath Test. Compartments 1 and 2 represent the new bicarbonate/CO_2 biokinetic model. Compartments inside the dashed lines comprise total body.

The ^{14}C was assumed to be immediately absorbed into the stomach wall and was assumed to leave the stomach wall via three independent pathways, corresponding to urea, bicarbonate/CO_2, and a long-term retention compartment of ^{14}C labeled molecules. In Figure 1, these three pathways are referred to as "Stomach-Urea", "Stomach-CO_2", and "Stomach-Other", respectively. The distribution of activity to these three pathways was determined by the observed cumulative excretion and retention. The percent excreted in the urine and breath defined the percentage removed via the urea and bicarbonate/CO_2 pathways, respectively. All activity unaccounted for in the excreta was assumed to be uniformly distributed in the total body, and removed with a 1,000 hr biological half-time. The biological removal rates from the stomach wall into

each of these pathways were iteratively determined in a manner that provided the best fit between the simulated and observed excreta (and total-body retention) time-activity curves.

The averaged urinary excretion data for the HP- and HP+ subjects were fit to monoexponential functions using a nonlinear-least-squares regression algorithm (CONSAM30, Resource Facility for Kinetic Analysis, Seattle, Washington). The urea biokinetic model assumes a rapid absorption of ^{14}C urea from the stomach wall with uniform distribution of the activity in the total body. This activity is assumed to be excreted directly into the urine. The resulting urinary excretion fractions and their associated biological removal half-times were estimated and used as input data for the dynamic bladder model of Cloutier et al (6). The dynamic bladder model, with a bladder voiding interval of 4.8 hours, was used for estimating the residence times for the urinary bladder contents.

The Stubbs and Marshall biokinetic model for bicarbonate/CO_2 was applied to the average percentage of the activity exhaled in the breath of the HP- and HP+ subjects. This multicompartmental model was modified to remove the long-term storage compartment (compartment 3). Again, the stomach wall was the input route for activity utilizing this model.

The long-term retention (activity not excreted in breath or urine during the five days of excreta measurement) was modeled as a single compartment and the biological removal half-time fixed at 1000 hours (per ICRP 30, removal half-time for ^{14}C labeled organic molecules, (7). This biokinetic model assumes a rapid absorption of ^{14}C labeled molecules from the stomach with uniform distribution of the activity in the body.

Total-body retention of ^{14}C activity was modeled as the sum of activities in each of the three previously described biokinetic models (dashed box of Figure 1). The total-body retention biokinetic model has the property of conservation of activity.

Total-body residence times were calculated by numerical integration of the simulated total body time-activity curve. The stomach wall residence times were found by analytical integration, i.e., multiplying the fraction of activity leaving via a given pathway by 1.443, and its biological removal half-time (in hours). For example, consider the HP- group which excreted an average of 84.3 % of the activity in the urine. The biological removal rate for this activity, from the stomach wall to the total body, was 1.54 hours. Thus, the stomach residence time for activity leaving the stomach wall via this pathway was $1.443 \times (0.843) \times (1.54 \text{ hr}) = 1.87$ hours. The remainder of the body residence time was calculated by subtracting the lung and stomach wall residence times from the total-body residence time. Spleen residence times were negligible, therefore the spleen was neglected as a source organ.

Stomach wall and lung residence times were determined using the modified method of the Radiation Internal Dose Information Center report (RIDIC) (5). The RIDIC calculations used the modification for lung only. In this study, applying the modified residence time calculation method to the determination of stomach wall residence times was also warranted. Therefore, the full set of organ dose estimates were calculated explicitly apportioning, to the lungs, $1/70^{th}$ of the total-body residence time (ratio of lung mass to total body mass; 1kg/70kg). The stomach was treated in the same manner, where the apportionment of total-body residence time (ratio of stomach wall to total body mass; 0.15kg/70kg) was added to the stomach residence time, calculated as described in the previous paragraph. The remainder of the body residence times were reduced by the amount apportioned to stomach and lung. This results in lung absorbed doses slightly larger than those to nonsource organs. This modification resulted in stomach absorbed doses 20% larger than if the modification were not used.

Radiation absorbed doses for the HP- and HP+ subject groups were estimated using the MIRDOSE 3.1 software (8). The exception to this was absorbed dose to the stomach wall. The MIRDOSE 3.1 software assigns stomach residence times to the stomach contents and it was felt that the residence time for stomach would be more appropriately assigned to the stomach wall. The S

value for stomach wall irradiating itself (with ^{14}C as the radionuclide) was estimated as 7E-4 rad/μCi · hr, where the assumed mass of stomach wall was 150 grams. The stomach wall dose was obtained by multiplying the stomach wall residence time by this S value.

RESULTS

Breath test results revealed 9 HP-positive volunteers and 11 HP-negative volunteers in the study group. Serology and breath test results concurred in all but one of the 20 cases. The lone exception was an individual with positive serology and negative breath test. It was later learned that the volunteer had previously been treated for *H.pylori* which would account for the inconsistent result and would also indicate successful treatment. Individual cumulative excretion data for 24, 48 and 120 hours post administration of the PYtest capsule are shown in Table 1.

Table 1
Twenty-four hour, 48-hour and 120-hour Cumulative ^{14}C Excretion Results

	24 hr Totals			48 hr Totals			120 hr Totals		
Subj.	Urine %	Breath %	Total %	Urine %	Breath %	Total %	Urine %	Breath %	Total %
1*	76.4	0.6	77	88.1	0.6	89	91.8	0.6	92
2	84.2	3.9	88	90.4	3.9	94	91.4	4.7	96
3*^	7.7	76.7	84	8.8	76.7	85	9.7	77.4	87
4	75.5	1.1	77	85.6	1.1	87	87.2	2.8	90
5*^	56.6	24.5	81	64.0	24.5	88	65.0	24.9	90
6	75.3	0.9	76	87.1	0.9	88	89.1	1.3	90
7*^	44.4	36.0	80	50.7	36.0	87	51.7	36.4	88
8	76.7	1.1	78	85.4	1.1	86	85.6	1.1	87
9*^	29.9	54.1	84	35.8	54.6	90	37.4	55.9	93
10*^	35.2	73.2	108	37.6	73.4	111	37.8	77.1	115
11	60.5	2.3	63	68.7	3.9	73	69.2	4.5	74
12*^	56.8	37.3	94	60.2	37.3	97	60.3	38.4	99
13*^	26.4	59.9	86	30.2	60.2	90	30.5	61.7	92
14	50.0	5.4	55	55.8	5.4	61	57.8	5.4	63
15	88.5	1.4	90	92.6	1.4	94	92.9	1.4	94
16*^	28.2	52.2	80	30.1	52.2	82	30.4	53.7	84
17*^	30.9	63.2	94	34.7	63.2	98	35.5	63.6	99
18	75.6	0.7	76	83.2	0.7	84	83.9	0.7	85
19	73.9	1.5	75	80.9	1.5	82	82.7	1.5	84
20	91.1	1.7	93	95.3	1.7	97	95	2	98
Avg	57.2%	24.9%	82%	63.3%	25.0%	88%	64.3%	25.8%	90%
1SD	24%	28%	11%	26%	28%	10%	27%	29%	10%

* Indicates a case with HP-positive serology
^ Indicates a case with HP-positive breath test
1 SD = 1 standard deviation

The average recovery for the first 24 hours was 82%, 88% for the first 48 hours; 90% by 72 hours, a value which did not change significantly when the study concluded at 120 hr (90% ±10% {mean ± 1 SD}). The results were grouped into HP-positive and HP-negative categories. Total (120 hr) ^{14}C excretion values are shown in Tables 2 and 3.

Table 2

Cumulative (120-hour) ^{14}C Excretion Values, HP+ Volunteers (n=9)

Subject	Urine % Excreted	Breath % Excreted	Total % Excreted
3	10	77	87
5	65	25	90
7	52	36	88
9	37	56	93
10	38	77	115
12	60	38	99
13	31	62	92
16	30	54	84
17	35	64	99
Average	40%	54%	94%
1 SD	17%	18%	9%

Table 3

Cumulative (120-hour) ^{14}C Excretion Values, HP- Volunteers (n=11)

Subject	Urine % Excreted	Breath % Excreted	Total % Excreted
1	92	1	92
2	91	5	96
4	87	3	90
6	89	1	90
8	86	1	87
11	69	4	74
14	58	5	63
15	93	1	94
18	84	1	85
19	83	2	84
20	95	2	98
Average	84%	2%	87%
1 SD	11%	2%	10%

The cumulative results show that an average of 94% of ^{14}C from the PYtest is excreted from HP+ volunteers and 87% from HP- volunteers in the first 5 days following administration of a PYtest

capsule. When combined, these results show that on average 90% of the ^{14}C from a PYtest capsule is excreted within the first five days following ingestion.

Radiation Dose Estimates

Table 4 lists the biological model parameters and residence times for the 37 kBq (1 μCi) ^{14}C Urea breath test.

Table 4

Biological Model Parameters and Residence Times for the 37-kBq ^{14}C Urea Breath				
	HP- (n=11)		HP+ (n=9)	
	Measured Values*	T_B‡	Measured Values*	T_B‡
%Urea (urine)	84.3%	(T_B=1.54 h)	39.8%	(T_B=1.54 h)
%Pulmonary/($C0_2$)	2.4%	(T_B=0.99 h)	54.3%	(T_B=0.11 h)
%Other	13.3%	(T_B=0.17 h)	5.9%	(T_B=0.17 h)
*Averaged over the respective subject groups ‡Biological removal half-times from stomach wall to total body				

	Residence Times	
Source Organs	HP- τ(hr)	HP+ τ(hr)
Stomach Wall	2.37	1.17
Lungs	2.86	1.29
Urinary Bladder Contents	2.21	1.03
Remainder of Body	195	87.7

HP- Subjects

The cumulative urinary excretion was in the range of 58% - 95%, with only two subjects' values below 82.7%. The HP- subjects excreted an average of 84.2% (84.2% simulated, 84.3% observed) of the administered ^{14}C in their urine with a biological removal half-time of 7.46 hours. These subjects excreted an average of 2.4% of the administered activity in the breath.

The stomach wall was estimated to receive the largest absorbed dose (0.38 mGy/kBq, 1.4 mrad/μCi), followed by the urinary bladder wall (0.19 mGy/kBq, 0.70 mrad/μCi), and lungs (0.081 mGy/kBq, 0.30 mrad/μCi). All other organs were estimated to receive an absorbed dose of 0.078 mGy/kBq (0.29 mrad/μCi). The effective dose equivalent was 0.10 mSv/kBq (0.38 mrem/μCi).

HP+ Subjects

The cumulative urinary excretion was in the range of 9.7% - 65%, with only three subjects' values falling outside one standard deviation of the mean (39.8% ± 17%). The HP+ subjects excreted an average of 39.9% (39.9% simulated, 39.8% actual) of the administered ^{14}C in their urine with a biological removal half-time of 9.16 hours. These subjects excreted an average of 54.3% of the

administered activity in the breath.

The stomach wall was estimated to receive the largest absorbed dose (0.22 mGy/kBq, 0.82 mrad/μCi), followed by the urinary bladder wall (0.086 mGy/kBq, 0.32 mrad/μCi), and lungs (0.038 mGy/kBq, 0.14 mrad/μCi). All other organs were estimated to receive an absorbed dose of 0.035 mGy/kBq (0.13 mrad/μCi). The effective dose equivalent was 0.049 mSv/kBq (0.18 mrem/μCi).

All Subjects

Table 5 shows a comparison of several dosimetric variables from this study as well as those from the RIDIC calculations (5). The simulated urinary excretion for the HP- group was nearly identical (84.2% vs 85.5%), however, the HP+ group demonstrated 46% higher recovery of activity in the urine (39.9% vs 27.3%). The mean biological removal half-times for urinary excretion were 7.46 hours and 9.16 hours for the HP- and HP+ subjects, respectively. These values are very similar to those reported in the RIDIC dose estimate; 7.0 hours and 10 hours for the HP- and HP+ subjects, respectively.

Table 5
Comparison of Dosimetry Parameters for the ^{14}C Urea Breath Test

	This Study		RIDIC Calculations①	
Parameter	HP-	HP+	HP-	HP+
f_U	84.2%	39.9%	85.5%	27.3%
f_B	2.4%②	54.3%②	14.5%③	72.7%②
T_B	7.46 h	9.16 h	7.0 h	10 h
τ_{UBC}	2.21 h	1.03 h	2.2 h	0.73 h
τ_{RB}	195 h	87.7 h	45.7 h	195 h
τ_{Lung}	2.86 h	1.29 h	0.68 h	2.94 h
τ_{Stom}	2.37 h	1.17 h	0.11 h	0.11 h
D_{Stom} (mGy/kBq)	0.38	0.22	0.015	0.046
D_{UBW} (mGy/kBq)	0.19	0.086	0.16	0.089
D_{Lung} (mGy/kBq)	0.081	0.038	0.019	0.084
D_{other} (mGy/kBq)	0.078	0.035	0.018	0.078
EDE (mSv/kBq)	0.10	0.049	0.027	0.078

f_U = simulated percentage of activity excreted in the urine
f_B = measured percentage of activity excreted in the breath
T_B = biological removal half-time (hours) for activity excreted in urine
EDE = effective dose equivalent

① RIDIC dose estimates (April 7, 1995) for ^{14}C Urea Breath Test(5)
② measured values
③ calculation assumed all activity not excreted in urine was excreted in breath

DISCUSSION

The results obtained from this study reveal that not more than 10% (average for all 20 subjects) of administered ^{14}C is retained by the body long-term. This amount is similar to the 3.7 kBq (0.1 μCi) normally found in the body. The results presented here are consistent with previous excretion studies in which breath and urine samples were obtained (1,2). The study lasted 2 days longer than necessary

since the amount recovered after 72 hours did not increase significantly. This also shows that Munster's study was of sufficient duration. The results (HP-, 77% initial 24 hours; HP+, 88% initial 24 hours) are consistent with those obtained in our first excretion study (74% HP-, 75% HP+).

The remaining activity is assumed to be excreted from the body with a 1,000 hour half-time. This long-term component is included in our dosimetry estimates. The 1,000-hour value is based on the recommendations of the International Commission on Radiological Protection (7) which state that the use of a 40-day (960 hour) biological half-life would lead to realistic or conservative dose estimates for ^{14}C labeled organic compounds.

The major improvement of this absorbed dose estimate compared to prior dose estimates is the existence and use of the long-term breath excretion data. Availability of this data brought to light the need for changing the bicarbonate/CO_2 biokinetic model used in previous dose estimates.

The stomach wall absorbed doses for our calculations are substantially larger than that of the RIDIC dosimetry calculations(5). This increase is due entirely to the assumptions used in estimating stomach wall residence times. The RIDIC calculations used the stomach residence time of 0.11 hours as reported by Stubbs and Marshall, whereas this work directly apportions some of the total body residence time to the stomach based on the ratio of the stomach wall mass to that of the total body, as well as directly calculating estimated stomach wall residence times based on the ^{14}C absorption pathways. The net result is larger stomach wall residence times. It should be noted that this work calculated the stomach wall absorbed dose outside of the MIRDOSE 3.1 software, because that program assumes the activity in the stomach is in the contents of the stomach rather than the wall. Assuming that the activity is in the wall results in a near doubling of the stomach wall absorbed dose compared to assuming an equivalent amount of activity in the contents. This assumption also results in a more conservative estimate of absorbed dose to the stomach wall than would a distribution of activity in the stomach's contents.

All absorbed dose values for HP- subjects are higher than previously estimated and those for HP+ subjects are lower than previously estimated, with the exception of stomach wall. These changes are simply due to a more accurate accounting of activity not excreted during the course of the clinical investigation. For HP- subjects, an average of 2.4% of the administered activity was measured in the breath, with 13.3% not excreted within five days. The biokinetic model in this study assumed that the 13.3% was retained with a long biological half-time (1000 hr), whereas the previous estimates (which had no breath excretion data to indicate otherwise) assumed all activity not excreted in the urine went to the bicarbonate pathway. The previous bicarbonate model predicted, for activity reaching this pathway, rapid excretion of 84.4% (in the breath) with the remaining 15.6% retained in a long-term storage compartment with a long biological removal half-time. With that model, HP- subjects would have had 15.8% of the administered activity (observed activity in the urine was 84.2%) assumed to enter the bicarbonate pathway. Therefore, 13.3% ($0.158 \times 84.4\% = 13.3\%$) of the 15.8% reaching the bicarbonate pathway would be excreted rapidly in the breath and 2.5% would be retained in the body with a long removal half-time. Since 2.4% was measured in the breath of HP- subjects, rather than 13.3%, this aspect of the bicarbonate modeling was inaccurate in the previous model.

To more accurately simulate the observed excreta data (both urinary and pulmonary), the bicarbonate model was altered. The long-term retention compartment was removed from the bicarbonate model and incorporated as a separate excretion pathway. This modification produced a very accurate simulation of cumulative urinary and pulmonary excretion data, as well inferred total-body retention, for the HP- subjects. Because the original biokinetic model was altered for HP- subjects, the same alteration was required for HP+ subjects. Application of the new biokinetic model to the HP+ subjects' average excretion data resulted in accurate simulations, confirming the reasonability of the model alterations for dosimetric purposes.

Using the effective dose equivalent as an index of radiological risk for this procedure, one can compare the radiological risks of the 37 kBq (1-μCi) breath test to natural background or another radiological procedure. The United Nations Scientific Committee on the Effects of Atomic Radiation (9) reported a global average of 2.4 mSv/year for natural background radiation. By comparison, an HP- person (EDE = 0.10 mSv/kBq) would need to have 630 37 kBq Breath Tests to equal a year's background exposure (1300 tests for HP+ persons). Alternatively, a single 37 kBq Breath Test is equivalent to 14 hours or 7 hours of background radiation exposure for HP- and HP+ persons, respectively. These are trivial exposures compared to background or virtually any other radiological (medical) procedure.

Although the radiation dose estimate calculated from this study is higher than the previous calculation for HP- subjects (EDE 0.10 versus 0.027 mSv/kBq), this is due to the change in assumptions and additional data for the model. This increase does not significantly impact the risk associated with the test, especially when compared to other diagnostic procedures and radiation doses received from environmental sources. A comparison of doses from various diagnostic procedures is provided in Table 6.

Table 6

Comparison of Effective Dose Equivalents of Common Nuclear Medicine Procedures

Radiopharmaceutical/Procedure	EDE (mSv)
370 MBq Kr-81m Gas (lung perfusion)	0.01
37 kBq Co-57-Cyanocobalamin (Schilling's test)	0.16
370 MBq Tc-99m-DTPA (renal function)	3.0
740 MBq Tc-99m-MDP (bone scan)	5.4
370 MBq F-18-FDG (brain scan)	10.7
18.5 MBq In-111-WBC (infection imaging)	12.5
185 MBq Ga-67-citrate (tumor imaging)	23.0
37 kBq ^{14}C urea (PYtest)	**0.002-0.004**

As Table 6 shows, the radiation dose received from the PYtest is much smaller than most diagnostic nuclear medicine procedures. In fact, the PYtest gives an absorbed dose which is 40 times lower than a nonimaging test with the same administered activity (37 kBq) of a much shorter-lived radionuclide (Co-57, 270 days). The dose from the PYtest is also lower, but on the same order of magnitude as a 370 MBq (10,000 μCi) inhalation of Kr-81m-gas (13-second half-life) for lung perfusion assessment.

The absorbed dose from this procedure is also small in relation to background radiation levels. We normally receive between 0.88 and 2.4 mSv annually from background radiation (10). The annual dose received from naturally occurring ^{40}K (0.17 mSv) is 42 times higher than that received from the PYtest(6).

The dosimetry model used in this study is the best available for ^{14}C urea dosimetry. It is based on a widely accepted, published method and this study provided a significant improvement in the model.

REFERENCES

1. Combs MJ, Stubbs JB, Buck DA and Marshall BJ. Dosimetry and reproducibility of a capsule-based C-14 urea breath test. J Nucl Med 36(5);P98, 1995 (Abst.).

2. Munster DJ, Chapman BA, Burt MJ, Dobbs BR, Allardyce RA, Bagshaw PF, Troughton WD and Cook HB. The fate of ingested 14C urea in the urea breath test for Helicobacter pylori infection. Scand J Gastroenterol 28(8):661-666, 1993.
3. Diem K, Lentner C, eds. Geigy Scientific Tables, 7th edition. Basel; CIBA-GEIGY, pp 536-540, 1975.
4. Stubbs JB and Marshall BJ: Radiation dose estimates for the carbon-14 labeled urea breath test. J Nucl Med 34:821-825, 1993.
5. Dose Estimate for C-14 Urea - Orally Administered. Radiation Internal Dose Information Center, Oak Ridge Institute for Science and Education, Oak Ridge, TN, personal communication April 7, 1995.
6. Cloutier R, Smith S, Watson E, Snyder W and Warner G. Dose to the fetus from radionuclides in the bladder. Health Phys 25:147-161, 1973.
7. ICRP 30 Part 3. Limits for Intakes of Radionuclides by Workers. Pergamon Press, New York, pp 4-7, 1978.
8. Stabin MG. MIRDOSE: Personal computer software for internal dose assessment in nuclear medicine. J Nucl Med 37(3):538-546, 1996.
9. Sources, Effects and Risks of Ionizing Radiation. United Nations Scientific Committee on the Effects of Atomic Radiation 1988 Report to the General Assembly, with annexes. New York: United Nations; 1988.
10. Kathren RL. Radioactivity In The Environment: Sources, Distribution, and Surveillance. Harwood Academic Publishers, pp 78-90, 1985.

BIOKINETICS AND DOSIMETRY OF ^{111}In-DTPA-D-Phe-1-OCTREOTIDE IN PATIENTS

Leide-Svegborn S, Nosslin B and Mattsson S
Department of Radiation Physics,
Malmö University Hospital,
S-205 02 Malmö, SWEDEN

ABSTRACT

^{111}In-DTPA-D-Phe-1-octreotide (^{111}In-pentetreotide) is a recently developed radiopharmaceutical used for diagnosis of neuroendocrine tumors. The purpose of this study was to investigate the biokinetics and dosimetry of ^{111}In-pentetreotide in patients with such tumors. Ten patients underwent whole-body scanning (anterior and posterior projections) with a gamma camera, 15 minutes, 4, 24 and 48 hours after an intravenous injection of 110 MBq ^{111}In-pentetreotide. Blood samples were taken after each scan. Urine was collected for 24 hours starting immediately after the injection. The activity in whole body and various organs was determined by geometric mean of the anterior and posterior number of counts, corrected for physical decay, attenuation in patient and gamma camera couch and for the sensitivity of the gamma camera. From time-activity curves for whole body and various organs, initial uptake, biological half-time and corresponding fraction of uptake were derived. These parameters were used to calculate the normalized cumulated activity. Using an ICRP53 computer code and MIRDOSE3.1, the absorbed dose to individual organs and the effective dose were calculated.

^{111}In-pentetreotide is rapidly cleared from the blood with a half-time of 1.2 hours. Fifteen minutes after the injection ^{111}In activity can be seen in liver (5%), spleen (3%), kidneys (8%), urinary bladder (8%), heart (6%), lungs (4%) and thyroid (0.2%). The substance is excreted predominantly via the renal system. Eighty-five percent is excreted in 24 hours. For the whole body and most of the organs, the retention can be described by a biexponential function. The absorbed dose is highest for kidneys (0.54 mGy/MBq), spleen (0.53 mGy/MBq), urinary bladder (0.27 mGy/MBq) and liver (0.11 mGy/MBq). The effective dose is 0.08 mSv/MBq. These figures include contribution of up to 3% from the impurity ^{114}In^{m}. An investigation with 110 MBq of ^{111}In-pentetreotide gives an effective dose of around 9 mSv which is comparable with that of other ^{111}In-labeled radiopharmaceuticals.

INTRODUCTION

The recently developed ^{111}In-DTPA-D-Phe-1-octreotide (^{111}In-pentetreotide) (1, 2) is a radiopharmaceutical which is used for diagnosis of neuroendocrine tumors such as carcinoid, islet cell tumor, paraganglioma, medullary thyroid carcinoma, pheochromocytoma, small cell lung cancer and pituitary tumor. ^{111}In-pentetreotide is, however, not specific for neuroendocrine tumors as scintigraphy is also positive in many other tumors, granulomas and autoimmune diseases (3).

The purpose of this study was to measure the biodistribution and retention of ^{111}In-pentetreotide and to calculate the absorbed dose to various organs as well as the effective dose.

MATERIALS AND METHODS

Radiopharmaceutical

Pentetreotide was supplied as a dry frozen kit to which approximately 120 MBq ^{111}In-chloride was added, followed by an incubation period of 30 minutes. Both pentetreotide (10 microgram) and ^{111}In-chloride were supplied from Mallinckrodt Medical B.V. (Petten, The Netherlands). Prior to the injection of each patient, quality control was performed with instant thin layer chromatography (ITLC/SG strip, Gelman Sciences Inc. Michigan, USA.) and with gel chromatography (Bond Elut, VARIAN, Switzerland) to assure a labeling yield of better than 98%.

Patients

Ten consecutive patients referred to the Department of Nuclear Medicine at Malmö University Hospital, for scintigraphy of potentially somatostatin receptor positive tumors, were included in the study (Table 1). The activity given to the patient was thoroughly determined by measuring the syringe in an ionization chamber (Capintec, New Jersey, USA) before, as well as after the injection. The patients were given a laxative (Pico-Salax and Microlax, Ferring, Sweden) in order to minimize the influence from activity in the gastrointestinal tract and thus improve the detectability of small tumors in the area.

Table 1
Patient data

Patient No.	Sex	Tumor type	Age (years)	Weight(kg)	Given activity (MBq)
1	F	Gastrinoma	71	75	116
2	F	Carcinoid	48	65	107
3	F	Endocrine pancreatic tumor	21	60	112
4	F	Medullary thyroid carcinoma	54	66	108
5	F	Pheochromocytoma	47	75	120
6	F	Medullary thyroid carcinoma	56	68	53
7	M	Pituitary tumor	36	128	102
8	M	Endocrine pancreatic tumor	61	80	104
9	M	Carcinoid	51	82	118
10	M	Pheochromocytoma	53	108	117
Mean			50	81	106

Acquisition of Retention Data

Whole-body scanning, both in anterior and posterior projections, was done with a square field-of-view gamma camera (Toshiba GCA 901 A, Tokyo, Japan) equipped with a medium-energy general purpose collimator (MEGP). Twenty percent energy windows (±10%) were symmetrically centered around each of the full-energy photon peaks - 171 keV and 245 keV.

All patients were scanned 15 minutes (scanning speed: 20 cm/min), 4 hours (15 cm/min) and 24 hours (10 cm/min) after an intravenous bolus injection of ^{111}In-pentetreotide. Five patients were also

scanned 48 hours (10 cm/min) after injection. Measurements were performed with the patient lying in supine position on the gamma camera couch.

Blood Samples and Urine Collection

Heparinized blood samples were drawn immediately after the scanning. The count rates (cps) in the blood samples were measured with two opposed NaI(Tl)-detectors (Φ=127 mm and h= 102 mm) in a low background room.

Urine was collected into two-liter plastic bottles (Kautex, Germany) during 24 hours, starting directly after the injection. One of the patients had an additional urine collection 24-48 hours after the injection. The count rate (cps) was measured with a high-purity coaxial Ge-detector (HPGe) (Φ=46 mm and h= 37 mm), after adjustment of the urine volume up to 2000 ml using distilled water and 200 ml hydrochloric acid.

Calibration Measurements

The sensitivity F (counts/MBq) for the gamma camera was determined by phantom studies. The phantom was made of two-liter and one-liter cylindrical plastic bottles (Kautex, Germany) placed to simulate a 70 kg person according to Schmier (4). Thirty-seven MBq of ^{111}In was dispersed in the various bottles corresponding to the distribution of the ^{111}In-activity in the patients. The amount of activity in each bottle was determined by measuring the syringe before and after the ^{111}In was inserted into the bottle. Plasma was added to the ^{111}In in order to prohibit ^{111}In binding to the walls of the bottle.

Three scans (20,15 and 10 cm/min), both anterior and posterior, were performed with the gamma camera in the same way as for the patients, and since the activity in the phantom was known, the sensitivity F could be determined. Correction was made for attenuation in the phantom and in the gamma camera couch.

To account for attenuation in the body, the average linear attenuation coefficient (μ) in soft tissue was experimentally determined for photons of the energy distribution in question. This was done with the same equipment as in the patient studies using two different sizes of ^{111}In-sources (1 liter bottle and 10 ml bottle).

The sensitivity (cps/MBq) of the HPGe-detector system was determined with a two-liter plastic bottle filled with known amount of ^{111}In (incl. plasma). The measurement was done with the same geometry as the urine samples. In the same way, the sensitivity for the NaI(Tl)-detector system was determined by measurement of blood samples with known amount of ^{111}In. Hence the activity in the blood and urine samples could be calculated.

Analysis of the Gamma Camera Images

Regions of interest (ROI) were drawn around those organs that were visualized on the images - liver, spleen, kidneys, lungs, heart, thyroid, urinary bladder, small intestine (SI), upper large intestine (ULI), lower large intestine (LLI) and whole body. Background ROI was placed at the right hip, carefully done to avoid scattered radiation from the urinary bladder. For the whole-body regions, detector background next to the calves of the patients and well outside the margin of the leg was used. For those patients whose liver and right kidney were overlapping, correction was made using the count density in the undisturbed liver region multiplied by the projected area of the liver. The image of the right kidney was treated in the same way. As a test of the number of counts in the right kidney, the number of counts in the left kidney was doubled assuming equal distribution between the

two kidneys. There was no difference in the results from the two methods used. The number of counts in the posterior image was corrected for attenuation in the gamma camera couch.

The calculated activity in whole body and in the various organs was corrected for physical decay of ^{111}In to the time of injection. The activity A in an organ is given by

$$A = \left(N_a \cdot N_p\right)^{1/2} \times \left[\left(\frac{\sinh(\mu \cdot l/2)}{\mu \cdot l/2} \cdot \exp(-\mu \cdot L/2)\right) \cdot F\right]^{-1}, \qquad (5)$$

where

N_a and N_p are the number of counts in the regions of interest (anterior and posterior),

l is the thickness of the organ or tissue,

L is the thickness of the patient body at the region of interest,

μ is the average linear attenuation coefficient in soft tissue for photons of the energy distribution in question, experimentally determined to 0.13 cm^{-1} and

F is the sensitivity of the gamma camera (counts/MBq) obtained from phantom measurements.

Absorbed Dose and Effective Dose

The relative contents of ^{111}In in the whole body and in various organs (% of injected activity) was plotted as a function of time after the injection. The missing 48-hour data point for five of the patients was estimated from their 24-hour data and from the mean value of the long half-time of those patients who were scanned 48 hours after the injection (Fig.1, 3a, and 3b).

The initial uptake, biological half-time and corresponding fraction of uptake were derived from these curves and used to determine the normalized cumulated activity, $\tilde{A}/A_o$ (the cumulated activity per unit activity administered) according to the ICRP (6).To calculate the cumulated activity in the urinary bladder, the kidney-bladder model of the ICRP (6) was used.

The absorbed dose, D (mean absorbed dose to the whole organ) to various organs was calculated using an ICRP53 computer code (7) and MIRDOSE 3.1 (8). The effective dose was calculated according to the ICRP (9,10). The absorbed dose to various organs and the effective dose were determined for each patient as well as for the mean values of the organ uptake in the ten patients. In these calculations, the mathematical adult phantom was used for the men and the mathematical 15-year old phantom was used for the women (11).

The contribution to the absorbed dose from $^{114}In^m$ impurities was also calculated, assuming an $^{114}In^m$ activity concentration of 0.05 % of the total activity at reference time and that 95.7% of $^{114}In^m$ decays to ^{114}In.

RESULTS

Blood Samples and Urine Collection

After an injection of ^{111}In-pentetreotide, ^{111}In was rapidly cleared from the blood a with a dominating half-time of 1.2 hours. Clearance was predominantly via the kidneys and urinary bladder, where 85% of the administered activity was excreted in 24 hours. For the patient who had urine collected between 24 and 48 hours after the injection, approximately 98% was excreted in 48 hours. Even though the patients were given a laxative, some activity (about 2 % of the injected activity) can be observed in the gastrointestinal tract on the gamma camera images after 48 hours.

Distribution and Biokinetics

The shape of the whole-body retention curve is similar for the ten patients. The average retention is described by a biexponential function with a short half-time of 2.6 hours (72%) and a long half-time of 59 hours (28%) (Figure 1).

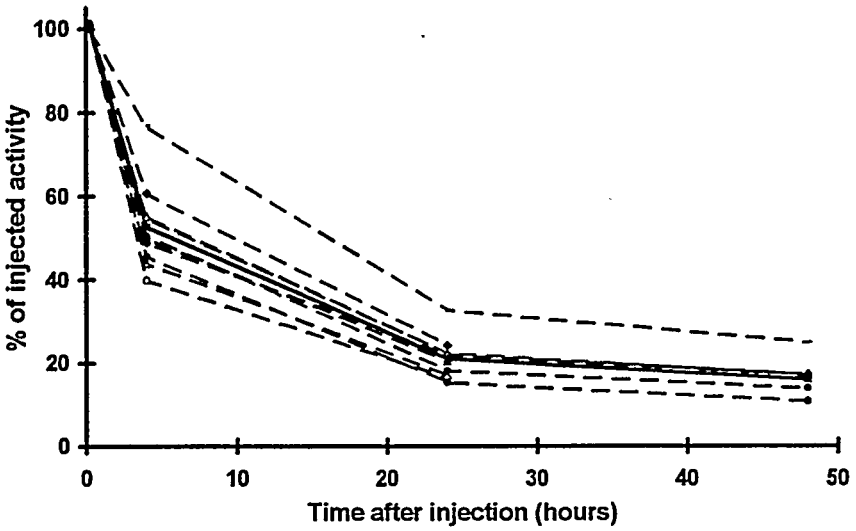

Figure 1. Whole-body retention as function of time after an intravenous injection of ^{111}In-pentetreotide. Dashed lines represent patient data and solid line is the mean.

In the initial gamma camera images ^{111}In was clearly evident in several organs such as liver (5.0% of injected activity), spleen (3.3%), kidneys (7.9%), lungs (4.0%), heart (6.0%), urinary bladder (8.0%) and thyroid (0.19%) (Figure 2a). After 4 and 24 hours ^{111}In activity could still be seen in liver, spleen, kidneys and urinary bladder. Even 48 hours after the injection spleen, the liver and kidneys were visible (Figure 2b).

For all organs, except spleen and kidneys, the retention of the substance is described by a biexponential function for a majority of the patients. For the heart and lungs, clearance is very rapid. For the spleen, a rapid uptake phase can be seen followed by a monoexponential elimination (Figure 3A). There were minor differences in uptake and retention for the ten patients. Data presented in Table 2 represent mean values of normalized cumulated activities for the source organs.

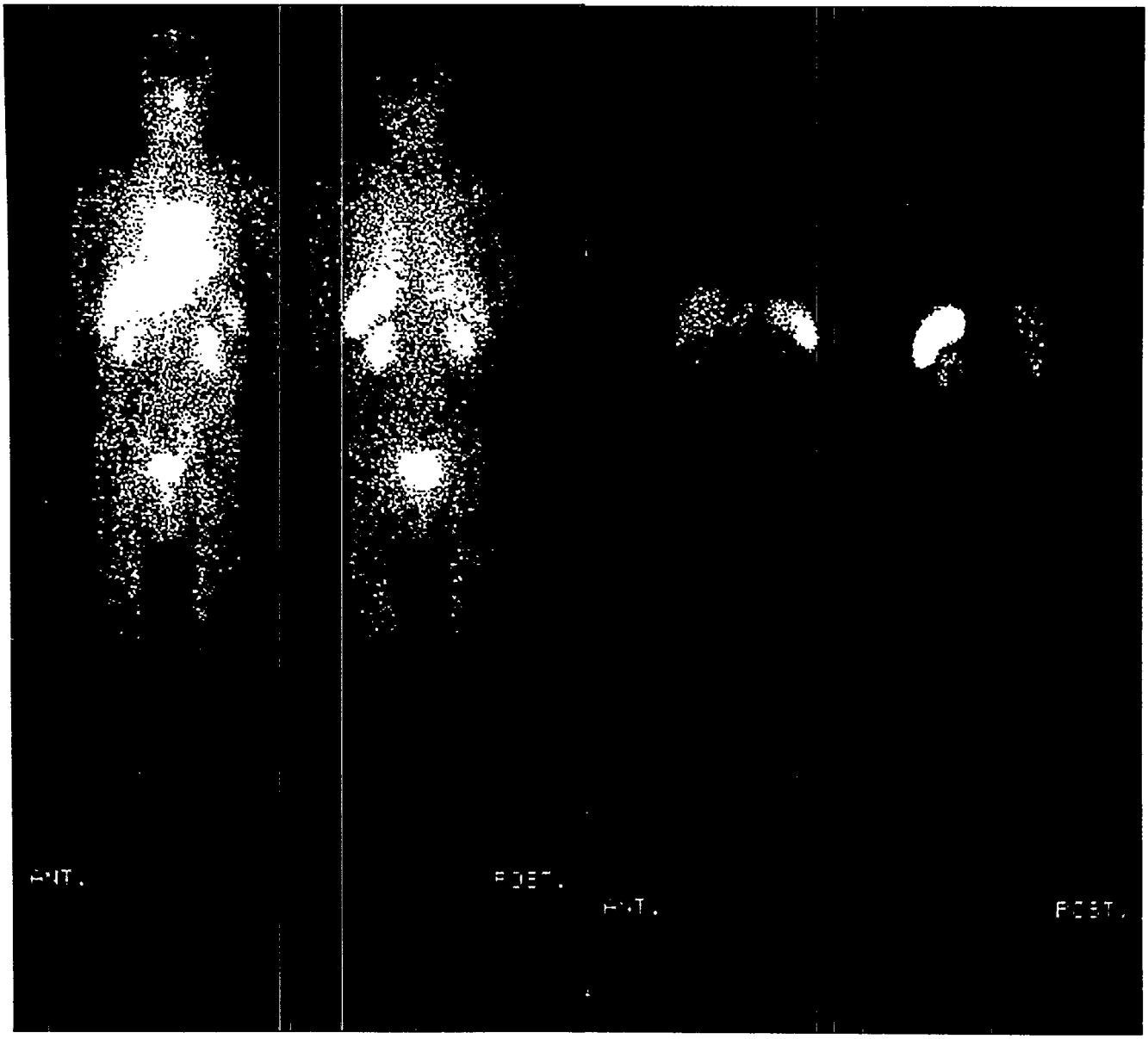

Figure 2a. Whole-body scintigram 15 minutes after an injection of ^{111}In-pentetreotide.

Figure 2b. Whole-body scintigram 48 hours after an injection of ^{111}In pentetreotide.

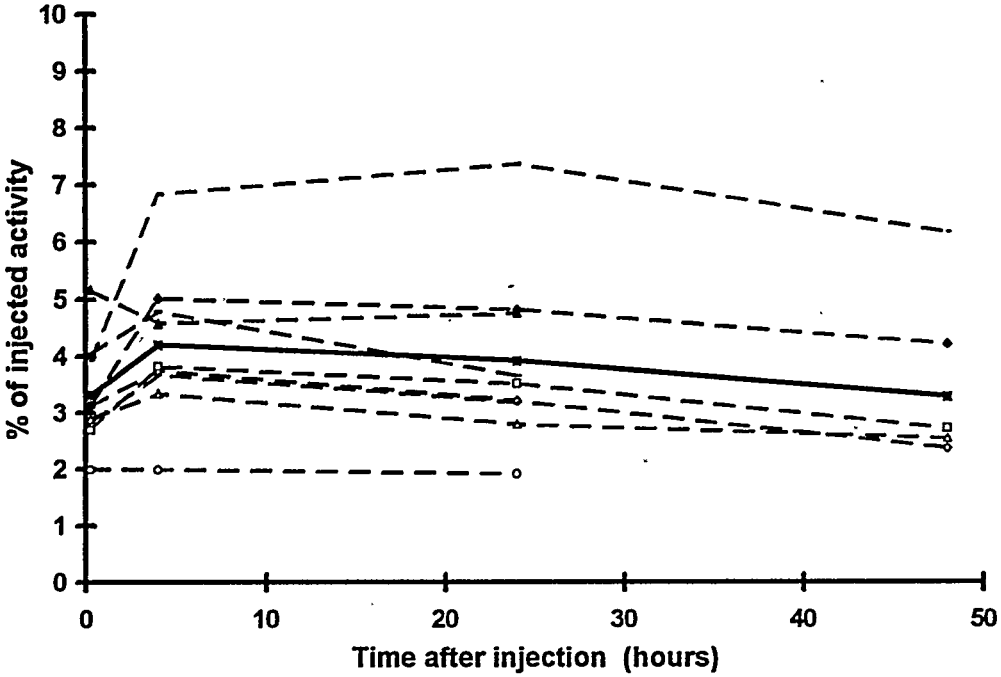

Figure 3a. Retention of ^{111}In in spleen after an intravenous injection of ^{111}In-pentetreotide. The dashed lines are the patients and the solid line is the mean.

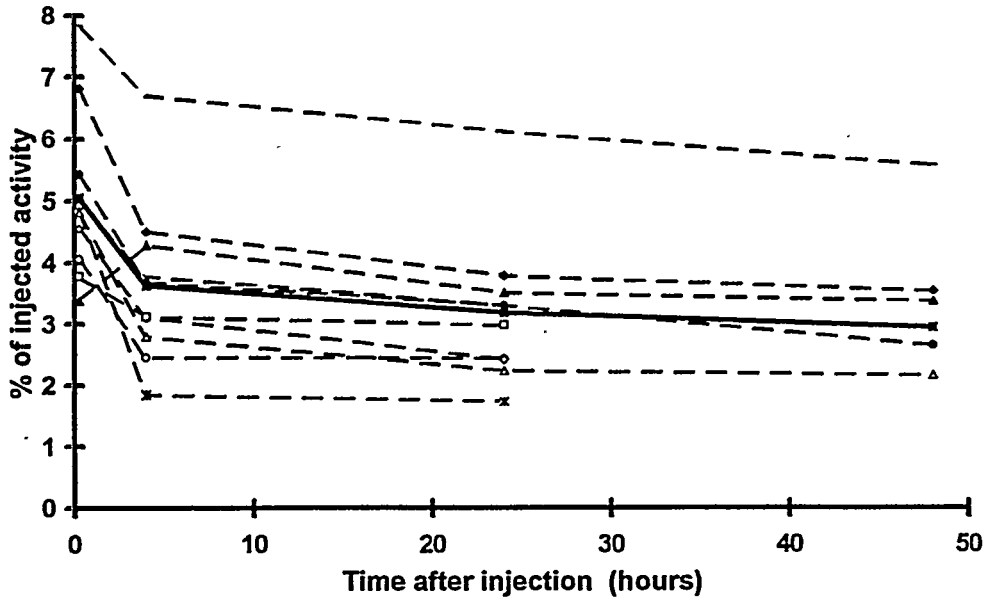

Figure 3b. Retention of ^{111}In in liver after an intravenous injection of ^{111}In-pentetreotide.

Table 2
Normalized Cumulated Activities ($\tilde{A}/A_o$)

Organ	$\tilde{A}/A_o$
Liver	2.2 hours
Kidneys	3.4 hours
Spleen	1.8 hours
Heart	27min
Lungs	25 min
Thyroid	1.3 min
Small intestine (SI)	17 min
Upper large intestine (ULI)	19 min
Lower large intestine (LLI)	7.2 min
Urinary bladder	1.6 hours
Remainder of the total body	9.6 hours

Absorbed Dose and Effective Dose

The absorbed dose to various organs was calculated for each patient and the data presented in Table 3 are the mean values of six women and four men.

Table 3
Absorbed Dose to Various Organs from ^{111}In-Pentetreotide

Organ	Mean abs.dose (mGy/MBq)	Range (min - max) (mGy/MBq)
Adrenals	0.08	(0.05 - 0.12)
Urinary bladder	0.27	(0.19 - 0.33)
Bone surface	0.04	(0.03 - 0.05)
Brain	0.02	(0.01 - 0.02)
Breasts	0.02	(0.01 - 0.03)
Stomach	0.05	(0.03 - 0.08)
SI wall	0.06	(0.03 - 0.08)
Colon	0.06	(0.03 - 0.09)
(ULI wall	0.07	(0.03 - 0.12))
(LLI wall	0.05	(0.03 - 0.06))
Kidneys	0.54	(0.36 - 0.78)
Liver	0.11	(0.07 - 0.19)
Lungs	0.05	(0.02 - 0.08)
Red marrow	0.03	(0.02 - 0.04)
Muscles	0.03	(0.02 - 0.04)
Ovaries	0.05	(0.03 - 0.06)
Pancreas	0.08	(0.05 - 0.13)
Skin	0.02	(0.01 - 0.02)
Spleen	0.53	(0.25 - 0.95)
Testes	0.02	(0.02 - 0.03)
Thymus	0.03	(0.02 - 0.04)
Thyroid	0.05	(0.02 - 0.08)
Uterus	0.06	(0.04 - 0.07)
Heart wall	0.06	(0.03 - 0.10)
Gall bladder	0.07	(0.05 - 0.10)
E* (mSv/MBq)	0.08	(0.05 - 0.10)
H_E* (mSv/MBq)	0.12	(0.08 - 0.17)

*E = Effective dose and H_E = Effective dose equivalent

An investigation using 110 MBq of ^{111}In-pentetreotide gives the highest absorbed doses to the kidneys and the spleen (both 60 mGy), and to the urinary bladder (30 mGy). $^{114}In^{m}$ and ^{114}In contribute to the total absorbed dose up to 2.8% and to the effective dose with 1.1 %. The effective dose for an investigation with 110 MBq ^{111}In-pentetreotide is calculated to be 8.8 mSv. The contribution to the effective dose from various organs and tissues is shown in Figure 4.

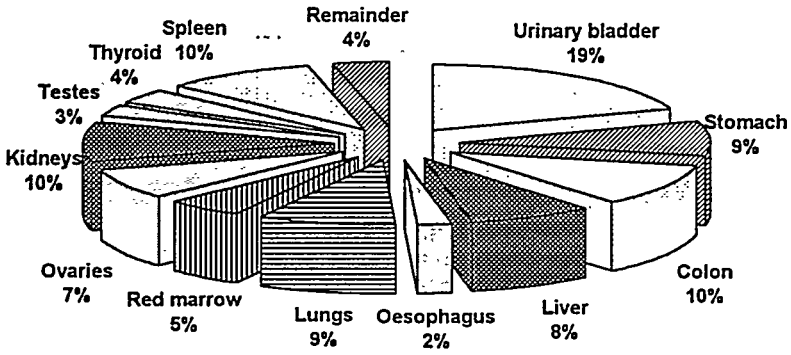

Figure 4. The contribution to the effective dose from various organs.

DISCUSSION

Even though there were some individual differences, both in biokinetic data and in absorbed doses, no significant differences could be observed between the results based on the average absorbed doses of the 10 patients and the absorbed doses calculated from the mean of the organ uptake of ^{111}In-pentetreotide.

The activity in various organs has been calculated according to Fleming (5) as well as according to Myers et al. (12). The results show that the amount of ^{111}In differs, up to 11% for the thickest organ, using the two methods.

The results show that the absorbed dose to the kidneys and the spleen can be as high as 60 mGy for an investigation with 110 MBq. It is not unusual however, that double the amount of ^{111}In-pentetreotide is administered (especially when SPECT is performed), which gives an absorbed dose to these organs of 120 mGy.

When calculating the effective dose, the kidneys and the spleen are normally included in the "remainder" which has a tissue weighting factor of 0.05. However, if a single one of the remainder tissues or organs receives an equivalent dose in excess of the highest dose in any of the organs for which a weighting factor is specified, a weighting factor of 0.025 should be applied to that tissue or organ and a weighting factor of 0.025 to the average dose in the rest of the remainder (9). In this special case, the absorbed dose to kidneys and spleen is similar and a tissue weighting factor of 0.0125 is applied to each of them.

The new way of applying the tissue weighting factor to the colon ($H_{colon} = 0.57*H_{ULI} + 0.43*H_{LLI}$) (10) causes only a minor effect on the effective dose.

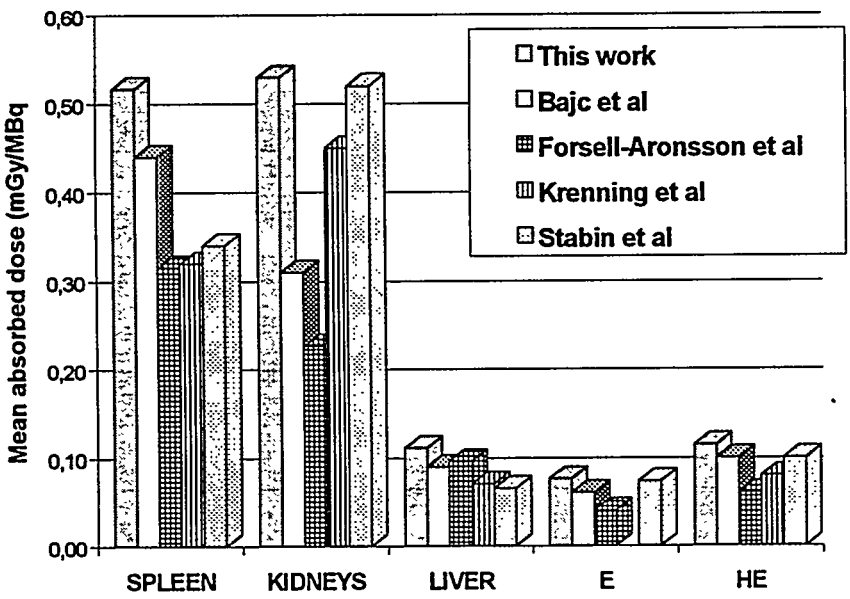

Figure 5. Comparison between the results of this work and published data (Krenning 1992 (2), Bajc 1994 (13), Stabin 1995 (14) and Forssell-Aronsson 1996, (15)) regarding the mean absorbed dose to some organs as well as the effective dose equivalent and the effective dose. Six of the ten patients in Stabin et al (1995) are the same as those used by Krenning et al (1992) although the results have been determined in two different ways.

As shown in Figure 3a and b, there are individual differences in organ uptake between patients. The differences in absorbed doses between various studies (Figure 5) may be, to a considerable extent, due to varying definition of background region around the spleen and the kidneys and also due to uncertainties in the determination of the attenuation in the patient.

An additional study was performed to determine how to treat the final slope of the retention curves. The absorbed dose to various organs was estimated first assuming that the slope between 4 and 24 hours was the final slope, and then assuming that the slope between 24 and 48 hours was the final slope. This was done for four patients and four source organs. This investigation showed that the absorbed dose to various organs was higher when the slope between 24 and 48 hours after injection was assumed to be the final slope. When the biokinetic study is done for only 24 hours, the biological half-time of the final slope is too short and the absorbed dose becomes underestimated. This justifies the method we used for estimating the 48-hour data that are lacking for 5 patients.

The liver had a much longer biological half-time than the other organs. The reason for this could be that there is a dissociation of ^{111}In from ^{111}In -DTPA-D-Phe-1-octreotide (16). This is also indicated by the long retention in the spleen.

CONCLUSION

Biodistribution studies on ^{111}In-pentetreotide demonstrated uptake in liver, spleen, kidneys, heart, lungs and thyroid. The substance is excreted predominantly via the renal system (85% in 24 hours). The highest absorbed doses were estimated for the kidneys (0.54 mGy/MBq) and for the spleen (0.53 mGy/MBq). The effective dose for an investigation with ^{111}In-pentetreotide is calculated to be 0.08 mSv/MBq.

ACKNOWLEDGMENT

This paper is based on research carried out under contract with the Swedish Radiation Protection Institute (P 787.93). We want to thank Dr. Eva Forssell-Aronsson for discussions and cooperation and Jan Svegborn, Senior lecturer, for linguistic support.

REFERENCES

1. Bakker WH, Krenning EP, Breeman WA, Krooij PPM, Reubi JC, Koper JW, deJong M, Lameris JS, Visser TJ and Lamberts SW. In vivo use of a radioiodinated somatostatin analogue: Dynamics, metabolism and binding to somatostatin receptor-positive tumors in man. J Nucl Med 32:1184-1188, 1991.
2. Krenning EP, Bakker WH, Krooij PPM, Breeman WAP, Oei HY, deJong M, Reubi JC, Visser TJ, Bruns C, Kwekkeboom DJ, Reijs AEM, van Hagen PM, Koper JW and Lamberts SWJ. Somatostatin receptor scintigraphy with indium-^{111}-DTPA-D-Phe-1-Octreotide in man: Metabolism, dosimetry and comparison with Iodine-123-Tyr-3-Octreotide. J Nucl Med 33:652-658, 1992.
3. Hoefnagel CA. Metaiodobenzylguanidine and somatostatin in oncology: role in the management of neural crest tumors. Eur J Nucl Med 21:561-581, 1994.
4. Schmier H. Kalibrierungsvergleich von Ganzkörperstrahlungs-Messanlagen in den Ländern der Europäischen Gemeinshaften. Bundesgesundheitsamt, Abteilung fur Strahlenhygiene, Berlin, Bakker WH, Krenning EP, Breeman WA, Krooij PPM, Reubi JC, Koper JW, deJong M, Lameris JS, Visser TJ and Lamberts SW. In vivo use of a radioiodinated somatostatin analogue: Deutschland 1972.
5. Fleming JS. A technique for the absolute measurement of activity using a gamma camera and a computer. Phys Med Biol 24:176-180, 1979.
6. ICRP, Radiation Dose to Patients from Radiopharmaceuticals, ICRP Publication 53. Annals of the ICRP, 18 (1-4), Pergamon Press, Oxford, 1988.
7. Johansson L. ICRP Task Group on Radiation Dose to Patients from Radiopharmaceuticals. Personal communication, 1995.
8. Stabin MG. MIRDOSE: Personal computer software for internal dose assessment in nuclear medicine. J Nucl Med 37:538-546, 1996.
9. ICRP, 1990 Recommendations of the International Commission on Radiological Protection, ICRP Publication 60. Annals of the ICRP 21 (1-3), Pergamon Press, Oxford, 1991a.
10. ICRP, Age-dependent Doses to Members of the Public from Intake of Radionuclides: Part 2, ICRP Publication 67. Annals of the ICRP 23 (3-4), Pergamon Press, Oxford, 1993.
11. Cristy M and Eckerman K. Specific absorbed fractions of energy at various ages from internal photons sources. ORNL/TM-8381, Oak Ridge National Laboratory, Oak Ridge, TN, USA ,1987.

12. Myers MJ, Lavender JP, de Oliveira JB and Maseri A: A simplified method of quantitating organ uptake using a gamma camera. Br J Radiol 54:1062-1067, 1981.
13. Bajc M, Palmer J, Ohlsson T and Edenbrandt L. Distribution and dosimetry of ^{111}In DTPA-D-phe-octreotide in man assessed by whole body scintigraphy. Acta Radiol 35; Fasc.1:53-57, 1994.
14. Stabin MG, Kooij PPM, Bakker WH, Inoue T and Endo K. The radiation dosimetry of In-111 pentetreotide. J Nucl Med 36(5):182, 1995.
15. Forssell-Aronsson E, Lanhede B, Fjälling M, Wängberg B, Tisell LE, Ahlman H and Mattsson S. Pharmacokinetics and dosimetry of ^{111}In-DTPA-D-Phe^{1}-octreotide in patients with neuroendocrine tumors. This publication: 643-655, 1999.
16. Claessens RAMJ, Koenders EB, Boerman OC, Oyen WJG, Borm GF,van der Meer JWM and Corstens FHM. Dissociation of indium from indium-111-labelled diethylene triamine penta-acetic acid conjugated non-specific polyclonal human immunoglobulin G in inflammatory foci. Eur J Nucl Med 22:212-219, 1995.

PHARMACOKINETICS AND DOSIMETRY OF ^{111}In-DTPA-Phe^{1}-OCTREOTIDE IN PATIENTS WITH NEUROENDOCRINE TUMORS

Forssell-Aronsson E[1], Lanhede B[1], Fjälling M[2], Wängberg B[3],
Tisell LE[3], Ahlman H[3] and Mattsson S[4]
Departments of [1]Radiation Physics, [2]Nuclear Medicine and [3]Surgery, Göteborg University,
Sahlgrenska University Hospital, S-413 45 Göteborg, Sweden and
[4]Department of Radiation Physics, Lund University,
Malmö University Hospital, S-205 02 Malmö, Sweden

ABSTRACT

The pharmacokinetics of ^{111}In-DTPA-Phe^{1}-octreotide were studied in 13 patients with previously verified neuroendocrine tumors. After I.V. administration, the biodistribution was followed by gamma camera imaging up to 72 h after injection.

The activity in whole body and visualized organs was estimated using the geometric mean of the anterior and posterior counts. Corrections were made for detector and tissue background and for attenuation in tissue. The parameters in an open one- or two-compartment model were fitted to the measured time-activity curve for each source organ, giving the fractional uptakes and effective half-times for clearance. Absorbed doses were calculated following the MIRD formalism.

The mean absorbed dose in the whole body was 0.024 mGy/MBq. The mean effective dose equivalent was 0.062 mSv/MBq, and the mean effective dose 0.040 mSv/MBq. The contribution to the absorbed dose from ^{114m}In and ^{114}In was always below 1.5 % of corresponding absorbed dose from ^{111}In, and could thus be neglected. The effective dose for a common clinical investigation using 120 or 240 MBq ^{111}In-DTPA-Phe^{1}-octreotide will be about 5 or 10 mSv, respectively.

INTRODUCTION

The somatostatin analogue octreotide can be labeled with ^{111}In using DTPA as a chelating agent (1). Somatostatin-receptor scintigraphy using ^{111}In-DTPA-D-Phe^{1}-octreotide has high sensitivity and specificity for localization of primary and metastatic neuroendocrine tumors, which frequently express somatostatin receptors (e.g. 2-6). ^{111}In-DTPA-D-Phe^{1}-octreotide has also been used for intraoperative localization of such tumors by a hand-held scintillation detector (7).

The pharmacokinetics and dosimetry of ^{111}In-DTPA-D-Phe^{1}-octreotide have previously been studied for patients using gamma camera techniques and in some cases examination of blood, urine and feces (8-11). Most of these studies involved a limited number of patients. ^{111}In-DTPA-D-Phe^{1}-octreotide has also been tried for therapy of neuroendocrine tumors (11, 12). To evaluate the possibility of using radiolabeled octreotide for tumor therapy, it is necessary to obtain detailed information on activity concentrations and absorbed doses in both tumor and normal tissue for the

individual patient. In one such study, the concentration of ^{111}In in tissue samples was measured at various times after injection of ^{111}In-DTPA-D-Phe^1-octreotide (13).

The aim of the present study was to further investigate the uptake, retention and dosimetry of ^{111}In-DTPA-Phe^1-octreotide.

MATERIAL AND METHODS

Radiopharmaceutical

Radiolabeling of the DTPA-D-Phe^1-octreotide with ^{111}In was performed according to the instructions from the manufacturer (Mallinckrodt Medical B.V., Petten, Netherlands). Chromatography of the radiopharmaceutical was performed using instant thin layer chromatography (ITLC-SG, Gelman Instrument Company, Michigan, U.S.A.) with Na-citrate (0.1 M, pH 5) as the mobile phase. The fraction of peptide-bound ^{111}In was always more than 98 %.

Patients

Thirteen patients (9 men and 4 women; mean age 64 y, range 35-78 y) with histologically verified neuroendocrine tumors and metastatic disease were included in this study. Ten of the patients had liver metastases at the time of the study. All patients were on daily octreotide treatment (median 200 μg/d s.c., range 100-300 μg/d), but discontinued the treatment 3 days prior to injection of the radiopharmaceutical. Treatment with octreotide was again initiated after the last examination. The patients received 200-240 MBq (20 μg) ^{111}In-DTPA-Phe^1-octreotide by I.V. injection. The activity of the syringe was measured with a well-type ionization chamber (CRC-120, Capintec, U.S.A.) before and after administration of the radiopharmaceutical. The study was approved by the Ethical Committee of Göteborg University and the Isotope Committee of Sahlgrenska University Hospital, and informed consent was given by the patients.

Measurements

The distribution of ^{111}In was followed by a gamma camera (General Electric 400 ACT, USA) equipped with a medium-energy parallel-hole collimator. Data acquisition was performed with energy windows around the 173 and 247 keV peaks (20 % window width).

Anterior and posterior whole-body scanning (256 x 1024 matrix, 4-10 min/m) was performed at about 0.5, 4, 24, 48 and 72 h after injection. No urinary bladder voiding was performed between the injection and the first image acquisition.

Regions of interest were drawn around the whole body, thorax, legs, kidneys, liver, spleen and urinary bladder. For some images, correction for overlapping regions involving the kidneys and liver and/or spleen was made, assuming homogeneous activity concentration within each kidney.

The activity content in the whole body and in the visualized organs (liver, spleen, kidneys, and urinary bladder) was determined mainly according to the "conjugate-view method" (15). The activity content in the remainder of the body was calculated as the content in whole body minus the content in the visualized organs. The activity content was expressed as the percent of the injected activity, %IA.

Calibration of the gamma camera was performed using both a trunk phantom with dimensions according to MIRD (16) and a thin surface source, according to the method of Fleming (15). The relation between the sensitivity of the ionization chamber and the gamma camera was then determined.

When determining the activity content in the whole body, correction for attenuation was made. Each of the anterior and posterior images of the body was divided into three regions: thorax, legs and the rest of the body. The effective thickness of each of these regions was estimated from CT images

of patients of similar size, and assuming a lung density of 0.3 g/cm^3. The same attenuation correction was subsequently applied to all patients. After geometric averaging of the number of anterior and posterior counts and multiplication by the calibration factor, the activity content in the whole body was calculated as the sum of the ^{111}In activity in these three regions.

Corrections were also made for detector background. For the whole-body content, a region well outside the body was used. For the organs, an appropriate region in the abdomen was used. In order not to underestimate the activity in the organs, the activity in tissues located anterior and posterior to the organ was subtracted, assuming homogeneous activity distribution in the background region. Background correction from over- and underlying tissue was based on the mean thickness of the organ. As the mean thickness of the liver and spleen, the values published by Fleming (15) were used. For the urinary bladder, the same correction as for the kidneys was made. Correction was also made for radioactive decay.

Dosimetry

The time-activity curve for an open one- or two-compartment model was fitted to the measured time-activity data for each source organ, giving the fractional uptakes and clearance effective half-times. In this study, the source organs were the kidneys, liver, spleen, urinary bladder and remainder. The remainder was estimated as the activity in the whole body minus the activities in the other source organs. The cumulated activity was obtained by integrating the time-activity curve to infinity. The residence time was calculated as the ratio of the cumulated activity and the injected activity.

Dose calculations were made individually for each patient. The mean absorbed dose was calculated following the Medical Internal Radiation Dose Committee (MIRD) formulation (17, 18), as implemented in the MIRDOSE computer software (version 3.1) (19). The absorbed dose from each source organ was then obtained by multiplying the cumulated activity (MBq*d) by the corresponding S value (absorbed dose per unit cumulated activity, mGy/MBq*d) (20). The female phantom model was used when applicable. The effective dose equivalent was calculated by the MIRDOSE 3.1 program according to ICRP 26 (21) and ICRP 28 (22) and the effective dose according to ICRP 60 (23), respectively.

According to the manufacturer, there might be impurities of ^{114m}In and ^{114}In in the ^{111}In solution from the production of the radiopharmaceutical. A separate estimate of the mean absorbed doses from ^{114m}In and ^{114}In was made, assuming an amount of 0.05% ^{114m}In of the injected ^{111}In activity at the time of injection, and the same biokinetics as for ^{111}In.

RESULTS

Pharmacokinetics

The gamma-camera images showed a clear visualization of the liver, spleen, kidneys and the urinary bladder. On the first images (about 0.5 h after injection), activity in blood caused visualization of the heart and large vessels. The normal thyroid and pituitary glands were visualized in nine and five patients, respectively.

Figure 1 shows the ^{111}In activity content in the whole body given as percent of injected activity (%IA) for all 13 patients. There was a rapid decrease during the first 24 h due to rapid excretion through the kidneys. Already at about 0.5 h 3-10 % IA was in the urinary bladder, and at 4 h after injection 30-70 % IA was excreted.

The time-activity curves for whole body, kidneys, liver, spleen and urinary bladder obtained from two of the patients are shown in Figure 2. The final biological half-time was about the same for whole body and the organs, except perhaps for the liver.

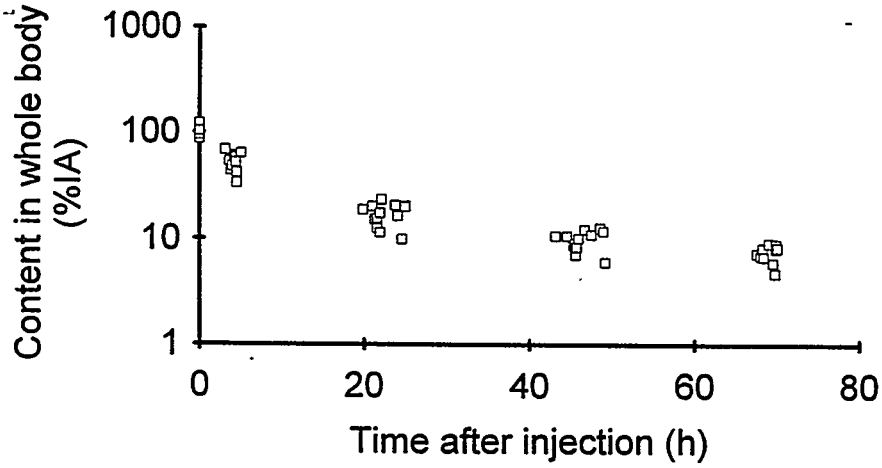

Figure 1. The content of ^{111}In in whole body for 13 patients with neuroendocrine tumors injected with ^{111}In-DTPA-Phe-1-octreotide. The values are corrected for physical decay to the time of injection.

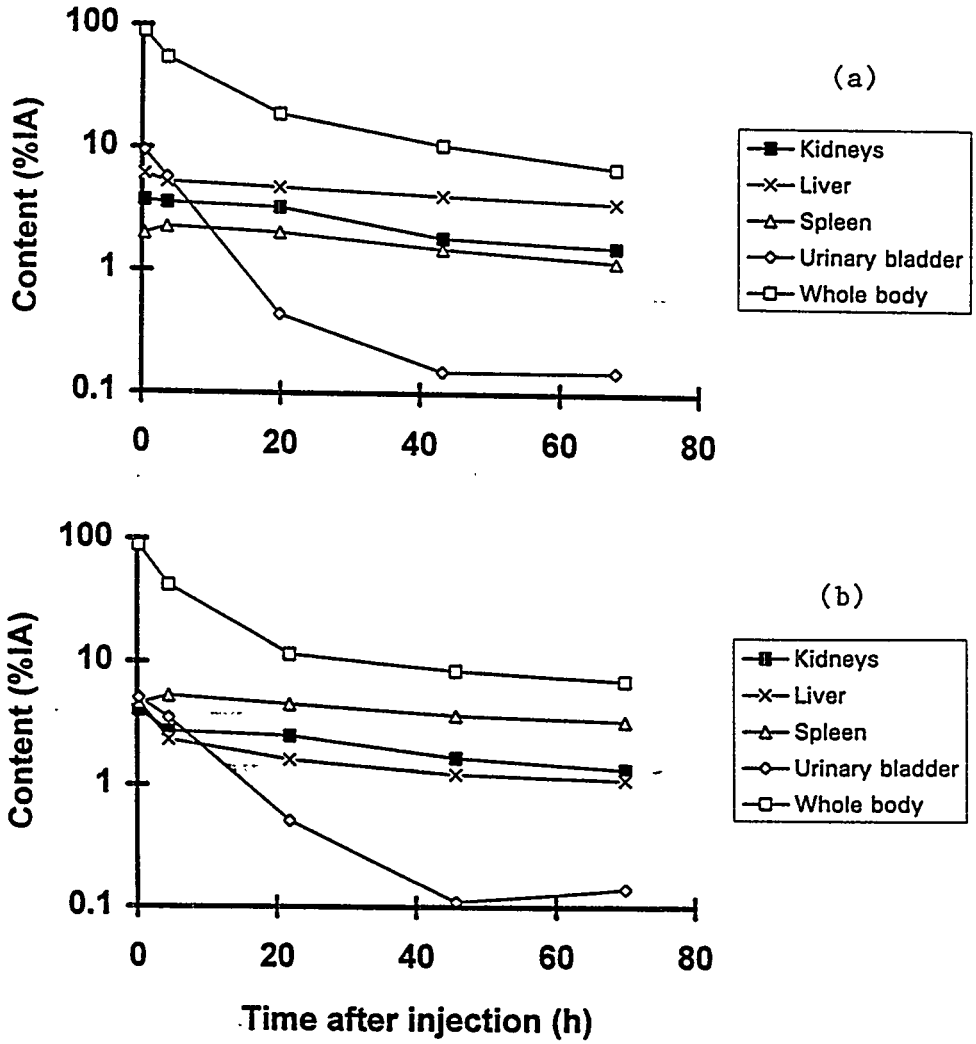

Figure 2. The time-activity curves for whole body, kidneys, liver, spleen and urinary bladder from a) a patient with, and b) a patient without liver metastases. The values are corrected for physical decay to the time of injection.

The ^{111}In activity content in kidneys for all patients is shown in Figure 3a. There was a rapid decrease during the first 4 h; thereafter the biological half-time was much longer. The highest interindividual variation was about a factor of four, with one extreme case. Figure 3b shows the ^{111}In activity content in liver. The content decreased with time for all patients. The highest interindividual variation was about a factor of six. For the time-activity curves for the spleen (Figure 3c), the maximum value was found at 4 h for half of the patients and at 0.5 h for the rest. The highest interindividual variation was about a factor of four.

Table 1 shows the mean residence times for the various source organs. The mean residence time for ^{111}In was highest for the remainder of the body, followed by the liver, kidneys, spleen and urinary bladder. The variation between the patients was at most a factor of 4-6. For ^{114m}In, the mean residence time was highest for the spleen, followed by the kidneys, remainder of the body, urinary bladder and liver.

Table 1

Mean Residence Times for ^{111}In and Estimated Mean Residence Times for ^{114m}In in Patients after Injection of ^{111}In-DTPA-D-Phe^1-Octreotide

	Mean residence time, ^{111}In (h)		Mean residence time, ^{114m}In (h)	
	mean	(range)	mean	(maximum)
Kidneys	1.4	(0.8-3.0)	0.0006	(0.003)
Liver	2	(1.2-4.6)	0.0001	(0.0004)
Spleen	1.2	(0.5-2.4)	0.001	(0.003)
Urinary bladder	0.5	(0.2-1.2)	0.0002	(0.0005)
Remainder	9.1	(6.3-13)	0.0003	(0.003)
Total body	14	(9-17)	0.002	(0.004)

Dosimetry

The estimated absorbed doses together with the effective dose equivalent, H_E, and effective dose, E, from ^{111}In are shown in Table 2.

DISCUSSION

This paper presents pharmacokinetic and dosimetric data for ^{111}In-DTPA-D-Phe^1-octreotide from a study in which individual calculations have been done for 13 patients. Previous studies have shown that even a low amount of ^{114m}In may give a relatively high contribution to the absorbed dose in the organs (24). In this study, the contribution from ^{114m}In and ^{114}In to the absorbed doses was always below 1.5 % of the corresponding absorbed doses from ^{111}In, and was thus neglected. Furthermore, the value 1.5 % is an overestimate, since the administration of the radionuclide was done 1-2 days prior to the time of calibration.

There were large differences in pharmacokinetics between the patients. The highest interindividual variation of the ^{111}In activity content in the liver was about a factor of six and was about a factor of four for the other organs studied. The variation of the ^{111}In activity in the liver could be expected to be higher than that for the other organs, since the tumor burden in the liver varied significantly between the patients. The two lowest liver time-activity curves (Figure 3b) were generated from the patients without liver metastases. The highest interindividual variation of effective dose equivalent and effective dose was a factor of two in this study. The mean absorbed doses to the

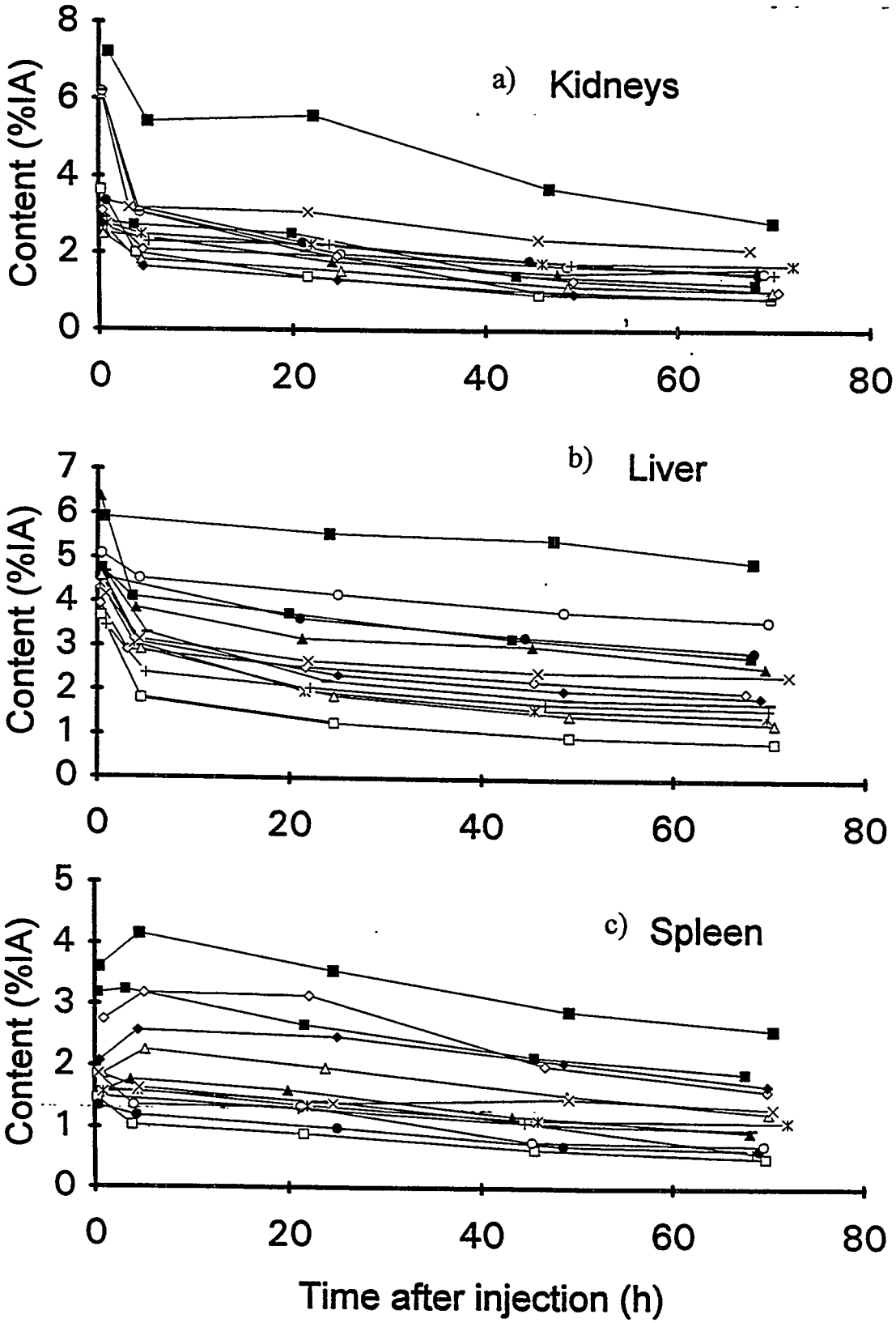

Figure 3. The ^{111}In activity content in a) kidneys, b) liver, and c) spleen for each of the 13 patients after I.V. injection of ^{111}In-DTPA-D-Phe^{1}-octreotide. The values are corrected for physical decay to the time of injection.

Table 2

Absorbed Doses per Unit Injected Activity, Effective Dose Equivalent, H_E, and Effective Dose, E, from I.V. Injected ^{111}In-DTPA-D-Phe^1-Octreotide Estimated from 13 Patients Using MIRDOSE 3.

Target organ	Absorbed dose per unit injected activity (mGy/MBq),	
	mean	(range)
Adrenals	0.047	(0.030-0.062)
Brain	0.014	(0.009-0.023)
Breasts	0.014	(0.010-0.022)
Gallbladder	0.047	(0.029-0.068)
LLI wall	0.024	(0.016-0.040)
SI wall	0.027	(0.019-0.040)
Stomach	0.035	(0.023-0.048)
ULI wall	0.029	(0.019-0.043)
Heart	0.027	(0.018-0.039)
Kidneys	0.23	(0.13-0.45)
Liver	0.094	(0.051-0.17)
Lungs	0.024	(0.016-0.036)
Muscle	0.020	(0.014-0.031)
Ovaries	0.025	(0.017-0.041)
Pancreas	0.054	(0.033-0.070)
Red marrow	0.022	(0.015-0.032)
Bone surfaces	0.030	(0.020-0.046)
Skin	0.012	(0.008-0.019)
Spleen	0.32	(0.14-0.57)
Testes	0.015	(0.011-0.019)
Thymus	0.018	(0.012-0.030)
Thyroid	0.016	(0.011-0.024)
Urin. bladder	0.082	(0.042-0.22)
Uterus	0.028	(0.020-0.047)
Total body	0.024	(0.016-0.047)
H_E *	0.062	(0.037-0.080)
E *	0.040	(0.025-0.057)

*mSv/MBq
LLI = lower large intestine
SI = small intestine
ULI = upper large intestine

organs in women were 6-120 % higher than those for men. The mean values for the effective dose equivalent and the effective dose were 30 % higher for women than men. However, these results are based on data from only four women.

Similar biokinetic and dosimetric estimations have been done by other investigators for both diagnostic amounts (8-10) and for therapeutic amounts of ^{111}In-DTPA-D-Phe^1-octreotide (11, 12). All studies except the study by Leide-Svegborn et al. (10) contain a limited number of patients, and some of these patients were regarded as "atypical", and thus their data were not included in all results. Also, extrapolation of missing data was sometimes attempted. In general the present dosimetric values (absorbed dose per unit ^{111}In activity) were similar to, or lower than those reported previously

for diagnostic amounts of the radiopharmaceutical (Table 3). Leide-Svegborn et-al. (10) reported generally higher values than the others. The results of this study mainly agree with our results with therapeutic amounts of ^{111}In-DTPA-D-Phe^1-octreotide (12) for the various organs. However, the absorbed dose per unit activity in the liver was much higher in the therapeutic study, most likely due to the extensive tumor burden in the liver of that patient. In the therapeutic study by Krenning et al. (11) the total hepatic tumor volume was smaller (as judged from CT), and their patient had no contribution from the spleen (a splenectomy had been performed).

Table 3

Absorbed Dose per Unit Injected Activity for Various Organs and Whole Body(mGy/MBq), and Effective Dose Equivalent, H_E and Effective Dose, E (mSv/MBq) from ^{111}In-DTPA-D-Phe^1-Octreotide Reported in the Literature

	Present Study	Krenning et al., 1992 (8)	Bajc et al., 1994 (9)	Leide-Svegborn et al., 1996 (10)	Krenning et al., 1994§ (11)	Andersson et al., 1996§ (12)
Kidney	0.23 0.13-0.45	0.45 0.19-0.80	0.31	0.54 0.36-0.78	0.25	0.32-0.56
Liver*	0.09 0.05-0.17	0.07 0.04-0.15	0.09	0.11 0.07-0.19	0.12	0.73-1.2
Spleen	0.32 0.14-0.57	0.32 0.10-0.66	0.44	0.53 0.25-0.95	-**	0.50-0.87
Urinary bladder wall	0.08 0.04-0.22	0.18	0.20	0.27 0.19-0.33	0.06	0.07-0.22
Red marrow	0.022 0.02-0.03	0.020 0.02-0.03	0.03	0.03 0.02-0.04		0.05-0.09
Total body	0.02 0.02-0.05					0.07-0.12
H_E ***	0.06 0.04-0.08	0.08 0.05-0.12	0.10	0.12 0.08-0.17		
E ***	0.04 0.02-0.06		0.06	0.08 0.05-0.10		

Values are given as mean or median values and, when possible, ranges are supplied
§ indicates results for therapeutic amounts of the radiopharmaceutical
*including possible liver metastases
**splenectomy
***mSv/MBq

The apparent variability in results between different studies can be explained by both biological and methodological factors. Some biological factors are: different tumor types with individual expression of somatostatin receptor subtypes, differences in total tumor burden and distribution, cardiovascular and renal function, age, sex, and possibly ongoing, or previous, hormonal treatment (e.g. octreotide). In the therapeutic studies, repeated examinations were performed in the same patients over a prolonged time, with several administrations of ^{111}In-DTPA-D-Phe^1-octreotide in quantities higher than the diagnostic amounts (both regarding ^{111}In activity and peptide weight).

Methodological factors include differences in calibration of the gamma camera, attenuation correction, background correction, measurement technique (simultaneous anterior and posterior imaging), quantitation method and follow-up time. In the case of therapy, the correction for dead-time losses of the gamma camera is also important.

One of the most important parameters in these studies is the calibration. In some studies, the gamma camera is assumed to be calibrated by doing the first measurement of the patient immediately after injection (before voiding). The whole-body content is then assumed to be 100% of the injected activity. However, this method might give false results due to redistribution within the body during the initial measurement or due to different biodistribution between the first and the following measurements, since the density and thickness (and thus the attenuation) is different in various body regions. Such an error will rescale the activity in the organs with the same factor. However, the whole-body content may be scaled differently at various times after injection, due to redistribution in the body (if no attenuation correction is performed). Therefore, in this study, the gamma camera was carefully calibrated in two ways, using a trunk phantom and a surface source. After attenuation correction, the results from the two calibrations showed a very good agreement; the difference was only about 5%. One problem with calibration for ^{111}In is potential adsorption of ^{111}In to glass or plastic surfaces, rendering the sensitivity of the gamma camera too high. This effect can be reduced if the phantom is rinsed with stable indium chloride or if extra DTPA is added to the ^{111}In solution prior to calibration.

If there is considerable redistribution of the radionuclide within the body during the period of study, it is important to correct for differences in attenuation in different body regions, e.g. the lungs, when the content of ^{111}In in the whole body is calculated. Since there was no access to reliable transmission measurements of the whole body at the time of the study, attenuation correction was performed separately for the selected body regions. Although the effective thicknesses were estimated for a standard patient (individual data was not available), the whole-body content at 0.5 h was between 90 and 110% IA, except for one patient (120% IA). This low variability may be due to the fact that this patient group with malignant disease was rather homogeneous in terms of body mass index (BMI<25). A 1 cm error in body thickness gives an error in activity of about 5% (15). If no attenuation correction and separate calibration had been used in this study, the initial whole-body content had reached 70-200% IA (mean value 150% IA). This would have resulted in low estimates of mean activity and absorbed dose values.

Due to the initially rapid redistribution within the body, the early whole-body images should be acquired during a very short time. In this study, the scan velocity was higher for the early images. Regarding the high counting statistics, the scan velocity could have been even higher. One should also consider the mode of image acquisition. Simultaneous scanning of the anterior and posterior images, using a double-headed gamma camera, would best suit accurate determination of organ activities at a specific time. However, this technique might still give misleading values of the whole-body content due to redistribution during measurement.

Two kinds of background corrections were applied: 1) correction for detector background (always applied), and 2) correction for background activity in over- and underlying tissues (when organ activities were determined). The last correction requires information about the thickness of each organ, but depends also on a homogeneous activity distribution in surrounding tissues. The method of Fleming was used, where a 1 cm error in organ thickness gives an error in activity determination of 2% (15).

The follow-up time is important for determination of the biological half-times and the number of exponential functions for curve fitting. In this study each patient was followed to about 72 h after injection (vs. 24-48 h in the other studies with diagnostic amounts), which probably permits

resolution of longer half-times. Still, there were problems with the curve-fitting for some organs, mainly due to the fact that the maximum value was obtained at 4 h (spleen), or that the values at 4 h were sometimes only slightly higher than that at 24 h (e.g. liver, kidneys, and urinary bladder). Due to the rapid clearance from blood, more frequent measurements during the first few hours should have been done, especially for a more correct time-activity curve in the kidneys. However, the absorbed dose would probably not be much different, due to the relatively short half-life of ^{111}In.

In a well performed pharmacokinetic and dosimetric study of a radiopharmaceutical, it should be possible to reach an accuracy of about 20-30% in the organ absorbed doses. Although the measurement and calculation procedures differ between the published studies on the dosimetry of ^{111}In-DTPA-D-Phe^1-octreotide (8-12), the discrepancies in mean absorbed doses per unit ^{111}In activity to the organs still did not exceed a factor of two. This must be regarded as acceptable for these types of studies with large variations in patient kinetics.

ACKNOWLEDGMENTS

We thank Mallinckrodt Medical B.V. for the generous supply of the radiopharmaceutical. This work was supported by grants from the Swedish Cancer Society (3427), the Swedish Medical Research Council (5220), the King Gustav V Jubilee Clinic Cancer Research Foundation and Assar Gabrielsson Research Foundation, Göteborg, Sweden.

REFERENCES

1. Bakker WH, Albert R, Bruns C et al. [^{111}In-DTPA-D-Phe^1]-octreotide, a potential radiopharmaceutical for imaging of somatostatin receptor-positive tumors: synthesis, radiolabeling and in vitro validation. Life Sci 49:1583-1591, 1991.
2. Krenning EP, Kwekkeboom DJ, Bakker WH, Breeman WAP, Kooij PPM, Oei HY, van Hagen M, Postema PTE, de Jong M, Reubi JC, Visser TJ, Reijs AEM, Hofland LJ, Koper JW and Lamberts SWJ. Somatostatin receptor scintigraphy with [^{111}In-DTPA-D-Phe^1]- and [^{123}I-Tyr^3]-octreotide: The Rotterdam experience with more than 1000 patients. Eur J Nucl Med 20:716-731, 1993.
3. Maini CL, Tofani A, Sciuto R, Carapella C, Cioffi R and Crecco M. Somatostatin receptors in meningiomas: A scintigraphic study using ^{111}In-DTPA-D-Phe-1-octreotide. Nucl Med Commun 14:550-558, 1993.
4. Kwekkeboom DK, van Urk H, Pauw BKH, et al. Octreotide scintigraphy for the detection of paragangliomas. J Nucl Med 34:873-878, 1993.
5. Ahlman H, Wängberg B, Tisell LE, Nilsson O, Fjälling M and Forssell-Aronsson E. Clinical efficacy of octreotide scintigraphy in patients with midgut carcinoid tumors and evaluation of intraoperative scintillation detection. Br J Surg 81:1144-1149, 1994.
6. Tisell LE, Ahlman H, Wängberg B, Hansson G, Mölne J, Nilsson O, Lindstedt G, Fjälling M and Forssell-Aronsson. Somatostatin receptor scintigraphy in medullary thyroid carcinoma. Br J Surg, in press, 1996.
7. Wängberg B, Forssell-Aronsson E, Tisell LE, Nilsson O, Fjälling M and Ahlman H. Intraoperative detection of somatostatin-receptor-positive neuroendocrine tumors using indium-111-labeled DTPA-D-Phe^1-octreotide. Br J Cancer 73:770-775, 1996.
8. Krenning EP, Bakker WH, Kooij PPM, Breeman WAP, Oei HY, de Jong M, Reubi JC, Visser TJ, Bruns C, Kwekkeboom DJ, Reijs AEM, van Hagen PM, Koper JW and Lamberts SWJ. Somatostatin receptor scintigraphy with indium-111-DTPA-D-Phe-1-octreotide in man:

Metabolism, dosimetry and comparison with iodine-123-tyr-3-octreotide. J Nucl Med 33:652-658, 1992.
9. Bajc M, Palmer J, Ohlsson T and Edenbrandt L. Distribution and dosimetry of ^{111}In-DTPA-D-Phe-octreotide in man assessed by whole body scintigraphy. Acta Radiol 35:53-57, 1994.
10. Leide-Svegborn S, Nosslin B, Mattsson S. Biokinetics and dosimetry of ^{111}In-DTPA-D-Phe-1-octreotide in patients. In: Sixth International Radiopharmaceutical Dosimetry Symposium, Proceedings of a Conference held at Gatlinburg, Tennessee, May 7-10, 1996 (Edited by AT S-Stelson et al.), pp: 631-642, 1999.
11. Krenning EP, Kooij PPM, Bakker WH, Breeman WAP, Postema PTE, Kwekkeboom DJ, Oei HY, de Jong M, Visser TJ, Reijs AEM and Lamberts SWJ. Radiotherapy with a radiolabeled somatostatin analogue, [^{111}In-DTPA-Phe^1]-octreotide. A case history. In: Molecular and Cell Biological Aspects of Gastroenteropancreatic Neuroendocrine Tumor Disease. Wiedenmann B, Kvols LK, Arnold R and Rieken EO, Editors. Ann N Y Acad Sci 733:496-506, 1994.
12. Andersson P, Forssell-Aronsson E, Grétarsdóttir J, Johansson V, Wängberg B, Nilsson O, Fjälling M and Ahlman H. Biokinetics and dosimetry after repeated injections of ^{111}In-DTPA-D-Phe^1-octreotide. In: Sixth International Radiopharmaceutical Dosimetry Symposium, Proceedings of a Conference held at Gatlinburg, Tennessee, May 7-10, 1996 (Edited by AT S-Stelson et al.), pp: 127-136, 1999.
13. Fjälling M, Andersson P, Forssell-Aronsson E, Grétarsdóttir J, Johanson V, Tisell LE, Wängberg B, Nilsson O, Berg G, Michanek A, Lindstedt G and Ahlman H. Systemic radionuclide therapy using indium-111-DTPA-D-Phe-1-octreotide in a patient with midgut carcinoid syndrome. J Nucl Med 37(9):1519-1521, 1996.
14. Forssell-Aronsson E, Fjälling M, Nilsson O, Tisell LE, Wängberg B and Ahlman H. ^{111}In activity concentration in human tissue samples after i.v. injection of ^{111}In-DTPA-D-Phe^1-octreotide. J Nucl Med 36:7-12, 1995.
15. Fleming JS. A technique for the absolute measurement of activity using a gamma camera and computer. Phys Med Biol 24(1):176-180, 1979.
16. Snyder WS, Ford MR and Warner GG. Estimates of Specific Absorbed Fractions for Photon Sources Uniformly Distributed in Various Organs of a Heterogeneous Phantom. Medical Internal Radiation Dose (MIRD), Pamphlet No. 5, Rev., Society of Nuclear Medicine, New York, 1978.
17. Loevinger R and Berman M. A Revised Schema for Calculating the Absorbed Dose from Biologically Distributed Radionuclides. Medical Internal Radiation Dose (MIRD), Pamphlet No. 1, Society of Nuclear Medicine, New York, 1976.
18. Watson EE, Stabin M and Siegel JA. MIRD formulation. Med Phys 20(2):511-514, 1993.
19. Stabin MG. MIRDOSE: Personal computer software for internal dose assessment in nuclear medicine. J Nucl Med, 37:538-546, 1996.
20. Snyder WS, Ford MR, Warner GG and Watson SB. "S", Absorbed Dose per Unit Cumulated Activity for Selected Radionuclides and Organs. Medical Internal Radiation Dose (MIRD), Pamphlet No. 11, Society of Nuclear Medicine, New York, 1975.
21. ICRP Publication 26. Recommendations of the International Commission on Radiological Protection. Pergamon Press, Oxford, 1977.
22. ICRP Publication 28. Statement from the 1978 Stockholm Meeting of the ICRP. Pergamon Press, Oxford, 1978.
23. ICRP Publication 60. 1990 Recommendations of the International Commission on Radiological Protection. Pergamon Press, Oxford, 1991.
24. Bjurman B, Johansson L and Mattsson S. ^{114}In^m in ^{111}In-radiopharmaceuticals and its contribution to the absorbed dose in the patients at investigation with ^{111}In-labeled blood cells. edited by

Raynaud C. In: Proceedings from the 3rd World Congress of Nuclear Medicine and Biology, Paris. Pergamon Press, Oxford, pp: 2403-2406, 1992.

QUESTIONS

Roesch: These are well performed studies, congratulations. However, I wonder what the radiation dose is to the tumor. Because ^{111}In-octreoscan is applied for the diagnosis of somatostatin receptor expressing tumors it would be of interest to compare the radiation doses for the tumor with those for the other organs.

Leide: Thank you. The primarily interest of this study was not to measure tumor uptake and dose to tumor tissues, but to determine the absorbed dose to normal organs and tissues. The investigation was done mainly for radiation protection purposes.

Aronsson: In Göteborg we are now working with the tumor dosimetry. Some results have been presented at this symposium (Andersson et al.), showing that the tumor receives 0.5-2.5 mGy/MBq. Even higher absorbed doses per unit activity were found for the liver metastases in this patient. More data, based on measurements on tumor biopsies and the biokinetics in visible tumors will soon be available.

Kagan: How did you correct your count data for attenuation?

Aronsson: In Göteborg we performed attenuation correction for the organs according to the method by Fleming, 1979, using the effective thickness of the organs and the body. When estimating the content of ^{111}In in the whole body, separate attenuation correction was performed in three regions of the body: thorax, legs and the rest of the body, using the effective thickness of each region. Further details are given in the paper.

Leide: When calculating the activity in each source organ the equation of Fleming (1979) was used. Thus attenuation correction was made for the body thickness of the patient in different regions as well as for the thickness of the different organs. The average attenuation coefficient, μ was measured with plastic bottles filled with ^{111}In surrounded with varying thickness of tissue - equivalent material. This was done with bottles of different sizes. Furthermore, the count data in the image from the posterior projection was corrected for attenuation in the gamma camera couch.

Rao: Could you compare the results of Malmö and Göteborg studies on the absorbed doses to different tissues?

Leide: Figure 1a and 1b. Absorbed dose to kidneys, spleen, liver and the effective dose from ^{111}In-pentetreotide. Comparison between the results of Forssell-Aronsson et al. (o) and Leide-Svegborn et al (▪).

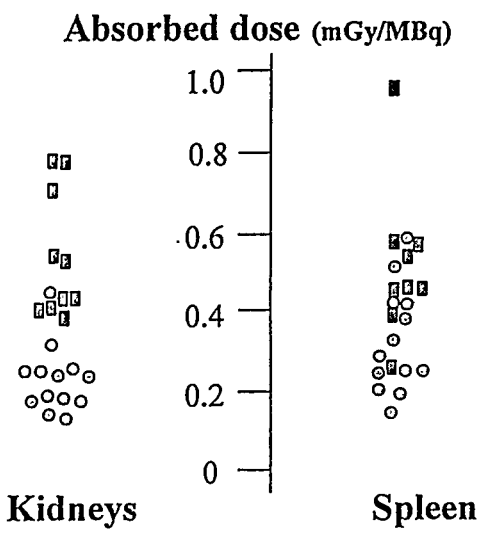

1a

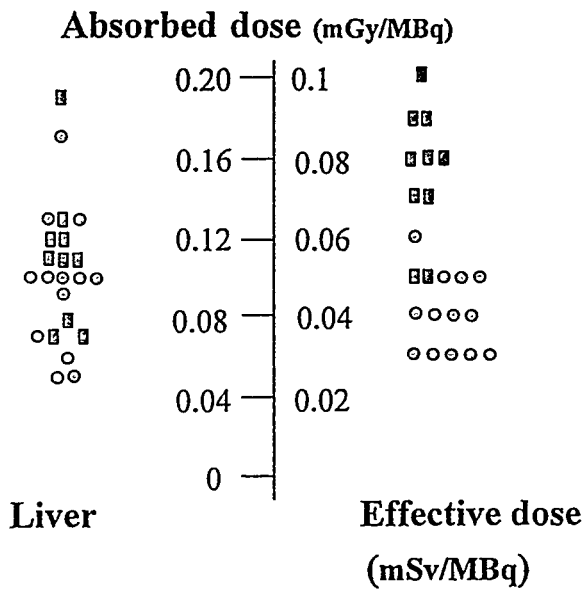

1b

The differences between the results of Forssell-Aronsson et al. (Göteborg) and Leide-Svegborn et al. (Malmö) in the absorbed dose to different organs may be due to individual variations between the patients such as sex, age, weight, tumor burden and possible ongoing octreotide treatment. Other factors that may contribute to the differences are various methods for background- and attenuation correction, differences in the calibration procedure and different number of source organs. Minor differences might also be explained by different amounts of injected peptide, 20μg (220 MBq) in Göteborg and 10μg (110 MBq) in Malmö.

RADIATION ABSORBED DOSE FROM ^{111}In CYT-356, AN IV-ADMINISTERED ANTI-PROSTATE ANTIBODY FOR PROSTATE CANCER STAGING AND A PROPOSED INFUSIONAL BRACHYTHERAPY APPLICATION

Brill AB[1], Mardirossian G[1], Menon M[2], and Maguire R[3]
[1]University of Massachusetts Medical Center, Nuclear Medicine Department
[2]University of Massachusetts Medical Center, Urology Department
Worcester, MA. 01655
[3]Cytogen Corporation, Princeton, NJ. 08450

ABSTRACT

The fraction of the injected dose that targets tumors in human studies has been adequate for diagnostic studies but marginal for radioimmunotherapy. Recent work by a number of investigators has led to renewed interest in infusional brachytherapy. We have conducted dosimetry studies on an IgG antibody, originally designated CYT356, which targets a prostate-specific membrane antigen (PSMA). Dosimetry studies were performed on data obtained from sequential (up to 7-10 days post injection) conjugate imaging of organ uptake in prostate cancer (PCa) patients who received 185 MBq administrations of ^{111}In-CYT-356. The data were analyzed using SAAM and the MIRD methodology. Measurements were made using a quantitative conjugate emission imaging protocol along with transmission imaging, and a thickness-dependent camera sensitivity calibration . Uptake in the testes and transit through the GI tract were included in the dose analyses.

Previous attempts to use I.V. administrations of ^{111}In-OncoScint (the first anti-tumor antibody approved for patient diagnosis in the United States) when labeled with a beta emitting tumor seeker (^{90}Y-CYT 103), revealed disappointingly low absorbed tumor doses in patients with colorectal and ovarian cancers. The location of the prostate makes it accessible for implant and infusional brachytherapy. The fact that many patients with histologically-negative lymph nodes have molecular biological evidence of tumor in these nodes indicates that up to half the patients undergoing radical prostatectomy have disease extending beyond the prostate, and new approaches need to be considered to deal with this common problem.

We are proposing two means of boosting the dose to regional lymph node metastases to a therapeutic range: 1) preoperative pericapsular infusion of ^{90}Y-CYT 356 administered under ultrasound control, to patients with no known metastases and to patients with known lymph node metastases who will not be operated upon, and 2) injection of ^{90}Y-CYT 356 into the tumor bed in patients found at surgery to have lymph node metastases. Initial studies will be conducted using infusions of ^{111}In-CYT 356 injected as proposed for therapy to ascertain feasibility of the approach based on the observed pharmacokinetics and dose distribution. A dose-escalation study with ^{90}Y-CYT 356 will then be pursued if nodal uptake is high enough to anticipate good results. Infusional

brachytherapy appears to be a potentially-useful means for increasing the dose to regional metastases using radioimmunotherapy along with primary surgical therapy or interstitial brachytherapy.

INTRODUCTION

The history of nuclear medicine reveals a cycling between the development of tracers for diagnosis, followed by therapy trials, and a series of iterations thereafter to improve delivery and measurement systems to increase both diagnostic and therapeutic effectiveness. Clearly agents which don't localize strongly, even if useful for diagnosis, are not candidates for therapy . Nuclear medicine started with tracer kinetic studies in plants (1), followed by physiologic studies in patients (2) and treatment (3), the latter, shortly after the first radioisotopes came from the Berkeley medical cyclotron. With the exception of ^{131}I and ^{32}P, most of the early therapy trials failed to live up to expectations due to relatively low tumor to normal organ uptake ratios.

Implanted radioactive isotopes and seeds placed in the primary tumor deliver extremely high tumor doses, but metastases are not treated and the tumor dose is heterogeneous allowing some tumor cells to survive. Nonetheless, brachytherapy is an excellent means of delivering large doses to the tumor with minimum dose to surrounding normal tissue. Many nuclear medicine groups have attempted to use the I.V. and intracavitary routes of administration to target both primary and metastatic lesions, and work continues in this area. Molecular technology now provides highly selective molecules in clinically useful amounts which recognize and target specific tumors. Molecular recognition agents, including monoclonal antibodies, increase the efficiency of targeting both the primary and metastatic lesions following I.V. administration. But early results have been disappointing, as most I.V.-injected materials do not accumulate sufficiently strongly in most solid tumors to provide successful therapy. New interest in interstitial injections is witnessed by the growing number of investigators attempting to inject diffusible materials for cancer diagnosis and therapy . Here again, heterogeneous distribution is a problem that must be overcome for successful therapy. Early results are promising in locating the sentinel node (the first node to which the tumor drains). Pathologic analysis of this node provides a sensitive index of tumor dissemination, and has some advantage over the use of dye markers. When the sentinel node accumulates the radiolabeled antibody, radioimmuno-guided surgery (RIGS) using intraoperative probes can assist the surgeon in finding other tumor-involved nodes. There is growing interest in local drug instillation for diagnosis and staging, using external imaging and RIGS. It is for these reasons that we are now proposing to test a combination of these methods to treat prostate cancer regional metastases using infusional brachytherapy.

Our interest was pointed in this direction by the recent report in which ^{32}P-colloid was percutaneously infused to the pancreas in patients with inoperable pancreatic cancer (4). Macroaggregates were preinfused to block the egress of subsequently injected ^{32}P labeled colloid, thereby increasing retention in and dose to the pancreas. Very large doses were delivered, up to more than a million rads, and tumor shrinkage occurred in several of these terminally-ill patients.

The ability to deliver large doses to the tumor was especially impressive when compared to doses from I.V.-administered antibodies we experienced analyzing ^{90}Y-labeled OncoScint dosimetry (4). Even assuming infinite retention of the antibody in sampled tumor-containing lymph nodes, the estimated dose was in the order of several gray from a projected 1110 MBq (30 mCi) administration, which clearly was too low to expect effective use in therapy.

At the time of the 1994 interstitial brachytherapy report (5), we were investigating the biodistribution and clinical utility of ^{111}In-CYT-356 (ProstaScint) for staging prostate cancer patients. It is an IgG murine monoclonal antibody developed by CYTOGEN directed at a prostate-specific

membrane antigen. The antibody does not react with PSA or PAP (6), and is the kind of agent that could be most useful for infusional radiotherapy. Unlike the pancreas cancer protocol, we are not considering this for treatment of the primary prostate lesion, but are proposing to use it to treat local metastases by infusing beta-emitting labeled material into the prostate capsule and/or the prostate bed. Thus, we want leakage from the injection site to target local metastases, unlike what was done in the pancreas infusion protocol where they used microsphere blockade to increase dose to the primary tumor to limit loss from the infused sites.

METHODS

Dosimetry Studies

Data from 21 prostate cancer patients were collected at three sites using a common protocol. All patients signed informed consent forms approved by their respective Institutional Review Boards. Five patients were from the University of Massachusetts Medical Center (UMMC), 11 from the University of Washington Medical Center (UWMC) and five from the Iowa City Veterans Administration Medical center (ICVAH) (7). Each patient received (I.V.) 0.5 mg of CYT356 labeled with approximately 185 MBq (5 mCi) of ^{111}In. The activity administered was determined by measuring syringe activity in a dose calibrator before and after infusion. Only ^{114m}In and ^{111}In were included in the dose calculations. The amount of ^{114m}In was assumed to be 0.06% of the injected activity at time of administration, and this contaminant was assumed to follow the same biological kinetics as ^{111}In.

Sequential biodistribution studies included measurements of whole-body and organ activity content, including serum, liver, spleen, kidneys, testes and red marrow out to 10 days postinjection. Urine was measured frequently during the first day, and daily thereafter. Whole-body counts were obtained at each session. Stool was not collected. A standard quantitative conjugate-emission imaging protocol included transmission imaging, and a thickness-dependent camera sensitivity calibration method was employed (8).

A Macintosh computer and DIP Station (Jandel) image analysis software was used for drawing regions of interest (ROIs) about the specified source organs and background regions. The fraction of the injected dose in source organs was analyzed based on counts obtained from flagged anterior regions of interest, which were flipped horizontally to overlay the posterior images. ROIs were linked together so that consistent organ placement of ROIs could be interrogated at successive imaging sessions. The source organs included the liver, spleen, kidneys, testes, bone marrow, heart chamber, lungs, urinary bladder contents and remainder of the body along with the GI tract organs, i.e. gall bladder contents, LLI, SI and ULI. The calculated activity in the GI tract organs was based on a compartmental model proposed by Stabin, using the model shown in Figure 1 (9).

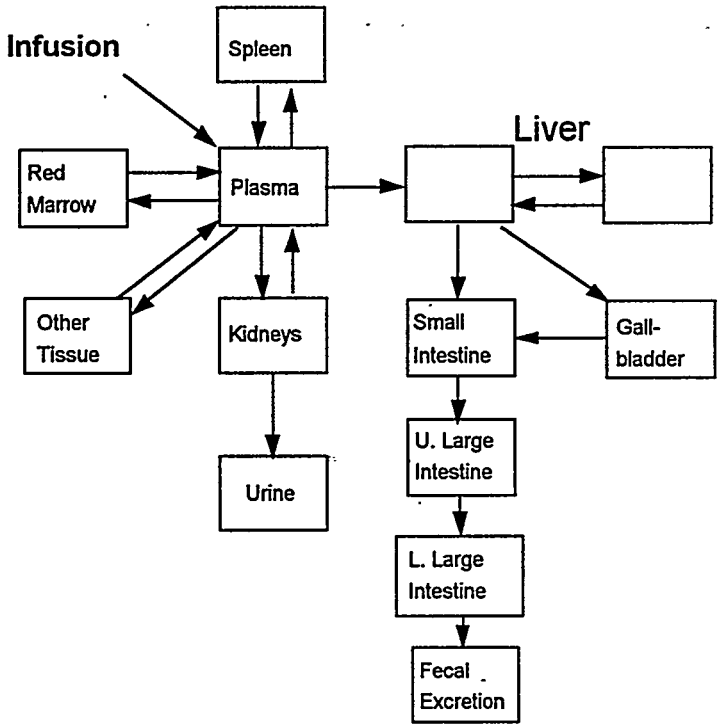

Figure 1. Compartmental Model.

The total content of radioactivity in the bone marrow was estimated from measurements over L2 and L3 vertebrae multiplied by a factor (22.5), which scales the sampled activity to total marrow content (10). The remainder of the body activity at each sampling period was considered to be 100% of the injected activity minus the sum of all activities otherwise accounted for in the measured source organs, the simulated fecal loss, and activity lost in urine. The partition of plasma activity included an assignment of 10% of the plasma pool to the heart and lungs respectively (11). Serum clearance and urine excretion data were established based on the counting of serum, and urine samples and standards, at the end of the collection period. Organ data were quantitated after correction for physical decay.

The activity measured in each organ reflects tissue fixed activity plus circulating activity. The CONSAM program (12), was used to produce least squares best fit curves for organs, using the plasma data as a forcing function to separate blood from organ uptake kinetics. The urine data were fit assuming a 4.8 hr. voiding schedule. The temporal pattern of GI transit and fecal excretion was estimated using a compartmental analysis method (8)for three UMASS patients. The model includes all measured source organs, rest of body and urine data, and was fit using the CONSAM program. The model assumed that the liver is connected to the GI tract with 30% leaving via the gallbladder, with the rest excreted directly into the small intestine. The transit times of the material through the GI tract were based on ICRP data (13).

The area under the curve (AUC) for each source organ was determined from the best-fit curves extrapolated to infinity. The only losses (besides stool and urine) were assumed to come from physical decay of the tracer. The residence times (AUC/Injected activity) so obtained (blood plus fixed activity) for each patient were calculated, and average values computed for each site for ^{111}In and ^{114m}In, separately. These values were entered into the MIRDOSE3 program (14) for each patient separately and calculations were made using the S factors for ^{111}In and ^{114m}In and the MIRD formalism (15,16).

Although the dose to the prostate was not derived from direct measurements, we estimated the dose based on several assumptions. These were: uptake of 0.01%/g in a 16 g prostate with infinite retention. Calculations were made based upon the method and using S factors tabulated and presented by Stabin (17).

RESULTS

Figure 2 shows the computer fit data (FIA, i.e. fraction of injected activity) versus time for a typical patient. The excreted material in each segment of the GI tract was calculated, and these values along with organ content data were entered into MIRDOSE 3 for subsequent analyses.

The individual organ doses and effective dose are given in Table 1. The greatest variation was seen in the dose to kidneys (range 0.28-1.7 mGy/MBq) and dose to the testes; when considered as a source organ there was a great variation in testicle dose between patients. In several patients, the testes were only barely visualized, while in others the activity was clearly visible. Testicular dose estimates ranged from 0.14 - 0.54 mGy/MBq. The total-body absorbed dose from ^{111}In-CYT 356 was found to be 0.14 mGy/MBq, and the effective dose was 0.25 mSv/MBq. If the dose from simulated transit through the GI tract is included, the effective dose is further increased by 18 %.

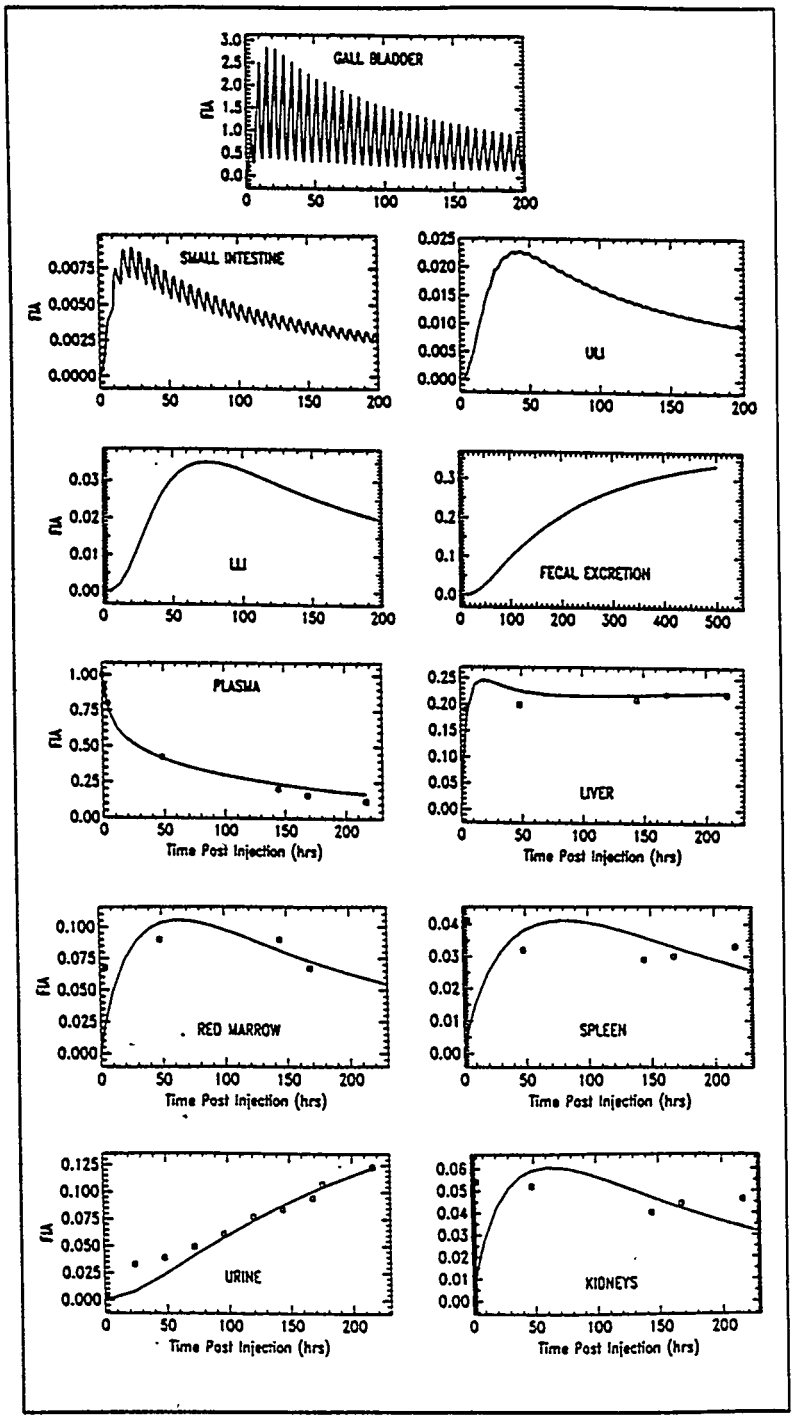

Figure 2. Observed data and computer best fit values (for a typical patient).

Table 1

Average Absorbed Dose Estimates (mGy/MBq)

ORGAN	In-111	In-114m	TOTAL
Adrenals	0.28	0.004	0.28
Brain	0.05	0.004	0.06
Gallbladder Wall	0.39	0.003	0.39
LLI Wall	0.40	0.009	0.41
Small Intestine	0.18	0.002	0.18
Stomach	0.16	0.004	0.17
ULI Wall	0.27	0.004	0.27
Heart Wall	0.40	0.015	0.42
Kidneys	0.65	0.024	0.67
Liver	0.96	0.037	1.00
Lungs	0.29	0.012	0.31
Muscle	0.10	0.004	0.11
Pancreas	0.27	0.004	0.27
Red Marrow	0.23	0.004	0.23
Bone Surfaces	0.21	0.004	0.22
Skin	0.06	0.004	0.06
Spleen	0.84	0.037	0.88
Testes	0.27	0.033	0.30
Thymus	0.14	0.004	0.14
Thyroid	0.07	0.004	0.08
Urine Blad Wall	0.12	0.002	0.12
Total Body	0.14	0.005	0.14
ED*	0.28	0.014	0.29
*mSv/MBq			

DISCUSSION

Dose estimates for the patients studied at the different institutions included in this study are in reasonable agreement, i.e. for individual organ doses within study sites, as well as between different sites. The greatest variation was seen in the dose to kidneys (range 0.28-1.7 mGy/MBq) and dose to the testes. There was a great variation in testicle dose between patients. In many patients the testes were only barely visualized while in others the activity was clearly visualized. The inclusion of the testes as source organs increased the contribution to the ED on the average from 0.21 to 0.25 mSv/MBq, i.e. by 16%. In addition to the testicular uptake per se, part of the increased dose is due to the relatively long blood residence time (45 hrs. vs. 38 hrs for OncoScint CR/OV) (18), which contributes to increased dose to all organs. Despite the long physical half-life of ^{114m}In , its contribution to the total dose is not large (3.5% of the total ED).

Excretion through the GI tract was modeled, and 10.8% of the activity was assigned (using the ICRP 30 GI tract feature (19) in MIRDOSE 3) to the excretory path. The use of the GI tract as a modeled source organ increased the dose to the lower large intestine by a factor of four.

Therapy Proposal

Given that tumor uptake of I.V. injected monoclonal antibodies is of the order of 0.01% per gram or less, it is unlikely that effective tumor therapy for solid organ malignancies can be achieved by I.V. administration. Current therapy procedures combine surgery, external beam, and/or interstitial

brachytherapy (using sealed sources) with hormonal therapy. To this end, we propose to add intratumoral or peritumoral infusion of a radiolabeled antibody to target regional metastases.

The rationale for the therapy proposal is two-fold. The first is that many patients who at surgery are found to be node negative subsequently manifest progressive disease, indicative of undetected metastases at surgery. About half of the patients undergoing radical prostatectomy for apparently localized prostate cancer have histological evidence of disease outside the prostate, and a substantial proportion of these patients have positive surgical margins (20). The presence of positive surgical margins is highly predictive of biochemical and clinical recurrence. The second factor is the location of the prostate which is accessible to both implant and infusional brachytherapy. Together these can deliver very high doses to the treatment field (implants to the prostate, and infusions to the lymphatic and vascular drainage routes). The recent finding that 44% of node-negative patients (based on standard pathology review) actually have molecular markers in pelvic lymph nodes indicative of disseminated prostate cells, suggests that the likelihood of cure could be increased if the patients could be treated while the metastatic spread is still at the microscopic level (20).

Prostate cancer patients with no evidence of spread are prime candidates for infusional brachytherapy. We propose injecting ^{90}Y labeled CYT 356 into the prostate capsule under ultrasound control. The patient would be treated surgically several days later, at which time intraoperative radiation probes would be used to assist the surgeon (radioimmunoguided surgery, RIGS) to remove nodes with high levels of tumor and antibody. The radioimmunotherapy (RIT) dose can also be injected into the prostate bed just prior to closing. In any case, it will be important to follow these patients along with a group treated in the usual fashion to determine how outcome is affected by RIT.

CYT 356 is the natural choice for the ligand, but there are many possibilities for choice of optimum radionuclide. $^{186/188}$Re would be a good choice, but its low specific activity and high cost argue against its use. We chose ^{90}Y for several reasons: its 67 hour half-life is appropriate, it is available from an on-site generator (^{90}Sr/^{90}Y), it is cheap and always available, and last, but not least, CYTOGEN has an IND for ^{90}Y-CYT356 which we will cross-reference. Other labels with shorter range particulate emissions, including alpha-particle emitters, would be better for treating microscopic metastases, and in the final planning, the final selection will be made based upon pilot-study findings.

The initial goal is to do a treatment planning study administering ^{111}In CYT 356 under ultrasound guidance to determine the biodistribution following periprostate infusion, and to optimize the drug delivery system. The external imaging protocol used for the dosimetry study will be used to determine normal organ dose (including the bone marrow). Uptake in tumor-involved nodes removed at operation will be used to estimate tumor dose by this route of injection. Based on the absorbed dose to tumor and normal organs (especially the bone marrow), we will inject a safe amount of ^{90}Y-CYT356 and escalate this amount until a reasonable compromise is reached before embarking on an efficacy trial.

The object is to deliver as high a dose as possible to the tumor while avoiding severe bone marrow toxicity. If we assume that the residence time of the antibody labeled with ^{111}In and ^{90}Y are the same, even if all the activity was injected, the worst case estimate of marrow dose from 1.1 GBq (30 mCi) of ^{90}Y- labeled material would be 2.2 Gy, assuming infinite retention of material that locates in the marrow, i.e. a higher dose than calculated based on model-derived pharmacokinetics.

CONCLUSIONS

The total-body absorbed dose from ^{111}In-Capromab Pendetide was 0.14 mGy/MBq, and the effective dose was 0.25 mSv/MBq (including the testes as a source organ). If one includes the dose from simulated transit through the GI tract the ED dose is further increased by 18 %. These dose

estimates are similar in magnitude to the total-body and effective doses listed in the package insert for OncoScint CR/OV (0.15 mGy/MBq and 0.23 mSv/MBq respectively), an agent approved for use in colorectal and ovarian cancer diagnosis and management.

If experience with other infusional brachytherapy applications is a valid guide, ^{90}Y-CYT 356 injected perioperatively to the prostate capsule could significantly irradiate loco regional micrometastases. This boost dose may kill these small tumor cells, which otherwise can go on to manifest their presence as late treatment failures. This proposal is in the early planning stage and we hope to present early results in the near future.

ACKNOWLEDGMENT

Figures 1 and 2 reprinted by permission of the Society of Nuclear Medicine from: Mardirossian G, Brill AB, Dwyer KM, Kahn D and Nelp W. Radiation absorbed dose from indium-111-CYT-356. Journal of Nuclear Medicine 37:1583-1588, 1996.

REFERENCES

1. Hevesy G. The absorption and translocation of lead by plants. Bioch 17:439-445, 1923.
2. Blumgart HL and Yens OC. Studies on the velocity of blood flow. I. The method utilized J Clin Invest 4:1-13, 1926.
3. Lawrence JH. Cited in GT Seaborg. The First 50 Years. Published in Nuclear Medicine. 100 Years in the Making. SNM Press, 1996.
4. Unpublished data from a CYTOGEN therapy trial. Data calculated at the Univ. of Mass Medical Center.
5. Order SE, Siegel JA, Lustig RA et al. Infusional brachytherapy in the treatment of non-resectable pancreatic cancer: A new radiation modality. Antibody, Immunoconjugates, and Radiopharmaceuticals 7:11-17, 1994.
6. Wynant GE, Murphy GP, Horoszewicz JS et al. Immunoscintigraphy of prostatic cancer: Preliminary results with ^{111}In-labeled monoclonal antibody 7E11-C5.3 (CYT-356). The Prostate 18:229-241, 1991.
7. Mardirossian G, Brill AB, Dwyer KM, Kahn D and Nelp W. Radiation absorbed dose to patients from ^{111}In CYT-356, J Nucl Med 37(9):1583-1588, 1996.
8. Doherty P, Schwinger R, King M and Gionet M. Distribution and dosimetry of indium-111 labeled F(ab')2 fragments in humans, pp:464-476, In: Fourth International Radiopharmaceutical Symposium, Oak Ridge, TN, 1985, CONF-851113 (DE86010102), 1986.
9. Stabin MG. Prediction of radiation dose to the GI tract from analysis of blood and liver time-activity curves, In: Fifth International Radiopharmaceutical Dosimetry Symposium, May 7-10, 1991. Oak Ridge, TN, Oak Ridge Associated Universities, CONF-910529 pp:202-215, 1992.
10. Report on the Task Group on Reference Man, ICRP Publication 23, Pergamon Press, 1974.
11. Poston JW, Aissi A, Hui TY and Jimba BM. A preliminary model of the circulating blood for use in radiation dose calculations. In: Fourth International Radiopharmaceutical Dosimetry Symposium, Nov. 5-8, 1985. Oak Ridge, TN, Oak Ridge Associated Universities, CONF-851113, p. 574-586, 1986.
12. Berman M, Beltz WF, Greif PC, Chabay R and Boston RC. CONSAM User's Guide. Laboratory of Mathematical Biology, National Institutes of Health, Bethesda, Maryland 20205. Manual Version: July 1983.

13. Eckerman K. Chapter 13. Dosimetric Methodology of the ICRP. In: Internal Radiation Dosimetry. Ed. OG Raabe. Health Physics Society 1994 Summer School. Medical Physics Publishing, Madison, WI, 1994.
14. Stabin MG, MIRDOSE: Personal computer software for internal dose assessment in nuclear medicine. J Nucl Med37:538-546, 1996.
15. Watson EE. The MIRD Internal Dose Formalism. Chapter 15. In: Internal Radiation Dosimetry. Ed. OG Raabe. Health Physics Society 1994 Summer School. Medical Physics Publishing Co. Madison, WI, 1994.
16. Loevinger R and Berman M. A Revised Schema for Calculating the Absorbed Dose from Biologically Distributed Radionuclides. MIRD Pamphlet No 1 (Revised). New York: The Society of Nuclear Medicine, 1976.
17. Stabin M. A model of the prostate gland for use in internal dosimetry. J Nucl Med 35:516-520, 1994.
18. OncoScint and ProstaScint residence times determined in Univ. of Mass. Dosimetry studies.
19. Annals of the ICRP, Publication 30, Part 1: Limits for Intakes of Radionculides by Workers, Section 6:30-34, 1974.
20. Edelstein RA, Zietman AL, Morenas ADL et al. Implications of prostate micrometastases in pelvic lymph nodes: An archival tissue study. Urology 47:370-375, 1996.

QUESTIONS

R. Dunn: Given the fact that ^{111}In goes to the bone marrow, whereas ^{90}Y is a bone seeker, can an accurate correlation between marrow dose from the diagnostic study be made for therapy? Has any analysis been performed to ascertain the amount of radionuclide (either ^{111}In or ^{90}Y) which may come off the conjugate? A possible lesion (mets vs. fracture) was seen on the bone scan image but not on the Mab scan. What is the possibility/probability of not targeting lesions?

Brill: The problem of estimating dose from ^{90}Y based on ^{111}In studies is due to the small amount of ^{90}Y that can detach from the antibody during its biological sojourn. Thus, it can deliver a slightly larger dose to bone and bone marrow than predicted from the ^{111}In treatment planning study, the amount dependent upon the chelator binding properties. In the case of the GYK linker, the incremental dose from free ^{90}Y is not large. The rationale for choosing ^{90}Y is that we derive it from a ^{90}Sr long-lived generator, and hence, cost and availability are strong positives. We could have made three other choices. One, would have been to administer ^{114m}In as the therapeutic nuclide. We have done this in rat studies, and this would have permitted a radionuclide in the same family. The difference in half-life, however, creates large uncertainties, and further, ^{114m}In is not available in the amounts needed for human therapy since the ANL cyclotron closed. The second possibility would have been to use ^{86}Y, a positron emitter, but we do not have the appropriate measurement systems, and tracer availability is also a problem. The last possibility would have been to use ^{186}Re, or ^{188}Re, and again cost and availability led us in a different direction. Furthermore, CYTOGEN has an IND for ^{90}Y-CYT 356 which we plan to amend for our use. Thus, although ^{90}Y-CYT 356 which we plan to amend for our use. Thus, although ^{90}Y is not ideal, it is the best compromise available to us.

The focal uptake in the rib on the bone scan was interpreted as a small nonpathologic fracture.

TC-99M DMSA IN CHILDREN: BIODISTRIBUTION, DOSIMETRY, RADIOPHARMACEUTICAL SCHEDULE AND AGE DEPENDENCY

Smith T, Evans K, Lythgoe MF, Anderson PJ and Gordon I
Department of Radiology, Great Ormond Street Hospital for Children
London WC1N 3JH, UK

ABSTRACT

The variation of radiation dose in children undergoing diagnostic Tc-99m DMSA studies was examined using a radiopharmaceutical schedule (RPS) based on body surface area. Twenty-four children (5 weeks - 14.8 years; 15 normal renal function, 9 renal pathology) were investigated by gamma-camera imaging, whole-body counting and urinalysis up to 30h p.i. Uptakes in kidneys, liver, spleen, knees (metaphyseal growth regions) and urinary bladder were estimated using an attenuation-corrected geometric mean method. In normal children, maximal kidney uptake (42.4 ± 5.4%) was attained after 6-7h with half-times of uptake and elimination of 1h and 3.2d respectively. Mean liver, spleen, and knee uptakes were 4.6%, 1.9% and 1.4% respectively. In renal pathology, kidney uptake was reduced to 15.8 ± 8.2%, but there were normal uptakes in other organs. Twenty-four hour urinary excretion was significantly lower in normals under 1y compared with older children. The MIRDOSE 3 program was used to estimate equivalent doses in 24 target organs, from which the value of effective dose (E) per administered activity was estimated for each child. Interpolation by inverse body weight between pairs of five discrete pediatric phantoms was used to obtain E values for individual children, leading to large differences (up to 46%) in some cases compared with values using discrete phantoms by age. Using a RPS based on surface area, the value of E in normal children was 0.91 ± 0.08 mSv and showed less variation over the measured age range compared with a RPS based only on body weight. In normals, the mean kidney dose of 17 ± 2 mSv contributed 46% of the effective dose. Renal pathology reduced the value of E to about 85% of the normal value. There was little evidence of age-dependency of the biokinetic parameters examined.

INTRODUCTION

Tc-99m DMSA (dimercaptosuccinic acid) has been used successfully in nuclear medicine for more than 20 years to examine renal dysfunction by gamma scintigraphy (1-3). Radiation dose estimates based on these studies were performed when this radiopharmaceutical was first introduced. Although most information relates to adults, some studies on children have been reported (2). However, they are mainly concerned with clinical diagnosis and we are not aware of any systematic pediatric studies to establish factors which would allow an investigation of the age dependence of biokinetic data and dosimetry. The latter requires accurate translation of the measured biological parameters to radiation dose estimates, and this is critically dependent on the application of

appropriate S values derived from mathematical anthropomorphic phantoms (4), which convert organ residence times to organ doses. Currently, five discrete pediatric phantoms have been designed for this purpose to cover the age range 0 - 15 years (5), and it is clear that some form of interpolation is necessary to allow sensible estimation of dose to children of varied age and physical size. We have previously reported on pediatric studies of biodistribution (6) and dosimetry (7) of Tc-99m DMSA. The purpose of the present paper is to examine the results of these studies for age dependence and to investigate the internal dose implications of a radiopharmaceutical schedule based on body surface area. For the latter purpose, the application of a method of interpolation between discrete anthropomorphic pediatric phantoms is described.

MATERIALS AND METHODS

Patients

Twenty-four children (15 boys and 9 girls) aged from 5 weeks to 14.8 years (mean 5.6y) were selected from patients undergoing routine diagnostic Tc-99m DMSA imaging for investigation of renal impairment at the Nuclear Medicine Department, Great Ormond Street Hospital for Children NHS Trust. Fifteen of these children, investigated for urinary tract infection, were categorized as having normal renal function: ultrasound examination and biochemistry (e.g. serum creatinine) were normal and the 3h static DMSA image failed to reveal any focal abnormality. One patient had a single kidney with compensatory hypertrophy and was included in this group. The remaining nine showed abnormal renal function: seven had chronic renal failure for various reasons while of the remaining two, with normal serum creatinine levels, one had acute renal failure secondary to urinary tract infection in an obstructed renal pelvis and the other was suffering from steroid resistant nephrotic syndrome with proteinuria.

As one of the objectives of the study was to examine the observed biokinetic data for evidence of age dependence, a reasonable spread of ages between 1 and 15 years was achieved, particularly for the normal children. Furthermore, as any differences in biological handling of the radiopharmaceutical might be expected to be most pronounced in very young children, a reasonable number of patients was chosen below the age of 1 year. The distribution of ages in our patients is shown in Figure 1. This study was approved by the ethics committee of Great Ormond Street Hospital.

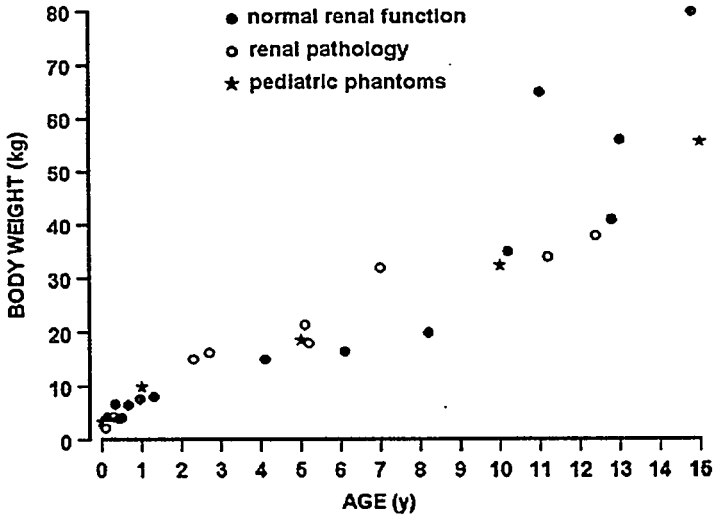

Figure 1. Age and weight distribution of patients and phantoms.

Radiopharmaceutical Schedule

The amount of Tc-99m DMSA administered to patients was determined using the value of the body surface area (S.A.) to scale down the amount normally used for adults (100 MBq), assuming an adult S.A. of $1.73m^2$. A curve relating scaled administered activity A_0 (MBq) to body weight W (kg) was compiled previously for 100 children of varied age and size, whose S.A. values were calculated from their height and weight, according to the formula of Du Bois & Du Bois (8). The equation of this curve is given by

$$A_o\ (MBq) = 5.29 \cdot W^{0.714}. \quad (1)$$

Tc-99m DMSA (Amersham International plc) was prepared according to the manufacturer's recommendations and chromatographically checked for free pertechnetate, which was always less than 0.1%.

Measurements

Biodistribution measurements were obtained using a static gamma camera (Elscint SP6 with low energy, high sensitivity collimator) at the following approximate times; 0.5, 1, 2, 4, 6, 24 and 30h. Anterior and posterior views included kidneys, liver, spleen, urinary bladder and knees, which showed increased uptake of Tc-99m DMSA relative to other tissues. Attenuation corrections for these organs and tissues were obtained from preliminary transmission imaging of the injection syringe through the body regions which included them.

Whole-body retention was measured following the imaging procedures, using the same gamma camera in the vertical position with collimator removed. The patients were measured in both anterior and posterior reference positions at a reproducible distance from the camera. The amount of excreted radioactivity was estimated in total timed urine collections up to 30h. Activity in urine containers, or diapers of very young patients, was determined using a calibrated counting method on the gamma camera. No evidence of excretion via the GI tract was seen on camera images.

Background-corrected regions-of-interest (ROI) were used to obtain conjugate count rates in the above organs which were corrected for attenuation to give organ retention values as fractions of the administered activity. After decay correction, biological retention in organs was described by mono- or biexponential equations. Rates of kidney uptake and elimination were derived from these data, as well as the rates of elimination from other measured organs. The whole-body retention data were corrected by subtracting residual activity in bladder contents and were then expressed as biexponential equations.

Statistical Methods

Investigation for evidence of age dependence was primarily performed by testing the significance of differences between mean biokinetic parameters obtained for the two groups of children aged less than or more than 1year. Immature development of organ function and handling of DMSA should make this comparison a sensitive indicator of any age-dependent changes. Differences were tested using Student's t-test and by the paired sample t-test where appropriate. Correlations between various biokinetic data sets were also tested by t-test.

Dosimetry

Whole-body (less bladder contents) and organ retention curves were integrated to give residence times in kidneys, liver, spleen, knees and remaining body. Kidneys, liver, spleen, bladder contents and remaining body were used as source organs and their residence times were used with the MIRDOSE

3 dose calculation program (Oak Ridge Institute for Science and Education) to estimate doses ($mGy \cdot MBq^{-1}$) in 24 target organs. For this purpose, residence time in bladder contents was estimated by choosing the dynamic bladder model included in the program and determined by the whole-body retention parameters. Bladder voiding periods for children of different ages were taken from ICRP Publication 62 (9), namely 2h (newborn, 1 and 5 y), 3h (10y) and 3.5h (15y). We have assumed, on the basis of 'worst case' dosimetry, that the activity measured in knees resides entirely in the metaphyseal growth complexes. Since there are no published S values for this tissue, we have calculated them independently (7) following the method of Gelfand et al. (10) using the data of Widman and Powsner (11).

Pediatric Phantoms

MIRDOSE 3 incorporates S values for five pediatric phantoms appropriate for newborn, 1y, 5y, 10y and 15y children, as well as that for a 70kg adult. Our dose calculations were made in two ways: firstly by choosing the phantom closest in age to the individual child and secondly, by performing linear interpolation, on the basis of inverse body weight, between organ doses estimated for the two adjacent phantoms whose weight range included that of the child. The latter method was adopted because the variation in age and body weight of our patients (Figure 1) suggested that large errors in dose estimates could arise by age-matching of patient to phantom. For example, one 11 year old child, who would have been age-matched to the 10y phantom, was heavier (65 kg) than the 15y phantom. Furthermore, there is a good linear relationship between dose ($mGy \cdot MBq^{-1}$) and inverse body weight for the kidneys, which receive the highest dose, and for other organs.

Effective Dose

From values of equivalent dose to 24 target organs calculated using MIRDOSE 3, the effective dose (E) was calculated for each patient using relevant tissue weighting factors (12). Following current practice, the effective dose is presented to allow a single dose for comparison with other radiopharmaceuticals used in pediatric investigations. For the estimation of E, we have used the latest ICRP recommendations regarding colon and oesophagus (13) and the gonad dose appropriate for the sex of individual children. Kidneys, which receive a much higher dose than other organs, were ascribed a tissue weighting factor of 0.025 with a similar value for the mass-weighted average dose to remainder tissues.

RESULTS AND DISCUSSION

Biodistribution, Biokinetics and Age Dependency

Typical gamma camera images are shown in Figures 2 and 3 and organ retention patterns are shown in Figure 4. The main biodistribution and biokinetic data are summarized in Tables 1 and 2. For kidneys, both uptake and elimination rates of Tc-99m DMSA are given. For liver, spleen and knees, uptakes were too rapid for accurate assessment and we have assumed instantaneous uptake by these organs and tissues. For normal patients (Table 1), data are presented separately for two groups of children, younger or older than 1 year, and the significance of differences in biokinetic parameter values for the two groups are indicated. The 24h urinary excretion and uptake in knees were both significantly lower in the younger group, but these were the only significant age-dependent effects observed. Correlations between various biokinetic data sets were tested and significant negative correlations were found only between kidney uptake and urinary excretion in all patients, and

Figure 2. Posterior abdominal image of a 13-year old child 20 min after injection of Tc-99m DMSA.

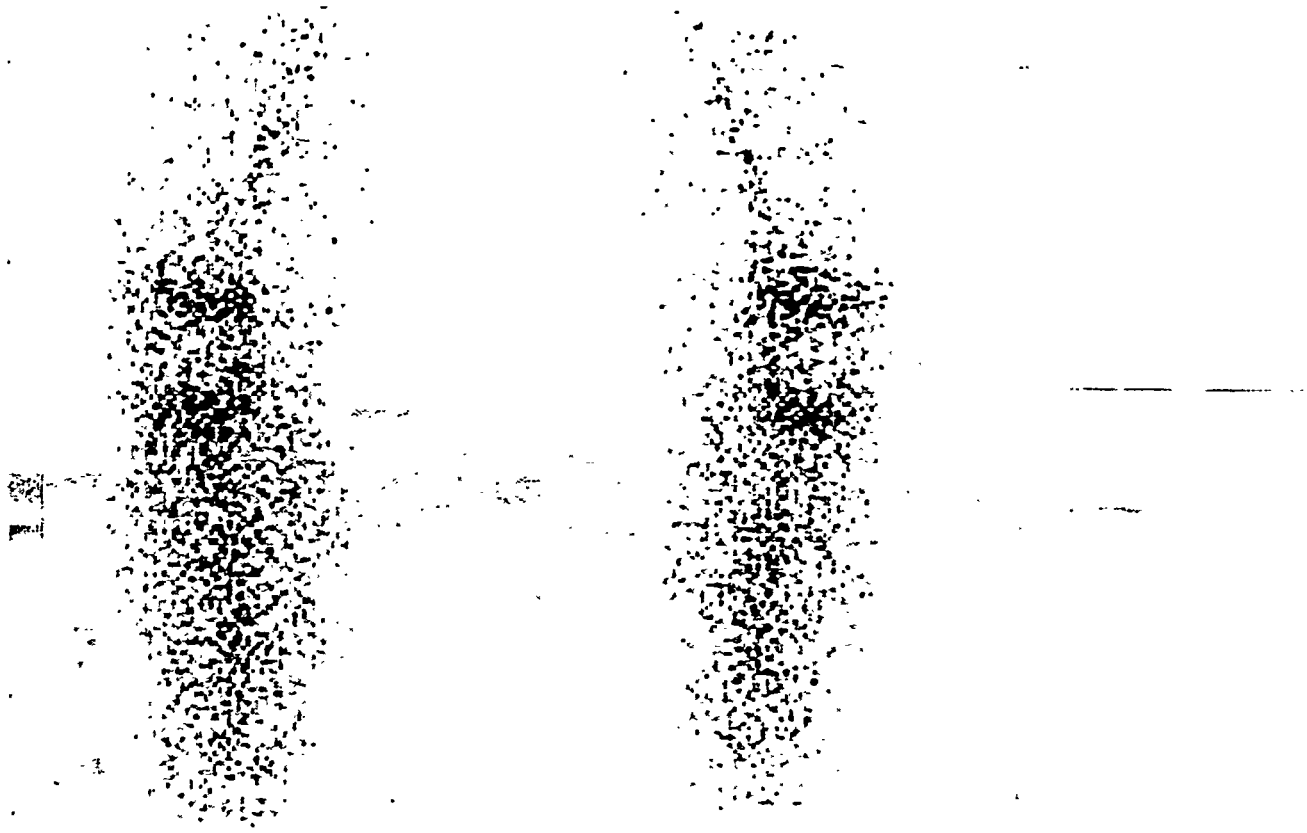

Figure 3. Concentration of Tc-99m DMSA in knees of a 13-year old child 20 min after injection.

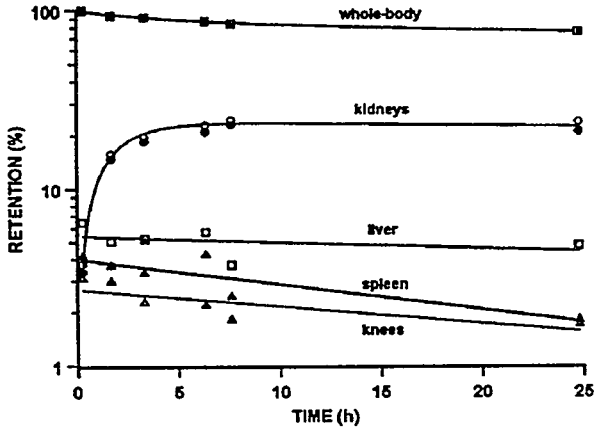

Figure 4. Retention of Tc-99m DMSA in a child with normal renal function.

Table 1
Measured Biological Parameters in Patients with Normal Renal Function

Observed parameter	< 1 year (n = 6)	> 1 year (n = 9)	p	All patients
Kidneys:				
max uptake (%)	41.8 ± 6.4	42.9 ± 4.9	NS	42.4 ± 5.4
uptake rate (h^{-1})	0.67 ± 0.13	0.72 ± 0.14	NS	0.70 ± 0.14
elim. rate (h^{-1})	0.010 ± 0.005	0.008 ±0.007	NS	0.009 ± 0.006
Liver:				
max uptake (%)	4.8 ± 2.8	4.4 ± 1.5	NS	4.6 ± 2.0
Spleen:				
max uptake (%)	1.6 ± 0.6	2.0 ± 1.2	NS	1.9 ± 1.0
Knees:				
max uptake (%)	0.77 ± 0.31	1.8 ± 1.1	< 0.05	1.4 ± 1.0
24h Urinary excretion (%)	14.9 ± 3.7	20.6 ± 3.2	< 0.01	18.0 ± 4.4

Table 2
Measured Biological Parameters in Patients
with Abnormal Renal Function

Observed parameter	All patients (n = 9)	p (cf normals)
Kidneys:		
max uptake (%)	15.8 ± 8.2	< 0.001
elim. rate (h^{-1})	0.010 ± 0.009	NS
Liver:		
max uptake (%)	4.9 ± 1.7	NS
Spleen:		
max uptake (%)	1.8 ± 1.1	NS
Knees:		
max uptake (%)	1.4 ± 0.4	NS
24h Urinary excretion (%)	32.4 ± 11.1	< 0.005

between liver uptake and urinary excretion in normals. Whilst the amount of residual body activity varied considerably in the total group of patients, as a result of variable renal uptake, there was no evidence that this affected uptake in liver and spleen.

Our normal kidney uptake values were in good agreement with those of other workers for adults (3,14) and for children (15); combined uptake in liver and spleen was similar to other reported values (2,14); and whereas our 24h urinary excretion values were similar to some published values they were lower than others (1,3) reported for normal adults.

In addition to the expected significant reduction in renal uptake, children with abnormal renal function (Table 2) excreted a significantly greater amount of administered Tc-99m DMSA in 24h urine samples compared with the normal group. Although the difference in the rate of kidney uptake was significant, this result was largely due to the very low rate of uptake in one abnormal patient. No other significant differences between measured parameters in children with normal or abnormal renal function were observed.

Our studies revealed very little evidence of age-dependence of biokinetic parameters, even though comparisons were made between groups of normals younger or older than 1 year. Indeed, our youngest normal child (7 weeks) had a global kidney uptake of 39.4% which was similar to the mean for the entire normal group (42.4 ± 5.4%). Thus it would appear that large numbers of investigations on very young children would be necessary to elucidate any significant age-dependent characteristics using DMSA. From our results we have concluded that a single dosimetry model for DMSA will reasonably predict dose estimates for the entire pediatric range (7). If biokinetic differences are subsequently found to exist to any significant extent in very young children due to immature organ function, the reduced organ uptakes will lead to lower radiation doses than predicted by the model, which thus errs on the side of caution.

Dosimetry

Interpolation of organ dose values from pediatric phantoms The results of using the two different methods of applying phantom data for the normal children are shown in Figure 5. Our method of interpolating organ doses between phantoms on the basis of inverse body weight leads to a much lower variation in effective dose (mean 0.91 ± 0.08 mSv) over the entire age range, compared to the method of age-matching to the phantoms (mean 0.98 ± 0.29 mSv). It should be noted that the abscissa in Figure 5 has been extended in the 0-1 year range for the sake of clarity.

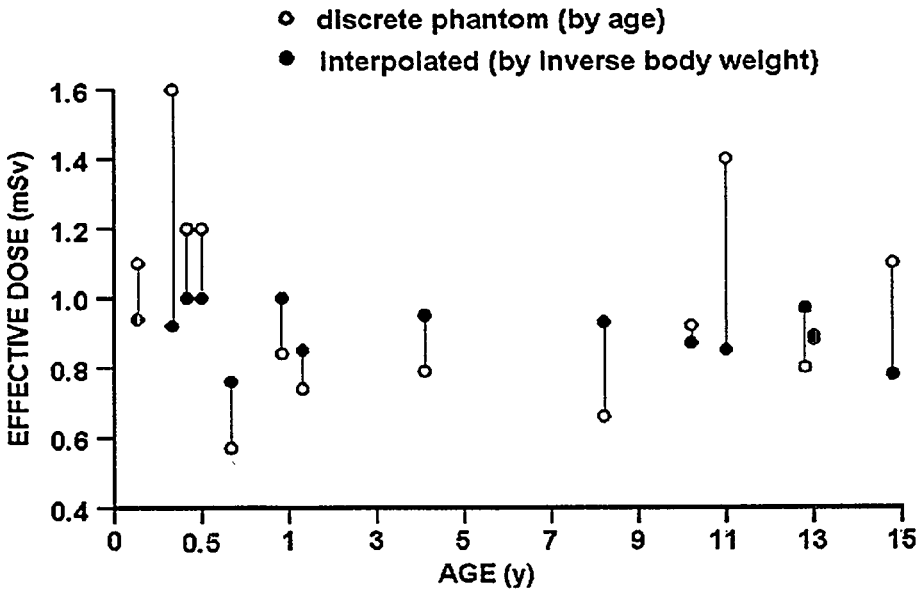

Figure 5. Effect on effective dose per administered activity of using the interpolation method of deriving pediatric organ doses.

Dose Values

Organ dose values, calculated using the interpolation method and for administered activities based on body surface area, are shown in Table 3 for both the normal and abnormal groups of children. The dose to kidneys was the highest in both groups, followed by doses to spleen, adrenals, urinary bladder wall, liver and pancreas. However, the estimated dose to the metaphyseal growth complexes ranged from 0.7 to 10.8 mSv in all 24 patients with a mean value of 3.9 ± 2.7 mSv. There was a significant correlation between dose to growth complex and age of the patient ($r = +0.44$; $p < 0.05$). The latter doses, however, are probably overestimates since we have assumed that the metaphyseal growth complexes contain all the activity measured in knees and we have made an *ad hoc* calculation of S values, which are not generally available. Because of these uncertainties, and since the fraction of the total bone surfaces they represent is unknown, we have not included this tissue dose in the calculation of effective dose. For the latter purpose, the residence time in knees was included with that of the remaining body.

Table 3

Dose Estimates (Equivalent Dose per Administered Activity, mSv(sd))
for Children with Normal or Abnormal Renal Function

Organ or tissue	Normals (mSv)	Abnormals (mSv)	Organ or tissue	Normals (mSv)	Abnormals (mSv)
adrenals	1.3 (0.2)	0.86 (0.16)	ovaries	0.51 (0.10)	0.59 (0.03)
brain	0.27 (0.06)	0.37 (0.08)	pancreas	0.94 (0.17)	0.77 (0.08)
breast	0.26 (0.06)	0.31 (0.08)	red marrow	0.44 (0.03)	0.45 (0.06)
gall-bladder	0.82 (0.10)	0.75 (0.09)	bone surfaces	0.71 (0.09)	0.73 (0.09)
LLI	0.49 (0.09)	0.57 (0.05)	skin	0.26 (0.06)	0.30 (0.07)
SI	0.66 (0.06)	0.63 (0.06)	spleen	2.5 (0.8)	1.9 (0.9)
stomach	0.62 (0.05)	0.60 (0.07)	testes	0.33 (0.06)	0.42 (0.08)
ULI	0.62 (0.06)	0.62 (0.06)	thymus	0.33 (0.06)	0.42 (0.08)
heart wall	0.44 (0.05)	0.50 (0.08)	thyroid	0.33 (0.08)	0.44 (0.09)
kidney	16.7 (2.3)	8.9 (5.6)	bladder	1.2 (0.4)	1.6 (0.5)
liver	0.93 (0.23)	0.88 (0.20)	uterus	0.54 (0.09)	0.62 (0.03)
lung	0.42 (0.07)	0.46 (0.08)	total body	0.53 (0.07)	0.50 (0.07)
muscle	0.41 (0.06)	0.44 (0.07)	m.g.c.*	3.5 (2.9)	4.5 (2.3)

* metaphyseal growth complex

Effective dose

The mean effective dose per administered activity, was 0.91 ± 0.08 mSv for normal children and 0.77 ± 0.13 mSv in children with abnormal renal function. The kidney dose contributed as much as 46% of the effective dose in normals. There is a close linear correlation between E/A_0 ($mSv \cdot MBq^{-1}$) and inverse body weight W^{-1} (kg^{-1}) for normal children (Figure 6), except for the heavier children (W > 57 kg). The regression line has the equation

$$E/A_o\ (mSv \cdot MBq^{-1}) = 0.00581 + 0.261 \cdot W^{-1}. \quad (2)$$

Radiopharmaceutical Schedule

Figure 7 shows the estimated values of effective dose versus body weight for the normal children from administered activities based on body surface area and also the values that would have resulted for a radiopharmaceutical schedule based on body weight alone. Whereas the former remain reasonably constant over the entire range of body weight with a coefficient of variation of 9%, the latter values decrease progressively as body weight decreases until, at an arbitrary minimum level of administered activity, the effective dose rises rapidly. The minimum administered activity is imposed to ensure adequate image quality. In the radiopharmaceutical schedule based on body surface area, the lowest administered activity was 14 MBq and this value has been used as the minimum activity to apply to the schedule based only on body weight. The values affected by this adjustment are indicated by arrows in Figure 7. The result obtained using the schedule based on surface area can be explained by the combination of Equations 1 and 2 leading to

$$E\ (mSv) = 0.0307 \cdot W^{0.714} + 1.381 \cdot W^{-0.286}, \quad (3)$$

which is the equation of a curve with a broad minimum at 18 kg body weight, and is shown by the line (A) in Figure 7. On the other hand, a radiopharmaceutical schedule based on body weight alone, relative to that of the 70 kg adult (administered activity (MBq) = 100 · W/70), when combined with equation (2) gives

$$E\ (mSv) = 0.373 + 0.0083 \cdot W, \qquad (4)$$

which is the equation of line (B) in Figure 7.

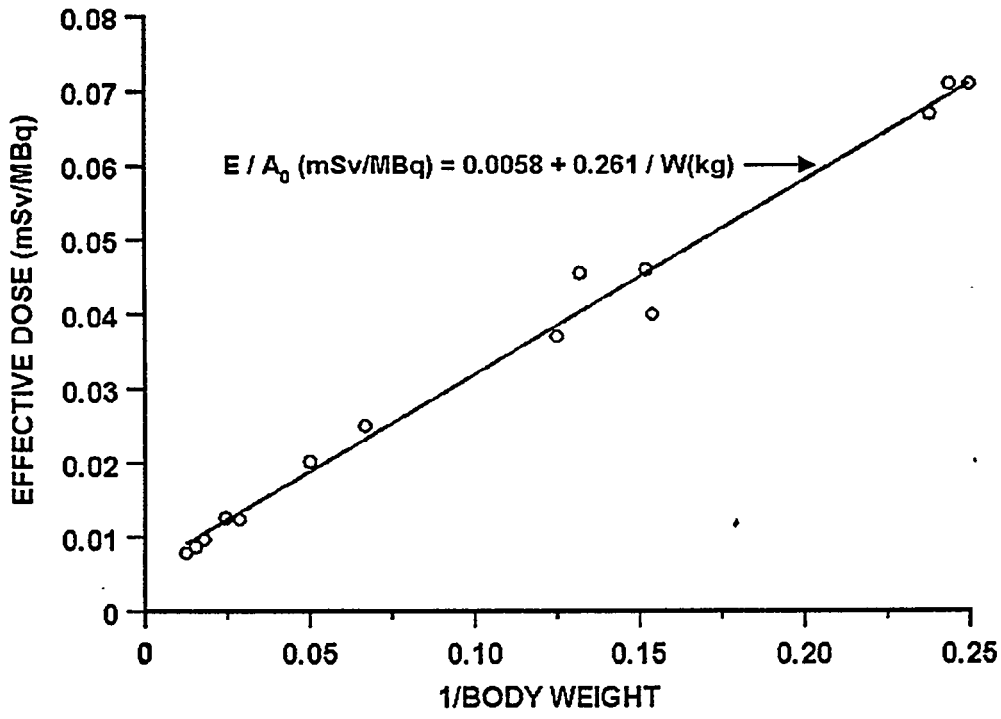

Figure 6. Relationship between effective dose per MBq Tc-99m DMSA and inverse body weight in children with normal renal function.

As pointed out earlier, Equation 2 does not hold for weights over about 57kg, the weight of the 15y phantom, but the deviation at higher body weights ensures good uniformity of E per administered activity over the complete range of our patients (Figure 7). Indeed, the values for the heavier children were better fitted by the inverse of Equation 1 multiplied by 0.91, implying a constant value of 0.91 mSv for E using the surface area schedule. In these circumstances, the body weight schedule leads to the expression $E = 0.246\ W^{0.286}$.

There has been considerable discussion in the past concerning the appropriate radiopharmaceutical schedules for pediatric nuclear medicine investigations; these schedules have been based mainly on age, body weight or body surface area. With the requirement to administer the lowest amount of activity compatible with satisfactory diagnostic information, the usefulness of the various methods has been examined (16). It is recognized that different criteria apply in different types of nuclear medicine procedures. The important consideration in imaging concerns the statistics

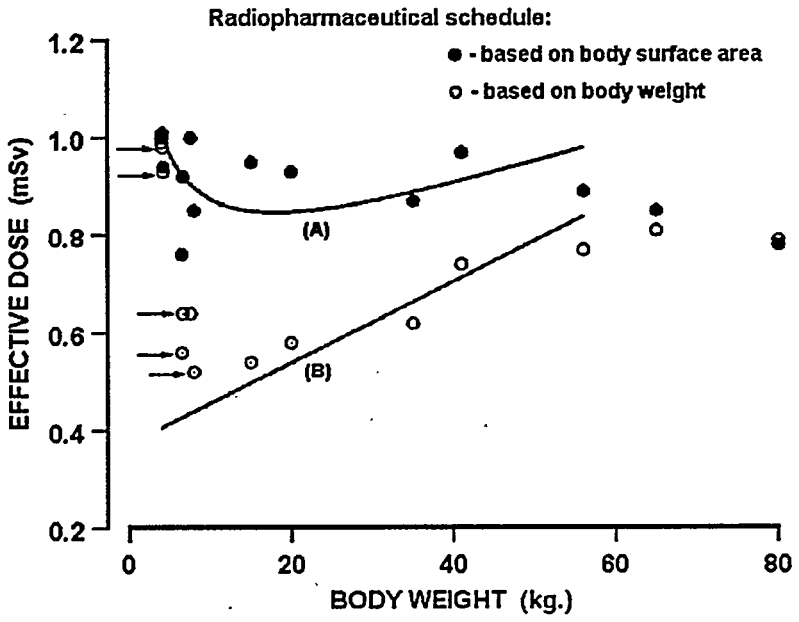

Figure 7. Relationships between effective dose and body weight for two radiopharmaceutical schedules in children with normal renal function.

of photon detection and is based on the maintenance of constant activity per unit area of organ, the logical extension of which is a schedule based on body surface area. The Pediatric Task Group of the European Association of Nuclear Medicine has compiled values of fractional administered activities for various radiopharmaceuticals on the basis of body surface area for children of different weights (17). In addition to these considerations, there may be advantages in having a radiopharmaceutical schedule which results in a uniform effective dose over the pediatric range, as observed in the present work on DMSA for a schedule based on body surface area. It appears to offer simpler control of patient dose and overcomes the need to apply a minimum administered activity except perhaps for babies. Furthermore, it may be possible to reduce the maximum (adult) activity in the knowledge that dose levels will be reduced equally for all children, with the proviso that image quality is not impaired by this change to protocol. However, it is likely that an appropriate administered activity, based on image quality criteria for the adult weight, will be satisfactory for use with the surface area schedule over the entire pediatric range. A schedule based on body weight alone leads to a more variable dose response and therefore is more affected by the need to apply a minimum administered activity as body weight, and hence administered activity, decreases. Thus, although this method follows as far as possible the principle of reducing dose to "as low as reasonably achievable", there could be a greater risk of administering too little activity resulting in scans of poor image quality, especially for children with body weights around 10 - 20 kg where the relative difference in administered activity between the two schedules is greatest.

CONCLUSIONS

The uptake of Tc-99m DMSA in the knees, and the possible resultant dose to metaphyseal growth complexes, increased with increasing age of normal children while children younger than 1 year excreted less radioactivity in urine than older children: these were the only age-dependent

parameters revealed by these studies. In children with renal pathology, kidney uptake of Tc-99m DMSA was predictably reduced but other organ uptakes were similar to normal values.

A radiopharmaceutical schedule, by which amounts of activity administered to children were determined on the basis of body surface area, resulted in a fairly constant value of effective dose (mean 0.91 ± 0.08 mSv) over the complete range of normal children. The variance was significantly lower than that for a schedule based only on body weight.

Organ dose estimates in individual children were obtained using a method of interpolation between discrete pediatric phantoms on the basis of inverse body weight. In normal children, this resulted in a large reduction in the variation of effective dose values compared with a method of matching children to the nearest phantom by age.

ACKNOWLEDGMENT

This work was supported in part by the Commission of European Communities (Contract F13P-CT920052)

REFERENCES

1. Enlander D, Weber PM and Dos Remedios LV. Renal cortical imaging in 35 patients: superior quality with ^{99m}Tc-DMSA. J Nucl Med 15(9):743-749,1974.
2. Handmaker H, Young BW and Lowenstein JM. Clinical experience with ^{99m}Tc-DMSA (Dimercaptosuccinic acid), a new renal-imaging agent. J Nucl Med 16(1):28-32, 1975.
3. Arnold RW, Subramanian G, McAfee JG, Blair RJ and Thomas FD. Comparison of ^{99m}Tc complexes for renal imaging. J Nucl Med 16(5):357-367, 1975.
4. Snyder WS, Ford MR, Warner GG and Watson SB. "S", Absorbed Dose per Unit Cumulated Activity for Selected Radionuclides and Organs. Medical Internal Radiation Dose Committee, Pamphlet No. 11, Society of Nuclear Medicine, New York, 1975.
5. Cristy M. Mathematical Phantoms Representing Children of Various Ages for Use in Estimates of Internal Dose. ORNL/NUREG/TM-367, Oak Ridge, TN: Oak Ridge National Laboratory; 1980.
6. Evans K, Lythgoe MF, Anderson PJ, Smith T and Gordon I. The biokinetic behavior of ^{99m}Tc-DMSA in children. J Nucl Med, 37(8):1331-1335, 1996.
7. Smith T, Evans K, Lythgoe MF, Anderson PJ and Gordon I. Radiation dosimetry of ^{99m}Tc-DMSA in children. J Nucl Med, 37(8): 1336-1342,1996.
8. Du Bois D and Du Bois EF. A formula to estimate the approximate surface area if height and weight be known. Arch Intern Med 17:863-871, 1916.
9. International Commission on Radiological Protection. Radiological Protection in Biomedical Research. ICRP Publication 62. Ann ICRP 22, Pergamon, Oxford, 1991.
10. Gelfand MJ, Thomas RS and Kereiakes JG. Absorbed radiation dose from routine imaging of the skeleton in children. Ann Radiol 26:421-423, 1983.
11. Widman JC and Powsner ER. Energy absorption in cylinders containing a uniformly distributed source. J Nucl Med 8:179-186, 1967.
12. International Commission on Radiological Protection. 1990 Recommendations of the ICRP. ICRP Publication 60. Ann ICRP 21, Pergamon, Oxford, 1990.

13. International Commission on Radiological Protection: Age-dependent Doses to Members of the Public from Intake of Radionuclides: Part 2. ICRP Publication 67. Ann ICRP 23(3-4), Pergamon, Oxford, 1990.
14. Elliott AT, Britton KE, Brown NJG, Pearce PC, Smith FR and Barnasconi EW. Dosimetry of current radiopharmaceuticals used in renal investigation, in: Radiopharmaceutical Dosimetry Symp (Proc Conf, Oak Ridge, Tennessee). HEW Publication (FDA 76-8044), pp. 293-304, Department of Health Education and Welfare, Bureau of Radiological Health, Rockville, Maryland, 1976.
15. Gordon I, Evans K, Peters AM, Kelly J, Morales BN, Goldraich N and Yau A. The quantitation of ^{99m}Tc-DMSA in pediatrics. Nucl Med Comm 8:661-670, 1987.
16. Webster EW, Alpert NM and Brownell GL. Radiation doses in pediatric nuclear medicine and diagnostic X-ray procedures, in Pediatric Nuclear Medicine, edited by AE James, HN Wagner and RE Cooke, pp. 34-58, WB Saunders, Philadelphia, 1974.
17. Piepsz A, Hahn K, Roca I, Ciofetta G, Toth G, Gordon I, Kolinska J and Gwidlet J. A radiopharmaceuticals schedule for imaging in pediatrics: Pediatric Task Group European Association Nuclear Medicine. Eur J Nucl Med 17:127-129,1990.

QUESTIONS

Eckerman: The relationship between organ masses and total-body weight are inherent in the design of the pediatric phantom series for many organs. Thus your procedure is quite appropriate. Could you comment on the regional distribution of the active marrow?

Smith: I am afraid that I have no knowledge as to whether the regional distribution of bone marrow in children scales according to inverse body weight.

Eckerman: In the abnormal patients how were the differences in left/right kidney addressed?

Smith: The majority of normal children had bilateral kidney function with very similar uptakes in both kidneys. In a small number of patients there were significant differences between kidney uptakes. In those cases we estimated the doses to the individual kidneys. For purposes of calculating the effective dose, we used the higher kidney dose.

In one normal patient and three or four patients with renal pathology there was only a simple functioning kidney. In these cases the kidney dose estimated by MIRDOSE 3 was doubled to account for the fact that all kidney residence time was associated with a single kidney.

Muller: You might validate the linear interpolation method by inverse body weight by comparing the outcome for the fourth phantom with the result of interpolation between the third and the fifth (and similarly for the second and third phantom).

Smith: We have shown that using a common ^{99m}Tc-DMSA biokinetic model with all the five pediatric phantoms leads to good linear correlation between effective dose per MBq and inverse body weight. Similarly there were good linear correlations between organ dose/MBq and inverse body weight for various organs and particularly for the most important kidney doses. I believe these linear relationships prove the validity of the interpolation method based on inverse body weight.

Kagan: When you obtained raw data counts from the ROIs, did you account for organ overlapping such as kidney-spleen or lung-heart?

Smith: The presence of early activity in heart and lungs is due to blood pool activity. We were unable to calculate residence times due to this component as we did not obtain data on the activity content of blood. Consequently the residence times for these organs were included with that of the remaining body. Left and right kidney uptake values were obtained separately and this was relatively easy in view of the high kidney uptake. A region surrounding each kidney was used for background correction. The liver and spleen regions of interest were drawn to include the right and left kidneys, respectively, and subsequently corrected for background and the measured kidney activity.

PLACENTAL TRANSFER OF RADIOPHARMACEUTICALS AND DOSIMETRY IN PREGNANCY

Russell JR[1], Stabin MG[2] and Sparks RB[2]
[1]University of Maryland at Baltimore
Baltimore, MD 21201
[2]Oak Ridge Institute for Science and Education
Oak Ridge, TN, 37831-0117

ABSTRACT

The calculation of radiation dose estimates to the fetus is often important in nuclear medicine. To obtain the best estimates of radiation dose to the fetus, the best biological and physical models should be employed. In this paper, after identification of radiopharmaceuticals often administered to women of childbearing age, the most recent data available on the placental crossover of these radiopharmaceuticals was used (with standard kinetic models describing the maternal distribution and retention and with the best available physical models) to obtain fetal dose estimates for these radiopharmaceuticals at all stages of pregnancy. From a survey of thirty medical institutions, 19 radiopharmaceuticals were identified as those most commonly administered to women of childbearing years. The literature yielded information on placental crossover of 15 radiopharmaceuticals, from animal or human data. Radiation dose estimates are presented in early pregnancy and at 3-, 6-, and 9-months gestation for these radiopharmaceuticals, as well as for many others used in nuclear medicine (the latter considering only maternal organ contributions to fetal dose).

INTRODUCTION

In the evaluation of risks and benefits in nuclear medicine, the calculation of radiation doses is an essential element. In the case of administration of radiopharmaceuticals to women of childbearing years, doses estimates for the embryo or fetus are needed for evaluation of possible risks to the unborn child from the procedure. The estimation of fetal doses has long been an area of active inquiry, but has been hampered by a lack of a good physical model of the adult female at different stages of pregnancy as well as a paucity of reliable data on the placental crossover of radiopharmaceuticals. The former need has been addressed in the pregnant female phantom series of Stabin et al. (1). The latter issue is only partially addressed in this study. After identifying radiopharmaceuticals commonly used in women of childbearing years, we sought to obtain all available data from the literature reporting any quantitative estimates of the amount of these radiopharmaceutical which might cross the placenta at any stage of pregnancy. As expected, we found quantitative information on placental crossover for only a fraction of the radiopharmaceuticals routinely administered, and most of the data have been gathered in animal studies. We applied this

information to the estimation of fetal doses at all stages of pregnancy; using the phantoms of the pregnant female phantom series, and the best available kinetic models for the general behavior of the radiopharmaceutical within the mother's body.

METHODS AND MATERIALS

Medical Institution Survey

A survey of 30 medical institutions of various size and mission was conducted. The institutions were selected randomly from the data base of requests received at the Radiation Internal Dose Information Center, operated by Oak Ridge Associated Universities in Oak Ridge, Tennessee. The institutions were asked to respond to a questionnaire by phone, facsimile or mail. Of the thirty medical institutions approached in this study, twenty-six responded to the survey.

The survey was conducted to determine the diagnostic nuclear medicine procedures most commonly used for women of childbearing age. Childbearing age for this survey was defined to be 13 to 45 years of age. The survey was also designed to solicit information regarding the procedures in place at each institution to prevent the inadvertent administration of a radiopharmaceutical to a pregnant woman.

Radiation Absorbed Dose Estimates

The MIRD schema for estimating the radiation absorbed dose to organs, tissues, and other structures from internally deposited emitters (2) was employed, as implemented in the MIRDOSE personal computer software (3). Residence times for the mother's organs were assigned based on the best available kinetic models for the radiopharmaceuticals studied. The biokinetic models for each radiopharmaceutical used in this study were compiled by the Radiation Internal Dose Information Center (RIDIC). Most of the models were based on data obtained in humans and were analyzed either by compartmental modeling or least squares analysis to obtain the residence times for the relevant source organs. The biokinetic models are assumed to represent the average normal adult, and thus the nonpregnant woman. An assumption was made that no changes occurred in the biodistribution of the radiopharmaceutical in maternal organs during pregnancy. This assumption was necessary because little information exists regarding the changes in the kinetic behavior of radiopharmaceuticals that may occur during pregnancy. In a few special cases, models were available which described the biodistribution including activity transfer involving the placenta and/or fetus.

The fetal dose from penetrating radiations (e.g. x-rays, gamma rays) from the radiopharmaceutical in the maternal organs was computed. Information on the placental localization and/or transfer of some radiopharmaceuticals in the pregnant woman was found during an extensive literature search. When available, the data for the fetal and placental accumulation of radioactivity were used to determine the absorbed dose to the embryo/fetus from the penetrating and nonpenetrating radiations (e.g. beta particles, Auger and conversion electrons) originating from radionuclides within the embryo/fetus.

Most of the available information concerning the localization and transfer of radiopharmaceuticals in fetal and placental tissues was obtained in experiments using animals. This required that several extrapolation methods be investigated before the data could be used to estimate the absorbed dose to the human embryo/fetus. Generally the percent of the administered activity localizing in the placenta or crossing into the fetus of the animal was assumed to be the same percent that would localize in the human placenta or cross into the human fetus. Another method used was to normalize tissue concentration data according to body weight. When the animal data was provided in units of "percent dose in whole organ" or "percent dose per % body weight" (i.e. if an organ

comprised 5% of the animal's total body weight, the % in the organ was divided by 5); the data may be extrapolated as follows:

$$\left(\frac{\%\ dose}{\%\ animal\ body\ wt}\right) x \left(\frac{human\ organ\ wt}{human\ body\ wt}\right) x \left(\frac{1}{100\%}\right). \quad (1)$$

The second and third term express the human organ weight as a percentage of the human total body weight. The result of this calculation is the equivalent percent of administered activity in the human. Another method of extrapolation is to calculate an "equivalent time" factor derived for each species, (4) defined as:

$$\frac{W^{0.33}\ MAN}{W^{0.33}\ ANIMAL} \quad (2)$$

This factor is then multiplied by the times at which data were gathered in the animal study to obtain the "equivalent times" for a human study.

Frequently, the animal data provided were obtained only for one stage of gestation. The developmental stages of the animal used during the experiments were compared to those of the human (5). When practical, the data were used with the stage of gestation in the human embryo/fetus that most closely corresponded to that of the animal fetus. The data from the later stages of gestation in the animals, when used for dose estimates at earlier stages, were not corrected for the possible alterations in biodistribution that may result during the different stages of gestation. The placental and fetal accumulation provided for animals during the later stages of gestation were assumed to be the greatest values for all gestation periods because of the mature nature of the placenta (6,7). In cases where information from several sources were available for fetal and placental accumulation, the largest values reported were used for determining the absorbed dose estimate to the human fetus. Data for placental crossover in early pregnancy were generally not available. Thus, the absorbed dose estimates for early pregnancy (i.e. using the nonpregnant adult female model) reported in this study include maternal contributions only.

Although it was not always clear in the original reference, it was assumed that placental and fetal uptakes reported were the maximum values observed in the experiments, and these values were applied in the human dose estimates. Information was also not often available on the mechanism or rate of loss of the activity from the fetal or placental tissues. Therefore, the observed activity was assumed to remain in these regions indefinitely. This simplified the residence time calculation to

$$\tau_h = 1.443(T_{1/2})\ A_h \quad (3)$$

where $T_{1/2}$ is the physical half life of the radionuclide (hr) and A_h is the fraction of administered activity in the source.

The model for the pregnant woman at 3-months gestation (1) does not include a placenta. The placenta is reported to function as a fully mature organ at about four months gestation (7). Therefore, no attempt was made to assign activity to the placenta in the dose estimates for the woman at 3-months gestation. However, the fetus at 3-months gestation was assumed to accumulate activity similar to the fetus in later stages of gestation. This assumption may result in overestimates of cumulated activity in the fetus at this stage of gestation.

RESULTS

A. Responses to Questionnaire

Thirty medical institutions of various size and mission were surveyed. Twenty-six of the institutions responded to the questionnaire either completely or in part. The patient workload of the nuclear medicine department at each institution per year was requested. Eleven percent of the institutions had less than 4000 patients per year, 39% had between 4000 and 6000, 31% had between 6000 and 8000, 8% had between 8000 and 10,000, and 11% had greater than 10,000. Over one half of the institutions reported that 45-65% of the patient population were females between 12 and 45 years of age (childbearing age).

The medical institutions were questioned on the deliberate or inadvertent administration of a radiopharmaceutical to a pregnant woman in the past operational history of the nuclear medicine department. Nine institutions reported that between one and five planned procedures per year are performed on known pregnant patients, while three institutions reported that between 6 and 12 planned procedures are performed on known pregnant women. Fifty-seven percent of the institutions replied than no procedures had been performed inadvertently on pregnant patients and 43% replied that one or two procedures had been performed.

The institutions were asked if procedures were taken to prevent the inadvertent administration of a radiopharmaceutical to a pregnant woman and if these procedures are in written form. One hundred percent of the institutions had procedures in place and only two of the twenty-six institutions surveyed did not have these procedures in written form.

Several of the institutions provided the full written procedures to prevent the inadvertent administration of a radiopharmaceutical, other institutions provided abbreviated information concerning the subject. The most common procedure cited was the use of a patient worksheet or questionnaire which requires the patient's signature verifying that she is not pregnant. The second most commonly cited procedure was the posting of signs warning the patient to notify the physician or technician if the patient is or may be pregnant. Four of the institutions reported using the "10 day rule" which implies that a procedure is least likely to pose any hazard to a developing embryo if performed during the first 10 days following the onset of menstruation as determined by questioning the patient (8).

One institution reported that a pregnancy test was required for all women of childbearing age unless mitigating circumstances existed to warrant an exception, such as a hysterectomy or other surgical birth control measure. Several institutions reported that pregnancy tests were required prior to all diagnostic or therapeutic uses of iodine. Over 50% of the institutions reported that if the patient was uncertain of the last day of her previous menstrual period or uncertain if she was pregnant, the nuclear medicine procedure would be postponed until such time as she is certain, or else a pregnancy test would be conducted. Over 75% of the respondents added that if the patient is pregnant, the decision to perform or postpone the procedure is left to the attending physician and patient, often requiring written consent from the patient. One institution reported that even if pregnancy is confirmed, the nuclear medicine procedure should be performed. The 19 radiopharmaceuticals identified by the survey as most commonly used in women of childbearing age are presented in Table 1 in the order from the most commonly used to the least commonly used.

Table 1

Radiopharmaceuticals Most Commonly Used in Women of Childbearing Age

1. Tc-99m Methylene Diphosphonate (MDP)	10. Tc-99m Diethylenetriaminepentaacetic Acid (DTPA)
2. Tc-99m Macro Aggregated Albumin(MAA)	11. Tc-99m DTPA Aerosol
3. I-123 Sodium Iodide	12. Tc-99m White Blood Cells
4. Ga-67 Citrate	13. Tc-99m Sulfur Colloid
5. Xe-133	14. Tc-99m Hydroxymethylene Diphosphonate (HDP)
6. Tl-201 Chloride	15. I-131 Sodium Iodide
7. Tc-99m Benzoylmercaptoacetyl-triglycine (MAG3)	16. Tc-99m Pertechnetate
8. Tc-99m Methoxyisobutylisonitrile (MIBI)	17. Tc-99m Disofenin
9. Tc-99m Mebrofenin	18. In-111 White Blood Cells
	19. Tc-99m Red Blood Cells

B. Placental Crossover Information for Specific Radiopharmaceuticals

1. Tc-99m Methylene Diphosphonate (MDP)

The biokinetic data for Tc-99m MDP in normal patients used to determine the absorbed dose estimates were taken from MIRD Dose Estimate Report No. 13 (9). Data available for the biodistribution of Tc-99m MDP in pregnant patients was gathered from both human (10, 11) and animal investigations (6, 12).

The placental and fetal uptakes of Tc-99m MDP obtained by Palmer in guinea pigs during the 7th and 8th week of gestation were determined to be the most appropriate for use in determining the fetal absorbed dose provided for Tc-99m MDP. Palmer reported that the maximum fetal uptake for Tc-99m MDP was 0.27% and the placental uptake was 0.024%. Several assumptions were made in determining the absorbed dose estimates using Palmer's data. It was assumed that the guinea pig gestational period of 9 weeks corresponds to the 9-month gestational period of the human. The data collected from the 7 and 8 week pregnant guinea pig were assumed to be valid for use with the 6-month and 9-month pregnant phantoms based on a comparison of the developmental stages of the animal and human. The data for accumulation in the fetal tissue were also used with the 3-month pregnant phantom to obtain an estimate of the absorbed dose at 3-months gestation in the human fetus. These dose estimates also assume that no changes occur in the biodistribution of Tc-99m MDP in maternal organs during pregnancy. The standard model for the distribution of Tc-99m MDP (9) was used with these data. The absorbed dose estimate for early pregnancy includes maternal contributions only.

2. Tc-99m Macroaggregated Albumin (MAA)

The biodistribution data in the normal patient used to determine the absorbed dose estimates were taken from ICRP Publication 53 (13). Uptake and retention of Tc-99m MAA by the fetus and placenta were published by Palmer (12) and Malone and Ennis (14). The data of Palmer were used for the estimates provided.

Tc-99m MAA was administered intravenously to guinea pigs during the 7th to 8th week of gestation. The animals were sacrificed between 1/2 and 6 hours post administration to determine the maximum fetal and placental uptake. The maximum reported fetal uptake for Tc-99m MAA was 0.6%, and the placental uptake was 9.1%.

For the fetal dose calculations based on Palmer's data, the biodistribution of Tc-99m MAA in the pregnant guinea pig was assumed to be similar to that of the human and that this distribution remained constant throughout gestation. The fetal and placental uptake determined in guinea pigs in the 7-8 week period of gestation was also assumed to be acceptable for use with the 6-month and the 9-month pregnant woman phantom. The accumulation in the fetal tissue was used with the 3-month pregnant phantom to obtain the dose estimate at 3-months gestation in the human fetus. Additionally, activity was assumed to enter the fetus and placenta and remain there indefinitely (i.e. loss occurred only by radioactive decay). The absorbed dose estimate for early pregnancy includes maternal contributions only.

3. I-123 Sodium Iodide

Biodistribution data for normal patients for I-123 sodium iodide were taken from MIRD Dose Estimate Report No. 5 (15). This model applies to the intravenous administration of iodide; however, the oral administration of iodide will delay the appearance of iodide in the blood by 10 to 15 minutes, which will have only a minimal effect on the activity level in the blood and little effect on the thyroid uptake. The distribution data used for the dose estimates in this section assumed a 25% maximum thyroid uptake level which corresponds to a 24-hour uptake of 23.6%. The MIRD Dose Estimate Report provides metabolic models for three different assumed maximum thyroid uptakes. The actual percentage of administered radioiodine in tissues of the body at various times after administration varies with the maximum thyroid uptake. According to the model, radioiodine distributes throughout the extracellular-extravascular space, thyroid, intestine, and liver (15).

Several studies concerning the biodistribution of iodide in the fetus and the fetal thyroid have been conducted (16, 17, 18, 19, 20). Watson stated that after about 13-weeks gestation, the fetal thyroid begins to concentrate iodine and continues to do so throughout gestation (21). Watson also stated that the concentration of iodide in the fetal blood increases with gestation to approximately 75% of that in the mother's blood.

Watson compiled information from a number of sources to develop a biokinetic model for iodide administered to a pregnant woman. Her model, shown in Figure 1, includes the model proposed by Berman (22) for a maximum maternal thyroid uptake of 25%. Watson incorporated compartments representing the fetal thyroid and fetal organic compartment. The transfer rate coefficients for the mother determined by Watson are shown in Table 2. Watson determined that these coefficients remained unchanged throughout gestation. The transfer rate coefficients for the fetus are shown in Table 3. Watson suggested that these transfer rates did not remain constant throughout gestation.

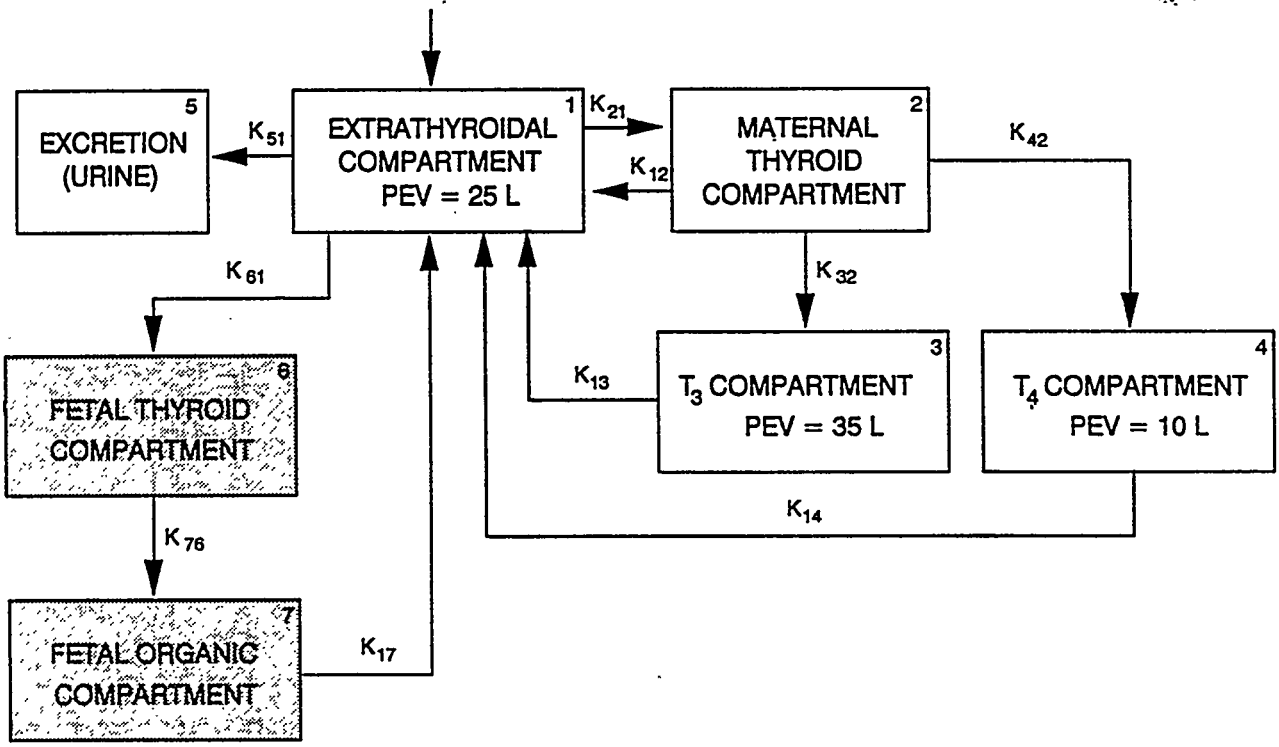

Figure 1. Compartmental Model for Iodine Metabolism in the Fetus and the Pregnant Woman (PEV is the Plasma Equivalent Volume).*

The Simulation, Analysis, And Modeling (SAAM) software (23) was used with Watson's proposed model to determine the residence times for iodide in the pregnant woman and fetus at 3, 6 and 9-months gestation. These residence times were combined with the residence times for other organs determined from MIRD Dose Estimate Report No. 5 (15) to provide the dose estimate.

Table 2*

Transfer Rate Coefficients for the Model of the Nonpregnant Woman

Transfer Pathway	day^{-1}
k_{21}	0.727
k_{12}	0.005
k_{32}	0.002
k_{42}	0.007
k_{13}	0.56
k_{14}	0.1
k_{51}	2.0

Table 3*

Transfer Rate Coefficients for Model of Fetus (day^{-1})

Gestational Age (month)	k_{61}	k_{17}	k_{76}
3	0.00084	0.05	0.003
6	0.0290	0.50	0.036
9	0.058	0.30	0.027

*Source: Watson EE. Radiation Absorbed Dose to the Human Fetal Thyroid. In: Fifth International Radiopharmaceutical Dosimetry Symposium. Oak Ridge, Tennessee: Oak Ridge Associated Universities, pp 179-187, 1992.

4. Ga-67 Citrate

MIRD Dose Estimate Report No. 2 (24) describes the biokinetics of gallium citrate in normal patients. Watson compiled information from a number of sources to develop a biokinetic model for Ga-67 citrate administered to a pregnant woman (7). Her model includes the biokinetic model of gallium in the adult from MIRD Dose Estimate Report No. 2, time-activity data from Wegst (25) and from unpublished data by Lathrop (26), and data from Mahon et al. (27). This model was considered applicable to the pregnant woman from about the fourth month of gestation "when the placenta begins functioning at a mature level" until term (7).

Watson extrapolated to humans the data presented by Mahon et al. (27), involving administration of Ga-67 citrate to a rabbit in the third trimester of pregnancy. Her results indicated that approximately 7.5% of the administered activity would be in the human placenta and about 0.75% would be in the human fetus (7). Watson also presented a biokinetic model of the pregnant woman after 3-months gestation. The residence times she determined from her model were used with the current 3-, 6- and 9-month pregnant woman phantoms. The dose estimate for early pregnancy includes maternal contributions only.

5. Xe-133

The residence times provided in MIRD Dose Estimate Report No. 9 (28) for the adult must be scaled to provide the residence times in the adult female. This scaling is based on the discussion by Hilyer and Snyder (29) that the air space and lung mass have an effect on the absorbed doses and that body fat content has an effect on whole body retention of Xe-133. The residence times for the adult lung must be reduced by the ratio of the adult and adult female lung volumes, Equation 4. The residence time for the component of the model representing fatty tissue (compartment 5) must be reduced by a ratio of the fat content of the adult male and adult female, Equation 5.

$$\tau_{lung,\ adult\ female} = \tau_{lung,\ adult\ male} \times \frac{V_{lung,\ adult\ female}}{V_{lung,\ adult\ male}} \qquad (4)$$

Using the information provided by Hilyer and Snyder (29), the volume of the female lung is 2.8 liters and of the adult male is 4.0 liters; the fat contents are 17% and 20% for the female and male, respectively.

$$\tau_{fat,\ adult\ female} = \tau_{fat,\ adult\ male} \times \frac{fat\ content_{adult\ female}}{fat\ content_{adult\ male}} \qquad (5)$$

No quantitative information was found concerning the placental and fetal accumulation of radioxenon. Biodistribution data in normal patients are described in MIRD Dose Estimate Report No. 9 (28). The residences times for blood are 0.103, 0.0276, and 0.0618 hour for 5, 7.5, and 10 liter spirometers, respectively. Of the Xe-133 that is present in blood, it is reasonable to assume that only a small fraction of the activity would locate in the placenta or cross into fetal tissue. Therefore, it is reasonable to assume that, given the small amount in blood, it is unlikely that this contribution would be of significance compared to the contribution from maternal organs. The dose estimates for Xe-133 given are thus from maternal contributions only.

6. Tl-201 Chloride

Biodistribution data for the intravenous administration of Tl-201 chloride in normal patients without exercise were taken from Krahwinkel et al. (30). Biodistribution studies to determine the behavior of Tl-201 chloride during pregnancy were conducted by Wegst on pregnant guinea pigs. On days 53-55 of a 68 day gestational period, the animals were injected with 3.7 MBq (100 μCi) of Tl-201 Chloride. The animals were sacrificed at various times following injection, dissected, and counted to determine the Tl-201 content of the maternal organs and fetal tissue (31). Wegst's data demonstrated that Tl-201 was transported across the placenta and localized in fetal tissues. Quantitative data to determine the amount of activity that localized in the placenta and fetal tissues were not available. Thus, the dose estimates for Tl-201 chloride include maternal contributions only.

7. Tc-99m Diethylenetriaminepentaacetic Acid (DTPA)

Biodistribution data for the intravenous administration in normal patients of Tc-99m DTPA were found in MIRD Dose Estimate Report No. 12 (32). Biodistribution studies to determine the behavior of Tc-99m DTPA during pregnancy were conducted by Wegst on pregnant Fisher rats on the 15th, 17th 19th, and 21st days of a 22 day gestational period. The animals were sacrificed at various times following an intravenous tail vein injection of Tc-99m DTPA. The animals were dissected, and maternal tissue, placental and fetal tissue were counted against a standard. Wegst provided cumulated activities for maternal organs, placental and fetal tissues (31).

Wegst determined that the maternal biodistribution of Tc-99m DTPA does not remain constant throughout gestation. Her article also states that the fetal activity and fetal weight increase exponentially with gestation, while the placental activity and placental weight increase linearly with gestation (31).

The data presented by Wegst for several maternal organs, fetus and placenta were extrapolated to the human at 3, 6 and 9-months gestation through the use of two extrapolation factors: 1) a ratio of the weight of the female Fischer rat to the weight of the female human multiplied by the weight of the human organ at the stage of gestation corresponding to the gestational period of the rat, and 2) the "equivalent time" factor presented by McAfee and Subramanian (4). Absorbed dose estimates

were calculated using the residence times for all organs determined from Wegst's extrapolated data. These estimates were compared to the dose estimates determined at all stages of gestation from maternal contributions only using the standard model from MIRD Report No. 12. The doses determined using Wegst's data, which included maternal and fetal contributions, were consistently lower than the dose estimates determined using the standard model. Therefore, it was determined that, even with extrapolation, the distribution data provided by Wegst for all organs was not acceptable for use. The absorbed dose estimate provided in this report for Tc-99m DTPA used Wegst's values for the placenta and fetus in the rats only extrapolated using the weight ratio described above.

The developmental stages of the rat were compared to those of the human. The 15th day of gestation in the rat is roughly comparable to the end of the second trimester in the human, while the 21st day of gestation in the rat is roughly comparable to the end of the third trimester in the human. This comparison indicates that the data collected by Wegst at 15 days and 21 days are best used with the human phantom at 6 and 9-months gestation, respectively. The data collected by Wegst from the 15 day rat were also used to extrapolate the cumulated activity in the human fetus at 3-months gestation. The dose estimate provided for early pregnancy includes maternal contributions only.

A study on a 17 year old pregnant girl using Tc-99m DTPA was conducted during her 14th week of pregnancy by Griffith et al. (33). A positive visualization of the uterus was seen in this patient. No quantitative data were provided for the amount or location of the radioactivity. The authors reported that the increase in blood flow to the uterus during pregnancy, combined with the increased metabolic and physiologic functions within the uterus and fetus may cause the increased uptake of the radionuclide.

8. Tc-99m DTPA Aerosol

The biological distribution data for Tc-99m DTPA aerosol in normal patients was found in MIRD Dose Estimate Report No. 16 (34). No quantitative information was found concerning the placental and fetal accumulation of Tc-99m DTPA aerosol. The dose estimates for the fetus from Tc-99m DTPA aerosol were based on the assumption by Atkins et al. that once in the blood, the Tc-99m DTPA follows the distribution described in MIRD Dose Estimate Report No. 12 for injected Tc-99m DTPA (32). The amount of Tc-99m DTPA that enters the blood and is then available for fetal and placental uptake was estimated based on the ICRP 30 lung model (35) for a particle size of 0.25 μm Activity Median Aerodynamic Diameter (AMAD) and consideration of the rate at which activity enters the blood relative to the rate of loss by radioactive decay (36). The estimated amount of Tc-99m DTPA available in the blood was approximately 0.435 Bq/Bq (434.7 μCi/mCi) administered.

The biodistribution data for cumulated activities in the rat for the placenta and the fetus at 15 and 21 days gestation provided by Wegst (31) were used for the dose estimates. Wegst's cumulated activity values given for the placenta and fetus in the rats were extrapolated using the weight ratio. The residence times for the fetus and placenta were then scaled by a factor of 0.434 to account for the amount of activity in the blood available for uptake by the fetus and placenta.

The biodistribution data for the normal patient found in MIRD Dose Estimate Report No. 16 (34) were used with Wegst's extrapolated data to determine the absorbed dose to the human fetus. The absorbed dose estimate provided for early pregnancy includes maternal contributions only.

9. Tc-99m Sulfur Colloid

The biokinetic data for Tc-99m sulfur colloid in normal patients used to determine the absorbed dose estimates were taken from MIRD Dose Estimate Report No. 3 (37). Data in Mahon's article provided distribution information at 1 hour after intravenous injection of Tc-99m sulfur colloid to

New Zealand albino rabbits in the third trimester of gestation (27). The animals were sacrificed, dissected and counted to determine the radionuclide content of selected organs. Mahon reported the distribution of Tc-99m Sulfur Colloid in the pregnant rabbit in terms of "percent dose in whole organ" and "percent dose per 1 % body weight". Assuming the New Zealand albino rabbits weigh 2770 grams each, extrapolation of the values given for the fetus and placenta to humans yields 0.29% and 0.79%, respectively, at 6-months gestation and 0.51% and 1.16%, respectively, at 9-months gestation. The extrapolation at 3-months gestation yields fetal uptake of 0.089%.

The estimated fetal doses Tc-99m sulfur colloid were calculated using Mahon's rabbit data, given several assumptions. The activity was assumed to reach a maximum in the fetus and the placenta at 1 hour after injection, and remained there indefinitely (i.e.. loss occurred only by radioactive decay). The data collected from the albino rabbits in the third trimester of gestation was assumed to be acceptable for use with the 3-, 6- and 9-month pregnant woman phantoms. The absorbed dose estimate for early pregnancy includes maternal contributions only.

10. Tc-99m Hydroxymethylene Diphosphonate

The biokinetic data for Tc-99m hydroxymethylene diphosphonate (HDP) in normal patients were found in MIRD Dose Estimate Report No. 13 (9). Tc-99m HDP follows a distribution path in the human patient similar to that of ^{99m}Tc MDP (9). Therefore, the fetal and placental accumulation data for Tc-99m MDP was assumed to be appropriate for use with the maternal distribution for Tc-99m HDP. The fetal and placental uptakes reported by Chandra and Pizzarello (6) Tc-99m MDP were higher than either Hedrick et al. (10) or Palmer (12); therefore their data were used to provide a conservative estimate for the absorbed dose to the human fetus from Tc-99m HDP. During a conversation with Chandra, he reported that the placental uptake of Tc-99m HDP was 0.5% of the administered activity, and that the fetal uptake of Tc-99m HDP was 0.5% of the administered activity (38).

Other assumptions were needed to determine the absorbed dose estimates using Chandra and Pizzarello's data for Tc-99m HDP; as for Tc-99m MDP, refer to section on Tc-99m MDP for these assumptions. The model for the distribution of Tc-99m HDP in the MIRD Dose Estimate Report No. 13 (9) was used with Chandra's data to obtain the dose estimates for the human fetus. The absorbed dose estimate provided for early pregnancy includes maternal contributions only.

11. I-131 Sodium Iodide

Biodistribution data for normal patients for I-131 sodium iodide was found in MIRD Dose Estimate Report No. 5 (15). The absorbed dose estimates for the fetus from the administration of I-131 sodium iodide to the mother were determined by applying the same procedure used for I-123 sodium iodide described previously in this paper. The transfer rate coefficients for the mother determined by Watson for iodide are shown in Table 2. The transfer rate coefficients for the fetus are shown in Table 3. The SAAM software (23) was used with Watson's proposed model to determine the residence times for I-131 sodium iodide in the pregnant woman and fetus at 3, 6 and 9-months gestation. The dose estimate provided for early pregnancy includes maternal contributions only.

12. Tc-99m Pertechnetate

The model for the biodistribution of Tc-99m pertechnetate in normal patients used to determine the absorbed dose estimates was taken from MIRD Dose Estimate Report No. 8 (39). Biodistribution studies to determine the behavior of Tc-99m pertechnetate during pregnancy were conducted by Wegst (40) on pregnant Fisher rats and by Palmer (12) in guinea pigs.

The placental and fetal uptakes of Tc-99m pertechnetate obtained by Palmer in guinea pigs

during the 7th and 8th week of gestation were determined to be the most appropriate for use in determining the fetal absorbed dose provided. Palmer reported that the maximum fetal uptake for Tc-99m pertechnetate was 3.85% and that the placental uptake was 1.1%. During a conversation with Dr. Palmer, she stated that she observed no alterations in the maternal distribution of the pregnant animals relative to nonpregnant animals (41).

Several assumptions were made in determining the absorbed dose estimates using Palmer's data. The guinea pig gestational period of 9 weeks was assumed to correspond to the 9-month gestational period of the human. The data collected from the 7- and 8-week pregnant guinea pig was assumed to be valid for use with the 6-month and 9-month pregnant phantoms based on a comparison of the developmental stages of the animal and human. The data for accumulation in the fetal tissue were also used with the 3-month pregnant phantom to obtain the absorbed dose at 3-months gestation in the human fetus. These dose estimates also assumed that no changes occur in the biodistribution of Tc-99m pertechnetate in maternal organs during pregnancy. The standard model for the distribution of Tc-99m pertechnetate (39) was used with these data. The absorbed dose estimate for early pregnancy includes maternal contributions only.

13. Tc-99m Red Blood Cells

The biokinetic data for Tc-99m red blood cells (RBCs) in normal patients used to determine the absorbed dose estimates were taken from MIRD Dose Estimate Report No. 14 (42). Placental and fetal uptakes of Tc-99m RBCs were obtained in guinea pigs during the 7th and 8th week of gestation by Palmer (12). Palmer reported that the maximum fetal uptake for Tc-99m RBCs was 0.1% and the placental uptake was 1.1%. During a personal conversation with Dr. Palmer, she explained that she observed no alterations in the maternal distribution of the pregnant animals in relation to nonpregnant animals (41).

There were several assumptions needed for determining the absorbed dose estimates using Palmer's data. The guinea pig gestational period of 9 weeks was assumed to correspond to the 9-month gestational period of the human. The data collected from the 7- and 8-week pregnant guinea pig were assumed to be valid for use with the 6-month and 9-month pregnant phantoms, based on a comparison of the developmental stages of the animal and human. The data for accumulation in the fetal tissue were also combined with the 3-month pregnant phantom to obtain the absorbed dose estimate at 3-months gestation in the human fetus. These dose estimates also assume that no changes occur in the biodistribution of Tc-99m RBCs in maternal organs during pregnancy. The absorbed dose estimate for early pregnancy includes maternal contributions only.

14. Tc-99m Pyrophosphate (PYP)

The biokinetic data for Tc-99m pyrophosphate (PYP) in normal patients used to determine the absorbed dose estimates were taken from MIRD Dose Estimate Report No. 13 (9). Available biodistribution data for the accumulation of Tc-99m PYP in fetal and placental tissue was obtained using Swiss albino mice during the 17th to 19th day of a 20 to 22 day gestation period (6). During a conversation with Dr. Chandra, he reported that the distribution of Tc-99m PYP in the pregnant animal was comparable to the biodistribution of Tc-99m PYP in the nonpregnant animals. He also stated that the placental accumulation of Tc-99m PYP was 0.8% of the administered activity and the fetal accumulation of the Tc-99m PYP was 0.7% of the administered activity (38).

Several assumptions were made to estimate the absorbed dose to the fetus from Tc-99m PYP administered to the human mother. The accumulation of Tc-99m PYP in the mouse fetus and placenta was assumed to be equivalent to that of the human fetus and placenta. It was assumed that no changes occur in the biodistribution of Tc-99m PYP in maternal organs during pregnancy. The

model for the distribution in the MIRD Dose Estimate Report No. 13 (9) was used with Chandra's data to obtain the dose estimates to the human fetus.

The 17th to 19th day of gestation in the mouse was assumed to be roughly comparable to the later stages of gestation in the human. This assumption allows the data collected by Chandra be used with the human phantom at 9-months gestation and, to a lesser extent, with the 6-month phantom. The data for accumulation in the fetal animal tissue were also combined with the 3-month pregnant phantom to obtain the absorbed dose estimate at 3-months gestation in the human fetus. The reported uptake of activity in the fetus and the placenta were assumed to be the maximum values and that the activity remained there indefinitely (i.e.. loss occurred only by radioactive decay). The absorbed dose estimate for early pregnancy includes maternal contributions only.

15. Tc-99m 2,3 Dimercaptosuccinic Acid

The model for the biodistribution of Tc-99m 2,3 Dimercaptosuccinic Acid (DMSA) in normal patients used to determine the absorbed dose estimates was based on the data of Arnold et al. (43). Fetal uptake and placental transfer data of Tc-99m DMSA were available from studies on swiss albino mice during the 17th to 19th day of a 20 to 22 day gestation period (6). The data collection by Chandra and the assumptions made to estimate the human fetal dose are the same as for Tc-99m PYP above. During a conversation, Dr. Chandra reported the placental tissue contained 2.1% of the administered activity and the fetal tissue contained 0.3% of the administered activity (38).

16. Tc-99m Glucoheptonate

The model for the distribution of Tc-99m glucoheptonate (GHA) in normal patients used to determine the absorbed dose estimates was based on the data of Arnold et al. (43). Placental and fetal uptakes of Tc-99m GHA were obtained in guinea pigs by Palmer (12) and Chandra (6) in swiss albino mice. The data obtained by Palmer were determined to be the most appropriate for use in determining the fetal absorbed dose provided for Tc-99m GHA. Palmer reported that the maximum fetal uptake for Tc-99m GHA was 0.18% and the placental uptake was 0.23%. During a personal conversation with Dr. Palmer, she explained that she observed no alterations in the maternal distribution of the pregnant animals (41). The assumptions needed for determining the absorbed dose estimates using Palmer's data are the same as those used above.

C. Dose Estimates

Radiation dose estimates for early pregnancy, 3-months gestation, 6-months gestation, and 9-months gestation are shown in Table 4 for the fifteen radiopharmaceuticals studied, per unit activity administered to the mother. Table 5 shows the total absorbed dose to the fetus at these stages of gestation, assuming typical levels of administered activity for these studies. The residence times assumed for the mother's organs for these studies are given in a separate paper (44).

Table 4

Absorbed Dose Estimates to the Embryo/Fetus Per Unit Activity of Radiopharmaceutical Administered to the Mother (shading indicates maternal and fetal self dose contributions)

Radiopharmaceutical	Early mGy/MBq	3-Month mGy/MBq	6-Month mGy/MBq	9-Month mGy/MBq
Co-57 Vitamin B-1, Normal-Flushing	1.0E+00	6.8E-01	8.4E-01	8.8E-01
Co-57 Vitamin B-12, Normal-No Flushing	1.5E+00	1.0E+00	1.2E+00	1.3E+00
Co-57 Vitamin B-12, PA- Flushing	2.1E-01	1.7E-01	1.7E-01	1.5E-01
Co-57 Vitamin B-12, PA- No Flushing	2.8E-01	2.1E-01	2.2E-01	2.0E-01
Co-58 Vitamin B-12, Normal-Flushing	2.5E+00	1.9E+00	2.1E+00	2.1E+00
Co-58 Vitamin B-12, Normal-No Flushing	3.7E+00	2.8E+00	3.1E+00	3.1E+00
Co-58 Vitamin B-12, PA-Flushing	8.3E-01	7.4E-01	6.4E-01	4.8E-01
Co-58 Vitamin B-12, PA-No Flushing	9.8E-01	8.5E-01	7.6E-01	6.0E-01
Co-60 Vitamin B-12, Normal-Flushing	3.7E+01	2.8E+01	3.1E+01	3.2E+01
Co-60 Vitamin B-12, Normal-No Flushing	5.5E+01	4.2E+01	4.7E+01	4.7E+01
Co-60 Vitamin B-12, PA-Flushing	5.9E+00	4.7E+00	4.8E+00	4.5E+00
Co-60 Vitamin B-12, PA-No Flushing	8.3E+00	6.5E+00	6.8E+00	6.5E+00
F-18 FDG	2.7E-02	1.7E-02	9.4E-03	8.1E-03
F-18 Sodium Fluoride	2.2E-02	1.7E-02	7.5E-03	6.8E-03
Ga-67 Citrate	9.3E-02	2.0E-01	1.8E-01	1.3E-01
I-123 Hippuran	3.1E-02	2.4E-02	8.4E-03	7.9E-03
I-123 IMP	1.9E-02	1.1E-02	7.1E-03	5.9E-03
I-123 MIBG	1.8E-02	1.2E-02	6.8E-03	6.2E-03
I-123 Sodium Iodide	2.0E-02	1.4E-02	1.1E-02	9.8E-03
I-124 Sodium Iodide	1.4E-01	1.0E-01	5.9E-02	4.6E-02
I-125 HSA	2.5E-01	7.8E-02	3.8E-02	2.6E-02
I-125 IMP	3.2E-02	1.3E-02	4.8E-03	3.6E-03
I-125 MIBG	2.6E-02	1.1E-02	4.1E-03	3.4E-03
I-125 Sodium Iodide	1.8E-02	9.5E-03	3.5E-03	2.3E-03
I-126 Sodium Iodide	7.8E-02	5.1E-02	3.2E-02	2.6E-02
I-130 Sodium Iodide	1.8E-01	1.3E-01	7.6E-02	5.7E-02
I-131 Hippuran	6.4E-02	5.0E-02	1.9E-02	1.8E-02

Table 4 (Continued) Radiopharmaceutical	Early mGy/MBq	3-Month mGy/MBq	6-Month mGy/MBq	9-Month mGy/MBq
I-131 HSA	5.2E-01	1.8E-01	1.6E-01	1.3E-01
I-131 MAA	6.7E-02	4.2E-02	4.0E-02	4.2E-02
I-131 MIBG	1.1E-01	5.4E-02	3.8E-02	3.5E-02
I-131 Sodium Iodide	7.2E-02	6.8E-02	2.3E-01	2.7E-01
I-131 Rose Bengal	2.2E-01	2.2E-01	1.6E-01	9.0E-02
In-111 DTPA	6.5E-02	4.8E-02	2.0E-02	1.8E-02
In-111 Pentetreotide	8.2E-02	6.0E-02	3.5E-02	3.1E-02
In-111 Platelets	1.7E-01	1.1E-01	9.9E-02	8.9E-02
In-111 Red Blood Cells	2.2E-01	1.3E-01	1.1E-01	8.6E-02
In-111 White Blood Cells	1.3E-01	9.6E-02	9.6E-02	9.4E-02
Tc-99m Albumin Microspheres	4.1E-03	3.0E-03	2.5E-03	2.1E-03
Tc-99m Disofenin	1.7E-02	1.5E-02	1.2E-02	6.7E-03
Tc-99m DMSA	5.1E-03	4.7E-03	4.0E-03	3.4E-03
Tc-99m DTPA	1.2E-02	8.7E-03	4.1E-03	4.7E-03
Tc-99m DTPA Aerosol	5.8E-03	4.3E-03	2.3E-03	3.0E-03
Tc-99m Glucoheptonate	1.2E-02	1.1E-02	5.3E-03	4.6E-03
Tc-99m HDP	5.2E-03	5.4E-03	3.0E-03	2.5E-03
Tc-99m HEDP	7.2E-03	5.2E-03	2.7E-03	2.4E-03
Tc-99m HMPAO	8.7E-03	6.7E-03	4.8E-03	3.6E-03
Tc-99m Human Serum Albumin	5.1E-03	3.0E-03	2.6E-03	2.2E-03
Tc-99m MAA	2.8E-03	4.0E-03	5.0E-03	4.0E-03
Tc-99m MAG3	1.8E-02	1.4E-02	5.5E-03	5.2E-03
Tc-99m MDP	6.1E-03	5.4E-03	2.7E-03	2.4E-03
Tc-99m MIBI-Rest	1.5E-02	1.2E-02	8.4E-03	5.4E-03
Tc-99m MIBI-Stress	1.2E-02	9.5E-03	6.9E-03	4.4E-03
Tc-99m Pertechnetate	1.1E-02	2.2E-02	1.4E-02	9.3E-03
Tc-99m PYP	6.0E-03	6.6E-03	3.6E-03	2.9E-03
Tc-99m RBC-Heat Treated	1.7E-03	1.6E-03	2.1E-03	2.2E-03
Tc-99m RBC-In Vitro	6.8E-03	4.7E-03	3.4E-03	2.8E-03

Table 4 (Continued) Radiopharmaceutical	Early mGy/MBq	3-Month mGy/MBq	6-Month mGy/MBq	9-Month mGy/MBq
Tc-99m RBC-In Vivo	6.4E-03	4.3E-03	3.3E-03	2.7E-03
Tc-99m Sulfur Colloid-Normal	1.8E-03	2.1E-03	3.2E-03	3.7E-03
Tc-99m Sulfur Colloid-Liver Disease	3.2E-03	2.5E-03	2.8E-03	2.8E-03
Tc-99m Teboroxime	8.9E-03	7.1E-03	5.8E-03	3.7E-03
Tc-99m White Blood Cells	3.8E-03	2.8E-03	2.9E-03	2.8E-03
Tl-201 Chloride	9.7E-02	5.8E-02	4.7E-02	2.7E-02
Xe-127, 5 Minute Rebreathing, 5 Liter Spirometer Volume	4.3E-04	2.4E-04	1.9E-04	1.5E-04
Xe-127, 5 Minute Rebreathing, 7.5 Liter Spirometer Volume	2.3E-04	1.3E-04	1.0E-04	8.4E-05
Xe-127, 5 Minute Rebreathing, 10 Liter Spirometer Volume	2.3E-04	1.4E-04	1.1E-04	9.2E-05
Xe-133, 5 Minute Rebreathing, 5 Liter Spirometer Volume	4.1E-04	4.8E-05	3.5E-05	2.6E-05
Xe-133, 5 Minute Rebreathing, 7.5 Liter Spirometer Volume	2.2E-04	2.6E-05	1.9E-05	1.5E-05
Xe-133, 5 Minute Rebreathing, 10 Liter Spirometer Volume	2.5E-04	2.9E-05	2.1E-05	1.6E-05
Xe-133, Injection	4.9E-06	1.0E-06	1.4E-06	1.6E-06

TABLE 5
Fetal Dose Estimates from Various Nuclear Medicine Procedures
(shading indicates maternal and fetal self dose contributions)

	Activity Admin. MBq (mCi)	Early mGy (rad)	3-Month mGy (rad)	6-Month mGy (rad)	9-Month mGy (rad)
Co-57 Vitamin B-12 Normal-Flushing	0.04 (0.001)	4.0E-02 (4.0E-03)	2.7E-02 (2.7E-03)	3.4E-02 (3.4E-03)	3.5E-02 (3.5E-03)
Co-57 Vitamin B-12 Normal-No Flushing	0.04 (0.001)	6.0E-02 (6.0E-03)	4.0E-02 (4.0E-03)	4.8E-02 (4.8E-03)	5.2E-02 (5.2E-03)
Co-57 Vitamin B-12 Pernicious Anemia-Flushing	0.04 (0.001)	8.4E-03 (8.4E-04)	6.8E-03 (6.8E-04)	6.8E-03 (6.8E-04)	6.0E-03 (6.0E-04)
Co-57 Vitamin B-12 Pernicious Anemia-No Flushing	0.04 (0.001)	1.1E-02 (1.1E-03)	8.4E-03 (8.4E-04)	8.8E-03 (8.8E-04)	8.0E-03 (8.0E-04)

Table 5 (Continued)	Activity Admin. MBq	Early mGy	3-Month mGy	6-Month mGy	9-Month mGy
Co-58 Vitamin B-12 Normal-Flushing	0.03 (0.0008)	7.5E-02 (7.5E-03)	5.7E-02 (5.7E-03)	6.3E-02 (6.3E-03)	6.3E-02 (6.3E-03)
Co-58 Vitamin B-12 Normal-No Flushing	0.03 (0.0008)	1.1E-01 (1.1E-02)	8.4E-02 (8.4E-03)	9.3E-02 (9.3E-03)	9.3E-02 (9.3E-03)
Co-58 Vitamin B-12 Pernicious Anemia-Flushing	0.03 (0.0008)	2.5E-02 (2.5E-03)	2.2E-02 (2.2E-03)	1.9E-02 (1.9E-03)	1.4E-02 (1.4E-03)
Co-58 Vitamin B-12 Pernicious Anemia-No Flushing	0.03 (0.0008)	2.9E-02 (2.9E-03)	2.6E-02 (2.6E-03)	2.3E-02 (2.3E-03)	1.8E-02 (1.8E-03)
F-18 FDG	370 (10)	1.0E+01 (1.0E+00)	6.3E+00 (6.3E-01)	3.5E+00 (3.5E-01)	3.0E+00 (3.0E-01)
Ga-67 Citrate	190 (5)	1.8E+01 (1.8E+00)	3.8E+01 (3.8E+00)	3.4E+01 (3.4E+00)	2.5E+01 (2.5E+00)
Hg-197 Chlormerodrin	4 (0.1)	4.4E-02 (4.4E-03)	3.0E-02 (3.0E-03)	2.7E-02 (2.7E-03)	2.8E-02 (2.8E-03)
I-123 Hippuran	.75 (2)	2.3E+00 (2.3E-01)	1.8E+00 (1.8E-01)	6.3E-01 (6.3E-02)	5.9E-01 (5.9E-02)
I-123 IMP	200 (5.5)	3.8E+00 (3.8E-01)	2.2E+00 (2.2E-01)	1.4E+00 (1.4E-01)	1.2E+00 (1.2E-01)
I-123 MIBG					
Pheochromocytoma	350 (9.5)	6.3E+00 (6.3E-01)	4.2E+00 (4.2E-01)	2.4E+00 (2.4E-01)	2.2E+00 (2.2E-01)
Cecholamine Tumor	80 (2)	1.4E+00 (1.4E-01)	9.6E-01 (9.6E-02)	5.4E-01 (5.4E-02)	5.0E-01 (5.0E-02)
I-123 Sodium Iodide					
Thyroid Uptake Study	30 (0.8)	6.0E-01 (6.0E-02)	4.2E-01 (4.2E-02)	3.3E-01 (3.3E-02)	2.9E-01 (2.9E-02)
Thyroid Imaging	15 (0.4)	3.0E-01 (3.0E-02)	2.1E-01 (2.1E-02)	1.7E-01 (1.7E-02)	1.4E-02 (1.4E-03)
I-125 HSA	2 (0.05)	5.0E-01 (5.0E-02)	1.6E-01 (1.6E-02)	7.6E-02 (7.6E-03)	5.2E-02 (5.2E-03)
I-125 NaI	1 (0.03)	1.8E-02 (1.8E-03)	9.5E-03 (9.5E-04)	3.5E-03 (3.5E-04)	2.3E-03 (2.3E-04)
I-131 Hippuran					
Renal Function	1.3 (0.035)	8.3E-02 (8.3E-03)	6.5E-02 (6.5E-03)	2.5E-02 (2.5E-03)	2.3E-02 (2.3E-03)

Table 5 (Continued)	Activity Admin. MBq	Early mGy	3-Month mGy	6-Month mGy	9-Month mGy
Renal Imaging	1.3 (0.035)	8.3E-02 (8.3E-03)	6.5E-02 (6.5E-03)	2.5E-02 (2.5E-03)	2.3E-02 (2.3E-03)
I-131 HSA	0.5 (0.013)	2.6E-01 (2.6E-02)	9.0E-02 (9.0E-03)	8.0E-02 (8.0E-03)	6.5E-02 (6.5E-03)
I-131 MAA	55 (1.5)	3.7E+00 (3.7E-01)	2.3E+00 (2.3E-01)	2.2E+00 (2.2E-01)	2.3E+00 (2.3E-01)
I-131 MIBG	20 (0.5)	2.2E+00 (2.2E-01)	1.1E+00 (1.1E-01)	7.6E-01 (7.6E-02)	7.0E-01 (7.0E-02)
I-131 NaI (Diagnostic)					
Thyroid Uptake	0.55 (0.015)	4.0E-02 (4.0E-03)	3.7E-02 (3.7E-03)	1.3E-01 (1.3E-02)	1.5E-01 (1.5E-02)
Scintiscanning	4 (0.11)	2.9E-01 (2.9E-02)	2.7E-01 (2.7E-02)	9.2E-01 (9.2E-02)	1.1E+00 (1.1E-01)
Localization of Extrathyroid Metastases	40 (1.1)	2.9E+00 (2.9E-01)	2.7E+00 (2.7E-01)	9.2E+00 (9.2E-01)	1.1E+01 (1.1E+00)
I-131 NaI (Therapeutic)					
Hyperthyroidism	350 (9.5)	2.5E+01 (2.5E+00)	2.3E+01 (2.3E+00)	8.1E+01 (8.1E+00)	9.5E+01 (9.5E+00)
Ablation of Normal Thyroid Tissue	1900 (50)	1.4E+02 (1.4E+01)	1.3E+02 (1.3E+01)	4.4E+02 (4.4E+01)	5.1E+02 (5.1E+01
I-131 Rose Bengal	0.04 (0.001)	8.8E-03 (8.8E-04)	8.8E-03 (8.8E-04)	6.4E-03 (6.4E-04)	3.6E-03 (3.6E-04)
In-111 DTPA	20 (0.5)	1.3E+00 (1.3E-01)	9.6E-01 (9.6E-02)	4.0E-01 (4.0E-02)	3.6E-01 (3.6E-02)
In-111 Pentetreotide					
Planar Imaging	110 (3)	9.0E+00 (9.0E-01)	6.6E+00 (6.6E-01)	3.8E+00 (3.8E-01)	3.4E+00 (3.4E-01)
SPECT Imaging	230 (6)	1.9E+01 (1.9E+00)	1.4E+01 (1.4E+00)	8.0E+00 (8.0E-01)	7.0E+00 (7.0E-01)
In-111 Platelets	10 (0.25)	1.7E+00 (1.7E-01)	1.1E+00 (1.1E-01)	9.9E-01 (9.9E-02)	8.9E-01 (8.9E-02)
In-111 White Blood Cell	20 (0.5)	2.6E+00 (2.6E-01)	1.9E+00 (1.9E-01)	1.9E+00 (1.9E-01)	1.9E+00 (1.9E-01)
Kr-81m Gas	600 (15)	1.1E-04 (1.1E-05)	1.0E-04 (1.0E-05)	1.6E-04 (1.6E-05)	2.0E-04 (2.0E-05)

Table 5 (Continued)	Activity Admin. MBq	Early mGy	3-Month mGy	6-Month mGy	9-Month mGy
Tc-99m Disofenin	350 (9.5)	6.0E+00 (6.0E-01)	5.2E+00 (5.2E-01)	4.2E+00 (4.2E-01)	2.3E+00 (2.3E-01)
Tc-99m DMSA	220 (6)	1.1E+00 (1.1E-01)	1.0E+00 (1.0E-01)	8.8E-01 (8.8E-02)	7.5E-01 (7.5E-02)
Tc-99m DTPA					
Kidney Imaging & Glomerular Filtration	750 (20)	9.0E+00 (9.0E-01)	6.5E+00 (6.5E-01)	3.1E+00 (3.1E-01)	3.5E+00 (3.5E-01)
Brain Imaging & Renal Perfusion	750 (20)	9.0E+00 (9.0E-01)	6.5E+00 (6.5E-01)	3.1E+00 (3.1E-01)	3.5E+00 (3.5E-01)
1st Pass	350 (9.5)	4.2E+00 (4.2E-01)	3.0E+00 (3.0E-01)	1.4E+00 (1.4E-01)	1.6E+00 (1.6E-01)
Gastric Reflux	10 (0.27)	1.2E-01 (1.2E-02)	8.7E-02 (8.7E-03)	4.1E-02 (4.1E-03)	4.7E-02 (4.7E-03)
Hypertension	800 (22)	9.6E+00 (9.6E-01)	7.0E+00 (7.0E-01)	3.3E+00 (3.3E-01)	3.8E+00 (3.8E-01)
Residual Urine Determination	350 (9.5)	4.2E+00 (4.2E-01)	3.0E+00 (3.0E-01)	1.4E+00 (1.4E-01)	1.6E+00 (1.6E-01)
Tc-99m DTPA Aerosol	40 (1.1)	2.3E-01 (2.3E-02)	1.7E-01 (1.7E-02)	9.2E-02 (9.2E-03)	1.2E-01 (1.2E-02)
Tc-99m Glucoheptonate					
Renal Imaging	750 (20)	9.0E+00 (9.0E-01)	8.2E+00 (8.2E-01)	4.0E+00 (4.0E-01)	3.4E+00 (3.4E-01)
Brain Imaging	750 (20)	9.0E+00 (9.0E-01)	8.2E+00 (8.2E-01)	4.0E+00 (4.0E-01)	3.4E+00 (3.4E-01)
Tc-99m HDP	750 (20)	3.9E+00 (3.9E-01)	4.1E+00 (4.0E-01)	2.3E+00 (2.3E-01)	1.9E+00 (1.9E-01)
Tc-99m HMPAO	750 (20)	6.5E+00 (6.5E-01)	5.0E+00 (5.0E-01)	3.6E+00 (3.6E-01)	2.7E+00 (2.7E-01)
Tc-99m Human Serum Albumin	200 (5.5)	1.0E+00 (1.0E-01)	6.0E-01 (6.0E-02)	5.2E-01 (5.2E-02)	4.4E-01 (4.4E-02)
Tc-99m MAA					
Hepatic Artery Perfusion	150 (4)	4.2E-01 (4.2E-02)	6.0E-01 (6.0E-02)	7.5E-01 (7.5E-02)	6.0E-01 (6.0E-02)
Lung Imaging	200 (5.5)	5.6E-01 (5.6E-02)	8.0E-01 (8.0E-02)	1.0E+00 (1.0E-01)	8.0E-01 (8.0E-02)

Table 5 (Continued)	Activity Admin. MBq	Early mGy	3-Month mGy	6-Month mGy	9-Month mGy
Isotopic Venography	220 (6)	6.2E-01 (6.2E-02)	8.8E-01 (8.8E-02)	1.1E+00 (1.1E-01)	8.0E-01 (8.0E-02)
LeVeen Shunt Patency	110 (3)	3.1E-01 (3.1E-02)	4.4E-01 (4.4E-02)	5.5E-01 (5.5E-02)	4.4E-01 (4.4E-02)
Tc-99m MAG3	750 (20)	1.4E+01 (1.4E+00)	1.0E+01 (1.0E+00)	4.1E+00 (4.1E-01)	3.9E+00 (3.9E-01)
Tc-99m MDP	750 (20)	4.6E+00 (4.6E-01)	4.0E+00 (4.0E-01)	2.0E+00 (2.0E-01)	1.8E+00 (1.8E-01)
Tc-99m MIBI-rest	1100 (30)	1.7E+01 (1.7E+00)	1.3E+01 (1.3E+00)	9.2E+00 (9.2E-01)	5.9E+00 (5.9E-01)
Tc-99m MIBI-stress	1100 (30)	1.3E+01 (1.3E+00)	1.0E+01 (1.0E+00)	7.6E+00 (7.6E-01)	4.8E+00 (4.8E-01)
Tc-99m Pertechnetate					
Brain Imaging	1100 (30)	1.2E+01 (1.2E+00)	2.4E+01 (2.4E+00)	1.5E+01 (1.5E+00)	1.0E+01 (1.0E+00)
Thyroid Imaging	400 (11)	4.4E+00 (4.4E-01)	8.8E+00 (8.8E-01)	5.6E+00 (5.6E-01)	3.7E+00 (3.7E-01)
Salivary Gland Imaging	200 (5.5)	2.2E+00 (2.2E-01)	4.4E+00 (4.4E-01)	2.8E+00 (2.8E-01)	1.9E+00 (1.9E-01)
Placental Localization	110 (3)	1.1E+00 (1.1E-01)	2.4E+00 (2.4E-01)	1.5E+00 (1.5E-01)	1.0E+00 (1.0E-01)
Blood Pool Imaging	1100 (30)	1.1E+01 (1.1E+00)	2.4E+01 (2.4E+00)	1.4E+01 (1.4E+00)	1.0E+01 (1.0E+00)
Cardiovascular Shunt Detection	550 (15)	6.0E+00 (6.0E-01)	1.2E+01 (1.2E+00)	7.7E+00 (7.7E-01)	5.1E+00 (5.1E-01)
1st Pass	550 (15)	6.0E+00 (6.0E-01)	1.2E+01 (1.2E+00)	7.7E+00 (7.7E-01)	5.1E+00 (5.1E-01)
Tc-99m PYP					
Skeletal Imaging	550 (15)	3.3E+00 (3.3E-01)	3.6E+00 (3.6E-01)	2.0E+00 (2.0E-01)	1.6E+00 (1.6E-01)
Cardiac Imaging	700 (19)	4.2E+00 (4.2E-01)	4.6E+00 (4.6E-01)	2.5E+00 (2.5E-01)	2.0E+00 (2.0E-01)
Blood Pool Imaging	700 (19)	4.2E+00 (4.2E-01)	4.6E+00 (4.6E-01)	2.5E+00 (2.5E-01)	2.0E+00 (2.0E-01)

Table 5 (Continued)	Activity Admin. MBq	Early mGy	3-Month mGy	6-Month mGy	9-Month mGy
Tc-99m RBC - In Vitro Labeling	930 (25)	6.3E+00 (6.3E-01)	4.4E+00 (4.4E-01)	3.2E+00 (3.2E-01)	2.6E+00 (2.6E-01)
Tc-99m RBC - In Vivo Labeling					
Rest	550 (15)	3.5E+00 (3.5E-01)	2.4E+00 (2.4E-01)	1.8E+00 (1.8E-01)	1.5E+00 (1.5E-01)
Exercise	930 (25)	6.0E+00 (6.0E-01)	4.0E+00 (4.0E-01)	3.1E+00 (3.1E-01)	2.5E+00 (2.5E-01)
Lower GI Bleeding	930 (25)	6.0E+00 (6.0E-01)	4.0E+00 (4.0E-01)	3.1E+00 (3.1E-01)	2.5E+00 (2.5E-01)
Tc-99m Sulfur Colloid - Normal					
Liver-Spleen Imaging	300 (8)	5.4E-01 (5.4E-02)	6.3E-01 (6.3E-02)	9.6E-01 (9.6E-02)	1.1E+00 (1.1E-01)
Bone Marrow Imaging	450 (12)	8.1E-01 (8.1E-02)	9.5E-01 (9.5E-02)	1.4E+00 (1.4E-01)	1.7E+00 (1.7E-01)
Pulmonary Aspiration	20 (0.5)	3.6E-02 (3.6E-03)	4.2E-02 (4.2E-03)	6.4E-02 (6.4E-03)	7.4E-02 (7.4E-03)
LeVeen Shunt Patency	110 (3)	2.0E-01 (2.0E-02)	2.3E-01 (2.3E-02)	3.5E-01 (3.5E-02)	4.1E-01 (4.1E-02)
Tc-99m White Blood Cells	200 (5.4)	7.6E-01 (7.6E-02)	5.6E-01 (5.6E-02)	5.8E-01 (5.8E-02)	5.6E-01 (5.6E-02)
Tl-201 Chloride					
Planar Imaging	150 (4)	1.5E+01 (1.5E+00)	8.7E+00 (8.7E-01)	7.0E+00 (7.0E-01)	4.0E+00 (4.0E-01)
SPECT Imaging	110 (3)	1.1E+01 (1.1E+00)	6.4E+00 (6.4E-01)	5.2E+00 (5.2E-01)	3.0E+00 (3.0E-01)
Myocardial Perfusion	55 (1.5)	5.3E+00 (5.3E-01)	3.2E+00 (3.2E-01)	2.6E+00 (2.6E-01)	1.5E+00 (1.5E-01)
Thyroid Imaging	80 (2.2)	7.8E+00 (7.8E-01)	4.6E+00 (4.6E-01)	3.8E+00 (3.8E-01)	2.2E+00 (2.2E-01)
Xe-133, Injection					
Muscle Blood Flow	20 (0.5)	9.8E-05 (9.8E-06)	2.0E-05 (2.0E-06)	2.8E-05 (2.8E-06)	3.2E-05 (3.2E-06)
Pulmonary Function with Imaging	1100 (30)	5.4E-03 (5.4E-04)	1.1E-03 (1.1E-04)	1.5E-03 (1.5E-04)	1.8E-03 (1.8E-04)

DISCUSSION

A considerable number of radiopharmaceuticals are routinely administered to women of childbearing years (Table 1). This is reflected also in the large number of requests routinely received at RIDIC for radiation dose estimates in pregnancy for many pharmaceuticals. Considerable diversity is seen in the approaches taken to prevent inadvertent administration of radiopharmaceuticals to the pregnant patient, from brief questioning of the patient through administration of pregnancy tests for most appropriate subjects. Probably no one method will work for every medical institution, and this study does not purport to prescribe such procedures. However, *every* institution should consider this problem and formulate explicit procedures for attempting to prevent inadvertent administrations of radiopharmaceuticals to pregnant patients.

Unfortunately, only a small number of the radiopharmaceuticals that may be administered to women of childbearing years have been studied to determine potential placental and fetal uptakes. This should be an area of active study, and a plan should be formulated to systematically study the placental and fetal uptake of all of the radiopharmaceuticals in Table 1 in one or more animal species. In addition, nuclear medicine physicians who, either intentionally or inadvertently, administer radiopharmaceuticals to pregnant women should be encouraged to obtain at least one image in the abdominal area to be used to estimate the placental and fetal uptake.

Nonetheless, this study reports for the first time a significant amount of information on the placental and fetal uptake of many radiopharmaceuticals (Tables 3 and 4). Although much of these data are based on animal studies, they provide some estimates of the placental and fetal uptake as a function of gestation, and thus represent an important advance in the knowledge of fetal radiation doses in nuclear medicine.

The radiation doses in Table 3 should be useful in many institutions for estimating possible fetal doses from nuclear medicine studies performed on their pregnant patients. The estimates in Table 4, however, show the ranges of typical fetal doses that may be encountered in practice. The data in this table illustrate that the majority of studies will probably result in fetal doses less than 10 mGy (1 rad). Only studies with Ga-67 citrate, I-131 NaI, I-131 RBC's, and Tl-201 chloride appear to result in fetal doses in excess of 10 mGy, according to present knowledge. Therapeutic administrations of I-131 NaI, which are routinely contraindicated in the case of pregnancy or breast feeding, may result in fetal doses up to 500 mGy. In addition, beyond 10-13 weeks' gestation, the fetal thyroid may as well receive extremely high doses in such cases (21).

According to NCRP Commentary No. 9 (45), "...it seems clear that exposures resulting in doses to the whole body (i.e. effective doses) of 100 mSv or less will not cause detectable deterministic effects in the embryo or fetus, with the possible exception of the induction of small head size with a threshold perhaps as low as 50 mSv...If the dose to the embryo, fetus, or nursing child from an unintended exposure is less than or equal to an effective dose of 50 mSv, there is no harm from deterministic effects and the risk of stochastic effects is less than one percent." The data in this study indicate that a dose exceeding 50 mSv will rarely be encountered in routine practice.

We also performed radiation dose estimates for *all* of the radiopharmaceuticals reported to be administered to women of childbearing years. In the cases in which information was not available on placental crossover, we calculated fetal doses at all stages of pregnancy just from activity in the mother's organs. While these estimates may represent an underestimate of the fetal doses in cases in which significant placental crossover does occur, we feel that the numbers should be used until information on placental crossover becomes available. The numbers surely represent an improvement over the dose to the ovaries, nongravid uterus, or other surrogate that may have been used in the

past, especially in later stages of pregnancy.

This work considers only the average dose to the fetus, assuming that any activity within the fetus is uniformly distributed throughout the fetal tissues. If a radiopharmaceutical crosses the placenta, it is reasonable to assume that it may concentrate in certain fetal organs and give a dose to those organs which is higher than the average fetal dose reported here. Dyer and Brill (17) gave estimates of fetal liver and spleen dose from uptake of Fe-59 in the fetus in studies involving the administration of Fe-59 to pregnant women at Vanderbilt University in the 1940's, and these were recently reevaluated (46). Watson (21) has developed dose estimates for the fetal thyroid after administration of I-123, I-124, I-125, and I-131 sodium iodide to the mother. In one of the literature studies reviewed in this work (11), an image of a pregnant woman given Tc-99m MDP seemed to indicate uptake in the fetal skeleton. No models currently exist for the fetus in which individual fetal organs are described; this awaits future study. One can obtain some estimates of the dose to fetal organs from self-irradiation only using simple models such as spheres; however estimates of the uptakes and clearance half-times in the fetal organs for different pharmaceuticals cannot presently be determined. It is also possible in some cases that the radionuclide may cross the placenta in a chemical form other than that administered to the mother. Thus, the development of the dosimetry for individual fetal organs is clearly beyond the scope of this study. The reader should bear in mind, however, that this additional consideration may need to be made in some cases.

REFERENCES

1. Stabin MG, Watson EE, Cristy M, Ryman JC, Eckerman KF, Davis JL, Marshal D and Gehlen MK. Mathematical Models and Specific Absorbed Fractions of Photon Energy in the Nonpregnant Adult Female and at the End of Each Trimester of Pregnancy. (Oak Ridge, Tennessee: Oak Ridge National Laboratory) ORNL/TM-12907, 1995.
2. Loevinger R, Budinger TF and Watson EE. MIRD Primer for Absorbed Dose Calculations. The Society of Nuclear Medicine, New York, 1991.
3. Stabin MG. MIRDOSE - The personal computer software for internal dose assessment in nuclear medicine. J Nucl Med 37:538-546,1996.
4. McAffee JG and Subramanian G. Interpretation of Interspecies Differences in the Biodistribution of Radioactive Agents. HHS Publication FDA 81-8166, In: Proc. Third Radiopharmaceutical Dosimetry Symposium, FDA81-8166 (Oak Ridge, Tennessee: Oak Ridge Associated Universities), pp. 292-306 (1980).
5. United Nations Scientific Committee on the Effects of Atomic Radiation; 1977 Report to the General Assembly, with Annexes. Sources and Effects of Ionizing Radiation. United nations Publication, New York, 1977.
6. Chandra R and Pizzarello D. Fetal radiation dose from some technetium-99m labeled radiopharmaceuticals. Med Phys 9:800, 1982.
7. Watson EE. Radiation dose estimates for the fetus from intakes of gallium citrate by the mother. Radiation Protection Dosimetry 41(2/4):123-126, 1992.
8. ICRP Publication 26, Recommendations of the International Commission on Radiological Protection. The International Commission of Radiological Protection, Pergamon Press, Oxford, England, 1977.
9. Weber DA, Makler PT, Watson EE, Coffey JL, Thomas SR and London J. Radiation Absorbed Dose from Technetium-99m-Labeled Bone Imaging Agents. MIRD Dose Estimate Report No. 13, J Nucl Med 30:1117-1122, 1989.
10. Hedrick WR, DiSimone RN, Wolf BH, and Langer A. Absorbed dose to the fetus during bone

scintigraphy. Radiology 168:245-248, 1988.
11. McKenzie AF, Bud RS, Yang C, Shapiro B and Hicks RJ. Technetium-99m-Methylene Diphosphonate uptake in the fetal skeleton at 30 weeks gestation. J Nucl Med 35:1338-1341, 1994.
12. Palmer AM. Placental transfer of technetium labeled radiopharmaceuticals in the guinea pig. J Nucl Med 35(5): 159P, 1993.
13. ICRP Publication 53, Radiation Dose to Patients form Radiopharmaceuticals. The International Commission of Radiological Protection, Pergamon Press, Oxford, England, 1988.
14. Malone LA and Ennis JT. Dose rates to the fetus from vascular radionuclide studies. In: Nuclear Medicine and Biology Advances, Proceedings of 3rd World Congress of Nuclear Medicine and Biology, C. Raynaud, editor, Pergamon Press, Vol. 3:2969-2972, 1983.
15. Berman M, Braverman LE, Burke J, De Groot L, McCormack KR, Oddie TH, Rohrer RH, Wellman HN and Smith EM. MIRD Dose Estimate Report No. 5: I-123, I-124, I-126, I-130, and I-131 as Sodium Iodide. J Nucl Med 16:857-860, 1975.
16. Aboul-Khair SA, Buchanan TJ, Crooks J and Turnbill AC. Structural and functional development of the human foetal thyroid. Cain Sci 31:415-524, 1966.
17. Dyer NC and Brill AB. Maternal-fetal transport of iron and iodine in human subjects. In: Advances in Experimental Medicine and Biology. Vol 27: Drugs and Fetal Development. MA Klingberg, A Abromovici, and J Chemke, eds. Plenum Press, New York, pp. 351-365, 1972.
18. Evans TC, Kretzchmar RM, Hodges RE and Song CW. Radioiodine uptake studies of the human fetal thyroid. J Nucl Med 8(2):157-165, 1967.
19. Hodges RE, Evans TC, Bradbury JT, and Keettel WC. The accumulation of radioactive iodine by human fetal thyroids. J Cain Endocrine Metab 15:661-667, 1955.
20. Johnson JR. Fetal Thyroid Dose from intakes of radioiodine by the mother. Health Physics 43:573-582, 1982.
21. Watson EE. Radiation Absorbed dose to the human fetal thyroid. In: Fifth International Radiopharmaceutical Dosimetry Symposium. Oak Ridge, Tennessee: Oak Ridge Associated Universities, pp 179-187, 1992.
22. Berman M. Kinetic Models for Absorbed Dose Calculations. The Society of Nuclear Medicine, New York, 1977.
23. Berman M and Weiss MF. Users manual for SAAM (Simulation, Analysis, and Modeling). Version: SAAM27. U.S. Dept of health, Education and Welfare, National Institutes of Health, Bethesda, MD 20014, DHEW Publication No. (NIH) 78-180, 1978.
24. Cloutier RJ, Watson EE, Hayes RL, Nelson B and Smith EM. Radiation absorbed dose from Ga-66, Ga-67, Ga-68, and Ga-72 Citrate. MIRD Dose Estimate Report No. 2. J Nucl Med 14:755-756, 1973.
25. Wegst AV. Factors Affecting Dosimetry in Pregnancy, HHS Publication FDA 81-8166, In: Proc. Third Radiopharmaceutical Dosimetry Symposium, FDA81-8166 (Oak Ridge, Tennessee: Oak Ridge Associated Universities), pp. 421-446 (1980).
26. Lathrop KA, Unpublished data, 1991.
27. Mahon DF, Subramanian G and McAfee JG. Experimental comparison of radioactive agents for studies of the placenta. J Nucl Med 14:651-659, 1973.
28. Atkins HL, Robertson JS, Croft BY, Tsui B, Susskind H, Ellis KJ, Loken MK and Treves S. MIRD Dose Estimate Report No. 9. J Nucl Med 21(5):459-465, 1980.
29. Hilyer MJ and Snyder WS. Estimates of dose from xenon-133 to infants and children for immersion in an infinite cloud and for medical uses. In Health in the Healing Arts, Proceedings of the Seventh Midyear Topical Symposium of the Health Physics Society, San Juan, Puerto

Rico, 1972. U.S. Department of Health, Education, and Welfare, Rockville, MD; 131-140, 1973.
30. Krahwinkel W, Herzog H and Feinendegen LE. Pharmacokinetics of thallium-201after routine myocardial scintigraphy. J Nucl Med 29:1582-1586, 1988.
31. Wegst AV and Davis JM. Anatomy and physiology of the embryo, fetus and placenta. Radiat Protect Dosim Int J Nucl Med & Biol Vol. 41 No. 2/4 pp. 103-110, 1992.
32. Thomas SR, Atkins HL, McAfee JG, et al. MIRD Dose Estimate Report No. 12: Radiation absorbed dose from ^{99m}Tc diethylenetriaminepentaacetic acid (DTPA). J Nucl Med 25:503-505, 1984.
33. Griffith D, Alexander M, Gelman R, and Kotlyarov E. Normal uptake in a gravid uterus on Tc-99m DTPA imaging. Clinical Nuclear Medicine 17(9):736-7, 1992.
34. Atkins HL, Weber DA, Susskind Hand and Thomas SR. MIRD Dose Estimate Report No. 16: Radiation absorbed dose from Tc-99m diethylenetriaminepentaacetic acid aerosol. J Nucl Med 33:1717-1719, 1992.
35. International Commission of Radiological Protection. Limits for Intakes of Radionuclides by Workers. Oxford: Pergamon Press; ICRP Publication 30, Part 1, Vol 3/4, 1979.
36. Stabin MG and Watson EE. An alternative to convolution integrals for radiation absorbed dose calculations. In: Fifth International Radiopharmaceutical Dosimetry Symposium. Oak Ridge, Tennessee: Oak Ridge Associated Universities, pp 457-464, 1992.
37. Atkins HL, Cloutier RJ, Lathrop KA, Freeman LM, McAfee JG, Nelp WB, Patton DD and Smith EM. MIRD Dose Estimate Report No. 3: Technetium-99m-sulfur colloid in various liver conditions. J Nucl Med 16:108A-108B, 1975.
38. Chandra R, Personal conversation, March 1995.
39. Lathrop KA, Atkins HL, Berman M, Hays MT and Smith EM. Technetium-99m as sodium pertechnetate. MIRD Dose Estimate Report No. 8, J Nucl Med 17:74-77, 1976.
40. Wegst AV, Goin JE and Robinson RG. Cumulated activities determined from biodistribution data in pregnant rats ranging from 13 to 21 days gestation. I. Tc-99m Pertechnetate. Med Phys 10(6):841-845, 1983.
41. Palmer AM. Personal conversation, February 1995.
42. Atkins HL, Thomas SR, Buddemeyer U, and Chervu LR. MIRD Dose Estimate Report No. 14: Radiation absorbed dose from technetium-99m-labeled red blood cells, J Nucl Med 31:378-380, 1990.
43. Arnold RW, Subramanian G, McAfee JG, Blair R and Thomas FD. Comparison of ^{99m}Tc complexes for renal imaging. J Nucl Med 16:357-367, 1975.
44. Russell JR, Stabin MG, Sparks RB and Watson EE. Radiation absorbed dose to the embryo/fetus from radiopharmaceuticals. Health Physics 73(5):756-759, 1997.
45. Considerations Regarding the Unintended Radiation Exposure of the Embryo, Fetus or Nursing Child. NCRP Commentary No. 9, 17pp, 1994.
46. Stabin MG, Stubbs JB and Russell JR. Review of the radiation doses received by infants irradiated in-utero in Fe-59 Studies at Vanderbilt University in the 1940's. Health Phys 72(5):1-7, 1997.

QUESTIONS

Mattsson: The absorbed dose within a fetus may sometimes be very nonuniform. Does your study also include uptake and absorbed doses for individual fetal organs like the thyroid?

Stabin: Yes, absolutely. We did not perform new calculations on fetal thyroid dosimetry, as this was very nicely done by Evelyn Watson at the last symposium. But I agree with you that this may be important. We will include Evelyn's fetal thyroid doses in our published works, and one can perform dose estimates for individual fetal organs (as did Drs. Dyer and Brill for fetal spleen and liver for the Vanderbilt Fe-59 patients). The difficulty of course is in assigning the biokinetic parameters.

COMPARISON OF THE EFFECTIVENESS OF SOME COMMON ANIMAL DATA SCALING TECHNIQUES IN ESTIMATING HUMAN RADIATION DOSE

Sparks RB[1] and Aydogan B[2]
[1]Oak Ridge Institute for Science and Education
[2]University of Florida, Gainesville

ABSTRACT

In the development of new radiopharmaceuticals, animal studies are typically performed to get a first approximation of the expected radiation dose in humans. This study evaluates the performance of some commonly used data extrapolation techniques to predict residence times in humans using data collected from animals. Residence times were calculated using animal and human data, and distributions of ratios of the animal results to human results were constructed for each extrapolation method. Four methods using animal data to predict human residence times were examined: (1) using no extrapolation, (2) using relative organ mass extrapolation, (3) using physiological time extrapolation, and (4) using a combination of the mass and time methods. The residence time ratios were found to be log normally distributed for the nonextrapolated and extrapolated data sets. The use of relative organ mass extrapolation yielded no statistically significant change in the geometric mean or variance of the residence time ratios as compared to using no extrapolation. Physiologic time extrapolation yielded a statistically significant improvement ($p < 0.01$, paired t test) in the geometric mean of the residence time ratio from 0.5 to 0.8. Combining mass and time methods did not significantly improve the results of using time extrapolation alone.

INTRODUCTION

Preclinical animal studies are used in the development of new radiopharmaceuticals with the goal of determining a first approximation of radiation dose in humans. In previous attempts to use animal data for human dosimetry estimation, various data extrapolation techniques have been applied to compensate for the differences in metabolism, anatomy and biodistribution of radiopharmaceuticals between animals and humans. Success of these extrapolations for various radiopharmaceuticals have varied widely. This leaves the usefulness of animal data to predict human dosimetry in question. No comprehensive study of the general effectiveness of animal extrapolation for dosimetry purposes has been performed. This study will evaluate the performance of some commonly used data extrapolation techniques to predict residence times (which are directly proportional to organ self-doses) in humans using data collected from animals. Residence times were calculated using animal and human data, and distributions of ratios of the animal results to human results were constructed for each extrapolation method. Four methods using animal data to predict human residence times were examined: (1) using no extrapolation, (2) using relative organ mass extrapolation, (3) using physiological time extrapolation, and (4) using a combination of the mass and time methods. Direct use of animal data

simply assumes that the percent of injected activity (%IA) at any time in the human organ is the same as in the animal organ. Relative organ mass scaling is based on the assumption that the uptake of activity in human organs is related to uptake in animal organs by a function of total body mass fractions of the organs in animals and humans. Physiological time scaling scales the time axis based on some measure of relative metabolic rates. The combination method applies both the mass and time extrapolations to the animal data. Methods that require data in more than one animal species to predict human organ self dose were not considered in this study, since biodistribution data for dosimetry purposes often is only gathered in one animal species before proceeding to human trials.

METHODS

Organ time-activity data for animals and humans from radiopharmaceuticals labeled with H-3, F-18, Se-75, Tc-99m, In-111, I-123, I-125, I-131, Sn-117m, Re-186, and Tl-201 were gathered from the literature [1-42] and from the files at the Radiation Internal Dose Information Center (RIDIC). These included, but were not limited to, brain imaging agents, myocardial imaging agents, renal imaging agents, bone imaging agents, lung perfusion agents, pain palliation agents, vascular agents, tumor localization agents, and blood pool imaging agents. Data from 33 different radiopharmaceuticals in a total of 115 organs were used in this study. Data were only used when organ time-activity data for a particular radiopharmaceutical were available for both animals and humans. Data were also limited to cases where the time-activity curve was adequately defined for the purpose of estimating residence time in the organ. The residence times based on the human data were calculated with the same method as described below for the direct use of animal data.

Direct use of Animal Data

The data were converted to %IA per organ in the animal, decay corrected if necessary, and fit with a sum of exponentials as shown in Equation 1.

$$A_{ne}(t) = A_0 \sum_{i=1}^{N} C_i e^{-\lambda_i t}, \tag{1}$$

where:

A_{ne} is the animal organ activity as a function of time without extrapolation,
A_0 is the initial injected activity,
λ_i is the biological removal rate, and
C_i is the fraction associated with each exponential term.

The cumulated activities per unit injected dose or "residence times" were then calculated using Equation 2.

$$\tau_{ne} = \frac{\tilde{A}_{ne}}{A_0} = \sum_{i=1}^{N} \frac{C_i}{\lambda_i + \lambda_R} \tag{2}$$

Relative Organ Mass Scaling

In relative organ mass scaling, the %IA in the human organ is assumed to be equal to the ratio of the fraction of the total body mass of the organ in the human to the fraction of the total body mass of the organ in the animal multiplied by the % IA in the animal organ. [43,44]

$$\%\ \text{ID Human organ} = \%\ \text{ID Animal Organ} \frac{\left[\frac{\text{Organ Mass}_{Human}}{\text{Body Mass}_{Human}}\right]}{\left[\frac{\text{Organ Mass}_{Animal}}{\text{Body Mass}_{Animal}}\right]} \tag{3}$$

Thus, if the human brain is four times larger as a fraction of total body mass then the rat brain, the human brain is assumed to have a percent injected dose uptake four times greater than the rat brain.

The residence times for the relative organ mass scaling can be found in the same manner as with the unextrapolated data, using equations of the form of Equation 1 and Equation 2. However, the residence time for the relative organ mass scaling procedure can also be calculated without refitting the scaled data. This is done by multiplying the residence time for the unscaled data by the mass scaling factor k_{me}. This is shown by the following:

mass scaled activity in the organ, $A_{me}(t)$, is equal to

$$A_{me}(t) = k_{me} A_{ne}(t), \tag{4}$$

where the relative organ mass scaling factor k_{me} is equal to

$$k_{me} = \frac{\left[\frac{\text{Organ Mass}_{Human}}{\text{Body Mass}_{Human}}\right]}{\left[\frac{\text{Organ Mass}_{Animal}}{\text{Body Mass}_{Animal}}\right]}. \tag{5}$$

Thus,

$$\tilde{A}_{me} = \int A_{me}(t)dt = \int k_{me} A_{ne}(t)dt = k_{me} \int A_{ne}(t) = k_{me} \tilde{A}_{ne} \tag{6}$$

Dividing this expression by A_0, the initial administered activity, yields a similar expression for residence time.

$$\tau_{me} = k_{me} \tau_{ne}. \tag{7}$$

Physiological Time Scaling

The physiological time scaling method used in this study is based on the assumption that many physiological functions across various animal species are related as a function of total body mass. This has been shown for heart rate, breathing rate, clearance half lives, and many other physiological processes [45-54]. The method used in this study was the equivalent time concept as introduced by Dedrick [55]. In this method, the time axis is scaled by a power function of the ratio of the total body masses of the human and animal.

$$t_{Human} = t_{Animal}\left[\frac{\text{body mass}_{Human}}{\text{body mass}_{Animal}}\right]^{\frac{1}{4}} \tag{8}$$

As in the mass scaling method, the residence time for the time scaled data can be calculated without refitting the data. It is slightly more complex, since instead of just a direct scaling of the residence time, the time extrapolated residence time must be calculated using the parameters of the fit for the nonextrapolated data. The physiologically scaled time, t_{te}, is found using

$$t_{te} = k_{te} t_{ne}, \tag{9}$$

where

$$k_{te} = \left[\frac{\text{body mass}_{Human}}{\text{body mass}_{Animal}}\right]^{\frac{1}{4}}. \tag{10}$$

Using the above relationships, an expression for the physiological time-scaled cumulated activity can be derived. The activity levels are not scaled in the physiological time-scaling method. Thus,

$$A(t_{te}) = A(t_{ne}). \tag{11}$$

From Equation 1 it follows that:

$$A(t_{te}) = C_1 e^{-\lambda_{b_1} t_{ne}} e^{-\lambda_R t_{te}} + C_2 e^{-\lambda_{b_2} t_{ne}} e^{-\lambda_R t_{te}} + \ldots + C_N e^{-\lambda_{b_N} t_{ne}} e^{-\lambda_R t_{te}}. \tag{12}$$

Next, substituting $t_{ne} = \frac{t_{te}}{k_{te}}$ from Equation 9 yields

$$A(t_{te}) = C_1 e^{-\lambda_{b_1} k_{te}^{-1} t_{te}} e^{-\lambda_R t_{te}} + C_2 e^{-\lambda_{b_2} k_{te}^{-1} t_{te}} e^{-\lambda_R t_{te}} + \ldots + C_N e^{-\lambda_{b_N} k_{te}^{-1} t_{te}} e^{-\lambda_R t_{te}}. \quad (13)$$

Integrating this yields an expression for the physiological time-scaled residence time.

$$\tau_{te} = \frac{\tilde{A}_{te}}{A_0} = \frac{C_1}{\lambda_{b_1} k_{te}^{-1} + \lambda_R} + \frac{C_2}{\lambda_{b_2} k_{te}^{-1} + \lambda_R} + \ldots + \frac{C_N}{\lambda_{b_N} k_{te}^{-1} + \lambda_R}. \quad (14)$$

Simultaneous Relative Organ Mass Scaling and Physiological Time Scaling

In this case the activity is scaled as in the relative organ mass-extrapolation method, and the time axis is scaled as in the physiological time-extrapolation method. The residence time for this extrapolation technique is found by multiplying the time extrapolation residence time by the mass scaling factor k_{me}.

$$\tau_{tme} = k_{me} \tau_{te} \quad (15)$$

An alternate method would be to fit the extrapolated data using equations of the form of Equation 1 and Equation 2 in order to determine the residence times.

RESULTS

The animal residence times for each organ with each radiopharmaceutical using the various extrapolation methods were normalized using the residence time found using human data for the same organ. The normalized residence times for each extrapolation method were then formed into bins and the resulting distributions were analyzed. Figures 1 through 4 show the histograms for the normalized residence times. The residence time ratios using the raw animal data had a geometric mean of 0.45 with a variance of 16.8. The residence time ratios from the mass extrapolated animal data had a geometric mean of 0.43 with a variance of 16. The residence time ratios using the time extrapolated animal data had a geometric mean of 0.79 with a variance of 14.4.And finally, the residence time ratios using the time and mass extrapolated animal data had a geometric mean of 0.79 with a variance of 12.2. Appropriate statistical tests were applied to the distributions to determine distribution form, and to compare the mean and variance estimates. The "Crystal Ball" software [56] was used to determine what percentage of the residence time estimations fell within various limits as shown in Tables 1-3.

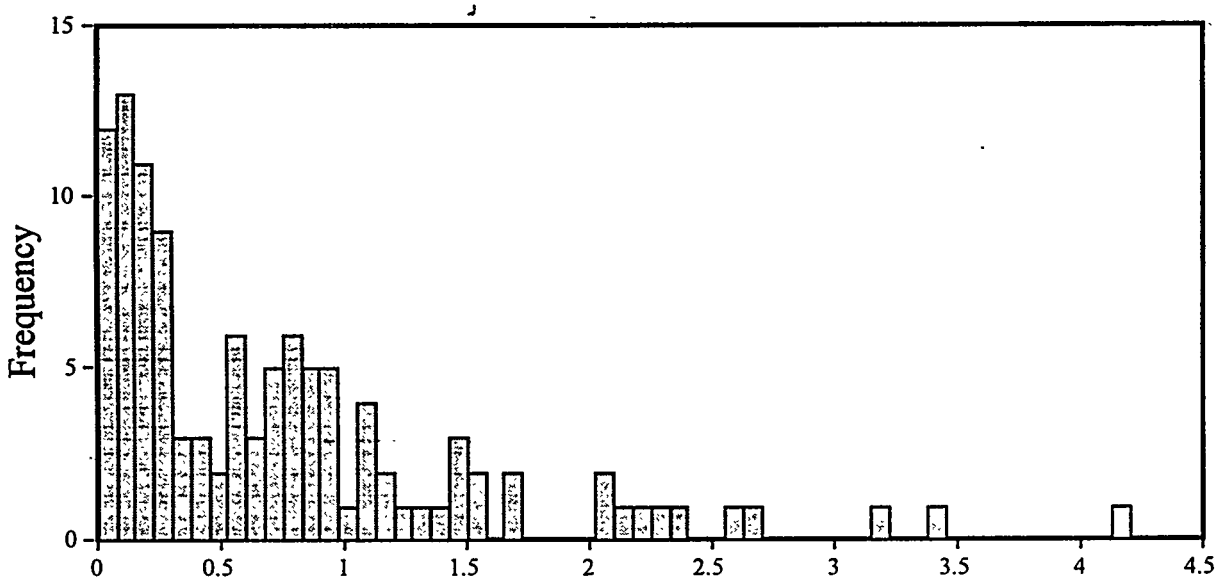

Figure 1. Frequency distribution of the ratio of the organ residence times found using the raw animal data to the residence times found using data from humans.

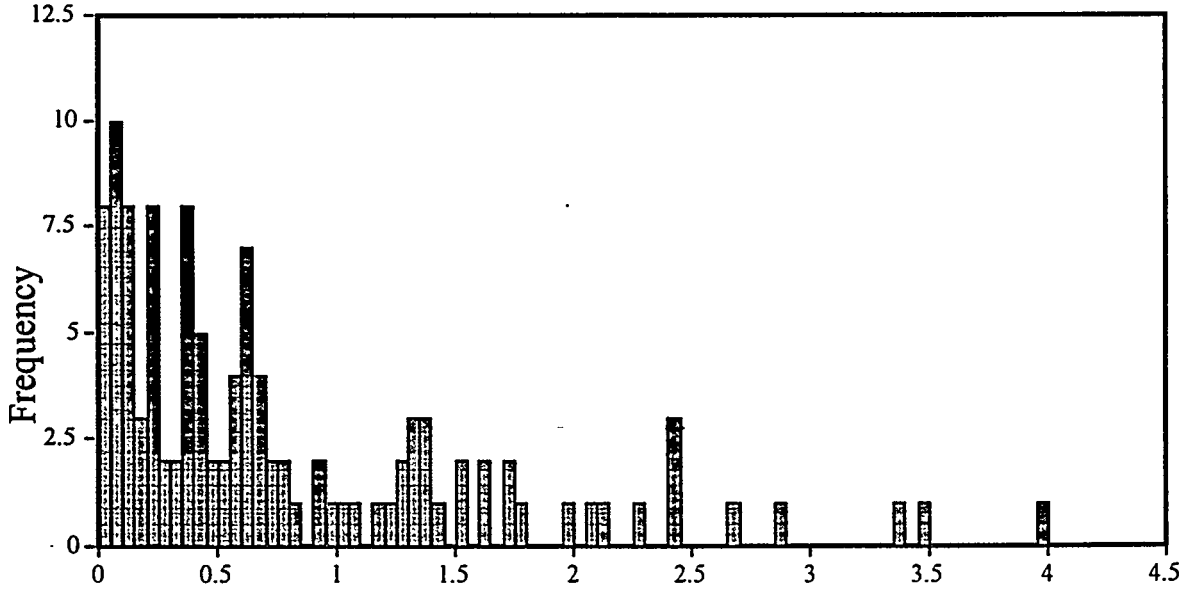

Figure 2. Frequency distribution of the ratio of the organ residence times found using the mass extrapolated animal data to the residence times found using data from humans.

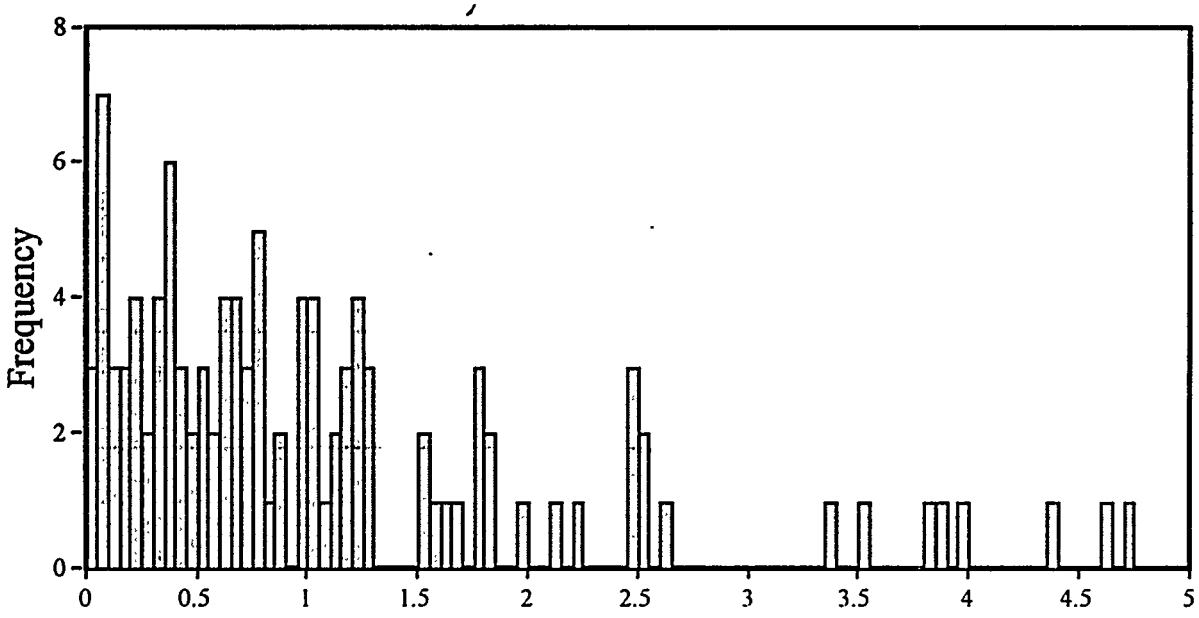

Figure 3. Frequency distribution of the ratio of the organ residence times found using the time extrapolated animal data to the residence times found using data from humans.

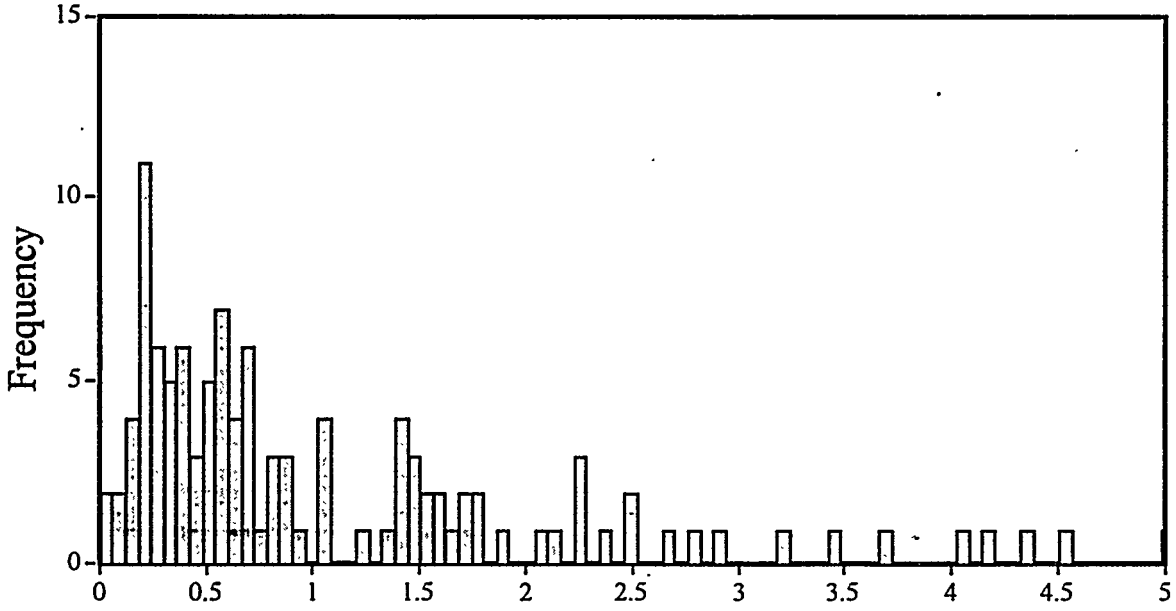

Figure 4. Frequency distribution of the ratio of the organ residence times found using the time and mass extrapolated animal data to the residence times found using data from humans.

Table 1
Percentage of Residence Times(or Organ Self Doses) Predicted with Animal Data that Were Successful within the Given Bounds

Extrapolation Type	Percentage Predicted Within Limits					
	±25%	±50%	±2x	±4x	±10x	±20x
None	18%	30%	39%	62%	84%	92%
Mass	8%	18%	40%	66%	85%	93%
Time	21%	32%	50%	74%	88%	91%
Time and Mass	8%	21%	46%	79%	94%	97%
Crawford CEDE†	32%	51%	59%	80%	92%	95%

Committed effective dose equivalents(Cedes) calculated by Crawford [57] in a smaller species that predicted the Cedes in a larger species.

Table 2
Percentage of Underestimation of Human Residence Times (or Organ Self Doses) as Predicted with Animal Data

Extrapolation Type	Percent Underestimates						
	>25%	>50%	>2x	>4x	>10x	>20x	Total
None	62%	54%	45%	34%	13%	6%	72%
Mass	67%	63%	49%	32%	14%	6%	70%
Time	50%	40%	31%	18%	7%	7%	60%
Time and Mass	56%	51%	34%	13%	3%	0%	62%

Table 3
Percentage of Overestimation of Human Residence Times (or Organ Self Doses) as Predicted with Animal Data

Extrapolation Type	Percent Overestimates						
	>25%	>50%	>2x	>4x	>10x	>20x	Total
None	21%	16%	13%	4%	2%	0%	28%
Mass	24%	17%	11%	1%	0%	0%	30%
Time	27%	27%	17%	6%	3%	0%	40%
Time and Mass	34%	26%	18%	6%	1%	1%	36%

DISCUSSION

The results of the search for data were disappointing. Insufficient data were found to investigate the total organ dose from all contributors in the body. Performing this analysis with complete data sets could possibly change the results. The results from Crawford listed in Table 1 might be an indication of how the results could change. However, since much of Crawford's data concerned extrapolation between various animal species, it could also indicate that extrapolation between various animal species is more reliable than extrapolation between animals and humans.

The original plan in this study included consideration of specific organs or species in terms of their performance using the given extrapolation techniques. However, insufficient data were found to evaluate these topics. The results might have changed if these analyses could have been performed.

The significance tests indicate that using time extrapolation improves the mean result. However, there appears to be some increase in severe overestimates (>10x) with the time extrapolation method. No statistically significant improvement was found using the relative organ mass extrapolation.

The log normal distribution along with the relatively large variances seen in this study indicate that extreme care should be taken when using animal data to predict results in humans when using the given extrapolation methods. This study indicates that the most likely result (the mode) of using the animal data directly or using relative organ mass extrapolation is a tenfold underestimation of the radiation exposure (self dose) in a specific organ. Using the time extrapolation reduces this to about a factor of 6 underestimation. Future work might investigate the effect of use of powers other than 1/4 in the time extrapolation method. It also might be possible to show that dose escalation procedures in human subjects would be able to provide the necessary biodistribution information without excessive radiation exposures in the human subjects, thus eliminating the need for reliance on animal data.

ACKNOWLEDGMENTS

The authors would like to thank Richard Toohey, Mike Stabin, John Melograna, Prantika Som, Andrew Wright, Roger Pickett, Bendi Lowery, Fanny Smith and Audrey Stelson for their assistance in this work.

REFERENCES

1. Arnold RW et al. Comparison of Tc-99m complexes for renal imaging. J Nucl Med 16(5):357-367, 1975.
2. Bossuyt A et al. Technetium-99m MRP20, a potential brain perfusion agent: In vivo biodistribution and SPECT studies in normal male volunteers J Nucl Med 32:399-403, 1991.
3. Bradley-Moore PR et al. Thallium-201 for medical use II: Biologic behavior J Nucl Med 16(2):156-160, 1975.
4. Chumpradit S et al. Fluorinated and iodinated dopamine agents: D2 imaging agents for PET and SPECT agents: D2 imaging agents for PET and SPECT. J Med Chem 36:221-228, 1993.
5. Doherty JE et al. The distribution and concentration of triated digoxin in human tissues. Ann Inter. Med. 66(1):116-124, 1967.
6. Ercan MT et al. Evaluation of Tc-99m dextran as a lymphoscintigraphic agent in rabbits. Eur J Nucl Med 11(2/3):80-84, 1985.
7. Frondoza CG et al. Metabolism of guanido-labeled(C-14) arginine in rats mice and man. J Nucl Med 21:52-58, 1980
8. Gallagher BM et al. Radiopharmaceuticals XXVII. F-18 labeled 2-deoxy-2-fluoro-D-glucose as a radiopharmaceutical for measuring regional myocardial glucose metabolism in vivo: Tissue

distribution and imaging studies in animals. J Nucl Med 18:990-996, 1977.
9. Goldstein DS et al. Dosimetric estimates for clinical positron emission tomographic scanning after injection of [F-18]-6-fluorodopamine. J Nucl Med 32:102-110, 1991.
10. Henze E et al. Tc-99m dextran: A new blood pool labeling agent for radionuclide angicardiography. J Nucl Med 23:348-353, 1982.
11. Higley B et al. Technetium-99m-1,2-bis[bis(2-ethoxyethyl) phosphino]ethane: Human biodistribution, dosimetry and safety of a new myocardial perfusion imaging agent. J Nucl Med 34:30-38, 1993.
12. Iturralde M, Reenen OR, Lötter MG et al. Clinical evaluation and dosimetry of Se-75 renal tubular pharmaceuticals. Proceed of IAEA and WHO sponsored Symp., Heidelberg, 1980, IAEA-SM-247/34, pp 363-376, 1981.
13. Kelly JD et al. Technetium-99m-tetrofosmin as a new radiopharmaceutical for myocardial perfusion imaging. J Nucl Med 34:222-227, 1993.
14. Klopper JF, Atkins HL. Tissue distribution of tritiated digoxin and ouabain in mice. BNL 22309, 1976.
15. Krahwinkel W et al. Pharmacokinetics of thallium-201 in normal individuals after myocardial scintigraphy. J Nucl Med 29:1582-1586, 1988.
16. Kubo A et. al. Indium-11-labelled liposomes, dosimetry and tumour detection in patients with cancer. Eur J Nucl Med 20:107-113, 1993.
17. Kung HF et al. A new brain perfusion imaging agent:[I-123]HIPDM:N,N,N'-trimethyl-N'-[2-hydroxy-3-methyl-5-iodobenzyl]-1,3-propanediamine. J Nucl Med 24:66-72, 1983.
18. Kung MP et al. The characterization of IBF as a new selective dopamine D-2 receptor imaging agent. J Nucl Med 31:648-654, 1990.
19. Leeb. J, Baumgartner WA, Lyons K and Lorber A. Uptake, distribution and excretion of sodium selenite in rheumatoid subjects. In: ERDA Symposium Series, pp 536-546, Biological Implications of Metals in the Environment, 1975.
20. MacGregor RR et al. 6-F-18 fluorodopamine as a potential adrenal scanning agent. J Nucl Med 15:6:513, 1974.
21. MIRD Dose Estimate Report No. 1 - Summary of current radiation dose estimates to humans from Se-75-selenomethionine J Nucl Med 14(1):49-50, 1973.
22. Morgan GF et al. Technetium-99m MRP20, a potential brain perfusion agent: In vivo biodistribution and SPECT studies in nonprimate animals J Nucl Med 32:500-505, 1991.
23. Moretti JL N-Isopropyl-[I-123]-p-Iodoamphetamine: An Agent for Brain Imaging with Single Photon Emission Computerized Tomography. Functional Radionuclide Imaging of the Brain. Editor: P. Magistretti, Raven Press, NY 1983
24. Narra RK et al. Absorbed radiation dose to humans from Tc-99m teboroximine. J Nucl Med 33:88-93, 1992.
25. Narra RK et al. A neutral Tc-99m complex for myocardial imaging. J Nucl Med 30:1830-1837, 1989.
26. Norets TA, VF Stepanenko and VP Komarov. Dose loads and genetic effects induced by single injection of selenomethionine containing small amounts of Se-75 report 1: Analysis of Distri. Radiobiology XVIII(6):87-94, 1978.
27. Othman I, Spyrou NM and Khan RAA. Study of the dose and distribution of technetium-99m-MDP in various bones and tissues. In: Proceedings of an International Symposium on Medical Radionuclide Imaging Organized by the International Atomic Energy Agency in Co-operation with the World Health Organization and held in Heidelberg, 1-5 September 1980, pp 599-612, IAEA-SM-247/113, Vol I, 1981.
28. Reske SN et al. 15(p-[I-123]iodophenyl)pentadecanoic acid as tracer of lipid metabolism:

Comparison with[1-C-14]palmitić acid in murine tissues. J Nucl Med 25:1335-1342, 1984.
29. Robbins PJ, Silberstein EB and Fortman DL. ^{111}In-bleomycin kinetics in mice bearing transplantable tumors of lung, skin and bone. J Nucl Med 15(4):273-277, 1974.
30. Seibyl JP et al. Whole-body biodistribution, radiation absorbed dose and brain SPECT imaging with I-123-b-CIT in healthy human subjects. J Nucl Med 35:764-770, 1994.
31. Soundy RG et al. The radiation dosimetry of Tc-99m exametazine. Nucl Med Comm 11:791-799, 1990.
32. Srivastava SC et al. The development and in-vivo behavior of tin containing radiopharmaceuticals I. Chemistry, preparation, and biodistribution in small animals. Int J Nucl Med Biol 12(3):167-174, 1985.
33. Srivastava SC, Richards P, Meinken GE, Som P, Knapp FF, Jr and Butler TA. In-vivo behavior of tin-117m(2+ and 4+)-labeled DTPA and MDP. Preparation, tissue distribution in mice and imaging in dogs. In: Nuclear Medicine and Biology, Proceedings of the Third World Congress of Nuclear Medicine and Biology 8/29-9/2, 1982, Paris, France, edited by: C Raynaud, pp 1635-1638, Pergamon Press, 1982.
34. Stabin MG. The radiation dosimetry of Re-186 HEDP. J Nucl Med 36(5) 180p, 1995.
35. Stabin MG et. al. Radiation dosimetry for technetium-99m-MAG3 technetium-99m DTPA, and iodine-131 OIH based on human biodistribution studies. J Nucl Med 33:33-40, 1992.
36. Stabin MG, Taylor A, Jr., Eshima D and Wooter W. Radiation dosimetry for technetium-99m-MAG_3, technetium-99m-DTPA, and iodine-131-OIH based on human biodistribution studies. J Nucl Med 33:33-40, 1992.
37. Subramanian G, McAfee JG, Blair RJ, Mehter A and Connor T. ^{99m}Tc-EHDP: A potential radiopharmaceutical for skeletal imaging. J Nucl Med 13(12):947-950, 1972.
38. Thakur ML, Merrick MV and Gunasekera SW. Some pharmacological aspects of a new radiopharmaceutical, ^{111}In-bleomycin. Symposium on Radiopharmaceuticals and Labeled Compounds, IAEA, Vol. II, 183-204, 1973.
39. Tse FLS, Jaffe JM. Preclinical Drug Distribution, A Laboratory Handbook. Marcel Dekker Inc., 1991.
40. Vallabhajosula S et al. Tc-99m ECD: A new brain imaging agent: In vivo kinetics and biodistribution studies in normal human subjects J Nucl Med 30:599-604, 1989.
41. Weber DA, Keyes, JW, Jr and Wilson GA. Significant differences among the ^{99m}Tc-polyphosphates, ^{99m}Tc-pyrophosphates and ^{99m}Tc-diphosphonates for bone imaging. In: Critical Reviews in Clinical Radiology and Nuclear Medicine. edited by Y Wang, J Edeiken and MK Loken, pp 369-390, CRC Press, Inc. 1977.
42. Williams ED, Merrick MV and Lavender JP. The distribution and dosimetry of ^{111}In-bleomycin in man. Brit J Radiol 48:275-278, 1975.
43. Kirschner AS et al. Radiation dosimetry of I-131-iodocholesterol: The pitfalls of using tissue concentration data - the author's reply. J Nucl Med 16(3):248-249, 1975
44. Crook JE et al. Radiation dose estimates for copper-64 citrate in man. In: Fourth International Radiopharmaceutical Dosimetry Symposium Proceedings, CONF-851113, p:212-215, 1985.
45. Animal Models in Radiotracer Design. Edited by RM Labrecht and WC Eckelman, Springer-Verlag, New York, Berlin, Heidelberg, Tokyo, 1983.
46. Boxenbaum H. Time concepts in physics, biology, and pharmacokinetics. J Pharm Sci 75(11):1053-1062, 1986.

47. Boxenbaum H. Interspecies scaling, allometry, physiological time, and the ground plan of pharmacokinetics. J Pharmacokin and Biopharm 10(2) 201-227, 1982.
48. Conney AH, Coutinho C, Koechlin B, Swarm R, Cheripko JA, Impellizzeri C and Baruth BS. From animals to man: Metabolic considerations. Clin Pharmacol & Therapeutics 16:176-182, 1974.
49. Lathrop KA, Tsui BMW, Chen C-T and Harper PV. Multiparameter extrapolation of biodistribution data between species. Health Physics 57(1):121-126, 1989.
50. McAfee JG and Subramanian G. Interpretation of interspecies differences in the biodistribution of radioactive agents. In: Proceedings of Third International Radiopharmaceutical Dosimetry Symposium held in Oak Ridge, TN, 10/7-10, 1980, edited and compiled by EE Watson, AT Schlafke-Stelson, JL Coffey and RJ Cloutier, pp 292-306, HHS Publication FDA 81-8166, 1981.
51. Mordenti J. Man versus Beast: Pharmacokinetic scaling in mammals. J Pharm Sci 75(11):1028-1040, 1986
52. Travis CC. Interspecies Extrapolation. CONF-8806280--1, DE89 002208, Oak Ridge National Laboratory, Oak Ridge, TN, 1988.
53. Tsui BMW, Lathrop KA and Harper PV. Extrapolation from animals to the human for the retention of radiothallium in the blood. In: Proceedings of Third International Radiopharmaceutical Dosimetry Symposium held in Oak Ridge, TN, 10/7-10, 1980, edited and compiled by EE Watson, AT Schlafke-Stelson, JL Coffey and RJ Cloutier, pp 283-291, HHS Publication FDA 81-8166, 1981.
54. Yates FE, Kugler PN. Similarity principles and intrinsic geometries: Contrasting approaches to interspecies scaling. J Pharm Sci 75(11) 1019-1027, 1986.
55. Dedrick RL et al. Interspecies correlation of plasma concentration history of methotrexate. Cancer Chemother Reports Part 1, 54:95-101, 1970.
56. Crystal Ball 3.0 Forecasting and Risk Analysis for Spreadsheet Users, Decisioneering, 1993.
57. Crawford DJ and Richmond CR. Epistemological considerations in the extrapolation of metabolic data from nonhumans to humans. In: Proceedings of Third International Radiopharmaceutical Dosimetry Symposium held in Oak Ridge, TN, 10/7-10, 1980, edited and compiled by EE Watson, AT Schlafke-Stelson, JL Coffey and RJ Cloutier, pp 181-197, HHS Publication FDA 81-8166, 1981.
58. Pharmacokinetics: Regulatory-Industrial-Academic-Prospectives. In: Drugs and Pharmaceutical Sciences, Vol 33, edited by PG Welling and FLS Tse, 1988.
59. Calabrese EJ. Animal extrapolation and the challenge of human heterogeneity. J Pharmaceutical Sci 75(11):1041-1046, 1986.
60. Thomas JM and Eberhardt JM. Can results from animal studies be used to estimate dose or low dose effects in humans? In: Proceedings of Third International Radiopharmaceutical Dosimetry Symposium held in Oak Ridge, TN, 10/7-10, 1980, edited and compiled by EE Watson, AT Schlafke-Stelson, JL Coffey and RJ Cloutier, pp 259-282, HHS Publication FDA 81-8166, 1981.
61. Thomas JM and Eberhardt LL. Extrapolation of Animal Radionuclide Retention Data to Man--The Use of Similarity Ratios. BNWL-SA-5366, 1973.
62. Calabrese EJ. Animal extrapolation - a look inside the toxicologist's black box. Environ Sci Technol 21(7):618-623, 1987.
63. Boxenbaum H and Fertig JB. Scaling of antipyrine intrinsic clearance of unbound drug in 15 mammalian species. Europ J of Drug Metabolism & Pharmacokinetics 9(2):177-183, 1984.

RADIATION DOSIMETRY ESTIMATES IN ANIMALS FOR DMP 444, A NEW THROMBUS-IMAGING AGENT

Lazewatsky J, Barrett JA, Bresnick M, Crocker A, Edwards DS, Harris AR, Kagan M, Liu S, Mazaika T, Ziegler MC and Carroll TR
Dupont Merck Pharmaceutical Co., Radiopharmaceutical Division
North Billerica, Massachusetts 01862

ABSTRACT

Preclinical studies using gamma camera imaging were performed using five rhesus monkeys to provide initial estimates of the radiation dosimetry of DMP 444, a new Tc-99m-labeled agent for the localization of intravascular thrombi. Each animal was initially anesthetized using ketamine-acepromazine and maintained thereafter with halothane. Following acquisition of an image using a collimated Tc-99m flood source, the animal was placed on the table and spot transmission images covering the whole body, with overlap, were obtained. The source was then removed, and, with no other change in the preparation, the animal was injected with DMP 444 (37 MBq per Kg). Spot images covering the whole body with overlap were obtained from both the anterior and posterior aspects over the next 6 hours and at 24 hours. Spot views were combined to produce whole-body images and regions drawn for all identifiable organs, plus appropriate background areas and whole-body. Urine and feces were not collected as whole-body data was obtained and prototype studies had indicated that there was no significant fecal excretion of the compound. This was confirmed in these experiments by virtue of the absence of measurable radioactivity in the gastrointestinal tract at all time points. Time-activity curves derived from region-of-interest data were fitted to multi-term exponential functions using Microsoft Excel and residence times obtained by substitution into the appropriate analytic expression. Correction for species was made using a metabolic rate method. As the animals did not urinate during the initial 4 to 6 hours of the study, good estimates of urinary kinetics could be obtained from time-activity data of the bladder. Radiation dose estimates were calculated using MIRDOSE 3.0. Results indicated that, for a two-hour voiding interval, the critical organ is the spleen with a dose of 0.038 mGy/MBq (0.140 rad/mCi). The whole-body dose under these conditions is estimated to be 0.00330 mGy/MBq (0.0122 rads/mCi). Using a 4.8-hour voiding interval, the urinary bladder becomes the critical organ, with a dose of 0.0040 mGy/MBq (0.148 rads/mCi). It is estimated that a 1220 MBq (33 mCi) injected dose yields a radiation dose of 50 mGy or less to the critical organ and no more than 30 mGy to any radiation-sensitive organ. Other organs containing moderate activity concentrations included the kidneys, lung, heart contents, and liver.

INTRODUCTION

This study provides an estimate of the radiation dose to patients during diagnostic procedures

using the thrombus-avid agent, DMP 444 . It is also intended to determine the injected (radioactivity) dose below which no radiosensitive organ receives more than 30 mGy and no other organ receives more than 50 mGy. The study uses biodistribution data obtained by gamma camera imaging of DMP 444 in monkeys. This study is intended to contribute to a demonstration of safety prior to Phase I trials of DMP 444.

DMP 444 is an antagonist for the platelet GPIIb/IIIa receptor that consists of a cyclic RGD (argenine-glycine-aspartic acid) component combined with a linker to a Tc-99m-containing moiety. Although this specific compound has not yet been described in the literature, a description of the chemistry and pharmacology of a similar related compound was recently published (1,2).

Under normal circumstances, platelets circulate through the blood in the resting state. When a thrombotic event occurs, they become activated and rapidly express a series of adhesion receptors and the platelet GPIIb/IIIa receptor site. The goal of our program was to develop a thrombus imaging agent that would detect a rapidly growing thrombus. Based upon its known functionality, the platelet GPIIb/IIIa receptor was chosen as a primary target.

The monkey was chosen for this study due to its size and because its RGD recognition site on the platelet is the most similar to human. The rodent platelet GPIIb/IIIa receptor differs significantly from the human receptor: It has low affinity for RGD containing oligopeptides and does not bind to the C-terminus of the gamma chain of human fibrinogen (3). In addition, similar data has been demonstrated in the rabbit (4).

Although it was possible to use dogs, since the RGD site in these animals is also similar to those of humans, the organ sizes and distributions (in particular, the spleen) are significantly different. We believe that this difference, in an organ likely to sequester a significant fraction of radioactivity under most conditions, made the dog a problematic subject. We also felt that the excretion pathways, which are most critical in the determination of the larger organ radiation doses, were more likely to be similar to humans in non-human primates than in dogs.

Although in-vitro testing indicated that there should be little or no pharmacological effect and no radiation effects on the animals, animal hematology was monitored throughout the course of the study to make certain that no unexpected physiological or pharmacological changes occurred as a result of administration of the test article.

MATERIALS AND METHODS

The complex DMP 444 was prepared by reconstituting lyophilized vials containing the formulation RP444-2A with 1.5 ml of aqueous sodium Tc-99m-pertechnetate and heating for 30 min in an 80 C water bath.

The concentration of the Tc-99m-pertechnetate solution was chosen to provide a 111MBq:1μg (3mCi:1μg) ratio of Tc-99m to starting XV066 (in the lyophilized vial) at the time of administration (typically 1.5 ± 0.75 h after reconstitution), accounting for radionuclidic decay. The material was analyzed by a radio-HPLC method immediately after heating. Just prior to administration, a sufficient volume of the kit was transferred to another vial and diluted to a concentration of 52 MBq/ml with saline to allow 37 MBq/kg to be administered and to retain sufficient sample for HPLC analysis. The retained sample is analyzed by the radio-HPLC method after infusion.

Five male Rhesus Monkeys (Macaca mulatta), 10-14 kg. in weight at dosing, were used. Two of these animals are approximately 11 years old and the other three animals are six years old.

Data Acquisition Procedure

Hematological parameters were monitored via blood samples at intervals beginning as soon after immobilization as was practical and continuing until the animal regained consciousness. Parameters were also monitored at intervals while taking data for the 24-hour time point starting as soon after immobilization as was practical and ending when the animal regained consciousness. Upon completion of the postsetup stabilization period (>30 min), control readings of physiological parameters were recorded. The gamma camera (Picker Digital Dyna Camera) was positioned and centered above a collimated flood source filled with approximately 740 MBq of Tc-99m. The camera energy window was then adjusted using the collimated source so that it was centered on the 140 KeV Tc-99m gamma ray energy with a width of 20% of the center value. A flood image was then taken.

For each animal, whole-body anterior-posterior transmission images were taken by moving the examination table holding the anesthetized animal between the camera and the flood source and acquiring a series of overlapping planar images from the animal's head to its feet. Four such images sufficed and the value of the positioning marker on the table base was noted for each view. This permitted accurate reproduction of the positioning for the emission views. Once this was completed, the flood source was removed. DMP 444 was then administered intravenously as an infusion over one to two minutes at a dose of 37 MBq per Kg body weight.

A series of whole-body image sequences were then acquired on the following schedule, with one "set" of images beginning at each time point following administration; 5, 30, and 45 minutes, 1, 1.5, 2, 3, 4, 6, and 24 hours. Each set of images consisted of eight views, four anterior views and four posterior views each at the track setting defined in the transmissions image. Each view was recorded with a unique name which was entered into the computer file, and the position of the table was recorded to verify proper positioning. The animal was allowed to recover from anesthesia following the 360-minute point and was anesthetized the next day to acquire the 1440-minute point .

Blood samples were taken at the following time intervals: less than 5 minutes prior, and 1.5, 15, 30, 45, 60, 90, 120, 180, 240, 360 and 1440 minutes after injection.

Data Analysis

For each time point, the individual views were assembled into whole-body anterior and posterior images and saved. Regions of interest were drawn for all identifiable organs and for the whole body. If the organ was not specifically visualized by a recognizable shape, then it was assumed that there was no measurable accumulation of radioactivity in that organ at that time. Any radioactivity present at such non-organ-specific locations were included in the whole body region.

Background regions of interest were drawn as necessary, but only where it was deemed necessary to correct a significant contamination of the organ of interest.

For each organ at each time point in each experiment, the organ radioactivity was determined using the following expression (from the work of Eary et al.(5) with modifications for author-confirmed typographic errors in the article):

$$A = \varepsilon f_c \sqrt{I_{ant} I_{post}},$$

where

$$f_c = \sqrt{\frac{I_0}{I}} \text{ (attenuation correction factor),}$$

ε = system sensitivity (MBq/cps),

I_{ant} = average observed count rate (cps) for a given organ from an anterior view,

I_{post} = average observed count rate (cps) for a given organ from the corresponding posterior view,
I = average measured intensity in a given organ for a transmission image, and
I_0 = average measured intensity in the corresponding region in the flood image.

Absolute radioactivity was not determined nor was the parameter ε above determined directly. Rather, relative organ radioactivity was determined by dividing the value obtained for each organ by the first whole-body value. Thus, throughout the initial calculations, ε was set to 1 and was eliminated subsequently.

Neither the data nor the images were corrected for radioactive decay. Background correction was applied to selected organs. For each organ to be corrected by a given background region, the background count density in each view (anterior and posterior) was multiplied by the organ area in pixels and 50% of the result subtracted from the organ counts.

As it was not practical to acquire lateral views to provide an estimate of organ sizes and depths, no correction was made for organ thickness either in the primary corrected count calculation or in the background subtraction. This results in an overestimation of dose for a given organ by no more than 25% for the largest organs in the primary calculation. The 50% subtraction of background is a conservative use of nontarget count densities that will also result in some small overestimation of dose. We believe that the combined overestimation that results is appropriately conservative.

All corrected organ counts were then divided by the whole-body count for the first time point, as discussed above. Combined biological translocation and radiological decay was then expressed as a percent of this injected dose in subsequent calculations.

It was possible to estimate excretion without obtaining urine and fecal samples. This was done first, by observing in pilot studies in rhesus monkeys and all other preclinical studies in dogs that there was no visualization in any animal of any organ in the hepatobiliary excretion pathway other than the liver (i.e., gall bladder, stomach, small intestine and large intestine). We therefore concluded that, for this purpose, all excretion was urinary.

Total excretion was then calculated as the difference between the initial value for the whole body and subsequent whole-body values. Since the anesthetized animals generally did not urinate during the first 6-hour portion of the experiment, it was not possible to determine total excretion from a curve fit to the whole-body data. Instead, we assumed that the total excretion was represented by the difference between the initial whole-body value and that measured at 24 hours.

Using Microsoft Excel's Solver add-in, a multiterm exponential expression was fit using nonlinear least sum-of-squares regression analysis to the time-activity data for each organ.

Expressions used for fitting were of the following form:

$$A = e^{-0.115t}\left(A_1 e^{\lambda_1 t} + A_2 e^{\lambda_2 t} + A_3 e^{\lambda_3 t}\right).$$

As there were no data between six and 24 hours, a relative weight of 20 was applied to the 24-hour time point. Rather than correct for radioactive decay, the physical decay was incorporated into the fit function in the form of the leading exponential coefficient. This permitted direct determination of the biological parameters from data that was not corrected for decay.

From the coefficients of the regression analysis, the cumulated activity, $\tilde{A}$, over time was calculated using the following expression (note that the term for the physical decay must be incorporated explicitly in this expression):

$$\tilde{A} = \int_0^\infty A(t)dt = \frac{A_1}{\lambda_1 + .115} + \frac{A_2}{\lambda_2 + .115} + \frac{A_3}{\lambda_3 + .115}$$

and the residence time, τ, may be determined by

$$\tau_i = \frac{\tilde{A}_i}{\textit{total injected dose } (MBq)}$$

for each organ, I.

A separate regression analysis of the urinary bladder data was performed to determine the biological parameters of its appearance. These are converted to a voiding-interval-dependent residence time using the method of Watson et al. (6) as implemented in MIRDOSE3 (7).

Residence time for the "remainder of the body" was calculated by subtraction of the sum of the residence times for all other organs from that of the whole body.

In general, it is necessary to make corrections to animal-derived data when estimating the corresponding parameters in human subjects. In this case, we chose to use a metabolic rate method (8), which has been shown to be widely applicable for drugs that are not actively incorporated into the cell. This appears to be a reasonable assumption for DMP 444.

To apply this method, the time scale must be corrected by the following factor:

$$T_H = T_a \left(\frac{W_H}{W_a} \right)^{.33} ,$$

where T_a represents a time interval for the animal, T_H is the corresponding one for a human being, W_a is the animal weight and W_H is the human weight. Residence times were computed by including this factor as a multiplier of the appropriate biological clearance constant.

Radiation dose estimates were obtained by use of the MIRD method (9). The calculated residence times for each organ other than the bladder were entered into MIRDOSE3 (7). The bladder residence time was determined as described above by MIRDOSE3. As no hepatobiliary (and therefore no fecal) clearance was assumed, the ICRP30 GI tract model was not used.

The program was set to use Tc-99m as the radionuclide, and the adult male phantom was chosen. MIRDOSE3 then calculated the radiation dose estimates, the effective dose equivalent and the effective dose for each input and output organ. Determination was also made of the injected dose yielding no more than 50 mGy to the organ with highest radiation dose and no more than 30 mGy to a radiation-sensitive organ. All organ doses were compiled by animal. Means, standard deviations, coefficients of variation, ranges and mean-normalized ranges were then computed.

Blood samples were assayed for radioactivity in an LKB model 1282 gamma well counter and the result corrected for radioactive decay by collection time and normalized by the initial value. This was then subjected to exponential curve-stripping analysis using JANA (10). Values were then determined for AUC (area under curve), and for the biological fractions and clearance constants for each exponential term. Once again, each parameter was summarized by simple descriptive statistics.

White cell, red cell and platelet counts were determined from blood samples using a K-1000 hematology analyzer. A Coagulation Analyzer (MCA-210), was used to determine prothrombin time

(PT), activated partial thromboplastin time (APTT), and fibrinogen concentration. Whole blood aggregation was obtained with a 560-Ca Lumi Aggregometer (using electrode impedance) and ATP release by platelet degranulation. Blood pressure was measured at intervals using a conventional pressure cuff sphygmomanometer and EKG tracings monitored with a Grass Polygraph.

RESULTS

The average radiochemical purity of the five preparations used for this experiment was 91.8±1.5% and ranging from a low of 88.8% to a high of 93.2%. Figure 1 depicts a typical image of the biodistribution of the compound in normal primates.

Figure 1. Anterior (L) and posterior (R) whole-body image of monkey J14 one hour after injection.

It is evident from this image that the primary organs in which concentration is observed are the heart, lungs, kidneys, spleen and urinary bladder and that the remainder of the compound seems to be distributed throughout the body in a pattern reflecting intravascular retention.

Tables 1 through 4 give the results of the radiation dosimetry calculations for all experiments. Tables 1 and 2 are summary tables containing descriptive statistics for each organ over all animals. Tables 3 and 4 are animal-by-animal radiation dose estimates. Tables 1 and 3 were calculated assuming a voiding interval of 2 hours; Tables 2 and 4 assumed a voiding interval of 4.8 hours. Figures 2 and 3 depict the mean and standard deviation values for the 2-hour void results and those for 4.8 hours, respectively.

Table 1
Summary Table of Estimated Preclinical Radiation Dose, Effective Dose Equivalent (EDE) and Effective Dose (ED) for DMP 444 Assuming a Regular 2-hour Voiding Interval (organ doses are in mGy/MBq, EDE and ED are in mSv/MBq)

	Mean (mGy/MBq)	*Std Dev (mGy/MBq)*	*CV (%)*
Adrenals	5.49E-03	5.27E-04	10%
Brain	1.58E-03	7.68E-05	5%
Breasts	2.38E-03	2.07E-04	9%
GB Wall	5.54E-03	5.38E-04	10%
LLI	3.19E-03	1.37E-04	4%
Small	3.27E-03	1.55E-04	5%
Stomach	4.32E-03	4.76E-04	11%
ULI	3.32E-03	1.88E-04	6%
Heart	1.36E-02	2.07E-03	15%
Kidneys	1.58E-02	2.25E-03	14%
Liver	1.19E-02	1.73E-03	15%
Lungs	9.92E-03	1.59E-03	16%
Muscle	2.61E-03	1.43E-04	5%
Ovaries	3.30E-03	1.30E-04	4%
Pancreas	6.43E-03	7.76E-04	12%
Red	2.81E-03	1.74E-04	6%
Bone	4.59E-03	2.73E-04	6%
Skin	1.55E-03	8.27E-05	5%
Spleen	3.78E-02	1.04E-02	28%
Testes	2.18E-03	8.73E-05	4%
Thymus	4.08E-03	4.11E-04	10%
Thyroid	2.15E-03	1.13E-04	5%
U. Bladder	1.81E-02	2.95E-03	16%
Uterus	4.24E-03	2.73E-04	6%
Total Body	3.22E-03	2.20E-04	7%
EDE	8.73E-03	9.16E-04	11%
ED	6.30E-03	5.11E-04	8%

Table 2

Summary Table of Preclinical Estimated Radiation Dose, Effective Dose Equivalent (EDE) and Effective Dose (ED) for DMP 444 Assuming a Regular 4.8-hour Voiding Interval (organ doses are in mGy/MBq, EDE and ED are in mSv/MBq)

	Mean (mGy/MBq)	*Std Dev (mGy/MBq)*	*CV (%)*
Adrenals	5.49E-03	5.19E-04	9%
Brain	1.58E-03	7.68E-05	5%
Breasts	2.38E-03	2.08E-04	9%
GB Wall	5.59E-03	5.30E-04	9%
LLI	4.30E-03	3.00E-04	7%
Small	3.70E-03	1.34E-04	4%
Stomach	4.35E-03	4.70E-04	11%
ULI	3.65E-03	1.51E-04	4%
Heart	1.36E-02	2.07E-03	15%
Kidneys	1.58E-02	2.24E-03	14%
Liver	1.19E-02	1.71E-03	14%
Lungs	9.92E-03	1.59E-03	16%
Muscle	2.86E-03	1.30E-04	5%
Ovaries	4.35E-03	2.65E-04	6%
Pancreas	6.46E-03	7.76E-04	12%
Red	2.95E-03	1.46E-04	5%
Bone	4.81E-03	2.44E-04	5%
Skin	1.62E-03	7.38E-05	5%
Spleen	3.78E-02	1.04E-02	28%
Testes	2.89E-03	1.95E-04	7%
Thymus	4.08E-03	4.11E-04	10%
Thyroid	2.15E-03	1.13E-04	5%
U. Bladder	4.00E-02	6.81E-03	17%
Uterus	6.65E-03	6.84E-04	10%
Total Body	3.46E-03	1.92E-04	6%
EDE	1.04E-02	8.76E-04	8%
ED	7.41E-03	6.54E-04	9%

Table 3
Absorbed Dose, Effective Dose Equivalent (EDE) and Effective Dose (ED) by Animal
Using a 2-hour Voiding Interval (organ doses are in mGy/MBq, EDE and ED are in mSv/MBq)

	J10	*J118*	*J14*	*T36*	*T54*
Adrenals	5.38E-03	6.41E-03	5.24E-03	5.14E-03	5.22E-03
Brain	1.54E-03	1.69E-03	1.62E-03	1.57E-03	1.49E-03
Breasts	2.49E-03	2.70E-03	2.22E-03	2.23E-03	2.27E-03
GB Wall	5.78E-03	6.32E-03	5.43E-03	5.05E-03	5.05E-03
LLI	3.00E-03	3.22E-03	3.16E-03	3.38E-03	3.14E-03
Small	3.14E-03	3.51E-03	3.27E-03	3.27E-03	3.14E-03
Stomach	3.95E-03	5.14E-03	4.05E-03	4.27E-03	4.16E-03
ULI	3.24E-03	3.65E-03	3.32E-03	3.27E-03	3.16E-03
Heart	1.54E-02	1.55E-02	1.09E-02	1.19E-02	1.42E-02
Kidneys	1.29E-02	1.85E-02	1.68E-02	1.41E-02	1.68E-02
Liver	1.35E-02	1.39E-02	1.14E-02	1.03E-02	1.03E-02
Lungs	1.11E-02	1.21E-02	8.54E-03	8.86E-03	8.97E-03
Muscle	2.56E-03	2.86E-03	2.55E-03	2.58E-03	2.51E-03
Ovaries	3.14E-03	3.35E-03	3.30E-03	3.49E-03	3.24E-03
Pancreas	5.92E-03	7.78E-03	5.97E-03	6.27E-03	6.16E-03
Red	2.76E-03	3.11E-03	2.73E-03	2.73E-03	2.68E-03
Bone	4.54E-03	5.08E-03	4.54E-03	4.49E-03	4.38E-03
Skin	1.52E-03	1.69E-03	1.54E-03	1.52E-03	1.47E-03
Spleen	2.54E-02	5.30E-02	3.16E-02	4.11E-02	3.76E-02
Testes	2.08E-03	2.19E-03	2.18E-03	2.32E-03	2.14E-03
Thymus	4.38E-03	4.62E-03	3.65E-03	3.76E-03	4.05E-03
Thyroid	2.13E-03	2.33E-03	2.15E-03	2.10E-03	2.03E-03
U.Bladder	1.65E-02	1.50E-02	1.68E-02	2.24E-02	1.95E-02
Uterus	4.00E-03	4.11E-03	4.16E-03	4.70E-03	4.27E-03
Total Body	3.19E-03	3.59E-03	3.11E-03	3.11E-03	3.05E-03
EDE	8.03E-03	1.02E-02	7.97E-03	8.78E-03	8.65E-03
ED	6.03E-03	7.14E-03	5.84E-03	6.43E-03	6.11E-03

Table 4
Absorbed Dose, Effective Dose Equivalent (EDE) and Effective Dose (ED) by Animal
Using a 4.8-hour Voiding Interval (organ doses are in mGy/MBq, EDE and ED are in mSv/MBq)

	J10	*J118*	*J14*	*T36*	*T54*
Adrenals	5.41E-03	6.41E-03	5.27E-03	5.16E-03	5.22E-03
Brain	1.54E-03	1.69E-03	1.62E-03	1.57E-03	1.49E-03
Breasts	2.49E-03	2.70E-03	2.22E-03	2.24E-03	2.27E-03
GB Wall	5.86E-03	6.38E-03	5.49E-03	5.16E-03	5.11E-03
LLI	4.03E-03	4.11E-03	4.22E-03	4.78E-03	4.38E-03
Small	3.54E-03	3.86E-03	3.68E-03	3.81E-03	3.62E-03
Stomach	3.97E-03	5.16E-03	4.11E-03	4.30E-03	4.19E-03
ULI	3.54E-03	3.89E-03	3.62E-03	3.68E-03	3.51E-03
Heart	1.54E-02	1.55E-02	1.09E-02	1.19E-02	1.42E-02
Kidneys	1.30E-02	1.85E-02	1.68E-02	1.41E-02	1.68E-02
Liver	1.35E-02	1.39E-02	1.15E-02	1.03E-02	1.03E-02
Lungs	1.11E-02	1.21E-02	8.54E-03	8.86E-03	8.97E-03
Muscle	2.78E-03	3.08E-03	2.78E-03	2.89E-03	2.78E-03
Ovaries	4.11E-03	4.19E-03	4.27E-03	4.78E-03	4.41E-03
Pancreas	5.95E-03	7.81E-03	6.00E-03	6.30E-03	6.19E-03
Red	2.89E-03	3.22E-03	2.89E-03	2.92E-03	2.86E-03
Bone	4.73E-03	5.24E-03	4.73E-03	4.76E-03	4.62E-03
Skin	1.59E-03	1.75E-03	1.61E-03	1.62E-03	1.55E-03
Spleen	2.54E-02	5.30E-02	3.16E-02	4.11E-02	3.76E-02
Testes	2.73E-03	2.76E-03	2.86E-03	3.22E-03	2.95E-03
Thymus	4.38E-03	4.62E-03	3.65E-03	3.76E-03	4.05E-03
Thyroid	2.13E-03	2.33E-03	2.15E-03	2.10E-03	2.03E-03
U. Bladder	3.68E-02	3.27E-02	3.73E-02	5.00E-02	4.38E-02
Uterus	6.22E-03	6.00E-03	6.38E-03	7.70E-03	6.92E-03
Total Body	3.41E-03	3.78E-03	3.32E-03	3.41E-03	3.32E-03
EDE	9.51E-03	1.15E-02	9.46E-03	1.08E-02	1.04E-02
ED	7.03E-03	8.41E-03	6.73E-03	7.65E-03	7.16E-03

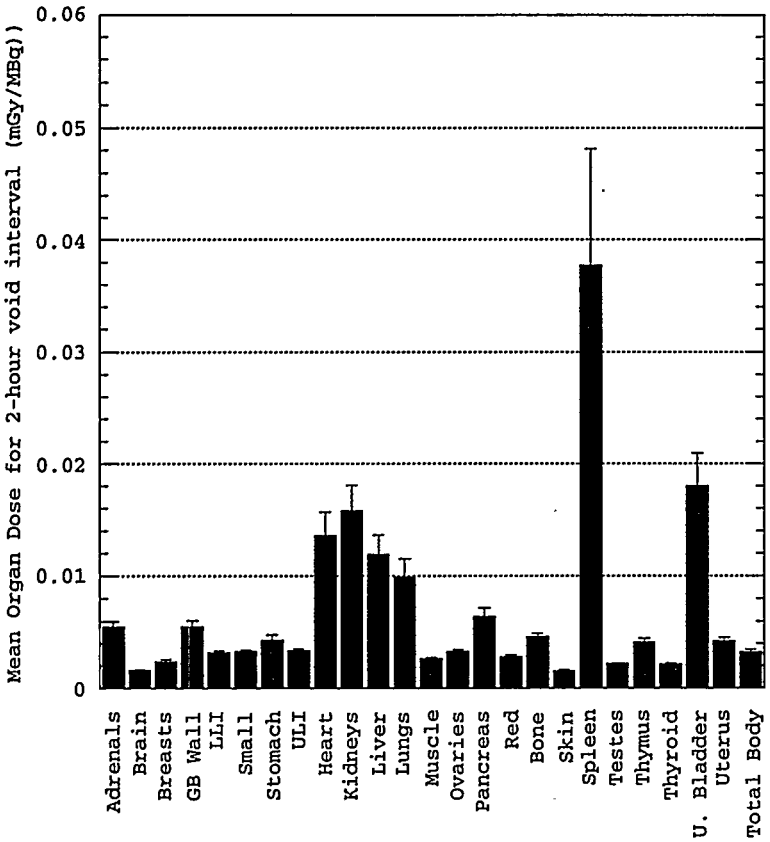

Figure 2. Bar chart of radiation dose estimates (mean of 5 animals) for DMP 444 with a 2 h voiding interval. Error bars represent one s.d.above and one s.d. below the mean.

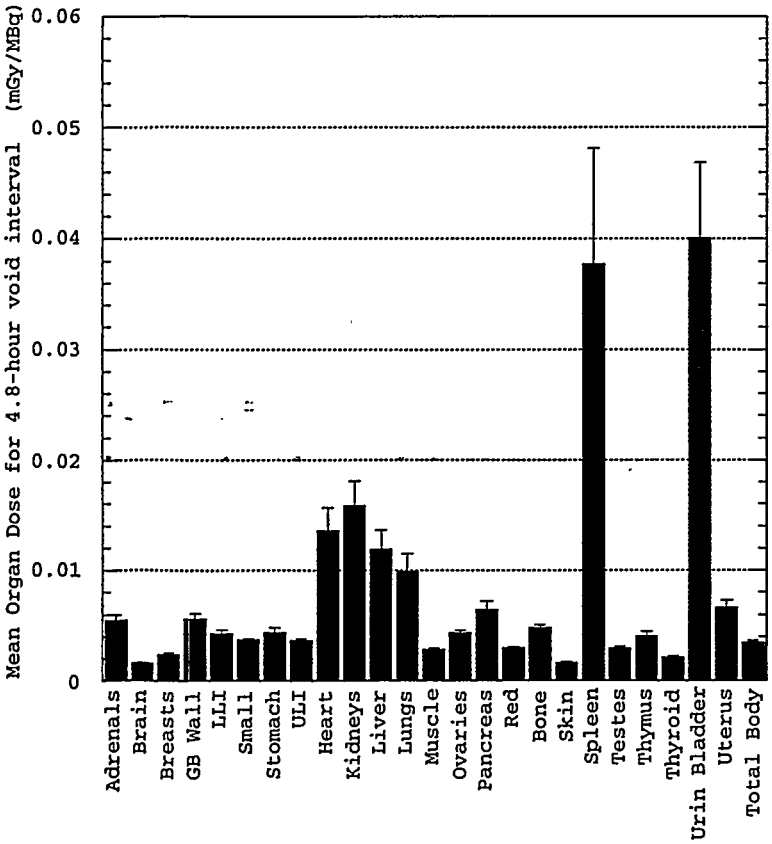

Figure 3. Bar chart of radiation dose estimates (mean of 5 animals) for DMP 444 with a 4.8 h voiding interval. Error bars represent one s.d. above and one s.d. below the mean.

For the 2-hour void interval, the spleen receives the highest radiation dose, 0.0378 mGy/MBq. As the spleen is not considered a radiation sensitive organ, the injected dose that would limit the radiation dose to the critical organ to 50 mGy under these conditions is 1323 MBq. For a 4.8 hour voiding interval, the urinary bladder becomes the critical organ at 0.040 mGy/MBq, yielding a maximum injected dose of 1247 MBq. For both voiding intervals, the next highest dose is received by the kidney. Neither the bladder nor the spleen are considered radiation-sensitive organs and all others (including the kidney) are less than or equal to 19.3 mGy under either voiding condition with an injected dose of 1221 MBq. Therefore it is estimated that an injected dose of 1221 MBq should result in no more than 50 mGy to any one organ and no more than 30 mGy to a radiation-sensitive organ.

Blood Clearance

Plots representing blood clearance of Tc-99m in each animal are shown in Figures 4 through 8. A two-component exponential curve fit (solid line) is superimposed on the data (circles).

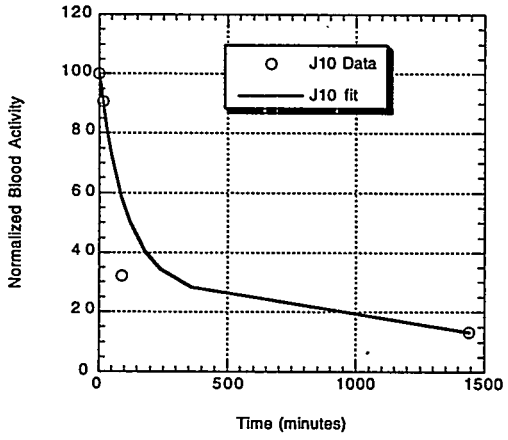

Figure 4. Blood data and regression line, J10.

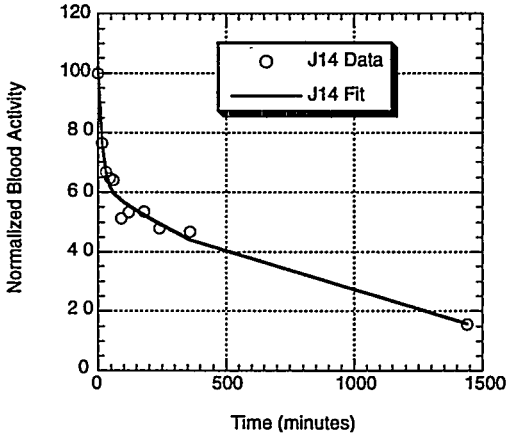

Figure 5. Blood data and regression line, J14.

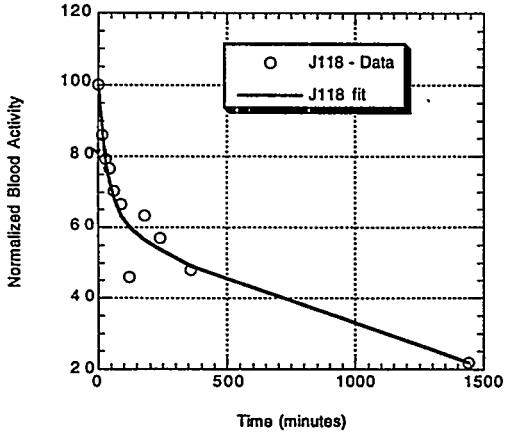

Figure 6. Blood data and regression line, J118.

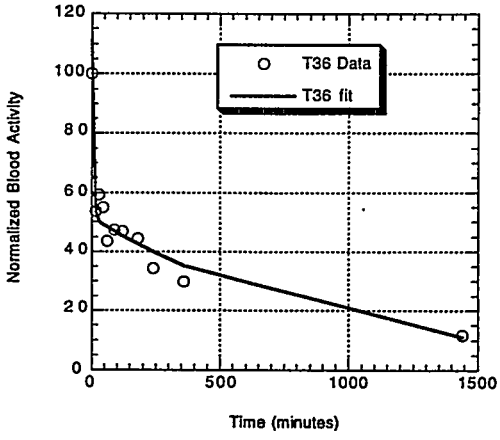

Figure 7. Blood data and regression line, T36.

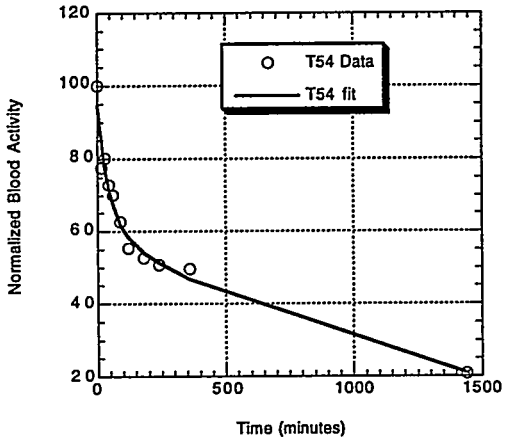

Figure 8. Blood data and regression line, T54

Table 5 summarizes the result of exponential curve fits to the data obtained from assay of radioactivity levels in blood samples.

Table 5
Summary Table for Blood Clearance Data for DMP 444 in Nonhuman Primates

	Mean	SD	CV%	Range	Range/mean
A1	54.7%	12.55	23%	30.41	56%
A2	46.9%	15.10	32%	33.22	71%
B1	0.000833 min^{-1}	0.000172	21%	0.00	50%
B2	0.0651 min^{-1}	0.0798	123%	0.19	296%
R^2 of curve fit	0.95	0.04	4%	0.10	11%
AUC	68818 min	16509	24%	38,714.66	56%

Hematology

Table 6 lists the hematology parameters obtained during the course of the five studies. Many samples are missing owing to continuing difficulties, particularly during the early experiments, obtaining sufficient blood due to problems maintaining catheter patency. PT, APTT and fibrinogen levels were not measured during the last three experiments as it became necessary in each case to establish a heparin lock to maintain patency. Under these conditions, these three parameters were not reflective of changes that might be attributed to the agent and thus the tests were omitted. In one case (animal J14), it appeared that the presence of heparin caused a noticeable decrease in platelet aggregation. In other cases, this remained relatively constant and within normal values. There was no observable thrombocytopenia indicating that the agent was not altering platelet function.
No clinically significant changes were observed in either blood pressure or electrocardiogram tracings during any experiment.

Table 6

Hematologic Values for All Five Animals during the Course of the Study

DATE Animal	averages	control	1 min	30 min	60 min	180 min	360 min	1440 min
4/6/95 T36	AGG (ohms)	26	31			36		29
	ATP (nm)	0.44	0.41			0.29		0.16
	platelets x 10E3/ul	333	320	291		295		250
	PT (sec)	10.3	10.6			11		9.9
	APTT (sec)	21.8	23.4			20.8		23.9
	Fg (mg/dl)	219	200			179		337
4/10/95 J10	AGG (ohms)	25						
	ATP (nm)	0.59						
	platelets x 10E3/ul	312	293					310
	PT (sec)	10.8						
	APTT (sec)	19.2						
	Fg (mg/dl)	256						
4/12/95 J118	AGG (ohms)	27	25	15	19	33		36
	ATP (nm)	0.22	0	0	0	0.22		0.59
	platelets x 10E3/ul	299	394	388	380	400		383
	PT (sec)							
	APTT (sec)							
	Fg (mg/dl)							
4/13/95 J14	AGG (ohms)	18	8	5	12	5		23
	ATP (nm)	0	0	0	0	0		0
	platelets x 10E3/ul	327	333		330	342		321
	PT (sec)							
	APTT (sec)							
	Fg (mg/dl)							
4/18/95 T54	AGG (ohms)	18	13	16	18	17		21
	ATP (nm)	0	0	0	0	0		0
	platelets x 10E3/ul	476	442	448	462	469		481
	PT (sec)							
	APTT (sec)							
	Fg (mg/dl)							

DISCUSSION

This study was conducted to estimate the radiation dose that a normal human subject would receive from DMP 444. It also contributes to the safety basis for the proposed injected dose of DMP 444 to be used in Phase I clinical trials. All other data generated (blood clearance, hematology) was acquired primarily as quality control to support the use of the primate and to make certain there were no significant compromising clinical abnormalities that would have affected the primary conclusions of the study.

The values for dosimetry obtained are consistent with expectations based on the persistence of the compound in the various organs and based upon its known mechanism of action. A compound that binds to platelet surface receptors would be expected to accumulate in the spleen as that organ serves as a reservoir for many cellular elements of the blood. As the platelet lifetime is several days, we would expect to see a prolonged retention of activity in the spleen. The rapid excretion of a substantial fraction of the radioactivity via the urine is also consistent with the high bladder dose that varies with voiding interval.

REFERENCES

1. Barrett JA, Edwards DS, Harris TD, Rajopadhye M, Lazewatsky J, Liu S, Damphousse DJ, Heminway SJ, Mzaika TJ, Thomas J, Carroll TR and Smith J. The development of a technetium-99m agent for imaging deep vein thrombosis, in Technetium and Rhenium in Chemistry and Nuclear Medicine 4, edited by Nicolini, M, Bandoli, G, and Mazzi, U, pp 275-280, SGEditoriali: Padova, 1995.
2. Barrett JA, Heminway S, Damphousse D, Crocker A, Mazaika T, Bresnick M, Kagan M, Lazewatsky J, Edwards DS, Liu S, Harris T, Rajopadhye M and Carroll T. DMP-444: A potential thrombosis imaging agent. 43rd Annual SNM Meeting, Denver, 1996.
3. Poncz M and Newman PJ. Analysis of rodent platelet glycoprotein IIb: Evidence for evolutionarily conserved domains and alternative proteolytic processing. Blood 75(6):1282-1289, 1990.
4. Harfenist EJ et al. Effects of the cell adhesion peptide, Arg-Gly-ASP-Ser, on responses of washed platelets from humans, rabbits and rats. Blood; 71(1):132-136, 1988.
5. Eary JF, Appelbaum FL, Durack L and Brown P. Preliminary validation of the opposing view method for quantitative gamma camera imaging. Med Phys 16(3):382-387, 1989.
6. Cloutier RJ, Smith SA, Watson EE, Snyder WS and Warnter GG. Dose to the fetus from radionuclides in the bladder. Health Physics 23:147-161, 1973.
7. Stabin M. MIRDOSE - Personal computer software for internal dose assessment in nuclear medicine. J Nucl Med 37:538-546, 1996.
8. McAfee JG and Subramanian G. Interpretation of interspecies differences in the biodistribution of radioactive agents. Third International Radiopharmaceutical Dosimetry Symposium, Oak Ridge, Tennessee, Oct 7-9, 1980, HHS Publication FDA 81-8166.
9. Loevinger R and Berman M. A Revised Schema for Calculating the Absorbed Dose from Biologically Distributed Radionuclides. MIRD Pamphlet No. 1, Revised, Society of Nuclear Medicine, 1976.
10. JANA program, Statistical Software Consultants, Lexington, KY.

UNCERTAINTY ANALYSIS FOR ABSORBED DOSE FROM A BRAIN RECEPTOR IMAGING AGENT

Aydogan B[1], Sparks RB[2], Stubbs JB[3] and Miller LF[1]
[1]Nuclear Engineering Department, The University of Tennessee, Knoxville, TN 37996
[2]Oak Ridge Institute for Science and Education, Oak Ridge, TN 37831-0117
[3]Radiation Dosimetry Systems of Oak Ridge, Inc., Knoxville, TN 37932

ABSTRACT

Absorbed dose estimates are known to contain uncertainties. A recent literature search indicates that prior to this study no rigorous investigation of uncertainty associated with absorbed dose has been undertaken. A method of uncertainty analysis for absorbed dose calculations has been developed and implemented for the brain receptor imaging agent ^{123}I-IPT. The two major sources of uncertainty considered were the uncertainty associated with the determination of residence time and that associated with the determination of the S values. There are many sources of uncertainty in the determination of the S values, but only the inter-patient organ mass variation was considered in this work. The absorbed dose uncertainties were determined for lung, liver, heart and brain. Ninety-five percent confidence intervals of the organ absorbed dose distributions for each patient and for a seven-patient population group were determined by the "Latin Hypercube Sampling" method. For an individual patient, the upper bound of the 95% confidence interval of the absorbed dose was found to be about 2.5 times larger than the estimated mean absorbed dose. For the seven-patient population the upper bound of the 95% confidence interval of the absorbed dose distribution was around 45% more than the estimated population mean. For example, the 95% confidence interval of the population liver dose distribution was found to be between 1.49E+07 Gy/MBq and 4.65E+07 Gy/MBq with a mean of 2.52E+07 Gy/MBq. This study concluded that patients in a population receiving ^{123}I-IPT could receive absorbed doses as much as twice as large as the standard estimated absorbed dose due to these uncertainties.

INTRODUCTION

Absorbed dose is calculated to predict the radiation risk as a result of exposure to ionizing radiation. In medical applications, the absorbed dose that a patient would receive is often calculated using the MIRD method (1). This method employs certain simplifying assumptions, and does not explicitly treat many of the complexities that arise in the anatomic and biokinetic variabilities of the population to which the standard dose estimates are applied. Patient-specific dosimetry is considered whenever more specific and accurate dose estimates are necessary as in radiotherapy. In most diagnostic applications, however, the standard absorbed dose estimates are routinely used in the evaluation of the risk/benefit relationship. The magnitude of the uncertainties of the method have not been systematically assessed.

This study was performed to evaluate the uncertainties in internal dose calculations. The absorbed dose uncertainties can be considered in two main categories. First, uncertainty associated with determination of residence time and second, uncertainty associated with determination of S values. Due to the difficulties in the determination of the uncertainties in some components of the S values, the major source of uncertainty considered in this study was the one associated with the determination of residence time. However, organ mass variabilities were incorporated to obtain some estimate of the S-value uncertainties. A method of uncertainty analysis which makes use of the "classical approach" was postulated. The Latin Hypercube method was used to determine uncertainty associated with the absorbed dose calculations of ^{123}I-IPT, a brain receptor imaging agent.

METHOD AND RESULTS

Determination of Residence Time Uncertainties.

Since the original biokinetic model for ^{123}I-IPT (2) was too complex for uncertainty analysis, a simplified biokinetic model including liver, lung, heart and brain was developed. This model simulated the biokinetics of the radiopharmaceutical using biexponential functions. The parameter estimates for the model and their uncertainties were obtained through least squares regression analysis. The SAAM (Simulation Analysis and Modeling) II software (3) was used to fit the data to the multiexponential function given in Equation 1.

$$\frac{A(h)}{A_0} = S_1 e^{-L_1 t} + S_2 e^{-L_2 t} \qquad (1)$$

The SAAM software iteratively adjusts the parameters of above equation until the simulated activity distribution fits the observed activity distribution. SAAM provides parameter estimates and their associated uncertainties. Although some of the uncertainty comes from the biokinetic data itself, most of the uncertainty is from the least-square parameter estimation procedure.

Several questions arise in parameter estimation and the determination of uncertainty. First, it is not practical to determine "true values" for parameters of a nonlinear model such as Equation 1. Parameters of a living system may vary considerably from one individual to another, between genders, and even from one experiment to the next. One of the common problems with curve fitting is that the fit can be very good, yet the parameter estimates can have large variances. In nonlinear regression, large variances from least-squares analysis may indicate one or more of the following:

- overparameterization
- inadequate data
- an inappropriate model
- highly interrelated parameters in terms of their influence on the model output
- nonuniqueness in the fit.

The nonuniqueness problem is directly related to the local/global minimum concept. If a relatively good fit is obtained the residence time, in most cases, will be similar regardless of whether a local or global minimum is obtained. However, the parameter uncertainties may vary substantially.

No general statistical distribution theory exists for nonlinear estimators where only small data samples are available. Nevertheless, their approximate behavior can be studied empirically by using

the Monte Carlo simulation method, e.g. as employed in the Crystal Ball software (4). For a short-lived radionuclide, residence time can be approximated by

$$\tau = \int_0^\infty \left(S_1 e^{-L_1 t} + S_2 e^{-L_2 t}\right) e^{-\lambda_p} dt, \tag{2}$$

where λ_p is the physical decay constant of the radionuclide, and S1, S2, L1, and L2 are the parameters of the model. Solving the above integral yields

$$\tau = \frac{S_1}{L_1 + \lambda_p} + \frac{S_2}{L_2 + \lambda_p}. \tag{3}$$

Equation 3 was used to simulate the residence time calculations for ^{123}I-IPT by sampling from the parameter distributions at least 2,500 times. The residence-time distributions were obtained for each source organ. The parameter values, their associated standard deviations, and cross correlations were used as assumptions in sampling. Standard deviations associated with residence-time calculations were also calculated by using first-order error propagation (FOEP), and are listed in Table 1 for comparison purposes.

Table 1
Residence Times for the Source Organs and their Associated
Standard Deviations Calculated by Both FOEP and LHS

ORGAN	PATIENT : DF			PATIENT : RF		
	τ (h)	σ (LHS)	σ (FOEP)	τ (h)	σ (LHS)	σ (FOEP
Lung	1.17E+00	2.02E-02	2.46E-03	1.22E+00	1.36E-01	2.50E-01
Liver	1.02E+00	1.35E-01	2.75E-02	1.14E+00	1.36E-01	1.20E-01
Brain	3.20E-01	2.06E-02	2.08E-03	4.16E-01	9.72E-03	2.75E-03
Heart Wall	2.43E-01	2.04E-02	9.48E-03	2.94E-01	9.07E-03	7.00E-03
Total Body	1.07E+01	8.63E+00	1.07E+00	8.94E+00	1.08E+01	9.08E-01
Remainder of the Body	7.96E+00	8.63E+00		5.87E+00	1.08E+01	

	PATIENT : PT			PATIENT : VU		
	τ (h)	σ (LHS)	σ (FOEP)	τ (h)	σ (LHS)	σ (FOEP)
Lung	4.55E-01	2.41E-01	9.78E-03	1.20E+00	1.01E-01	9.30E-02
Liver	7.48E-01	2.24E-01	3.52E-02	7.53E-01	1.27E-02	9.90E-03
Brain	3.55E-01	6.71E-02	1.92E-02	4.06E-01	3.23E-03	1.71E-03
Heart Wall	2.54E-01	4.87E-02	5.43E-03	2.55E-01	4.07E-02	8.10E-03
Total Body	1.37E+01	1.37E+01	2.56E-01	1.33E+01	1.18E+00	3.21E-01
Remainder of the Body	1.19E+01	1.37E+01		1.07E+01	1.19E+00	

The first-order error propagation for calculating the residence-time variance is given by

$$Var(\tau)=\left(\frac{\partial\tau}{\partial P_1}\right)^2\sigma_{P_1}^2+\left(\frac{\partial\tau}{\partial P_2}\right)^2\sigma_{P_2}^2+\left(\frac{\partial\tau}{\partial P_3}\right)^2\sigma_{P_3}^2+\left(\frac{\partial\tau}{\partial P_4}\right)^2\sigma_{P_4}^2+$$

$$2\sum_{i}^{4}\sum_{j=i+1}^{4}\rho_{P_iP_j}\sigma_{P_i}\sigma_{P_j}\left(\frac{\partial\tau}{\partial P_i}\right)\left(\frac{\partial\tau}{\partial P_j}\right). \quad (4)$$

The results of the two methods , FOEP and LHS, were quite different in most cases. FOEP will yield relatively good results when underlying parameter distribution is normal. These results suggest that the parameter distributions are not normal. In fact, the parameter distributions obtained using the sampling method appeared to be log-normal in most cases.

S Values and Error Propagation

The S-value uncertainties were calculated by error propagation of the specific absorbed fraction uncertainties. Specific absorbed fractions for photon sources and their estimated coefficients of variance were obtained from Snyder et al. (5). The absorbed-fraction uncertainties are directly related to the statistical uncertainties of the Monte Carlo calculations and organ mass variabilities. All electrons were assumed to contribute only to self-organ dose for the organs considered. Therefore, no uncertainties other than the one associated with the organ-mass variabilities were taken into account for the nonpenetrating component. Two sets of S-value uncertainty calculations were carried out.

(1) In the first case, photon transport uncertainties associated with SAF values were considered as the only source of uncertainty in the S-value calculation.

$$S(r_k \leftarrow r_h)=\sum_{i=1}^{N}\Delta_i\Phi_i(r_k \leftarrow r_h) \quad (5)$$

Here $\Phi(r_k \leftarrow r_h)$ is the specific absorbed fraction for source region r_h irradiating target region r_k, and Δ_i is the mean energy emitted per nuclear transition i.

(2) Target-organ mass variabilities of the typical western adult male were determined and incorporated into the S-value calculations through the specific absorbed fraction in addition to uncertainties considered in the first case. The specific absorbed fraction (SAF) values from source organ r_k to target organ r_h can be calculated using the following equation.

$$\Phi(r_k \leftarrow r_h)=\frac{\phi(r_k \leftarrow r_h)}{m_k}, \quad (6)$$

where m_k is the target organ mass and ϕ is the absorbed fraction. The standard deviations associated with the SAF values were calculated by FOEP method.

$$\sigma^2_{\Phi_i} = \left(\frac{\phi_i}{m}\right)^2 \times \left[\left(\frac{\sigma_{m_k}}{m_k}\right)^2 + \left(\frac{\sigma_{\phi_i}}{\phi_i}\right)^2\right] \quad (7)$$

and

$$\sigma^2_{\Phi_{np}} = \left(\frac{1}{m_k}\right)^2 \sigma^2_{m_k}, \quad (8)$$

where subscript np represents the nonpenetrating emissions, in this case electrons only.

The resultant specific absorbed fractions and their associated uncertainties were then used to calculate the second set of S values and their associated uncertainties. This calculation yielded almost the same mean S values but with larger associated uncertainties.

Determination of Absorbed Dose Uncertainties

The dose per unit administered activity can be calculated as follows:

$$\overline{D_k}/A_0 = \sum_{h=1}^{n} \left[\tau_h \, S(r_k \leftarrow r_h)\right] + \tau_{RB} \, S(r_k \leftarrow RB). \quad (9)$$

The dose calculations were carried out in two categories in order to determine the contribution to the absorbed dose uncertainties from the biokinetic and biologic variabilities separately. The absorbed dose distributions for each patient were obtained. An example of an absorbed dose distribution is shown in Figure 1.

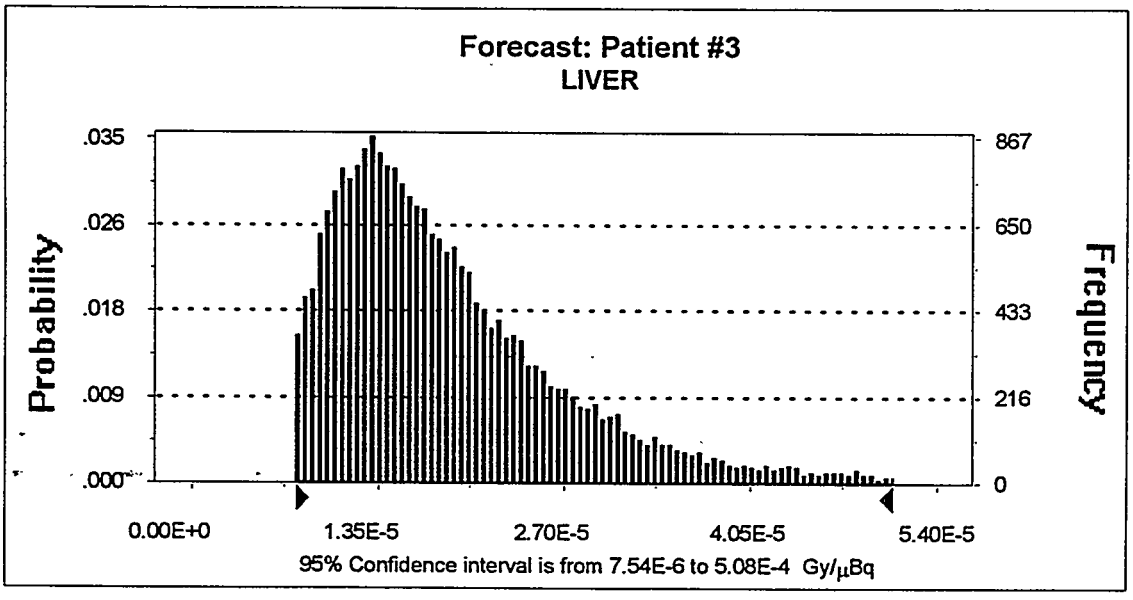

Figure 1. An example of absorbed dose distribution with 95% confidence interval.

The absorbed dose calculations were simulated using Equation 9, for at least 10,000 trials each by sampling from the residence time distributions and the first set of S-value distributions (which excluded the mass variabilities). The results are presented in Table 2. This table shows the mean

absorbed dose, standard deviations and the coefficients of variation of absorbed dose estimates for each patient.

Table 2
Mean Organ Doses and Associated Uncertainties as Standard Deviation and Coefficient of Variation for each Patient when the Organ Mass Variabilities are Neglected

PATIENT	LUNG			LIVER		
	MEAN DOSE (Gy/MBq)	SD (Gy/MBq)	CV%	MEAN DOSE (Gy/MBq)	SD (Gy/MBq)	CV%
1	2.05E+07	3.86E+06	19	2.49E+07	4.19E+06	17
2	3.30E+07	1.32E+06	4	2.14E+07	1.04E+06	4.8
3	1.92E+07	5.49E+06	29	2.06E+07	5.59E+06	30
4	3.08E+08	1.98E+06	6.4	3.24E+08	2.17E+06	6.7
5	2.52E+07	1.66E+06	6.6	2.97E+08	2.13E+06	7.2
6	2.08E+07	4.08E+06	20	2.69E+07	4.11E+06	15
7	2.97E+08	2.86E+06	9.3	2.13E+07	3.16E+06	15.3
FOR THE POPULATION	2.56E+07	3.41E+06	13.26	2.52E+07	3.38E+06	13.44
	BRAIN			HEART		
1	1..04E+07	1.39E+06	13	2.69E+07	4.43E+06	18
2	1.09E+07	7.32E+05	6.7	2.42E+07	1.08E+06	4.5
3	1.23E+07	3.51E+06	26.2	2.89E+07	7.35E+06	26.2
4	1.14E+07	5.32E+05	4.7	4.89E+07	1.52E+06	4.6
5	1.32E+07	5.59E+05	4.2	2.95E+07	1.70E+06	5.9
6	1.27E+07	1.69E+06	13.1	3.03E+07	4.05E+06	12.1
7	1.05E+07	1.00E+06	9.5	2.24E+07	1.96E+06	8.7
FOR THE POPULATION	1.16E+07	1.66E+06	14.3	3.00E-05	3.81E+06	13.56

SD=Standard Deviation CV=Coefficient of Variation

The absorbed dose coefficients of variation (CVs) were between 4% and 29%. The S-value CVs were between 1% and 4%. This would indicate that the calculated uncertainties were mainly due to the biokinetic data analysis. The relatively large uncertainties may have been caused by a lack of sufficient biokinetic data to perform a good least-squares parameter analysis. For instance, the data set for patient number three consisted of seven observations for the target organs, whereas the average number of measurements was about 10. Other patients with less than 10 measurements, such as patients one and six, also showed relatively larger organ dose uncertainties. Urine data also consisted of fewer measurements, which may have been the cause of larger remainder of the body residence time uncertainties. Among the four organs considered in this study, the liver showed the highest absorbed dose uncertainties in almost every patient. There are several possible causes for this. The model to simulate liver activity might be too simplistic to accurately describe the true kinetics of the drug in liver. For instance, in the simplified biokinetic model, gastrointestinal (GI) tract excretion was ignored. Another possible cause could be the overlap of organs in the abdominal cavity and interference from other organ activity during the course of biokinetic data collection.

The absorbed dose simulation was repeated by using the second set of S values, which included the organ mass variabilities in addition to statistical uncertainties in the Monte Carlo calculations. The mean target organ absorbed doses remained almost the same. However, coefficients of variation of the organ absorbed doses were increased by a factor ranging from two to five, with values of between 17% and 57%. The results for the second case are listed in Table 3.

Table 3
Mean Organ Doses, and Associated Uncertainties as Standard Deviation and Coefficient of Variation for Each Patient when the Organ Mass Variabilities are Incorporated into Calculations

PATIENT	LUNG			LIVER		
	MEAN DOSE (Gy/MBq)	SD (Gy/MBq)	CV%	MEAN DOSE (Gy/MBq)	SD (Gy/MBq)	CV%
1	2.05E+07	5.38E+06	26.15	2.49E+07	7.46E+06	29.93
2	3.30E+07	6.51E+06	19.79	2.14E+07	4.95E+06	23.15
3	1.92E+07	9.46E+06	48.86	2.06E+07	1.17E+07	56.89
4	3.08E+08	6.11E+06	19.8	3.24E+08	7.05E+06	21.73
5	2.52E+07	3.97E+06	15.79	2.97E+08	5.81E+06	19.54
6	2.08E+07	7.65E+06	36.85	2.69E+07	7.54E+06	29.03
7	2.97E+08	6.08E+06	20.41	2.13E+07	5.46E+06	25.64
FOR THE POPULATION	2.56E+07	7.00E+06	27.35	2.52E+07	7.11E+06	28.26
	BRAIN			HEART		
1	1..04E+07	2.45E+06	23.34	2.69E+07	6.76E+06	25.06
2	1.09E+07	1.91E+06	17.54	2.42E+07	7.51E+06	31.6
3	1.23E+07	5.73E+07	34.02	2.89E+07	9.70E+06	33.55
4	1.14E+07	1.99E+06	17.5	4.89E+07	1.00E+07	20.61
5	1.32E+07	2.22E+06	16.75	2.95E+07	5.22E+06	17.71
6	1.27E+07	3.76E+05	29.66	3.03E+07	7.73E+06	23.25
7	1.05E+07	2.19E+06	20.79	2.24E+07	4.00E+06	17.89
FOR THE POPULATION	1.16E+07	2.52E+06	21.72	3.00E+07	7.57E+06	25.23

SD=Standard Deviation CV=Coefficient of Variation

Patients two, four and five showed dramatic increases in their absorbed dose uncertainties. This is probably due to the availability of the better biokinetic data for good least-squares parameter analysis for these patients.

The absorbed dose results were used to compute the patient population absorbed dose uncertainties and the 95% confidence intervals for both cases. Table 4 summarizes the results of this work. In this table, the mean absorbed doses, standard deviations, upper and lover bounds of 95% confidence intervals, and the coefficients of variation for the seven-patient population absorbed dose estimates are listed.

Table 4
Comparison of the Absorbed Dose Uncertainties and the 95% Confidence Interval Values when Neglecting and Including Mass Variabilities

Absorbed Dose when Organ Mass Variabilities were Neglected (Gy/MBq)					
Organ	Mean Dose	Minimum	Maximum	SD	CV%
Population					
Lung	2.57E+07	2.04E+07	3.49E+07	3.41E+06	13.23
Liver	2.52E+07	1.99E+07	3.46E+07	3.49E+06	13.85
Heart	2.99E+07	2.22E+08	4.03E+07	3.81E+06	14.34
Brain	1.16E+07	8.95E+06	1.61E+07	1.66E+06	13.55
Individual Patient #3					
Liver	2.06E+08	7.54E+06	5.08E+08	1.17E+07	29.86

Absorbed Dose when Organ Mass Variabilities were Included (Gy/MBq)					
Organ	Mean Dose	Minimum	Maximum	SD	CV%
Population					
Lung	2.56E+07	1.53E+07	4.68E+07	7.00E+06	27.35
Liver	2.52E+07	1.49E+07	4.65E+07	7.11E+06	28.26
Heart	3.00E+07	1.91E+08	5.30E+07	7.59E+06	21.72
Brain	1.16E+07	7.84E+07	1.85E+07	2.52E+06	25.23
Individual Patient #3					
Liver	2.06E+08	7.54E+07	5.08E+07	1.17E+07	56.89

Incorporation of mass variabilities into the uncertainty calculations almost doubled the 95% confidence intervals of the population absorbed dose estimates. Based on this study, one may conclude that the absorbed dose that a patient receives could be twice as large as the estimated mean absorbed dose of the population. For instance, the liver dose a patient might receive could be between 1.49E+07 Gy/MBq and 4.65E+07 Gy/MBq, with a mean of 2.52 E+07 Gy/MBq.

DISCUSSION

It is well known that biokinetic data are very important for estimating the absorbed dose. A biokinetic data set must fully characterize the kinetics of the drug in the body. A biokinetic data set should consist of a certain minimum number of data to perform a reliable least-squares parameter estimation. In this study, the organs that had less than 10 measurements showed relatively larger uncertainties in the parameter estimation. For instance, lower availability of urine data measurements, with between four and seven data points, could be the cause of the larger remainder of the body absorbed dose uncertainties. Patients with fewer measurements, such as patient number one and three, also showed larger absorbed-dose uncertainties. Additional research could clarify the specific needs of biokinetic data collection and analyses for accurate determination of the uncertainty.

The patient population selected for this study was very homogeneous. They were all young adults with no known illness. Of the seven patients, five were male, and two were female. Therefore, the result of this study should not be used to form conclusions about a diverse population. In a more diverse patient group, interpatient biokinetic variability, organ mass variability, and anatomical differences are expected to be much larger, which might result in larger uncertainties. The results of this work should be considered as reflecting the lower limit of uncertainty in the determination of the absorbed dose from ^{123}I-IPT applications. Nevertheless, the results of this work provide an understanding of the limitations of the MIRD method in terms of the uncertainty associated with absorbed dose calculations. It should also be noted that the uncertainty estimates for other compounds and different patient populations could be very different from the ones estimated here for ^{123}I-IPT.

CONCLUSION

This work established a general method for determining absorbed-dose uncertainties. The method was implemented on a study group for ^{123}I-IPT. It was found that the absorbed dose a patient would receive could be as much as twice as large as the estimated mean absorbed dose. This factor should be included in any risk/benefit evaluation. Physicians should be aware of these uncertainties when they use a radiolabeled pharmaceutical in therapy or diagnosis.

In this work, the sources of uncertainty were restricted to the uncertainty associated with the least squares parameter estimation procedure, interpatient biokinetic variabilities, and interpatient organ mass variabilities. It is clear that properties like mass, size and geometry of source and target organs are the major factors in the determination of the uncertainty in the associated absorbed fractions. Future studies might include the determination of correlation between absorbed fractions and such properties. This information could then be incorporated into uncertainty calculations, which would result in more accurate and complete absorbed dose uncertainty estimates.

REFERENCES

1. Loevinger R and Berman M. A Revised Schema for Calculating the Absorbed Dose from Biologically Distributed Radionuclides, MIRD Pamphlet No. 1, Revised, Society of Nuclear Medicine 1976.
2. Personal communication, Radiation Internal Dose Information Center, Oak Ridge, TN, 1995.
3. Berman M, Beltz WF, Grief PC, Chabay R and Boston RC. CONSAAM User's Guide. US Department of Health and Human Services, 1983.
4. Crystal Ball, Version 3.0, User manual, Decisioneering, 1993.
5. Snyder WA, Ford MR, Warner GG and Fisher HL. Estimates of Specific Absorbed Fractions for Photon Sources Uniformly Distributed in Various Organs of a Heterogeneous Phantom. MIRD Pamphlet No. 5. The Society of Nuclear Medicine, New York, 1969.

QUESTIONS

Muller: Comment. Although it is very important to calculate the uncertainties in dosimetric calculations, it is important to emphasize that these are still only estimated uncertainties. Only by actual measurements (difficult if not impossible) can the real uncertainty be determined.

NEURAL NETWORKS FOR PARAMETER IDENTIFICATION IN COMPARTMENTAL MODELS

Narayana NG and Miller LF
The University of Tennessee
Knoxville, Tennessee 37996-2300

ABSTRACT

In health physics and nuclear medicine, numerous situations arise in which it is required to model the transport of radionuclides in biological systems. As is the case with most areas of science and engineering, methods for evaluating model performance and for parameter identification are necessary. In this study, neutral networks are evaluated for identification of model parameters, initial conditions, and residual activities.

Information for training the neural networks, "synthetic data," was generated by models that simulate biokinetic processes. The networks were evaluated on synthetic data and on positron-emission tomography scan data. In addition, several neural network models were developed and trained using different mathematical features of the synthetic data. Then, the performance of these network models was evaluated by testing with patterns not used in training.

The results show that the network models predicted the model parameters with more than 95% accuracy. Myocardial blood flow (MBF) estimated by neural network models correlated well with MBF obtained by a conventional method (correlation (r) = 0.96, slope = 0.977). MBF obtained by neural network models also agreed well with MBF specified for compartment models (r = 0.99, slope = 1.005) not used in training sets. Good agreement of the MBF estimates from neural network models was also observed for data containing small amounts of noise (r = 0.97, slope 1.0092). Results from these studies demonstrate that neural network models are reliable tools for estimation of parameters in some compartmental models, and that their computational efficiency of suitably trained neural networks far exceeds that of conventional nonlinear minimization algorithms.

INTRODUCTION

Internal exposure and movement of radionuclides is monitored based on the measurement of radionuclides in specific organs, excreta and the whole body. Biokinetic models that describe the behavior of material in the body or in a specific organ are used to establish a relationship between the levels in the body or organs, and they are used to estimate intake and the resulting dose. In nuclear medicine, imaging techniques are used to determine the movement of activity in organs, to identify the kinetics of metabolic processes, and to verify transport properties in the myocardium, for example. This information permits one to calculate activity as a function of time and to determine tissue viability at a given location.

Several excellent methods that use linear and nonlinear algorithms are available for identification of parameters from data. However, the computational efficiency of these techniques is too low for

clinical applications when thousands of parameters must be identified to determine tissue viability. This situation occurs when time-dependent data are obtained for many spatial locations in organs.

In this study, neural network models are developed for predicting transfer rate constants, initial amounts of radioactive materials, and other important diagnostic indicators. Although computer algorithms for solving compartment models and parameter identification are well established, they are often less robust relative to noise and complexity than neural networks. Neural network models can be developed to identify important model parameters for which nonlinear minimization algorithms are computationally inefficient. Neural networks were utilized to estimate the translocation rates between compartments, to determine initial amounts of radioactive material present in a specified compartment, and to calculate regional myocardial blood flow in nuclear medicine applications. Information for training was generated by many executions (simulations) of models with parameters that were varied over feasible ranges relative to the nuclear medicine or health physics applications of interest. Results from simulations were used as input to the Neuralware Software package (1) to develop the neural network models. Several neural network models were developed and trained using different mathematical features of the data. These features included function evaluations at selected points, moments of the data sets, and integrals over fractions of the domain scaled to the total integral over the domain. The networks were also tested for perturbation and sensitivity by introducing noise into the system and observing changes in the desired outputs.

In nuclear medicine applications, effective half-life of radionuclides in the body may be few minutes; however, in some health physics applications, radioactivity may be in the body for many years. Thus, performance of neural networks for parameter identification was evaluated for two-, three- and four-compartment models. A computer program for solving general compartmental models was written to provide training and testing information.

NEURAL NETWORK TOPOLOGY

The history of neural networks began forty-eight years ago with the work of a neurobiologist, Warren Mcculloch (2), and a statistician, Walter Pitts. This effort was followed by Frank Rosenblatt, Hebb and others in the 1950's and 1960's (3,4). In 1957, Rosenblatt's perceptron generated a great amount of research interest in neural computing. However, research in neurocomputing came almost to a halt in 1969 due to a book by Minsky and Papert (5) that proved perceptrons cannot classify inputs that are visually nonlocal. The funding agencies shifted their investment to other artificial intelligence areas, which started to a achieve significant successes. Other researchers continued their work in neural computing despite Minsky and Papert's book. With the development of new theories and algorithms and with the availability of faster and parallel hardware, interest in neural computing was rekindled. In 1982, John Hopfield's first paper presentation since the 1960's prompted researchers to become interested again in the field of neural computing. Also, there was a realization that the solution of certain problems requires a significant amount of computational power, and the recognition that traditional sequential computing, however fast, was inadequate for the solution of some problems.

Artificial neural networks (ANNs) are computational systems formed by a number of nonlinear information processing elements (PE) that are highly interconnected and operate in parallel. These processing elements are arranged in layers, and they are connected by weights to resemble the structure of neurons in the cerebral cortex portion of the brain. Neural networks are trained by exposing them to specified data sets of information, which enable self-organizing and learning capabilities to produce desired goals. Artificial neural networks generally encompass a wide variety of applications. Notable examples are pattern and speech recognition, data compression and signal

processing. In theory, ANNs are capable of exactly reproducing any continuous function and its first derivative. The functional representation of the processing units are not specified by this theoretical development, however.

The processing element, also referred to as a logistic function or transfer function, acts as an automatic scaling and gain control factor. The processing element used most commonly is the sigmoid function defined by

$$F(x) = \frac{1.}{1+e^{-\alpha x}} \quad (\alpha > 0),$$

where x is the input to the function, and α is the shaping parameter. In theory, the algorithm only requires that the function be bounded and everywhere differentiable. Values of F(x) range from zero for large negative values of x to one for large positive values of x. Other processing elements in common use are the hyperbolic tangent and the arc tangent where the values vary between -1 and 1 as x changes from a large negative value to a large positive value. In the fully connected model, every processing element in a layer is connected to all PEs in the next higher layer with no lateral connections. A processing element calculates the scalar product of each input vector and its corresponding connection weights, it then filters this product using the logistic function illustrated above.

One notable advantage of neural networks is the speed of computation. Another advantage is the robustness. Perhaps the most important characteristic of neural networks is their ability to model processes and systems from data. The neural network is supplied with data and then "trained" to reproduce the input-output relationships of the process or system. This is called the learning phase. During this phase, the connection weights associated with each processing elements (PE) are adjusted by a learning algorithm. The training time depends on the complexity of the application, the network model, the extent of the training data, and the training algorithm. The next phase is the recall phase, where performance of the network is examined and evaluated by presenting inputs of unseen patterns (not used in the training) to the network. Several trials on both the network structure and the amount of training time may be required to obtain a suitable network for a given application.

Backpropagation is a systematic method for training multiple layer artificial neural networks and is the method used for training neural networks in this study. The training method quantifies the contribution from individual units to the global error, and it adjusts weights between connected processing elements so that the difference between the actual output and the desired output is minimized in a least-squares sense. Backpropagation networks (BPN) operate either in autoassociative or heteroassociative modes, depending upon the objective of the network. For an autoassociative network, the input vector and the output vector are identical. A heteroassociative network learns associations between different input and output vector pairs. The basic BPN algorithm is presented by Rumelhart and McClelland (6), which has an input layer, an output layer and at least one hidden layer. The input layer acts as a buffer, or fanout, for the inputs to the system. It receives information (input vectors) and transmits the information to the hidden layers through weighted connections. The hidden layers are used by the network to develop its own internal representations of the input patterns which represent the nonlinear characteristics of the data. Backpropagation trains the hidden layers by propagating the adjusted error back through the network, layer by layer, adjusting the weight of each layer.

The input layer receives the input to the system and passes it to the first hidden layer. In the output layer, the overall error is calculated. The error is the difference between the ideal (desired)

output and the actual output generated by the network. This error is propagated back through the layers, and the weights are adjusted at each layer. This training process is repeated for each associated input/output pair until the error is reduced to a predefined level, or for a specific number of iterations, according to the criteria for termination. During training, the information flows forward from the input layer to the output layer, and the error is propagated backwards through the weights to calculate the weight adjustments. Training involves the modification of the weights until the error is minimized. The general topology of a neural network is as shown in Figure 1.

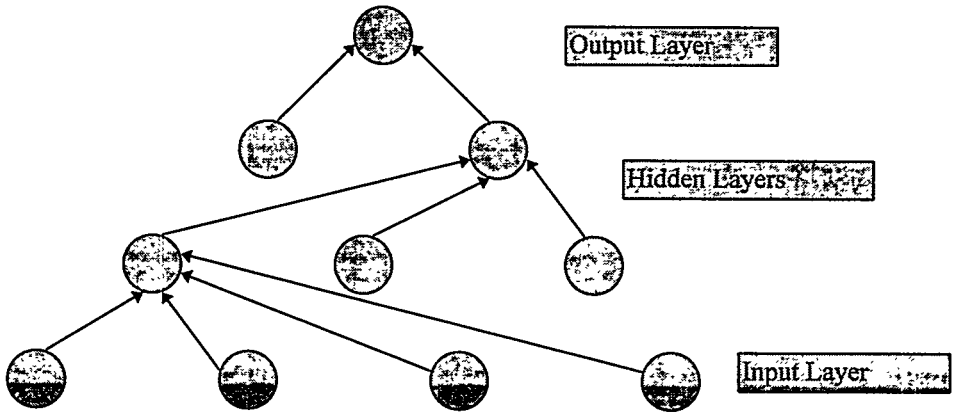

Figure 1. Topology of a Neural Network. Only connections to one node are illustrated. All nodes are usually connected to the next layer of nodes. Each circular region represents a processing element.

MODELS FOR SIMULATION AND PARAMETER IDENTIFICATION

Two models were used to generate training information for compartmental models. One solves a general set of linear first order differential equations using a matrix exponential with a "reduced" matrix formulation, and the other solves an analytical formulation of a two-compartment model for myocardial blood flow.

Solution of a Set of First Order Differential Equations

Most time dependent phenomena associated with physiological processes can be modeled by a general set of first order linear differential equations with constant coefficients, as illustrated below.

$$\dot{\underline{X}}(t) = \underline{A}\,\underline{X}(t) + \underline{B}\,\underline{U}(t)$$
$$\underline{Y}(t) = \underline{C}\,\underline{X}(t) + \underline{D} \quad ,$$

where: X(t) = the state vector of independent variables,
A = the system matrix,
B = input matrix,
U = input vector,
C = output matrix, and
D = a disturbance matrix.

The general solution to a these equations is as follows:

$$\underline{x(t)} = \underline{\underline{e}}^{\underline{\underline{At}}} \underline{x_0} + \int_0^t \underline{\underline{e}}^{\underline{\underline{A(t-\tau)}}} \underline{\underline{B}}\, \underline{u(\tau)} d\tau,$$

where

exp(At) = a matrix exponential and
X_0 = initial values of the independent variables.

The key numerical component for efficient solution is to evaluate the matrix exponential. Direct series expansion of the exponential often requires excessive computer time due to the slowness of convergence, which is the case when terms of the A matrix are large. Elements of the matrix exponential can be scaled, or "reduced," by powers of 2n for evaluation of the exp(At), and the unscaled result can be obtained from the following identity

$$\underline{\underline{e}}^{\underline{\underline{A}}} = \left[\underline{\underline{e}}^{\underline{\underline{A}}/2^n} \right]^{2^n}.$$

The reduced matrix exponential is evaluated from the series expression

$$\underline{\underline{e}}^{\underline{\underline{A}}} = \sum_{k=0}^{\infty} \frac{\underline{\underline{A}}^k}{k!}.$$

A computer program which solves the reduced matrix formulation was written to generate training data for two-, three-, and four-compartment models.

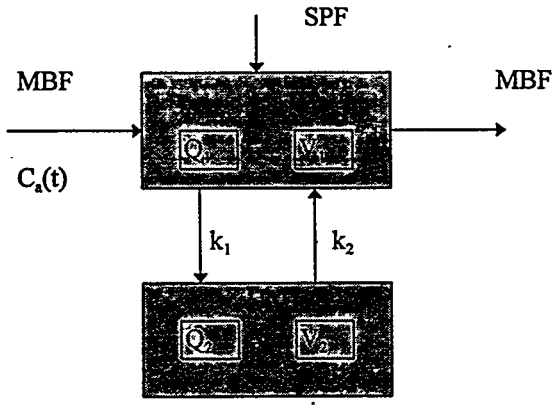

Figure 2. A two-compartment model representing the tracer dynamics in the myocardium. MBF = myocardial blood flow, SPF = spillover factor, Ca(t) = arterial blood flow, Q_1 and Q_2 =compartment activities, and V_1 and V_2 = compartment volumes.

A Two-compartment Model for the Heart

A two-compartment model, shown in Figure 2, is used to describe the tracer dynamics in the heart tissue. The model consists of vascular space $Q_1(t)$ (counts/pixel/min) representing ^{13}N-ammonia activity in the freely diffusible compartment and $Q_2(t)$ (counts/pixel/min) representing the trapped ^{13}N-ammonia activity within the heart tissue. The activities in each compartment as a function of time are $Q_1(t)$ and $Q_2(t)$. The transfer rate constants between the two compartments are k_1(ml/min/g) and k_2(ml/min/g). The terms V_1 (ml/g) and V_2 (ml/g) represent the distribution volume of free ^{13}N-ammonia in each compartment respectively. The arterial input function is represented by $C_a(t)$, and SPF is the spillover fraction of activity from blood to myocardium. The rate of radioactivity change in the freely diffusible compartment and in the trapped compartment can be approximated by first order differential equations as follows (7,8):

$$\frac{dQ_1(t)}{dt} = -\frac{k_1 + F}{V_1} Q_1(t) + \frac{k_2}{V_2} Q_2(t) + F\, C_a(t) \text{ and}$$

$$\frac{dQ_2(t)}{dt} = \frac{Q_1(t)}{V_1} k_1 - \frac{Q_2(t)}{V_2} k_2,$$

where F is the myocardial blood flow (MBF) in ml/min/g. Myocardial blood flow (MBF) can be determined by solving the differential equations in the two-compartment model and by fitting to the myocardial tissue time-activity curves. The total activity Q(t) is measured and is the sum of the activity of freely diffusible ^{13}N-ammonia $Q_1(t)$, ^{13}N-metabolites in the trapped pool $Q_2(t)$ and the product of spillover factor (SPF) times the arterial blood radioactivity AB(t). In particular,

$$Q(t) = Q_1(t) + Q_2(t) + (SPF) A_b(t).$$

In practice, Q(t) is obtained from a positron-emission tomography (PET) scanner, and the relationship between k_1 and F can be assumed to be

$$k_1 = F\left[1.65\, e^{1.25/F} - 1\right].$$

This relationship can be derived by equating the extraction fraction (E_m) defined by the two-compartment model

$$E_m = \frac{k_1}{k_1 + F},$$

with the following correlation for blood flow

$$E_m = 1 - 0.607\, e^{-1.25/F}.$$

The arterial input function, $C_a(t)$, is experimentally determined to be well approximated by a gamma variate function, $C_a(t) = at e^{-\beta t}$ in which 'a' varies from 0.1 to 0.6, β is 0.1(7), and k_2 may be neglected. The analytical solution to this modified two-compartment model is as follows:

$$Q_1(t) = \frac{Fa}{(k-\beta)} te^{-\beta t} - \frac{Fa}{(k-\beta)^2} e^{-\beta t} + C_1 e^{-kt},$$

where

$$k = \frac{k_1 + F}{V_1}$$

and

$$C_1 = \frac{Fa}{(k-\beta)^2}.$$

The constant C_1 is obtained by using the initial condition $Q_1(0) = 0$. Substituting C_1, as defined above into the expression above, one obtains

$$Q_1(t) = \frac{Fa}{(k-\beta)}[te^{-\beta t} - \frac{1}{(k-\beta)} e^{-\beta t} + \frac{1}{(k-\beta)} e^{-kt}].$$

Integration of the differential equation for Q_2, and assuming $Q_2(0) = 0$, yields the following:

$$Q_2(t) = \frac{FaC}{(k-\beta)}[-\frac{1}{\beta}(te^{-\beta t} + \frac{1}{\beta} e^{-\beta t}) + \frac{1}{(k-\beta)\beta} e^{-\beta t} - \frac{1}{(k-\beta)k} e^{-kt} - (-\frac{1}{\beta^2} + \frac{1}{(k-\beta)\beta} - \frac{1}{(k-\beta)k})],$$

where $C = k_1/V_1$. Synthetic data representing the activity of a PET scan region of interest is generated by

$$Q(t) = Q_1(t) + Q_2(t) + (SPF)\, C_a(t).$$

Estimation of Regional Myocardial Blood Flow Using Patlak Graphical Analysis

The Patlak graphical analysis method is used to estimate myocardial blood flow since it is computationally straightforward and requires only linear regression. Integrating equations for Q_1 and Q_2, and assuming k_2 to be negligible, results in

$$Q_1(t) = -\frac{k_1 + F}{V_1} \int_0^t Q_1(\tau) d\tau + F \int_0^t C_a(\tau) d\tau$$

and

$$Q_2(t) = \frac{k_1}{V_1} \int_0^t Q_1(\tau) d\tau.$$

By substituting these expressions for $Q_1(t)$ and $Q_2(t)$ into the equation for $Q(t)$, by expressing the time integral of $Q_1(t)$ in terms of $C_a(t)$, and by using the asymptotic form

$$Q_1(t) = \frac{FV_1C_a(t)}{k_1+F},$$

one obtains the following "Patlak" equation:

$$\frac{Q(t)}{C_a(T)} = K\frac{\int_0^t C_a(\tau)d\tau}{C_a(t)} + \frac{F^2}{F+K_1^2} + SPF\frac{A_b(t)}{C_a(t)}.$$

Note that K is the slope of the straight portion of the Patlak plot, which is defined by

$$K = F\frac{k_1}{F+k_1}.$$

Thus,

$$K = F\,E_m \text{ and}$$

$$K = F\left[1 - 0.607\,e^{1.25/F}\right].$$

Myocardial blood flow (MBF) can be estimated by assuming that $k_2 = 0$ and by determining the slope, K, of the straight portion of a plot which consists of $Q(t)/C_a(t)$ as the vertical (y) axis, and

$$\int_0^t C_a(\tau)d\tau / C_a(t)$$

as the horizontal axis. This plot is referred to as a Patlak plot.

RESULTS AND DISCUSSION

Network for Myocardial Blood Flow

The network for identifying the regional myocardial blood flow consisted of 12 nodes in the input layer, 10 nodes in the first hidden layer and 6 nodes in the second hidden layer. The output layer has only one node. Approximately 150 patterns of synthetic data were used for training the network, which were obtained from the analytical solution of the two-compartment model for myocardial blood flow. The training process continued until the RMS error between the desired and predicted output was reduced to 0.03. The network was then tested with 20 patterns of data different from the ones used in training where the MBF was known. The network predicted 18 patterns with an accuracy of 97% and the other 2 with 92%. The results, shown in Figure 3, show a good correlation between predicted and specified estimates. The network was also tested with 18 patterns of normalized data obtained from positron emission tomography (PET) scans, as shown in Figure 4. The values for MBF were obtained by Patlak analyses of PET data. The neural network predicted the regional MBF with about 96% accuracy.

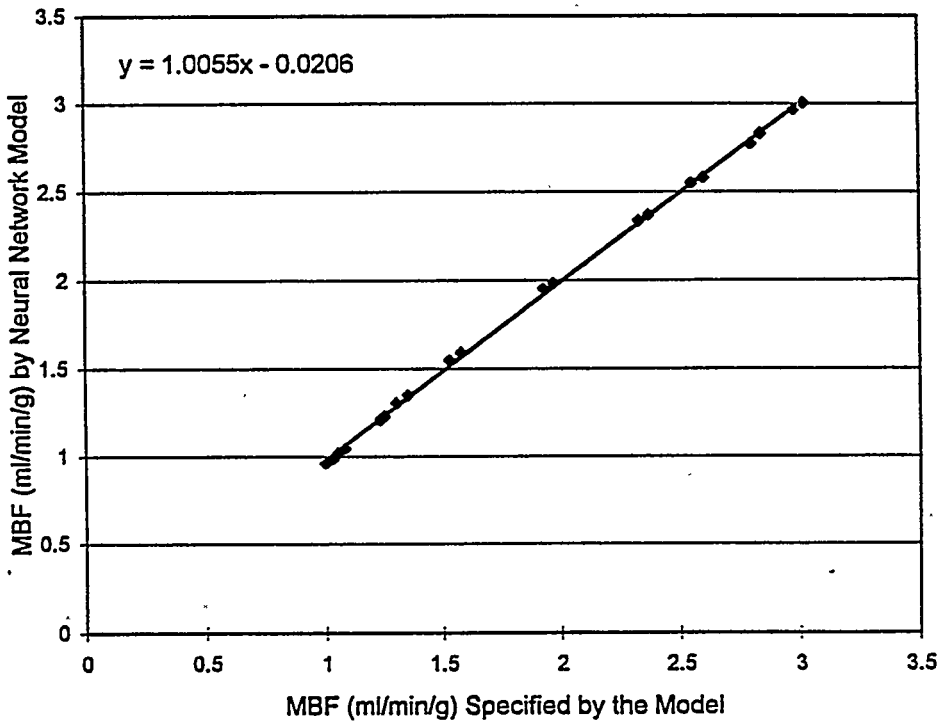

Figure 3. Correlation between neural network predictions of MBF and values specified in simulated data. Twelve input nodes that correspond to selected time points were used as inputs to the network.

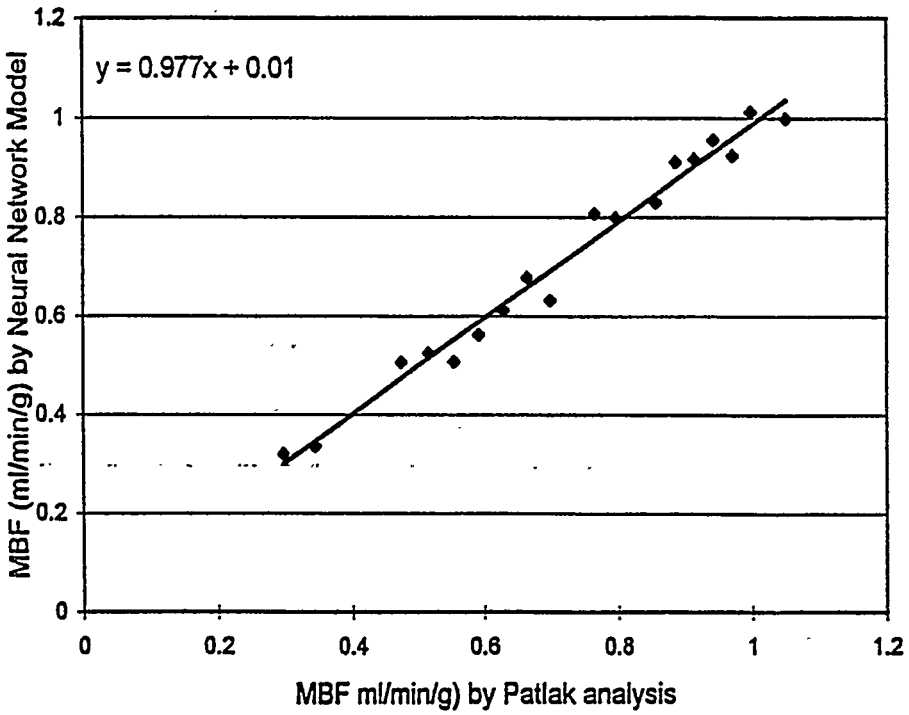

Figure 4. Correlation of neural network predictions of MBF with values obtained by a Patlak analysis of PET scans. Twelve input nodes that correspond to selected time points were used as inputs to the network.

Network Based on Noisy Data

The performance of the model was also evaluated with noise contaminated data since the data normally contains some level of measurement noise. This was accomplished by adding 2 , 4 and 6 % noise to the original testing patterns. The following relationship was used to add noise to the data:

$$X_n(t) = X(t)[1 + \alpha\, n(t)],$$

where: $X_n(t)$ = noisy data ,
$X(t)$ = simulated data,
$n(t)$ = noise data, and
α = noise fraction.

The noise was generated by using a random number generator with a Gaussion distribution whose mean and variance were 0.0 and 1.0, respectively. The correlation of predicted and observed MBF estimates was 0.97 for each case. Thus, one can conclude that the neural network models are not very sensitive to noise in the data.

Network Based on Moments of Data

Another network model was developed to identify the regional MBF by training the neural network with moments about the mean of the normalized data. The network consisted of 5 nodes in the input layer, 3 nodes in the hidden layer, and one in the output layer. The training data, consisting of moments, were presented to the network and trained until the RMS error was reduced to 0.05. The network was tested with 20 patterns of data not used for training. The predicted results differed from the specified values by ~12%, and the correlation coefficient, r, was 0.98. One advantage of this approach is that it can be used for arbitrary scan times and scan methods, since the input data are only functions of shape and are independent of time. The correlation between values predicted by the neural network and values specified for the generation of the synthetic data is illustrated by Figure 5.

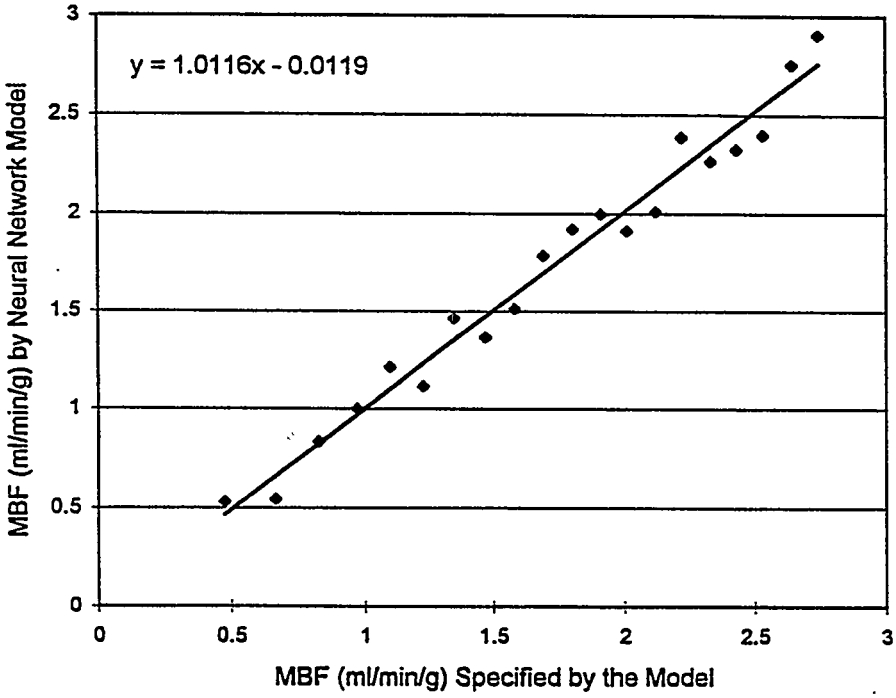

Figure 5. Correlation between neural network predictions of MBF and values specified in simulated data. Five input nodes corresponding to moments about the mean were used as inputs to the network.

Network Based on Numerical Integration of the Data

Another network was developed based on numerical integration of normalized training data over selected time intervals, which also eliminates time dependent factors associated with data acquisition. This network model consisted of 11 nodes in the input layer, 8 nodes in the first hidden layer, 6 nodes in the second hidden layer, and one output node. One hundred patterns of data were presented to the network for training and 25 unseen patterns were used for testing. The results show that the predicted regional MBF has an accuracy of 97% and that there is a good correlation, r = 0.98, between the neural network model estimates. These results are illustrated by Figure 6.

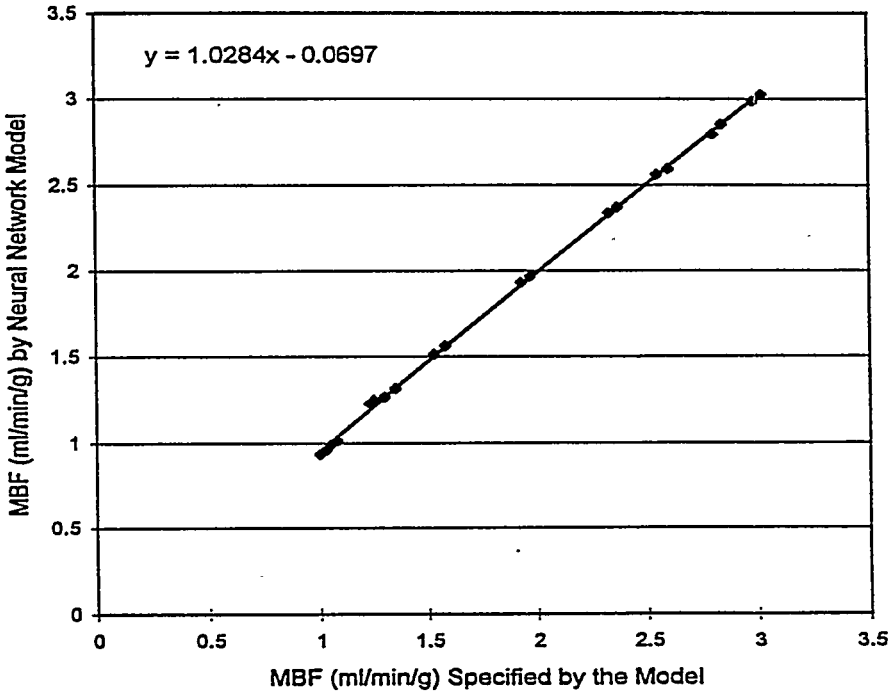

Figure 6. Correlation between neural network predictions of MBF and values specified in simulated data. Eleven input nodes that correspond to normalized integrals were used as inputs to the network

Three-compartment Models

Two three-compartment neural network models were studied, one for identifying the initial amount of material in each compartment and the other for identifying the output after time 't'. It is assumed that compartment activities can be measured and that model parameters can be identified.

Network for identifying initial amount of radioactive material present in the compartments

The network for identifying the initial amounts in each compartment consisted of 7 nodes in the input layer with one representing the time 't', three for translocation rates between compartments and three for specified amount of material after time 't'. The hidden layer consisted of 7 nodes. The output layer was composed of 3 nodes each representing the initial amount of material that was present in each of the three compartments. Approximately 70 patterns of data were presented to the network for training. The network was trained until the maximum error for each pattern was reduced to 0.02, and it was tested with 20 patterns of data different from the ones used in the training. The results indicated that the predicted initial amount of material in each compartment has an accuracy of more than 90%. Initial amounts of radioactive material estimated by neural network model correlate well with the values specified for the models used to generate the test cases.

Network for identifying specified amounts of radioactive material remaining in the compartments after time 't' The network for identifying the specified amounts in each compartment at time t included 7 nodes in input layer with one node representing the time t, three for translocation rates and three for initial amount of material. The hidden layer was composed of 7 nodes. The output layer consisted of 3 nodes each representing the final amount of material that will be present after time 't' in each of the compartments. Approximately the same number of patterns were presented to the network as in the previous case, until the maximum error reduced to 0.01. The network was examined with unseen patterns, to evaluate its performance. The predicted specified amount of material in each of the 3 compartments at time 't' had an error less than 10% with a correlation coefficient of $r = 0.86$.

Four-compartment Models

As was the case for the three-compartment models, two four-compartment neural network models were studied, one for identifying the initial amount of material in each compartment and the other for identifying the output after time 't'. It is again assumed that compartment activities can be measured and that model parameters can be identified.

Network for identifying initial amount of radioactive material present in the compartments The network for identifying the initial amounts in each compartment consisted of 11 nodes in the input layer with one node representing time 't', six for translocation rates between the compartments and four for specified amounts of material after time 't'. The hidden layer included 10 nodes. The output layer consisted of 4 nodes each representing the initial amount of material that was present in each of the 3 compartments. Approximately 85 patterns of data were presented to the network for training. The network was then tested with 25 patterns of data different from the ones used in training. The network predicted the initial amount of material in each compartment with more than 90% accuracy.

Network for identifying the specified amount of radioactive material left in the compartments after time 't' The network for identifying the specified amounts in each compartment consisted of 11 nodes in the input layer with one node representing time 't', six for translocation rates and four for initial amount of material. The hidden layer consisted of 10 nodes. The output layer consisted of 4 nodes each representing the final amounts of material that will be present after time t in each of the compartments. About the same number of patterns were presented as in the previous case until the maximum error was reduced to 0.01. The network predicted the final amount of material in each of the compartments with an error less than 10%. The regression lines and correlation coefficients were $y = 0.4738 + 0.8299x$, $r = 0.86$.

CONCLUSION AND RECOMMENDATIONS

Backpropagation neural networks were evaluated for identification of parameters in Nuclear Medicine and Health Physics biokinetic models, for estimation of intakes, and for determination of residual activities in biokinetic model compartments. These assessments included a two-compartment model for myocardial blood flow (MBF), a three-compartment model, and a four-compartment model. Comparisons between MBF obtained from conventional methods and from neural networks generally agreed to within 5 percent. Agreement between MBF values predicted by neural networks and values specified by models were generally within 3 percent, and addition of noise to data did not significantly affect predictions of the networks. Predictions of initial values, or intakes, and residual

concentrations after various times for three- and four-compartment models were within 10 percent. Results demonstrated that neural networks are suitable tools for identifying parameters from data when the model structure is known. They are also capable of predicting initial values and residual activities associated with compartments of models.

Networks obtained from the backpropagation method of training are acceptable for applications cited in this study; however, more sophisticated approaches are available and would probably obtain networks with better performance than achieved in this study.

REFERENCES

1. Neuralware Inc. Neural Computing, Manuals for Neuralworks Professional II and Neuralworks Explorer Software, Vol.1, Pittsburgh, PA, 1990.
2. McCulloch WS, Pitts W. "A logical calculus of the ideas imminent in nervous activity", Bulletin of Mathematical Biophysics, 5:115-133, 1943.
3. Rosenblatt R. Principles of Neurodynamics, Spartan Books, New York, 1949.
4. Hebb DO. The Organization of Behavior, John Wiley & Sons, New York, 1949.
5. Minsky ML and Papert S. Perceptions, MIT Press, Cambridge, MA 1969.
6. Rumelhart DE and McClelland JL. Parallel Distributed Processing, MIT Press, Cambridge, MD, 1986.
7. Smith GT, Huang SC, Neinabar CA, Krivokapich J, Schwaiger M and Schelbert HR. Noninvasive quantification of regional myocardial blood flow with N-13 ammonia and dynamic PET J Nucl Med 29:950, 1988.
8. Miller LF, Smith GT, Wu Y and Uhrig RE. Evaluation of Neural Networks for Parameter Identification from Positron Emission Tomography Scans. Transactions of the American Nuclear Society, November 11-16, 1990.

SUMMARY AND HIGHLIGHTS OF THE 6TH INTERNATIONAL RADIOPHARMACEUTICAL DOSIMETRY SYMPOSIUM GATLINBURG, May 7-10, 1996

Richard E. Toohey
Director, Radiation Internal Dose Informaion Center

When I became director of the Radiation Internal Dose Information Center on Evelyn Watson's retirement two years ago, the position description I received did not include hosting these Radiopharmaceutical Dosimetry Symposia, much less summarizing one. It has been a daunting task, and I must begin by acknowledging the efforts of our staff who have contributed so much to organizing and conducting this meeting: Mrs. Audrey Stelson, Mrs. Fanny Smith, Mrs. Sue Holloway, Ms. Bendi Lowrey, Mr. Mike Stabin, Mr. Rick Sparks, and Mr. Jeff Evans. As an experienced manager, I delegated, which means they did all the work; however, it is now time for me to earn my keep.

The symposium was truly international: 39 papers were presented by authors from the United States, while 34 were presented by authors from other countries. Countries represented included Canada, France, Sweden, the United Kingdom, the Netherlands, Belgium, Germany, Australia, Hong Kong, Denmark and Norway. Several themes emerged throughout the meeting, spread across the scientific sessions, and I will summarize the meeting according to the themes I perceived.

The first theme is patient-specific dosimetry for radiopharmaceutical therapy applications. Dr. Sgouros introduced us to treatment planning; we then heard from Drs. Tagesson, Dunn, Akabani, Parsai, Brihaye, and Muller how to use SPECT imaging and quantitative curve fitting to obtain patient-specific biokinetics, and Dr. Miller described the use of neural networks for rapid modeling. Thus we can obtain residence times, but we also need the other terms in the dose equation, patient-specific S factors. These are normally obtained from three-dimensional voxel phantoms based on MRI scans of the patient; Dr. Zubal described his head phantom, and Dr. Tagesson showed his brain model. However, we still have a problem with automatically identifying organ boundaries; neural network technology may be of assistance here.

Patient-specific dosimetry requires extensive data processing resources, which leads me to the second theme of the meeting: desktop computing power. We heard about seven different programs: MIRDOSE, MABDOS, MARCEL, SIMDOS, 3DID, SAAM II, and PLEIADES, all addressing various aspects of dosimetry and risk assessment. No doubt in a few years, increases in processing speed, memory, and and image manipulation technology will enable desktop computers to serve as adequate platforms for patient-specific dosimetry based on Monte Carlo generation of S factors in individualized voxel phantoms. Dr. Shen then reminded us of the errors we need to consider enroute to patient-specific dosimetry.

The third theme I call "diversity in dosimetry." We no longer compute doses exclusively for a few reference adult phantoms. The ICRP has now published age-specific dose coefficients for public exposure to effluents from nuclear facilities; and the pediatric phantoms for the MIRD schema are in routine use, with an interesting interpretation by Dr. Smith of data on pediatric dosimetry for Tc-99m

DMSA. Embryo/fetal dosimetry has also come of age, so to speak, as presented by Stabin and Sparks. Dr. Grafstrom presented a dosimetry model for extravasation, and our French colleagues discussed biological dosimetry, including lymphocyte damage by labeling of white blood cells with Tc-99m, and morphological damage to the lung from Tc-99m labeled microspheres. Another "diverse" paper was Dr. Roeske's presentation on ovarian doses to radium dial painters, the exposure group which led to the development of standards and regulations for internal dose.

This diversity extends to the fourth theme, which I call "small-scale dosimetry and small-scale dosimeters." Dr. Flux told us about dosimetry for intralesional therapy, and we then moved to the cellular level, with Dr. Humm's presentation that showed the dose distribution is nonuniform, even at that level, while Dr. Gardin presented another cellular dosimetry model. Dr. Bolch presented another small-scale dose model for suborgan dosimetry using cubical S values. Finally, Drs. Allen and Strandh told us about developments in MOSFET pin diodes and TLDs that may someday enable us to actually measure internal dose.

The fifth theme, and to my mind the most significant of the meeting, was a shift from diagnostics to therapy. The magnitude of this shift can be seen by a brief comparison with the 5th Symposium in 1991. That symposium comprised 48 papers, which by my count included 10 in general dosimetry, with 19 each on diagnostics and therapy. In contrast, this 6th symposium comprised 71 papers, of which only 11 pertained to diagnostics, with 30 each on general dosimetry and therapeutics. A new topic in this symposium was α-emitter therapy, as presented by Drs. Fisher and Roeske. Another change is that in 1991, all the papers on therpeutics were about radiolabeled monoclonal antibodies; this symposium included that topic, but also discussed therapy applications of antibody fragments, Sn-117m DTPA, P-32 infusion, Y-90 and Tl-201, as well as papers on neutron capture therapy, using both boron and gadolinium.

The final theme is one that has long been the norm in occupational radiation protection, and now seems to be emergining in nuclear medicine, and that is optimization. We have new models for the GI tract, the blood, the spine and cerebrospinal fluid, bone and marrow, and the salivary glands. We have learned Bayesian methods for biokinetic modeling, sampling methods for uncertainty analysis, error analysis even in physical parameters, and scaling of animal data to humans. All these methods are intended to give us more realistic dosimetry models, with the hope of actually relating computed doses to clinical effects, and thereby optimizing benefit versus risk to the patient.

I must apologize to those participants whose contributions I have not cited explicitly; by no means do I wish to denigrate the value of your work--I am merely constrained by space and time limitations.

Perhaps one way to measure the progress of our field since the last symposium is to review Dr. Mattsson's concluding look to the future from that meeting; as it turns out, Soren was remarkably prescient. Some goals he set included: measurement standardization, and we are getting there for SPECT and PET; better biokinetic data, and we can now do patient-specific modeling; dose reduction to normal tissues, and we now have more high-specificity agents; age- and gender-specific models, which are now in routine use; fetal dosimetry, which is also in place, although more and better data on cross-placental transport are needed; SPECT quantitation, which is in place; investigations of heterogeneity of tumor uptake, which is under investigation through both imaging and modeling; and improved marrow dosimetry, where there has been progress, but there is also still a ways to go.

I will now expose myself to the same risk that Dr. Mattsson undertook by predicting the future. My personal feelings are that we will see some decrease in diagnostic uses of radiopharmaceuticals, in favor of other imaging modalities such as MRI, but therapeutic applications will increase dramatically, and in fact become the focus of our work. Alpha emitters will see more applications in therapy. There will be more regulatory concerns, especially in research. There will be more application of

methodologies developed for occupational radiation protection to nuclear medicine, including the concept of optimization espoused by the ICRP. Cost effectiveness will drive technology, which will also affect optimization. Finally, patient-specific dosimetry will become the norm for therapy, using both individual biokinetic models and voxel phantoms; this will be controlled solely by the pace of development of desktop computers. I look forward to an evaluation of my clairvoyance at the next symposium.

Let me conclude by thanking our sponsors for their support; this symposium would have been nowhere near as productive and enjoyable without them. Specifically, we express our gratitude to Oak Ridge Associated Universities, the U.S. Department of Energy, the U.S. Food and Drug Administration, Bracco Research USA, DuPont Pharma, Mallinkrodt Medical, Radiation Dosimetry Systems of Oak Ridge, Syncor International, and TriMed Specialties. Finally, I wish all of you a safe and pleasant journey home, and perhaps we will meet again in the first year of the third millenium of the common era.

PARTICIPANT LIST

SIXTH INTERNATIONAL RADIOPHARMACEUTICAL DOSIMETRY SYMPOSIUM HELD IN GATLINBURG, TENNESSEE MAY 7-10, 1996

Akabani, Gamal
Department of Radiology
Division of Nuclear Medicine
Duke Medical Center
Box 3949
Durham, NC 27710

Allen, Barry J.
University of Wollongong
Department of Physics
Wollongong, NSW, 2522 Australia

Alvarez, Mauricio
Swedish Radiation Protection Institute
S-17116 Stockholm, Sweden

Amer, Mamun
The University of Tennessee
Department of Nuclear Engineering
207 Pasqua Engineering Building
Knoxville, TN 37996-2300

Andersson, Peter
Sahlgrenska University Hospital
Department of Radiation Physics
Göteborg, Sweden

Atcher, Robert
Chemical Science and Technology Div.
CST-18, MS J514
Los Alamos National Laboratory
Los Alamos, NM 87545

Aydogan, Bulent
University of Florida
Department of Nuclear Engineering
202 Nuclear Science Center
Gainesville, FL 32611-8300

Bardies, Manuel
INSERM U.211
9 Quai Moncousu
44035 Nantes, France

Beaumier, Paul
NeoRx Corporation
410 West Harrison St.
Seattle, WA 98119

Behr, Thomas M.
University of Göttingen
Department of Nuclear Medicine
Robert-Koch-Str. 40
D - 37075 Göttingen
Germany

Bolch, Wesley E.
University of Florida
Department of Nuclear Engineering
202 Nuclear Science Center
Gainesville, FL 32611-8300

Bouchet, Lional
700 S.W. 66th Blvd.
Gainesville, FL 32607

Breitz, Hazel
NeoRx-Virginia Mason
Clinical Research Unit
1407 E. Boston
Seattle, WA 93112

Brihaye, Claude
Universite De Liège
Centre De Recherches Du Cyclotron
Bat B30 - SART TILMAN
B-4000 Liège 1, Belgium

Brill, A. Bertrand
Department of Radiology
Vanderbilt University School of Medicine
MCN-R 1302
Nashville, TN 37232-2675

Clairand, Isabelle
Institue Gustave-Roussy
Physics Department-39
rue C. Desmoulins
Villejuif Cedex 94805, France

Cloutier, Roger
168 Cumberland View Drive
Oak Ridge, TN 37830

Combs, Matthew J.
Tri-Med Specialties, Inc.
1500 Avon Street Ext'd
Charlottesville, VA 22902

Crane, Paul
DuPont Merck Radiopharmaceuticals
331 Treble Cove Rd.
North Billerica, MA 01862

Cutler, P. Duffy
Mallinckrodt Radiology
510 S. Kingshighway Blvd.
St. Louis, MO 63110

Davidson, Claudette
Bureau of Biologics & Radiopharmaceuticals
Health Canada
Radiopharmaceuticals Division
Drugs Directorate
Postal Locator: 0603C4, Building #6
Tunney's Pasture
Ottawa ON K1A OL2, Canada

de Labriolle-Vaylet, Claire
Service de Medecine Nucleaire
Hopital Saint Antoine
184 rue du Faubourg Saint Antoine
75012 Paris, France

Dunn, Robert M.
Garden State Cancer Center
520 Belleville Avenue
Belleville, NJ 07109

Dunn, William L.
Mayo Clinic
Department of Nuclear Medicine
Charlton Building, Room 2N-325
200 First Street Southwest
Rochester, Minnesota 55905

Eckerman, Keith
Oak Ridge National Laboratory
Dosimetry Research Group
1060 Commerce Park, MS 64803
Oak Ridge, TN 37831

Fisher, Darrell R.
Pacific Northwest National Laboratory
P.O. Box 999, P57-52
Richland, WA 99352

Flux, Glenn
The Institute of Cancer Research
Joint Department of Physics
The Royal Marsden NHS Trust
Downs Road, Sutton, Surrey
SM2 5PT, U.K.

Forssell-Aronsson, Eva
Sahlgrenska University Hospital
Department of Radiation Physics
S-413 45 Göteborg, Sweden

Foster, David M.
The SAAM Institute, FL-20
Box 352255
Center for Bioengineering
University of Washington
Seattle, WA 98195

Gardin, Isabelle
Service de Médecine Nucléaire
Hopital Beaujon
100, Bd du Général-Leclerc
92110 Clichy, France

Grafstrom, Gustav
Lund University
Lund University Hospital
S-221 85 Lund, Sweden

Green, Alan J.
Royal Free Hospital School of Medicine
Department of Clinical Oncology
Rowland Hill Street
London NW3 2PF, U.K.

Groer, Peter
The University of Tennessee
Department of Nuclear Engineering
315 Pasqua Engineering Building
Knoxville, TN 37996-2300

Guo, Shuntong
Purdue University
126-11 Marshall Drive
West Lafayette, IN 47906

Hansen, Soren Baarsgaard
Aarhus University Hospital
PET Center
Norrebrogade 44
Aarhus C., 8000 Denmark

Harper, Paul V.
University of Chicago Hospitals
5841 South Maryland MC/2026
Chicago, IL 60637

Herzberg, Benno
Hospital of Free University Berlin
Nuclear Medicine
Hindenburgdamm 30
D-12200 Berlin, Germany

Hetherington, Eric L.R.
Australian Nuclear Science and
Technology Organization (ANSTO)
Private Mail Bag
Menai, NSW, Australia 2234

Hindorf, Cecilia
Lund University Hospital
Division of Radiation Physics
S-221 85 Lund, Sweden

Holloway, Sue
Oak Ridge Institute for Science
and Education
REAC/TS
P.O. Box 117
Oak Ridge, TN 37831-0117

Howe, Donna-Beth
Nuclear Regulatory Commission
Mail Stop TWFN 8-F-5, OWFN
Washington, DC 20555

Howe, Duncan
University of South Carolina
School of Medicine
Department of Radiology
Columbia, SC 29208

Humm, J.L.
Memorial Sloan-Kettering Cancer Center
Department of Medical Physics
1275 York Avenue
New York, NY 10021

Johansson, Lennart
Umeå University Hospital
Radiation Physics Department
90185 Umeå, Sweden

Johnson, Cherry
Cancer Research Campaign Labs
Royal Free Hospital School of Medicine
Rowland Hill Street
London NW3 2PF, U.K.

Johnson, Timothy K.
University of Colorado Health Sciences Center
Department of Radiology
Campus Box C278
4200 East Ninth Avenue
Denver, Colorado 80262-0278

Johnson, Thomas E.
Purdue University
29 Tower Drive #5
West Lafayette, IN 47906

Jones, Troyce
Oak Ridge National Laboratory
Health & Science Research Division
Building 4500-S, M.S. 6101
P.O. Box 2008
Oak Ridge, TN 37831-6101

Jönsson, Helene
Malmö University Hospital
Department of Radiation Physics
S-205 02 Malmö, Sweden

Kagan, Mikhail
DuPont Merck Radiopharmaceuticals
331 Treble Cove Road
North Billerica, MA 01862

Kassing, William M.
Univ. of Cincinnati
727 M.L. King Drive #716
Cincinnati, OH 45220

Kennel, Stephen J.
Lockheed Martin Energy Systems (Y-12)
Biology Division, Bldg. 9220 MS 8077
P.O. Box 2009
Oak Ridge, TN 37830

Kiser, William
Purdue University
208D Waterford Ct.
Lafayette, IN 47905

Konijnenberg, Mark W.
Mallinckrodt Medical BV
Westerduinweg 3
1755 LE PETTEN
The Netherlands

Kopp, Jürgen
Stabsstelle Medizinische Physik und
Strahlenschutz
Krankenhauszweckverband
Stenglinstr. 2
D-86156 Augsburg, Germany

Kwok, Cheuk S.
Department of Optometry
and Radiography
The Hong Kong Polytechnic University
Hung Hom, Kowloon
Hong Kong

Lassmann, Michael
University of Wuerzburg
Josef-Schneider - Str. 2
97080 Wuerzburg, Germany

Lathrop, Katherine
The University of Chicago
Department of Radiology
5841 South Maryland Avenue
MC 2026
Chicago, IL 60637

Lazewatsky, Joel
DuPont Merck Radiopharmaceuticals
331 Treble Cove Road
North Billerica, MA 01862

Leide-Svegborn, Sigrid
Malmö University Hospital
Department of Radiation Physics
S-205 02 Malmö, Sweden

Lovins, Ken (Duke)
Radiation Physics
Suite Q-1
400 Oak Street
Cincinnati, OH 45219

Lowery, Bendi
Oak Ridge Institute
for Science and Education
Radiation Internal Dose
Information Center
P.O. Box 117
Oak Ridge, TN 37831-0117

Ma, Kwok-Man
Tuen Mun Hospital
Department of Nuclear Medicine
Ching Chung Koon Road
Tuen Mun, N.T., Hong Kong

Mardirossian, George
University of Massachusetts Medical Center
Department of Nuclear Medicine
55 Lake Avenue North
Worchester, MA. 01655

Mattsson, Sören
Malmö General Hospital
& Lund University
S-205 02 Malmö, Sweden

McCullough, Steven
The University of Texas
M.D. Anderson Cancer Center
1515 Holcombe Blvd.
Houston, TX 77030

McQuarrie, Steve M.
University of Alberta
Faculty of Pharmacy
Edmonton, Alberta, T6G2N8 Canada

Melograna, John
Food and Drug Administration
5600 Fishers Lane, HFD-160
Rockwell, MD 20857

Meredith, Ruby
Univ. of Alabama Hospital, Birmingham
Dept. of Radiation Oncology and Radiation Therapy
619 South 19th Street
Birmingham, AL 35233-6832

Miller, Laurence F.
The University of Tennessee
Department of Nuclear Engineering
207 Pasqua Engineering Building
Knoxville, TN 37996-2300

Mills, George
FDA Center for Biologics
Department of Clinical Trials
Woodmont Building, 208C, II
1401 Rockville Pike
Rockville, MD 20852

Muller, Sara H.
NKI-AvL, Nuclear Medicine
Plesmanlaan 121
1066 CX Amsterdam
The Netherlands

Noska, Michael A.
National Institutes of Health
21 Wilson Drive, MSC-6780
Bethesda, MD 20892

Nosske, Dietmar
Federal Office for Radiation Protection - ISH
Ingolstädter Landstr. 1
D-85764 Oberschleissheim, Germany

Parsai, E. Ishmael
Medical College of Ohio
Department of Radiation Therapy
3000 Arlington Avenue
Toledo, OH 43699-0008

Phipps, Allen W.
National Radiological Protection Board
Chilton, Didcot, Oxon
OX11 ORQ England

Rao, Dandamudi V.
University of Medicine
and Dentistry of New Jersey
Department of Radiology
185 South Orange Ave.
Newark, NJ 07103

Roberson, Peter L.
The University of Michigan Medical School
UH-B2C490, Box 0010
1500 E. Medical Center Drive
Ann Arbor, Michigan 48109

Robinson, Marjorie
Université Paris VII
Faculté de Médecine Xavier Bichat Hospital
Laboratoire de Biophysique
BP 416
75870 Paris Cedex 18, France

Roedler-Vogelsang, Traute
Strahlenbiologisches Institut der Universität
Schillerstr. 42
D-80336 München, Germany

Roeske, John C.
University of Chicago Medical Center
5841 South Maryland Avenue, MC 0085
Chicago, IL 60637

Rösch, Frank
Johannes Gutenberg University
Fritz - Strassmann - Weg 2
D-55099 Mainz, Germany

S-Stelson, Audrey T.
Oak Ridge Institute
for Science & Education
Radiation Internal Dose
Information Center
Oak Ridge, TN 37831-0117

Saha, Gopal
Cleveland Clinic Foundation
Department of Nuclear Medicine
Cleveland, OH 44195

Schlyer, David J.
Brookhaven National Laboratory
Bldg 555A
Upton, NY 11973

Sgouros, George
Memorial Sloan-Kettering Cancer Center
Medical Physics
1275 York Avenue
New York, NY 10021

Shen, Sui
University of California at Davis
School of Medicine
1508 Alhambra Boulevard
Sacramento, CA 95816

Skretting, Arne
The Norwegian Radium Hospital
Ullernchausseen 70, Montebello
0310 Oslo, Norway

Smith, Terry
Great Ormond Street Hospital for Children
WCIN 3JH, Department of Radiology
Great Ormond Street
London WC1N 3JH, U.K.

Smith, Fanny B.
ORISE, Radiation Internal Dose Information Ctr
P.O. Box 117
Oak Ridge, TN 37831-0117

Sparks, Richard
ORISE, Radiation Internal Dose Information Ctr.
P.O. Box 117
Oak Ridge, TN 37831-0117

Srivastava, Suresh C.
Brookhaven National Laboratory
Medical Department, Bldg 801
Upton, NY 11973

Stabin, Michael G.
Departamento de Energia Nuclear/UPPE
Av. Prof. Luiz Freire, 1000-Cicade Univ
CEP 50740 - 540
Recife - PE, Brazil

Strandh, Margareta
Jubileumsinstitutionen
Radiation Physics Department
Lund University
S-221 85 Lund, Sweden

Stubbs, James
Proxima Therapeutics, Inc.
1111 Alderman Drive, Suite 280
Alpharetta, GA 30005-4143

Tagesson, Magnus
Lund University Hospital
Department of Radiation Physics
S-221 85 Lund, Sweden

Toohey, Richard E.
ORISE, Radiation Internal Dose Information Ctr.
P.O. Box 117
Oak Ridge, TN 37831-0117

Van Baalen, Mary
University of Texas Medical Branch
G-103 Microbiology Building
Galveston, TX 77555-0633

Verkh, Lèv
Alpha Therapeutic Corporation
5555 Valley Blvd.
Los Angeles, CA 90032

Wang, Wei-Hsung
Purdue University
School of Health Science
1338 Civil Engineering Building
West Lafayette, IN 47907

Wang, C-K Chris
Georgia Institute of Technology
3480 Evans Ridge Drive
Chamblee, GA 30341

Watson, Evelyn
104 New Bedford Lane
Oak Ridge, TN 37830

Wendt, Richard E. III
4812 Spruce Street
Bellaire, TX 77401

Wright, Andrew
Amersham International plc
Building 9, White Lion Road
Little Chalfont, Bucks
HP79LL England

Yu, Ming-Der
Purdue University
221-13 Arnold Drive
West Lafayette, IN 47906

Zasadny, Kenneth R.
University of Michigan
Division of Nuclear Medicine
3480 Kresge III
Ann Arbor MI 48109-0552

Zubal, George
Yale University
School of Medicine
333 Cedar Street
P.O. Box 208042
New Haven, Connecticut 06520-8042